WVMP SAR Reference 3-17

Significant of Tests and Properties of Concrete and Concrete-making Materials, ASTM Report STP 169D, J. F. Lamond and J. H. Pielert, ASTM International, West Conshohocken, Pennsylvania, 2006.

Page 564

The mixing technique should be compatible with the type of mixture, its ingredients, the job requirements, and the method of placement. Mixing should efficiently mix the cement and water and properly blend them with the other ingredients including the preformed foam. Paddle, high shear, continuous, and rotary drum mixers may all be acceptable for specific applications depending on the quality requirements of the final product.

Cellular concrete mixtures are typically job-site produced and placed. If ready-mix trucks are used for sanded mixtures (floor-fill applications), the grout is delivered to the job site and the preformed foam is added just prior to placement. This maintains the quality and freshness of the material. The rotary drum action of a ready-mix truck is acceptable for sanded mixtures with densities greater than 800 kg/m^3 (50 lb/ft^3).

For low-density applications (roof deck and engineered fill) with neat-cement slurries at densities less than 800 kg/m^3 (50 lb/ft^3), rotary drum mixing action is not ideal. Instead, paddle type or shear mixers are common methods for both batch and continuous mixing procedures. After the cement/water slurry is produced in these mixers, the preformed foam is added and blended prior to or during placement with a positive displacement pump. As the mixture is pumped, density is measured at the point of placement for quality control. Mix adjustments can then be made to account for pumping distances and other special application conditions.

Pumping is the most common method of placement, but other methods can be used. Positive displacement pumps such as Moyno or peristaltic pumps are used for low-density mixtures. Although piston pumps are efficient for grout mixtures at densities greater than 1440 kg/m^3 (90 lb/ft^3), they do not efficiently pump low-density mixtures.

Casting techniques are different for each type of cellular concrete application. The thinner floor-fill mixtures utilize a rolling screed to provide a constant thickness. Since roof deck applications are cast slope-to-drain, string lines provide guides for casting and darby finishing the material by experienced tradesmen. Screed rails may also be used. Finishing operations, in general, should be kept to a minimum; smoothing with a darby or bullfloat is usually sufficient [20].

Geotechnical fill applications have the greatest variation in casting techniques. Generally, these fills are several meters (feet) thick so that they are cast in lifts of up to 1.0 m (3.3 ft) thick based on the available area to be cast. The succeeding lifts are cast on a daily basis until the final fill profile is reached.

Physical Properties

Several studies investigated the physical and mechanical properties of cellular concrete cast at different densities and with or without aggregates in the mix [1,18–21]. Because the density of cellular concrete may be varied over a wide range, 320–1920 kg/m^3 (20–120 lb/ft^3), it is considered as an additional variable that significantly impacts the physical properties and the mix design of the material. The lower density cellular concrete has lower thermal conductivity (higher insulation), accompanied by lighter weight and reduced strength. As the density

Density

When referring to the density of cellular concrete, confusion may be avoided by stating the moisture condition of the material at that specific density. Significant moisture conditions include as-cast density (wet density or plastic concrete density), air-dry density (at a stated age and curing condition), and the oven-dry density.

The as-cast or wet density is usually determined at the point of placement in accordance with ASTM C 796. In determining the wet density, the concrete should be consolidated by tapping the sides of the container and not by rodding. The ratio of the wet density to oven-dry density for the different cellular concrete mixtures varies due to the different water content requirements. The wet density of the cellular concrete is an important job-site quality assurance tool to control uniformity of the mixtures.

The air-dry density of cellular concrete usually represents the condition of the in-place material. The change in density due to air drying is a function of temperature, duration of the drying period, humidity, the wet density of the concrete, the water-cement ratio, and the surface-area ratio of the element. Although the relationship between air-dry density and wet density seems complicated, the air-dry density of cellular concrete is usually about 80 kg/m^3 (5 lb/ft^3) less than its wet density. Cellular concrete cast, cured, and air dried under job conditions in low-humidity environments may have density losses approaching 160 kg/m^3 (10 lb/ft^3).

Oven-dry density is commonly used to relate the physical properties of various types of cellular concretes, and for the determination of the thermal conductivity by the guarded hot plate method in accordance with ASTM Standard Test Method for Steady-State Heat Flux Measurements and Thermal Transmission Properties by Means of the Guarded-Hot-Plate Apparatus (C 177). For the latter purpose, the oven-dry density may be calculated with sufficient accuracy from the mixture data by assuming that the water required for hydration of the cement is 20 % of the weight of the cement. The oven-dry density (D) is calculated as follows:

$$D = [1.2\ C + A]\ \text{kg/m}^3 \text{ or } [(1.2\ C + A)/27]\ \text{lb/ft}^3$$

where

C = weight of cement, kg/m^3 (lb/yd^3) of concrete; and
A = weight of aggregate, kg/m^3 (lb/yd^3) of concrete.

Workability

Cellular concrete in the low-density range (less than 800 kg/m^3 (50 lb/ft^3)) is a flowable material with excellent workability. As a result, it is handled as a liquid and poured or pumped into place without the need for consolidation. It should be pointed out that the slump test, which is used to measure the consistency in normal weight concrete, is meaningless in the case of cellular concrete since the material is placed in fluid consistency.

Thermal Conductivity

The thermal conductivity (k) of a material is the time rate of transfer of heat by conduction, through a unit thickness, across a unit area for a unit difference of temperature. The units of k

J. F. Lamond and J. H. Pielert, Significant of Tests and Properties of Concrete and Concrete-making Materials, ASTM Report STP 169D, ASTM International, West Conshohocken, Pennsylvania (2006), p. 564.

WVMP SAR Reference 3-18

ACI Manual of Concrete Inspection, 10th ed., American Concrete Institute Committee 311 Report SP-2(07), American Concrete Institute, 2008.

Page 126

16.3.2 *Foams for cellular concrete*—Both preformed and mixer-generated foams are used in cellular low-density concrete. Preformed foam is generated by introducing controlled quantities of air, water, and foaming agent under pressure into a foaming nozzle. The foam is blended with a cement or cement-aggregate slurry, either in batched volumes or by continuous batching. The foam should have sufficient stability to maintain its structure until the concrete hardens.

Mixer-generated foams are produced by high-speed, high-shear mixing of water, foaming agent, cement, and aggregate (if required) with simultaneous air entrapment. Air bubbles are large initially, but become smaller as mixing proceeds.

Trial mixtures should be used to determine the quantity of preformed foam or foaming agent required. Up to 80% of the volume of the final concrete mixture may be air, depending on the desired concrete density.

16.3.3 *Mixture proportioning and control*—For most applications, proportions should be chosen for insulating concrete to provide a specified dry density, because thermal properties are primarily a function of density. If the concrete is to be conveyed by pumping, all laboratory mixtures should be trial-pumped under field conditions before construction begins. Pumping can affect water requirements, wet and dry densities, and mixture uniformity. It may be necessary to start with additional amounts of air or foam to make up for losses in air caused by mixing, pumping, and placing of insulating concrete.

16.3.3.1 *Aggregate type*—Mixtures containing lightweight aggregate often are specified in terms of cubic feet (bulk volume) of aggregate per bag of cement. A 1:6 mixture, for example, would contain one bag of portland cement and 6 ft^3 (0.17 m^3) of aggregate. A better method is to specify the total loose bulk volume of lightweight aggregate per cubic yard of concrete along with the weight of cement and the slump and air content required for the mixture. Required cement contents generally range from 330 to 630 lb/yd^3 (195 to 375 kg/m^3).

Insulating concrete made with lightweight aggregates typically includes an air-entraining admixture to act as a wetting agent, lower the specific gravity of the paste, and increase relative specific gravity of the coarse-aggregate particles. This reduces the mixing water content and substantially reduces the tendency of the aggregate to float. The use of an air-entraining admixture is particularly important in fluid, nearly self-leveling mixtures that are to be pumped through small (2 to 4 in. [50 to 100 mm] diameter) hose lines. It is often necessary to adjust the amount of air entrainment to produce concrete with the required dry density.

Water requirements of insulating concretes made with lightweight aggregates vary greatly with the absorption of the aggregates and the desired fluidity of the mixture. Vermiculite aggregate is highly absorptive, and typically requires 600 to 700 lb (355 to 415 kg) of water per cubic yard (meter) of concrete for fluid mixtures. Most perlites are less absorptive, with water requirements of 300 to 500 lb/yd^3 (180 to 295 kg/m^3).

16.3.3.2 *Cellular (foam type)*—Cement contents for cellular concrete range from 470 to 940 lb/yd^3 (280 to 560 kg/m^3). No aggregate is used when the desired dry density is less than 30 lb/ft^3 (480 kg/m^3). When densities greater than 30 lb/ft^3 (480 kg/m^3) are desired, fine sand usually is added, and the cement contents then range from 470 to 550 lb/yd^3 (280 to 325 kg/m^3). The water contents of cellular insulating concretes without aggregate are generally 300 to 500 lb/yd^3 (180 to 295 kg/m^3); with sand in the mixture, water contents are 200 to 375 lb/yd^3 (120 to 220 kg/m^3).

16.3.4 *Testing*—Laboratory tests of trial mixtures of low-density concrete are generally limited to compressive strength and plastic (freshly mixed) and dry densities. Compressive-strength and dry-density specimens (molded 3 x 6 in. [75 x 100 mm] cylinders) should be tested in accordance with ASTM C495. Plastic densities should be determined in a manner similar to that for other concretes (ASTM C138/C138M), but the concrete should be consolidated by tapping the sides of the container rather than by rodding. To permit construction control based on plastic density, the plastic density should be correlated with the dry density.

Once satisfactory mixture proportions have been established, other laboratory tests may be required. Because these concretes are used for insulation, the thermal resistivity is measured with a guarded hot plate (ASTM C177) or a calibrated hot conductometer (ASTM C518). Specific heat and thermal diffusivity are sometimes needed for design purposes.

If measurements of tensile strength, modulus of elasticity, Poisson's ratio, and drying shrinkage are required, the same techniques should be used as those for structural concrete. The testing equipment, however, should have sufficient sensitivity for the low values generally encountered. Drying shrinkage of insulating concrete is greater than that of structural concrete (as much as 0.5%).

Penetration resistance is sometimes used to define the ability of low-density concrete to sustain normal construction foot traffic. For acceptable resistance to foot traffic, the Proctor penetrometer reading should indicate an average bearing value of 200 psi (1.4 MPa) or greater.

A measure of nailing characteristics of low-density concrete may also be required. For satisfactory nailing, the concrete should be able to receive a specified type of nail without shattering and withstand a withdrawal force of 40 lb (0.18 kN).

Field control tests are typically limited to compressive strength and plastic density. Because of variations in the weights of the aggregates, cement, and water, density measurements accurate within ±1% are generally acceptable. Unless otherwise specified, an ordinary galvanized 10 quart pail (approximately 1/3 ft^3 [9.5 L]) or similar calibrated container and a scale should be used to determine density. The pail should be calibrated before using, and the scale's accuracy checked at least once a week during use.

16.3.5 *Batching and mixing*—To ensure uniform density at the point of placement, all materials should be added to the mixer at a constant rate, in their correct proportions and in the correct sequence. The required amount of water goes into the mixer first, followed by the cement, air-entraining admixture or foaming agent, aggregate, preformed foam, and other additives. Materials should be mixed so that the design plastic density is obtained at the point of placement. Any

WVMP SAR Reference 3-19

Response of High Performance to Fire Conditions: Review of Thermal Property Data and Measurement Techniques, NIST Report GCR 99-767, D. R. Flynn, March 1999.

NIST GCR 99-767

RESPONSE OF HIGH PERFORMANCE CONCRETE TO FIRE CONDITIONS: REVIEW OF THERMAL PROPERTY DATA AND MEASUREMENT TECHNIQUES

Daniel R. Flynn

MetSys Corporation
Millwood, VA 22646-0317

United States Department of Commerce
Technology Administration
National Institute of Standards and Technology

NIST GCR 99-767

RESPONSE OF HIGH PERFORMANCE CONCRETE TO FIRE CONDITIONS: REVIEW OF THERMAL PROPERTY DATA AND MEASUREMENT TECHNIQUES

Prepared for

U.S. Department of Commerce
Building and Fire Research Laboratory
National Institute of Standards and Technology
Gaithersburg, MD 20899

By

Daniel R. Flynn

MetSys Corporation
Millwood, VA 22646-0317

Final Report

December 1998
Issued March 1999

[redacted]

[redacted]

Notice

This report was prepared for the Building and Fire Research Laboratory of the National Institute of Standards and Technology under Contract number 43-NANB-809607. The statement and conclusions contained in this report are those of the authors and do not necessarily reflect the views of the National Institute of Standards and Technology or the Building and Fire Research Laboratory.

[redacted]

[redacted]

[redacted]

MetSys Report No. 98-01-101

December 1998

[redacted]

Response of High Performance Concrete to Fire Conditions:

Review of Thermal Property

Data and Measurement Techniques

[redacted]

by

[redacted]

Daniel R. Flynn

[redacted]

MetSys Corporation

Millwood VA 22646-0317

[redacted]

This report is based upon work supported by the Department of Commerce/National Institute of Standards and Technology (NIST) under contract No. 43-NANB-809607. Any opinions, findings, and conclusions or recommendations expressed in this publication are those of the author and do not necessarily reflect the views of the Department of Commerce/NIST.

[redacted]

Abstract

The NIST Building and Fire Research Laboratory (BFRL) has undertaken a project concerning the effect of fire on high strength concrete. Heating concrete to sufficiently high temperatures results in water of hydration being driven off, with a resultant irreversible loss of concrete strength. In addition, it has been observed that rapid heating of high strength concrete can result in spalling of the concrete. Computer models for prediction of temperature and pore pressure distributions in heated concrete typically include consideration of (1) mass transfer of air and water by diffusion and by forced convection, conversion of liquid water to vapor, and release of water of hydration and (2) heat transfer by conduction, mass diffusion, and forced convection. In order to make valid predictions, the computer models require reliable data as to the physical properties of the concrete. Mass transport properties are being investigated by the Building Materials Division. Thermal transport properties, the subject of this report, are being investigated by the Building Environment Division. The present report addresses (1) identification of material properties critical to prediction of heat and mass transfer in high strength concrete at high temperatures, (2) variation of the thermal properties with temperature, pressure, and thermal history, (3) examination of correlations between concrete composition and thermal properties, (4) identification of appropriate experimental techniques for determination of the thermal properties of high strength concrete, (5) identification of available equipment and testing services for carrying out such measurements, and (6) preliminary design of special equipment that needs to be constructed for measurement of the thermal conductivity of concrete.

Acknowledgements

The Principal Investigator thanks the following organizations for permission to reproduce copyrighted figures and tables:

American Society for Testing and Materials

NRC Research Press (National Research Council – Canada)

Pearson Education Limited (Longman Group Limited)

Portland Cement Association

The Principal Investigator also thanks Robert R. Zarr, the NIST Contracting Officer's Technical Representative for the contract under which this report was prepared, for his guidance and his review of earlier drafts of the report and James R. Lawson, of NIST, for assisting with the preparation of this report.

Table of Contents

Page

Abstract iv

Nomenclature xii

1. Introduction 1

2. Modeling of Simultaneous Heat and Mass Transfer in Porous Media 3

    2.1 Overview of Heat and Mass Transfer in Concrete Exposed to Fire 4
    2.2 Irreversible Thermodynamics Approach for Diffusion of a Gas 8
    2.3 Heat Transfer and Diffusive Mass Transfer 11
    2.4 Ahmed Model 14

3. Existing Data on Thermal Properties of Concrete and Its Constituents 16

    3.1 Mass, Volume, and Density 16
    3.2 Enthalpy, Specific Heat, and Heats of Reaction 32
    3.3 Thermal Conductivity and Thermal Diffusivity 37

4. Correlations and Prediction of Thermal Properties 55

    4.1 Mass, Volume, and Density 56
    4.2 Enthalpy, Specific Heat, and Heats of Reaction 58
    4.3 Thermal Conductivity and Thermal Diffusivity 59

5. Experimental Techniques for Determination of Thermal Properties 71

    5.1 Mass, Volume, and Density 71
    5.2 Enthalpy, Specific Heat, and Heats of Reaction 72
    5.3 Thermal Conductivity and Thermal Diffusivity 72
        5.3.1 Steady-State Methods 74
        5.3.2 Transient Methods 77

6. Availability of Apparatus and Testing Services 86

7. Design of New Apparatus for High-Temperature Thermal Conductivity Measurements ... 90

8. References 99

Appendix A. Analysis Procedures for Transient Hot-Wire or Probe Techniques for Thermal Conductivity Measurement A-1

A.1 Ideal Line Heat Source A-1
A.2 Finite-Diameter Probe A-2
A.3 Numerical Results A-7
A.4 References A-12

Appendix B. Analysis Procedures for Transient Plane-Source Techniques for Thermal Conductivity Measurement B-1

List of Figures

Figure 1. Thermogravimetric and dilatometric curves for Cement Paste C 18

Figure 2. Typical relationships between weight loss, corresponding length change, and temperature for Portland cement paste 19

Figure 3. Weight loss of calcareous and siliceous aggregates and concretes caused by heating 20

Figure 4. Weight loss as a percentage of initial weight for various concretes caused by heating 20

Figure 5. Mass loss of various concrete types as a function of temperature 21

Figure 6. Mass loss of high strength concrete at elevated temperatures (heating rate of 2 K/min) 23

Figure 7. Mass loss of high strength concrete at elevated temperatures (heating rate of 20 K/min) 24

Figure 8. Mass loss of high strength concrete at elevated temperatures (heating rate of 50 K/min) 25

Figure 9. Change of weight with temperature of concrete containing silica fume 26

Figure 10. Length change of Portland cement paste specimens at various temperatures 26

Figure 11. Dilatometric curves for the ten rocks described in Table 3 27

Figure 12. Dilatometric curves for three normal-weight concretes and three lightweight concretes. Aggregates: LI, limestone; SI siliceous rock; AD, andesite; SG, expanded shale; CL, expanded clay; PU, pumice 28

Figure 13. Linear thermal expansion of concretes made with various conventional aggregates, as a function of temperature ((a) quartzite; (b) sandstone; (c) limestone; (d) basalt; (e) expanded slag 28

Figure 14. Thermal expansion, as a function of temperature, of the three concrete types described in Table 1 29

Figure 15. Correlation between the coefficient of thermal expansion of the aggregate and that of the concrete 29

Figure 16. True density (ρ_t), bulk density (ρ_{pt}), and porosity (P_{pt}) of Cement Paste C (calculated) 30

Figure 17. Effect of temperature on density of concrete made with limestone aggregate 30

Figure 18. Effect of temperature on mass density of concretes made with quartzite, bauxite, and expanded shell aggregates 31

Figure 19. Density versus temperature curves used in the Ahmed model 31

Figure 20. Computed specific heat of Model Pastes A, B, and C 33

Figure 21. Measured specific heat of Cement Pastes A, B, and C 33

Figure 22. Volumetric specific heats (computed) for four hypothetical concretes: normal-weight, Concretes 1 and 2; lightweight, Concretes 3 and 4 34

Figure 23. Effects of temperature on measured specific heats of various concretes: (1) granite aggregate concrete; (2) limestone aggregate concrete; (3) limestone aggregate concrete; (4) siliceous aggregate concrete; (5) limestone aggregate concrete; (6) siliceous aggregate concrete. 35

Figure 24. Specific heat, as a function of temperature, of the three concrete types described in Table 1 36

Figure 25. Specific heat versus temperature curves used in the Ahmed model 36

Figure 26. Thermal conductivities of Cement Pastes A, B, and C and thermal conductivity of a hypothetical pore-less cement paste 39

Figure 27 Thermal conductivity of 15 materials described in Table 4 40

Figure 28. Histogram of the thermal conductivity of limestones 42

Figure 29. Thermal conductivity of limestones 42

Figure 30. Plot of thermal conductivity against the moisture content of concrete 43

Figure 31. Variation range of thermal conductivity of concretes, plotted against the porosity 43

Figure 32. Thermal conductivity of granite-aggregate concrete as a function of temperature under heating and subsequent cooling 44

Figure 33. Thermal conductivity of limestone-aggregate concretes 44

Figure 34. Thermal conductivity of siliceous-aggregate concretes 45

Figure 35. Thermal conductivity of different structural concretes 45

Figure 36. Thermal conductivity of various concretes that were not oven-dried before test, as a function of temperature: (a) limestone aggregate concrete; (b) barytes aggregate concrete; (c) gravel aggregate concrete; (d) quartzite aggregate concrete; (e) quartzite aggregate concrete 46

Figure 37. Thermal conductivity, as a function of temperature, of the three concrete types described in Table 1 46

Figure 38. Thermal conductivity versus temperature for the five high-strength concretes described in Table 2 47

Figure 39. Thermal conductivity of oven-dried high-strength concrete mix No. 5, as determined by three different techniques 48

Figure 40. Thermal conductivity versus temperature curves used in the Ahmed model 49

Figure 41. Thermal diffusivity of limestones 49

Figure 42. Thermal diffusivity of normal and lightweight concrete, mortar, and cement stone 50

Figure 43. Thermal diffusivity of limestone concrete 50

Figure 44. Thermal diffusivity of siliceous concrete 51

Figure 45. Thermal diffusivity of different concretes 51

Figure 46. Effect of temperature on thermal diffusivity of concrete made with siliceous and calcareous aggregates and with lightweight aggregates 52

Figure 47. Thermal diffusivity versus temperature for the five high-strength concretes described in Table 2 53

Figure 48. Thermal diffusivity of oven-dried high-strength concrete mix No. 5, as determined by two different techniques 54

Figure 49. Two-phase material with phases distributed as parallel slabs 61

Figure 50. Effective thermal conductivity of a laminated material with heat flow parallel or perpendicular to laminations 62

Figure 51. Cross-section of the model in which a disperse second phase is considered to be a cubic array of cubes 63

Figure 52. Computed effective conductivity of a dispersion of 0.1 volume fraction of a material of conductivity λ_d in a continuous matrix of material of conductivity λ_c 66

Figure 53. The effect of porosity on thermal conductivity as computed by series-slabs expression, parallel-tubes expression, and Maxwell dilute expression 68

Figure 54. Effective thermal conductivity of a mixture as computed by Bruggeman mixture expression; Maxwell dilute dispersion expression, high-conductivity phase continuous; and Maxwell dilute dispersion expression, low-conductivity phase continuous 70

Figure 55. Pattern of copper and nickel strips used by Brydsten and Bäckström 79

Figure 56. Possible boundary conditions for transient plane source methods for determination of thermal conductivity or thermal diffusivity 80

Figure 57. Experimental arrangement suggested by Vernotte 81

Figure 58. Experimental arrangement used by Clarke and Kingston 81

Figure 59. Isometric view of experimental setup used by Harmathy 82

Figure 60. Specimen assembly used by Harmathy 83

Figure 61. Specimen geometry used by Dzhavadov 84

Figure 62. Experimental layout of the pulse method used by Kubičár and colleagues 84

Figure 63. Cross section of proposed apparatus for high-temperature thermal conductivity measurements 91

Figure 64. Cross section of the thin foil heater 92

Figure 65. Elevation view of the foil heater showing the support structure that also serves as current leads 93

Figure 66. The support frame from which the foil heaters, specimens, and cold plates are suspended 95

Figure 67. Elevation view of the apparatus if the loading force is provided by a weight inside the furnace 96

Figure 68. Elevation view of the apparatus if the loading force is provided by a weight below the furnace 97

Figure 69. Elevation view of the apparatus if the loading force is provided by a weight and pulley system above the furnace 98

Figure A1. The function $G(\beta, \alpha, \tau)$ versus τ, with α as a parameter, for $\beta = 0$ A-9

Figure A2. This figure is the same as Figure A1, but with a different vertical scale A-9

Figure A3. The function $G(\beta, \alpha, \tau)$ versus τ, with α as a parameter, for $\beta = 1$ A-10

Figure A4. The function $G(\beta, \alpha, \tau)$ versus τ, with α as a parameter, for $\beta = 2$ A-10

Figure A5. The function $G(\beta, \alpha, \tau)$ versus τ, with α as a parameter, for $\beta = 3$ A-11

Figure A6. The function $G(\beta, \alpha, \tau)$ versus τ, with α as a parameter, for $\beta = 4$ A-11

List of Tables

Table 1. Batch quantities and properties of concrete mix 21

Table 2. Composition of concrete mixtures 22

Table 3. Some characteristics of the ten rocks whose dilatometric curves are shown in Figure 11 27

Table 4. Some characteristics of the 15 materials whose thermal conductivities are plotted in Figure 27 41

Nomenclature

The nomenclature list below is limited to those symbols that are used in the main body of this report. The symbols used in Sections 2.1, 2.2, and 2.3 are not included, since the symbols used there, and defined there, are those of the various investigators whose work is being cited and they are not used elsewhere in this report. The symbols used for the various equations in Appendices A and B are not included since they are defined as they are used in those appendices.

A relative mass [kg/kg] = [1] of water that would fill voids

B bulk modulus [Pa]

C specific heat [J/kg·K] at constant pressure

$\bar{C}$ sensible heat contribution to the specific heat [J/kg·K]

D mass diffusivity [m^2/s]

f volume fraction [m^3/m^3] = [1]

H enthalpy [J/kg]

K permeability [m^2]

ℓ length [m]

m dimensionless constant used in the Bruggeman mixture rule (Eq. (55)

$\dot{m}$ mass flux [$kg/m^2 \cdot s$]

n index of summation

p partial pressure [Pa]

P pressure [Pa], porosity [m^3/m^3] = [1], or fraction of area or of length (Eq. (75))

q heat flux [W/m^2]

S source term [$kg/m^3 \cdot s$] for creation of liquid or vapor

t time [s]

T temperature [K]

v volume fraction [m^3/m^3] = [1]

V volume [m^3]

W mass [kg]

x coordinate axis [m]

Greek

α coefficient of linear thermal expansion [$m/m \cdot K$] = [K^{-1}]

β coefficient of volumetric thermal expansion [$m^{-3}/m^{-3} \cdot K$] = [K^{-1}]

γ dimensionless constant in Harmathy's form of Hamilton-Crosser mixture rule (Eqs. (58)-(59))

δ mass diffusivity [kg/m·s·Pa] when the partial pressure gradient is the driving force; this quantity is usually called "permeability" in the building research literature

ΔH_p heat of reaction, or latent heat contribution to the specific heat [J/kg·K]

ζ degree of conversion of a chemical reaction ($0 \leq \zeta \leq 1$)

η dimensionless constant used in the Hamilton-Crosser mixture rule (Eq. (57))

κ thermal diffusivity [m^2/s]

λ thermal conductivity [W/m·K]

μ viscosity [kg/m·s]

ξ moisture capacity [kg/kg] = [1]

π 3.14159265...

ρ density [kg/m^3]

ϕ a particular property of interest

ω mass fraction [kg/kg] = [1]

Subscripts

0 reference

1,2 component

c forced convection, cement, or continuous phase

d diffusion, or dispersed phase

i component

m mass

n non-evaporable water

P at constant pressure

s saturation

u energy

w water

1. Introduction

The NIST Building and Fire Research Laboratory (BFRL) has undertaken several projects concerned with the performance of high strength concrete. One of these projects concerns the effect of fire on high strength concrete. Heating concrete to sufficiently high temperatures results in water of hydration being driven off, with a resultant irreversible loss of concrete strength. In addition, it has been observed that rapid heating of high strength concrete can result in spalling of the concrete. The most common explanation for this phenomenon is that, because of the very low permeability of high strength concrete, the moisture freed during dehydration (release of chemically bound water) cannot escape quickly enough to prevent a large buildup in pore pressure, which "blows off" some of the concrete. Another possible explanation for the observed spalling is that it occurs due to the large thermal stresses encountered under fire conditions.

Several computer models have been developed to predict temperature and pore pressure distributions in concrete exposed to simulated fire conditions. It probably will be necessary to develop a companion computer program to predict spalling and strength loss. BFRL is examining such computer programs to ascertain how reliably they can predict the overall response of high strength concrete structures to fire conditions and, hopefully, can provide insights into possible spalling prevention procedures.

The computer models for prediction of temperature and pore pressure distributions utilize an analysis procedure that involves the strongly coupled heat and mass transfer within the concrete. Such models typically include consideration of **mass transfer** of air and water by diffusion and by forced convection, conversion of liquid water to vapor, and release of water of hydration and **heat transfer** by conduction, mass diffusion, and forced convection with inclusion of the effects of the heat of vaporization of water, the heat of dehydration, and the thermal capacity of the concrete. Regardless of how good the computer programs are, in order to make valid predictions, they require reliable data as to the physical properties of the concrete. Mass transport properties are being investigated by the Building Materials Division. Thermal transport properties, the subject of this report, are being investigated by the Building Environment Division.

The present report addresses (1) identification of material properties critical to prediction of heat and mass transfer in high strength concrete at high temperatures, (2) variation of these properties with temperature, pressure, and thermal history, (3) examination of correlations between concrete composition and thermal properties, (4) identification of appropriate experimental techniques for determination of the thermal properties of high strength concrete, (5) identification of available equipment and testing services for carrying out such measurements, and (6) preliminary design of special equipment that needs to be constructed for measurement of one or more thermal properties.

Section 2 of this report provides an overview of heat and mass transfer in porous media, identifies the properties that are required in mathematical modeling of heat and mass transfer, and provides the mass and energy conservation equations for several different models that have been previously developed. Section 3 provides an overview of the available data on thermal properties of normal and high strength concrete. Section 4 is a discussion of various correlations and procedures that might be useful in prediction of the thermal properties of concrete. In Section 5, various experimental

techniques for determination of the needed thermal properties are described. The current availability of apparatus and testing services, for these properties, is covered in Section 6, with the aim of determining whether NIST has the appropriate capabilities, should procure or build appropriate equipment, or should rely on testing at outside laboratories. It is concluded that no suitable equipment for high temperature thermal conductivity measurements is available and that NIST needs to develop such capability. Accordingly, Section 7 provides a preliminary design of the apparatus that is proposed to be built for high temperature thermal conductivity measurements.

2. Modeling of Simultaneous Heat and Mass Transfer in Porous Media

When moisture is present, a very complex analysis can be required to deal with the coupled heat and mass transfer that can occur, involving both liquid mass transfer and vapor mass transfer. In general, moisture transport may include air-vapor mixture flow due to forced convection, free convection, and infiltration through cracks and pores; vapor transport by diffusion; flow of liquid due to diffusion, capillary action, or gravity; and the further complications associated with phase changes due to condensation/evaporation, freezing/thawing, ablimation/sublimation, and adsorption/desorption. There is a vast literature concerned with moisture transfer in materials and with simultaneous heat and mass transfer. The literature concerning moisture flow in porous materials encompasses the development of analytical/mathematical models, experimental studies, combined experimental and analytical studies, field studies, and retrofit studies. Much theoretical and experimental work has been done on the development of the theory of heat and mass transfer, separately and together, in porous media. This work comes mainly from the fields of drying, chemical processing, and building research, as well as from geophysics. However, in general it is fair to state that consistent and universally reliable analytical approaches and test methods are yet to be achieved for predicting combined heat and moisture transfer through porous media.

While analytical approaches differ, in general it is customary to write a set of coupled equations in which there are three "currents," such as heat flow, liquid water flow, and water vapor flow. Each current has three components, driven by one of three "forces," the temperature gradient, the gradient in liquid water content, and the gradient in water vapor content. Thus there are nine coefficients corresponding to the nine "conductivities" or "diffusivities" relating the currents and the forces. The Onsager reciprocal relations reduce the number of independent coefficients to six. Depending upon the application and the investigator, the moisture contents may be written in a variety of ways (e.g., mass or volume or relative humidity of moisture per mass or volume of medium). There also is a variety of choices used for the currents and for the forces. A few of the approaches used are discussed below.

The "apparent" thermal conductivity can be thought of as the ratio of the heat flux to the temperature gradient, even though the heat flux is also affected by the gradients in liquid-phase and vapor-phase moisture content. If moisture is migrating slowly, it can appear as if the apparent thermal conductivity is constant. However as the local moisture content changes over time, the true thermal conductivity will change, the heat transport associated with the fluxes of liquid and vapor will change, and thus the apparent thermal conductivity will change.

Obviously, the extensive theoretical literature concerned with heat and mass transfer in porous media cannot be reviewed in this report. Rather the approach taken is to (1) provide an overview of what happens when a concrete wall is exposed to fire conditions (and define various terms), (2) use the principles of irreversible thermodynamics to derive the much simpler problem of diffusion of a single gas through a porous media, (3) summarize the theoretical results which three different investigations found for the mass flux densities and energy flux density of coupled heat and moisture transfer through a porous medium in the absence of convective mass transfer, and (4) summarize the equations used in the Ahmed model (which does include convection) for predicting temperatures and pore pressures in concrete exposed to fire conditions.

2.1 Overview of Heat and Mass Transfer in Concrete Exposed to Fire

For concrete, particularly at high temperature, one cannot predict heat transfer from just the traditional thermal properties: thermal conductivity and volumetric specific heat (or, under some conditions, one of these properties plus thermal diffusivity). Movement of air, water, and possibly carbon dioxide through the concrete is accompanied by significant energy transfer, particularly associated with the latent heat of water and the heats of hydration and dehydration. Because of the high pore pressures that result when high-strength concrete is exposed to a fire, it is necessary to consider forced convection as well as diffusion.

Consider a concrete slab that initially may have small temperature gradients, e.g., due to indoor-to-outdoor temperature differences. Further, the extent of hydration of the concrete may not be uniform throughout the structure. Because of the heat released during initial curing and drying out of the concrete near one or both surfaces, there may be a higher amount of hydration in the middle of the material than near the surfaces. The free moisture content also may vary throughout the concrete if the different surfaces have been exposed to different humidities.

At the beginning of a fire, the temperature of the exposed side of the concrete slab will rise rapidly. Free moisture, both liquid and vapor, will migrate toward the cold side of the concrete. Initially, this moisture movement occurs by diffusion processes, where the driving force may be considered to be the gradient in moisture content (commonly expressed as partial pressure, humidity, molar or mass fraction, or molar or mass density). As the temperature of the fire-exposed side increases, any free liquid water will boil off and migrate toward the colder side where some of it will condense. The latent heat required to boil the liquid water will retard the rate of temperature rise at that location. When water vapor is transported into a colder region, some of it is absorbed into the concrete, with a heat of sorption that is approximately equal to the latent heat associated with condensation of free water vapor into liquid, so that significant heat is released. As moisture moves into the slab and the interior temperature rises towards 100 °C, portions of the slab may experience additional hydration (conversion of free water to chemically bound water), with an attendant release of heat. When the temperature of any portion of the concrete slab exceeds (roughly) the boiling point of water (at the local pressure) some dehydration (release of chemically bound water) will begin to take place, with an attendant absorption of heat. The dehydration reactions continue to temperatures in excess of 800 °C, with the most pronounced reaction being the dehydration of calcium hydroxide between 400 and 600 °C. The free water introduced into the concrete tries to diffuse toward the cold side. However, high-strength concrete is not very permeable to water vapor and is even less permeable (by, say, roughly two orders of magnitude) to liquid water. Thus the moisture cannot escape as rapidly as it is being released and the pore pressure in the concrete will rise substantially. Eventually, liquid water may fill the concrete pores at a location ahead of the temperature front, creating a condition known as moisture clog, where the liquid water blocks the transfer of water vapor toward the cold side of the slab. Under such conditions, the pore pressure will result in forced convective mass transfer of superheated steam and air to the heated side of the slab.

For concrete with carbonate aggregates, the situation is further complicated. Between 660 and 980 °C, calcium carbonate breaks down into calcium oxide with the release of carbon dioxide. Magnesium carbonate is similarly decomposed between 740 and 840 °C. Both reactions are

endothermic, thus absorbing heat and delaying temperature rise in the concrete. Quartz undergoes a pronounced phase transformation, with an accompanying volume increase, at about 573 °C.

During temperature exposure of the concrete, its transport properties for both heat and mass can change quite significantly due to differential thermal expansion opening up microcracks and changes to the solid structure associated with chemical decomposition of the cement paste (dehydration) and of any carbonate aggregates (conversion to oxides), both processes leading to less dense material and thus lower thermal conductivity (and thermal diffusivity) and higher mass transport properties.

In the absence of mass transfer and chemical reactions, conductive heat transfer is described by

$$\rho_o C \frac{\partial T}{\partial t} = \frac{\partial}{\partial x}\left(\lambda \frac{\partial T}{\partial x}\right) \quad , \tag{1}$$

where T is temperature [K], t is time [s], ρ_o is the bulk **density** [kg/m^3] of the medium, C is **specific heat** [J/kg·K], and λ is **thermal conductivity** [W/m·K]. If there are no other mechanisms of heat transfer and if λ can be assumed to be constant, this equation can be replaced by

$$\frac{1}{\kappa}\frac{\partial T}{\partial t} = \frac{\partial^2 T}{\partial x^2} \quad , \tag{2}$$

where $\kappa = \lambda/\rho_o C$, the ratio of thermal conductivity to volumetric specific heat, is known as the **thermal diffusivity** [m^2/s]. For a boundary value problem with prescribed surface temperatures as functions of time, the interior temperatures versus time depend only on the thermal diffusivity and it is not necessary to know the thermal conductivity or the specific heat separately. (Correspondingly, in measuring thermal diffusivity it is only necessary to measure a geometrical factor and a temperature variation with time; no power or energy measurements are required.) For a boundary value problem with a prescribed heat flux or with a radiation boundary condition, the temperature variation with time depends upon both thermal conductivity and thermal diffusivity (or upon one of these properties plus the volumetric heat capacity).

When exothermic or endothermic chemical reactions, or phase changes in the solid concrete, take place, it is preferable to replace Eq. (1) with

$$\rho\left(\frac{\partial H}{\partial T}\right)_P \frac{\partial T}{\partial t} = \frac{\partial}{\partial x}\left(\lambda \frac{\partial T}{\partial x}\right) \quad , \tag{3}$$

where H is **enthalpy** [J/kg] and P is **pressure** [Pa]. If the **degree of conversion** from the reactants into the products is designated by ζ ($0 \le \zeta \le 1$), Eq. (3) can be rewritten as

$$\rho\left(\bar{C} + \Delta H_P \frac{\partial \zeta}{\partial T}\right)\frac{\partial T}{\partial t} = \frac{\partial}{\partial x}\left(\lambda \frac{\partial T}{\partial x}\right) \quad , \tag{4}$$

where $\bar{C}$ represents the **sensible heat** contribution to the specific heat at a given degree of conversion, and the term involving ΔH_P, the **heat of reaction**, is the latent heat contribution. Sometimes the latent heat term is written as a heat source/sink term.

Turning now to mass transfer, diffusion is first considered. Assuming that Fick's law for diffusion holds, the mass flux due to a gradient in the density of the diffusing fluid is simply

$$\dot{m}_d = -D \frac{\partial \rho}{\partial x} \quad , \tag{5}$$

where $\dot{m}_d$ is the mass flux [kg/m^2·s] due to diffusion, ρ is the density [kg/m^3] of the fluid, and D is the **mass diffusivity** [m^2/s]. In the building research literature, for moisture transfer this equation is often expressed in terms of partial pressures as

$$\dot{m}_d = -\delta \frac{\partial p}{\partial x} \quad , \tag{6}$$

where p is the partial pressure [Pa] and δ is usually called the "permeability" [kg/m·s·Pa] rather than being called a mass diffusivity. For diffusion of water vapor, a similar expression is often seen with the driving force being the gradient in the humidity.

For forced convection through a porous medium, the mass flux is given approximately by

$$\dot{m}_c = -K \frac{\rho}{\mu} \frac{\partial P}{\partial x} \quad , \tag{7}$$

where P is the total pressure [Pa], ρ is the density [kg/m^3] of the moving fluid, μ is the **viscosity** [kg/m·s] of the moving fluid, and K is the **permeability** [m^2] of the medium for the particular fluid. (Often experimental results will indicate that K is not really a constant but varies with the pressure gradient so that a more complex expression may be required.)

The energy transport (heat flux) associated with a mass flux is simply

$$q = \dot{m} H \quad , \tag{8}$$

where H is the enthalpy of the moving fluid. The net energy content per unit volume (i.e., the additional term to be included in the energy differential equation, Eq. (4)) is

$$\dot{m} \frac{\partial H}{\partial x} = \dot{m} \left(\frac{\partial H}{\partial T} \right)_P \frac{\partial T}{\partial x} = \dot{m} C \frac{\partial T}{\partial x} \quad , \tag{9}$$

where C is the heat capacity of the moving fluid. If, as is the case with water, a phase change and the associated latent heat are involved, it is necessary to deal appropriately with the step function in the enthalpy.

In the case of diffusion or forced convection of a gas, absorption and desorption by the medium (concrete) probably can be ignored. However, for moisture transfer at temperatures below the boiling point of water (at the local pressure), absorption effects are quite important and the mass storage of water, and the associated enthalpy storage, need to be considered. Absorption/desorption of water vapor is usually described in terms of **sorption isotherms**, curves which relate the equilibrium absorbed moisture content of a medium, at a specific temperature, to the moisture content (usually expressed as vapor pressure or humidity) to which it is exposed. At low humidities, absorption is mainly by adsorption, first in monomolecular layers and then in multimolecular layers. Above about 40 percent relative humidity, capillary condensation begins in the smallest micropores of the material and then, as the humidity increases, there is condensation in larger pores and cracks, due to the depression of vapor pressure over the curved menisci of the water-filled capillaries. Porous materials exhibit hysteresis, so that absorption isotherms differ from desorption isotherms. The **moisture capacity** of a material is defined as the slope of the sorption isotherm (analogous to the heat capacity being the slope of the enthalpy-versus-temperature curve). The moisture capacity increases markedly as the water vapor pressure increases toward the saturation vapor pressure. Above a relative humidity of about 97 percent, it is customary to treat the moisture as being a liquid. Here the moisture capacity of a material is related to the capillary suction pressure by what is known as a **suction curve**, which also exhibits hysteresis.

Consideration of the mass flux (e.g., Eq. (5) or (6)) and the moisture capacity results in a differential equation, for diffusive mass transfer, that is analogous to Eq. (1) for heat transfer. A source term is added to this differential equation to represent the mass of moisture that is created or annihilated by hydration or dehydration, respectively. If the driving potential is taken as the density of the water vapor, mass conservation plus Eq. (5) results in

$$\frac{1}{D}\frac{\partial \rho}{\partial t} = \frac{\partial^2 \rho}{\partial x^2} + \frac{S}{\rho} \quad , \tag{10}$$

where S is the source term [kg/m^3·s] included to deal with conversion of liquid to vapor, or vice versa, or with the creation of water by dehydration of the medium. Comparison of the form of Eq. (10) with that of Eq. (2) shows the analogy between mass diffusivity and thermal diffusivity. The form of Eq. (10) does not explicitly show the dependence upon moisture capacity. If partial pressure or, equivalently, relative humidity is used as the driving potential and Eq. (6) is used to obtain the mass flux, mass conservation yields

$$\frac{\rho_o \xi}{\delta p_s}\frac{\partial p}{\partial t} = \frac{\partial^2 p}{\partial x^2} + \frac{S}{\delta} \quad , \tag{11}$$

where ρ_o is the bulk density of the medium, p_s is the saturation pressure [Pa] at the local temperature of the medium, and ξ is the moisture capacity obtained as the slope of the sorption curve, plotted as mass of water vapor per unit mass of the medium versus relative humidity (so ξ is dimensionless).

Some investigators explicitly consider two moisture fluxes, one for vapor and one for liquid, while others use a single moisture flux, with the moisture capacity being used to deal with the change of phase, or the absorption and desorption, of the water. An equation analogous to Eq. (11) can be

derived for transfer of liquid water, with the moisture capacity being obtained from capillary suction curves.

Forced convection of moisture through the medium also requires consideration of the moisture capacity of the medium. For sufficiently small flows, one might assume that the moisture absorbed or desorbed can be predicted from the moisture capacity as determined from sorption curves or suction curves measured under steady-state conditions. In such a case, differential equations analogous to Eq. (11) could be written. However, for concrete under simulated fire conditions and high pore pressures, it is questionable whether there would be time for such equilibrium to be achieved.

2.1 Irreversible Thermodynamics Approach for Diffusion of a Gas

Before discussing the rather complex analysis of two-phase (liquid and vapor) flow of moisture through a porous solid, the more simple case of diffusion of a gas through a stationary medium is considered. This is done most conveniently by the methods of irreversible thermodynamics, applying the Onsager Reciprocal Relations [1-24]. A set of current densities is defined as

$$\mathbf{J}_i = \sum_j L_{ij} X_j \quad , \tag{12}$$

where X_j are the "conjugate forces," such that

$$R(S) = \sum_j \mathbf{J}_i \cdot X_i \quad , \tag{13}$$

where $R(S)$ is the rate of entropy production in the system. The Onsager Reciprocal Theorem states that

$$L_{ij} = L_{ji} \quad . \tag{14}$$

The rate of entropy production is uniquely defined by the system under consideration, but since $R(S)$ can be split into a sum of products in many ways, one is left with a choice of current densities and conjugate forces. We choose a mass current density $\mathbf{J}_m$, an internal energy current density $\mathbf{J}_u$, and an entropy current $\mathbf{S}$, so that the divergence of each of these current densities is the rate of change per unit volume of the corresponding thermodynamic variable. With these definitions for the current densities,

$$T\mathbf{S} = \mathbf{J}_u - \mu \mathbf{J}_m \quad , \tag{15}$$

where T is the absolute temperature and μ is the chemical potential of the diffusing gas. The rate of production of entropy is

$$R(S) = \nabla \cdot \mathbf{S} = \mathbf{J}_m \cdot \nabla \left(-\frac{\mu}{T} \right) + \mathbf{J}_u \cdot \nabla \left(\frac{1}{T} \right) \quad . \tag{16}$$

The current densities are

$$\mathbf{J}_m = L_{mm}\nabla\left(-\frac{\mu}{T}\right) + L_{mu}\nabla\left(\frac{1}{T}\right) \tag{17}$$

$$\mathbf{J}_u = L_{mu}\nabla\left(-\frac{\mu}{T}\right) + L_{uu}\nabla\left(\frac{1}{T}\right) \quad . \tag{18}$$

In order to put these expressions in terms of measurable gradients, it is noted that

$$\nabla\left(\frac{\mu}{T}\right) = \frac{v}{T}\nabla P - \frac{Ts + \mu}{T^2}\nabla T = \frac{v}{T}\nabla P - \frac{h}{T^2}\nabla T \quad , \tag{19}$$

where v is the specific volume, s is the specific entropy, and h is the specific enthalpy. Substitution of Eq. (19) into Eqs. (17) and (18) yields

$$\mathbf{J}_m = -\frac{L_{mm}v}{T}\nabla P + \frac{L_{mm}h - L_{mu}}{T^2}\nabla T \tag{20}$$

$$\mathbf{J}_u = -\frac{L_{mu}v}{T}\nabla P + \frac{L_{mu}h - L_{uu}}{T^2}\nabla T \quad . \tag{21}$$

Thermal conductivity is defined as

$$\lambda = \left[\frac{-\mathbf{Q}}{\nabla T}\right]_{\mathbf{J}_m = 0} = \left[\frac{-\mathbf{J}_u}{\nabla T}\right]_{\mathbf{J}_m = 0} \quad , \tag{22}$$

where $\mathbf{Q}$ is the heat current density, since when $\mathbf{J}_m = 0$, $\mathbf{J}_u = \mathbf{Q}$. Setting Eq. (20) equal to zero yields

$$\left(\frac{\nabla P}{\nabla T}\right)_{\mathbf{J}_m = 0} = \frac{h - L_{mu}/L_{mm}}{vT} \quad . \tag{23}$$

This ratio of the pressure gradient to the temperature gradient, when there is no mass flow, is called the thermomolecular pressure difference. Combining Eqs. (21)-(23) yields the following expression for the thermal conductivity in terms of the Onsager coefficients

$$\lambda = \frac{L_{uu}L_{mm} - L_{mu}^2}{T^2 L_{mm}} \quad . \tag{24}$$

When the system is isothermal, $\nabla T = 0$ and the two current densities are simply

$$\mathbf{J}_m = -\frac{L_{mm}v}{T}\nabla P \qquad \text{and} \qquad \mathbf{J}_u = -\frac{L_{mu}v}{T}\nabla P \quad , \tag{25}$$

Under such conditions, the two currents are related to each other by

$$\mathbf{J}_u = \frac{L_{mu}}{L_{mm}}\mathbf{J}_m = \alpha \mathbf{J}_m \quad , \tag{26}$$

where α is a quantity that can be determined experimentally by measuring both heat flow and mass flow for isothermal conditions. Permeability is defined as

$$\beta = \left[\frac{-\mathbf{J}_m}{\nabla P}\right]_{\nabla T=0} = \frac{L_{mm}}{\rho T} \quad , \tag{27}$$

where $\rho = 1/v$ is the density of the gas.

The Onsager coefficients can be expressed in terms of the measurable quantities λ, α, and β (other measurable quantities could have been selected of course):

$$L_{mm} = \beta T \qquad L_{mu} = \alpha\beta T \qquad L_{uu} = \lambda T^2 + \alpha^2\beta T \quad . \tag{28}$$

With these substitutions into Eqs. (20) and (21), the current densities become

$$\mathbf{J}_m = -\beta\nabla P + \frac{\beta(h-\alpha)}{T}\nabla T \tag{29}$$

$$\mathbf{J}_u = -\alpha\beta\nabla P - \left(\lambda - \frac{a\beta(h-\alpha)}{T}\right)\nabla T \quad . \tag{30}$$

Note that the use of the Onsager reciprocal relation results in only three measurable parameters being required, rather than four (h does not have to be measured since accurate data for the specific enthalpy are available for most gases and liquids of interest and certainly for water). Note that the quantity α requires thermal measurements even though it is defined under isothermal conditions.

Consider now the case of moisture transfer through a hygroscopic material. Even though there is no liquid water entering or leaving the specimen, there will be adsorbed water and, at moderately high humidities, liquid water inside the pores and capillaries. In general, proper understanding of simultaneous heat and mass transfer for such circumstances requires that both the vapor phase and

the liquid phase be explicitly considered. The current densities, analogous to those in Eqs. (17) and (18), are

$$\mathbf{J}_v = L_{vv}\nabla\left(-\frac{\mu_v}{T}\right) + L_{vl}\nabla\left(-\frac{\mu_l}{T}\right) + L_{vu}\nabla\left(\frac{1}{T}\right) \tag{31}$$

$$\mathbf{J}_l = L_{lv}\nabla\left(-\frac{\mu_v}{T}\right) + L_{ll}\nabla\left(-\frac{\mu_l}{T}\right) + L_{lu}\nabla\left(\frac{1}{T}\right) \tag{32}$$

$$\mathbf{J}_u = L_{uv}\nabla\left(-\frac{\mu_v}{T}\right) + L_{ul}\nabla\left(-\frac{\mu_l}{T}\right) + L_{uu}\nabla\left(\frac{1}{T}\right) \quad . \tag{33}$$

where $\mathbf{J}_v$ is the mass current density for water vapor, $\mathbf{J}_l$ corresponds to mass flow of liquid water and, as before, $\mathbf{J}_u$ is the current of internal energy. The nine coefficients can be reduced to six by invoking the Onsager reciprocal relations. Further reduction in the number in coefficients requires that certain assumptions be made, or other information be used, concerning the relationship between water vapor and liquid water. For example if the sorption isotherm curve is known for the specimen of interest, one can infer how much water will be adsorbed and/or absorbed in a specimen that is exposed to a particular temperature and relative humidity. The Kelvin equation can be used to relate hydraulic pressure inside a capillary to the relative humidity. Several workers have developed theories to describe simultaneous heat and mass transfer due to moisture migration in hygroscopic materials. Such derivations are quite complex and space and time do not permit showing the details in this report. Rather, the results obtained by several prominent workers in the field are given and differences and similarities are pointed out. There are many differences among these several developments in the definitions of terms and the symbols used; here the same nomenclature of the original workers is used so as not to add further confusion.

2.2 Heat Transfer and Diffusive Mass Transfer (no convection)

One comment is in order before proceeding to list the expressions which previous workers have obtained for the mass and heat fluxes associated with moisture transfer. In the derivation given above, a single gas was diffusing through a porous medium under the combined effects of a temperature gradient and a pressure gradient. In the case of moisture transfer, the water vapor pressure is normally very small compared to the total pressure of the moist air. Therefore in most derivations in the moisture literature it is assumed that the total pressure in the medium is uniform and that the water vapor diffuses under the combined influence of a concentration gradient (which may be expressed as a vapor pressure gradient or a humidity gradient) and a temperature gradient. If one wished to allow for the effects of a gradient in the total pressure, as is the case for concrete exposed to a fire, it would be necessary to add a convective term to the expressions given below. Similarly, the effects of gravitational forces are usually neglected in the case of moisture transfer through a hygroscopic medium.

Philip and de Vries [18-20] defined liquid flux density as

$$\mathbf{q}_l = -\rho_l (D_{\theta l} \nabla \theta_l + D_{Tl} \nabla T + K \mathbf{k}) \quad , \tag{34}$$

where

$$D_{\theta l} = K \partial \psi / \partial \theta_l \qquad \text{and} \qquad D_{Tl} = K \partial \psi / \partial T \quad . \tag{35}$$

In these equations ρ_l is liquid density, θ_l is volumetric liquid moisture content, $D_{\theta l}$ is macroscopic diffusivity for liquid transport due to $\nabla \theta_l$, T is temperature, D_{Tl} is macroscopic diffusivity for liquid transport due to ∇T, K is hydraulic conductivity, $\mathbf{k}$ is the unit vector in the z-direction, and ψ is moisture potential (see Eq. (39), below).

Philip and de Vries defined vapor flux density as

$$\mathbf{q}_v = -\rho_l (D_{\theta v} \nabla \theta_l + D_{Tv} \nabla T) \tag{36}$$

where

$$D_{\theta v} = f(a) D \frac{P}{P - p_v} \frac{Mg}{RT} \frac{\rho_v}{\rho_l} \frac{\partial \psi}{\partial \theta_l} \tag{37}$$

$$D_{Tv} = f(a) D \frac{P}{P - p_v} \frac{\rho_v}{\rho_l} \frac{\zeta}{p_{vs}} \frac{dp_{vs}}{dT} \tag{38}$$

$$p_v = h p_{vs} = p_{vs} \exp(Mg\psi / RT) \tag{39}$$

$$f(a) = a + \theta_l = S \quad , \qquad \text{for} \quad \theta_l \le \theta_{lk} \tag{40}$$

$$f(a) = a + a(S - a)/(S - \theta_{lk}) \quad , \qquad \text{for} \quad \theta_l > \theta_{lk} \tag{41}$$

$$\zeta = (\nabla T)_a / \nabla T \quad . \tag{42}$$

In these equations θ_v is volumetric moisture vapor content, $D_{\theta v}$ is macroscopic diffusivity for vapor transport due to $\nabla \theta_v$, D_{Tv} is macroscopic diffusivity for vapor transport due to ∇T, a is volumetric air content, D is the diffusion coefficient of water vapor in air, P is total gas pressure, M is molar mass, g is acceleration due to gravity, R is the universal gas constant, ρ_v is vapor density, p_{vs} is the partial pressure of water vapor at saturation, h is relative humidity, and S is porosity. They also define a total moisture flux density as

$$\mathbf{q}_m = \mathbf{q}_l + \mathbf{q}_v = -\rho_l (D_\theta \nabla \theta_l + D_T \nabla T + K \mathbf{k}) \quad . \tag{43}$$

Philip and de Vries defined the heat flux density as

$$\mathbf{q}_h = -\lambda^* \nabla T + c_l (T - T_o)\mathbf{q}_m - L\rho_l D_{\theta v} \nabla \theta_l \tag{44}$$

or

$$\mathbf{q}_h = -\lambda^+ \nabla T + c_l (T - T_o)\mathbf{q}_m - L\rho_l D_{\theta v} \nabla \theta_l \tag{45}$$

where λ^* is the (apparent) thermal conductivity associated with macroscopic inclusion of water vapor, λ^+ is the (apparent) thermal conductivity associated with microscopic inclusion of water vapor, c_l is specific heat of liquid water, T_o is a reference temperature, and L is the latent heat of evaporation. In this expression, the first term represents normal heat conduction, the second term represents the sensible heat transfer due to mass transfer, and the third term corresponds to the latent heat transfer due to mass transfer.

Fortes and Okos [21-22] derived the following heat and mass transfer equations, applicable to hygroscopic capillary-porous media:

Liquid mass flux:

$$\mathbf{j}_l = -K_l \left(\rho_l R_v \ln H \nabla T - \rho_l \frac{R_v T}{H} \frac{\partial H}{\partial M} \nabla M \right) \tag{46}$$

Vapor mass flux:

$$\mathbf{j}_v = -K_v \left[\left(\rho_{vo} \frac{\partial H}{\partial T} + H \frac{\mathrm{d}\rho_{vo}}{\mathrm{d}T} \right) \nabla T - \left(\rho_{vo} \frac{\partial H}{\partial M} \right) \nabla M \right] \tag{47}$$

Heat flux:

$$\mathbf{j}_q = -K_T \nabla T - \left[\rho_l K_l R_v \ln H + K_v \left(\rho_{vo} \frac{\partial H}{\partial T} + H \frac{\mathrm{d}\rho_{vo}}{\mathrm{d}T} \right) \right] \frac{R_v T^2}{H} \frac{\partial H}{\partial M} \nabla M \ . \tag{48}$$

In these equations K_l is "liquid conductivity," ρ_l is liquid density, R_v is the gas constant per unit mass of water vapor, H is relative humidity, M is moisture content expressed as mass of moisture per unit mass of dry medium, K_v is "vapor conductivity," ρ_{vo} is the saturation density of water vapor, and K_T is apparent thermal conductivity. Note that everywhere ∇M appears it is multiplied by $\partial H/\partial M$ so that the equations are effectively given in terms of the humidity gradient.

Luikov [23-24] combines the mass current density for water vapor and the mass current for liquid water into a single mass current density for moisture,

$$\mathbf{J}_m = -a_m \rho_o \nabla u - a_m \rho_o \delta \nabla T \ , \tag{49}$$

where u is moisture content, a_m is "moisture diffusivity," ρ_o is the density of the dry medium, and δ is the "thermogradient coefficient." The corresponding heat current density is

$$\mathbf{J}_u = -\lambda \nabla T - r \epsilon \mathbf{J}_m \quad , \tag{50}$$

where λ is thermal conductivity (Luikov put conductive heat transfer in terms of the thermal diffusivity $a = \rho_o c \lambda$, where c is the effective heat capacity of the moist medium), r is the latent heat of vaporization, and ϵ is the "phase conversion factor" of liquid into vapor.

The final expressions of Philip and de Vries, Fortes and Okos, and Luikov are all of the general form of Eqs. (31)-(33) but without some of the "cross" terms. For example, Philip and de Vries expressed the liquid flux density in terms of the gradient of liquid moisture content and the temperature gradient but did not have a term involving the gradient of moisture vapor content. Similarly, their expression for the vapor flux density involved the vapor concentration but not the liquid content. Fortes and Okos effectively used relative humidity, along with temperature, as the driving force for both liquid and vapor flow. Luikov combined liquid and vapor and only considered total moisture content (in his derivations this simplification was accomplished by using the sorption isotherm to infer liquid content from vapor concentration and vice versa).

2.3 Ahmed Model

Since the NIST parties involved with this project have access to the papers by Ahmed, *et al.*, describing the model used to simulate coupled heat and mass transfer in concrete slabs, only the three coupled differential equations which they use are shown here.

The differential equation for conservation of mass for water vapor is

$$\frac{\partial}{\partial t}\left(\rho_v \epsilon_g \phi\right) - \frac{\partial}{\partial x}\left(\rho_v \epsilon_g K_p \frac{\partial P}{\partial x}\phi\right) - \frac{\partial}{\partial x}\left(\rho_g \epsilon_g D \frac{\partial \phi}{\partial x}\right) = \Gamma \quad , \tag{51}$$

where ρ_v and ρ_g are the density [kg/m^3] of, respectively, the water vapor and the gaseous mixture of water vapor and air, ϵ_g is the volume fracture [m^3/m^3] of gaseous mixture in the porous medium, ϕ is the mole fraction [kmol/kmol] of water vapor in the gaseous mixture, K_p is the "coefficient of permeability" [m^3•s/kg], P is the pore pressure [Pa] of the gaseous mixture in the porous medium, D is the "modified diffusivity" [m^2/s] of the gaseous mixture, and Γ is the mass rate of evaporation of water per unit volume of porous medium [kg/m^3•s]. The coefficient of permeability, K_p, is defined as $K_p = K_g / g \rho_g \epsilon_g$, where K_g is the "permeability" [m/s] of the gaseous mixture and g is the acceleration [m/s^2] due to gravity. The modified diffusivity, D, [m^2/s] is $D = (M_v M_a / M^2) D'$, where M, M_a, and M_v are the molecular weights [kg/kmol] of, respectively, the gaseous mixture, the air in the gaseous mixture, and the water vapor in the gaseous mixture and D' is the diffusivity [m^2/s] of the gaseous mixture. Ahmed, *et al.* identify the four terms of Eq. (51) as the transient term, the convection term, the diffusion term, and the source term.

Ahmed, *et al.*, use a different definition for permeability than the one that is normally used. Apparently $K_g = (\rho g/\mu) \cdot K$, where ρ is density, μ is viscosity, and K is the permeability as normally defined (see Eq. (7), above).

The differential equation for conservation of mass of the mixture of water vapor and air is

$$\frac{\partial}{\partial t}\left(\rho_g \epsilon_g\right) - \frac{\partial}{\partial x}\left(\rho_g \epsilon_g K_p \frac{\partial P}{\partial x}\right) = \Gamma \quad , \tag{52}$$

where the three terms are the transient term, the convective term, and the source term. The differential equation for conservation of energy is

$$\rho C_p \frac{\partial T}{\partial t} - \rho_g \epsilon_g C_{p_g} \frac{\partial P}{\partial x} \frac{\partial T}{\partial x} - \left(\rho_g \epsilon_g (C_{p_v} - C_{p_a}) D \frac{\partial \phi}{\partial x}\right) \frac{\partial T}{\partial x} = \frac{\partial}{\partial x}\left(k \frac{\partial T}{\partial x}\right) - Q\Gamma \quad , \tag{53}$$

where C_p, C_{p_g}, C_{p_v}, and C_{p_a} are, respectively, the (total) effective heat capacity of the porous medium, the heat capacity of the gaseous mixture, the heat capacity of water vapor, and the heat capacity of air, k is the effective thermal conductivity of the medium, and the source term (evaporation/dehydration) is defined as

$$Q\Gamma = -\left(Q_\ell \frac{\partial \delta_{\ell f}}{\partial t} + (Q_\ell + Q_{dh}) \frac{\partial \delta_{td}}{\partial t}\right) \quad , \tag{54}$$

where Q_ℓ is the latent heat of evaporation [J/kg] of free water vapor, Q_{dh} is the heat of hydration [J/kg] of chemically bound water in the porous medium, $\delta_{\ell f}$ is the mass concentration of free liquid water in the pores per unit volume of porous medium [kg/m^3], and δ_{td} is the mass concentration of chemically bound water (in the cement paste) per unit volume of porous medium [kg/m^3]. The five terms in Eq. (53) represent the transient term, the convection term, the diffusion term, the conduction term, and the source term, respectively.

3. Existing Data on Thermal Properties of Concrete and Its Constituents

Since the data available for the properties of high strength concrete are quite limited and since most of the thermal properties of high strength concrete are not expected to differ considerably from the properties of normal concrete, this section addresses data available for both normal and high strength concrete.

The most important references, over the past thirty years, that contain data on the thermal properties of concrete, mortar, or cement paste over extended temperature ranges include [25-50]; these references in turn refer to many other publications. The vast majority of data on thermal properties of concrete correspond to temperatures close to normal room temperature. Reference [51] contains an extensive compendium of data on rocks and minerals, including materials that can be used as fine and coarse aggregates in Portland cement concrete. Although this reference has a 1989 copyright date, it was originally written in the late 1970's and all of the references are to publications dated 1978 or earlier, with very few references for 1977 or 1978. Other references relevant to the thermal properties of rocks include [52-59].

3.1 Mass, Volume, and Density

The density of concrete and its constituents is needed to compute volumetric heat capacity, which is needed for the various theoretical models used to predict heat transport in fire-exposed concrete; however, since the density does not vary by much over the temperature range of interest, only relatively small corrections to the room temperature density are required.

In addition, the variation of mass with time and temperature is an important indicator of the degree of conversion from the reactants to the products in a chemical reaction, such as dehydration or loss of carbon dioxide. Accordingly, information as to mass variation is important in determining the enthalpy of a specimen. Similarly, since a material may expand or contract when a chemical reaction takes place, thermal expansion data can be useful in determining the degree of conversion for a chemical reaction.

Thermal expansion data also will be needed to predict thermal stresses that might contribute to spalling. In addition, post-test measurements of thermal expansion would provide sensitive indicators of the degree of dehydration due to the temperature-time exposure that took place during a real or simulated fire.

Figure 1 shown the mass loss and the thermal expansion of a particular cement paste as functions of temperature when the specimen is heated at a nominally uniform rate from room temperature to 1000 °C. At 1000 °C, the one-dimensional length change is about 3.3 percent so that the volumetric contraction is approximately 10 percent. Since the same type of cement paste lost 15 percent of its mass, the bulk density would decrease by a rather small percentage between room temperature and 1000 °C (see Figure 16, below).

Figure 2 shows mass loss and temperature change for a sample of Portland cement paste that was heated to 260 °C over a period of 4.75 h, held at 260 °C for 44 h, and then allowed to cool to room temperature.

Curves A and C in Figure 3 show mass loss versus temperature for, respectively, a calcareous aggregate, containing carbonate (lime or limestone), and a siliceous aggregate, containing silica. The much greater mass loss for the carbonate aggregate is due to the dissociation of the carbonate and the attendant release of carbon dioxide. Curves B and D correspond to concretes made with the two types of aggregate. Figure 4 shows mass loss for various concretes, including measurements by two different investigators on limestone concrete. Another set of data for carbonate concrete is shown in Figure 5, with this concrete having the composition indicated in column 2 of Table 1 (the other two specimens for which data are shown in Figure 4 contained reinforcing steel fibers, which would not be expected to change the mass loss versus temperature curve significantly).

Table 2 shown the constituents of five high-strength concretes recently studied by investigators at the Portland Cement Association. The mass loss versus temperature for these specimens are shown in Figures 6, 7, and 8, corresponding to the different heating rates listed at the bottom of each figure.

Figure 9 shows how the amount of silica fume in a high-strength concrete affects the loss of mass with increasing temperature.

As mentioned above, in addition to mass loss, Figures 1 and 2 showed thermal expansion versus temperature for Portland cement paste. Additional thermal expansion data for cement paste are shown in Figure 10.

With regard to potential aggregates, Figure 11 shows thermal expansion data on the ten different types of rocks that are listed in Table 3. The data for limestone are shown by the curve labeled LI.

Thermal expansion versus temperature for several different types of concrete are shown in Figures 12, 13, and 14. Each of these figures includes data for a limestone-aggregate concrete. Figure 15 indicates how the room-temperature thermal expansion coefficient for concretes is related to the thermal expansion coefficient of the aggregate.

Figure 1 presented information on the mass loss and thermal expansion of a particular cement paste. Figure 16, shows, for that same paste, how the true density, the bulk density, and the porosity are believed to change with increasing temperature.

Figures 17 and 18 show the effect of temperature on the density of concretes with different types of aggregate. The data in Figure 17 correspond to limestone-aggregate concrete, which loses considerable density when the carbonate disassociates. Figure 19 shows the density versus temperature curves used in the version of the Ahmed model (see Section 2.3, above) that is currently available at NIST. Type 1 refers to carbonate aggregate concrete and Type 2 to siliceous concrete.

(Text continued on p. 32)

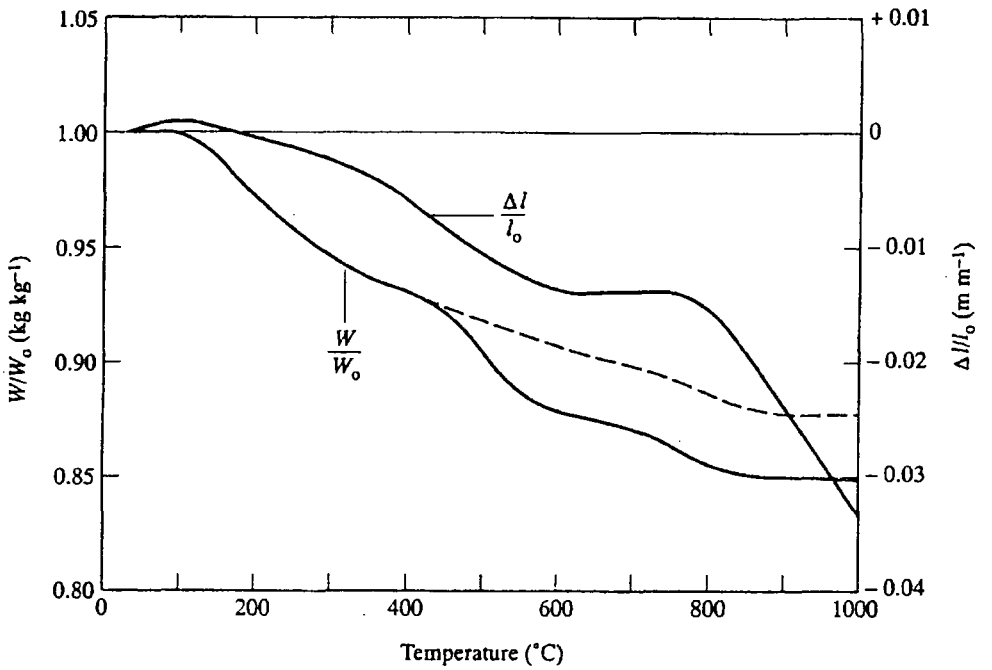

Figure 1. Thermogravimetric and dilatometric curves for Cement Paste C [27,41].

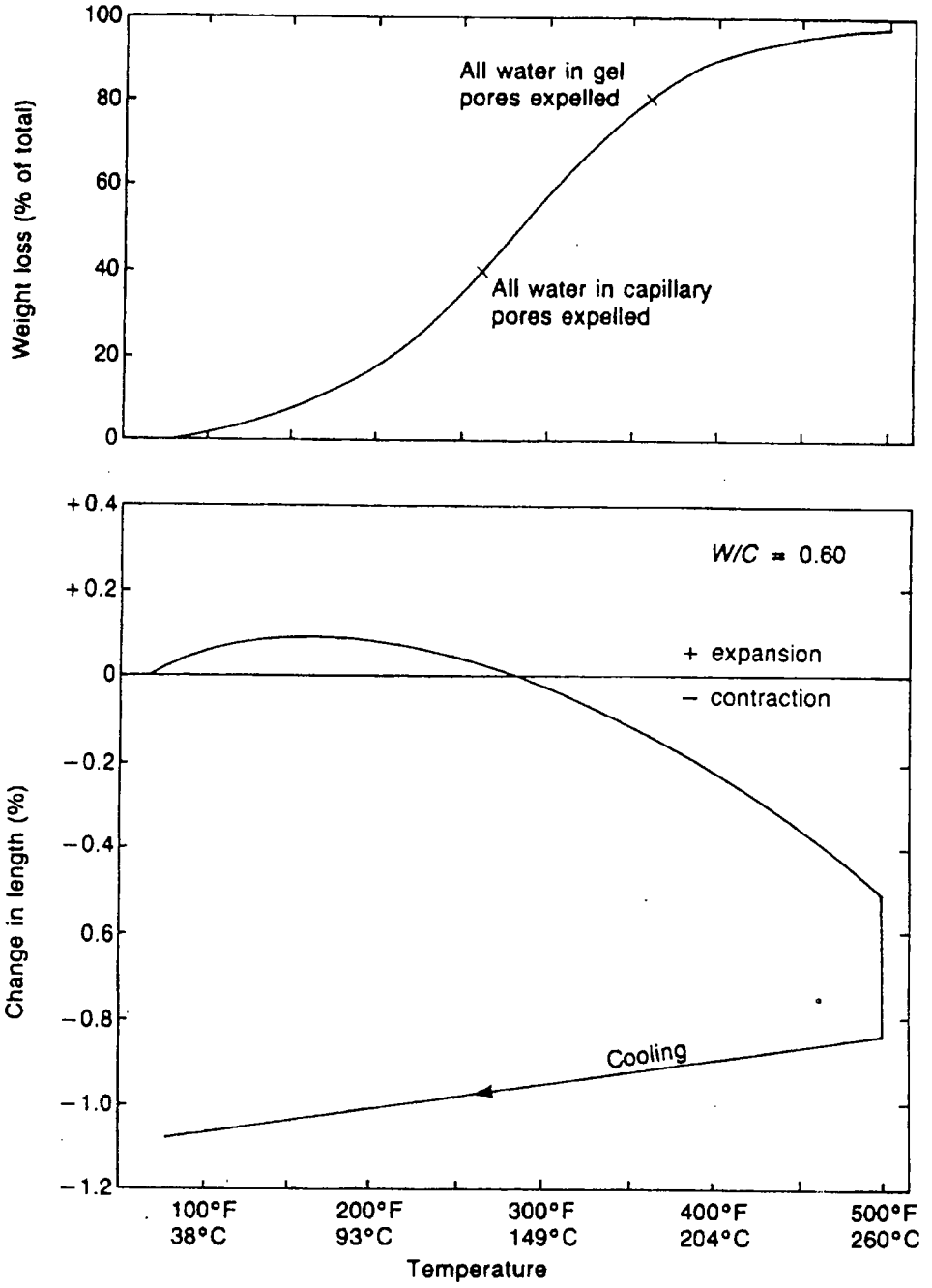

Figure 2. Typical relationships between weight loss, corresponding length change, and temperature for Portland cement paste: + expansion; − contraction [45].

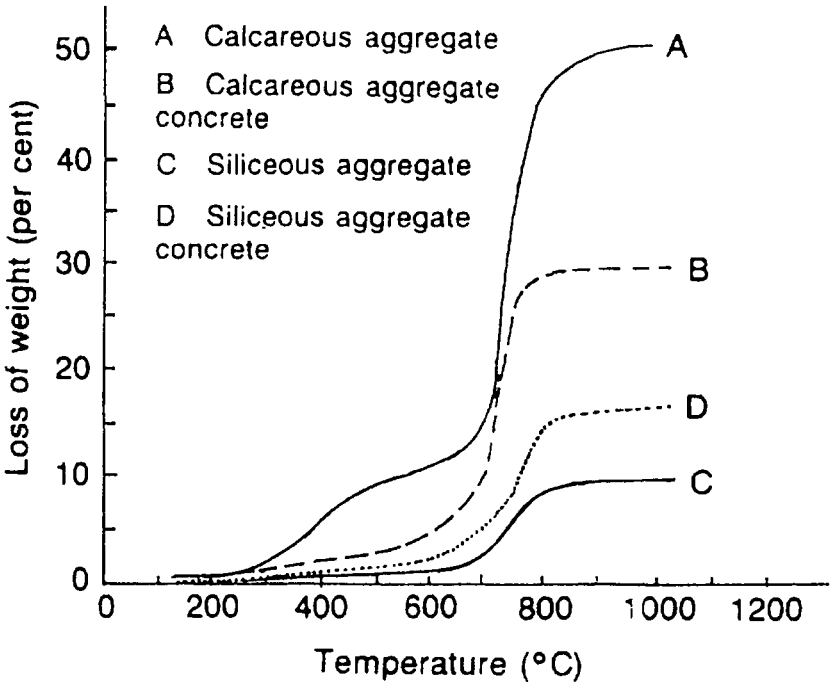

Figure 3. Weight loss of calcareous and siliceous aggregates and concretes caused by heating [45].

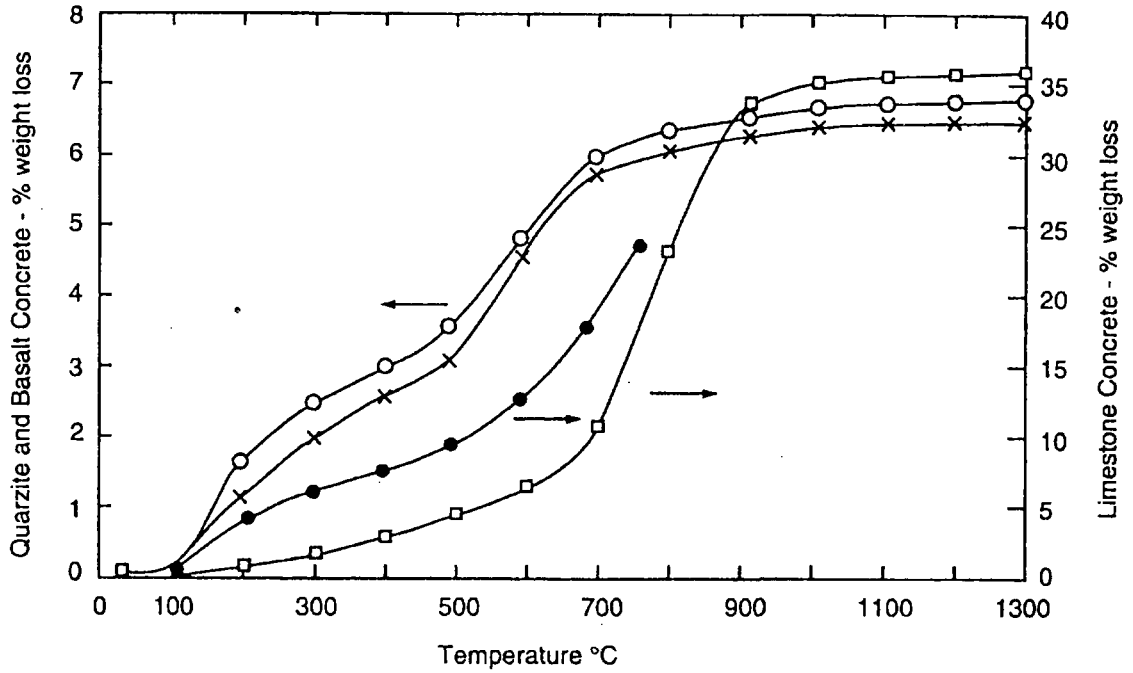

Figure 4. Weight loss as a percentage of initial weight for various concretes caused by heating (Kühl, 1958; Schneider, 1982): quartzite concrete (○); basalt concrete (×); limestone concrete (□) (all by Schneider, 1982); limestone concrete (●) – Philleo (1958) [45].

Property	Batch (specimen type)		
	1 (NRC1)	2 (NRC2)	3 (NRC3)
Cement content (kg/m^3)	380	439	439
Fine aggregate (kg/m^3)	673	621	621
Coarse aggregate (kg/m^3)			
19 mm	678	788	788
9.5 mm	438	340	340
Total	1162	1128	1128
Aggregate type	Siliceous	Carbonate	Carbonate
Water (kg/m^3)	167	161	161
Water–cement ratio	0.44	0.37	0.37
Retarding admixture (mL/m^3)	745	—	—
Superplasticizer (mL/m^3)	2500	300	1200
Steel fibre (kg/m^3)	42	—	42
28-day compressive strength (MPa)	39.9	32.6	43.2
Compressive strength at test date (MPa)	40.9	37.1	43.3

Table 1. Batch quantities and properties of concrete mix [44].

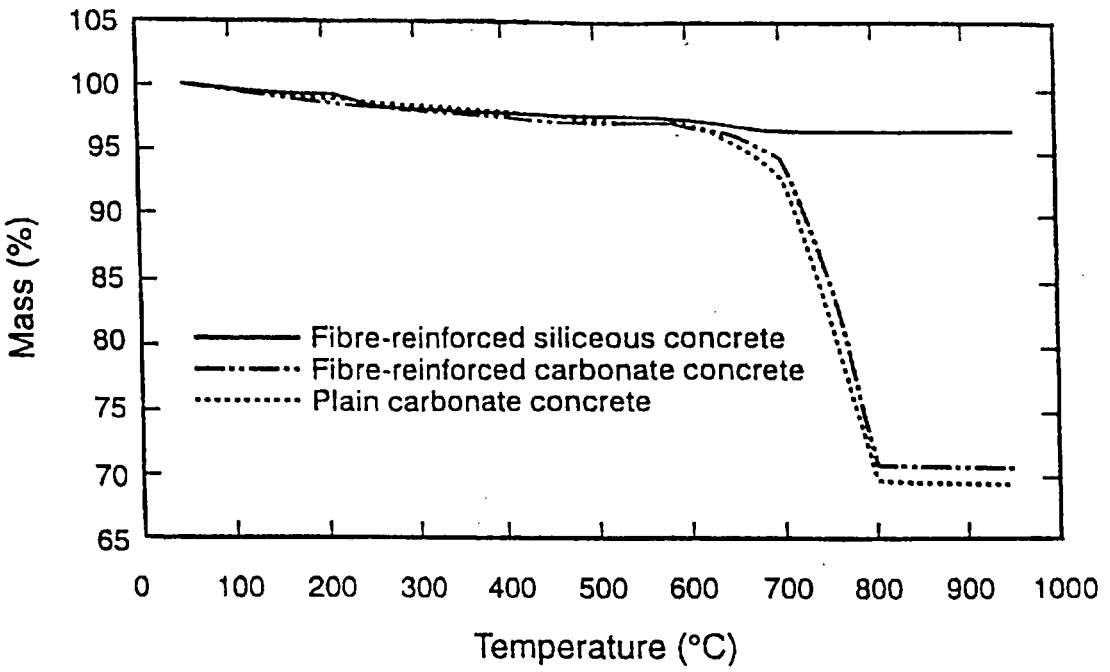

Figure 5. Mass loss of various concrete types as a function of temperature [44].

Parameter Units per cubic meter	Number identifying type of mix				
	1	2	3	4	5
Cement Type I, kg	564	475	487	564	475
Silica Fume, kg (1)	-	24	47	89	74
Fly Ash, kg	-	59	-	-	104
Coarse Agg. SSD, kg. (2)	1068	1068	1068	1068	1068
Fine Agg. SSD, kg.	647	659	676	593	593
HRWR Type F, liter	11.60	11.60	11.22	20.11	16.44
HRWR Type G, liter	-	-	-	-	-
Retarder Type D, liter	1.12	1.05	0.97	1.46	1.50
Total Water, kg. (3)	158	160	155	144	151
Water/Cement Ratio	0.281	0.338	0.320	0.255	0.318
Water/Cementitious Ratio	0.281	0.287	0.291	0.220	0.321

Note: As reported by ready-mix supplier
(1) Dry weight
(2) Maximum aggregate size: 12 mm
(3) Weight of total water in mix including admixtures

Table 2. Composition of concrete mixtures [47-48].

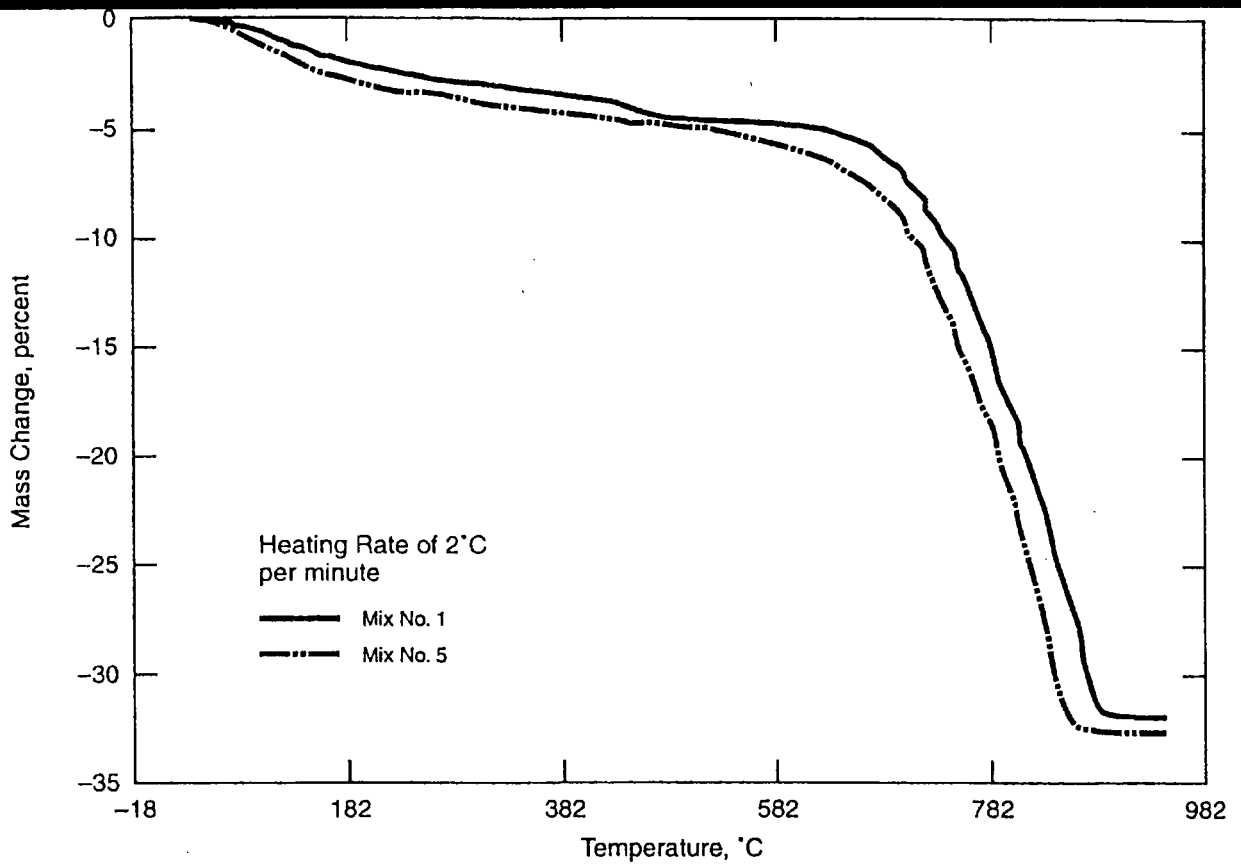

Figure 6. Mass loss of high strength concrete at elevated temperatures [47-48]

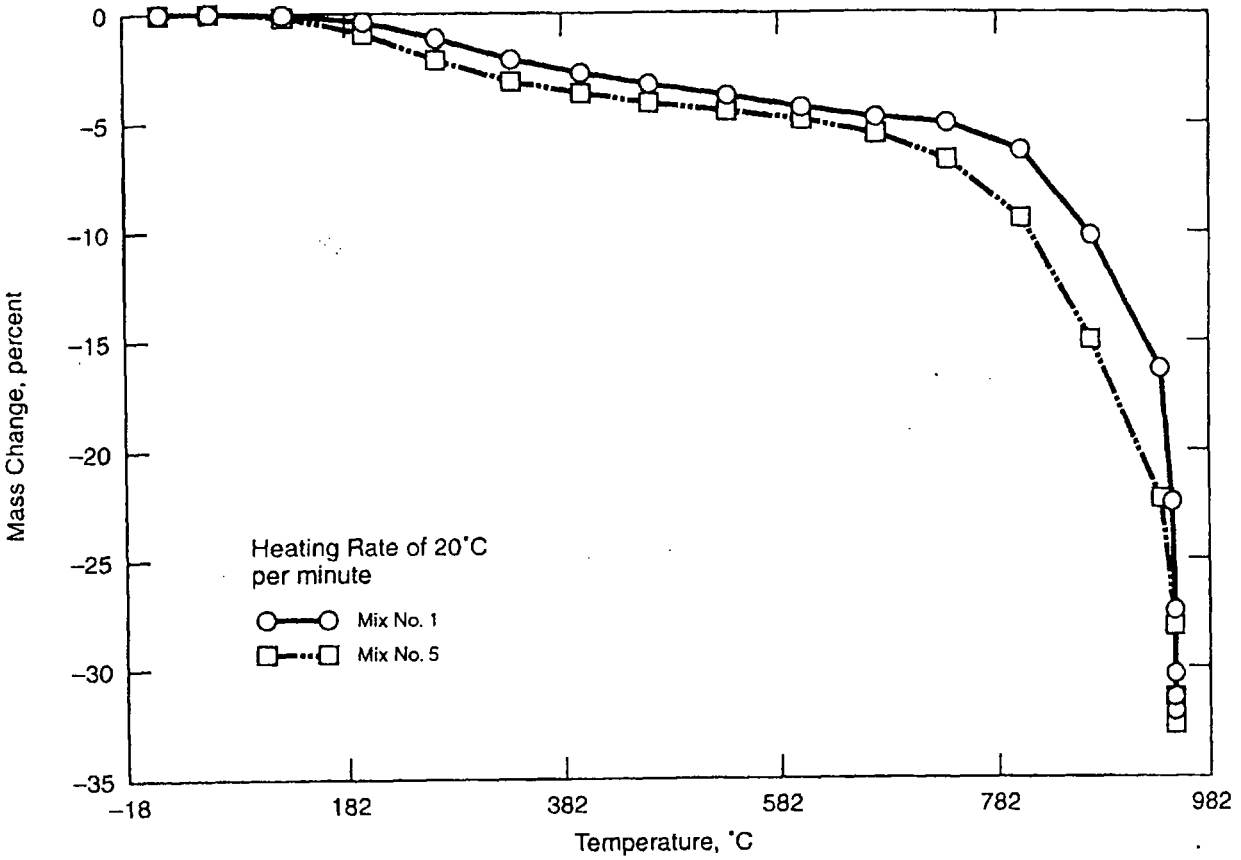

Figure 7. Mass loss of high strength concrete at elevated temperatures [47-48]

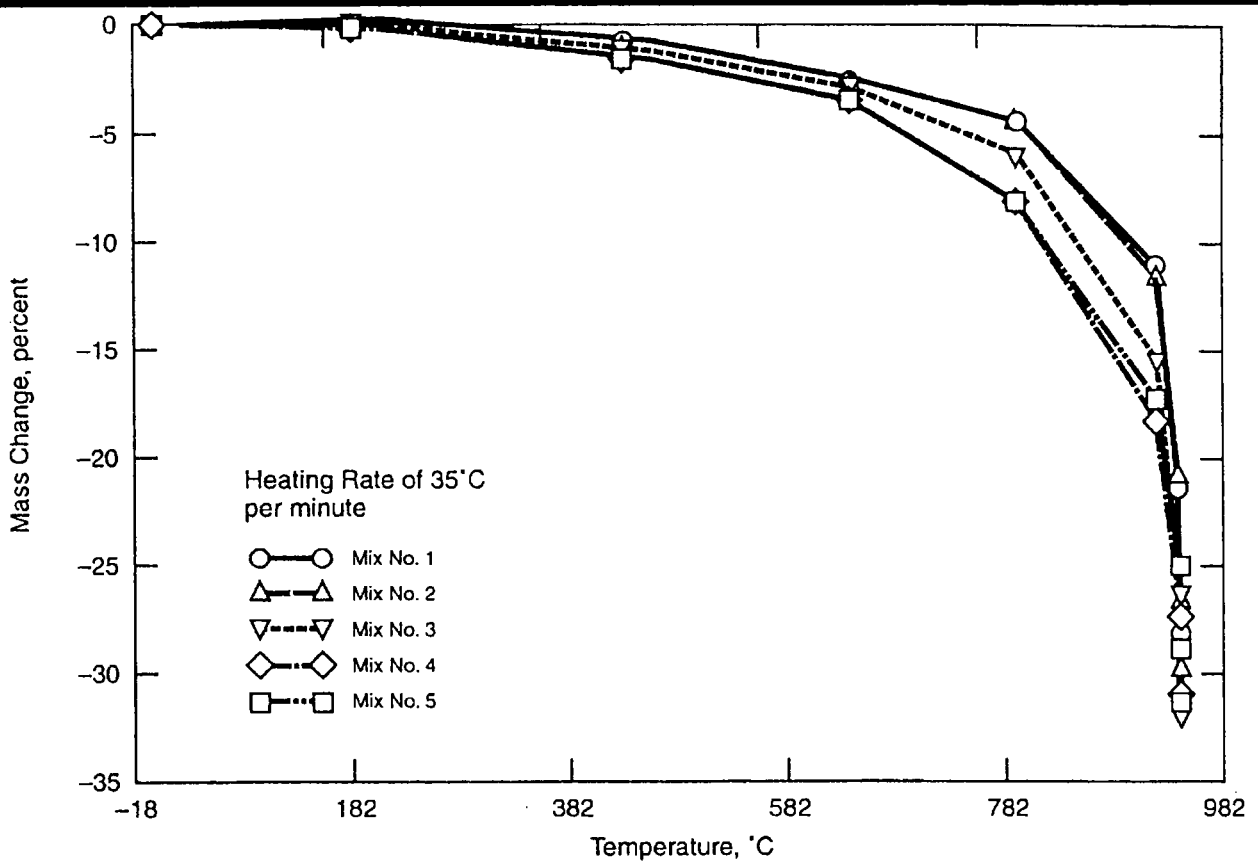

Figure 8. Mass loss of high strength concrete at elevated temperatures [47-48]

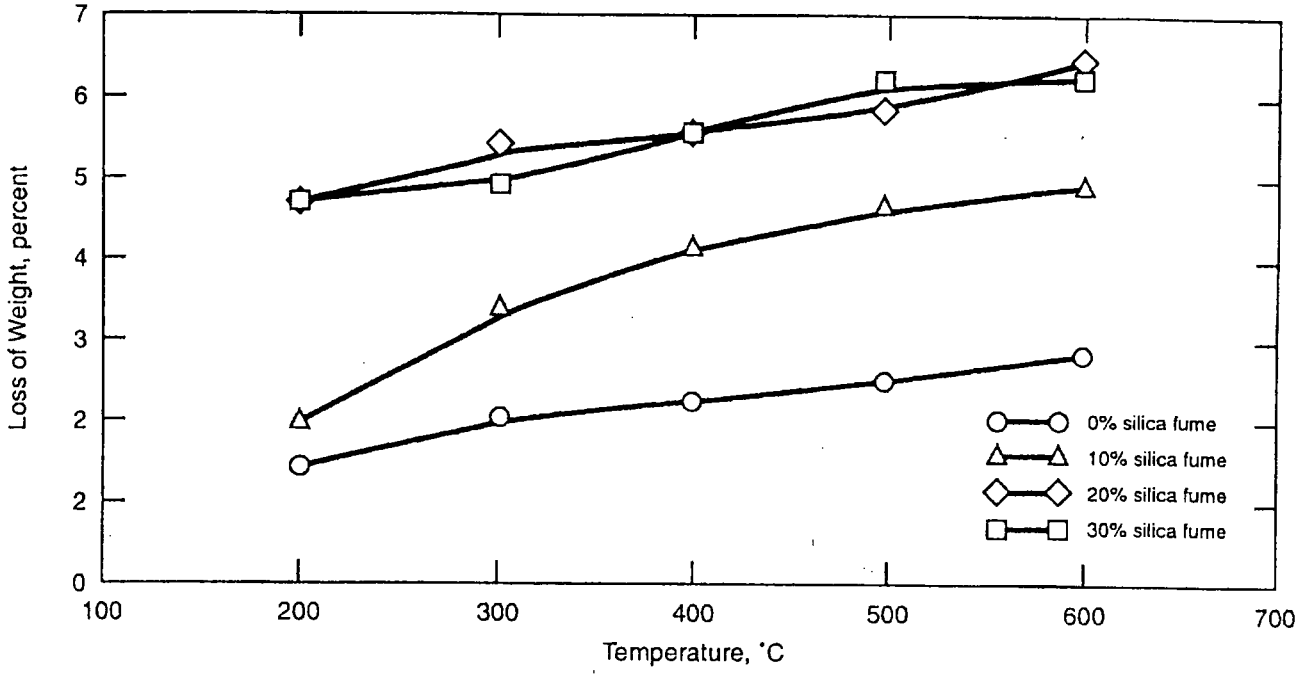

Figure 9. Change of weight with temperature of concrete containing silica fume [46].

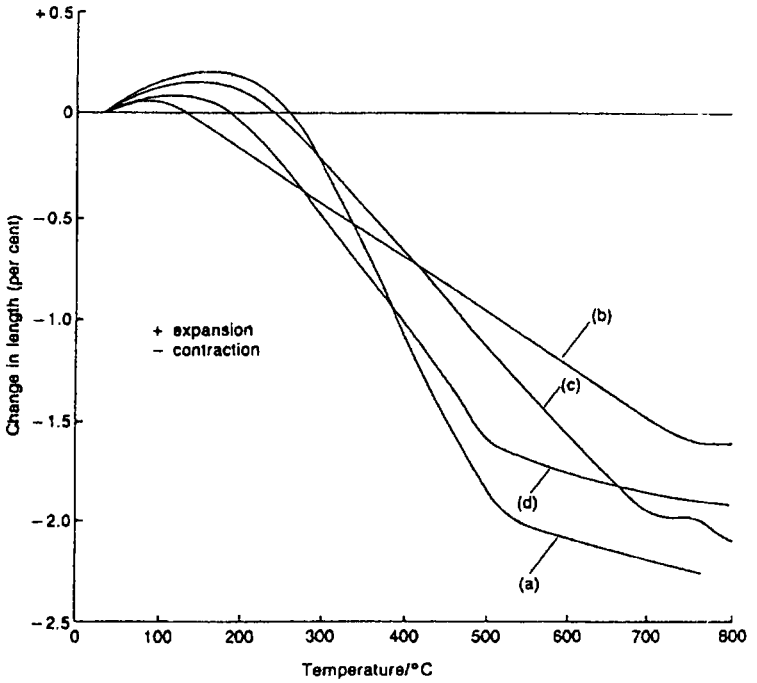

Figure 10. Length change of Portland cement paste specimens at various temperatures: (a) Philleo (1958); (b) Harada *et al.* (1972); Cruz and Gillen (1980); (d) Crowley (1956) [45].

Name	Symbol	Geological Origin	Composition	Density (kg/m^3)	Grain size (mm)
Anorthosite	AN	Igneous	Almost all plagioclase feldspars	2770	0.05-20
Basalt	BA	Igneous	Mainly epidotes, pyroxenes and plagioclase feldspars	3040	0.005-0.08
Dolomite	DO	Sedimentary	Almost all dolomite	2490	0.1-7
Granodiorite	GD	Igneous	Plagioclase feldspars, quartz amphiboles and micas	2750	0.05-4
Granite	GR	Igneous	Mainly potash and plagioclase-feldspars, quartz	2620	0.05-5
Limestone	LI	Sedimentary	Mainly calcite	2700	0.002-2
Quartz Monzonite	QM	Igneous	Mainly potash and plagioclase-feldspars and quartz	2645	0.5-7
Quartz	QR	Igneous	All quartz	2650	0.2-10
Rhyolite	RH	Igneous	Mainly potash and plagioclase-feldspars, and quartz	2640	0.05-3
Syenite	SY	Igneous	Mainly potash and plagioclase-feldspars, and amphiboles	2715	0.1-10

Table 3. Some characteristics of the ten rocks whose dilatometric curves are shown in Figure 11 (Geller, *et al.* 1962) [41].

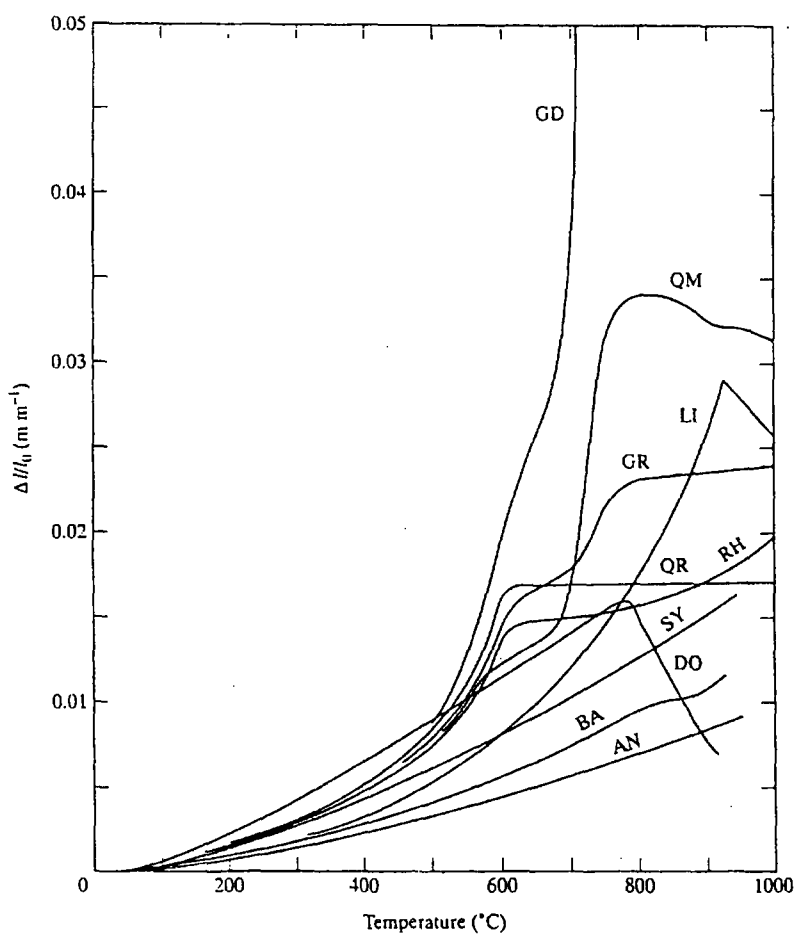

Figure 11. Dilatometric curves for the ten rocks described in Table 3 (Geller, *et al.* 1962) [41].

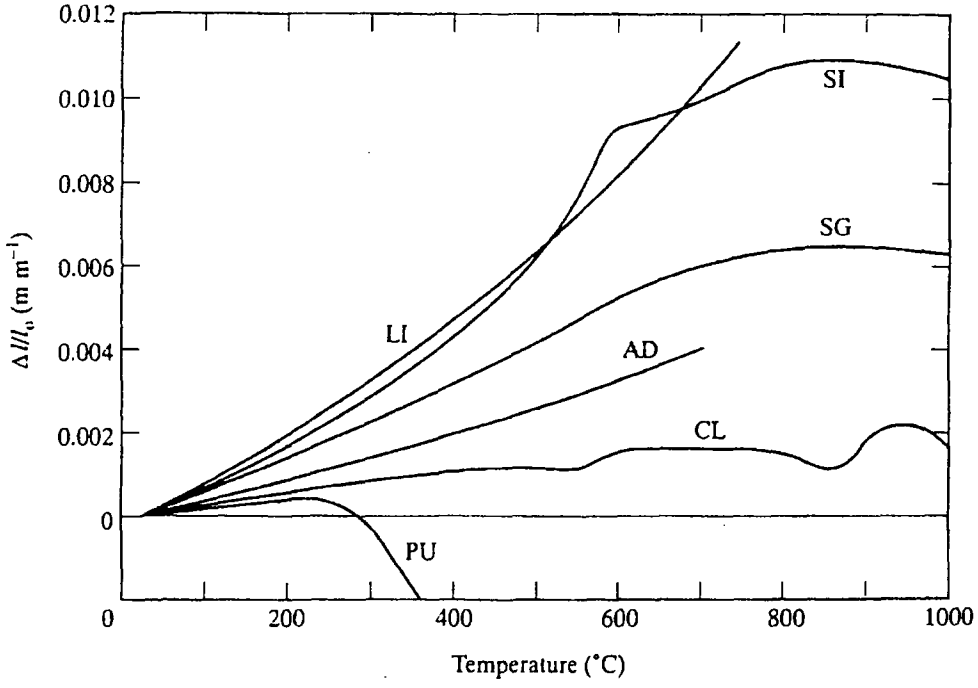

Figure 12. Dilatometric curves for three normal-weight concretes and three lightweight concretes. Aggregates: LI, limestone; SI siliceous rock; AD, andesite; SG, expanded shale; CL, expanded clay; PU, pumice (Harada, *et al.* 1972; Harmathy and Allen 1973) [41].

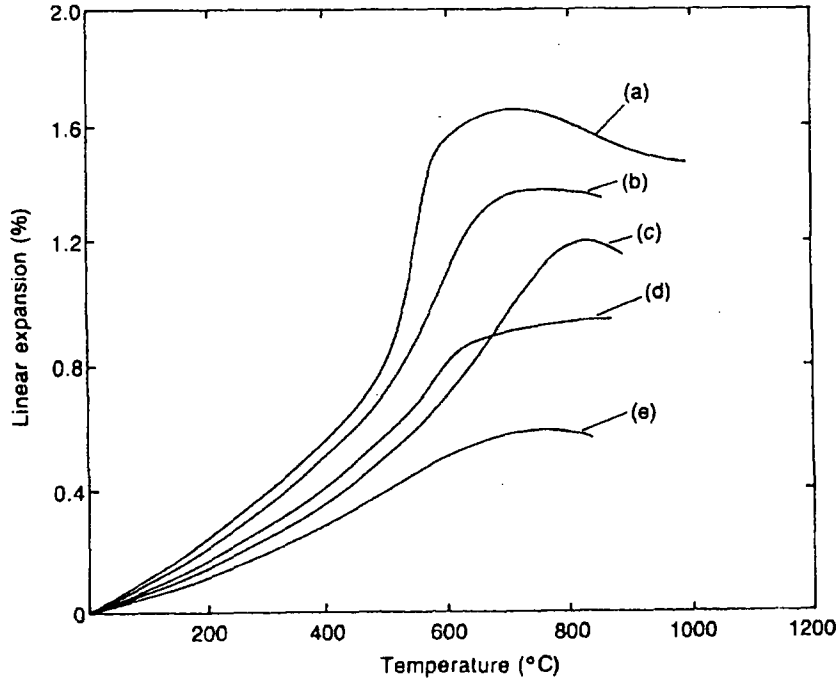

Figure 13. Linear thermal expansion of concretes made with various conventional aggregates, as a function of temperature (adapted from Schneider (1982)): (a) quartzite; (b) sandstone; (c) limestone; (d) basalt; (e) expanded slag [45].

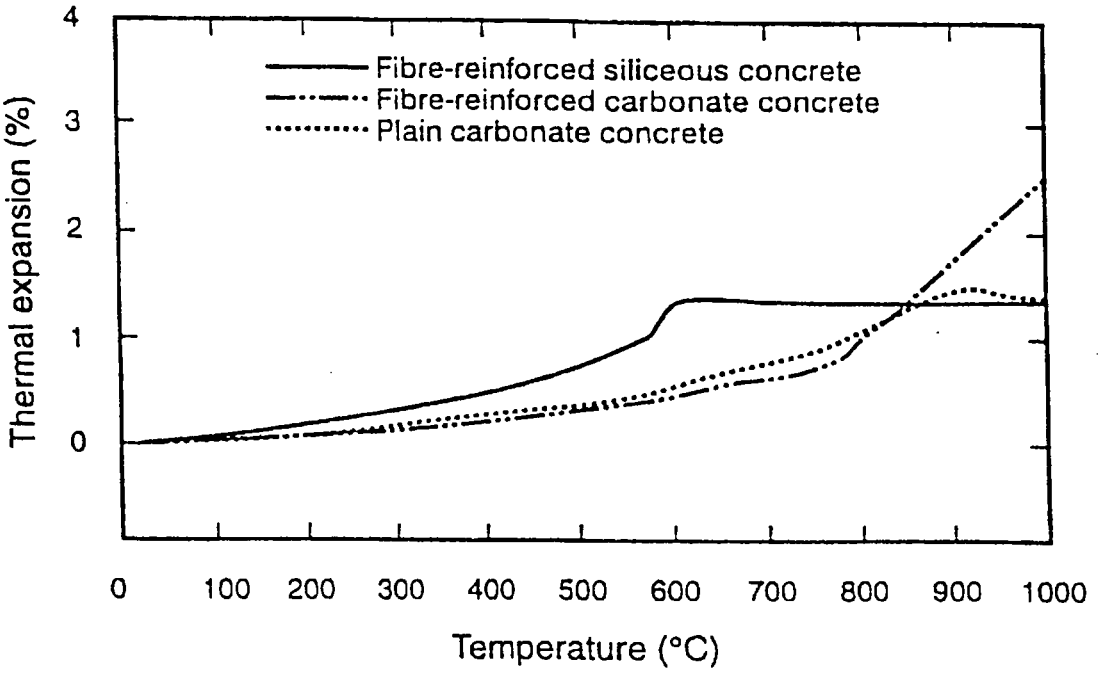

Figure 14. Thermal expansion, as a function of temperature, of the three concrete types described in Table 1 [44].

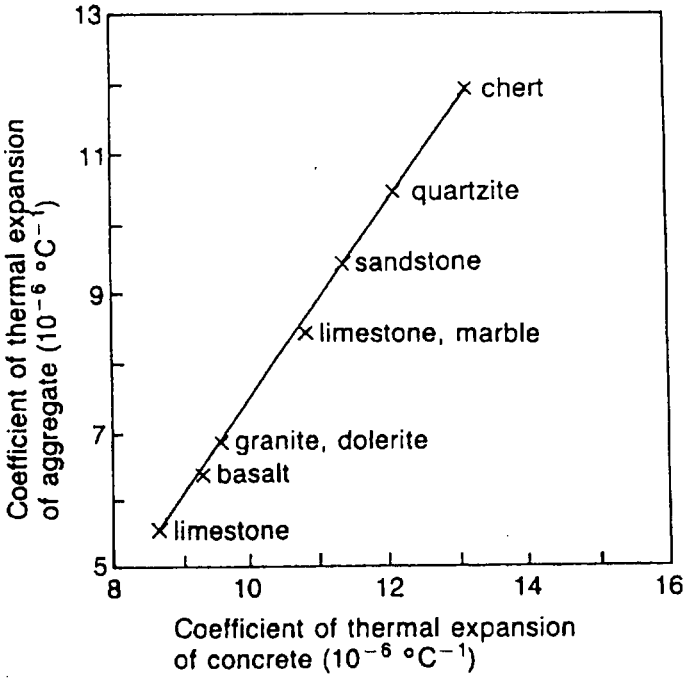

Figure 15. Correlation between the coefficient of thermal expansion of the aggregate and that of the concrete [45].

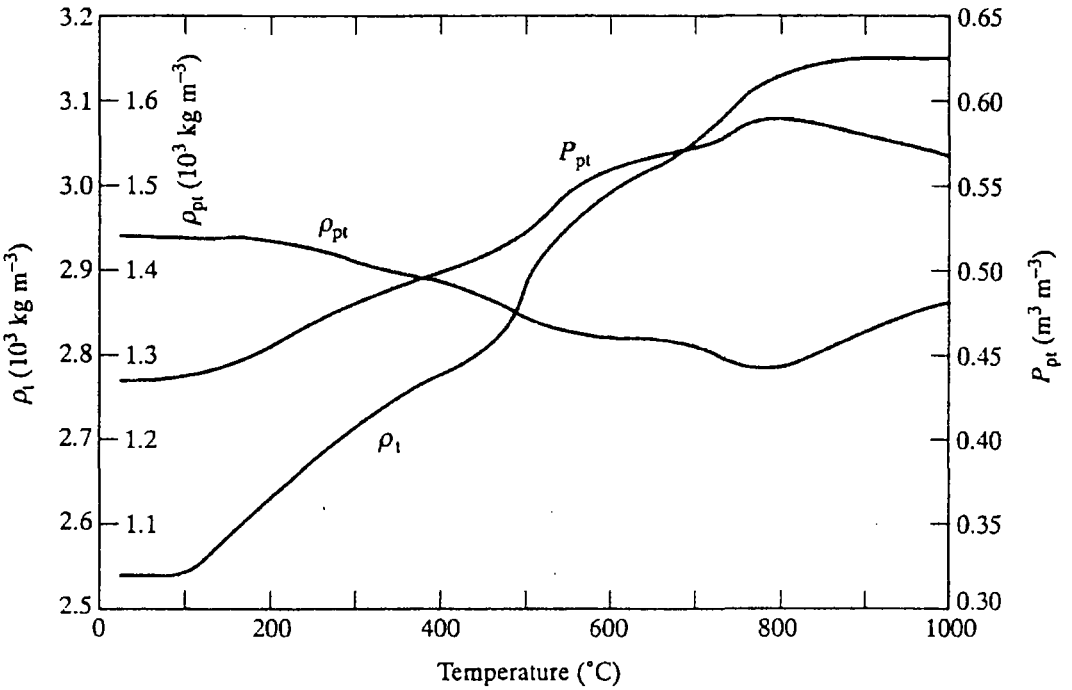

Figure 16. True density (ρ_t), bulk density (ρ_{pt}), and porosity (P_{pt}) of Cement Paste C (calculated): note the different scales for the three properties [27,41].

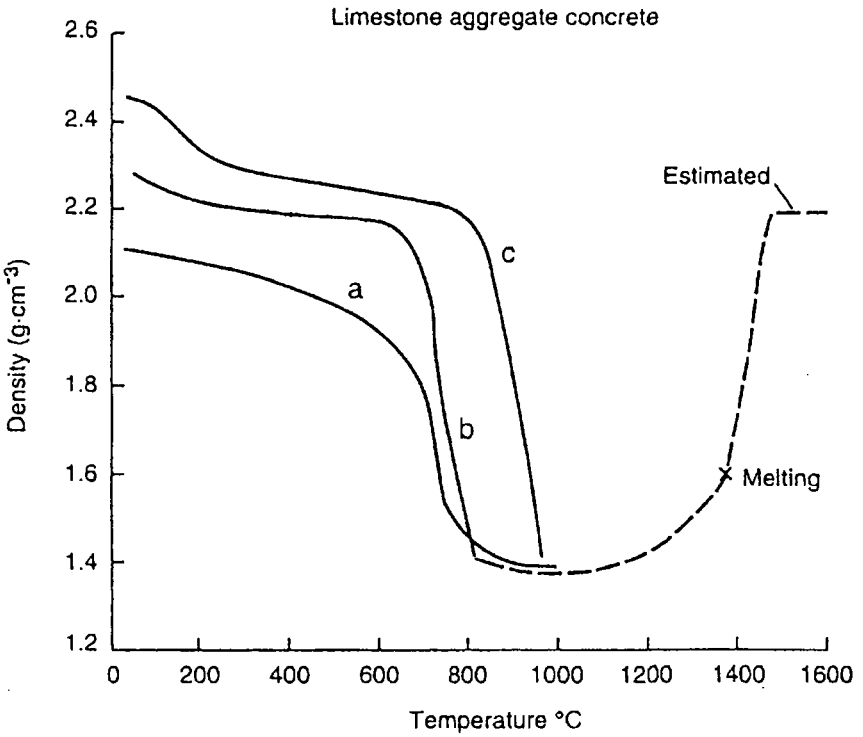

Figure 17. Effect of temperature on density of concrete made with limestone aggregate (Schneider, 1982): (a) Harmathy and Allen (1973); (b) cured at 20 °C and 65 percent RH (Schneider, 1982); (c) water cured (Schneider, 1982) [45].

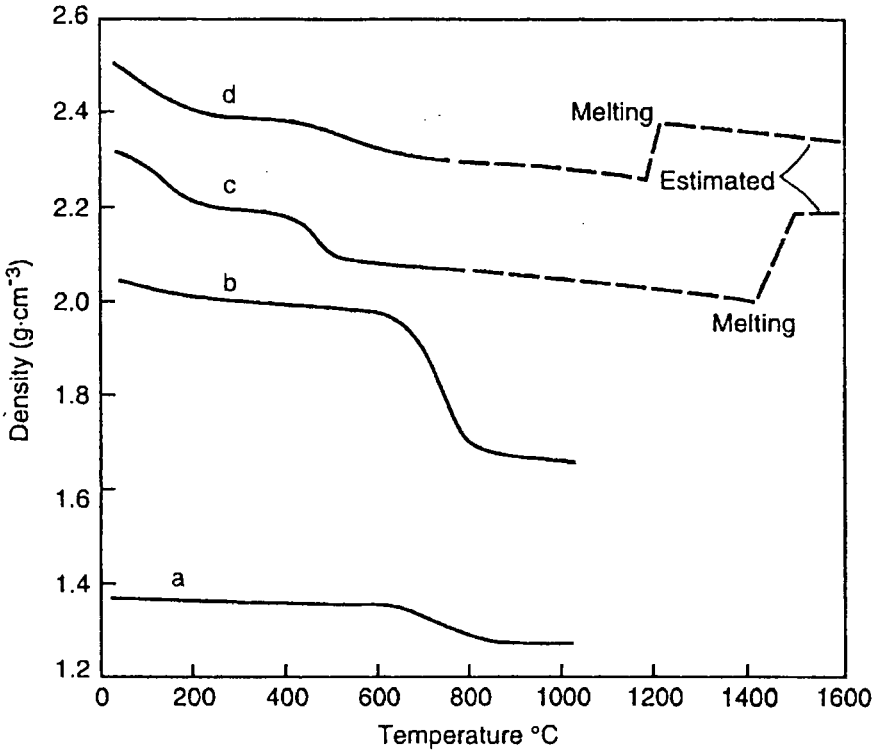

Figure 18. Effect of temperature on mass density of concretes made with quartzite, bauxite, and expanded shell aggregates: (a) expanded shale aggregate concrete (Harmathy and Allen, 1973); (b) siliceous aggregate concrete (Harmathy and Allen, 1973); (c) quartzite aggregate concrete (Schneider, 1982); (d) basalt aggregate concrete (Schneider, 1982) [45].

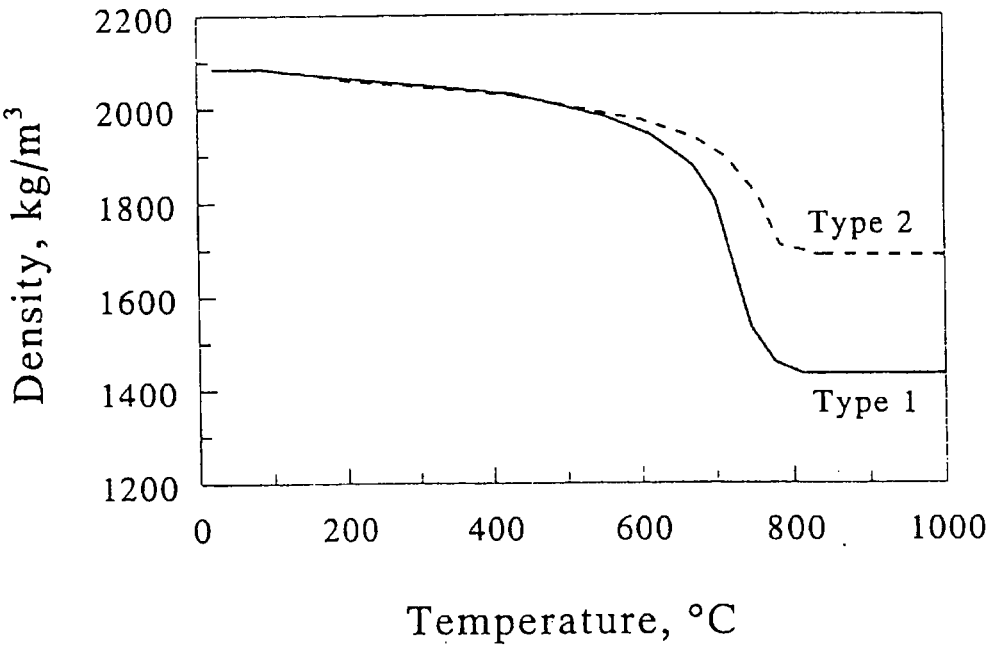

Figure 19. Density versus temperature curves used in the Ahmed model (see text).

3.2 Enthalpy, Specific Heat, and Heats of Reaction

The enthalpy or the specific heat, the derivative of enthalpy with respect to temperature, and the heats of reaction of any chemical reaction are required for modeling heat and mass transfer through concrete. These quantities are briefly discussed on pp. 5-6 of this report. Their inclusion in various models is indicated in Section 2.

Harmathy [27,41] has developed detailed procedures, which are briefly addressed in Section 4.2 of this report, for predicting the specific heat of cement paste and of concrete. Figure 20 shows his predicted specific heats for three different cement pastes; Figure 21 shows his later experimental results for those same cement pastes. The large peaks near 500 °C correspond to the release of bound water. The width and height of such peaks will depend significantly on the heating rate; the area under the curve represents the total energy absorption or release associated with a chemical reaction and thus will be much less dependent upon the heating rate. Some the models for predicting heat and mass transfer through concrete or other materials do not include the latent heat of reaction in the specific heat of the material but treat it separately. Thus, one must be careful to select the "proper" specific heat for use in a particular model.

Fu and Chung [50] recently published room temperature values of the specific heat of cement paste with various admixtures. For a plain cement paste with a water/cement ratio of 0.45, the density was 1.99 g/cm^3 and the specific heat was 0.703 J/g•K, corresponding to a volumetric heat capacity of 1.40 J/cm^3•K. A cement paste with 15 percent (by weight of cement) silica fume, 3 percent (by weight of cement) water reducing agent, and a water cement ratio of 0.35 had a density of 1.72 g/cm^3 and a specific heat of 0.765 J/g•K, corresponding to a volumetric heat capacity of 1.32 J/cm^3•K.

Figure 22 shows the volumetric specific heats that Harmathy [27,41] computed for four hypothetical concretes that he believed were "limiting cases," at least with regard to thermal conductivity. It is seen that the computed volumetric specific heats are very nearly identical for the two normal-weight concretes, one of which (Concrete 1) had crystalline quartz aggregate while the other one had crystalline anorthosite aggregate.

Figures 23 and 24 show the specific heat (per unit mass) of various types of Portland cement concrete as functions of temperature. Curve 6 in Figure 23 appears questionably low at higher temperatures. The curve for plain carbonate concrete in Figure 24 clearly shows the heat absorbed at high temperatures when the carbonate converts to the oxide with carbon dioxide being released. Note also, in this figure, that the specific heat is significantly lower at temperatures above this transition than it is at temperatures just below the carbonate decomposition temperature. Figure 25 shows the specific heat versus temperature curves used in the version of the Ahmed model that is currently available at NIST. As stated on p. 17, Type 1 concrete has a carbonate aggregate and Type 2 a siliceous aggregate. Both of these curves appear to be in error at high temperatures. For the Type 1 concrete, the specific heat should drop drastically from the peak at temperatures near 800 °C, in a manner similar to that seen for carbonate concrete in Figure 24. For the Type 2 concrete, there is no apparent reason to expect a high-temperature peak at all.

(Text continued on p. 37)

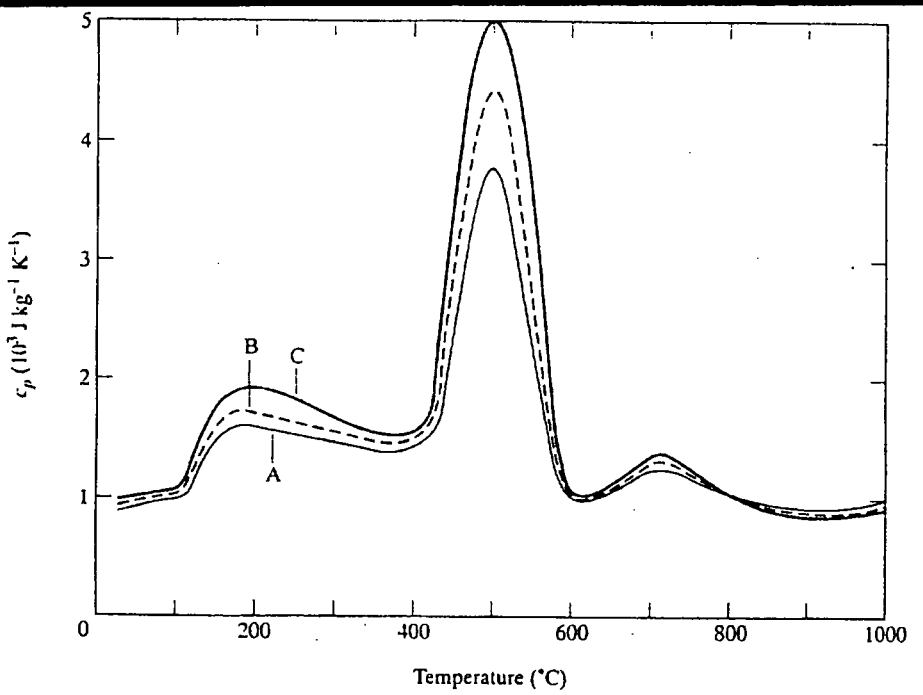

Figure 20. Computed specific heat of Model Pastes A, B, and C [27,41].

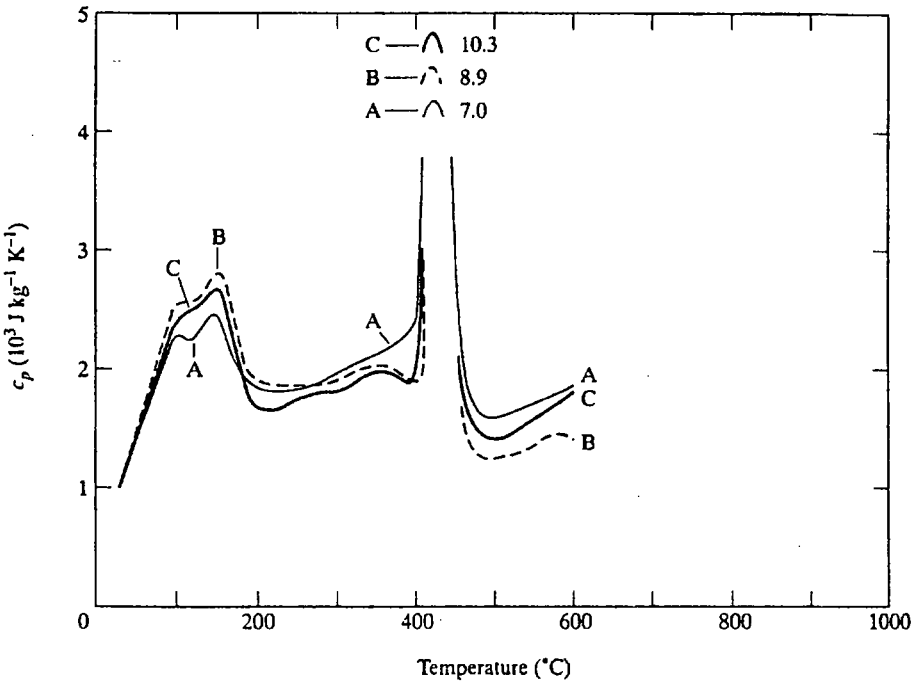

Figure 21. Measured specific heat of Cement Pastes A, B, and C [41].

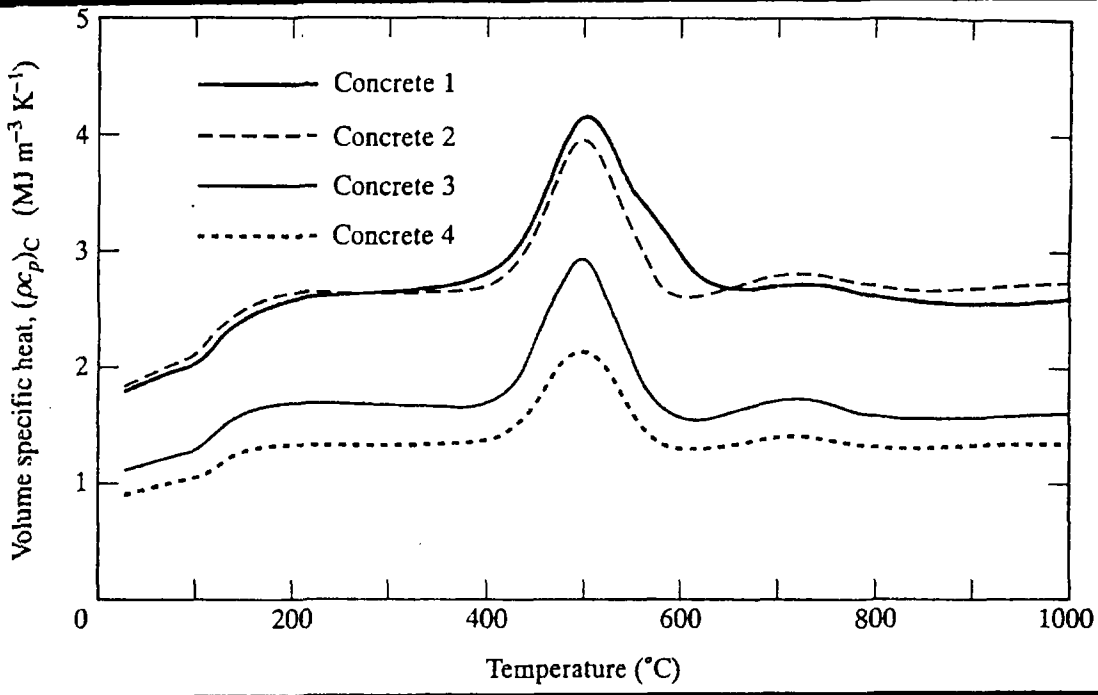

Figure 22. Volumetric specific heats (computed) for four hypothetical concretes: normal-weight, Concretes 1 and 2; lightweight, Concretes 3 and 4 [27,41].

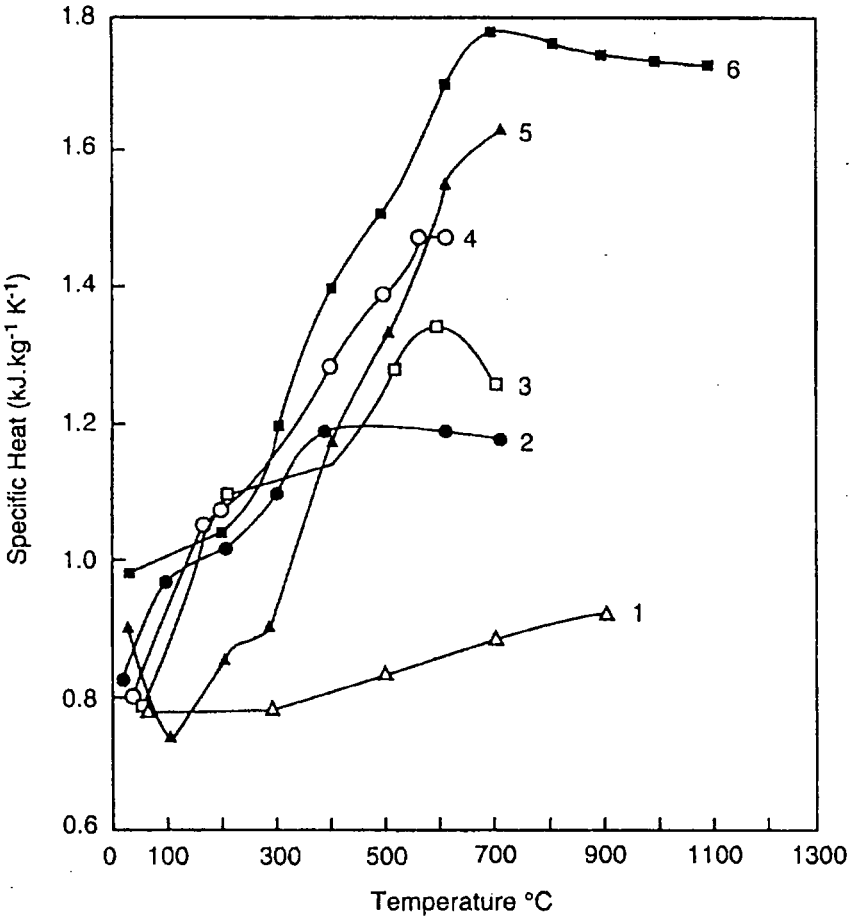

Figure 23. Effects of temperature on measured specific heats of various concretes: (1) granite aggregate concrete (Ödeen, 1968); (2) limestone aggregate concrete (Collet and Tavernier, 1976); (3) limestone aggregate concrete (Harmathy and Allen, 1973); (4) siliceous aggregate concrete (Harmathy and Allen, 1973); (5) limestone aggregate concrete (Hildenbrand, *et al.*, 1978); (6) siliceous aggregate concrete (Hildenbrand, *et al.*, 1978) [45].

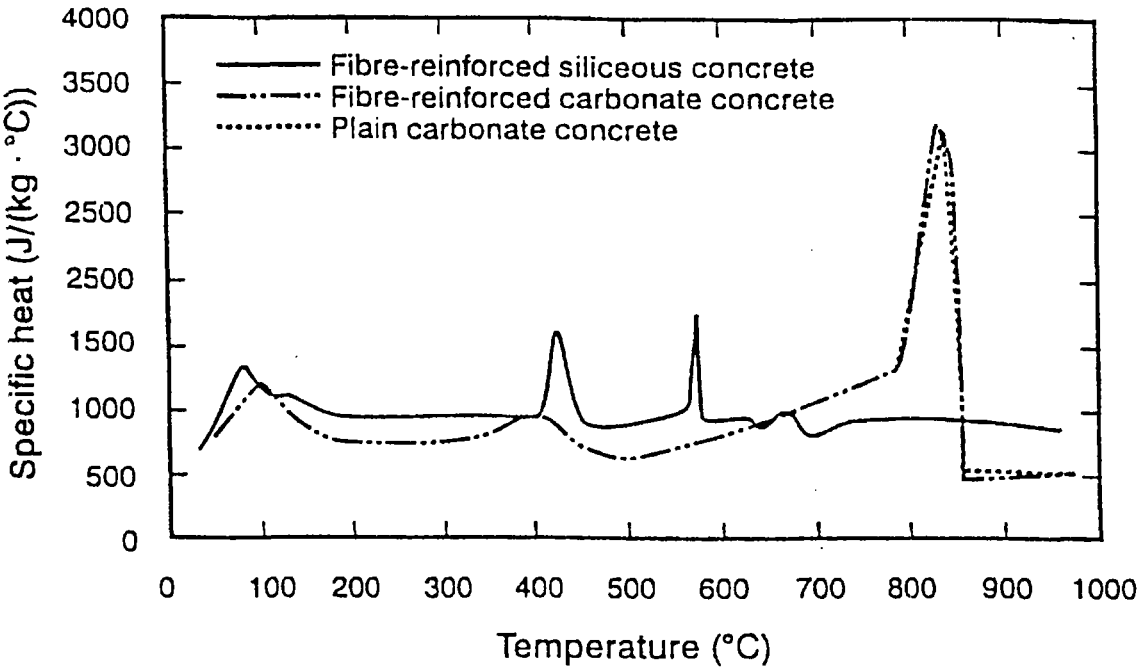

Figure 24. Specific heat, as a function of temperature, of the three concrete types described in Table 1 [44].

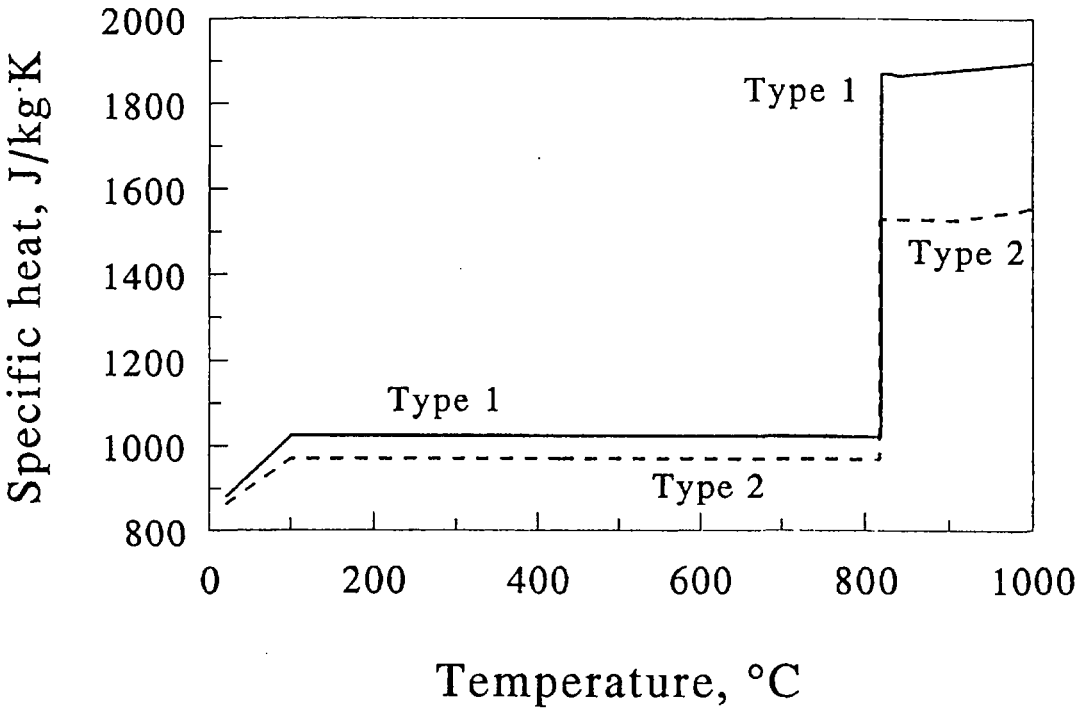

Figure 25. Specific heat versus temperature curves used in the Ahmed model (see text).

3.3 Thermal Conductivity and Thermal Diffusivity

Thermal conductivity is a key thermal property in predicting heat and mass transport in concrete exposed to fire conditions. As mentioned on p. 5, thermal diffusivity can be used if there are no mechanisms of heat transfer other than conduction and if the thermal conductivity can be considered to be constant. For modeling simultaneous heat and mass transfer, thermal diffusivity, in general, should not be used. However, rather than to measure thermal conductivity directly, many investigators have chosen to measure thermal diffusivity and then compute thermal conductivity from the thermal diffusivity and the specific heat.

Harmathy determined the thermal conductivities of several cement pastes, which have significant porosity and cracks, over a wide temperature range and then extrapolated these results to obtain an estimate of the thermal conductivity of a hypothetical pore-less cement paste, as shown in Figure 26. This curve can then be used to estimated the thermal conductivity of pastes of various porosities.

Fu and Chung measured the room-temperature specific heat, thermal diffusivity, and density of a plain cement paste and one containing silica fume (see p. 32 of this report for compositions) and then computed the thermal conductivity. The measured thermal diffusivities of the plain cement paste and the silica fume cement paste were 0.37 mm^2/s and 0.27 mm^2/s, respectively. The corresponding thermal conductivities were 0.52 W/m•K and 0.36 W/m•K, respectively, indicating that the higher porosity of the silica fume cement paste resulted in the room-temperature thermal conductivity being lowered by about 30 percent.

Figure 27 shows the thermal conductivity of 15 rocks and minerals at temperatures up to 300 °C; these materials are described in Table 4. Harmathy based his "limiting cases," discussed briefly on p. 32 of this report, for the thermal conductivity of concrete by selecting Curve QS (quartzitic sandstone) and Curve AN (anorthosite) as the thermal conductivity of the aggregates. The thermal conductivity of rocks and minerals can vary widely depending upon the source and the porosity. Touloukian, *et al.* [51] provide extensive data on the thermophysical properties of rocks, taken from the literature through the mid-1970s. They comment that because the properties of rocks and minerals can vary widely over relatively small distances and because the specimens used for thermophysical property measurements are relatively small, the measured properties can vary widely on specimens taken from nominally the same location. Figure 28 is a histogram showing the variation in the room-temperature thermal conductivity of limestone samples taken from two locations. It is clear that tests on numerous samples would be required to obtain statistically significant results.

Figure 29 shows the thermal conductivity of limestone, versus temperature, as measured by three different investigators. The two curves on samples taken in Nazareth, Pa., were from the same study as the curves shown in Figure 27.

Figure 30 shows the measured roon-temperature thermal conductivity of several different types of concrete, plotted versus the moisture content. These data were taken using a hot-wire method that allows measurements to be completed before the moisture has time to migrate significantly. It is seem that 10 percent moisture content can cause the thermal conductivity to be roughly doubled.

Obviously, this effect would be much smaller at higher temperatures. However, as pointed out by Thompson [60] many years ago, and as is known by competent workers in the field of thermal conductivity, it is very difficult to obtain values of thermal conductivity without some moisture movement and/or drying out occurring.

The thermal conductivity of concrete will depend upon the porosity of the cement paste and upon the type, quantity, and porosity of aggregates. Figure 31 shows one set of data indicating how the thermal conductivity of different types of concrete varies with porosity.

The thermal conductivity of concrete is known to show considerable hysteresis, although there appear to have been very few quantitative studies of this effect. Figure 32 indicates one set of data indicating how the thermal conductivity of a concrete changes due to the loss of moisture of hydration.

There has been considerable variation in thermal conductivity values reported by different investigators on nominally similar concretes. Part of the variations seen may be attributed to sample differences but it appears quite likely that large experimental errors have occurred in some cases. Figures 33 and 34 shown the thermal conductivity of, respectively, limestone-aggregate concrete and siliceous aggregate concrete.

Figures 35-37 show the thermal conductivity of different types of normal-strength concrete as functions of temperature.

In Section 3.1 curves were shown of the mass loss versus temperature of five high-strength concretes studied by investigators at the Portland Cement Association (PCA). The constituents of these materials were shown in Table 2. Figure 38 shows the thermal conductivity values obtained for these materials using a guarded hot plate apparatus. Thermal conductivity data on these materials were also obtained, by a different testing laboratory, using a hot-wire method (ASTM C1113). In addition, thermal diffusivity data were obtained by the same testing laboratory using a radial heat flow method and then thermal conductivity values were computed, apparently using specific heat values computed from the specific heats of the several components of the concrete. For one of these high-strength concretes, the three sets of thermal conductivity values are shown plotted in Figure 39. The differences are rather startling.

Figure 40 shows the thermal conductivity versus temperature curves used in the version of the Ahmed model that is currently available at NIST (one obvious typo in the program was corrected).

Turning to thermal diffusivity, Figure 41 shows the range of values for the thermal diffusivity of limestone from three different investigations.

Figures 42-46 show thermal diffusivity versus temperature for a number of types of normal-strength concrete. Figure 47 shows thermal diffusivity data obtained at PCA on the five high-strength concretes described in Table 2; these data were obtained in their guarded hot plate apparatus, run in a transient mode with the hot plate removed. For one of these samples, these data are shown in Figure 48 along with data obtained elsewhere by the radial heat flow method mentioned above.

(Text continued on p. 55)

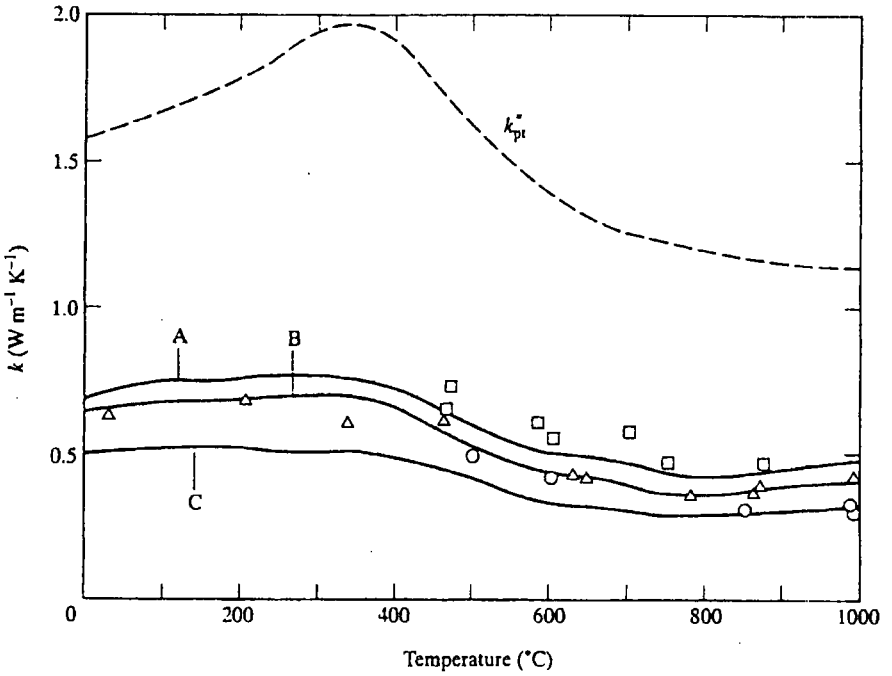

Figure 26. Thermal conductivities of Cement Pastes A, B, and C (points and solid-line curves), and thermal conductivity of a hypothetical pore-less cement paste (broken-line curve): □, Paste A; open triangle, Paste B; ○, Paste C [27,41].

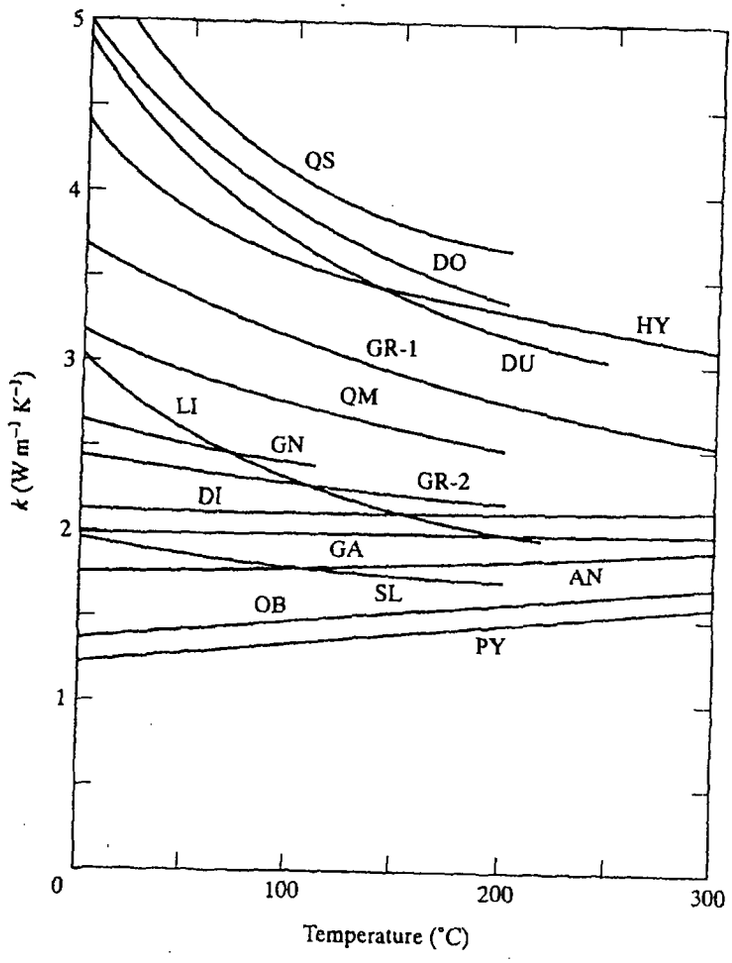

Figure 27. Thermal conductivity of 15 materials (rocks, minerals, glass) described in Table 4 (Birch and Clark 1940) [41].

Name	Symbol	Geological origin	Composition	Density (kg/m^3)	Mean grain size (mm)
Anorthosite	AN	Igneous	Almost all plagioclase feldspars	2700	0.5
Diabase	DI	Igneous	Mainly plagioclase feldspars and pyroxenes	2960	0.5
Dolomite	DO	Sedimentary	Carbonate group	2830	0.01
Dunite	DU	Igneous	Almost all olivines	3250-3270	1.0
Gabbro	GA	Igneous	Mainly plagioclase feldspars, pyroxenes and olivines	2860-2880	3.0
Gneiss	GN	Metamorphic	Layered mineral, mainly feldspar and quartz	2640	0.2
Granite-1	GR-1	Igneous	Mainly potash feldspars and quartz	2610	1.5-2.0
Granite-2	GR-2	Igneous	Mainly potash and plagioclase-feldspars, quartz	2640	0.5
Hypersthenite	HY	Igneous	Pyroxene group	3290	2.0
Limestone	LI	Sedimentary	Carbonate group, mainly calcite	2610	0.001-0.01
Obsidian	OB	Igneous	Glassy potash feldspar and quartz	2440	
Pyrex	PY	Artificial		2230	
Quartz monzonite	QM	Igneous	Mainly potash and plagioclase-feldspars and quartz	2640	1.0
Quartzitic sandstone	QS	Sedimentary	Mainly quartz	2640-2650	0.3
Slate	SL	Metamorphic	Layered clay minerals	2760	

Table 4. Some characteristics of the 15 materials (rocks, minerals, glass) whose thermal conductivity are plotted in Figure 27 (Birch and Clark, 1940) [41].

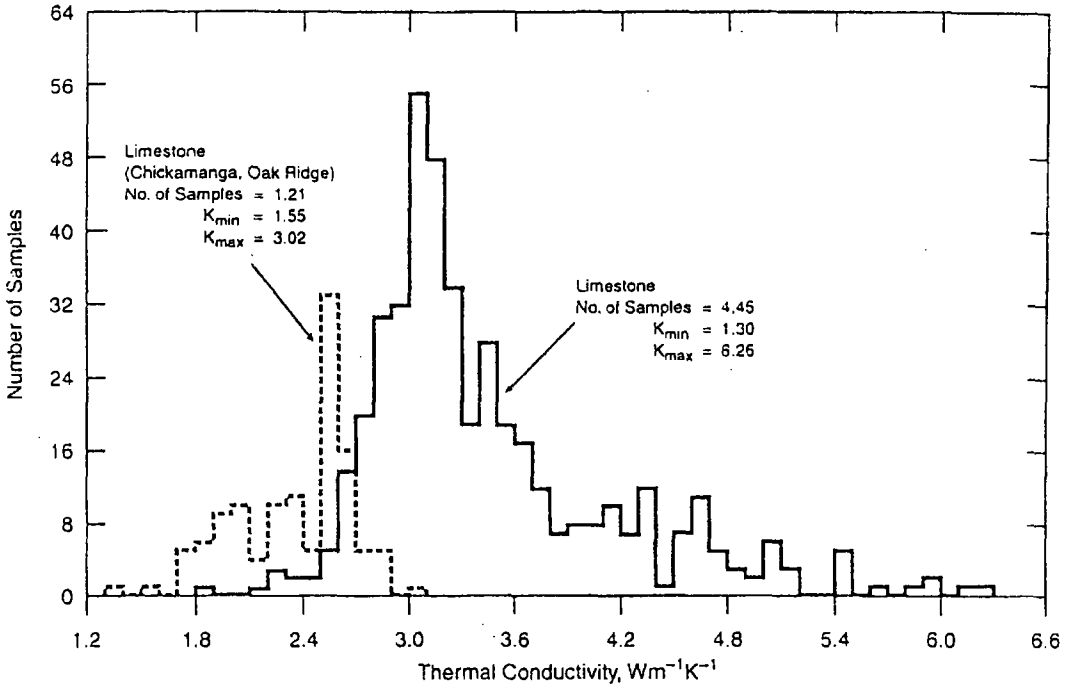

Figure 28. Histogram of the thermal conductivity of limestones [51].

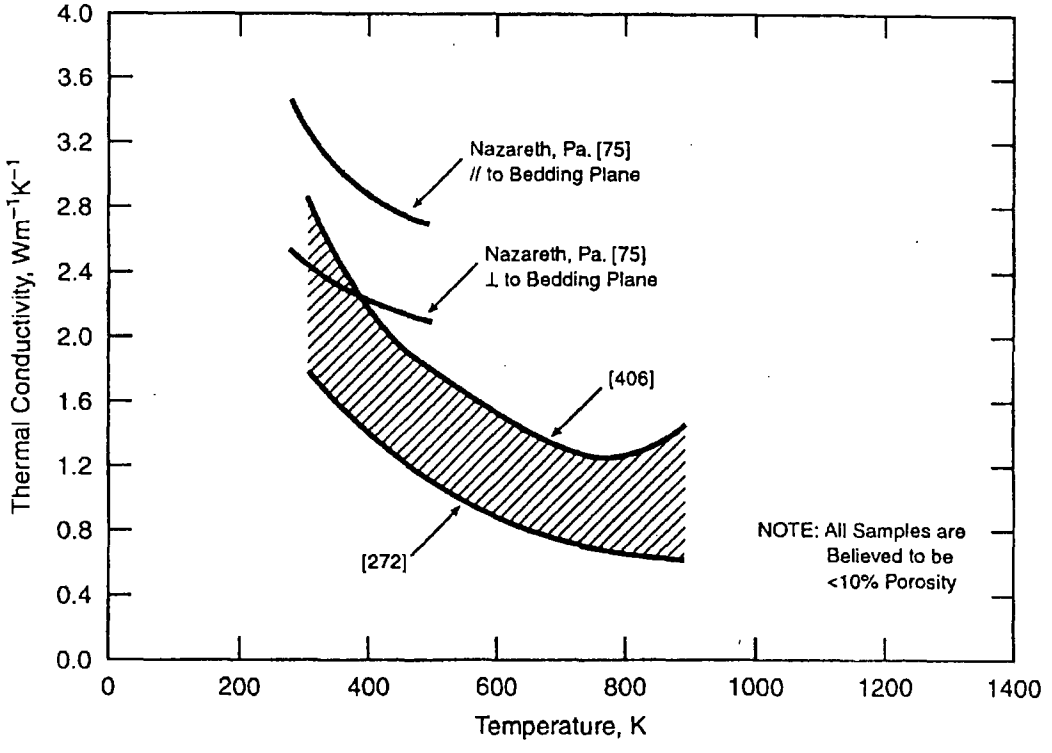

Figure 29. Thermal conductivity of limestones [51].

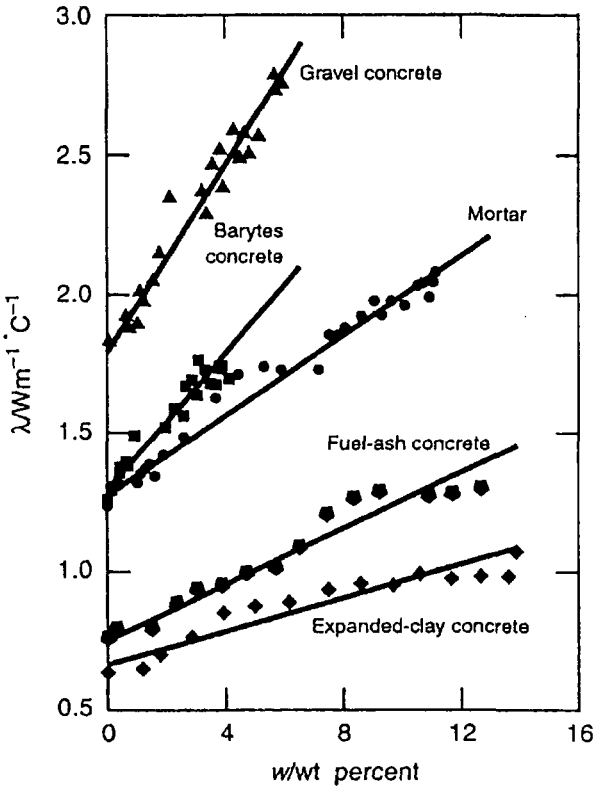

Figure 30. Plot of thermal conductivity against the moisture content of concrete [40].

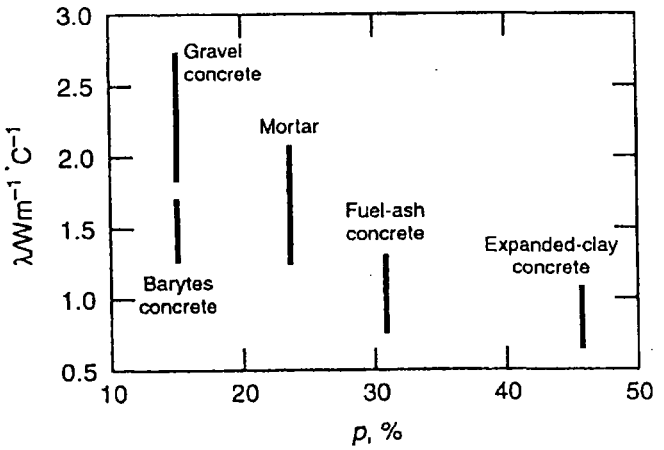

Figure 31. Variation range of thermal conductivity of concretes, plotted against the porosity [40].

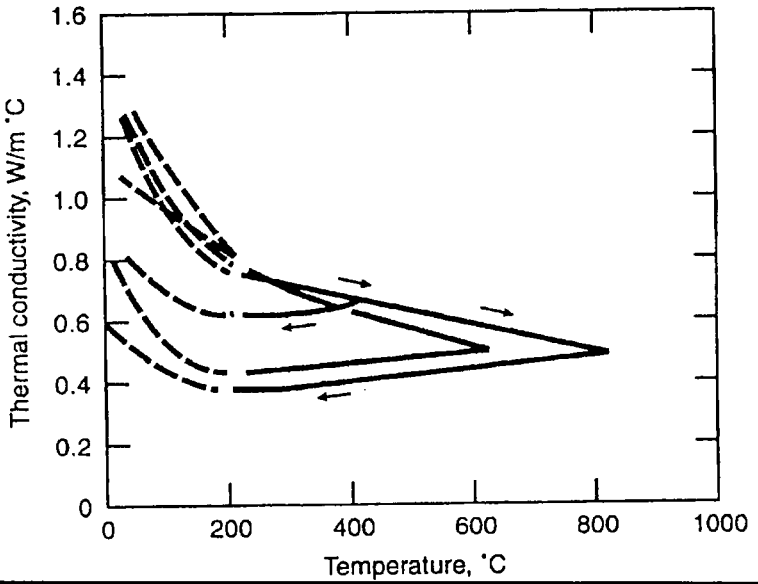

Figure 32. Thermal conductivity of granite-aggregate concrete as a function of temperature under heating and subsequent cooling [32].

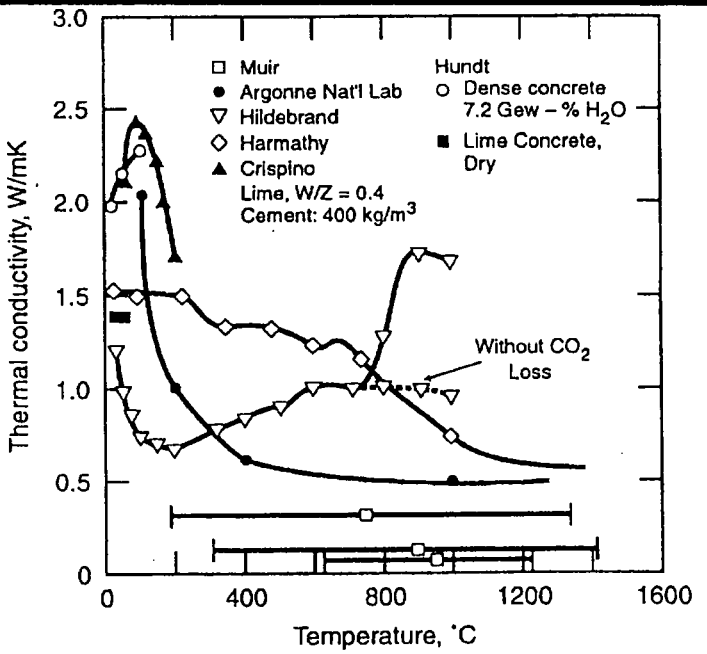

Figure 33. Thermal conductivity of limestone-aggregate concretes [35].

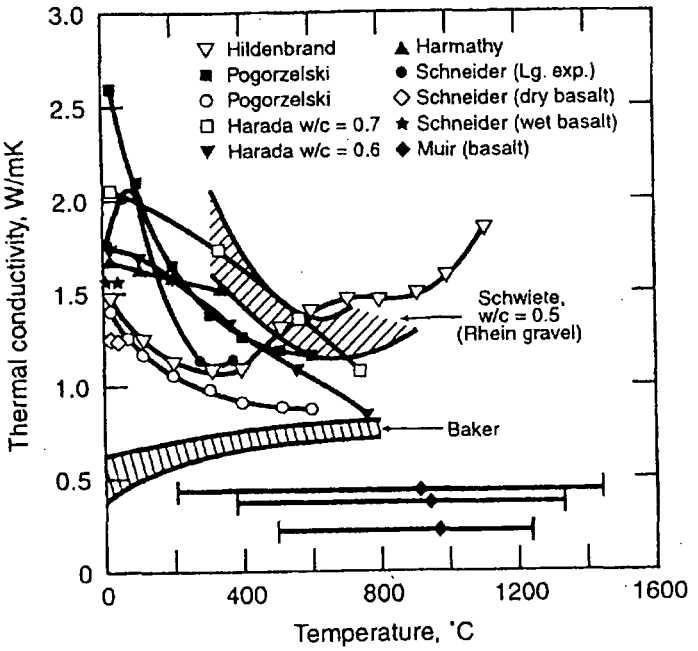

Figure 34. Thermal conductivity of siliceous-aggregate concretes [35].

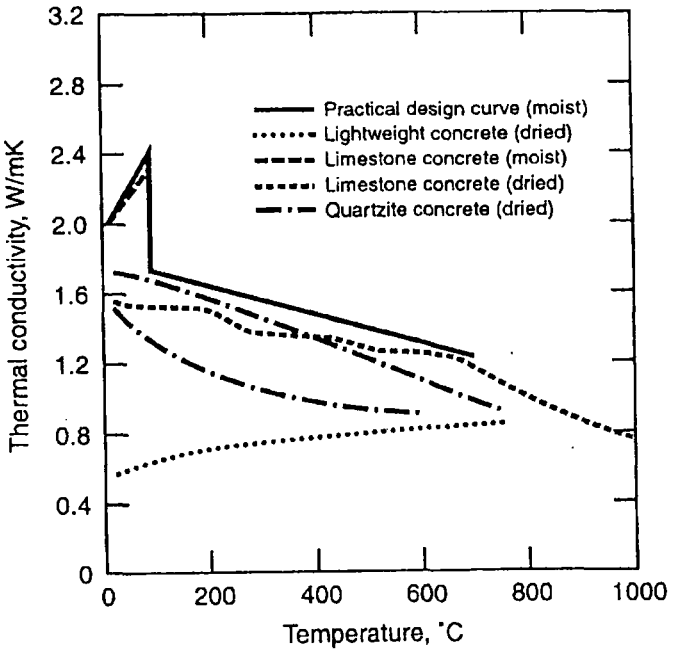

Figure 35. Thermal conductivity of different structural concretes [38].

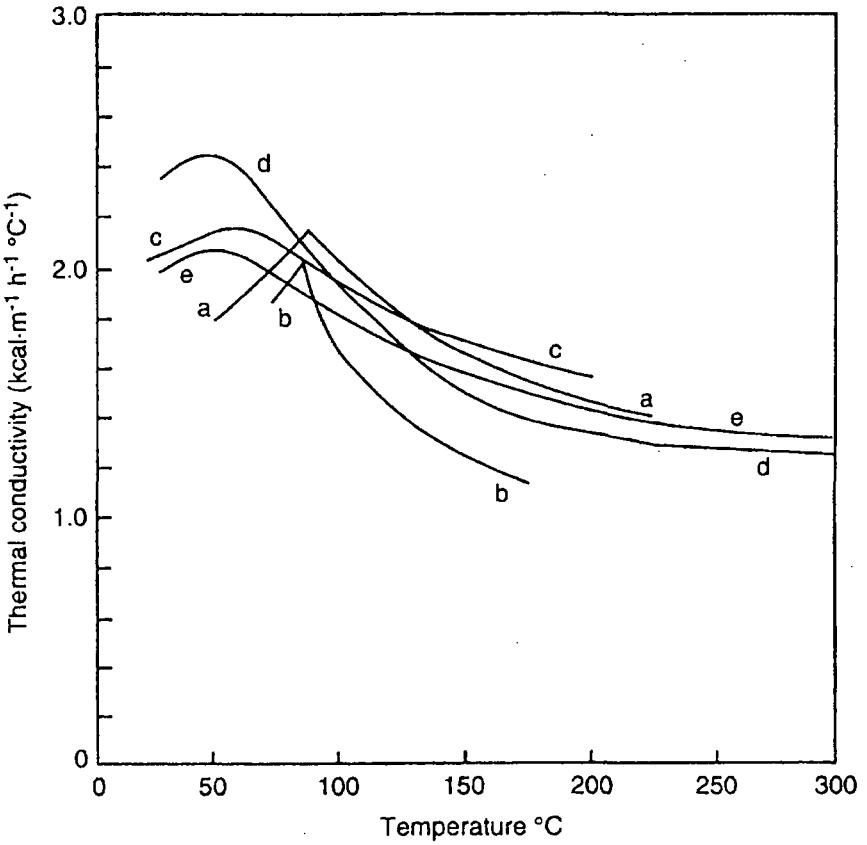

Figure 36. Thermal conductivity of various concretes that were not oven-dried before test, as a function of temperature: (a) limestone aggregate concrete (Crispino, 1972); (b) barytes aggregate concrete (Crispino, 1972); (c) gravel aggregate concrete (Abe, *et al.*, 1972); (d) quartzite aggregate concrete (Maréchal, 1972); (e) quartzite aggregate concrete (Maréchal, 1972) (1 kcal m^{-1} h^{-1} $°C^{-1}$ = 1.16 W/m•K) [45].

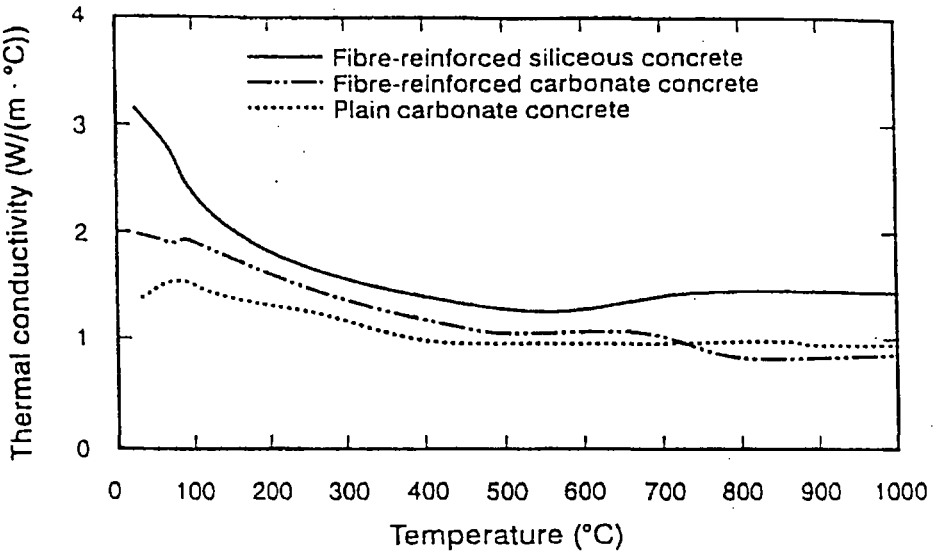

Figure 37. Thermal conductivity, as a function of temperature, of the three concrete types described in Table 1 [44].

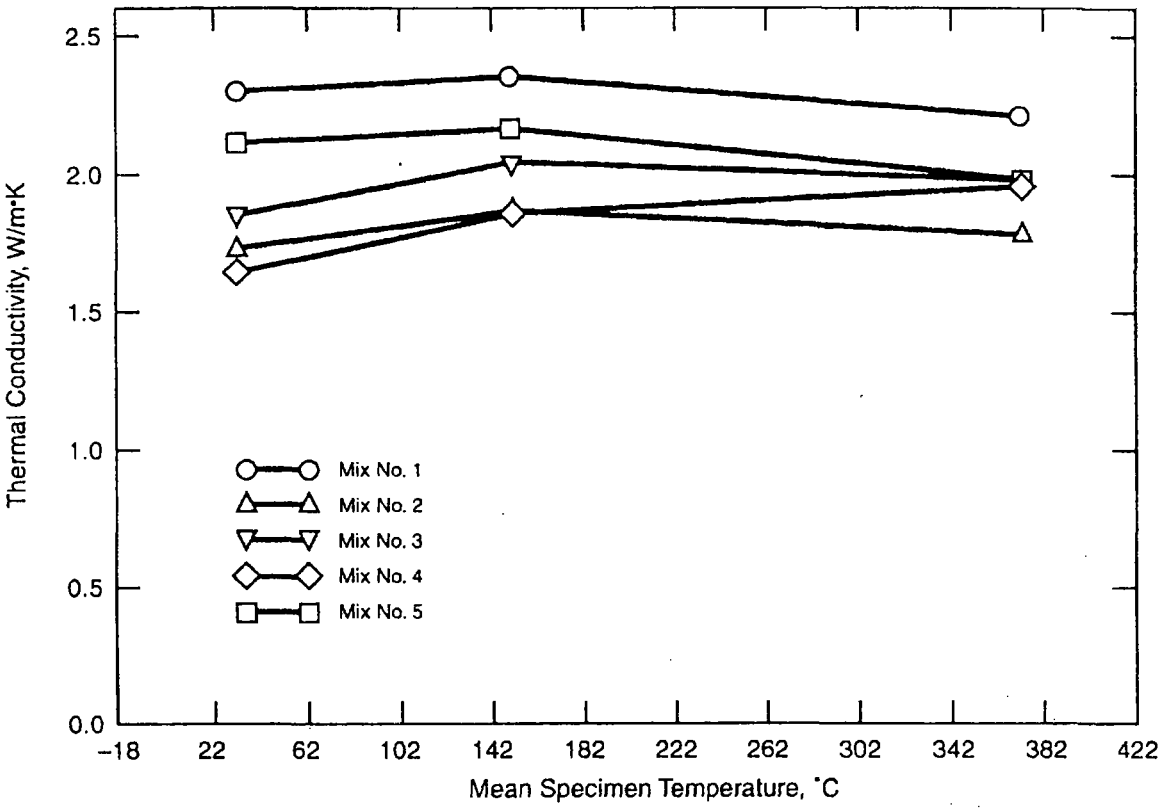

Figure 38. Thermal conductivity versus temperature for the five high strength concretes described in Table 2 [47-48]

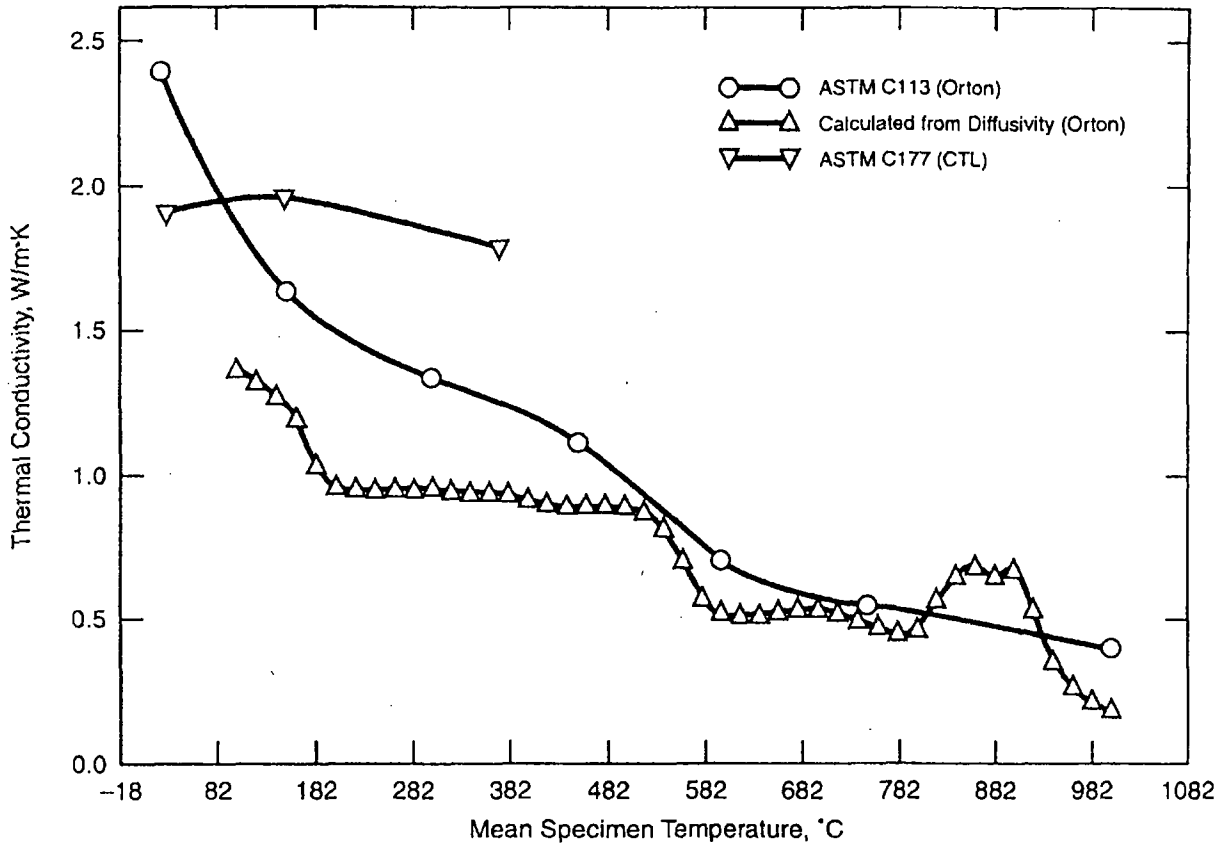

Figure 39. Thermal conductivity of oven-dried high-strength concrete mix No. 5, as determined by three different techniques [47-48]

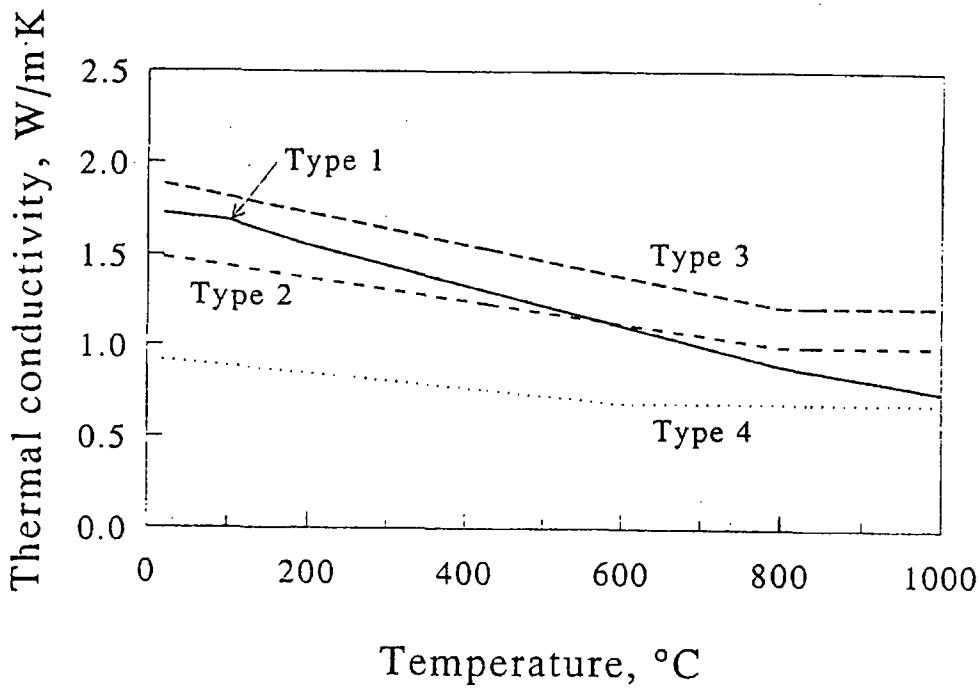

Figure 40. Thermal conductivity versus temperature curves used in the Ahmed model (see text).

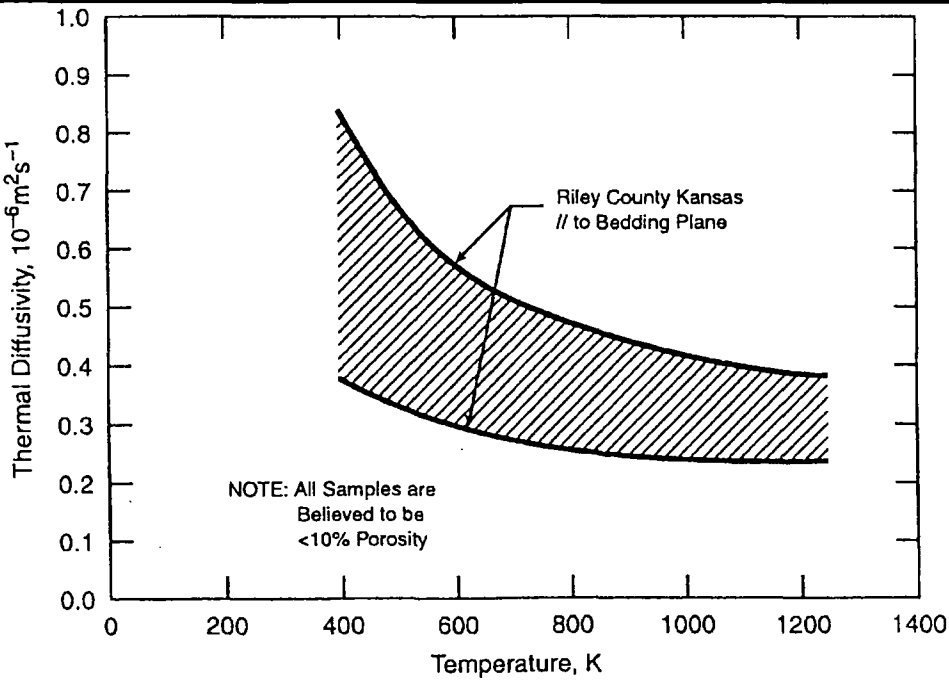

Figure 41. Thermal diffusivity of limestones [51].

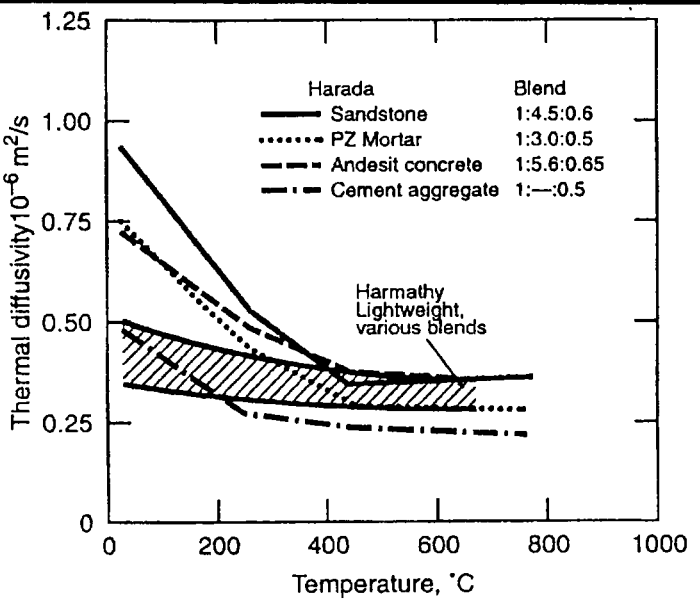

Figure 42. Thermal diffusivity of normal and lightweight concrete, mortar, and cement stone [35].

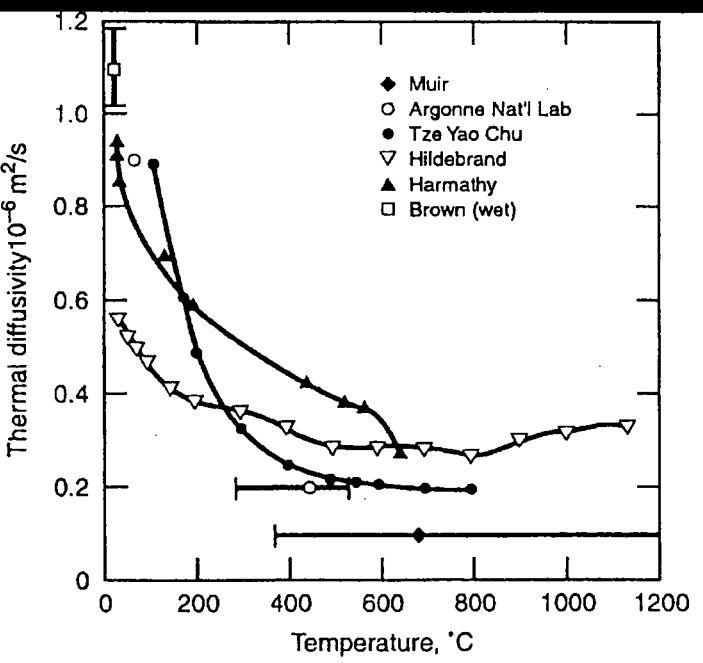

Figure 43. Thermal diffusivity of limestone concrete [35].

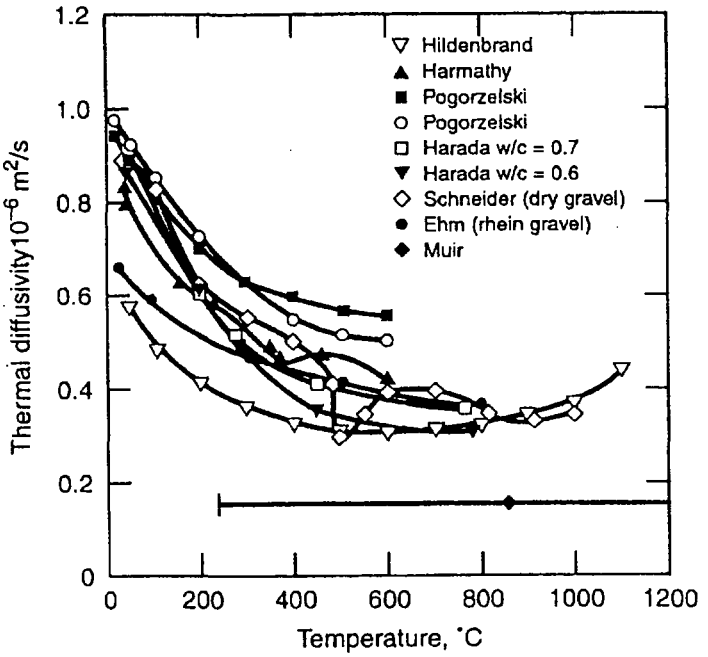

Figure 44. Thermal diffusivity of siliceous concrete [35].

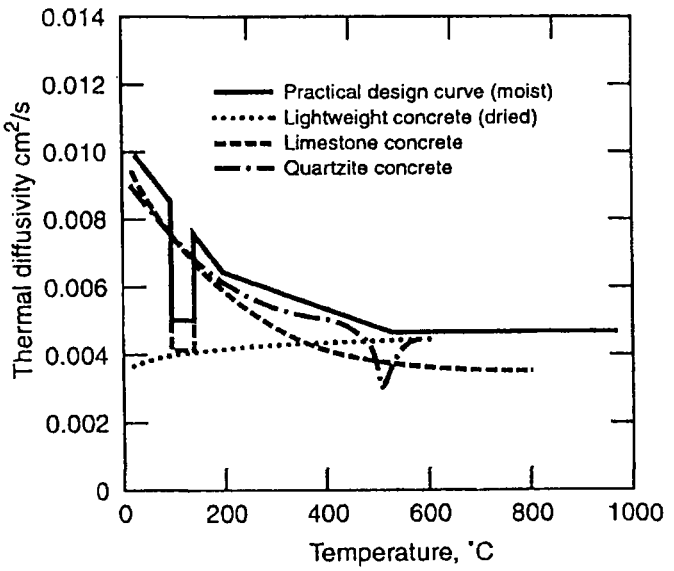

Figure 45. Thermal diffusivity of different concretes [38].

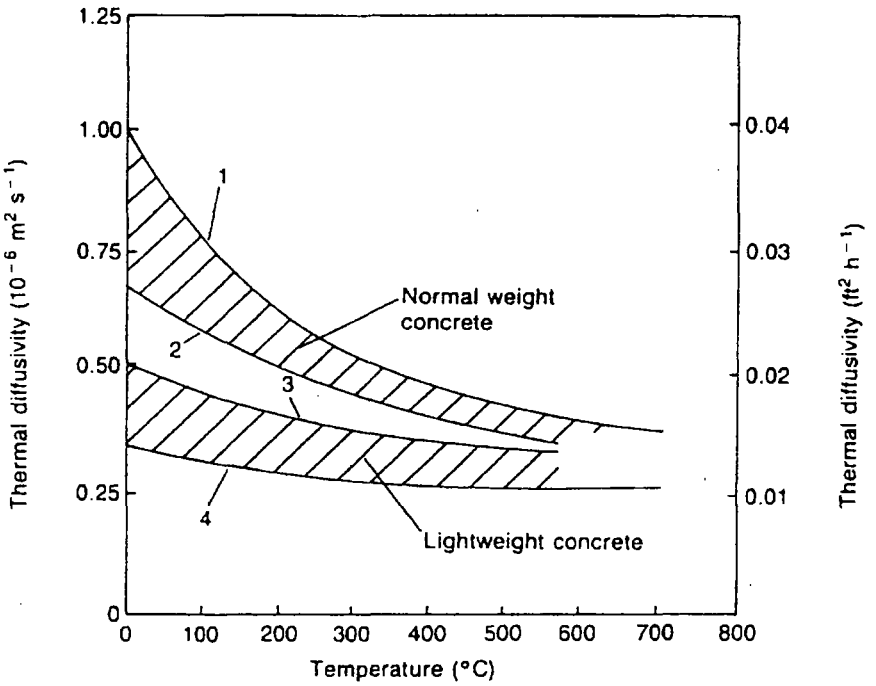

Figure 46. Effect of temperature on thermal diffusivity of concrete made with siliceous and calcareous aggregates and with lightweight aggregates [45].

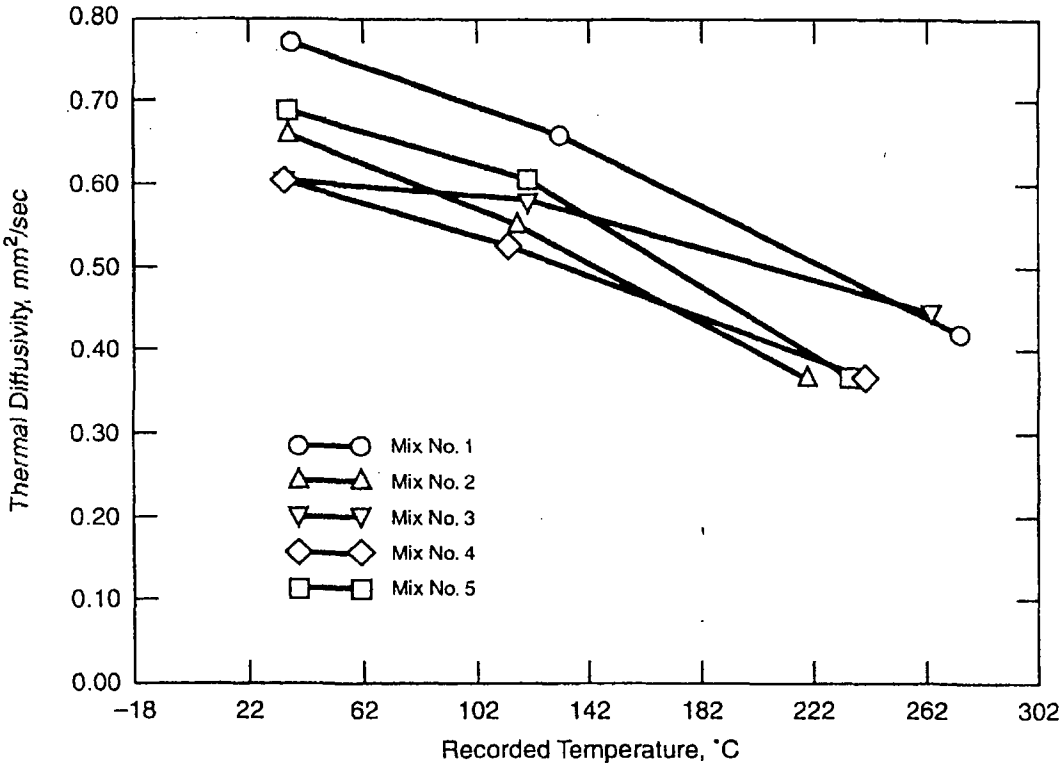

Figure 47. Thermal diffusivity versus temperature for the five high strength concretes described in Table 2 [47-48]

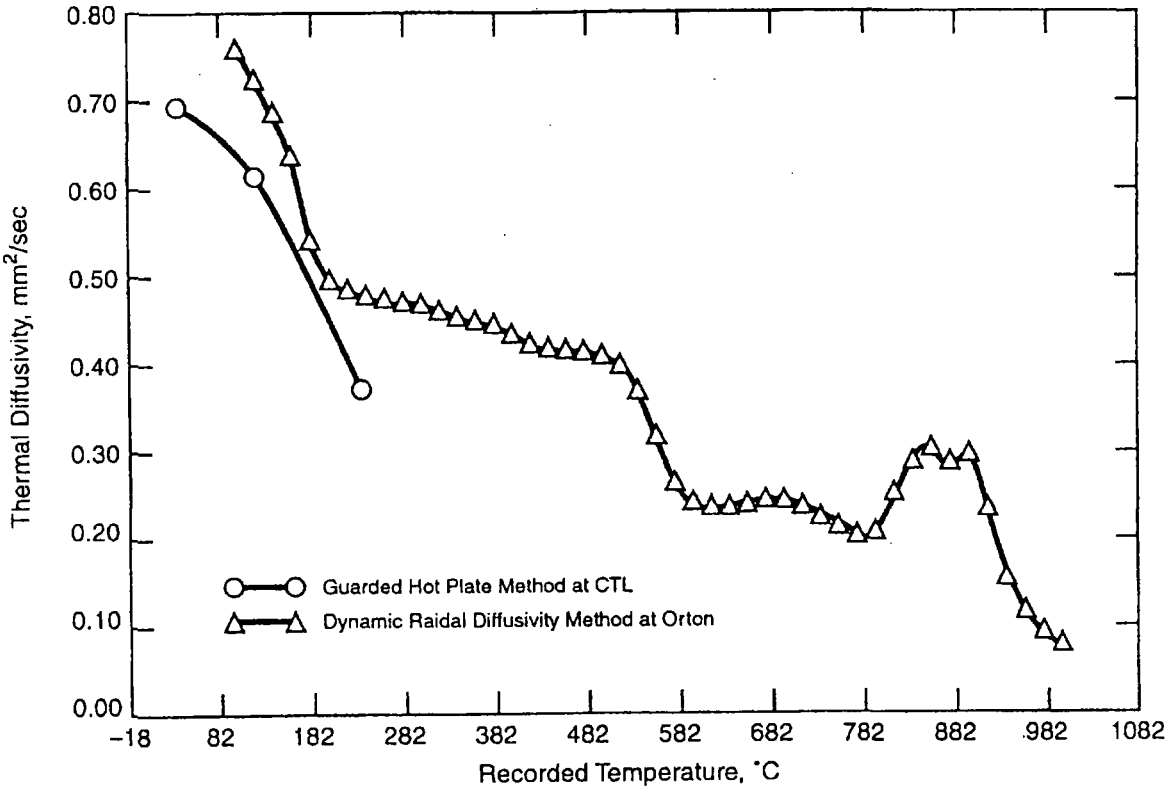

Figure 48. Thermal diffusivity of oven-dried high-strength concrete mix No. 5, as determined by two different techniques [47-48]

4. Correlations and Prediction of Thermal Properties

Concrete is a mixture of cement paste, fine aggregate, and coarse aggregate, with capillary pores and gel pores and some evaporable (as opposed to chemically bound) water. The general approach taken in this section is to examine various equations that can be used to predict a particular property of a mixture from the composition of the mixture and from the (same) property of each of the constituents. Two "mixture rules" are identified below. For the density and the heat capacity of a mixture, these rules reduce to very simple forms that are almost intuitively obvious. For a transport property such as conductivity or diffusivity, that depends upon how the different constituents or components are arranged, the situation gets more complicated, as is discussed in Section 4.3, below.

The simplest mixture rule is that of Bruggeman [61,41] which is

$$\phi^m = \sum_i v_i \phi_i^m \quad , \tag{55}$$

where ϕ is the particular property of interest for the mixture, ϕ_i is the property of the ith component, v_i is the volume fraction [m^3/m^3] of the ith component, and m is a dimensionless constant having a value between -1 and $+1$. The components of a mixture are often stated in terms of the mass fraction ω_i [kg/kg]. The volume fraction and the mass fraction are related to each other by

$$\omega_i = \frac{v_i \rho_i}{\sum_i v_i \rho_i} \qquad \text{and} \qquad v_i = \frac{\omega_i/\rho_i}{\sum_i \omega_i/\rho_i} \quad , \tag{56}$$

where ρ_i is the density of the ith component, $\sum_i v_i = 1$, and $\sum_i \omega_i = 1$.

A rather versatile mixture rule is that of Hamilton and Crosser [62] who suggest that the property (they were interested in thermal conductivity) of a two-component mixture be expressed as

$$\phi = \phi_1 \left[\frac{\phi_2 + (\eta - 1)\phi_1 - (\eta - 1)v_2(\phi_1 - \phi_2)}{\phi_2 + (\eta - 1)\phi_1 + v_2(\phi_1 - \phi_2)} \right] \quad , \tag{57}$$

where component 1 is the continuous component and η is an empirical constant. Harmathy [41] has rewritten this expression in the form

$$\phi = \frac{v_1 \phi_1 + \gamma v_2 \phi_2}{v_1 + \gamma v_2} \quad , \tag{58}$$

where

$$\gamma = \frac{\eta \phi_1}{(\eta - 1)\phi_1 + \phi_2} \tag{59}$$

depends upon η and upon the property value for the two components, but does not depend upon the volume fractions of the components. When $\eta \to \infty$, Eqs. (58) and (59) reduce to the form of Eq. (55) with $m = 1$. When $\eta \to 1$, they reduce to the form of Eq. (55) with $m = -1$. Other limits of these mixture equations are examined in Section 4.3, below.

4.1 Mass, Volume, and Density

The density ρ of a mixture is given simply by Eq. (55) with $m = 1$, which is the same as Eq. (58) with $\gamma = 1$:

$$\rho = \sum_i v_i \rho_i \quad , \tag{60}$$

where ρ_i is the density of the ith component. The overall porosity of a composite solid consisting of several porous components is

$$P = \sum_i v_i P_i \quad , \tag{61}$$

where P_i is the porosity of the ith component.

Harmathy [41, pp. 75-84] states that the bulk density of cement paste can be predicted from the equation

$$\rho = \frac{W_c + W_n}{W_c/\rho_c + W_{wn}/\rho_w} = \frac{1 + (\bar{W}_n/W_c)\zeta}{1/\rho_c + (W_w/W_c)(1 + A)/\rho_w} \quad , \tag{62}$$

where W_c is the mass [kg] of cement in the original cement mixture, W_w is the "effective" [41] mass [kg] of water in the original mixture, W_n is the mass [kg] of non-evaporable water, as determined by drying over dry ice, for the cement paste in its present condition, $W_{wa} = W_w(1 + A)$ is the "adjusted" mass [kg] of water in the original mixture, $\bar{W}_n$ is the mass [kg] of non-evaporable water that would be present on complete hydration of the cement paste, A is the mass [kg/kg] of water, relative to W_w, that would fill the voids created by entrained or entrapped air in the original mixture, $\rho_c \approx 3150$ kg/m^3 is the true density of the solid cement used to make the paste, $\rho_w \approx 1000$ kg/m^3 is the density of free water and capillary water, and ζ [dimensionless] is a measure of the extent of hydration of the cement paste.

Since, for the present project, the room-temperature mass, volume, and bulk density of concrete specimens can easily be determined simply by measuring the mass and volume of a specimen, there is no need to examine further any correlations to attempt to predict these room-temperature values from the composition of the concrete.

The bulk density of a material at elevated temperatures can be computed as

$$\rho(T) = \rho_0 \cdot \frac{W(T)/W_0}{[\,1 + \Delta\ell(T)/\ell_0\,]^3} \quad , \tag{63}$$

where ρ_0 is the room temperature density, $W(T)/W_0$ is the ratio of the mass of a specimen at temperature T to the room temperature mass, usually obtained by thermogravimetry (TG), and $\Delta\ell(T)/\ell_0$ is the linear thermal expansion of a specimen at temperature T, usually obtained by dilatometry. The form of Eq. (63) implicitly includes the assumption that specimens have been at temperature long enough to reach steady-state conditions, i.e., long enough for moisture to be driven off or for chemical reactions, such as dehydration, to come to completion. Otherwise, the density will depend upon the thermal history of the material.

Assuming such steady-state conditions, the mass of the concrete is simply the sum of the masses of its constituents so that $W(T)/W_0$ is easily computed from the corresponding curves for the various constituents -- cement paste, fine aggregate, and coarse aggregate.

The linear-thermal-expansion coefficient is defined, at constant pressure P, as

$$\alpha = \frac{1}{\ell}\left(\frac{\partial \ell}{\partial T}\right)_P , \tag{64}$$

where ℓ is length and T is temperature. The volumetric expansion coefficient is

$$\beta = \frac{1}{V}\left(\frac{\partial V}{\partial T}\right)_P = -\frac{1}{\rho}\left(\frac{\partial \rho}{\partial T}\right)_P , \tag{65}$$

where V is volume and, as before, ρ is density. If the material is isotropic, $\beta = 3\alpha$.

Normally coefficients of thermal expansion are not measured directly but are obtained by differentiation of curves of measured length versus temperature. For example, the observed change in length might be represented by a least-squares-fit power series such as

$$\frac{\Delta\ell}{\ell_0} = \frac{\ell - \ell_0}{\ell_0} = a_0 + a_1 T + a_2 T^2 + a_3 T^3 + \cdots , \tag{66}$$

where ℓ_0 is the length at a reference temperature such as 20 °C. Then the linear thermal expansion coefficient would be computed as

$$\alpha = \frac{a_1 + 2a_2 T + 3a_3 T^2 + \cdots}{1 + a_0 + a_1 T + a_2 T^2 \cdots} . \tag{67}$$

For the present project, it is really not necessary to compute thermal expansion coefficients since the density of concrete can be computed from $\Delta\ell/\ell_0$, as shown in Eq. (63). However, in the literature, correlations for predicting the thermal expansion of mixtures are expressed in terms of expansion coefficients rather than $\Delta\ell$.

Turner [63] recommended that the thermal expansion coefficient of a mixture of isotropic constituents be computed using

$$\alpha = \frac{\sum_i \alpha_i B_i \omega_i / \rho_i}{\sum_i B_i \omega_i / \rho_i} \quad , \tag{68}$$

where α_i, B_i, ω_i, and ρ_i are, respectively, the coefficient of linear thermal expansion [m m^{-1} K^{-1}], the bulk modulus [Pa], the mass fraction [kg/kg], and the density [kg/m^3] of the ith component. This equation implicitly assumes that thermal shear stresses are low enough to be neglected, which may be the case for concrete since cement paste has a low shear modulus. If the bulk moduli are not known but it can be assumed that the various components of the mixture have similar values of Poisson's ratio, the bulk moduli will be nearly proportional to the corresponding Young's moduli and the Young's moduli, rather than bulk moduli, can be used in Eq. (68). If it can be assumed that all of the components of the mixture have very similar bulk moduli, Eq. (68) reduces to

$$\alpha = \sum_i v_i \alpha_i \quad , \tag{69}$$

where v_i is the volume fraction of the ith component. This simple mixing rule corresponds to the Bruggeman rule (Eq. (55) with $m = 1$ and to the Hamilton-Crosser rule (Eqs. (58) and (59)) with $\gamma = 1$ ($\eta \to \infty$). For normal strength or high strength concrete, the curve of thermal expansion versus temperature tends to be rather similar to that of the principal aggregate, which typically occupies roughly 70 percent of the volume of the concrete.

Equations (68) and (69) are known to provide bounds on the thermal expansion coefficient of composite materials. There are other, more complicated, formulae in the technical literature [64-68] that provide somewhat tighter bounds than these two equations. Some of these expressions require knowledge of the shear modulus of each of the constituents, in addition to the bulk modulus. In general, such information will not be available and so these other expressions are of little practical value for the present project. The bulk modulus of different rocks or minerals that might be used as aggregates vary considerably with their origin and their porosity [51] so that even Eq. (68) is of rather limited value unless bulk modulus data are available for the particular lot of aggregate. Since it is much easier to measure high temperature thermal expansion than it is to measure high temperature bulk modulus, Eq. (68) and the other expressions referred to at the beginning of this paragraph are of limited use.

Typical normal strength concretes expand in length by roughly 0.5 to 1.5 percent between room temperature and 1000 °C, corresponding to a decrease in density of roughly 1.5 to 4.5 percent. Thus, for the purposes of this project, it is not necessary to know the thermal expansion of the concrete very accurately. If approximate values for the bulk moduli of the constituents are known, Eq. (68) is probably the most practical formula for predicting the density of the concrete. Otherwise, the simple rule of mixtures, Eq. (69), should provide a fairly reliable estimate.

4.2 Enthalpy, Specific Heat, and Heats of Reaction

The good news is that (1) the enthalpy of a mixture of materials, such as those contained in concrete, can be computed from the masses and enthalpies of the individual components, provided that the

degree of hydration is known or measured; (2) the sensible specific heat will not vary much with changes in type and quantity of aggregate; and (3) the heat of sorption for water will not differ much from the heat of vaporization except for extremely small pores and any difference can be estimated theoretically from the pore size. The bad news is that the rate of heat release or absorption due to chemical reactions will vary with temperature, rate of temperature rise, degree of hydration, absorbed moisture content, and pore pressure.

The specific heat of a mixture does not depend upon how the components are distributed but simply upon the mass fraction and the specific heat of each component:

$$C = \sum_i \omega_i C_i \quad . \tag{70}$$

Harmathy [41] has described a detailed approach to estimating the specific heat of the various constituents of concrete, cement paste, fine aggregate, and coarse aggregate from the estimated chemical composition of each constituent and then computing the specific heat of concrete using Eq. (70). He goes into considerable detail and it does not seem necessary to replicate his work here. It is recommended that this approach be used for the present project, supplemented by experimental verifications.

In Harmathy's method of computing specific heats, he includes the enthalpy associated with release of water of hydration as part of an effective specific heat. In the PCA model for predicting temperatures and pore pressures of concrete exposed to fire conditions, that enthalpy is handled separately from the sensible specific heat of the concrete. Thus care will be required to ensure that the specific heats that are computed treat heats of vaporization, heats of sorption, and heats of dehydration in a manner consistent with that used in the model.

4.3 Thermal Conductivity and Thermal Diffusivity

Heat transfer through a two-component medium, in the absence of large-scale convection, can be considered as having three mechanisms: (a) true thermal conduction through the continuous and discontinuous components, (b) natural thermal convection within the pores or cells of the material, and (c) thermal radiation within the continuous and/or the discontinuous components. These several components of heat transfer are additive but in general are not independent. For a material with reasonably small cells or pores, such as concrete, heat transfer due to natural convection within the pores is small and can either be neglected or can be lumped in with the true conduction component. Large-scale convection, e.g., due to air and water vapor being driven through the concrete by a gradient in pore pressure is not explicitly considered in this section.

Since the sensible portion of the specific heat of concrete will not vary greatly with changes in the type and quantity of aggregate or even with degree of dehydration, the thermal conductivity and the thermal diffusivity will be affected in similar amounts by changes in the concrete. For concrete, both of these thermal transport properties are relatively weak functions of temperature, but they will change quite significantly as functions of porosity, absorbed moisture content, and extent of dehydration. Heating of concrete will result in differential thermal expansion between the cement

paste (which shrinks as it is heated) and the fine and coarse aggregates. Such expansion can greatly affect thermal contact resistance at the interfaces between different components and hence significantly change both thermal conductivity and thermal diffusivity. Pore pressure probably would not directly affect these properties very much but it will affect the extent of dehydration and the absorbed moisture content and thus could indirectly cause significant changes in thermal conductivity and thermal diffusivity.

Thermal conductivity is defined in terms of the ratio of the heat flux to the temperature gradient, in the absence of any mass flow. In general, there is no practical way to stop mass flow from occurring. For materials with low permeability and low mass diffusivity, the diffusive mass flow may be small enough that it should be possible to carry out transient thermal tests to determine thermal conductivity and/or thermal diffusivity before significant mass transfer can occur. However, evaporation and subsequent condensation of moisture can transfer large quantities of heat even for small mass flows so separation of conducted heat from the heat associated with mass transfer can be very difficult and tricky.

For a homogeneous material, thermal conductivity is defined as

$$\lambda = -\frac{q}{\nabla T} \quad , \tag{71}$$

where q is the heat flux and ∇T is the temperature gradient. For a heterogeneous material, this definition is extended to

$$\lambda_{effective} = -\frac{q}{\langle \nabla T \rangle} \quad , \tag{72}$$

where $\langle \nabla T \rangle$ is the average value of the temperature gradient over a region large in comparison with the size of the inhomogeneities. Unless the sample is large in comparison with the inhomogeneities, it is scarcely meaningful to attempt to define an effective thermal conductivity.

In a multi-component material the effective thermal conductivity will depend upon:

1. The thermal conductivity of each component.
2. The proportions of each component.
3. The manner in which the components are distributed; in particular
    a. whether or not the component is continuous in the direction of heat flow,
    b. whether the component distribution is ordered or random,
    c. the size, shape, and orientation of each segment of each component.
4. The nature of the contacts between the different components.
5. The emissive and absorptive properties of the components if there is significant radiative heat transfer through one or more of the components.

The problem of computing the effective thermal conductivity of a mixture from the thermal conductivities of the components is mathematically the same as the problem of computing the electrical conductivity, dielectric constant, or magnetic permeability of a heterogeneous mixture. There exists a large body of pertinent literature, much of which is covered in review articles [69-76].

The following discussion covers a few of the available mathematical relations for correlating the effective thermal conductivity of a mixture with the thermal conductivities of the individual components.

The simplest model for purposes of analysis is that in which the two components are arrayed in alternative parallel layers as shown in Figure 49. If the heat flow is parallel to the layers, the effective thermal conductivity is given by

$$\lambda = f_1 \lambda_1 + f_2 \lambda_2 \quad , \tag{73}$$

where f_1 and f_2 are the volume fractions of the components having thermal conductivities λ_1 and λ_2, respectively; this expression is simply the Bruggeman mixture rule, Eq. (55), with $m = 1$. If the heat flow is perpendicular to the component layers,

$$\lambda = \frac{\lambda_1 \lambda_2}{f_2 \lambda_1 + f_1 \lambda_2} \quad ; \tag{74}$$

this expression is the Bruggeman mixture rule with $m = -1$. Equations (73) and (74) represent the extreme limits of the thermal conductivity of a two-component mixture. These limits are shown in Figure 50 for the case $\lambda_1 = 10 \lambda_2$. Although both Eq. (73) and (74) predict thermal conductivity values intermediate between the conductivities of the individual components, the conductivity obtained is very different for the two cases. Thus these limits are of relatively little use except for laminated materials.

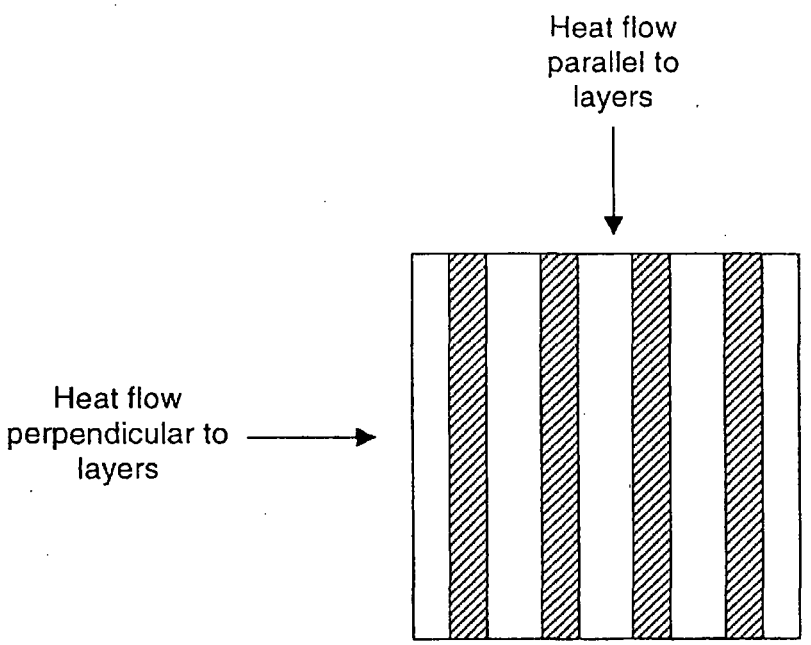

Figure 49. Two-phase material with phases distributed as parallel slabs.

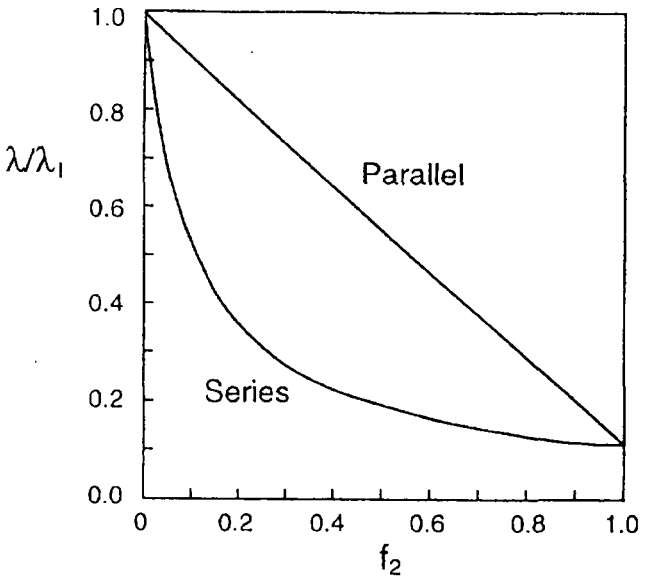

Figure 50. Effective thermal conductivity of a laminated material with heat flow parallel or perpendicular to laminations.

It is possible to obtain tighter limits for the thermal conductivity of a two-component mixture by calculating the apparent effective conductivity by each of two simple methods:

Series Slabs

The material is divided into thin slabs perpendicular to the direction of principal heat flow. The effective conductivity of each slab is computed by assuming that the two components act as conductors in parallel. The effective conductivity of the mixture is then computed by assuming that the slabs act as conductors in series.

Parallel Tubes

The material is divided into thin tubes or rods parallel to the direction of principal heat flow. The effective conductivity of each tube is computed by assuming-a that the two components act as conductors in series. The effective conductivity of the mixture is then computed by assuming that the tubes act as conductors in parallel.

Jackson and Coriell [77] have shown that these two methods provide upper and lower bounds for the true effective conductivity of a mixture. In order to calculate these bounds it is necessary to assume some sort of model representing the manner in which the components are deployed. Several investigators have represented a disperse second component by a cubic array of cubes as shown in Figure 51. The two methods described above can then be used to calculate limits for the effective conductivity of the mixture. Since there is some confusion in the literature on these calculations, it is worthwhile to spell out the steps and assumptions involved.

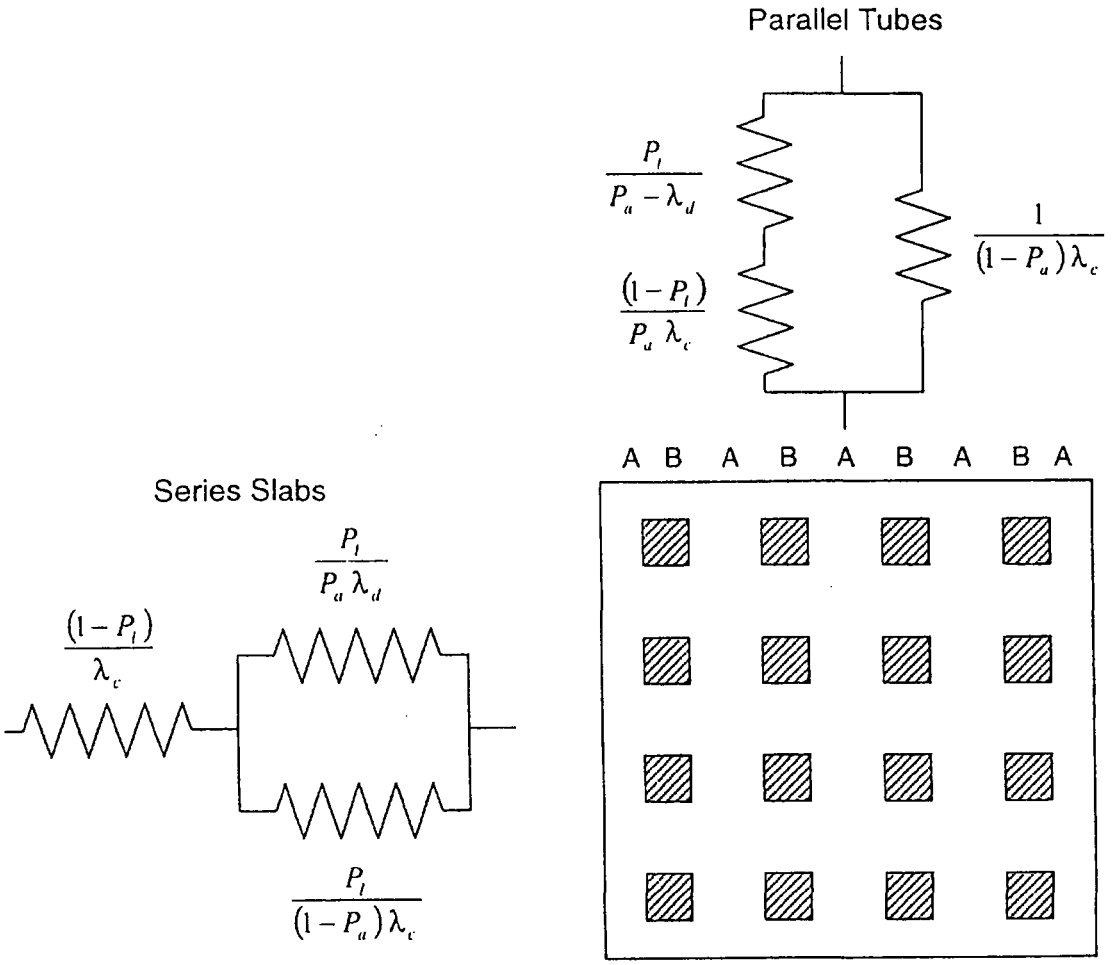

Figure 51. Cross-section of the model in which a disperse second phase is considered to be a cubic array of cubes.

Series Slabs

1. As shown in Figure 51, the mixture is divided into slabs (A) containing no disperse second component and into slabs (B) containing both continuous and disperse components. The effective conductivity of the B-slabs is computed, using Eq. (73), by assuming the disperse and continuous components act as conductors in parallel:

$$\lambda_B = P_a \lambda_d + (1 - P_a) \lambda_c \quad ,$$

where P_a is the fraction of the total area which contains the disperse component of conductivity λ_d and $(1 - P_a)$ is the fraction of the area which contains the continuous component of conductivity λ_c

2. The effective conductivity of the mixture is computed, using Eq. (74), by taking the A-slabs and the B-slabs in series:

$$\lambda = \frac{\lambda_A \lambda_B}{P_\ell \lambda_A + (1 - P_\ell)\lambda_B}$$

where $\lambda_A = \lambda_B$, λ_B was given above, and P_ℓ is the fraction of the total length containing the disperse component. Evaluation of this equation yields

$$\frac{\lambda}{\lambda_c} = \frac{(1 - P_a) + P_a \lambda_d/\lambda_c}{(1 - P_a + P_a P_\ell) + P_a(1 - P_\ell)\lambda_d/\lambda_c} \quad . \tag{75}$$

Parallel Tubes

1. In this approximation, the mixture is divided into parallel "tubes" (A) containing no disperse second component and "tubes" (B) containing, both components.

2. The effective conductivity of the B-tubes is computed, using Eq. (74), by assuming the disperse and continuous components to be in series:

$$\lambda = \frac{\lambda_c \lambda_d}{P_\ell \lambda_c + (1 - P_\ell)\lambda_d}$$

3. The effective conductivity of the mixture is computed, using Eq. (73), by assuming the A-tubes and B-tubes to be in parallel:

$$\lambda = P_a \lambda_B + (1 - P_a)\lambda_A \quad .$$

Evaluation of this equation yields:

$$\frac{\lambda}{\lambda_c} = \frac{P_\ell(1 - P_a) + (1 - P_\ell + P_a P_\ell)\lambda_d/\lambda_c}{P_\ell + (1 + P_\ell)\lambda_d/\lambda_c} \quad . \tag{76}$$

In the above derivations, it was stated that the model was a cubic array of cubes. In fact, it is not necessary to be so restrictive. For Eq. (75) to be valid, it is only necessary that the model can be divided into two types of slabs (perpendicular to the flow of heat)-one containing no disperse component and one having a fraction, P,, of disperse component which can be distributed in any manner. For Eq. (76) to be valid, it is only necessary that the model can be divided into-the two types of "tubes" (parallel to the flow of heat). Thus Eqs. (75) and (76) are, in principle, also applicable to dispersions of, for example, fibers or platelets oriented parallel or perpendicular to the flow of heat. However, these equations will not necessarily bound the true effective conductivity unless both are based on the same component deployment.

For a disperse component in the form of cubes, or in which cubes may be used to approximate an isometric disperse component, equations (75) and (76) may be recast in terms of the volumetric fraction of disperse component, which is designated as f. For the model used, it is easily seen that $P_a = f^{1/3}$ and $P_\ell = f^{2/3}$; with these substitutions, the forms usually seen are obtained:

Series Slabs

$$\frac{\lambda}{\lambda_c} = \frac{(1 - f^{2/3}) + f^{2/3}\,\lambda_d/\lambda_c}{(1 - f^{2/3} + f) + (f^{2/3} - f)\,\lambda_d/\lambda_c} \quad , \tag{77}$$

Parallel Tubes

$$\frac{\lambda}{\lambda_c} = \frac{(f^{1/3} - f) + (1 - f^{1/3} + f)\,\lambda_d/\lambda_c}{f^{1/3} + (1 - f^{1/3})\,\lambda_d/\lambda_c} \quad . \tag{78}$$

Although one would appear to be, on the face of things, considering a fairly complicated model in deriving Eqs. (77) to (78), a little thought reveals that the model reduces to the two simple electrical networks shown in Figure 51. In the series-slabs model, one effectively assumes that the continuous component has an infinite thermal conductivity normal to the principal flow of heat; thus this approach, resulting in Eqs. (75) and (77), always overestimates the effective thermal conductivity: In the parallel-tubes model, one effectively assumes that the continuous component has zero thermal conductivity normal to the principal flow of heat; thus this approach, resulting in Eqs. (76) and (78), always underestimates the effective thermal conductivity.

Maxwell derived an expression for the conductivity of a two-component dispersion of spherical particles of conductivity λ_d, imbedded in a medium of conductivity λ_c. This expression is rigorously valid for dilute dispersions where the average distance between dispersed particles is much larger than the particle size. Maxwell's relation can be written in the form:

$$\frac{\lambda}{\lambda_c} = \frac{2 - 2f + (1 + 2f)\,\lambda_d/\lambda_c}{2 + f + (1 - f)\,\lambda_d/\lambda_c} \quad . \tag{79}$$

The behavior of Eq. (79) for small f is more easily seen by expanding it in the form:

$$\frac{\lambda}{\lambda_c} = 1 - \frac{3f(1 - \lambda_d/\lambda_c)}{2 + \lambda_d/\lambda_c} + \frac{3f^2(1 - \lambda_d/\lambda_c)^2}{(2 + \lambda_d/\lambda_c)^2} - \cdots, \quad f \ll 1 \quad . \tag{80}$$

In Figure 52, the predictions of the series-slabs expression (Eq. (73)), the parallel-tubes expression (Eq. (74)), and the -Maxwell dilute dispersion expression (Eq. (79)) are compared for the case $f = 0.1$. For values of λ_d/λ_c near 1, all three expressions agree. However, if the thermal conductivities of the two components differ significantly, the series-slabs and parallel-tubes expressions disagree with the Maxwell expression, which should be very accurate for $f \leq 0.1$.

To predict the thermal conductivity of a dispersion having less than about 0. 1 volume fraction of isometric dispersed component imbedded in an isotropic continuous component, one should use the

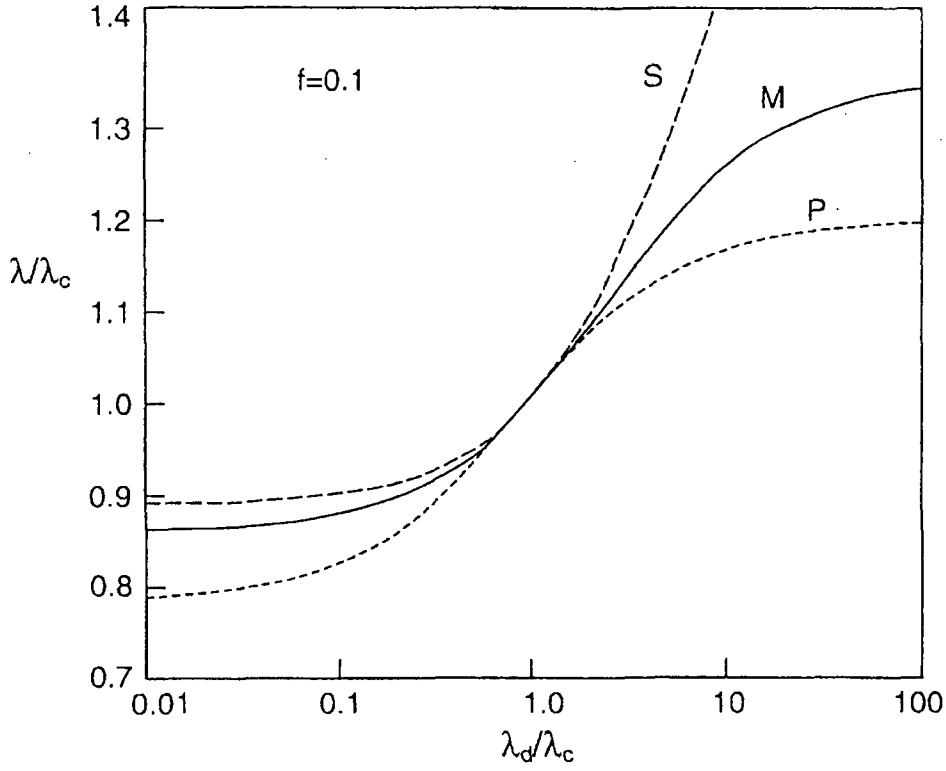

Figure 52. Computed effective conductivity of a dispersion of 0.1 volume fraction of a material of conductivity λ_d in a continuous matrix of material of conductivity λ_c.

S Series-slabs expression, Eq. (77)
P Parallel-tubes expression, Eq. (78)
M Maxwell dilute expression, Eq. (79)

Maxwell dilute dispersion expression, Eq. (79) or (80). The expressions obtained from the cubic array of cubes, Eqs. (75) to (79), should not be used for dilute dispersions in media having an isotropic continuous component. For anisotropic media, the Maxwell expression would have to be modified. For highly anisotropic media, the implicit assumptions of either infinite or zero lateral thermal conductivity of the continuous component might be more nearly met so that one of the series-slabs or the parallel-tubes expressions (Eqs. (75) to (79)) might be more accurate than in isotropic materials. For heat conduction in the poorest conducting direction, the series-slabs expressions, Eqs. (73) and (75), should be more accurate while for heat conduction in the best-conducting direction, the parallel-tubes expressions, Eqs. (74) and (76) should be more accurate.

The two expressions (Eqs. (77) and (78)) derived from the model of a cubic array of cubes disagree seriously with one another in the limiting case of small volume fractions of disperse component. However, for volume fractions of the disperse component approaching unity, Eqs. (77) and (78) converge to a common expression which, quite interestingly, is identical to the Maxwell dilute dispersion expression, Eq. (74).

A special case of interest is the effect of porosity on thermal conductivity. If the thermal conductivity of the continuous material is much greater than the effective conductivity of the pores, $\lambda_d/\lambda_c = 0$ and the above expressions reduce to:

Series-Slabs

$$\frac{\lambda}{\lambda_c} = \frac{1 - f^{2/3}}{1 - f^{2/3} + f} \quad , \quad \lambda_d \ll \lambda_c \quad , \tag{81}$$

which for small f reduces to

$$\frac{\lambda}{\lambda_c} = 1 - f - f^{5/3} + \cdots, \quad \lambda_d \ll \lambda_c \quad . \tag{82}$$

Parallel-Tubes

$$\frac{\lambda}{\lambda_c} = 1 - f^{2/3} \quad , \quad \lambda_d \ll \lambda_c \quad . \tag{83}$$

Maxwell Dilute Dispersion

$$\frac{\lambda}{\lambda_c} = \frac{2 - 2f}{2 + f} \quad , \quad \lambda_d \ll \lambda_c \quad , \tag{84}$$

which for small f reduces to

$$\frac{\lambda}{\lambda_c} = 1 - \frac{3}{2}f + \frac{3}{2}f^2 - \cdots, \quad \lambda_d \ll \lambda_c \quad . \tag{85}$$

In Figure 53 the predictions of Eqs. (81), (83), and (84) are shown for void volume fractions up to 0.1. Over this porosity range the Maxwell equation should be rather accurate if the porosity is in the form of dispersed, disconnected, isometric pores. For cement paste and porous aggregates, this generally will not be the case and Eq. (84) should then serve only as an upper limit for the effective thermal conductivity of a porous material.

For dispersions which are sufficiently dilute for Eq. (79) to be valid, neither the size distribution of the disperse particles nor the manner in which they are deployed are of consequence. However, these factors must be considered if the concentration of the dispersed component is increased. Lord Rayleigh treated the case of uniform spheres arrayed in a cubic lattice distribution. Meredith and Tobias extended Rayleigh's derivation by an additional term and obtained [70]:

$$\frac{\lambda}{\lambda_c} = 1 - \frac{3f}{\dfrac{2 + \lambda_d/\lambda_c}{1 - \lambda_d/\lambda_c} + f - \dfrac{1.315\,(1 - \lambda_d/\lambda_c) f^{10/3}}{4/3 + \lambda_d/\lambda_c + 0.409\,(1 + \lambda_d/\lambda_c) f^{7/3}}} \tag{86}$$

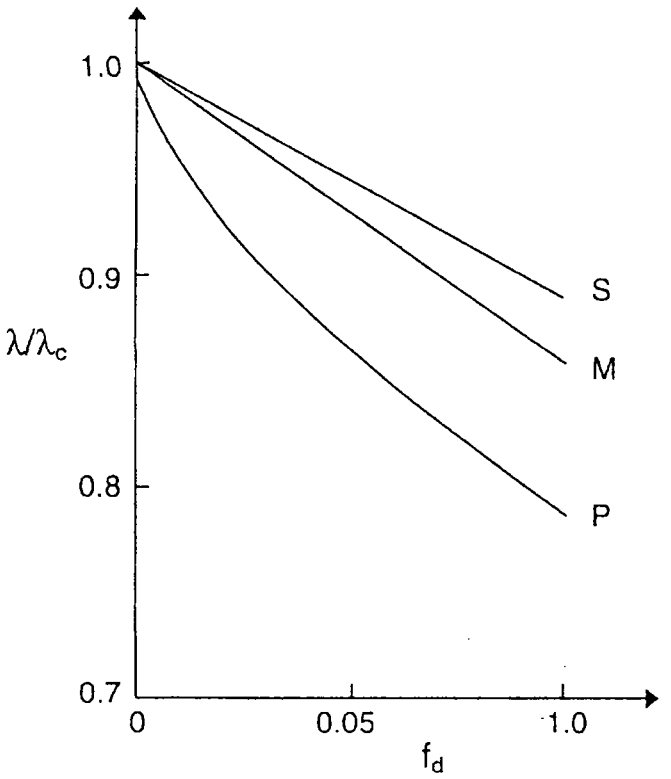

Figure 53. The effect of porosity on thermal conductivity as computed by:

S Series-slabs expression, Eq. (81)
P Parallel-tubes expression, Eq. (83)
M Maxwell dilute expression, Eq. (84)

for the conductivity normal to a side of the cube. If the term involving $f^{10/3}$ in the denominator of the right hand side is dropped, this expression reduces to the Maxwell dilute dispersion expression, Eq. (79). Equation (86) should be more accurate than Eq. (79) for values of f up to $\pi/6 = 0.524$, which is the maximum possible value for a cubic array of spheres.

A rigorous solution for the effective conductivity of a concentrated random array of particles of varying sizes has not been achieved. Several approximations have been developed which are useful in many cases. Bruggeman (see, e.g., [61,69-70]) developed an expression,

$$\frac{\lambda - \lambda_d}{\lambda_c - \lambda_d}\left(\frac{\lambda_c}{\lambda}\right)^{1/3} = 1 - f \quad , \tag{87}$$

which has proved rather effective in predicting the conductivity of a dispersion containing a wide range of particle sizes. For $\lambda_d \to 0$, Eq. (87) reduces to

$$\frac{\lambda}{\lambda_c} = (1 - f)^{3/2} \quad , \quad \lambda_d \ll \lambda_c \quad , \tag{88}$$

while for $\lambda_d \rightarrow \infty$,

$$\frac{\lambda}{\lambda_c} = \frac{1}{(1 - f)^3} \quad , \quad \lambda_d \gg \lambda_c \quad , \tag{89}$$

For a concentrated dispersion containing only a narrow range of particle sizes, the Bruggeman variable dispersion expression (Eq. (87)) tends to. overestimate the effect of the disperse component while the Maxwell expression (Eq. (74)) tends to underestimate. Meridith and Tobias [70] suggested an alternative semiempirical expression that predicts conductivity values intermediate between the Bruggeman variable dispersion equation and the Maxwell dilute dispersion equation:

$$\frac{\lambda}{\lambda_c} = \left[\frac{2(\lambda_d/\lambda_c + 2) + 2(\lambda_d/\lambda_c - 1)f}{2(\lambda_d/\lambda_c + 2) - (\lambda_d/\lambda_c - 1)f}\right]\left[\frac{(2 - f)(\lambda_d/\lambda_c + 2) + 2(\lambda_d/\lambda_c - 1)f}{(2 - f)(\lambda_d/\lambda_c + 2) - (\lambda_d/\lambda_c - 1)f}\right] \tag{90}$$

which reduces to:

$$\frac{\lambda}{\lambda_c} = \frac{8(2 - f)(1 - f)}{(4 + f)(4 - f)} \quad , \lambda_d \ll \lambda_c \quad , \tag{91}$$

and

$$\frac{\lambda}{\lambda_c} = \frac{(1 + f)(2 + f)}{(1 - f)(2 - f)} \quad , \quad \lambda_d \gg \lambda_c \quad . \tag{92}$$

Meredith and Tobias [70] contrast the predictions of the various expressions given above. For a given two-component system, all of these expressions predict two different conductivities, dependent on which component is assumed to be disperse. Bruggeman (see [61,69]) derived another approximate expression that should be applicable to mixtures where neither component is necessarily continuous:

$$f_1 \frac{\lambda_1 - \lambda}{\lambda_1 + 2\lambda} + f_2 \frac{\lambda_2 - \lambda}{\lambda_2 + 2\lambda} = 0 \quad . \tag{93}$$

In Figure 54, the predictions of the Bruggeman mixture equations are compared with those from the Maxwell dilute dispersion equation. It is seen that for small values of f_2, the Bruggeman mixture equation is in agreement with a dilute dispersion of particles of conductivity λ_2 in a matrix of conductivity λ_1, while for values of f_2 approaching unity the mixture equation predicts a conductivity due to particles of conductivity λ_1 dispersed in a matrix of conductivity λ_2.

There have not been enough accurate measurements of the thermal conductivity of well-characterized concretes to provide adequate experimental confirmation of any of the above equations. For well-defined systems (such as spheres dispersed in a continuous matrix) which are in good correspondence to the models used in deriving these equations, measurements of electrical

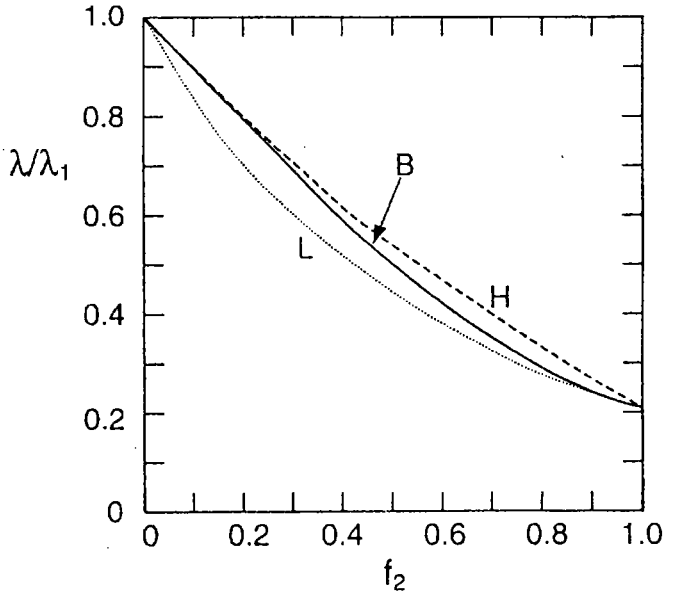

Figure 54. Computed effective thermal conductivity of a mixture.

B Bruggeman mixture expression, Eq. (93)
H Maxwell dilute dispersion expression, Eq. (79), high-conductivity phase continuous
L Maxwell dilute dispersion expression, Eq. (79), low-conductivity phase continuous

conductivity or dielectric constant have shown good agreement with the theoretical predictions of these equations. Concretes, in general, cannot be readily described in terms of a simple model such as spheres dispersed in a uniform medium, and hence in many cases the expressions cited above will indicate qualitatively the effect of an additional component but should not be relied upon for accurate quantitative predictions.

5. Experimental Techniques for Determination of Thermal Properties

5.1 Mass, Volume, and Density

At room temperature, the mass is easily determined by conventional weighing techniques and the volume easily computed from the measured dimensions of a specimen of well-defined geometry. The bulk density of the specimen is then computed from the mass and volume. In this report, the determination of porosity and of "true" density are not addressed.

The change in mass as a specimen is heated is conventionally determined using thermogravimetry (TG or TGA), which is a fancy way of saying that the sample is weighed while it is being heated. There are numerous commercial TGA apparatus available. Typically, a crucible containing the sample material is suspended, inside a vertical tube furnace, from a wire connected to an electronic balance above the furnace. The furnace is equipped with a temperature controller that permits increasing the furnace temperature at a pre-selected constant rate. Provision is made to minimize convection effects on the weighing process and to measure the sample temperature. Usually the furnace is purged with air or some other gas, at a very slow rate, to remove gases that evolve from the test sample. Some TGA apparatus is designed so that the pressure of the gas surrounding the sample can be controlled over a broad range.

Concrete and its components present a few challenges that homogeneous materials do not. Because concrete is a mixture, with the large aggregate typically being 1 to 5 cm in mean diameter, it is either necessary to use a rather large test sample of solid concrete in order to be statistically reliable or else it is necessary to grind up a large sample into a powder, blend it thoroughly, and test a small portion of the powder. Using a large sample of solid concrete presents several difficulties: (1) many TGA apparatus cannot handle a large sample, (2) a large sample will not be isothermal and it is therefore difficult to know what temperature to assign to the test results, and (3) a large sample will retard the evolution of gas – e.g., released water of hydration – from within the sample. Typically, one would expect TGA test results on large solid samples to be dependent upon the sample geometry and size, as well as upon the rate of heating. Using a small powdered sample means that the average temperature of the sample will be close to the temperature of the crucible and that the gas evolving from the sample can easily escape. However, mass loss data taken on a small powdered sample would not be representative of how the concrete would behave under fire conditions.

Rather than carrying out measurements on a solid or powdered sample of concrete, an alternative approach for determining mass change versus temperature is to measure, separately, the mass change of each of the components – cement paste, fine aggregate, and coarse aggregate – and compute the expected mass change for the concrete mixture. Unless fairly large samples can be tested, this latter approach is probably best, not only for mass change but for specific heat and heats of reaction.

As explained in Section 4.1, the change in volume due to heating is usually computed from data on the linear thermal expansion of a suitably large sample. Various techniques for measuring thermal expansion to high temperatures are described in [78-82]. Interferometric techniques, capacitance cells, and X-ray diffraction are more complex and expensive than necessary for engineering materials

such as ceramics or concrete. Thermal expansion measurements can be made using optical techniques, ranging from the use of a cathetometer to measure the change in position of fiducial marks on the specimen, to the use of more sophisticated laser equipment However, the simplest technique, and certainly the most commonly used technique, is push rod dilatometry. In this method the relative expansion of the specimen is transmitted out of the furnace using tubes or rods of some stable material. As described by Kirby [80], there are three variations of push rod dilatometry, with differential dilatometry being the preferred approach whenever possible. In differential dilatometry, the thermal expansion of the test specimen and the thermal expansion of a reference specimen, of nominally the same length, are brought out of the furnace using nominally identical push rods. Since the push rods hopefully experience the same longitudinal temperature distribution, their thermal expansions should be very nearly identical. Thus, the relative motion of the room-temperature ends of the push rods will be due to the relative thermal expansion of the test specimen and the (known) reference specimen.

Most high-temperature dilatometers use specimens no larger than 5 mm in diameter by 50 mm long. Considering that the high-strength concrete of interest to NIST in this project will have coarse aggregate nominally 13 mm in size, thermal expansion specimens of the order of 100 to 200 mm in length should be used if possible. If no other laboratory can handle such large specimens, it would not be too difficult to build a dilatometer at NIST that could handle such sizes.

5.2 Enthalpy, Specific Heat, and Heats of Reaction

There are numerous methods for determining specific heat and heats of reaction[83-93]. Most of the high-temperature techniques that would be suitable for concrete or its constituents are painfully slow and therefore data acquisition is expensive. An exception is differential scanning calorimetry (DSC), which is now the most commonly used procedure for measuring specific heat and for studying reaction kinetics. Most DSC equipment uses very small samples, typically a fraction of a gram in the form of powder, and can only handle measurements up to about 600 °C. For a material such as concrete, it would be very difficult to obtain representative samples of such small size. There are, however, a few commercial instruments that can accommodate large enough samples to be representative of concrete and that can make measurements at temperatures up to 1200 °C or higher. While the sensible heat capacity would not vary significantly with pressure, the reaction kinetics may be seriously affected by the high pore pressures that may occur in concrete exposed to fire conditions. Almost all commercial TGA and DSC equipment operates at atmospheric pressure or below. If commercial equipment can be found that can measure larger samples under controlled pressures, the enthalpy and mass loss measurements should be relatively straightforward. An alternative to using a pressurized system would be to measure on solid specimens of sufficient size that there will be significant internal pore pressures.

5.3 Thermal Conductivity and Thermal Diffusivity

In determining thermal conductivity or thermal diffusivity of concrete, it is important to recognize and deal with the influence of moisture migration. Traditionally, most thermal conductivity

measurements are made under steady-state conditions with thermal conductivity being computed from a geometrical factor, a heat input, and a temperature difference. The apparatus is operated either under conditions of constant heat input, with the resultant temperature difference being measured, or under conditions of constant temperature difference, with the resultant required heat flux being measured. Under such conditions, it may not be possible to measure the thermal conductivity corresponding to a given uniform moisture content in the specimen since the imposed temperature gradient can drive the moisture to the cold side of the specimen where it will collect or escape, depending upon the experimental configuration. Sometimes the moisture migration is sufficiently slow that it appears as if steady-state conditions have been achieved but the data may not yield appropriate thermal conductivity values.

For moist materials, it often is preferable to determine the apparent thermal conductivity or apparent thermal diffusivity under transient or periodic conditions so that data can be acquired without the moisture being driven away. Considerable care and understanding are required to ensure that the technique selected will yield property values that are appropriate for the end-use application. Analysis and interpretation of the results obtained from transient or periodic tests requires caution and an understanding of the limitations of the technique selected. For example, the differential equation that describes conductive heat transfer in an isotropic material of thermal conductivity λ, density ρ, and specific heat C is $\nabla\cdot(\lambda\nabla T) = \rho C(\partial T/\partial t)$, where T is temperature and t is time. If the thermal conductivity is independent of position and of temperature, it may be factored out on the left-hand side, yielding $\nabla^2 T = (1/\kappa)(\partial T/\partial t)$, where $\kappa = \lambda/\rho C$ is the thermal diffusivity. Thermal diffusivity is a questionable parameter if the thermal conductivity is not constant or if there are terms in the differential equation representing other forms of heat transfer, such as radiation or, in the present context, heat transfer associated with moisture migration. Even if an apparent thermal diffusivity is defined for a given test method, analysis would be required to determine whether or not it would be appropriate for use in predicting heat transfer under field use conditions. In general, it is better to use the appropriate analysis of the experimental data to obtain the volumetric specific heat and the apparent thermal conductivity.

The first concern in most techniques for measuring thermal conductivity is to force the heat flow to be unidirectional. Since, under steady-state conditions, heat flow is proportional to a geometric factor, a thermal conductivity, and a temperature difference, the direction of heat flow must be controlled by controlling one or more of these variables. The experimenter's freedom in adjusting these parameters is constrained, sometimes severely, by the often-conflicting requirements of being able to accurately measure total heat flow, geometry, and temperature differences. Very practical considerations, such as available specimen size, frequently constitute severe constraints on apparatus design.

It is not possible to directly measure the heat flow *in* a specimen; one must, rather, measure the heat flow *into* a specimen or *out of* a specimen. This necessitates that not only must transverse heat losses or gains from or to the specimen be prevented or accounted for but, further, there must be no unaccounted-for losses or gains between the specimen and the location at which the heat flow is measured. The most common method of measuring heat flow into a thermal conductivity specimen is to measure the electrical power dissipated in a heater at the hotter end of the specimen. In other "absolute" methods, the heat flow out of a specimen is sometimes measured by a "flow calorimeter,"

with which one observes the temperature rise and flow rate in a circulating liquid of known heat capacity, or by a "boil-off calorimeter," with which one observes the boil-off rate of a fluid of known heat of vaporization. In some types of apparatus, the heat flow is determined from the temperature difference or gradient in another material of hopefully known thermal conductivity that hopefully has the same heat flow; a special case of this type of apparatus would be one using a heat flow meter that is calibrated using one or more specimens of known thermal conductivity. This investigator's bottom line on comparative versus absolute methods is that one should not use comparative methods, including heat flow meter apparatus, unless there are absolute methods available that enable accurate testing of calibration specimens of the same size, and under the same environmental conditions, as are required in the comparison apparatus.

It is not possible to directly measure the temperature *gradient* in a specimen; one must, rather, measure the temperature *difference* between two or more locations and then compute the average temperature gradient. Consider a specimen held between a heat source and a heat sink. If the total thermal resistance of the specimen is large compared with the thermal contact resistances between the source and the specimen and between the specimen and the sink, then the temperature drop across the specimen can be taken as equal to the temperature of the source minus the temperature of the sink and it is not necessary to install temperature sensors in the specimen. However, if the specimen has a low thermal resistance such that thermal contact resistances are not negligible, it is necessary either to correct for these contact resistances or, what is usually done, to install temperature sensors in the specimen.

Measurement techniques, both steady-state and non-steady-state, for determination of thermal conductivity have been extensively reviewed [94,86,87]; for high-temperature measurements, the state-of-the-art has not changed significantly since these reviews were completed. Many of the test methods used for thermal conductivity and thermal diffusivity are described in the proceedings of the International Thermal Conductivity Conference, dating back to 1961.

5.3.1 Steady-State Methods

Most thermal conductivity measurements are made under steady-state conditions, which typically take some hours to achieve. For example, the NIST high-temperature guarded hot plate typically takes 4 to 6 hours to reach steady state. By that time, most of the moisture would be driven out of the specimen, so that the thermal conductivity values achieved would essentially correspond to a dry state.

The vast majority of the various techniques for steady-state measurement of thermal conductivity can be categorized under the headings given below (Types 1 through 7 utilize longitudinal heat flow).

Type 1. Absolute axial heat flow in a rod

This type of apparatus usually use a specimen whose length is very long compared to its diameter, with the specimen held coaxially in a guard cylinder whose inside diameter is typically two to four times the specimen diameter, the space between the specimen and the guard being filled with thermal

insulation. Such apparatus is mainly intended for good thermal conductors, such as metals or high density, high purity ceramics. For materials such as concrete that have quite low thermal conductivity, it would be very difficult to provide adequate guarding, particularly at high temperatures where the thermal conductivity of available insulations is not much lower than that of concretes. In addition, the time to reach thermal equilibrium increases approximately as the square of the specimen length so that long specimens should not be used when it is desired to attain equilibrium before moisture is driven off.

Type 2. Comparative cut-bar apparatus

This type of apparatus typically uses a specimen whose length is comparable (within a factor of, say, 2) with its diameter. The specimen is placed between two rods of known thermal conductivity and the thermal conductivity of the specimen computed from the ratio of the temperature gradients in the known and unknown specimens. As for Type 1 equipment, a coaxial guard and thermal insulation are used to control heat gains or losses. This design avoids the problems of providing the specimen with an attached heater and heat sink. Depending upon the thermal resistance of the specimen, thermocouples may be installed in it or the temperature difference across the unknown specimen may be computed by extrapolation of temperatures measured in the known specimens. For low-thermal-conductivity materials, adequate guarding is difficult. For the thermal conductivity range of concrete, there are not suitable reference materials over the temperature range of interest.

Type 3. Absolute cut-bar apparatus

This type of apparatus can accommodate specimens of similar geometry to those that are used in comparative cut-bar apparatus. However, the apparatus is "absolute," in that the heat flow is determined by measuring the input power to an electrical heater. The only apparatus of this type of which the principal investigator is aware is the one he designed and built at NBS in the early 1960s. By use of sophisticated mathematical analysis and careful experimental procedures, good data were acquired at temperatures up to 1200 °C. In order to make accurate measurements on a material with as low a thermal conductivity as that of concrete, a fairly large (e.g., 10 cm) specimen diameter would be required.

Type 4. Guarded hot plate apparatus

This type of apparatus, intended for use on specimens having relatively low thermal conductivity, utilizes a circular or square specimen whose diameter or edge length is typically an order of magnitude larger than the thickness of the specimen. A guarded hot plate apparatus consists of a heated metering plate, which may be square or circular, separated by a narrow insulating gap from a surrounding coplanar guard plate. Typically, similar specimens are placed on either side of the hot plate; the outside surfaces of the specimen are held between constant temperature cold plates. In operation, the electrical power input to the guard plate is adjusted, usually automatically, so that a multiple-junction differential thermocouple spanning the guard gap has zero output, indicating that there is no temperature difference across the guard gap. Thus the electrically generated heat input to the metering plate flows perpendicularly from both sides of the plate through the specimens to the cold plates. Guarded hot plate apparatus are typically quite reliable at moderate temperatures but

the agreement among different laboratories is not very good at elevated temperatures. The current high-temperature guarded hot plate apparatus at NIST can only be used to about 450 °C. NIST plans to design and build guarded hot plate apparatus for use to about 1200 °C, but that project will require several years. The only commercial high-temperature guarded hot plate apparatus that have been available in recent years are the Holometrix Model GHP-200, which accommodates circular specimens up to 20 cm in diameter, and the Holometrix Model GHP-300, for specimens up to 30 cm square. With the higher-temperature heaters from Holometrix, both models are advertised for use at temperatures up to 650 °C. Anter Laboratories plans to manufacture guarded hot plate apparatus based on the design of equipment developed at the National Physical Laboratory (United Kingdom). All such guarded hot plate apparatus requires a long time to reach equilibrium, thus precluding the possibility of obtaining valid thermal conductivity data before chemical reactions, such as loss of water of hydration, take place.

Type 5. Unguarded hot plate apparatus

This type of apparatus is similar to a guarded hot plate apparatus but the hot plate is made so thin and to have such a low lateral thermal conductance that is effectively self-guarding so that no separate guard is required. The hot plate for such an apparatus has a low thermal capacity so that it can have a fast thermal response, facilitating a rapid approach to thermal equilibrium. The absence of a guard simplifies the design and the operation of this type of apparatus, as well as allows more rapid operation. As will be discussed below under transient methods, an unguarded hot plate apparatus can be operated in either steady-state or transient mode.

Type 6. Guarded flat plate calorimeter

This type of apparatus typically uses a specimen in the form of a flat slab whose thickness is much less than its lateral dimensions. Rather than measure the electrical input to a heat on the hot side of the specimen, a calorimeter is used to measure the heat flow from a central region on the colder side of the specimen. Either a flow calorimeter or a boil-off calorimeter can be used. Since the heat capacities and heats of vaporization of pure fluids are well known, such calorimeters can, at least in principle, be quite accurate. The standardized flow calorimeter apparatus is known to have significant errors for specimens having low thermal conductivity. A disadvantage of either type of guarded flat plate calorimeter is that the colder side of the specimen remains at a temperature not too much greater than that of the calorimetric fluid so that for high hot-side temperatures there is a very large temperature difference across the specimen, making it more difficult to obtain accurate curves of thermal conductivity versus temperature.

Type 7. Heat flow meter apparatus

This type of apparatus also uses a slab-shaped specimen, held between a hot plate and a cold plate. A heat flow meter, which typically consists of a thin sheet of poorly conducting material with provision to measure a signal that is proportional to a temperature difference through the meter, is placed on one or both sides of the specimen. The apparatus is calibrated using specimens of known thermal conductance. Such apparatus is the workhouse of the building insulation industry since it can take data quite rapidly (typically it is operated with the hot and cold plates at fixed temperatures)

and is easy to operate. There do not appear to be any commercial heat flow meters of adequate sensitivity that can cover the temperature range of interest for this project. More critically, there are no suitable reference standards that could be used to calibrate a high-temperature heat flow meter apparatus.

Type 8. Radial heat flow apparatus

This type of apparatus typically uses a specimen in the form of a right circular cylinder, with heat flow radially outward from a heater located in a hole along the axis of the specimen. For solid specimens, it is customary to have temperature sensors located at different radii within the specimen, usually at several angular positions. The apparatus may have end heaters to provide guarding or the specimen may be long enough that it is self-guarding. Such equipment has been used quite successfully on materials ranging from powders to solid ceramics to metals and at temperatures well in excess of what is needed for the present project. Instrumenting the specimens typically is time consuming and the apparatus requires a long time to reach thermal equilibrium.

5.3.2 Transient Methods

Thermal diffusivity, which is a measure of the speed of propagation of heat into a material during changes of temperature with time, is arguably easier to measure than thermal conductivity since it does not require a power or heat flow measurement and since it does not require waiting for thermal equilibrium (steady-state) to occur. For materials and conditions where the only form of energy transport is via heat conduction, under conditions where the thermal conductivity can be assumed to be constant, and when the density and specific heat are very well known from other measurements, it is reasonable to measure thermal diffusivity and compute thermal conductivity values. For the present project, it is essential that **thermal conductivity, not thermal diffusivity**, be measured. Referring back to earlier parts of this report, it is easy to see (p. 5) that Eq. (2) follows from Eq. (1) if the thermal conductivity is constant. However, when there are other modes of energy transfer, thermal diffusivity is not a viable concept. For example, in the energy conservation equation (p. 15, Eq. (53)) for the Ahmed model, all of the material properties are complicated functions of temperature (and possibly of time and pore pressure) so that one cannot combine thermal conductivity and volumetric specific heat as a single property, such as thermal diffusivity. The models that might be used to predict simultaneous heat and mass transfer in porous media require thermal conductivity, not thermal diffusivity as a material property. Accordingly, thermal diffusivity measurements are not further considered in this report.

With one notable exception, there have been relatively few investigations that used transient techniques to obtain thermal conductivity directly (as opposed to measuring thermal diffusivity and computing thermal conductivity). There is a very extensive body of literature on hot-wire or probe methods of measuring thermal conductivity. These techniques have been used extensively for measurements on liquids, where it is important to complete a measurement before significant convection can occur, and for soils and rocks, where it is desired to complete a measurement before there is significant moisture migration. We will also refer to the "transient strip method," which is effectively a variant of the hot-wire method. There have been some studies concerned with thermal

conductivity measurements using one-dimensional transient heat flow through slabs of material; a variant of this approach is considered to be the most viable one for the present project and therefore such techniques are examined in some detail. Note that transient methods of measuring thermal conductivity do require measurement of power or heat flow, which is not the case for thermal diffusivity measurements.

Hot-Wire or Probe Methods

In the so-called hot-wire method, a heater wire is embedded in a specimen, or sandwiched between two slabs. When the heater is turned on, its temperature-time history, or that of a nearby temperature sensor, can be used to compute thermal transport properties. The values thus obtained correspond to a small region of the specimen close to the heater wire and again there are serious questions as to whether or not that small region is representative of a concrete sample with large aggregates. Normally, one would want to have an effective specimen thickness, or effective probing depth, that is roughly an order of magnitude larger than the largest aggregate.

The hot-wire technique and the variant known as or the probe method, both of which are sometimes called the line-heat-source method, were reviewed in 1969 by Pratt [95] and, briefly, by Danielson and Sidles [96]. At that time, the hot-wire method had been used mainly for fluids or for loose-fill or blanket-type insulating material. During the period since these reviews were completed, there has been rather extensive development, particularly in Europe, of the hot-wire method for use on refractory materials, including firebrick. These developments have been reviewed by Davis [97]. Line heat source techniques have, over the past two decades, become the method of choice for most determinations of the thermal conductivity of liquids. The probe method is a variant of the hot-wire technique in which a heater and temperature sensor are packaged in a rigid probe, or needle, that can be inserted into the specimen material. Recently Wechsler [98] reviewed probe methods for use on solids and insulating materials. Flynn has provided a recent extensive bibliography [99] of these methods, which includes abstracts for almost 300 relevant papers and reports. In the early 1980s, another group at NIST carried out an investigation of hot wire techniques for measuring the thermal conductivity of refractory materials at high temperatures [100].

Because of the extensive use of this technique on moist materials, and because of its possible applicability to the present project, a comprehensive discussion of the theoretical basis of this method is included in Appendix A. This discussion includes consideration of the effects of contact resistance between the probe and the specimen and the influence of the finite thermal capacity of the probe on the temperature-versus-time curves that are used to determine thermal conductivity.

There are several variations of the hot-wire method. Sometimes a thermocouple is used to measure the temperature rise of the heater wire with, typically, the thermocouple measuring junction being welded to the heater wire and the thermocouple leads going off perpendicularly to the heater wire. With regard to the present project, this approach has two major disadvantages. First, for a specimen with a fairly low thermal conductivity, the thermocouple leads may carry heat away from the junction, resulting in erroneous temperature measurement. Second, for an inhomogeneous material such as concrete, the temperature along the heater wire may vary with position and the use of a thermocouple at a single location provides very little averaging of that temperature distribution. A

better approach is to use the heater wire as a resistance thermometer to measure its own temperature, thus providing averaging over the region between the potential taps. A probe also may have either one or more discrete temperature sensors or may use the heater as a resistance thermometer. For radial heat flow in cylindrical coordinates, which is the goal with line-heat-source methods, measurement of the temperature-versus-time history of the heat source can provide, at least for homogeneous specimens, accurate data for thermal conductivity but can provide only very limited accuracy for specific heat or for thermal diffusivity. Better accuracy can be obtained for these two properties if the temperature is measured at a known radius from the axis of the heater, either instead of or in addition to the temperature at the axis. Thus, a separate temperature sensor (thermocouple or resistance thermometer), installed at a measured radius from the heater, is sometimes used instead of, or perhaps in addition to, the sensor used to measure the heater temperature.

When the hot-wire technique is used on solid specimens, it is customary to sandwich the heater and temperature sensors between two slabs of the specimen material, with one of them being grooved to accommodate the wire(s). Usually, the heater is turned on and assumed to provide constant power for the duration of the test. It is necessary for the specimens to be large enough that they can be assumed to behave as an infinite body during the duration of the measurements.

Transient Strip and Transient Patch Methods

Gustafsson [101-103] and his colleagues have developed a variant of the hot-wire technique that uses a narrow strip (typically a few millimeters wide) of pure metal as both a heater and a resistance thermometer. Their "transient hot-strip method" has been used with a strip of foil sandwiched between two specimens or by vapor deposition of a heater directly onto the specimen, the latter approach resulting in an extremely thin heater. The authors argue [101] that: "The fraction of the heat that is 'hindered' by the air-filled or oil-filled slots, created at the edges of the strip, when pressing it between the two plane test pieces, is consequently negligible. To achieve a similarly favourable geometrical configuration for the transient hot-wire method would be extremely difficult, or impossible. This fact actually limits the hot-wire method to fluids or to such solids that can be cast satisfactorily around the wire."

Brydsten and Bäckström [104] developed a technique wherein they deposited two metal strips on the specimen, with one strip serving as a heater and the other strip serving as a resistance thermometer, as shown in Figure 55.

The operational procedures for these two transient hot-strip techniques are essentially the same as those for the transient hot-wire or probe methods.

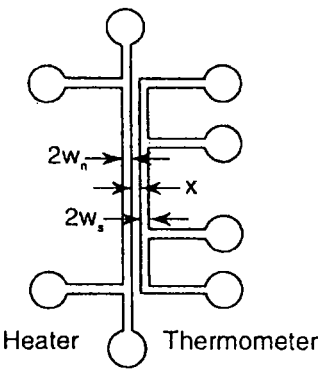

Figure 55. Pattern of copper and nickel strips used by Brydsten and Bäckström [104]. The strip on the left is the heater, and the strip on the right is the thermometer.

Gustaffsson and his colleagues [105-106] also have developed a technique, which they call the "transient plane source technique," in which the heater is a circular or rectangular patch that resembles a resistance strain gage. Since the heater does not cover the entire area of the specimen, as is the case for the methods described below, it seems more appropriate to refer to this technique as a transient patch method. Operationally, this technique is similar to the transient hot-wire and transient hot-strip methods.

Transient Plane Source Methods

In this report, the term "transient plane source methods" is used to designate transient methods in which the heater(s) is(are) nominally the same size, laterally, as the specimens and heat is constrained, by edge insulation or guarding, to flow in one direction, say, parallel to the z-axis, in Cartesian coordinates. Some of the possible boundary conditions for transient plane source methods are shown in Figure 56 [107]. Only the techniques in which the heat input is measured will provide values for thermal conductivity. The techniques with temperature boundary conditions can only provide thermal diffusivity values.

Vernotte [108] suggested that the adiabatic boundary condition required for the boundary conditions shown in Figure 56(a) could be achieved by using mirror images, as shown in Figure 57, where the four slabs in the center of the stack are the specimen material and the ebonite slabs are intended to provide thermal insulation. His assumption was that half of the power provided to each heater would flow toward the center of the stack, resulting in the desired temperature-time history at the mid-plane of the stack.

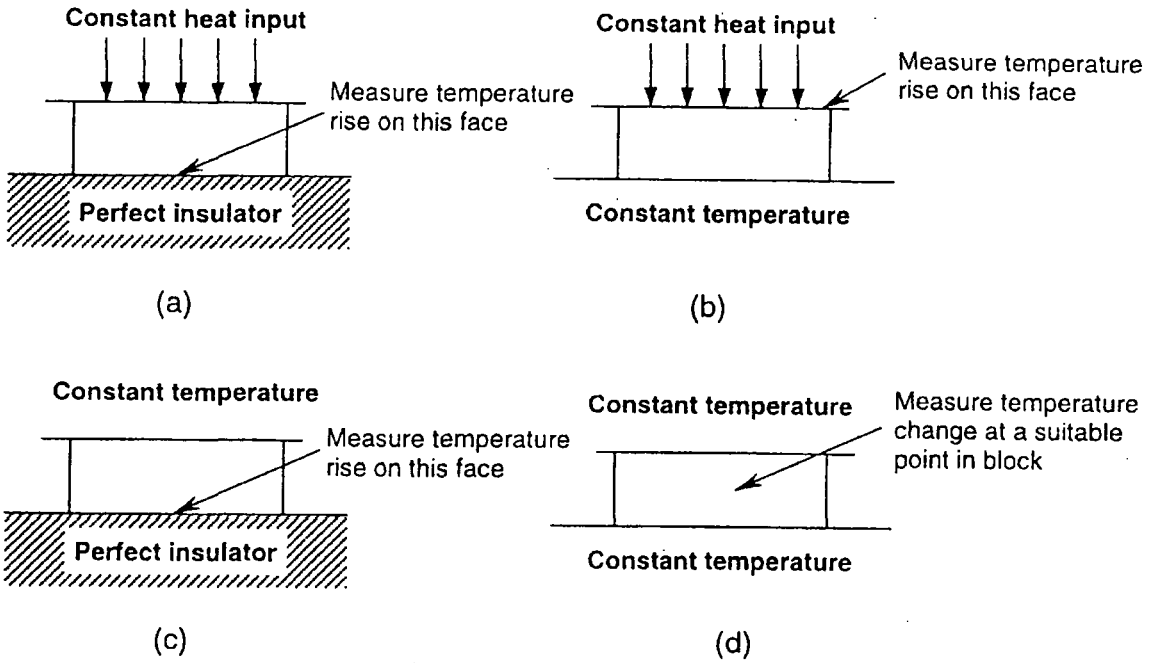

Figure 56. Possible boundary conditions for transient plane source methods for determination of thermal conductivity or thermal diffusivity [107].

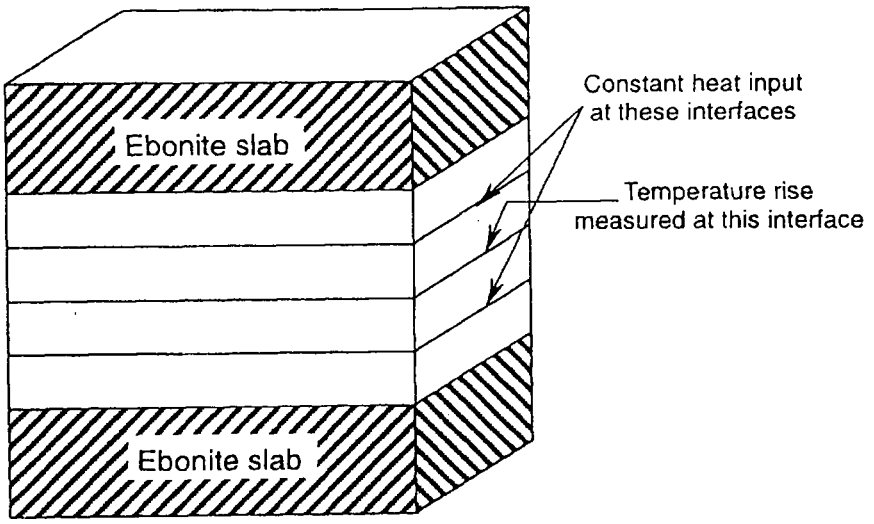

Figure 57. Experimental arrangement suggested by Vernotte [108,107].

Vernotte did not report having made any experimental measurements. When Clarke and Kingston [107,109] implemented the method suggested by Vernotte, they found that, for tests on good insulators, the assumption that half of the heat input flows toward the interface where temperatures are measured was not satisfied. They added additional slabs of specimen material, as shown in Figure 58 in order to provide "a further mirror image." Their heater consisted of a strip of foil interleaved through the stack as shown in Figure 58. In order to minimize the effects of the heat generated in the loops on the heater strip, they provided a "guard pile" of specimen material on either side of the "main pile." Basically this same technique was later used by several other investigators [110-113]. Bastian [113] carried out an extensive set of calculations to ascertain the effects of, among other things, the finite heat capacity of the heaters and thermal contact resistance between the heaters and the specimens.

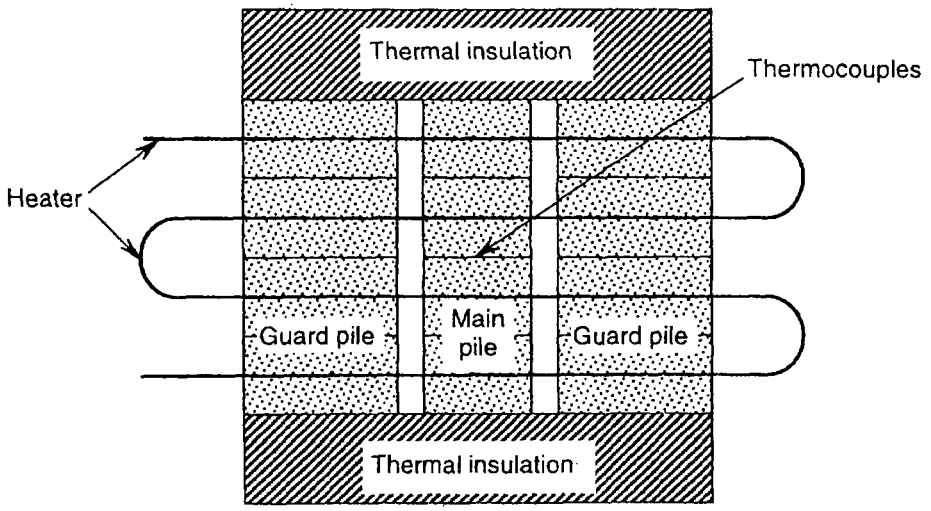

Figure 58. Experimental arrangement used by Clarke and Kingston [107,109].

For the present project, the use of such a thick stack of specimens is not appropriate since it would take so long to bring such a thick mass to a uniform temperature that any chemical reactions, such as loss of water of hydration, would have been completed long before the thermal conductivity test could even begin.

Before discussing other transient techniques, it is useful to make reference to the thin-heater thermal conductivity apparatus developed by Hager [114-120]. While this apparatus is normally allowed to achieve steady-state conditions, the construction of the hot plate is similar to the design that is proposed for the present project, and the Hager apparatus could be operated in a transient mode.

Figure 59 shows the apparatus used by Harmathy [121] to determine the thermal conductivity of concrete and other building materials to high temperatures under transient conditions. The arrangement of the various pieces of specimen material are shown in more clearly in Figure 60. The entire assembly was wrapped in a 1/2-inch layer of ceramic fiber insulation and placed in a furnace so as to minimize heat losses. For high-temperature tests, Harmathy used palladium foil as the heater. Normally, direct current was used to energize this heater. However, Harmathy states:

> For materials which are regarded as electrical insulators at room temperature, there are generally no experimental problems up to about 700°C. Above this temperature serious difficulties may arise, which are associated partly with a gradual increase in the electrical conductivity of such materials, and partly with **a slow charge build up on the metal foil and thermocouple wires following the switching on of the foil heating. This last phenomenon is caused mainly by space-charge polarization, and is less serious when alternating current is used for foil heating.** [emphasis added]

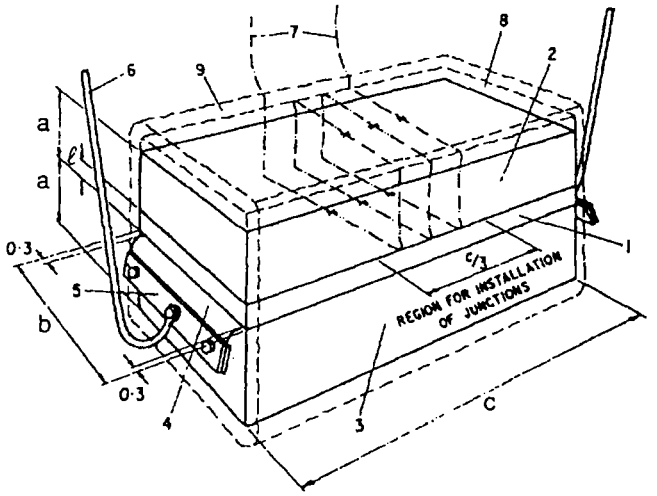

$\ell = \sqrt{262.5\ \kappa}$
a = 4 ℓ
b = 80 to 100 mm
c = 2 b

1 = measuring piece
2 = top piece
3 = bottom piece
4 = palladium foil
5 = Inconel clamps
6 = Alumel lead wire for foil heating
7 = thermocouple wires
8 = Fiberfrax cover
9 = over-all Fiberfax wrapping
X = thermocouple junctions

Figure 59. Isometric view of experimental setup used by Harmathy [121].

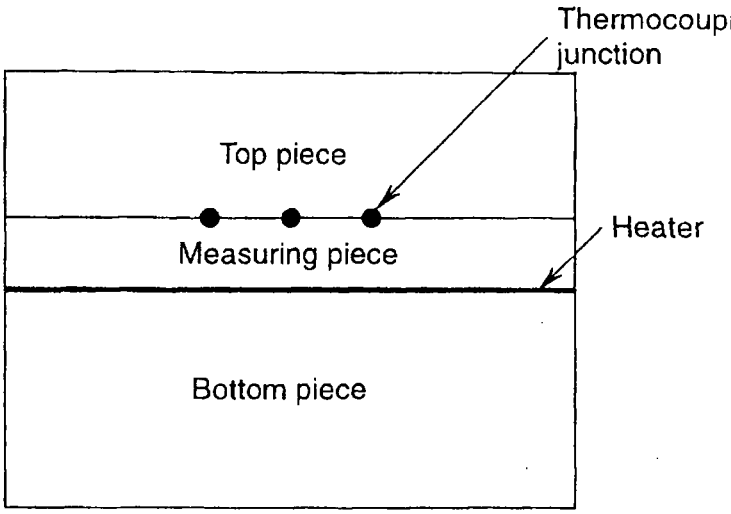

Figure 60. Specimen assembly used by Harmathy [121].

Harmathy used step-function heating, i.e., he turned on the heater and let it remain on until the desired temperature-time history had been recorded. The experiment had to be kept short enough for his assumption that the specimens were effectively of infinite thickness to be met. His mathematical analysis required that the power to the heater be constant, which is not really true for constant-current input to a heater made from a pure metal that has a significant increase in resistance with increasing temperature. His analysis also did not account for the finite heat capacity of the heater, or for contact resistance between the heater and the specimen pieces or between the "top piece" and the "measuring piece." Other investigators who have used Harmathy's method include [122-125]. The experimental setup used by Plummer, *et al.* [126], to measure the thermal diffusivity of ceramics to high temperatures was quite similar to that used by Harmathy although these investigators did not measure the power to the heater and thus could not obtain thermal conductivity.

The most popular method of measuring thermal diffusivity of homogeneous materials is the pulse method, in which the front side of a specimen is irradiated by a short pulse from a laser or a flash lamp and the temperature-versus-time history on the back side is recorded. In such tests it is difficult to measure accurately the energy input by the pulse so that thermal conductivity cannot be obtained directly. A few investigators have used a thin electrical heater to generate a short pulse of energy and measured the energy input so that thermal conductivity could be computed. Dzhavadov [127] used the experimental setup shown in Figure 61, in which three slabs of specimen material, of equal thickness, were sandwiched between two plates that were maintained at constant temperature. The heater at the lower interface was energized for a duration of the order of 0.1 s and the resultant temperature pulse at the upper interface was recorded. From these data the thermal conductivity, specific heat, and thermal diffusivity were computed.

The experimental technique used by Giedd and Onn [128] more closely resembles the classical pulse method in that only one slab of specimen material was used. The heater was a thin film of graphite sprayed onto one side of the specimen. A thermocouple was attached to the back side of the

specimen. A very short pulse was used. The thermal diffusivity was computed from the half rise-time on the back surface and the specific heat was computed from the overall temperature rise of the specimen after it reached thermal equilibrium.

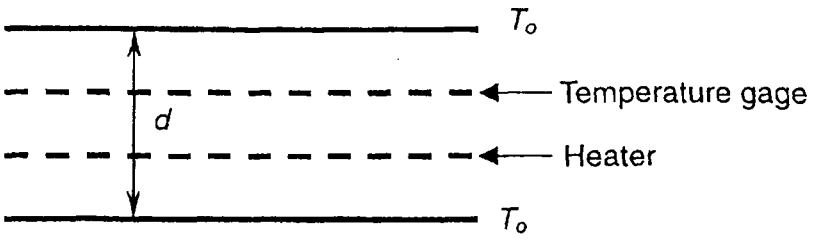

Figure 61. Specimen geometry used by Dzhavadov [127].

In a fairly recent book, Kubičár [129] describes, and references, the rather extensive work that has been carried out at the Institute of Physics of the Slovak Academy of Science, in Slovakia, using electrical pulse methods to determine thermal conductivity, specific heat, and thermal diffusivity. The general experimental approach used at that laboratory is shown in Figure 62. The thermal properties of the specimen are computed from the energy input to the heater, the maximum temperature reached, and the time at which that maximum occurred. These investigators generally used specimens of cylindrical geometry. Kubičár summarizes the procedures that have been developed to deal with the effects of heat loss from the convex surface of the specimens, the finite heat capacity of the heater, and thermal contact resistances between the specimen pieces.

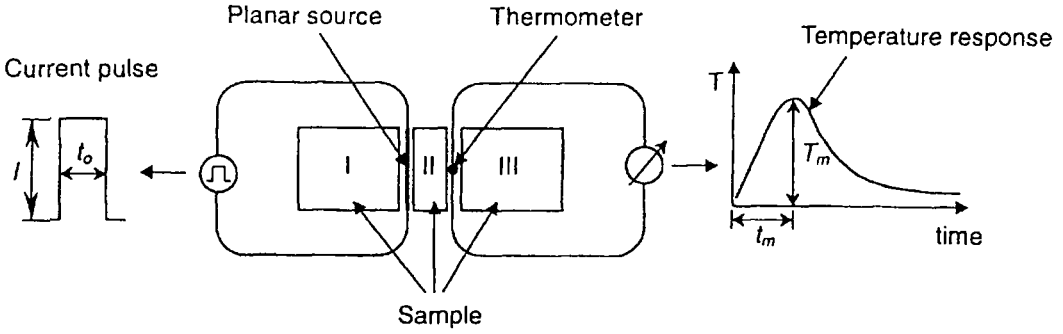

Figure 62. Experimental layout of the pulse method used by Kubičár and colleagues [129].

Piorkowska and Galeski [130-131] describe a transient technique for determining thermal conductivity in which the experimental layout is similar to that of a guarded hot plate apparatus. However, the operational procedure is rather unique. In effect, the "cold plates" are programmed such that their temperature increases linearly with time. Shortly, depending upon the specimen thickness, after this programmed ramp is initiated, the temperature drop across the specimens approaches a quasi-steady-state value. These investigators carried out two runs on the same specimens, with different

power inputs to the heater but with the cold plates increasing at the same rate. By subtracting the measured temperature differences for these two runs, the transient terms cancel out and the thermal conductivity can be obtained, even though true steady-state conditions are never achieved. The subtraction of the two temperature-difference histories also eliminates the influence of heat production or absorption associated with phase transformations. These authors provide extensive mathematical analysis of their method, including allowing the thermal conductivity of the specimen to be temperature dependent.

Some of the analysis procedures used for the above transient plane-source techniques are summarized in Appendix B.

6. Availability of Apparatus and Testing Services

The NIST Building and Fire Research Laboratory does not have in-house capability for carrying out the required thermal property measurements over the temperature range of concern (room temperature to 1200 °C). The NIST Ceramics Division, in the Materials Science and Engineering Laboratory (MSEL), has the capability to carry out measurements of specific heat, heats of reaction, and thermal expansion to temperatures higher than 1200 °C. However, their equipment uses rather small samples. The DTA or DSC measurements would be made on powdered samples of the order of a gram or so. The dilatometer uses a specimen nominally 5 mm in diameter by 25 mm long. The Ceramics Division has no capability to measure thermal conductivity or thermal diffusivity above room temperature. The NIST Metallurgy Division, in MSEL, can measure thermal diffusivity of small specimens only at temperatures above 900 °C.

In order to locate laboratories, outside of NIST, that could provide some or all of the needed measurements the following request was faxed to vendors of thermal property measurement equipment:

> The NIST Building and Fire Research Laboratory is working on a project concerning the response of concrete to fire conditions. My responsibilities include determining what thermal property measurements need to be made and locating laboratories where these measurements can be done reliably.
>
> The materials of interest are normal-strength and high-strength Portland cement concrete, with quartz sand as the fine aggregate and (nominally) 1/2-inch limestone as the coarse aggregate. We are primarily interested in the effective overall thermal properties of the mixture of cement paste, fine aggregate, and coarse aggregate. Thus for properties, such as thermal conductivity and thermal expansion, that depend upon the sizes and deployment of the various phases, the test samples need to be large compared to the size of the coarse aggregate. For properties such as heat capacity, heats of reaction, and mass loss, that only depend upon the mass fraction of the various components, either the test samples need to be large compared to the aggregate size or else it would be necessary to grind and blend rather large pieces of concrete and then take smaller representative samples from the resultant powder. Ideally, we would like to obtain data from room temperature to 1200 C but are interested in laboratories that could obtain data to temperatures above 800 C.
>
> We have not yet determined how many tests will be required for each type of measurement. However, there will be at least four types of concrete and it probably will be appropriate to make measurements at several heating rates. Thus we anticipate that approximately 10 to 12 tests for each property will be required. The thermal properties of interest include:
>
> Heat capacity and heats of reaction (probably DSC measurements)
>
> Mass loss versus temperature (TGA)

Thermal expansion

Thermal conductivity (direct measurements, not from thermal diffusivity)

Thermal diffusivity (?)

At this time, NIST does not wish to buy the instruments to carry out such measurements, but prefers to contract to have the measurements made elsewhere. If you only sell thermal measurement instrumentation and do not provide testing services, please let me know of laboratories that can provide such measurement services, either using your instrumentation or other types of equipment. It also would be helpful if you could indicate which models of your instrumentation would be most appropriate for which types of measurement.

If you do provide testing services, please let me know what types of measurements you can provide, along with the temperature range, estimated accuracy, and required sample size and geometry for each type of measurement. Also, please provide an estimate of the costs of such measurements.

A similar request was faxed to numerous laboratories, but with the next-to-last paragraph omitted.

As of the date of this report, the following vendors and laboratories have been contacted (for foreign vendors, the city of their U.S. subsidiary is given):

Anter Corporation (Pittsburgh, PA)

Ball Aerospace Systems (Boulder, CO)

Cahn Instruments (Madison, WI)

Colorado School of Mines (Golden, CO)

Concurrent Technologies Corporation (Johnstown, PA)

Coors Analytical Company (Golden, CO)

duPont Fibers Analytical Services (Wilmington, DE)

Geoscience Ltd. (San Diego, CA)

Hauser Laboratories (Boulder, CO)

Harrop Industries, Inc. (Columbus, OH)

Hazen Research, Inc. (Golden, CO)

Holometrix, Inc. (Bedford, MA)

Industrial Science & Technology Network, Inc. (York, PA)

Iowa State University (Ames, IA)

Itertek Testing Services (Richardson, TX)

Leach & Garner Technology (North Attleboro, MA)

Linseis Inc. (Princeton Junction, NJ)

Arthur D. Little, Inc. (Cambridge, MA)

Lockheed Martin (Orlando, FL)

Louisiana Productivity Center (Lafayette, LA)

The M&P Lab (Schenectady, NY)

Massachusetts Materials Research (Boylston, MA)

MATECH Associates (Scranton, PA)

Materials Research & Engineering, Inc. (Boulder, CO)

Mettler Toledo Inc. (Hightstown, NJ)

National Physical Laboratory (Teddington, Middlesex, United Kingdom)

Netzsch Instruments, Inc. (Paoli, PA)

Northrop (Rolling Meadows, IL)

Oak Ridge National Laboratory (Oak Ridge, TN)

Orton Ceramic Foundation (Westerville, OH)

Owens Corning Fiberglas Corporation (Granville, OH)

Polymer Solutions Inc. (Blacksburg, VA)

Precision Measurements and Instruments Corporation (Philomath, OR)

Research Triangle Institute (Research Triangle Park, NC)

SETARAM (Grand Prairie, TX)

Shimadzu (Columbia, MD)

Showa Denko America (New York, NY)

TA Instruments (New Castle, DE)

Texas Research Institute (Austin, TX)

Tg Technologies, Inc. (Freehold, NJ)

Theta Industries (Port Washington, NY)

TPRL, Inc. (West Lafayette, IN)

Tulane University (New Orleans, LA)

Ulvac Technologies, Inc. (Methuen, MA)

University of Illinois (Champaign, IL)

As replies from these organizations have come in, there have been numerous suggestions of other laboratories that might be able to carry out some of the measurements. Thus, it is anticipated that there will be further additions to the above list.

While it is too early to select particular laboratories to carry out the needed measurements, it is clear that there will be multiple laboratories with the capability to measure specific heat, heats of reaction, mass loss, and thermal expansion. A few laboratories can measure thermal conductivity (cut-bar method) or thermal diffusivity (flash method) on specimens that are too small to be representative of concrete. Thus far, only one laboratory has indicated that they can measure thermal conductivity using a guarded hot plate apparatus. As discussed earlier in this report, a guarded hot plate apparatus is too slow to allow measurements to be made before chemical reactions go to completion.

7. Design of New Apparatus for High-Temperature Thermal Conductivity Measurements

The cross section of the proposed test setup is shown in Figure 63 – it consists of a thin-foil heater sandwiched between two similar specimens, which are in turn sandwiched between two "cold plates." The specimens will be nominally 200 mm square with thicknesses in the range of 10 to perhaps 50 mm. The cold plates will simply be square, thin sheets of corrosion-resistance metal, such as nichrome or inconel; further analysis may indicate that it would be desirable to provide a guard gap in these cold plates in order to reduce lateral heat flow. NIST has purchased a high-temperature furnace for this project – the outside surfaces of the two cold plates will be exposed to the air in the furnace. The edges of the stack, shown in Figure 63, will be insulated with ceramic fiber insulation.

An expanded view of the thin-foil heater is shown in Figure 64 (not to scale). The heater will consist of a sheet of 0.025 mm platinum foil, folded to make a long, thin U. The interior of the U will be filled by a sheet of ceramic paper, with slots cut into it to accept potential leads to measure the voltage drop across the central portion of the heater. The two arms of the U will be attached to nickel busbars to provide the electrical current for the heater. The platinum heater will also act as a resistance thermometer to read its own temperature. In addition, the space within the U will be provided with Type N thermocouples to provide an independent check on the heater temperature. Several Type N thermocouples will also be attached to each of the two cold plates to provide their temperature.

The type of heaters used, e.g., by Harmathy [121] and by Plummer, *et al.*, are not folded back on themselves as is proposed here. Rather, the current leads for those heaters are at opposite ends of a flat strip heater. That design would be satisfactory if the heater were to be heated by direct current. However, it is proposed that the heater for the NIST apparatus be powered by alternating current, both to minimize the space-charge effects which Harmathy encountered (see the quotation on p.82 of this report) and to enable the use of an integrating digital voltmeter, with excellent ac common mode rejection, to read thermocouple voltages without serious errors due to leakage currents from the heater. With a single-pass heater, such as those used by Harmathy and by Plummer, there would be large inductances in the current loop and in the potential tap loop; such inductances could cause serious measurement errors unless very sophisticated equipment were used to measure the relative phases of the current and voltage signals. The folded heater design that is proposed will have minimal inductance so that the power to the heater is simply the product of the root-mean-square voltage drop across the central portion of the heater times the root-mean-square current through the heater, and the resistance of the heater will be simply the quotient of these two quantities.

Figure 65 shows how the thin-foil heater will be supported. To the right of these drawing can be seen two pieces of nickel angle stock that act as legs to support the right-hand-side of the twin busbars. At the left end of the busbars, they are electrically separated from each other by a thin ceramic washer through which a ceramic pin is inserted to provide a means of supporting that end of the busbars.

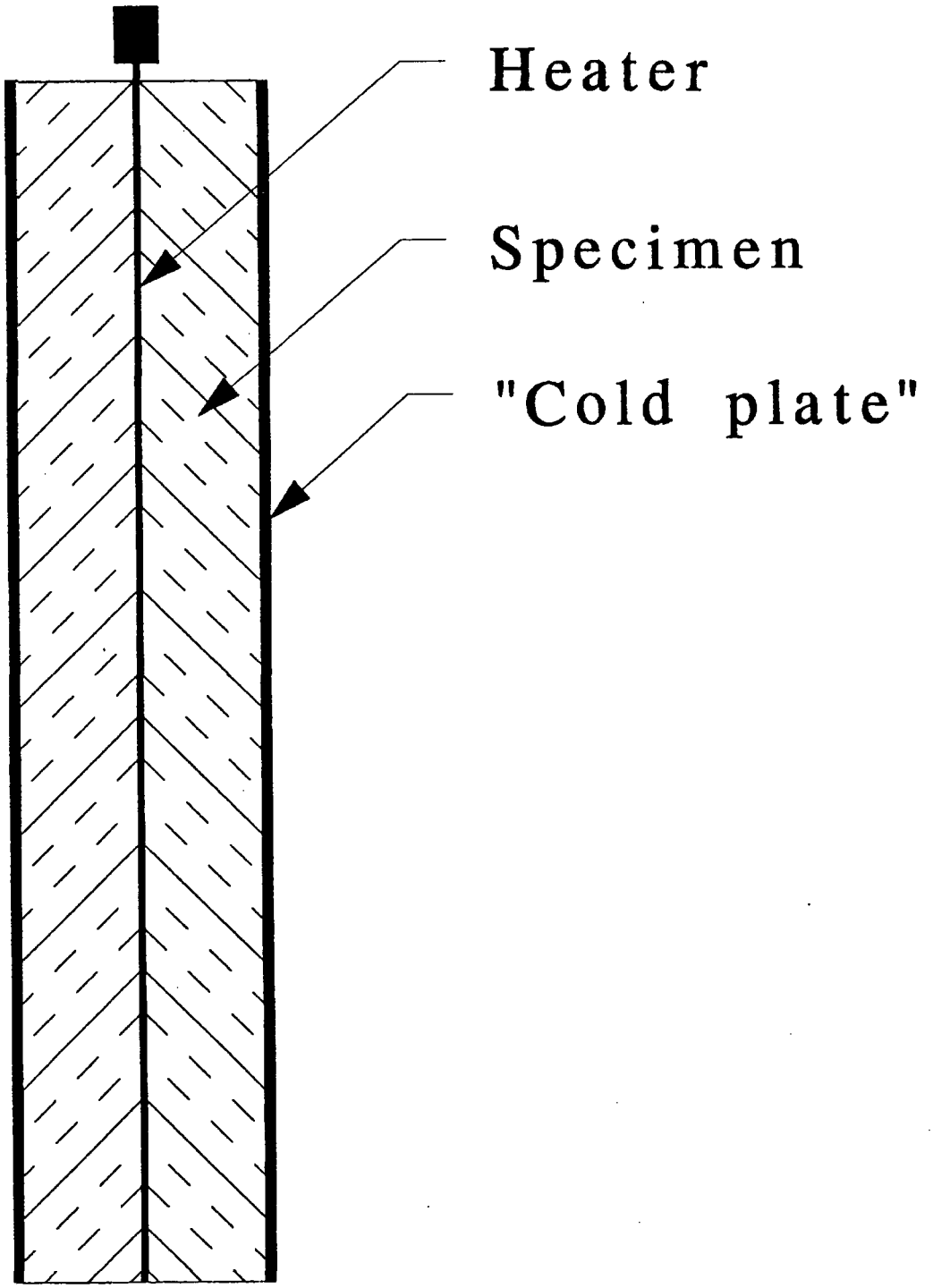

Figure 63. Cross section of proposed apparatus for high-temperature thermal conductivity measurements.

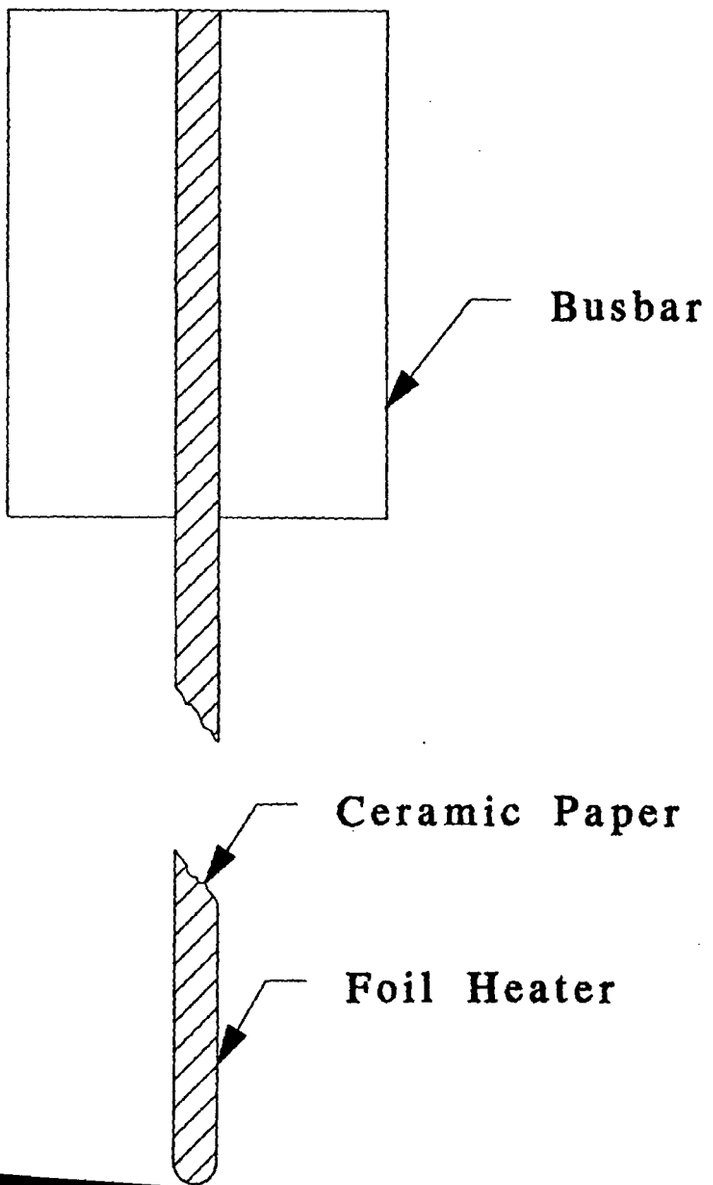

Figure 64. Cross section of the thin foil heater.

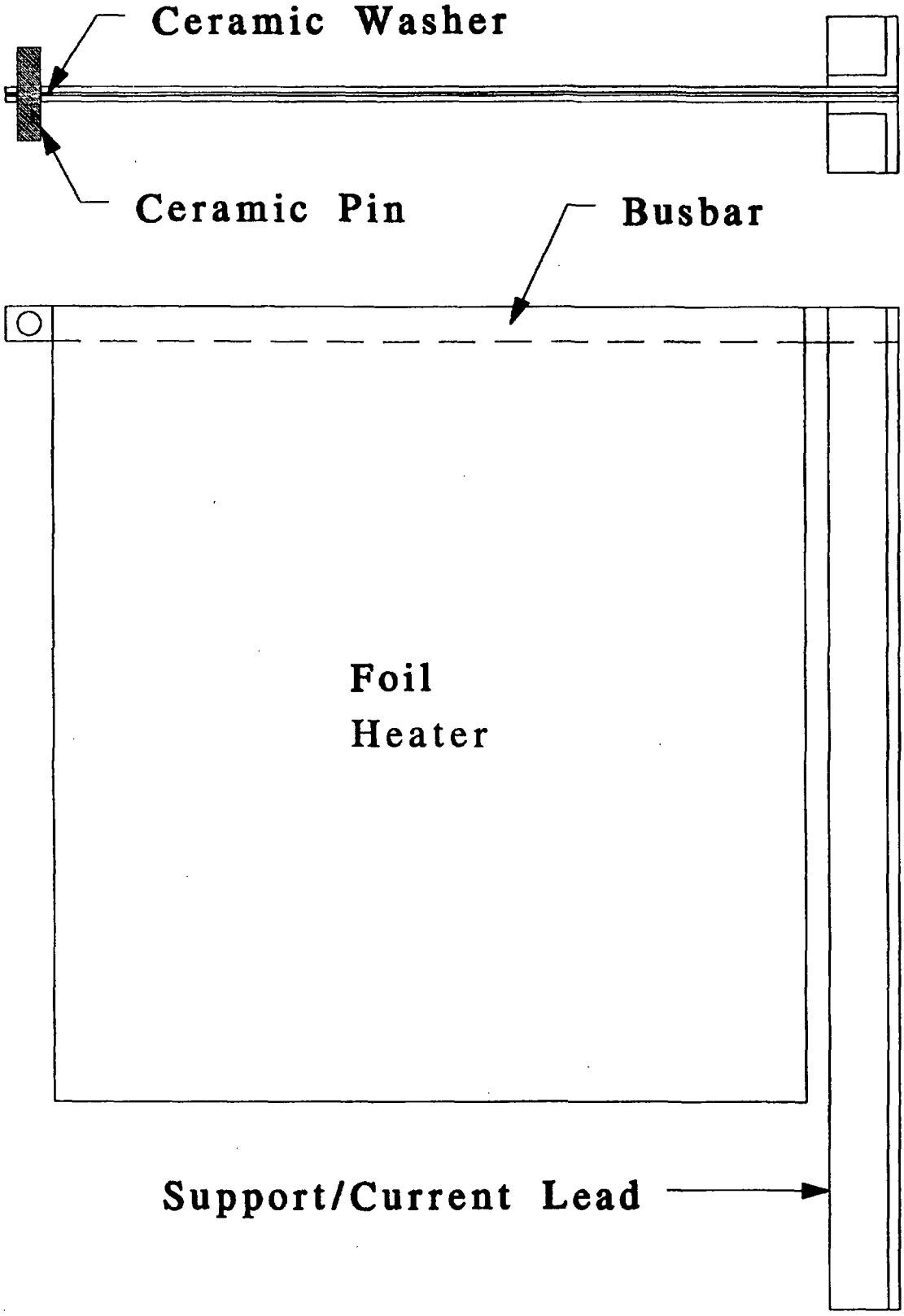

Figure 65. Elevation view of the foil heater showing the support structure that also serves as current leads. The free end of the busbar is supported from the support frame shown in the next figure.

Figure 66 is a conceptual view of the (nichrome or inconel) support frame from which the foil heater, specimens, and cold plates are suspended. The upper drawing is a plan view showing support rails, at each side, from which the components of the specimen assembly are hung. These support rails are held up by four legs, made of angle stock, as shown in the lower elevation view. Halfway up the rear legs a load screw plate is attached. The other load screw is supported from an angled arm attached to a fulcrum. The arrangement for the load screws can better be seen in Figure 67, which shows how a compressive load is applied to the specimen stack (for clarity, the support frame has been omitted in this drawing). Figure 67 represents the case where the weight that provides the compressive load is located inside the furnace. If possible, it would be preferable not too have the weight inside the furnace since it takes up a lot of space, provides a large thermal load for the furnace, and makes it difficult to change the applied force. A far preferable arrangement would be as shown in Figure 68, where the loading force is provided by a weight below the furnace, thus permitting the placement of two identical apparatus inside the furnace. The furnace that has been ordered by NIST is a bottom loading furnace and it may not be practical to have the weights located below the furnace. Figure 69 shows an arrangement whereby the weights can be located above the furnace with a pulley and cable (not shown) to reverse the direction of the force provided by each weight.

The intent is to run the tests in a manner analogous to that used by Piorkowska and Galeski [130-131], as described above on pp. 84-85. Since the changes to the specimens due to chemical reactions will be irreversible, it will not be possible to run tests on the same specimens at two different power levels. Rather, it is planned to run two tests simultaneously on two similar pairs of specimens, one test at a low power (just enough to enable obtaining accurate data for the heater resistance) and one test at a power large enough to cause a temperature drop of, say, 20 to 40 K across the specimens. The calculation procedure used by Piorkowska and Galeski is summarized in Appendix B.

With this apparatus, it also would be possible to carry out runs using Harmathy's method, which is described briefly on pp. 82-83, using his calculation procedure, which is summarized in Appendix B.

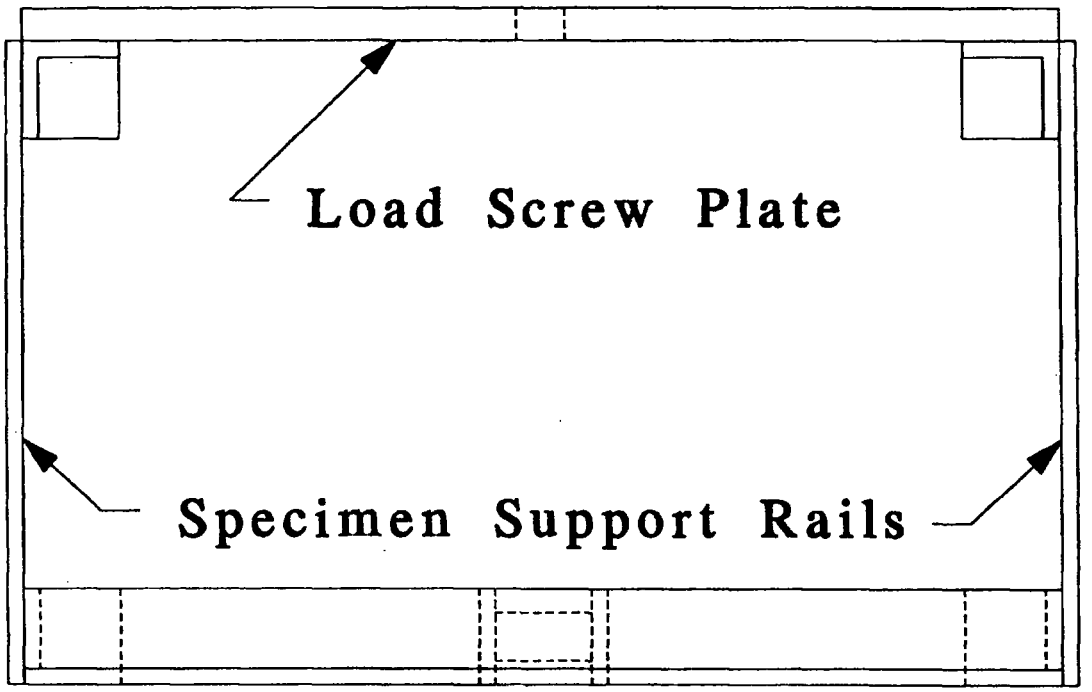

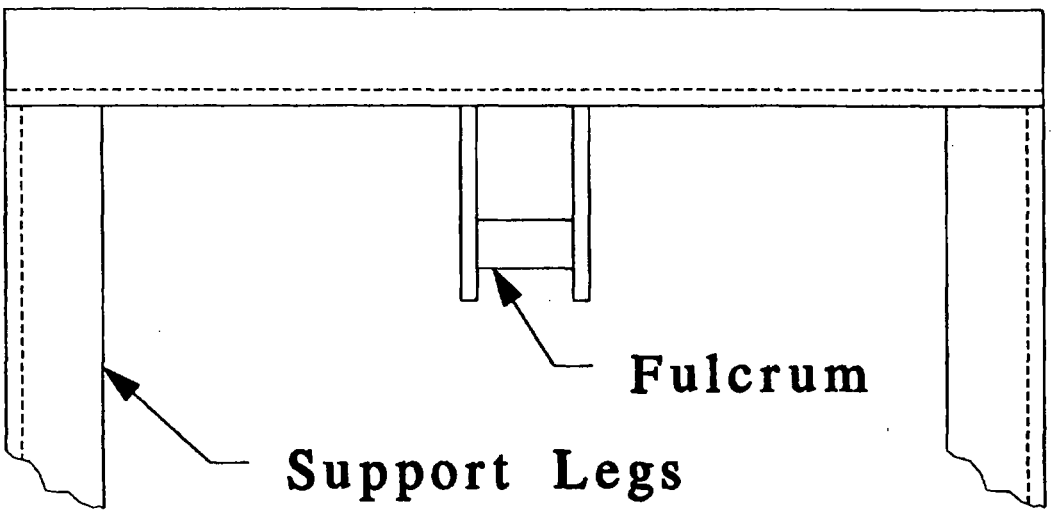

Figure 66. The support frame from which the foil heater, specimens, and cold plates are suspended. The fulcrum position would vary depending upon how the loading force is applied.

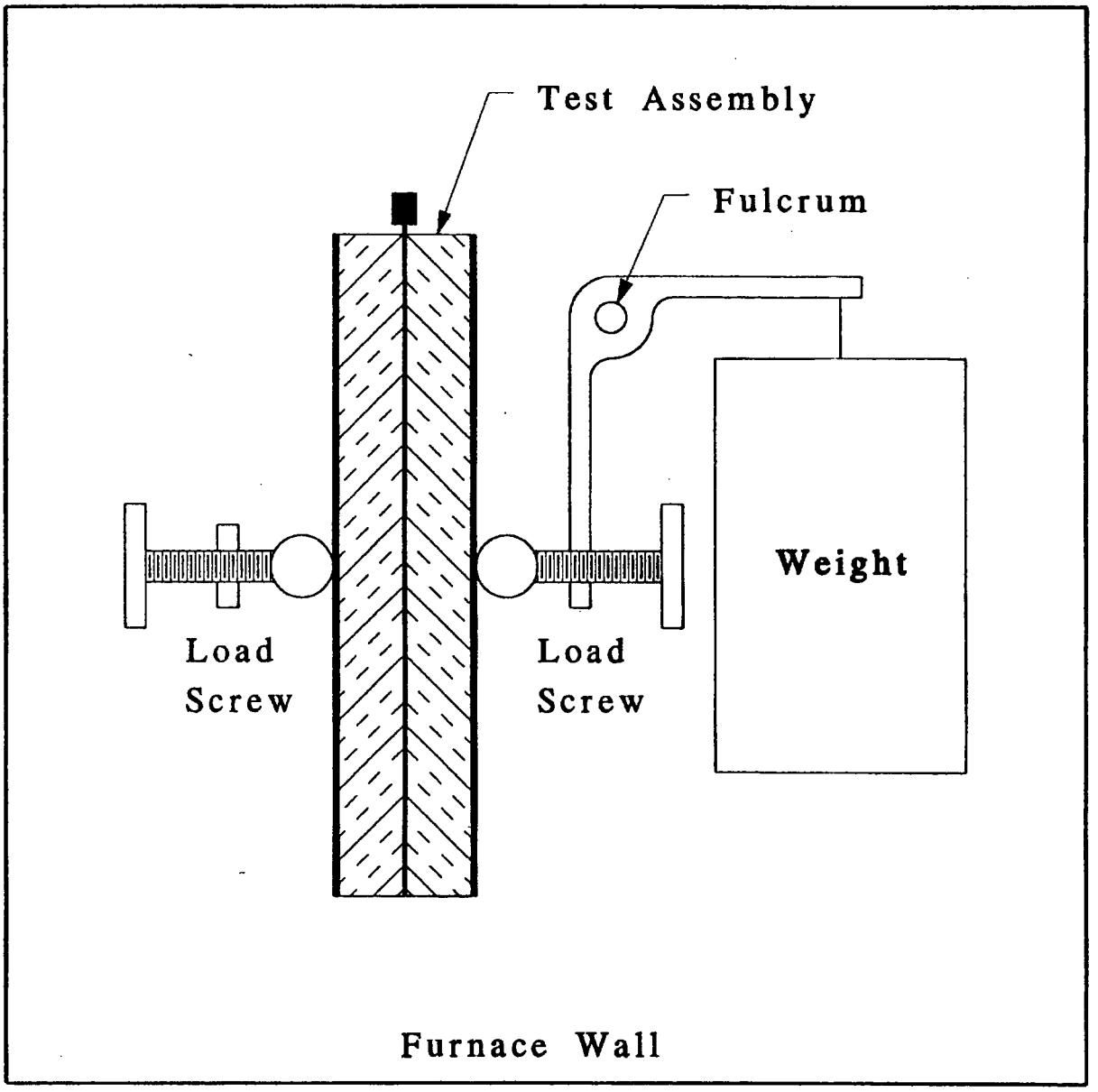

Figure 67. Elevation view of the apparatus if the loading force is provided by a weight inside the furnace.

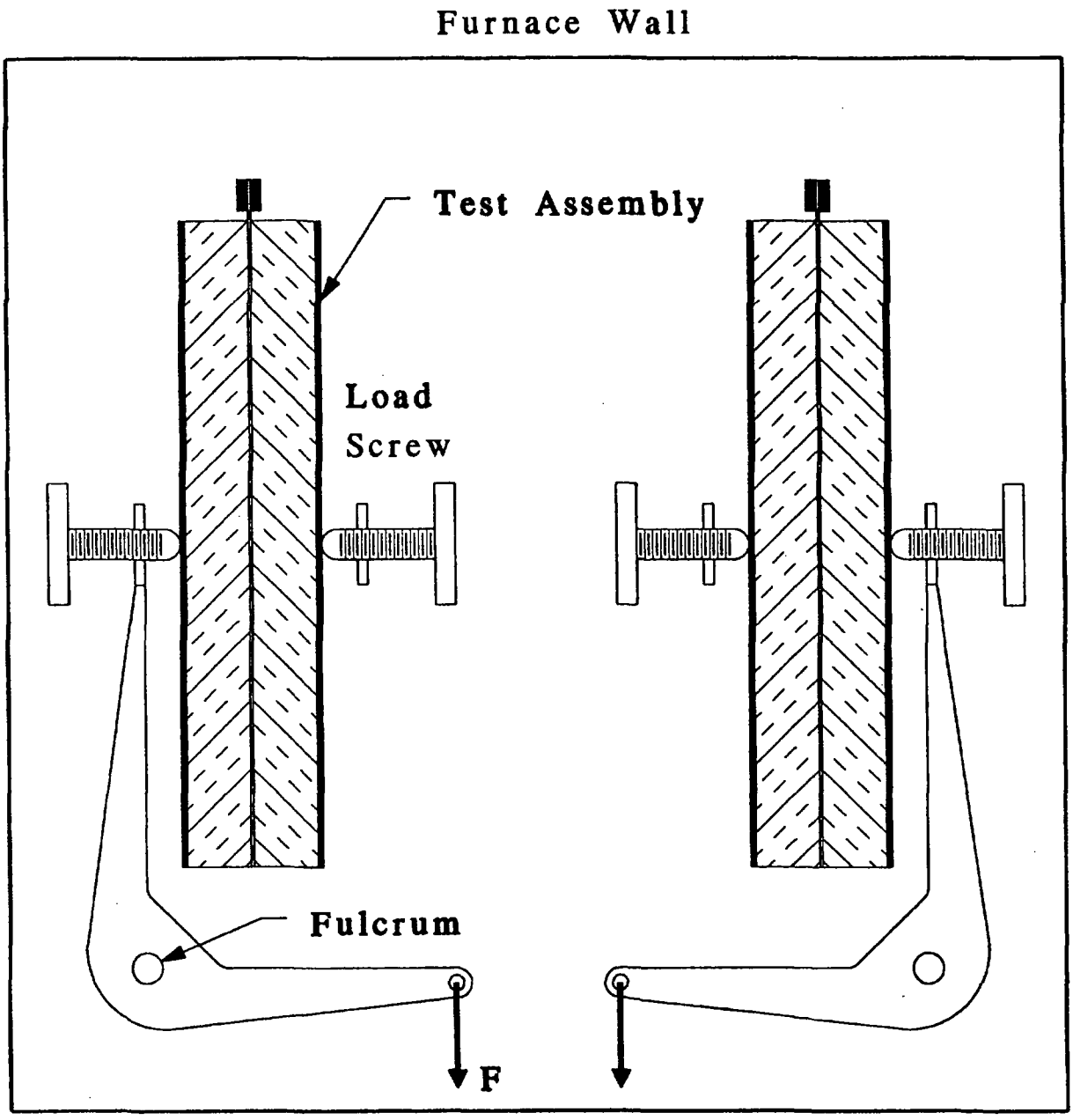

Figure 68. Elevation view of the apparatus if the loading force is provided by a weight below the furnace.

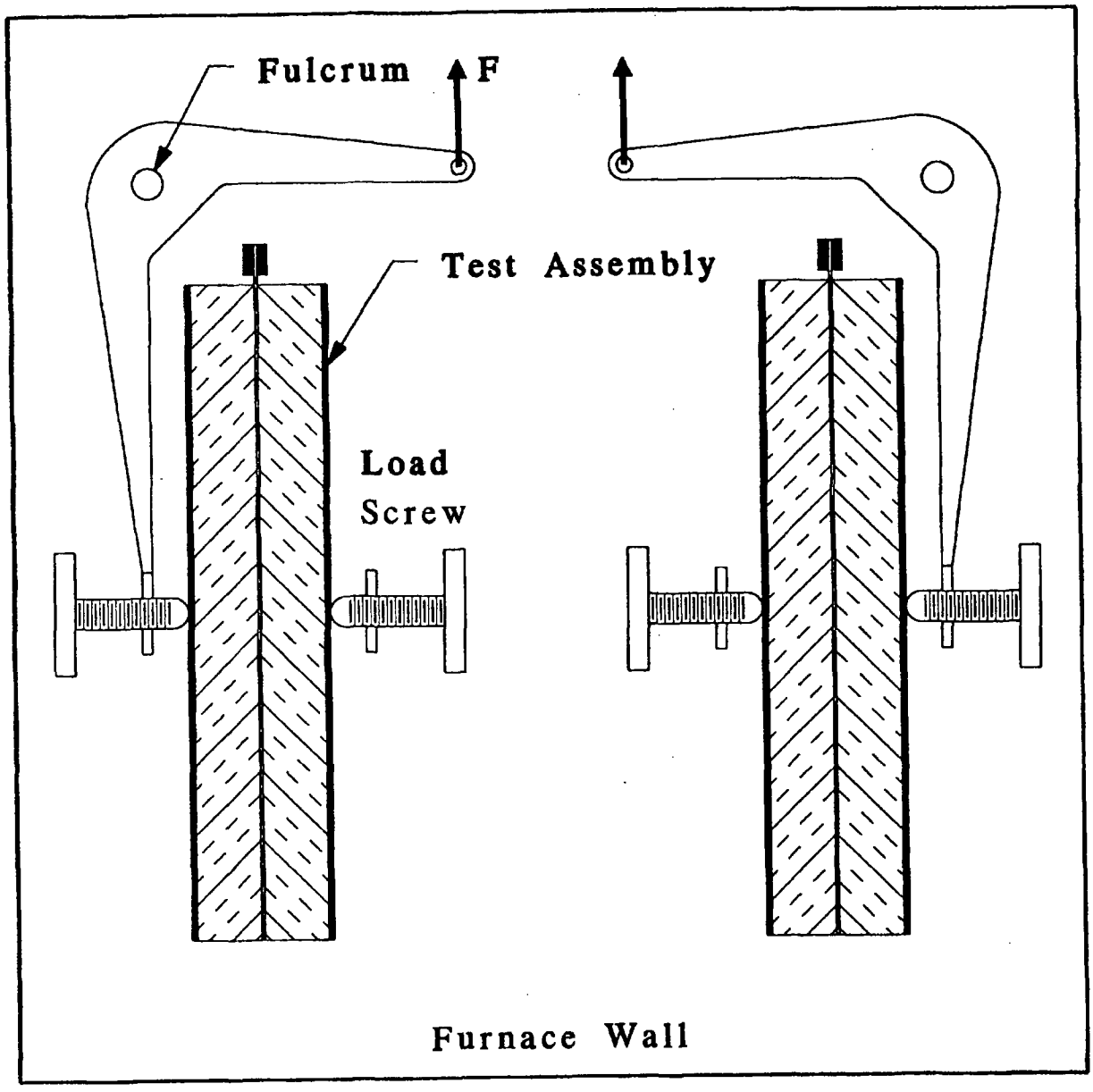

Figure 69. Elevation view of the apparatus if the loading force is provided by a weight and pulley system above the furnace.

8. References

[1] H. B. Callen, "The application of Onsager's reciprocal relations to thermoelectric, thermomagnetic, and galvanomagnetic effects," Phys. Rev. **73**, 1349-58 (1948).

[2] C. A. Domenicali, "Irreversible thermodynamics of thermoelectric effects of homogeneous, anisotropic media," Phys. Rev. **92**, 877-81 (1953).

[3] C. A. Domenicali, "Irreversible thermodynamics of thermoelectricity," Rev. Mod. Phys. **26**, 237-75 (1954).

[4] C. A. Domenicali, "Stationary temperature distribution in an electrically heated conductor," J. Appl. Phys. **25**, 1310-1 (1954).

[5] J. W. Leech, "Irreversible thermodynamics and kinetic theory in the derivation of thermoelectric relations, Canad. J. Phys. **37**, 1044-54 (1959).

[6] S. R. de Groot, "On the thermodynamics of irreversible heat and mass transfer," Intl. J. Heat Mass Transfer **4**, 63-70 (1961).

[7] S. R. de Groot and P. Mazur, *Thermodynamics of Irreversible Processes*, (North-Holland, Amsterdam, 1962).; reprinted by Dover Publications in 1984.

[8] I. Prigogine, *Introduction to Theory of Irreversible Processes* (Interscience Publishers, New York, 1967).

[9] R. Haase, *Thermodynamics of Irreversible Processes* (Addison-Wesley, Reading, MA, 1969); corrected, slightly enlarged edition reprinted by Dover Publications in 1990.

[10] I. Gyarmati, *Non-equilibrium Thermodynamics - Field Theory and Variational Principles* (Springer-Verlag, New York, 1970).

[11] B. H. Lavenda, *Thermodynamics of Irreversible Processes* (Wiley, New York, 1978).

[12] K. S. Forland, T. Forland, and S. K. Ratkje, *Irreversible Thermodynamics: Theory and Applications* (Wiley, Chichester, 1988).

[13] B. C. Eu, *Kinetic Theory and Irreversible Thermodynamics* (Wiley, New York, 1992).

[14] K. Gambár and F. Markus, "On the global symmetry of thermodynamics and Onsager's reciprocity relations," J. Non-Equilib. Thermodyn. **18**, 51-7 (1993).

[15] G. D. C. Kuiken, *Thermodynamics of Irreversible Processes. Applications to Diffusion and Rheology* (Wiley, Chichester, 1994).

[16] D. Jou, J. Casas-Vásquez, and G. Lebon, *Extended Irreversible Thermodynamics, 2nd Ed.* (Springer, New York, 1996).

[17] D. Jou, J. Casas-Vásquez, and G. Lebon, "Recent bibliography on extended irreversible thermodynamics and related topics (1992-95)," J. Non-Equilib. Thermodyn. **21**, 103-121 (1996).

[18] D. A. de Vries, "Simultaneous transfer of heat and moisture in porous media," Trans. Am. Geophys. Union **39**, 909-16 (1958).

[19] D. A. de Vries, "The theory of heat and moisture transfer in porous media revisited," Intl. J. Heat Mass Transfer **30** (7), 1343-50 (1987).

[20] J. R. Philip and D. A. de Vries, "Moisture movement in porous materials under temperature gradients,"Trans. Am. Geophys. Union **38**, 222-32, 594 (1957).

[21] M. Fortes and M. R. Okos, "A nonequilibrium thermodynamics approach to transport phenomena in capillary-porous media," in *Proc. 1st Intl. Symp. on Drying* (McGill Univ., Montreal, 1978).

[22] M. Fortes and M. R. Okos, "Heat and mass transfer in hydroscopic capillary extruded products," AIChE Journal **27**, 255-62 (1981).

[23] A. V. Luikov, *Heat and Mass Transfer in Capillary-porous bodies* (Pergamon, Oxford, 1966).

[24] A. V. Luikov, "Systems of differential equations of heat and mass transfer in capillary-porous bodies," Intl. J. Heat Mass Transfer **18**, 1-14 (1975).

[25] N. G. Zoldners, Thermal Properties of Concrete under Sustained Elevated Temperatures, pp. 1-31 in *Temperature and Concrete, Symposium on Effect of Temperature on Concrete*, ACI Publication SP 25 (American Concrete Institute, 1968).

[26] P. J. Sullivan and M. P. Poucher, The Influence of Temperature on the Physical Properties of Concrete and Mortar in the Range 20 C to 400 C, pp. 103-135 in *Temperature and Concrete, Symposium on Effect of Temperature on Concrete*, ACI Publication SP 25 (American Concrete Institute, 1968).

[27] T. Z. Harmathy, "Thermal properties of concrete at elevated temperatures," J. Matls. **5**, 47-74 (1970).

[28] T. Harada, J. Takeda, S. Yamane, and F. Furumura, Strength, Elasticity, and Thermal Properties of Concrete Subjected to Elevated Temperatures, pp. 377-406 in *Concrete for Nuclear Reactors, Vol. II*, ACI Special Publication SP-34 (American Concrete Institute, 1972).

[29] J. C. Marechal, Thermal Conductivity and Thermal Expansion Coefficients of Concrete as a Function of Temperature and Humidity, pp. 1047-57 in *Concrete for Nuclear Reactors, Vol. II*, ACI Special Publication SP-34 (American Concrete Institute, 1972).

[30] T. Z. Harmathy and L. W. Allen, "Thermal properties of selected masonry unit concretes," Amer. Concrete Inst. J. **70**, 132-42 (1973).

[31] A. M. Neville, *Properties of Concrete* (John Wiley and Sons, New York, 1973).

[32] Y. Anderberg, S. E. Magnusson, O. Pettersson, S. Thelandersson, and U. Wickstrom, An Analytical Approach to Fire Engineering Design of Concrete Structures, pp. 409-38 in Analytical Design of Fire Exposed Concrete Structures (Lund Institute of Technology, Lund, Sweden, 1978).

[33] J. A. Rhodes, Thermal Properties, Chapt. 17 in *Significance of Tests and Properties of Concrete and Concrete-Making Materials*, ASTM Special Technical Publication 169B (American Society for Testing and Materials, Philadelphia, 1978).

[34] C. R. Cruz and M. Gillen, "Thermal expansion of portland cement paste, mortar and concrete at high temperatures," Fire and Matls. **4**, 66-70 (1980).

[35] U. Schneider, *Behavior of Concrete at High Temperatures*, Deutscher Ausschuss für Stahlbeton, Heft 337 (Verlag W. Ernst und sohn, Berlin, 1982).

[36] H. C. Hirth, Jr., M. Polivka, and D. Pirtz, *Final Report on Thermal Properties of Concrete at High Temperatures*, Rept. No. ORNL/BRP-81/1 (Rev. 1) (Oak Ridge Natl. Lab., Oak Ridge, TN, 1984).

[37] U. Schneider (Ed.), *Properties of Materials at High Temperatures – Concrete*, for RILEM Committee 44-PHT (Dept. Civil Eng., Kassel Univ., 1985).

[38] U. Schneider, "Concrete at high temperatures – a general review," Fire Safety J. **13**, 55-69 (1988).

[39] R. Valore, Jr., A. Tuluca, and A. Caputo, *Assessment of the Thermal and Physical Properties of Masonry Block Products*, Rept. No. ORNL/Sub/86-22020/1 (Oak Ridge National Laboratory Oak Ridge, TN, 1988).

[40] P. Morabito, "Measurement of the thermal properties of different concretes," High Temperatures – High Pressures **21**, 51-59 (1989).

[41] T. Z. Harmathy, *Fire Safety Design & Concrete* (Longman Scientific & Technical, Essex, England, 1993).

[42] J. M. Scanlon and J. E. McDonald, Thermal Properties, pp. 229-239 in *Significance of Tests and Properties of Concrete and Concrete-Making Materials*, ASTM Special Technical Publication 169C , P. Klieger and J. F. Lamond, Eds. (American Society for Testing and Materials, Philadelphia, 1994).

[43] P. Smith, Resistance to Fire and High Temperatures, pp. 282-295 in *Significance of Tests and Properties of Concrete and Concrete-Making Materials*, ASTM Special Technical Publication 169C , P. Klieger and J. F. Lamond, Eds. (American Society for Testing and Materials, Philadelphia, 1994).

[44] T. T. Lie and V. K. R. Kodur, "Thermal and mechanical properties of steel-fibre-reinforced concrete at elevated temperatures," Canad. J. Civil Eng. **23**, 511-517 (1996).

[45] Z. P. Bažant and M. F. Kaplan, *Concrete at High Temperatures: Material Properties and Mathematical Models* (Longman (Addison-Wesley), London, 1996).

[46] M. Saad, S. A. Abo-El-Enein, G. B. Hanna, and M. F. Kotkata, "Effect of temperature on physical and mechanical properties of concrete containing silica fume," Cement & Concrete Res. **26**, 669-675 (1996).

[47] M. G. Van Geem, J. Gajda, and K. Dombrowski, *Thermal Properties of Commercially Available High-Strength Concretes*, PCA R&D Serial No. 2031 (Portland Cement Assoc., Skokie, IL, 1996).

[48] M. G. Van Geem, J. Gajda, and K. Dombrowski, "Thermal properties of commercially available high-strength concretes," Cement, Concrete, & Aggregates **19**, 38-53 (1997).

[49] F. Vodák, R. Černý, J. Drchalová, Š. Hošková, O. Kapičková, O. Michalko, P. Semerák, and J. Toman, "Thermophysical properties of concrete for nuclear-safety related structures, Cement & Concrete Res. **27**, 415-426 (1997).

[50] X. Fu and D. D. L. Chung. "Effects of silica fume, latex, methylcellulose, and carbon fibers on the thermal conductivity and specific heat of cement paste," Cement & Concrete Res. **27**, 1799-1804 (1997).

[51] Y. S. Touloukian, W. R. Judd, and R. F. Roy (Eds.), *Physical Properties of Rocks and Minerals*, CINDAS Data Series on Material Properties, Vol. II-2 (Hemisphere Publishing, New York, 1989).

[52] W. L. Sibbitt, J. G. Dodson, and J. W. Tester, Thermal Conductivity of Rocks Associated with Energy Extraction from Hot Dry Rock Geothermal Systems, p. 399 in *Thermal Conductivity 15*, Proc. 15th Intl. Conf. on Thermal Conductivity, V. V. Mirkovich, Ed. (Plenum, New York, 1978).

[53] W. L. Sibbitt, J. G. Dodson, and J. W. Tester, "Thermal conductivity of crystalline rocks associated with energy extraction from hot dry rock geothermal systems,," J. Geophys. Res. **84**, 1117-1124 (1979).

[54] M. T. Morgan and G. A. West, *Thermal Conductivity of the Rocks in the Bureau of Mines Standards Rock Suite*, Rept. No. ORNL/TM-7052 (Oak Ridge Natl. Lab., Oak Ridge, TN, 1980).

[55] M. T. Morgan and G. A. West, The Thermal Conductivity of the Rocks in the Bureau of Mines Standards Rock Suite, pp. 79-90 in *Thermal Conductivity 16*, Proc. 16th Intl. Conf. on Thermal Conductivity, D. C. Larsen, Ed. (Plenum, New York, 1983).

[56] F. E. Heuze, "High-temperature mechanical, physical and thermal properties of granitic rocks – a review," Intl. J. Rock Mech. Min. Sci. & Geomech. Abstr. **20**, 3-10 (1983).

[57] W. B. Durham, V. V. Mirkovich, and H. C. Heard, "Thermal diffusivity of igneous rocks at elevated pressure and temperature," J. Geophys. Res. **92**, 11615-11634 (1987).

[58] W. H. Somerton, *Thermal Properties and Temperature-Related Behavior of Rock/Fluid Systems* (Elsevier, Amsterdam, 1992).

[59] A. Bouguerra, J. P. Laurent, M. S. Goual, and M. Queneudec, "The measurement of the thermal conductivity of solid aggregates using the transient plane source technique," J. Phys. D: Appl. Phys. **30**, 2900-2904 (1997).

[60] N. E. Thompson, "A note of the difficulties of measuring the thermal conductivity of concrete," Mag. Concrete Res. **20**, 45-49 (1968).

[61] D. A. G. Bruggeman, "Über die Geltungsbereiche und die Konstaantenwerte der verscheidenen Mischkörperformeln Lichteneckers," Physikalische Zeit. **37**, 906-XXXX, Chapt. 5 (1936).

[62] R. L. Hamilton and O. K.Crosser, "Thermal conductivity of heterogeneous two-component systems," Ind. Eng. Chem. Fundamentals **1**, 187-91 (1962).

[63] P. S. Turner, "Thermal-expansion stresses in reinforced plastics," J. Research Natl. Bur. Stds. **37**, 239-50 (1946). RP1745

[64] E. H. Kerner, "The elastic and thermo-elastic properties of composite media," Proc. Phys. Soc. **69**, 808-13 (1956).

[65] V. M. Levin, "On the coefficients of thermal expansion of heterogeneous materials," Mech. Solids **2**, 58-61 (1967).

[66] R. A. Schapery, "Thermal expansion coefficients of composite materials based on energy principles," J. Composite Matls. **2**, 380-404 (1968).

[67] B. W. Rosen and Z. Hashin, "Effective thermal expansion coefficients and specific heats of composite materials," Intl. J. Eng. Sci. **8**, 157-173 (1970).

[68] A. A. Fahmy and A. N. Ragai, "Thermal-expansion behavior of two-phase solids," J. Appl. Phys. **41**, 5108-11 (1970).

[69] A. E. Powers, Conductivity in Aggregates, KAPL-2145, Knolls Atomic Power Laboratory (March 1961).

[70] R. E. Meredith and C. W. Tobias, "Conduction in heterogeneous systems," in *Advances in Electrochemistry and Electrochemical Engineering*, C. W. Tobias, Ed. (Wiley, New York, 1962).

[71] H. W. Godbee and W. T. Ziegler, "Thermal conductivities of MgO, Al_2O_3, and ZrO_2 powders to 850 °. II. Theoretical," J. Appl. Phys. **37**, 56-65 (1966).

[72] D. R. Flynn, "Thermal conductivity of ceramics," in *Mechanical and Thermal Properties of Ceramics*, NBS Spec. Pub. 303 (National Bureau of Standards, Gaithersburg MD, 1969).

[73] S. C. Cheng and R. I. Vachon, "A technique for predicting the thermal conductivity of suspensions, emulsions and porous materials," Intl. J. Heat Mass Transfer **13**, 537- (1970).

[74] R. C. Progelhof, J. L. Throne and R. R. Ruetsch, "Methods for predicting the thermal conductivity of composite systems: a review," Polym. Eng. Sci. **16**, 615- (1976).

[75] D. K. Hale, "Review: The physical properties of composite materials," J. Mater. Sci. **11**, 2105- (1976).

[76] R. Landauer, "Electrical conductivity in inhomogeneous media," in *Electrical Transport and Optical Properties of Inhomogeneous Media*, J. C. Garland and D. B. Tanner, Eds. (American Institute of Physics, New York, 1978).

[77] J. L. Jackson and S. R. Coriell, "Transport coefficients of composite materials," J. Appl. Phys. **39**, 2349-54 (1968).

[78] J. Valentich, *Tube Type Dilatometers* (Instrument Society of America, Research Triangle Park, NC, 1981).

[79] G. Ruffino, Thermal Expansion Measurement by Interferometry, pp. 689-706 in Compendium of Thermophysical Property Measurement Methods, Vol. 1 Survey of Measurement Techniques , K.D. Maglić, A. Cezairliyan, and V.E. Peletsky, eds. (Plenum Press, New York, 1984).

[80] R.K. Kirby, Methods of Measuring Thermal Expansion, pp. 549-567 in *Compendium of Thermophysical Property Measurement Methods, Vol. 2 Recommended Measurement Techniques and Practices,* K.D. Maglić, A. Cezairliyan, and V.E. Peletsky, eds. (Plenum Press, New York, 1992).

[81] G. Ruffino, Recent Thermal Expansion Interferometric Measuring Instruments, pp. 569-599 in *Compendium of Thermophysical Property Measurement Methods, Vol. 2 Recommended Measurement Techniques and Practices,* K.D. Maglić, A. Cezairliyan, and V.E. Peletsky, eds. (Plenum Press, New York, 1992).

[82] R. E. Taylor *et al.*, *Thermal Expansion of Solids* (ASM International, Materials Park, OH, 1998).

[83] J. P. McCullough and D.W. Scott, eds., *Experimental Thermodynamics. Volume I Calorimetry of Non-reacting Systems* (Plenum Press, New York, 1968).

[84] A. Cezairliyan, *et al.*, *Specific Heat of Solids* (Hemisphere, New York, 1988).

[85] W. Hemminger, *Calorimetry: Fundamentals and Practice* (Verlag Chemie, Weinheim, 1984).

[86] K.D. Maglić, A. Cezairliyan, and V.E. Peletsky, eds., Compendium of Thermophysical. Property Measurement Methods, Vol. 1 Survey of Measurement Techniques (Plenum Press, New York, 1984).

[87] K.D. Maglić, A. Cezairliyan, and V.E. Peletsky, eds., Compendium of Thermophysical Property Measurement Methods, Vol. 2 Recommended Measurement Techniques and Practices (Plenum Press, New York, 1992).

[88] W.W. Wendlandt, *Thermal Analysis* (Wiley, New York, 1986).

[89] M. E. Brown, *Introduction to Thermal Analysis: Techniques and Applications* (Chapman and Hall, New York, 1988).

[90] R.F. Speyer, *Thermal Analysis of Materials* (Marcel Dekker, New York, 1994).

[91] M. J. Richardson, Application of Differential Scanning Calorimetry to the Measurement of Specific Heat, pp. 669-685 in Compendium of Thermophysical Property Measurement Methods, Vol. 1 Survey of Measurement Techniques , K.D. Maglić, A. Cezairliyan, and V.E. Peletsky, eds. (Plenum Press, New York, 1984).

[92] M. J. Richardson, Application of Differential Scanning Calorimetry to the Measurement of Specific Heat, *Compendium of Thermophysical Property Measurement Methods, Vol. 2*

Recommended Measurement Techniques and Practices, K.D. Maglić, A. Cezairliyan, and V.E. Peletsky, eds. (Plenum Press, New York, 1992).

[93] S.C. Mraw, Differential Scanning Calorimetry, pp. 395-435 in, *Specific Heat of Solids*, A. Cezairliyan, ed. (Hemisphere, New York, 1988).

[94] R. P. Tye, ed., *Thermal Conductivity, Vols 1 and 2* (Academic Press, New York, 1969).

[95] A.W. Pratt, Heat Transmission in Low Conductivity Materials, pp. 301-405 in *Thermal Conductivity, Vol. 1*, R.P. Tye, ed. (Academic Press, New York, 1969).

[96] G.C. Danielson and P.H. Sidles, Thermal Diffusivity and Other Non-steady-state Methods, pp. 149-201 in *Thermal Conductivity*, Vol. 2, R.P. Tye, ed. (Academic Press, New York, 1969).

[97] W.R. Davis, Hot-Wire Method for the Measurement of the Thermal Conductivity of Refractory Materials, pp. 231-254 in *Compendium of Thermophysical Property Measurement Methods, Vol. 1 Survey of Measurement Techniques*, K.D. Maglić, A. Cezairliyan, and V.E. Peletsky, eds. (Plenum Press, New York, 1984).

[98] A.E. Wechsler, The Probe Method for Measurement of Thermal Conductivity," pp. 161-185 in *Compendium of Thermophysical Property Measurement Methods, Vol. 2 Recommended Measurement Techniques and Practices,* K.D. Maglić, A. Cezairliyan, and V.E. Peletsky, eds. (Plenum Press, New York, 1992).

[99] D.R. Flynn, *Development of a Measurement System for Field Determination of Thermal Properties of Soils and Rock: 1. Bibliography and Abstracts*, DRF R&D Report No. 97-02-101, April 1997, 110 p.

[100] R.R. Dils, J.D. Allen, J.C. Richmond, and M.B. McNeil, *Hot Wire Thermal Conductivity Measurements in High Temperature Refractories*, U.S. Department of Energy Rept. No. DOE/CS/40442-T1, 1982.

[101] S.E. Gustafsson, E. Karawacki, and M.N. Khan, "Transient hot-strip method for simultaneously measuring thermal conductivity and thermal diffusivity of solids and fluids," J. Phys. D: Appl. Phys. **12**, 1411-1421 (1979).

[102] S.E. Gustafsson and E. Karawacki, "Determination of the thermal-conductivity tensor and the heat capacity of insulating solids with the transient hot-strip method," J. Appl. Phys. **52**, 2596-2600 (1981).

[103] S.E. Gustafsson, K. Ahmed, A.J. Hamdani, and A. Maqsood, "Transient hot-strip method for measuring thermal conductivity and specific heat of solids and fluids: second order theory and approximations for short times," J. Appl. Phys. **53**, 6064-6068 (1982).

[104] U. Brydsten and G. Bäckström, "Hot strip determination of the thermal conductivity tensor and heat capacity of crystals," Int. J. Thermophysics **4**, 369-387 (1983).

[105] S.E. Gustafsson, "Transient plane source techniques for thermal conductivity and thermal diffusivity measurements of solid materials," Rev. Sci. Instrum. **62**, 797-804 (1991).

[106] S.E. Gustafsson, B. Suleiman, N.S. Saxena, and I. ul Haq, "The transient plane source technique: experimental design criteria," High Temperatures – High Pressures **23**, 289-293 (1991).

[107] L.N. Clarke and R.S.T. Kingston, "Equipment for the simultaneous determination of thermal conductivity and diffusivity of insulating materials using a variable-state method," Australian J. Appl. Sci. **1**, 172-187 (1950).

[108] P. Vernotte, "Détermination simultanée de la chaleur spécifique et de la conductiblité thermique des isolants. Method du signal," Comptes Rendus de L'Académie des Sciences **204**, 563-565 (1937).

[109] L.N. Clarke and R.S.T. Kingston, "Further investigation of some errors in a dynamic method for the determination of thermal conductivity and diffusivity of insulating materials," Australian J. Appl. Sci. **2**, 235-242 (1951).

[110] O. Krischer, "Über die Bestimmung der Wärmeleitfähigkeit, der Wärmekapazität und der Wärmeeindringzahl in einem Kurzzeitverfahren," Chemie-Ing.-Techn. **26**, 42-44 (1954).

[111] A.W. Pratt and J.M.E. Ball, "Thermal conductivity of building materials," J. Inst. Heating Ventilating Engrs. **24**, 201-226 (1956).

[112] A.P. Hatton, "Thermal conductivity and diffusivity measurements by an unsteady-state method with application to insulating materials containing moisture and ice," J. Mech. Engng. Sci. **2**, 45-51 (1960).

[113] G. Bastian, "Détermination de caractéristiques thermophysiques de matériaux de construction par la méthode de la source plane en régimes transitoire et asymtotique," Revue Phys. Appl. **22**, 431-444 (1987).

[114] N.E. Hager, Jr., "Miniature thin-heater thermal conductivity apparatus," ISA Trans. **8**, 104-109 (1969).

[115] N.E. Hager, Jr., "Thin-heater thermal conductivity apparatus," Rev. Sci. Instrum. **31**, 177-185 (1960).

[116] N.E. Hager, Jr., "Thin-heater thermal conductivity apparatus," J. Therm. Insul. **9**, 140-159 (1985).

[117] N.E. Hager, Jr., "Recent developments with the thin-heater thermal conductivity apparatus," J. Therm. Insul. **9**, 111-122 (1985).

[118] C.F. Gilbo, "Thermal conductivity measurement using a thin-heater apparatus," J. Therm. Insul. **9**, 92-101 (1985).

[119] G. Sirdeshpande, Thin-heater Thermal Conductivity Apparatus for Measuring Thermal Conductivity of Powdered Insulations, pp. 844-855 in *Thermal Conductivity 22. Proc. Twenty-Second Intl. Conf. On Thermal Conductivity*, T.W. Tong, ed. (Technomic Publishing, Lancaster, PA, 1994).

[120] ASTM C1114-95, Standard Test Method for Steady-State Thermal Transmission Properties by Means of the Thin-Heater Apparatus (Amer. Soc. For Testing and Materials, West Conshohocken, PA, 1995).

[121] T.Z. Harmathy, "Variable-state methods of measuring the thermal properties of solids," J. Appl. Phys. **35**, 1190-1200 (1964).

[122] R.C. Steere, "Thermal properties of thin-film polymers by transient heating," J. Appl. Phys. **37**, 3338-3344 (1966).

[123] A.B. Ng, M.S. Mirza, and T.T. Lie, "Response of direct models of reinforced concrete columns subjected to fire," ACI Structural J. **87**, 313-325 (1990).

[124] P.A. Miles and S.J. Grubits, *Measurement of the Thermal Diffusivity of Masonry. Review of Test Methods*, Report CIB W14/80/40, Experimental Building Station, North Ryde, New South Wales, Australia, 1980, 29 pp.

[125] N.H. Schilmoeller and D. White, Transient System for Measurement of Thermal Properties of Nuclear Fuel Powders of Varying Densities, pp. 857-870 in *Thermal Conductivity. Proc. Eighth Conf.*, C.Y. Ho and R.E. Taylor, eds. (Plenum Press, New York, 1969).

[126] W.A. Plummer, D.E. Campbell, and A.A. Comstock, "Method of Measurement of Thermal Diffusivity to 1000°C," J. Amer. Ceram. Soc. **45**, 310-316 (1962).

[127] L.N. Dzhavadov, "Measurement of thermophysical properties of dielectrics under pressure," High Temperatures – High Pressures **7**, 49-54 (1975).

[128] R.E. Giedd and D.G. Onn, Electronic Flash: A Rapid Method for Measuring the Thermal Conductivity and Specific Heat of Dielectric Materials, pp. 339-346 in *Thermal Conductivity 20. Proc. 20th* Intl. Thermal Conductivity Conf., D.P.H. Hasselman and J.R. Thomas, Jr., eds. (Plenum Press, New York, 1987).

[129] L. Kubičár, *Pulse Method of Measuring Basic Thermophysical Parameters, Part E of Vol. XII, Thermal Analysis, of Wilson and Wilson's Comprehensive Analytical Chemistry*, G. Svehla, ed. (Elsevier, New York, 1990).

[130] E. Piorkowska and A. Galeski, "Measurements of thermal conductivity of materials using a transient technique. I. Theoretical background," J. Appl. Phys. **60**, 485-492 (1986).

[131] E. Piorkowska and A. Galeski, "Measurements of thermal conductivity of materials using a transient technique. II. Description of the apparatus," J. Appl. Phys. **60**, 493-498 (1986).

[redacted]

(This page is blank)

[redacted]

[redacted]

[redacted]

Appendix A. Analysis Procedures for Transient Hot-Wire or Probe Techniques for Thermal Conductivity Measurement

Transient techniques for thermal conductivity measurement have been utilized with planar heat sources, point or spherical heat sources, and cylindrical heat sources, In this appendix, attention is confined to measurement systems utilizing a cylindrical geometry. For most of the analyses discussed below, an infinitely long heat source is assumed. The end effects due to a finite source length are briefly discussed.

A.1 Ideal Line Heat Source

The simplest analysis involves an ideal line heat source (i.e., a source of vanishing diameter) that is turned on at zero time and thereafter produces a constant heat output. Apparatus used for determining the thermal conductivity of liquids and gases usually approximates this ideal line heat source quite closely, the heater wire, which also serves as a resistance thermometer, typically being about 5 to 25 μm in diameter. Thin wire heaters also are frequently used for measuring the thermal conductivity of thermal insulation, including refractory materials. For *in-situ* measurements of, for example, soil thermal properties, a larger, more rugged probe is needed and it is necessary to account for the finite size and thermal capacity of the probe, as well as for thermal contact resistance between the probe and the surrounding medium. It is useful, however, to consider the analysis for an ideal line heat source since that solution serves as a limiting form of the solution for a probe as its diameter decreases and contact resistance becomes smaller.

In some implementations of the line heat source method, the temperature of the heater wire, or slender probe, is measured. In other implementations, the temperature is measured in the surrounding medium at some known radius from the axis of the heater or probe.

Following Carslaw and Jaeger [A1, pp. 261-262], we suppose heat to be released at the continuous rate Q per unit time per unit length along the z-axis. If the heat supply begins at the time $t = 0$, when the medium is isothermal at a temperature $T = 0$, the temperature at a distance r from the z-axis is given by

$$T(r,t) = \frac{Q}{4\pi\lambda} E_1\left(\frac{r^2}{4\kappa t}\right) , \tag{1}$$

where

$$E_1(x) = \int_x^\infty \frac{e^{-x}}{x} dx \tag{2}$$

is the exponential integral, λ is thermal conductivity, and κ is thermal diffusivity.. For small values of x, corresponding to small values of the radius r or large values of the time t, Eq. (2) reduces to

$$E_1(x) = -\gamma - \ell n\, x + \frac{x}{1\cdot 1!} - \frac{x^2}{2\cdot 2!} + \frac{x^3}{3\cdot 3!} - \frac{x^4}{4\cdot 4!} - \cdots , \tag{3}$$

where $\gamma = 0.577216...$ is Euler's constant. For values of x sufficiently small that x is negligible compared with $\ell n\ x$, the temperature is given simply by

$$T(r,t) = \frac{Q}{4\pi\lambda}\left(-\gamma + \ln\frac{4\kappa t}{r^2}\right) \quad . \tag{4}$$

For measurements at a fixed value of r,

$$T(a,t) = \frac{Q}{4\pi\lambda}(A + \ln t) \quad , \tag{5}$$

where A is a constant whose value need not be known if only thermal conductivity is needed. Thus the thermal conductivity can be computed from the strength of the heat source and the slope of a plot of temperature versus the logarithm of time. Note that in using Eq. (5) to obtain thermal conductivity, it is not necessary to specify the radius at which the temperature is measured, provided the value of $4\kappa t/r^2$ is large enough for Eqs. (4) and (5) to be valid. If it is desired to use Eq. (4) to compute thermal diffusivity values, it is necessary to know accurately the radius of the heater wire or probe. As pointed out, e.g., by Nieto de Castro [A2-A3], with the very thin probes used for measurements on fluids, and the very short times that are used in order to avoid convection effects, it generally is not possible to obtain thermal diffusivity (or specific heat) values with anywhere near the accuracy that is possible for thermal conductivity values.

For many investigations it is assumed that the line heat source probe is very thin and also very conductive in the radial direction so that the temperature across the probe can be considered to be constant at any given time. Under such conditions the temperature of the probe itself can be used to determine the thermal conductivity, provided the heated section of the probe is also sufficiently long, and of sufficiently low thermal conductance, that all of the power input to the portion of the probe where the temperature is measured can be assumed to flow radially into the surrounding medium whose thermal conductivity is to be determined.

Some investigators have used a two-wire or two-probe method in which the temperature is measured by a sensor located at some distance away from the line heat source. Under such conditions the value of $4\kappa t/r^2$ is usually not large enough for Eq. (5) to be valid so that the thermal conductivity needs to computed using Eq. (1).

A.2 Finite-Diameter Probe

Jaeger [A4; 2, pp. 344-345] has derived a solution for a finite-diameter probe, made of a perfect conductor , with finite thermal contact resistance between the probe and the surrounding medium. As above, the medium is assumed initially to be isothermal at $T = 0$ when the probe is energized at the constant rate Q per unit time per unit length. The temperature of the probe is given by

$$T(t) = \frac{Q}{\lambda} G(\beta, \alpha, \tau) \quad , \tag{6}$$

where

$$G(\beta, \alpha, \tau) = \frac{2\alpha^2}{\pi^3} \int_0^\infty \frac{[\,1 - \exp(-\tau u^2)\,]\, du}{u^3 \Delta(u)} \quad , \tag{7}$$

and J_i and Y_i are the Bessel functions of the first and second kind, respectively, of order I. The dimensionless parameters β, α, and τ are defined as

$$\beta = \frac{\lambda}{bh} \qquad \alpha = \frac{2\pi b^2 \rho C}{S} \qquad \tau = \frac{\kappa t}{b^2} \quad , \tag{9}$$

where the properties of the medium are thermal conductivity, λ [W/m·K], density, ρ [kg/m^3], specific heat, C [J/kg·K], and thermal diffusivity, κ [m^2/s]; the probe is of radius b [m]; S [J/m·K] is the thermal capacity per unit length of the probe; and h [W/m^2·K] is the heat transfer coefficient between the probe and the surrounding medium. The dimensionless parameter β is the ratio of the thermal contact resistance, $1/h$, at the probe-medium interface to the thermal resistance, b/λ, of a layer of the medium of thickness b. The dimensionless parameter α is twice the ratio of the thermal capacity of a cylinder of the medium material of radius b to the thermal capacity of an equal length of the probe. (Note that the probe could actually be a hollow cylinder, rather than a solid cylinder, with S being the thermal capacity of the actual probe material present.) The parameter τ is the usual dimensionless time that is used in transient heat conduction problems, obtained by multiplying the actual time by the ratio of the thermal diffusivity to the square of a characteristic dimension, in this case the radius of the probe (this parameter τ is often referred to as the Fourier number).

The integration shown in Eq. (7) cannot be carried out in closed form so it must be done numerically. For small values of τ, Jaeger [A4] shows that

$$G(\beta, \alpha, \tau) \approx \frac{\alpha}{2\pi}\left[\tau - \frac{\alpha}{2\beta}\tau^2 + \cdots\right] \tag{10}$$

when the heat transfer coefficient h is finite so that $\beta > 0$, and

$$G(\beta, \alpha, \tau) \approx \frac{\alpha}{2\pi}\left[\tau - \frac{4\alpha}{3\sqrt{\pi}}\tau^{3/2} - \cdots\right] \tag{11}$$

when h is infinite (perfect contact) so that $\beta = 0$. For large values of τ, Jaeger [A4] shows that

$$G(\beta, \alpha, \tau) \approx \frac{1}{4\pi}\left[2\beta - \gamma + \ln 4\tau - \frac{4\beta - \alpha}{2\alpha\tau} + \frac{\alpha - 2}{2\alpha\tau}(-\gamma + \ln 4\tau) + \cdots\right] . \quad (12)$$

For values of τ sufficiently large that the last two terms, involving τ^{-1}, can be neglected, Eq. (12) reduces to

$$G(\beta, \alpha, \tau) \approx \frac{1}{4\pi}[2\beta - \gamma + \ln 4\tau + \cdots] . \quad (13)$$

If the probe has a vanishingly small thermal capacity, so that $\beta \to 0$, Eq. (13) reduces to Eq. (4), the expression for an ideal line source. Two features of Eq. (13) are worthy of note. First, for long enough times, the thermal capacity of the probe is no longer a factor. Second, for long enough times, the effect of thermal contact resistance becomes independent of time so that one can compute thermal conductivity from a plot of temperature versus the logarithm of time without having to know either the thermal contact resistance or the thermal capacity of the probe. For a line heat source or a very slender probe such as those used for laboratory measurements on loose-fill materials, it is relatively easy to work in the region where Eq. (13) is valid. However, a probe for *in-situ* measurements of the thermal properties of soils must be rugged enough, and thus large enough in diameter, to be inserted 1 or 2 meters into the ground. Since τ is inversely proportional to the square of the radius of the probe, increasing the probe diameter by, say, an order of magnitude in order to achieve adequate strength, reduces the values of τ by two orders of magnitude. Thus, as is discussed in more detail below, for the probes to be developed for this project, it is necessary to use expressions that are more accurate than Eq. (13) for the values of τ that are of concern.

It also is of interest to examine the behavior of Eq. (7) in the limit when $\alpha \to \infty$. This limit corresponds to the case where the probe is of finite diameter but has negligible thermal capacity. Such a probe could be approximated by a very thin-walled hollow tube. As shown by Jaeger [A4], for $\beta = 0$ and $\alpha \to \infty$,

$$G(0, \infty, \tau) = \frac{2}{\pi^3}\int_0^\infty \frac{[1 - \exp(-\tau u^2)]\,du}{u^3[J_1^2(u) + Y_1^2(u)]} . \quad (14)$$

For finite values of thermal contact resistance (i.e., $\beta > 0$),

$$G(\beta, \infty, \tau) = \frac{\beta}{2\pi} + G(0, \infty, \tau) \quad ; \tag{15}$$

it is seen that β only shows up with respect to the constant temperature drop between the probe and the medium. Thus , for determinations of thermal conductivity, it is not necessary to know or to determine the thermal contact resistance. Equation (14) is the same as the solution for an infinite region with constant heat flux at $r = a$ [A1, p. 338].

Blackwell [A5] derived, with very different notation, the equivalent solution to Es. (6)-(9). In his short-time approximate solution, he included one more term that is given in Eq. (10); in our notation it is

$$G(\beta, \alpha, \tau) \approx \frac{\alpha}{2\pi}\left[\tau - \frac{\alpha}{2\beta}\tau^2 + \frac{8\alpha}{15\sqrt{\pi}\,\beta}\tau^{5/2} - \cdots\right] . \tag{16}$$

Blackwell's long-time approximation, with appropriate changes in notation agrees with Eq. (12), above. Blackwell [A5] also considered the problem of a hollow cylindrical probe, having a finite thermal conductivity, with heat supplied at the outer surface of the probe and the temperature measured at the inner surface. He obtained large-time and short-time solutions that agreed with Eqs. (12) and (16), above but with the inclusion of correction terms that account for the temperature difference between the inner and outer radii of the probe. As pointed out by Blackwell [A5] and by Wechsler [A6], the corrections in Blackwell's equations are quite small for well-designed probes. Furthermore, in the long-time solution given by Blackwell the correction term for finite probe thermal conductivity varies as τ^{-1} so that, for times long enough that Eq. (13) is valid, it drops out.

De Vries and Peck [A7] derived a long-time solution for a cylindrical probe, of finite thermal conductivity, with an ideal line heat source at its axis. With appropriate change of variables, their solution is identical to Eq. (12), with the addition of a term $(-1/\alpha)\,(\lambda/\lambda_p)\cdot\tau^{-1}$, where λ_p is the thermal conductivity of the probe material, inside the square brackets. For a homogeneous probe, this term reduces to $(-1/2)\,(\kappa/\kappa_p)\cdot\tau^{-1}$, where κ_p is the thermal diffusivity of the probe material. As with Blackwell's solution, the correction term for finite probe conductivity is not needed for times long enough that Eq. (13) can be used.

Christoffel and Calhaem [A8] give solutions, analogous to those of Carslaw [A4], for a perfectly conducting probe with no contact resistance, a perfectly conducting probe with contact resistance, and a probe having a finite thermal conductivity but no contact resistance. Although these authors do not indicate where the heat source is, their solution for a probe having a finite thermal conductivity appears to correspond to a probe heated at its outer surface. Their correction for finite probe conductivity is similar to that of Blackwell, whose solution is for a probe with heat supplied at its outer surface.

Bruijn, et al. [A9] used a "modified Jaeger model," which was a homogeneous solid cylindrical probe having the same thermal capacity per unit length as the real probe and an effective thermal contact resistance consisting of the contact resistance between the outer surface of the probe and the surrounding medium and an internal thermal resistance computed between the position of the temperature sensor and the outer radius of the probe. This internal resistance was computed for an idealized probe, with the heater at the axis, surrounded by a hollow cylinder of electrically insulating material (in which the temperature sensor was placed), and an outer metal cylinder. The internal resistance was assumed to be that computed for steady-state radial heat flow in the idealized probe, on the basis that the time constant of the probe is so short compared to the duration of a test that a steady-state temperature profile would be established in the probe.

Bruijn, et al., also give equations for a "four-regions model," consisting of coaxial cylinders: heating wire, insulating material, tube, and medium to be measured. These equations were left in terms of the Laplace-transformed temperatures and therefore are not suitable for use in data analysis.

Lin and Love [A10] give analytical solutions, similar to those of Jeager [A4] and of Blackwell [A5], for a system consisting of a probe, a well casing, and a surrounding medium. The probe and the well casing are assumed to have infinite radial thermal conductivity. They investigate the cases with and without thermal contact resistance at the interfaces and obtain integral solutions, large-time approximate solutions, and small-time approximate solutions. While their results are valuable, the extra complexity of three regions, rather than two, is not needed for the present project.

Bastian and Grosjean [A11] provide analytical solutions for probe consisting of a hollow pipe, open at the ends, with the unique feature that the material being tested in situated both outside and inside the probe.

All of the above theory was based on the assumption that the probe was infinite in length. In a separate paper, Blackwell [A12] examined the errors due to axial heat flow in a finite-length probe and provided guidelines for selecting a suitably long probe to avoid significant errors. Kierkus, et al.,[A13] have examined end effects in conjunction with a line heat source method for fluids.

As indicated previously, most investigators have used a simple large-time solution, such as Eq. (5) or (13), while a few investigators have used a somewhat more involved expression, such as Eq. (12). Very few workers have used an integral expression, such as Eqs. (6)-(9), that is valid over the entire time range.

In conjunction with the Thermal Property Analyzer (TPA) developed for EPRI by workers at Ontario Hydro [A14], a program was written that used a non-linear least squares fit to Blackwell's model [A5] to obtain thermal diffusivity and thermal contact resistance from the temperature versus time data, experimentally determined probe parameters ("effective probe radius" and probe thermal capacity), soil thermal conductivity, and probe power. It is not evident why these investigators elected to compute the thermal conductivity, separately, from the slope of the temperature-versus-time curve, rather than to have the computer program determine thermal conductivity as well. It appears that they computed thermal conductivity from the large-time data, where thermal diffusivity (or heat capacity) of the soil and contact resistance would cause relatively little effect, and then

computed the thermal diffusivity and contact resistance using small-time data. It would be preferable to have the computer use the entire temperature-time history and obtain self-consistent values for thermal conductivity, thermal diffusivity/heat capacity, and contact resistance. With the microprocessors that were available two decades ago, these investigators had to use a simpler approach for the software built into the TPA. They only used the non-linear curve fit program with a mainframe computer.

At about the same time, investigators at Sandia National Laboratories developed equipment and data analysis procedures [A15-A19] for using a probe method to determine the thermal conductivity of powders at high temperatures. These workers used Jaeger's analysis [A4], namely our Eqs. (6)-(9), (11), and (12), as well as finite element or finite difference techniques, to assist in designing their probes. For data analysis, they used a non-linear least squares fit, or parameter estimation technique, based on Jaeger's analysis. There is a significant gap between the range of validity of the small-time solution, Eq. (11), and that of the large-time solution, Eq. (12). There is an intermediate range of τ where neither solution even comes close to providing accurate results. The Sandia workers used the full integral solution, our Eqs. (6)-(9), for small and intermediate values of time and Eq. (12) for large times. They carried out a numerical study to determine what values of τ, for a given β and α, to use for the transition from one solution to the other, so as to obtain good continuity in temperature and its derivative with respect to time. (Discontinuity in either quantity, and particularly in the derivative, can wreck havoc with a non-linear least squares fit.) Koski [A17] indicated that the integral equation, our Eq. (7) proved difficult to integrate in a simple, rapid manner, particularly for larger values of τ, which is the reason they used the approximate solution for larger times.

A.3. Numerical Results

A FORTRAN program was written to compute values of $G(\beta, \alpha, \tau)$, using Eqs. (6)-(9), (14), and (15). Figure A1 shows G plotted versus τ with α as a parameter for $\beta = 0$, i.e., no contact resistance. Considering first the ideal probe with no thermal capacity, i.e., $\alpha \to \infty$, it is seen that, in this semi-log plot, the probe temperature curves rather slowly at small and medium times and asymptotically approaches a straight-line for values of τ greater than about 100, in accordance with Eqs. (5) and (13). Figure A1 includes curves corresponding to $\alpha = \infty$, 100, 50 , 20, 10, 5, 2, 1, 0.5, 0.2, and 0.1 Although the curves for the larger values cannot be distinguished, Figure A2 shows that as the thermal capacity of the probe approaches and then exceeds the thermal capacity of an equivalent volume of the surrounding medium (e.g., soil), a significant time delay is introduced at earlier times. When the contact resistance is zero, as in this case, or relatively small, the time lag due to a probe having a thermal capacity approximately equal to that of the medium (i.e., $\beta \approx 2$) actually results in the curve of temperature versus the logarithm of time approaching a straight line more rapidly than in the case where the probe has a very small thermal capacity. When the thermal capacity of the probe greatly exceeds that of an equivalent volume of the medium, the probe temperature lags behind until values of τ of the order of 1000 are attained. Inspection of Fig. A1 shows that if data over a rather limited range of temperatures, say τ going from 10 to 100, were used, it would be easy to be fooled into thinking the "straight-line region" had been reached but the slope thereby used to compute thermal conductivity could be significantly in error.

Figure A2 shows the same curves as those in Fig. 1, but plotted with a different vertical axis in order to facilitate comparison with the next four figures. Figure A3 shows how the curves change when contact resistance is present, in this case corresponding to $\beta = 1$ (i.e., the contact resistance is equal to the resistance of a plane layer of the surrounding medium having a thickness equal to the radius of the probe). For the case of a very light probe, with $\alpha \rightarrow \infty$, the contact resistance simply displaces the temperature-time curve upward, as shown by Eq. (15). For probes having large thermal capacity, the probe temperature cannot "jump" in response to the contact resistance so the temperature of such probes initially increases slowly and then accelerates to "catch up" with the curve for probes having very low thermal capacity. A potentially serious consequence of this behavior is that the curves of temperature versus the logarithm of time can have deceptively linear regions that are much steeper than the true final slope, thus exacerbating the potential error in thermal conductivity. Figures A4, A5, and A6 show the computed temperature-time curves for larger contact resistances, with $\beta = 2$, 3, and 4, respectively. The effects discussed above in this paragraph are exaggerated further as contact resistance increases.

The results shown in these figures clearly illustrate that great caution must be exercised in attempting to use the large-time solutions, such as Eq. (12) or Eq. (13), to determine thermal conductivity. This caution is required because the thermal capacity of the probe and the thermal contact resistance between the probe and the surrounding medium can seriously distort the shape of the temperature-time curve and result in serious measurement errors. The results in these figures also show that, for a given probe, the temperature-time curve is sensitive to the thermal capacity of the medium during the small and medium times but not at long times. Thus, if the heat capacity or the thermal diffusivity of the soil is desired, it is necessary to use information from the early part of the curve; these properties cannot be obtained from large-time data only. Finally, these curves and the above discussion demonstrate the importance of using the complete curve of temperature versus the logarithm of time if it is desired to obtain consistent, accurate values for thermal conductivity, thermal diffusivity, heat capacity, and thermal contact resistance.

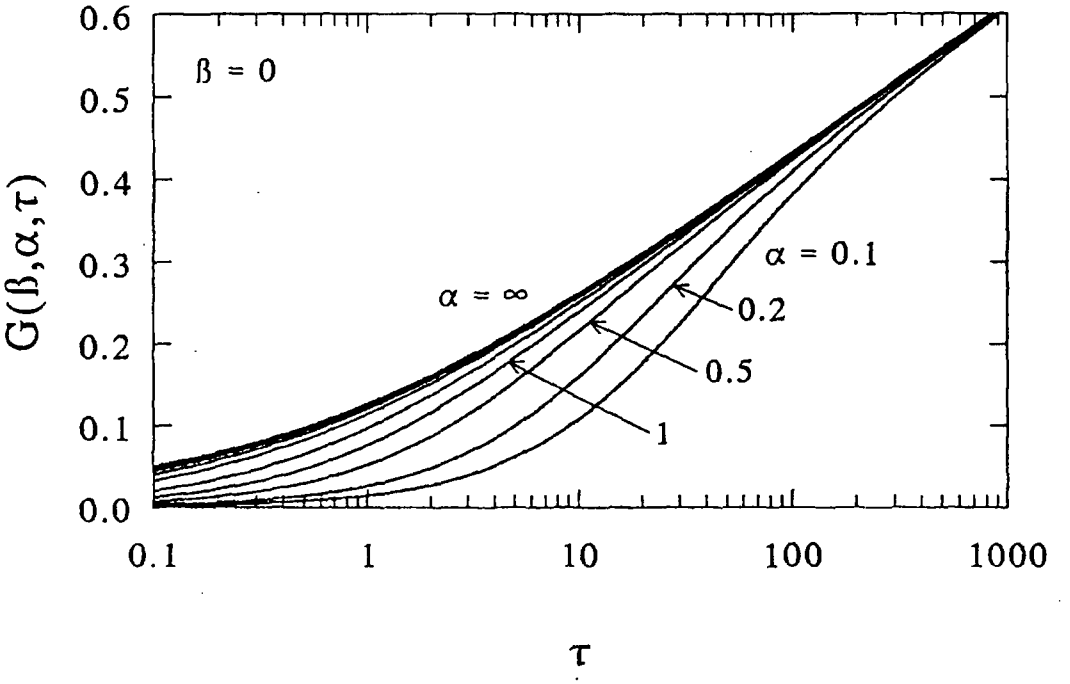

Figure A1. The function $G(\beta, \alpha, \tau)$ versus τ, with α as a parameter, for $\beta = 0$.

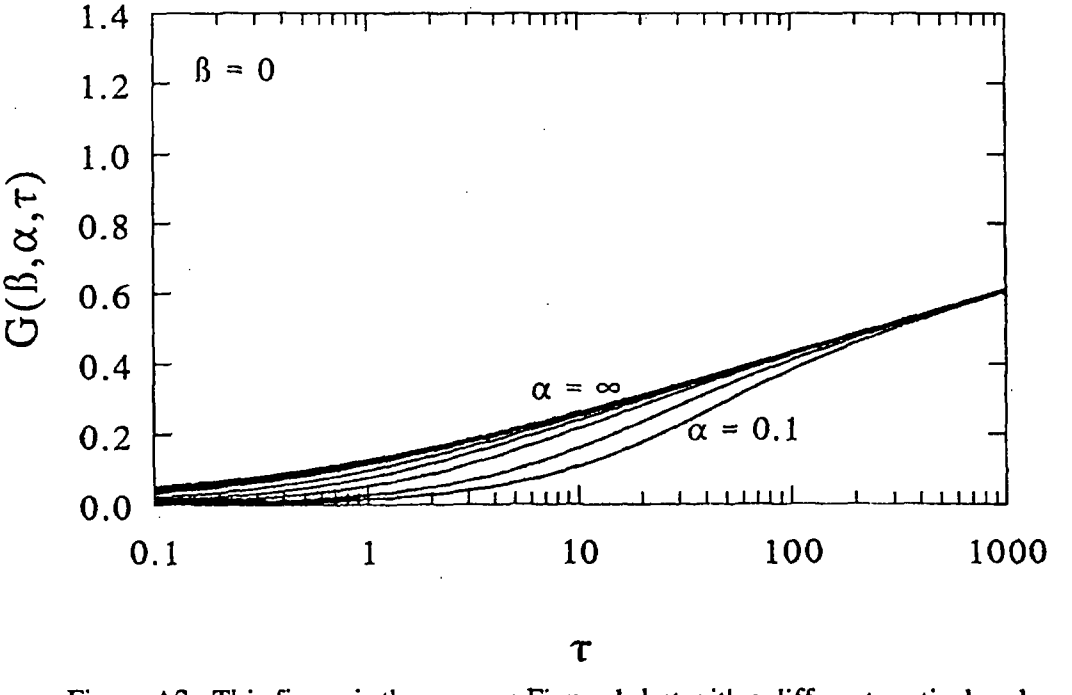

Figure A2. This figure is the same as Figure 1, but with a different vertical scale.

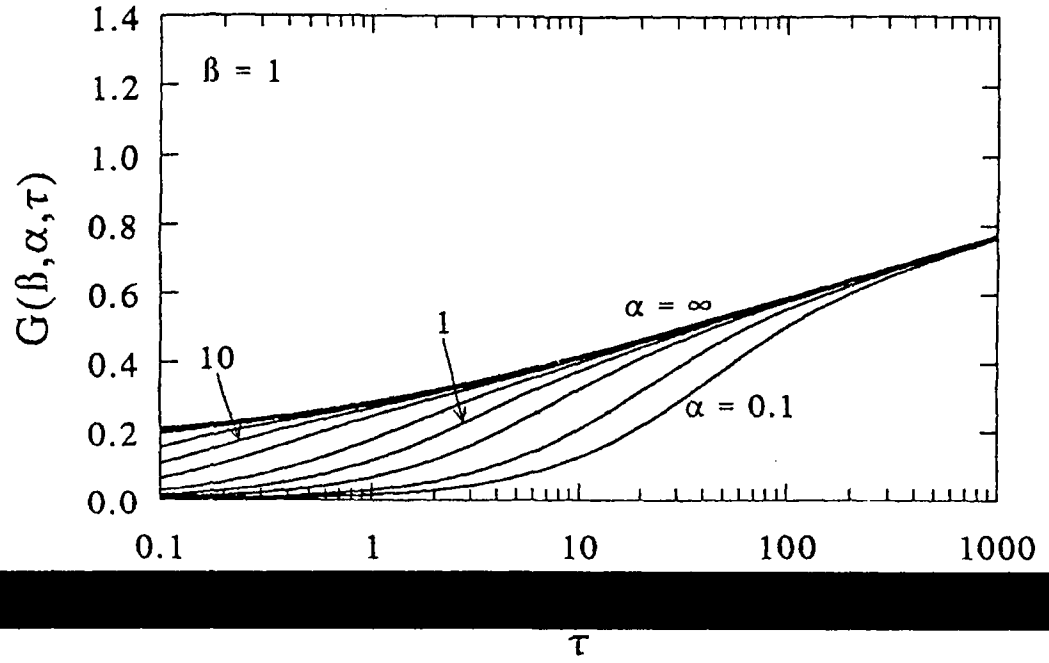

Figure A3. The function $G(\beta, \alpha, \tau)$ versus τ, with α as a parameter, for $\beta = 1$.

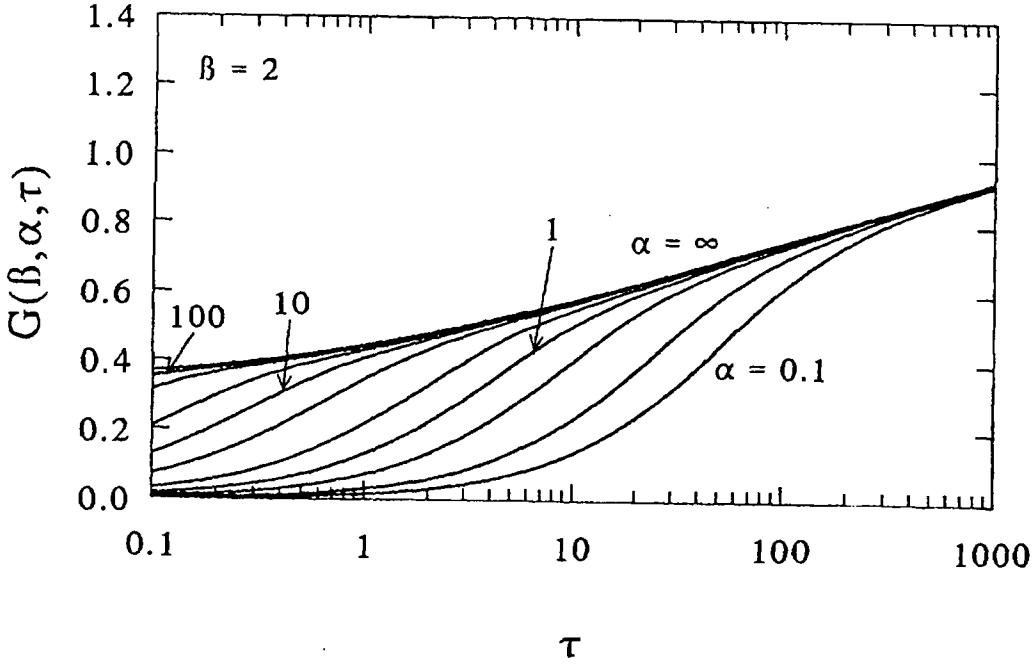

Figure A4. The function $G(\beta, \alpha, \tau)$ versus τ, with α as a parameter, for $\beta = 2$.

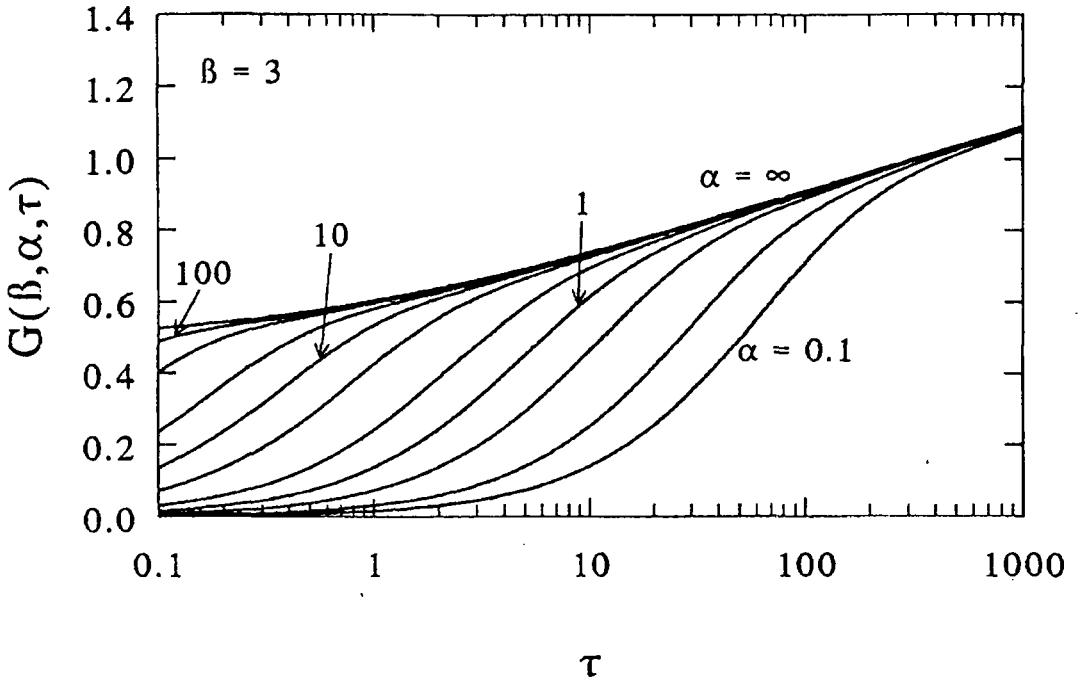

Figure A5. The function $G(\beta, \alpha, \tau)$ versus τ, with α as a parameter, for $\beta = 3$.

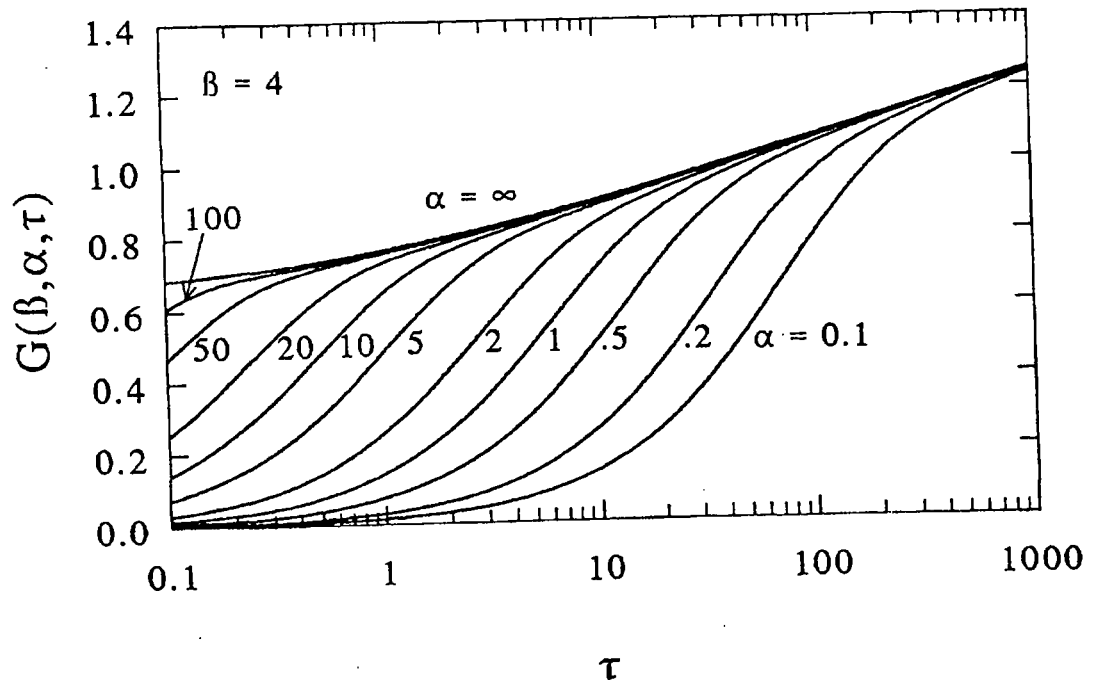

Figure A6. The function $G(\beta, \alpha, \tau)$ versus τ, with α as a parameter, for $\beta = 4$.

A.4. References

[A1] Carslaw, H.S. & Jaeger, J.C. (1959). *Conduction of Heat in Solids (2nd Ed.).* New York, NY: Oxford University Press.

[A2] Nieto de Castro, C.A., Taxis, B., Roder, H.M., and Wakeham, W.A. (1988). Thermal diffusivity measurement by the transient hot-wire technique: a reappraisal. *International Journal of Thermophysics, 9*(3), 293-316.

[A3] Fareleria, J.M.N.A. & Nieta de Castro, C.A. (1989). Simultaneous measurement of the thermal conductivity and thermal diffusivity of fluids. *High Temperatures - High Pressures, 21*(4), 363-371.

[A4] Jaeger, J.C. (1956). Conduction of heat in an infinite region bounded internally by a circular cylinder of a perfect conductor. *Australian Journal of Physics, 9*, 167.

[A5] Blackwell, J. H. (1954). A transient-flow method of determination of thermal constants of insulating materials in bulk. *Journal of Applied Physics, 25*, 137-144.

[A6] Wechsler, A.E. (1992). The probe method for measurement of thermal conductivity. In K. D. Maglic, A. Cezairliyan, and V. E. Peletsky (Eds.), *Compendium of Thermophysical Property Measurement Methods, Recommended Measurement Techniques and Practices* (Vol. 2, pp. 161-185). New York, NY: Plenum Press.

[A7] Vries, D.A. de & Peck, A.J. (1958). On the cylindrical probe method of measuring thermal conductivity with special reference to soils. I. Extension of theory and discussion of probe characteristics. *Australian Journal of Physics, 11*, 255-271.

[A8] Christoffel, D.A. & Calhaem, I.M. (1969). A geothermal heat flow probe for *in situ* measurement of both temperature gradient and thermal conductivity. *Journal of Scientific Instruments (Journal of Physics E), Series 2, 2*, 457-465.

[A9] Bruijn, P.J., van Haneghem, I.A., & Schenk, J. (1983). An improved nonsteady-state probe method for measurements in granular materials: Part I: theory. *High Temperatures - High Pressures, 15*, 359-366.

[A10] Lin, J. D. & Love, T. J. (1985). Analysis of a method of in-situ thermal properties determination for geologic formations. *Journal of Energy Resources Technology, Transactions of the ASME, 107*(1) 122-127.

[A11] Bastian, G. & Grosjean, R. (1991). A hollow cylindrical probe for the measurement of the thermophysical properties of loose materials. *High Temperatures - High Pressures 23*, 271-278.

[A12] Blackwell, J. H. (1956). The axial-flow error in the thermal-conductivity probe. *Canadian Journal of Physics, 34*, 412-417.

[A13] Kierkus, W.T., Mani, N. & Venart, J.E.S. (1973). Radial-axial transient heat conduction in a region bounded internally by a circular cylinder of finite length and appreciable heat capacity. *Canadian Journal of Physics, 51*, 1182-1186.

[A14] Boggs, S. A., Chu, F. Y., Radhakrishna, H. S. & Steinmanis, J. (1980). Measurement of soil thermal properties -- techniques and instrumentation. *IEEE Transactions Power Apparatus Systems PAS-99*(2), 747-752.

[A15] Drotning, W.D. (1983). An automated thermal conductivity probe and applications to powders. In T. Ashworth and D.R. Smith (Eds.) *Thermal Conductivity 18.* New York, NY: Plenum Press.

[A16] Drotning, W.D., Koski, J.A. & Havey, P.E. (1981). *Development of a technique for measurement of the thermal conductivity of powders at high temperatures.* (Report No. NUREG/CR-2287, SAND 81-0631). Albuquerque, NM: Sandia National Laboratories.

[A17] Koski, J.A. (1981). *Analysis of thermal conductivity probes for high temperature applications* (Report No. SAND 81-0106). Albuquerque, NM: Sandia National Labs.

[A18] Koski, J.A. (1982). *CONFIT: a computer code for thermal conductivity probe data reduction with the use of parameter estimation techniques*, (Report No. SAND 82-0741). Albuquerque, NM: Sandia National Labs.

[A19] Koski, J.A. & McVey, D.F. (1983). Application of parameter estimate techniques to thermal conductivity probe data reduction. In J.G. Hust (Ed.), *Thermal Conductivity 17.* New York, NY: Plenum Publishing Corporation.

Appendix B. Analysis Procedures for Transient Plane-Source Techniques for Thermal Conductivity Measurement

The literature concerning analysis procedures for transient plane-source techniques for thermal conductivity measurement is much less extensive than is the case for transient hot-wire or probe techniques. In particular, there is less information available concerning the effects of the heat capacity of the heater and the effects of contact resistance. Accordingly, as part of the development of a suitable apparatus for use at NIST, appropriate mathematical models need to be developed and programmed.

In this appendix, some of the mathematical models from the literature are briefly summarized. The references cited in this appendix are those from Section 8.

Gustafsson's Transient Strip Method [101-103]

Consider a thin strip heater of width $2d$, sandwiched between two slabs of material having density ρ, specific heat C, thermal conductivity λ, and thermal diffusivity $\kappa = \lambda/\rho C$. The assembly is initially isothermal and at time $t = 0$, the heater is energized with a constant electrical current, resulting in a power input Q per unit length. To first order, the voltage drop V across the heater of resistance R varies as

$$\frac{V}{V_0} = 1 + \frac{\alpha Q}{\lambda} \cdot g(\kappa t/d^2) \quad , \tag{1}$$

where V_0 is the voltage drop at $t = 0$ across the heater of resistance R_0, $\alpha = (1/R_0)\, dR/dT$ is the temperature dependence of the heater resistance, and $g(\,)$ is a mathematical function that is given by Gustafsson. When d is very small, Eq. (1) reduces, for reasonable values of t, to an expression equivalent to that given on p. A-2 for an ideal line heat source. The thermal conductivity can be obtained but it is not possible to obtain an accurate value for either the thermal diffusivity or the volumetric specific heat (ρC). When d is very large, Eq. (1) reduces, again for reasonable values of t, to the expression for an infinitely large plane heat source; the quantity known as the "effusivity," $\lambda \rho C = \lambda^2/\kappa$, can be obtained but it is not possible to obtain the individual thermophysical properties. A bit more needs to be said about "reasonable values of t." If d is very small, information about volumetric specific heat or thermal diffusivity could only be obtained for times that are so short that the thermal wave has barely begun to penetrate the test medium and further, so short that it would be difficult to make accurate measurements of the variation in the voltage drop across the heater. If d is very large, information about individual thermophysical properties could only be obtained for times that are so long that the assumptions of an infinitely large medium with negligible heat losses would not be valid. Gustafsson argues that if d is chosen so that, for reasonable times, the maximum argument of $g(\,)$ is approximately unity, it is possible to obtain reliable values for ρC, λ, and κ from a single experiment.

As mentioned above, Eq. (1) is a first-order expression. Gustafsson [103] also has derived a second-order expression for the time dependence of the voltage drop across the heater.

Brydsten and Bäckström Hot Strip Method [104]

As described on p. 79, Brydsten and Bäckström used one strip as a heater and a second strip as a thermometer. Their first-order mathematical analysis results in an expression analogous to Eq. (1) of this appendix, but with a different form for $g(\,)$. The use of a separate thermometer should make it possible to obtain reliable values for ρC, λ, and κ from a single experiment with less restriction on the width of the heater strip than is the case for Gustafsson's method; however, it would be necessary to carry out computations to confirm this supposition.

Gustafsson's Transient Plane Source Method [105-106]

As briefly described on p. 80, this technique uses a rectangular or circular patch heater, resembling a resistance strain gage, that also serves as a thermometer. Again the functional form of the first-order expression for the voltage drop across the heater is similar to Eq. (1) of this appendix, with a different form for $g(\,)$, depending upon the heater geometry.

Vernotte's Method [107-113]

There are several computational techniques presented in these papers. The technique originally used by Clarke and Kingston [107] is similar to that described below for Harmathy's method. Since it is not planned to use Vernotte's method for this project, the various computational techniques are not summarized here.

Harmathy's Method [121-125]

As described on pp. 82-83, Harmathy [121] used a heater that had essentially the same lateral dimensions as the specimen pieces so that, in contrast to Gustafsson's and Brydsten and Bäckström's methods, he obtained essentially one-dimensional heat flow. Neglecting the heat capacity of the heater and neglecting thermal contact resistance, Harmathy used a standard formula for the temperature rise, T, at position z in an infinite solid with constant heat flux in the $z = 0$ plane,

$$T = \frac{Pz}{\lambda} \cdot \left(\frac{\kappa t}{z^2} \right)^{\frac{1}{2}} \cdot \text{ierfc} \, \frac{1}{2} \left(\frac{z^2}{\kappa t} \right)^{\frac{1}{2}} \quad , \tag{2}$$

where $P/2$ is the heat flux into one specimen, of the pair, and ierfc( ) is the integrated complimentary error function. If the temperature rise at the heater were to be measured, Eq. (2) would reduce to

$$T = \frac{P}{\lambda} \cdot \left(\frac{\kappa t}{\pi} \right)^{\frac{1}{2}} = P \cdot \left(\frac{t}{\pi \lambda \rho C} \right)^{\frac{1}{2}} \quad , \tag{3}$$

and, as discussed following Eq. (1), it is only possible to determine the effusivity and not any of the normally defined thermophysical properties. This problem does not arise, however, if the temperature is measured at a sufficiently large distance from the location of the heater. Harmathy

let $z = \ell$, the thickness of the "measuring piece," as shown in Figures 59 and 60 of this report, wrote two equations of the form of Eq. (2), one at time t and the other at time $2t$, and formed the ratio

$$\frac{T(2t)}{T(t)} = \frac{\sqrt{2}\ \text{ierfc}\ \frac{1}{2}\left(\frac{\ell^2}{2\kappa t}\right)^{\frac{1}{2}}}{\text{ierfc}\ \frac{1}{2}\left(\frac{\ell^2}{\kappa t}\right)^{\frac{1}{2}}} \quad . \tag{4}$$

He computed this function and compared it to the experimental data in order to obtain κ and then inserted that value of κ into Eq. (2) to compute λ. With modern computers, it would probably be simpler to use non-linear parameter estimation techniques.

Pulse Methods [127-129]

For an instantaneous planar heat pulse in an infinite body, the resultant temperature at a distance ℓ from the heat source is given by [129]

$$T = \frac{H}{2\rho C\sqrt{\pi\kappa t}} \cdot \exp\left(-\frac{\ell^2}{4\kappa t}\right) \quad , \tag{5}$$

where H is the energy per unit area provided by the heater. This function has the form shown on the right-hand-side of Figure 62, on p. 84. The maximum temperature T_m occurs at the time t_m when $\kappa t/\ell^2 = 1/2$, and thus κ can be computed from

$$\kappa = \frac{\ell^2}{2t_m} \quad . \tag{6}$$

Substituting $\kappa t/\ell^2 = 1/2$ into Eq. (5), the value of the maximum temperature is given by

$$T_m = \frac{H}{\sqrt{2\pi e}\ \ell\rho C} \tag{7}$$

so that the volumetric heat capacity can be computed from

$$\rho C = \frac{1}{\sqrt{2\pi e}} \cdot \frac{H}{\ell T_m} = 0.2420 \cdot \frac{H}{\ell T_m} \quad . \tag{8}$$

The thermal conductivity is then computed from $\lambda = \kappa\rho C$.

If the pulse length is not short compared to t_m, it is necessary to use a more complicated expression, than Eq.(5), that properly accounts for the pulse shape and duration. Kubičár [129] addresses this issue as well as the effects of the heat capacity of the heater, thermal contact resistances, and heat losses from the edge of the specimen.

Dzhavadov [127] obtains expressions analogous to those above. However, his specimens were not treated as infinite bodies (see Figure 61, on p. 84 of this report) and the pulse width was not negligible.

Giedd and Onn [128] used thin specimens and assumed that there was no heat loss from these specimens. Thus their theoretical temperature-time histories do not go through a maximum but rather asymptotically approach a constant value. They compute thermal diffusivity from the time required for the backside temperature to reach half of its final value. Specific heat is computed from the overall rise in temperature of the specimen when it reaches its final isothermal equilibrium value.

Piorkowska and Galeski's Continuous Ramp Method [130-131]

Since it is proposed to use a variant of this method for the high-strength concrete project, it is worthwhile to provide some detail as to the analysis procedure used by Piorkowska and Galeski. Consider a pair of specimens, each of thickness ℓ, with a thin heater between them at $z = \ell$. The heater is assumed to have negligible heat capacity and there is assumed to be no thermal contact resistance between the heater and the specimens. At the beginning of a test, it is assumed that the outside surfaces of the specimens, $z = 0$ and $z = 2\ell$ are at a temperature $T = 0$ and that the heater has been providing a constant heat flux P for a sufficiently long time that steady-state conditions have been achieved. Thus the initial conditions are

$$T(z,0) = \frac{Pz}{2\lambda} \quad \text{for } 0 \le z \le \ell$$
$$\text{and} \qquad T(z,0) = \frac{P(2\ell - z)}{2\lambda} \quad \text{for } \ell \le z \le 2\ell \quad . \tag{9}$$

At time $t = 0$, the outer surfaces of the specimens are programmed to change in temperature according to

$$T(0,t) = T(2\ell,t) = vt \quad , \tag{10}$$

where v is the constant rate of change of temperature with time. As shown by Piorkowska and Galeski, the resultant temperature distribution within the lower specimen, $0 \le z \le \ell$, will be

$$T(x,t) = \frac{Pz}{2\lambda} + vt - vF(x,t) \quad , \tag{11}$$

with a similar expression for the other specimen, except that the leading term is replaced by the second line of Eq. (9). The function $F(x,t)$ is given by

$$F(x,t) = \frac{16\ell^2}{\kappa\pi^3}\sum_{n=0}^{\infty}\frac{1}{(2n+1)^3}\sin\left(\frac{(2n+1)\pi z}{2\ell}\right)\left[1 - \exp\left(-\frac{(2n+1)^2\pi^2\kappa t}{4\ell^2}\right)\right] \quad . \qquad (12)$$

Evaluating Eq. (11) at $z = 0$ and $z = \ell$, the temperature difference across each of the samples is

$$\Delta T(t) = \frac{P\ell}{2\lambda} - \frac{v\ell^2}{2\kappa} + \frac{16v\ell^2}{\kappa\pi^3}\sum_{n=0}^{\infty}\frac{(-1)^n}{(2n+1)^3}\exp\left(-\frac{(2n+1)^2\pi^2\kappa t}{4\ell^2}\right) \quad . \qquad (13)$$

Note that only the first term in this equation involves the power to the heater. Thus if two tests are run with the same value for v but different values for P, say P_1 and P_2, and the corresponding values of the temperature difference across the specimen, ΔT_1 and ΔT_2, are subtracted from each other, the second and third terms cancel leaving simply

$$\Delta T_1(t) - \Delta T_2(t) = \frac{(P_1 - P_2)\ell}{2\lambda} = \text{a constant} \quad . \qquad (14)$$

Thus the thermal conductivity can be computed from

$$\lambda = \frac{(P_1 - P_2)\ell}{2[\Delta T_1(t) - \Delta T_2(t)]} \quad . \qquad (15)$$

Piorkowska and Galeski also show that Eqs. (14) and (15) are valid when the thermal conductivity and thermal diffusivity are functions of temperature.

Although Piorkowska and Galeski do not discuss the determination of thermal diffusivity, it also is straightforward to compute. The simplest case would be to consider Eq. (13) at times long enough that the transient third term has died out enough to be negligible. The thermal diffusivity is then given by

$$\kappa = \frac{v\ell^2}{2\left(\frac{P\ell}{2\lambda} - \Delta T(t)\right)} \quad , \qquad (16)$$

where the value of λ computed from Eq. (15) can be substituted. However, for a test with no power to the heater, κ is given simply by

$$\kappa = -\frac{v\ell^2}{2\,\Delta T(t)} \quad , \qquad (17)$$

where $\Delta T(t)$ is simply the amount that the temperature at the heater lags the temperature at the two outer surfaces of the specimens when they are heated according to $T = vt$.

NIST-114
(REV. 6-93)
ADMAN 4.09

U.S. DEPARTMENT OF COMMERCE
NATIONAL INSTITUTE OF STANDARDS AND TECHNOLOGY

MANUSCRIPT REVIEW AND APPROVAL

(ERB USE ONLY)	
ERB CONTROL NUMBER	DIVISION
PUBLICATION REPORT NUMBER: NIST GCR 99-767	CATEGORY CODE
PUBLICATION DATE: March 1999	NUMBER PRINTED PAGES

INSTRUCTIONS: ATTACH ORIGINAL OF THIS FORM TO ONE (1) COPY OF MANUSCRIPT AND SEND TO THE SECRETARY, APPROPRIATE EDITORIAL REVIEW BOARD

TITLE AND SUBTITLE (CITE IN FULL)

Response of High Performance Concrete to Fire Conditions

CONTRACT OR GRANT NUMBER: 43-NANB-809607

TYPE OF REPORT AND/OR PERIOD COVERED: METSys Report No. 98-01-101, December 1998

AUTHOR(S) (LAST NAME, FIRST INITIAL, SECOND INITIAL)

Flynn, D.R.
MetSys Corporation, Millwood, VA 22646-0317

PERFORMING ORGANIZATION (CHECK (X) ONE BOX)
- [ ] NIST/GAITHERSBURG
- [ ] NIST/BOULDER
- [ ] JILA/BOULDER

LABORATORY AND DIVISION NAMES (FIRST NIST AUTHOR ONLY)

SPONSORING ORGANIZATION NAME AND COMPLETE ADDRESS (STREET, CITY, STATE, ZIP)

U.S. Department of Commerce
National Institute of Standards and Technology, Gaithersburg, MD 20899

PROPOSED FOR NIST PUBLICATION

[ ] JOURNAL OF RESEARCH (NIST JRES)	[ ] MONOGRAPH (NIST MN)	[ ] LETTER CIRCULAR
[ ] J. PHYS. & CHEM. REF. DATA (JPCRD)	[ ] NATL. STD. REF. DATA SERIES (NIST NSRDS)	[ ] BUILDING SCIENCE SERIES
[ ] HANDBOOK (NIST HB)	[ ] FEDERAL INF. PROCESS. STDS. (NIST FIPS)	[ ] PRODUCT STANDARDS
[ ] SPECIAL PUBLICATION (NIST SP)	[ ] LIST OF PUBLICATIONS (NIST LP)	[x] OTHER NIST GCR
[ ] TECHNICAL NOTE (NIST TN)	[ ] NIST INTERAGENCY/INTERNAL REPORT (NISTIR)	

PROPOSED FOR NON-NIST PUBLICATION (CITE FULLY) [ ] U.S. [ ] FOREIGN

PUBLISHING MEDIUM
- [ ] PAPER
- [ ] CD-ROM
- [ ] DISKETTE (SPECIFY)
- [ ] OTHER (SPECIFY)

SUPPLEMENTARY NOTES

ABSTRACT (A 2000-CHARACTER OR LESS FACTUAL SUMMARY OF MOST SIGNIFICANT INFORMATION. IF DOCUMENT INCLUDES A SIGNIFICANT BIBLIOGRAPHY OR LITERATURE SURVEY, CITE IT HERE. SPELL OUT ACRONYMS ON FIRST REFERENCE.) (CONTINUE ON SEPARATE PAGE, IF NECESSARY.)

The NIST Building and Fire Research Laboratory (BFRL) has undertaken a project concerning the effect of fire on high strength concrete. Heating concrete to sufficiently high temperatures results in water of hydration being driven off, with a resultant irreversible loss of concrete strength. In addition, it has been observed that rapid heating of high strength concrete can result in spalling of the concrete. Computer models for prediction of temperature and pore pressure distributions in heated concrete typically include consideration of (1) mass transfer of air and water by diffusion and by forced convection, conversion of liquid water to vapor, and release of water of hydration and (2) heat transfer by conduction, mass diffusion, and forced convection. In order to make valid predictions, the computer models require reliable data as to the physical properties of the concrete. Mass transport properties are being investigated by the Building Materials Division. Thermal transport properties, the subject of this report, are being investigated by the Building Environment Division. The present report addresses (1) identification of materials properties critical to prediction of heat and mass transfer in high strength concrete at high temperatures, (2) variation of the thermal properties with temperature, pressure, and thermal history, (3) examination of correlations between concrete composition and thermal properties.

KEY WORDS (MAXIMUM OF 9; 28 CHARACTERS AND SPACES EACH; SEPARATE WITH SEMICOLONS; ALPHABETIC ORDER; CAPITALIZE ONLY PROPER NAMES)

computer models; concretes; fire tests; heat transfer; literature reviews; mass transfer; spalling; temperature

AVAILABILITY
- [x] UNLIMITED
- [ ] FOR OFFICIAL DISTRIBUTION - DO NOT RELEASE TO NTIS
- [ ] ORDER FROM SUPERINTENDENT OF DOCUMENTS, U.S. GPO, WASHINGTON, DC 20402
- [x] ORDER FROM NTIS, SPRINGFIELD, VA 22161

NOTE TO AUTHOR(S): IF YOU DO NOT WISH THIS MANUSCRIPT ANNOUNCED BEFORE PUBLICATION, PLEASE CHECK HERE. [ ]

WORDPERFECT

WVMP SAR Reference 3-20

"Lightweight Insulating Concrete for Floors and Roof Decks,"
R. W. Steiger and M. K. Hurd, Concrete Construction,
23(7), 1978.

Lightweight insulating concrete for floors and roof decks

By R. W. Steiger, Designer, and
M. K. Hurd, Consultant
Farmington, Michigan

The cost of energy production and the consequences of its indiscriminate use impel us to thoughts of conservation and the construction technologies that make it possible. Just as the human head loses a disproportionate amount of heat when not properly insulated with a covering, so a building can manifest a disproportionately high level of thermal transfer through its roof to the outside atmosphere if it lacks adequate insulation. Designers, builders and owners today as never before must become aware of the energy-saving potential of lightweight concrete used as insulating fill for floors and roofs.

This article is restricted primarily to the thermal insulation qualities of lightweight concretes, although many of these concretes serve capably for other insulation purposes. The insulating lightweight concretes may be considered according to composition in three groups:

I—Concretes made with expanded perlite or vermiculite aggregate or expanded polystyrene pellets. Oven-dry weight ranges from 15 to 60 pounds per cubic foot.

II—Cellular concretes made by incorporating air voids in a cement paste or cement-sand mortar, through use of either preformed or formed-in-place foam. These concretes weigh from 15 to 90 pounds per cubic foot.

III—Concretes made with aggregates prepared by calcining, sintering, or expanding such products as slag, clay, fly ash, shale or slate; also made with aggregates processed from natural materials such as scoria, pumice, or tuff. Concretes in this group range in weight from 45 to 90 pounds per cubic foot.

Data are given here for Groups I and II, because generally the most effective thermal insulation is found in the lower density ranges of these groups. However, attractive combinations of insulating and strength properties may be achieved with Group III concretes, and the reader is alerted to these possibilities (see box).

Design considerations

Looking at the broad spectrum of lightweight concretes now available (Figure 1), we find an almost infinite variety of mixes and a wide range of densities. It is diffi-

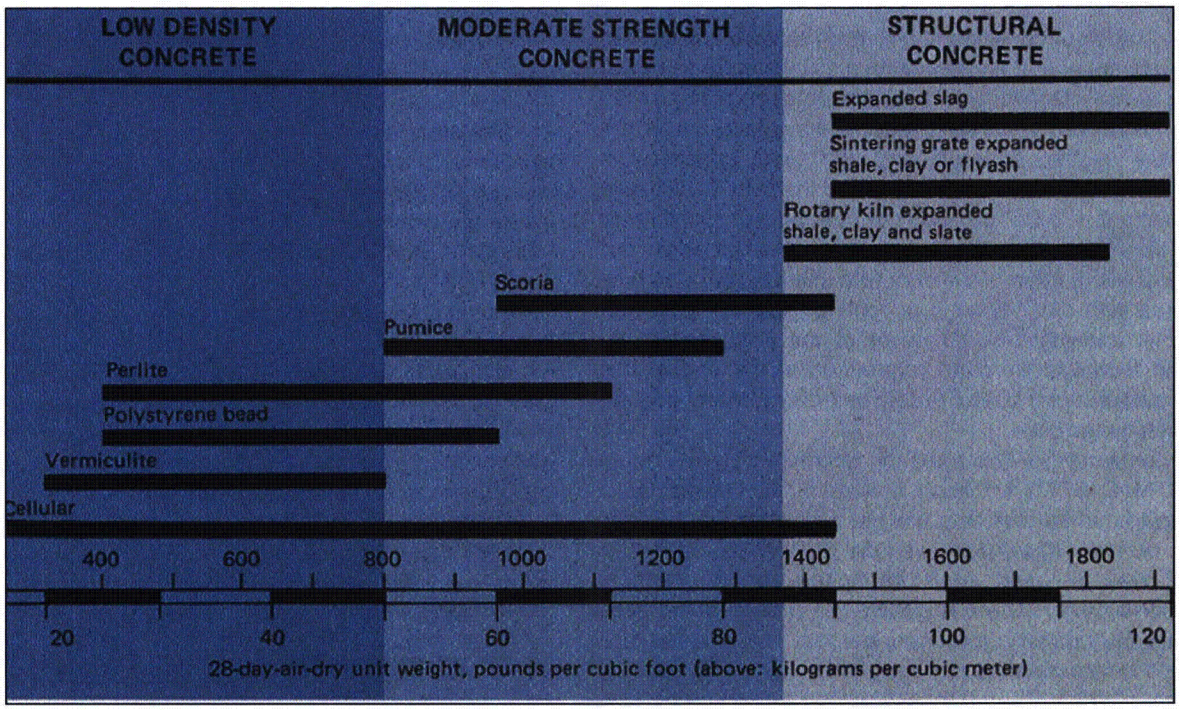

Figure 1. The full spectrum of lightweight concretes. Low density mixes discussed in this article (shaded band at left) offer best insulating properties. Chart adapted from ACI 213 report "Guide for Structural Lightweight Aggregate Concrete," *Journal of the American Concrete Institute*, August 1967, pages 433-469.

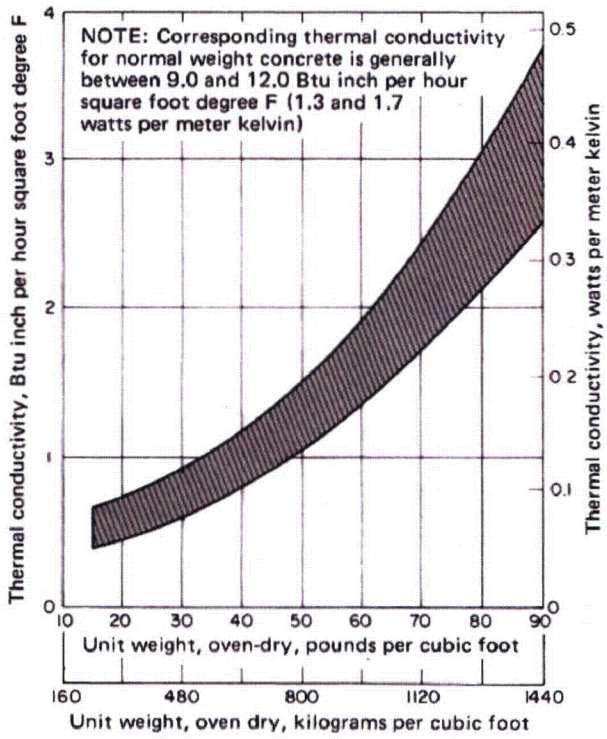

Figure 2. Approximate relationship between oven-dry unit weight and thermal conductivity of lightweight insulating concretes. From Special Types of Concrete, Portland Cement Association, Skokie, Illinois, Publication IS183T, 6 pages, 1977.

cult to draw a sharp line between structural and nonstructural capabilities, or to say at just what density a given type of concrete ceases to provide effective insulation. Generally, the heavier concretes in the group have higher strength and are less effective as insulation. The lightest concretes provide the best insulation—k-values from 0.4 to 0.7 Btu inch per hour square foot degree F—but very little strength. The designer must consider not only the insulating value of the concrete material, but also how it combines with other flooring or roofing materials and what the thermal transmittance (U-value) of the total system is. Trade and technical literature referenced at the end of this article provides much useful detail, and only general properties are mentioned here.

Thermal conductivity—This must be determined by laboratory test (ASTM C 177†) for each concrete mix design. As a general guide when test data are not available, the k-values (thermal conductivities) for oven-dry concretes shown in Figure 2 may be used. Moisture in the concrete affects thermal conductivity. There is generally a 5 percent increase in thermal conductivity for each percent increase in unit weight due to free moisture.

Compressive strength—As shown in Figure 3, compressive strength increases with increasing unit weight. Design requirements depend primarily on the installation. A compressive strength of 100 psi or even less may be quite acceptable for insulating underground steam lines; however, roof and floor fill requires enough early strength to withstand the traffic of workmen. Strengths of 100 to 200 psi are usually adequate, although up to 500 psi is sometimes specified.

Drying shrinkage—Shrinkage is not usually critical for low density fill or insulating concretes, although excessive shrinkage can cause curling. Moist cured cellular concretes made without aggregates do have high shrinkage.

Resistance to freezing and thawing—Lightweight insulating concrete is usually covered by roofing material such as hot mopped asphalt or pitch, and therefore not exposed directly to the elements. As for normal weight concretes, resistance to damage by freezing and thawing depends on the entrained air content of the mix.

Expansion joints: to use or not to use?– Follow the aggregate producers' recommendations. Some recommend insertion of a 1-inch expansion joint at the juncture of all roof projections and the concrete. Transverse expansion joints are used at a maximum spacing of 100

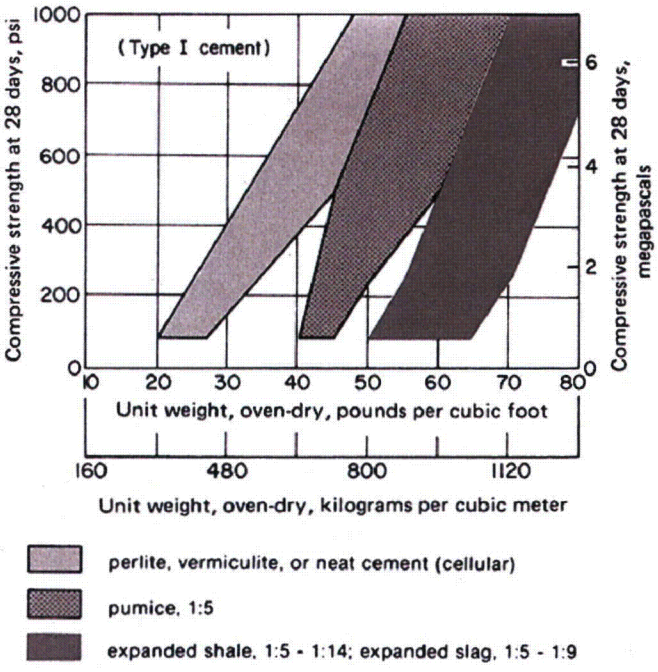

Figure 3. Approximate relationship between oven-dry unit weight and compressive strength of lightweight insulating concretes tested in air-dry conditions.
Note: mix **proportions for perlite and vermiculite concretes range from 1:3 to 1:10 by volume. From Special** Types of Concrete, **Portland Cement Association, Skokie, Illinois, Publication IS183T, 6 pages, 1977.**

† Standard Test Method for Seady-State Thermal Transmission Properties by Means of the Guarded Hot Plate.

feet in any direction to allow for a thermal expansion of 1 inch per 100 lineal feet. A joint material that will compress to one-half its thickness under a stress of 25 psi is generally used. With other aggregates, expansion joints may not be necessary because the initial shrinkage of the concrete is greater than any combination of thermal, moisture or freezing expansion that will occur in a roof deck.

Construction practices

Whether low density concrete is used as a floor fill or part of a roof deck, the form which supports it generally becomes a permanent part of the in-place construction. Typical forming or support systems include:

- Corrugated, galvanized sheet metal, appropriately vented and designed to carry the roof load.
- Insulating acoustical form board supported on flanges of steel subpurlins, with woven wire mesh reinforcement draped over the subpurlins to lie in the lower part of the concrete.
- Lath and mesh systems, where the concrete is placed on either paper backed wire mesh or a ribbed, expanded metal lath.
- Structural precast concrete or wood floors or roofs, where concrete serves as either leveling or insulating fill.

All of these systems require adequate venting in accordance with the recommendations of manufacturers and the National Roofing Contractors Association.

Mixing, placing and finishing—Proper consistency and uniform distribution of materials are necessary to achieve the required unit weight and can only be accomplished by mechanical means. Excessive mixing and handling can break down aggregate particles and should be avoided. Insulating concretes should be placed immediately after mixing by qualified technicians. Conventional placement methods can be used, but pumping is ideal and customarily used due to the normal consistency of lightweight insulating concrete.

Low density concrete should not be placed during rain or snow, nor should it be placed on a deck or form where standing water, snow or ice are present.

Workability—Insulating concretes have excellent workability because of their high air content. Appearance of the mix may be the most reliable indication of consistency. Slumps of 5 to 7 inches are usually quite satisfactory, and the mixtures are highly plastic and homogeneous.

Bleeding and segregation problems will not ordinarily be present. These mixtures can usually be placed simply by pouring and screeding, without further consolidation. This is particularly true with the cellular concretes which can be handled as liquids.

Curing and weather conditions—The surface of freshly smoothed low density concrete should be prevented from drying for not less than 3 days. If temperatures are above 40°F during the first 24 hours after placing, standard curing practices may be used. When temperatures during the first 24 hours are predicted to be from 30 to 40°F, high-early-strength cement and heated mixing water are recommended. Low density concrete should not be placed during freezing weather unless special cold weather procedures are followed.

Perlite concrete

Perlite, derived from the French word perle, resembles tiny clusters of pearls when viewed under the microscope. Perlite is a type of lava mined in large open pits in the western United States, and then crushed to sand sized particles for shipment to processing plants in 32 states. A small amount of water is locked inside the tiny particles and when heated to between 1500 and 2000° F the particles "pop" or expand, just like popcorn. The crude rock expands to about ten times its original volume.

Expanded perlite weighs only 7 1/2 to 10 pounds per cubic foot, approximately one-twelfth as much as sand. During the popping process, it changes to almost pure white from gray or black. The tiny perlite particles are composed of many minute glass-sealed dead air cells. The thermal conductivity of expanded perlite itself is 0.34 Btu inch per hour square foot degree F when graded for use as a concrete aggregate, which explains its excellent insulating value.

Perlite insulating concrete consists of a mixture of expanded perlite, portland cement, water and an air-entraining agent. The dry concrete weighs from 20 to 50 pounds per cubic foot, depending on the mix design selected. Perlite concrete can be placed monolithically on flat, uneven, curved or sloping surfaces. On flat roofs, the thickness of perlite concrete can be varied to provide specified drainage slopes.

The designer must select the strength and insulating value that he considers most appropriate to his project. The physical properties of perlite concrete are controlled by its dry density which is the principal factor in its specification. An ideal balance between reduced dead load, adequate compression and indentation strengths and good insulating value can be achieved with a density of 24 to 28 pounds per cubic foot. Greater densities can be specified if higher strengths or better nail holding capacity are more important than insulating value. For insulated floor slabs on grade, a density of 20 to 24 pounds per cubic foot is recommended.

Perlite roofs may have polystyrene insulation board sandwiched between layers of perlite concrete and supported on a metal deck. This system is capable of achieving U-values as low as 0.04 Btu per hour square foot degree F with a 2-hour fire rating.

Perlite concrete should meet the specified physical properties at the point of placement. It should be deposited and screeded in a continuous operation until the placing of a panel or section is completed. The 1-inch

expansion joints mentioned earlier should be installed through the full depth of the concrete around the perimeter of the roof deck and at the juncture of all roof projections (skylights, penthouses, ventilators, parapet walls) and perlite concrete.

The built-up roofing should be applied as soon as the perlite insulating concrete can carry construction traffic and is dry enough to develop adhesion with hot asphalt or pitch. Normally the perlite concrete should be permitted to cure at least three days.

For greater strength and corresponding higher density, blends of perlite and medium weight aggregates may be used. However, due to varying characteristics of naturally occurring aggregates in different parts of the country, the local perlite aggregate manufacturer should be consulted before specifying blends.

Vermiculite concrete

Vermiculite is a soft, laminated, mica-like material in its raw form. It is found in twelve states and mined commercially in seven. Vermiculite is a mineral that has few uses in its natural state but when heated and exfoliated becomes a lightweight aggregate of great value for fill and insulating concrete. The crude vermiculite is crushed, cleaned, dried and sized, and the resulting concentrate is shipped to processing centers, where it is heated in furnaces at temperatures of 1800 to 2000°F. Water molecules trapped in the flakes of vermiculite ore turn to steam and force the micaceous plates of the material to expand or exfoliate in an accordion-like fashion. Each individual granule is expanded to 10 to 15 times its original size. Air spaces thus formed convert the vermiculite into an aggregate that provides excellent insulating properties. Usually light brown or golden in color, the expanded product weighs from 6 to 10 pounds per cubic foot.

The components of vermiculite insulating concrete are expanded vermiculite aggregate, air-entraining admixture, portland cement, and water, all mixed and applied according to precise procedures. The ratio of cement to aggregate determines the density, strength and insulating value of the finished concrete. As used in the average roof deck, the ratio ranges from 1:4 to 1:8 by volume.

The resulting concrete mixture is usually pumped to the roof site and screeded into place over the structural base. Vermiculite concrete is installed in thicknesses of 2 inches and greater, depending on design needs and strength requirements. It weighs from 20 to 40 pounds per cubic foot, with compressive strengths from 90 to 500 psi.

Vermiculite roof deck assemblies have been developed using a slotted or perforated corrugated metal deck. These positive vented decks offer up to 3 percent open area in the steel form at no penalty or loss in structural performance. The openings help to speed up ventilating and drying of the insulating concrete. Insulation values are therefore quickly reached. In the event of subsequent roofing membrane leaks, the point of leakage is easily located on the underside of the metal decking.

Vermiculite concrete roof insulation, like perlite, can also be cast around a layer of polystyrene insulation board. A slotted opening pattern in the polystyrene permits vertical vapor flow through the board, in order to promote faster, more complete drying and venting of the concrete. The slots also ensure the positive locking and keying of the polystyrene board to the vermiculite concrete to enhance the shear strength of the insulation sandwich and provide a strong, composite roof insulation system. This system provides insulation with a U-value of 0.10 Btu per hour square foot degree F or less and a 1 1/2-hour fire rating.

Vermiculite lightweight concrete is best mixed and placed by experienced, licensed contractors. Current technology now permits contractors to pour quality decks in marginal weather, down to 32°F and even lower in certain cases.

Expanded polystyrene bead concrete

Expanded polystyrene, processed to a nominal density of 1 pound per cubic foot, serves as a stable, nonabsorptive aggregate in lightweight insulating concrete. Polystyrene, unlike perlite and vermiculite aggregate raw materials which are found in nature, is a polymer of styrene which is created by an involved chemical process from a liquid unsaturated hydrocarbon. The polystyrene is foamed to produce a lightweight aggregate. The polystyrene can be pre-expanded or supplied in an unexpanded form and foamed on the site by application of steam. During this process it expands to approximately 50 times its original size. Each closed cell aggregate particle contains prepackaged air and is

HEAVIER, STRONGER CONCRETES ALSO INSULATE

Low density concrete—50 pounds per cubic foot or less—provides the best insulation, but has limited strength. The user who needs greater strength without sacrificing all insulating properties should consider both aggregate and cellular concretes in the moderate density range. For information, consult the comprehensive (and encyclopedically titled) report of ACI Committee 523, "Guide for Cellular Concretes Above 50 pcf, and for Aggregate Concretes Above 50 pcf with Compressive Strengths Less Than 2500 psi." This report was published in the February 1975 issue of the Journal of the American Concrete Institute, pages 51-66, and is reprinted in Part 3 of the ACI Manual of Concrete Practice.

* Standard Method of Fire Tests of Building Construction and Materials

spherical in shape.

Typically, polystyrene bead lightweight insulating concrete consists of Type I or Type II portland cement, polystyrene aggregate expanded to a nominal density of pound per cubic foot, air-entraining agent and water. To enhance specific physical properties for a given application, additional mix components such as sand, limestone or pozzolans may be used. Depending upon the conditions of application, tensile stresses may be met by using mesh reinforcement, special bead aggregate coatings or a combination of the two.

Insulating roof fill of polystyrene bead concrete usually has a dry density of 26 to 30 pounds per cubic foot. Densities are available from 25 to 60 pounds per cubic foot. Fire resistance, verified by small scale ASTM E 119* fire tests conducted by the Portland Cement Association on 46-pound-per-cubic-foot-density concrete, resulted in the following ratings: 2 1/2-inch slab, 2 hours; 5-inch slab, 6 hours; 7-inch slab, 11 hours.

Polystyrene beads tend to resist absorption of water and are not readily wetted by water. Accordingly, cement paste or mortar does not adhere very well to them. Furthermore, their extremely low density makes them tend to segregate by floating out of the mix. To overcome this, the manufacturers have developed a number of bond-improving additives. Epoxy resin or an aqueous dispersion of polyvinyl propionate are recommended.

Shrinkage and swelling strains are high compared to dense concretes, and allowance must be made for this in the design. Polystyrene bead concrete has good workability, is quite pumpable, and requires minimum vibration in placement. Frost resistance is enhanced by entrained air, ranging from 5 to 10 percent of the matrix by volume.

As with all special types of concrete a technical consultant specializing in polystyrene lightweight concrete should be contacted for detailed recommendations covering formulations and mixing/placing techniques for your application.

Cellular concrete

Cellular insulating lightweight concrete owes its distinctive properties to a multitude of macroscopic, discrete air cells uniformly distributed throughout the mix. These cells may account for up to 80 percent of the total volume. Weight of the concrete may range from 12 to 90 pounds per cubic foot. Density and strength can be controlled to meet specific design requirements by varying the amount of air.

Numerous proprietary methods and agents are used to produce cellular concrete but essentially they can be considered in two groups, those using a preformed foam and those using formed-in-place foam. Formed-in-place foam is generated by special high speed mixing of water, foaming agent, cement and aggregates (if any) to allow foam to form in the mixer. Initially large air bubbles are reduced to a reasonably uniform size as mixing proceeds.

By the other method, a uniform preformed aqueous foam is blended with a portland cement and water slurry using only enough water to ensure proper hydration of the cement and facilitate the placing operation. The portland cement used may be Type I, II, III or portland blast-furnace slag cement, Type IS. The foam itself is made by blending a foam concentrate, water and compressed air in predetermined proportions in a foam generator calibrated for discharge rate. The concrete mix is blended in a mortar mixer or in a specially designed continuous blender. Each bubble of air in the foam is surrounded by a tough protein membrane which ensures stability during mixing and handling. However, since this membrane will eventually break down it is recommended that mixing and placing be completed within one hour. Use of high-early-strength cement (Type III) further ensures rapid setting and stability of cellular concrete, although good results are also obtained with regular portland cement (Type I) plus 2 percent calcium chloride, by weight of cement, as an accelerator.

As with other lightweight insulating concrete, the strength and thermal conductivity depend on density. The material can be made so light (down to 12 pounds per cubic foot) that its strength is only sufficient for it to retain its shape during handling. Thermal conductivities range from 0.51 Btu inch per hour square foot degree F for a density of 20 pounds per cubic foot to 2.3 Btu inch per hour square foot degree F for a density of 90 pounds per cubic foot.

Cellular concrete is totally incombustible (8 inches of concrete represents a fire rating of about 8 hours); yet it can be worked much like wood. Where prolonged working is likely, long-life tools are advised. These and other properties enhance the attractiveness of cellular concretes for floor and roof deck fill and insulation.

For more information

Obviously, subtle differences exist between the various lightweight insulating concretes available, which may recommend one type over another to satisfy some specific design objective. Costs and availability in the local market must also be considered.

Each type of insulating concrete, if mixed properly with high quality materials and placed and finished properly, will do an excellent job. Further research and study may reveal just the right characteristic that suits your need. A list of references for further information is given below.

REFERENCES

1. *Special Types of Concrete,* IS183T, Portland Cement Association, Skokie, Illinois, 1977, 8 pages.

2. Valore, R. C., Jr., "Insulating Concretes," *Journal of the American Concrete Institute,* November 1956, pages 509-532.

3. ACI Committee 523, *Guide for Cast-in-Place Low Density Concrete, American Concrete Institute,* Detroit, Michigan, 1967, 8 pages.

4. *The Roof Deck,* National Roofing Contractors Association, 1515 North Harlem Avenue, Oak Park, Illinois 60302.

5. "Vermiculite Roof Deck and Insulating Concrete," *Concrete Construction,* March 1961, pages 66-67.

6. "Perlite Roof Deck and Insulating Concrete," *Concrete Construction,* April 1961, pages 95-97.

7. "Perlite Insulating Concrete," 3.4d/Per, Perlite Institute Inc., 45 West 45th Street, New York, New York 10036.

8. Cook, D. J., "Polystyrene Aggregates," *Constructional Review* (Sidney, Australia), August 1972, pages 52-53.

9. *Cellular Concrete for Insulated Roof Decks,* Cellular Concrete Association Inc., 715 Boylston Street, Boston, Massachusetts 02116.

10. "Cellular Concrete," *Concrete Construction,* January 1963, pages 5-8.

11. Valore, Rudolph C. Jr., "Cellular Concretes, Parts 1 and 2," *Journal of the American Concrete Institute,* May and June 1954, pages 773-796 and 817-836.

PUBLICATION #C780411

WVMP SAR Reference 3-22

"Formation of Hydrated Calcium Silicates at Elevated Temperatures and Pressures," Flint, E.P., H. F. McMurdie, and L. S. Wells, J. Res. Nat. Bur. Stand., 21, 617-638, 1938.

III. Hydrothermal synthesis of hydrated calcium silicates—Continued. Page
4. Hydrothermal treatment of calcium silicates of varying molar ratios of lime to silica—Continued.
(g) Molar ratio CaO/SiO_2, 2:1 630
(h) Molar ratio CaO/SiO_2, 3:1 632
(i) Molar ratio CaO/SiO_2, 4:1 633
5. Cementitious material in sand-lime brick 634
IV. Discussion 635
V. Summary 636
VI. References 638

I. INTRODUCTION

The suggested application to portland cement [1] [1] of the autoclave test for soundness has renewed interest in the products of reactions between cement constituents and water at elevated temperatures and pressures. Among the possible products of such treatment are crystalline hydrated calcium silicates. Such compounds occur in nature as a group of rare but widely distributed minerals commonly found in contact zones of limestone and silicates and are evidently formed by hydrothermal processes. A number of unsuccessful attempts have been made to identify the cementing material of sand-lime brick with some of the naturally occurring calcium hydrosilicate minerals [2].

About a dozen apparently distinct varieties of these minerals are listed by J. W. Mellor [3], but several of these are based on analyses of impure specimens and inadequate optical data. For this reason it was necessary, first of all, to make a study of the natural minerals to ascertain which of these are actually distinct species. Hydrothermal syntheses of some, and determinations of the range of temperatures and pressures over which they are stable, were made. Certain difficulties were encountered. Chief among these was the slow crystallization rate of the hydrated calcium silicates, some of which apparently require months or even years to form at the lower temperatures. Consequently, the ranges of stability of the various phases have been only partially ascertained. Another difficulty lay in the close similarity in crystal habit and optical properties of most of the compounds. Confirmation by means of X-ray patterns was necessary in many cases.

II. X-RAY IDENTIFICATION OF HYDRATED CALCIUM SILICATE MINERALS

As many as possible of the hydrated calcium silicates already identified as distinctive minerals were obtained for further identification by means of X-ray diffraction patterns.[2] All were either from type localities or localities from which specimens described in the literature had been secured. Table 1 gives the name, locality, formula, and literature references accompanying the specimens of which X-ray diffraction patterns were made. Powder X-ray diffraction patterns were made also of the anhydrous calcium silicates: $3CaO.SiO_2$, β-$2CaO.SiO_2$, γ-$2CaO.SiO_2$, $3CaO.2SiO_2$, α-$CaO.SiO_2$ (artificial pseudowollastonite), and wollastonite.

[1] Figures in brackets indicate the literature references at the end of this paper.
[2] Practically all of these minerals were obtained from the United States National Museum, through the kindness of W. F. Foshag, Curator of Mineralogy.

TABLE 1.—*Hydrated calcium silicate minerals*

Name	Formula	Locality	Literature reference
Okenite	$CaO.2SiO_2.2H_2O$	Crestmore, Calif.	Eakle, Univ. Calif. Bul. Dept. Geol. 10, 327 (1917).
Centrallasite	$4CaO.7SiO_2.5H_2O$	Wet Weather Quarry, Crestmore, Calif.	Foshag, Am. Mineral. 9, 88 (1924).
Truscottite	$4(Ca,Mg)O.7SiO_2.5H_2O$	Benkoelen, Sumatra	Grutterink, Verh. Geol.-Mijnt. Genootschaap, Nederland, Geol. Series 8, 197 (1925).
Gyrolite	$4CaO.6SiO_2.5(H,Na,K)_2O$	Niakornat, Greenland	Boggild, Medd. am Grönl. 34, 93 (1908).
Crestmoreite	$2CaO.2SiO_2.3H_2O$	Crestmore, Calif.	Eakle, Univ. Calif. Bul. Dept. Geol. 10, 327 (1917).
Riversideite	$2CaO.2SiO_2.H_2O$	Crestmore, Calif.	Eakle, Univ. Calif. Bul. Dept. Geol. 10, 327 (1917).
Xonotlite	$5CaO.5SiO_2.H_2O$	Isle Royale, Mich.	Foshag and Larson, Am. Mineral. 7, 23 (1922).
Afwillite	$3CaO.2SiO_2.3H_2O$	Dutoitspan Mine, Kimberly, South Africa.	Parry and Wright, Mineralog. Mag. 20, 277–96 (1925).
Foshagite	$5CaO.3SiO_2.3H_2O$	Crestmore, Calif.	Eakle, Am. Mineral. 10, 97 (1925).
Hillebrandite	$2CaO.SiO_2.H_2O$	Velardena District, Durango, Mexico.	Wright, Am. J. Sci. 26, 551 (1908).

The results of this study were as follows: The minerals gyrolite, centrallasite, and truscottite, were found to be very closely related. All of the lines in the pattern of gyrolite were present in the same positions in the pattern of the truscottite sample. The truscottite sample, however, had additional lines, the more intense of which corresponded to the more intense lines of quartz. The sample of centrallasite also possessed lines common to gyrolite and truscottite as well as the more intense lines of quartz. The recorded optical properties of these minerals are also very similar; all three have the same maximum index of refraction, 1.549; all are optically negative; and gyrolite is unaxial, while centrallasite and truscottite are reported to have very small optic angles. All three of the samples studied contained perceptible amounts of isotropic material with low index of refraction occurring as microscopically thin crusts on the platy crystals or as fine laminae between the plates.

Of the hydrated monocalcium silicates, xonotlite has a pattern which is characteristic and distinctive. Some confusion has existed regarding the two minerals riversideite and crestmoreite, which possess crystallographic properties identical within experimental accuracy. Their discoverer, A. S. Eakle [4], distinguished between them by the greater water content of crestmoreite and presented a typical analysis of this mineral which corresponded to the ratios $1.09CaO:1.00SiO_2:1.27H_2O$, after correcting for the P_2O_5, SO_3, and CO_2 present. Similarly, the analysis given for riversideite conformed to the ratios $1.01CaO:1.00SiO_2:0.62H_2O$. The analyses showed that both minerals had the same impurities in comparable amounts.

In order to determine the significance of these reported differences in water content, some experiments were made on a sample of crestmoreite obtained from the United States National Museum. The loss on ignition to a temperature of 1,100° C was 13.09 percent. After heating the crestmoreite at 110° C for 3 hours, the loss on ignition (H_2O+CO_2) was reduced to 9.80 percent, which is only slightly higher than the water content of 8.11 percent reported for riversideite. The indices and appearance of the crystals were unchanged and the distinctive X-ray pattern of the original mineral was not altered, which indicated that the water was not constitutional.

Another characteristic of riversideite, according to Eakle, was its occurrence in narrow seams in mounds of vesuvianite, whereas crestmoreite was associated with calcite. However, a sample labelled "riversideite," from Ward's Natural Science Establishment, in which the hydrated calcium silicate appeared as narrow veins in lumps of vesuvianite, was found by its X-ray pattern to be identical with crestmoreite from the United States National Museum. Thus, crestmoreite may occur associated with the same mineral as was reported for riversideite.

A sample labelled "riversideite" from the United States National Museum showed complete identity of pattern with foshagite from the Museum. The identical X-ray diffraction pattern of a preparation obtained by treating $5CaO{\cdot}3SiO_2$ glass with water (as will be described later) indicates that both are foshagite.

Because no sample of riversideite could be obtained which was distinct from other minerals, and, in view of the fact that none of its reported properties are characteristic it is believed that riversideite does not exist as an independent compound.

A sample labelled "foshagite" from the Wet Weather Quarry, Crestmore, Calif., obtained from Ward's Natural Science Establishment, was found to be made up of two minerals. One gave an X-ray pattern identical with that of foshagite; the other was identical with that of hillebrandite from the Velardena Mines, Mexico—both samples were obtained from the United States National Museum. This may account for the fact that Vigfusson [5] found the X-ray patterns of foshagite and hillebrandite identical and concluded that they were the same mineral. The remaining minerals, okenite, afwillite, and hillebrandite, gave characteristic and distinctive X-ray patterns.

A sample of an unknown hydrated calcium silicate mineral obtained from the United States National Museum proved to be distinctive in X-ray pattern and optical properties. Analysis gave the following composition: 35.57 percent of CaO, 0.30 percent of MgO, 1.19 percent of R_2O_3, 42.7 percent of SiO_2, 19.76-percent ignition loss; total 99.61 percent. The amount of sample available was insufficient for a CO_2 determination, but petrographic examination indicated that the amount of carbonate present was probably less than 5 percent. Assuming the ignition loss to represent the water content, the analysis conforms to $0.89CaO:1.00SiO_2:1.54H_2O$, which does not correspond very closely to any simple CaO/SiO_2 ratio. The sample consisted of aggregates of fibrous crystals having parallel extinction, positive elongation, and indices of refraction[3] $\alpha=1.540 \pm 0.003$, $\gamma=1.548 \pm 0.003$. Some finely divided material as well as glassy isotropic impurity was present.

III. HYDROTHERMAL SYNTHESIS OF HYDRATED CALCIUM SILICATES

1. MATERIALS

The starting materials were precipitated hydrated calcium silicate, calcium silicate glass, and the crystalline anhydrous calcium silicates.

A previous investigation [6] had shown that solutions containing

[3] In this paper α and γ are used to indicate the minimum and maximum refractive indices, respectively, although, in some cases, it is not certain that the crystals are biaxial.

0.5 g SiO_2/l and about 0.05 g CaO/l can be prepared by boiling purified silica gel with dilute lime solution for several days. By adding saturated limewater to such a solution in varying proportions, hydrated calcium silicate precipitates were prepared having CaO/SiO_2 molar ratios ranging from 0.1 to 1.5. The precipitates were washed with alcohol and ether, dried in a desiccator over calcium chloride, and analyzed to determine their CaO/SiO_2 molar ratios. These preparations are designated in the tables by the letters "aq" to indicate their indefinite water content.

The calcium silicate glasses were prepared by quenching charges of the proper compositions wrapped in platinum foil from temperatures above the liquidus. Small amounts of boric oxide were added to some of these charges to bring the temperature of complete melting within the range of the furnace.

The anhydrous calcium silicates were laboratory preparations of high purity.

2. APPARATUS AND EXPERIMENTAL PROCEDURE

Four bombs were used in this investigation, three of which were constructed according to designs of the Geophysical Laboratory [7]. Two of these bombs are of stainless steel and of 40-ml capacity, and one is of tool steel and of 18-ml capacity. These bombs were heated in insulated Nichrome-wire furnaces having heating zones twice as long as the bombs. By means of modified bimetallic regulators, each furnace could be maintained at temperatures between 150° and 600° C within ±5°C for long periods of time.

Temperatures were measured by means of Chromel-Alumel thermocouples in conjunction with a portable potentiometer. The thermocouples were inserted in wells drilled in the bombs.

The calcium silicate starting materials were inclosed in platinum capsules of 3-ml capacity and placed with water in the bombs in such a way that the solid was in contact with the liquid at temperatures below the critical point of water. Sufficient water was always used so that the liquid phase was present up to the critical point (374° C, 218 atm.). The pressures below 374° C are therefore those of saturated steam in contact with liquid water; those above 374° C were read from the the curves of van Nieuwenburg and Blumendal [8], knowing the mass of water inserted and the volume of the bomb.

After completion of the heating period, the bomb was removed from its furnace and cooled by immersion in water; the product was then removed, washed with alcohol and ether, and dried in a desiccator over a mixture of calcium chloride and soda-lime or Dehydrite. Petrographic examinations, and, in some cases, chemical analyses were made on the products. X-ray diffraction patterns were taken of most of the preparations for comparison with those of the natural minerals.

The fourth bomb is of 2-liter capacity, is made of tool steel, and was used up to 225° C. As figure 1 shows, it was so designed that the liquid and solid phases could be quickly separated without opening the bomb. In use the bomb was first inverted and the materials were placed in the compartment designed as upper chamber in the figure. The bomb in this position was placed in a heating oven equipped with a fan. On completion of the heating period, the bomb

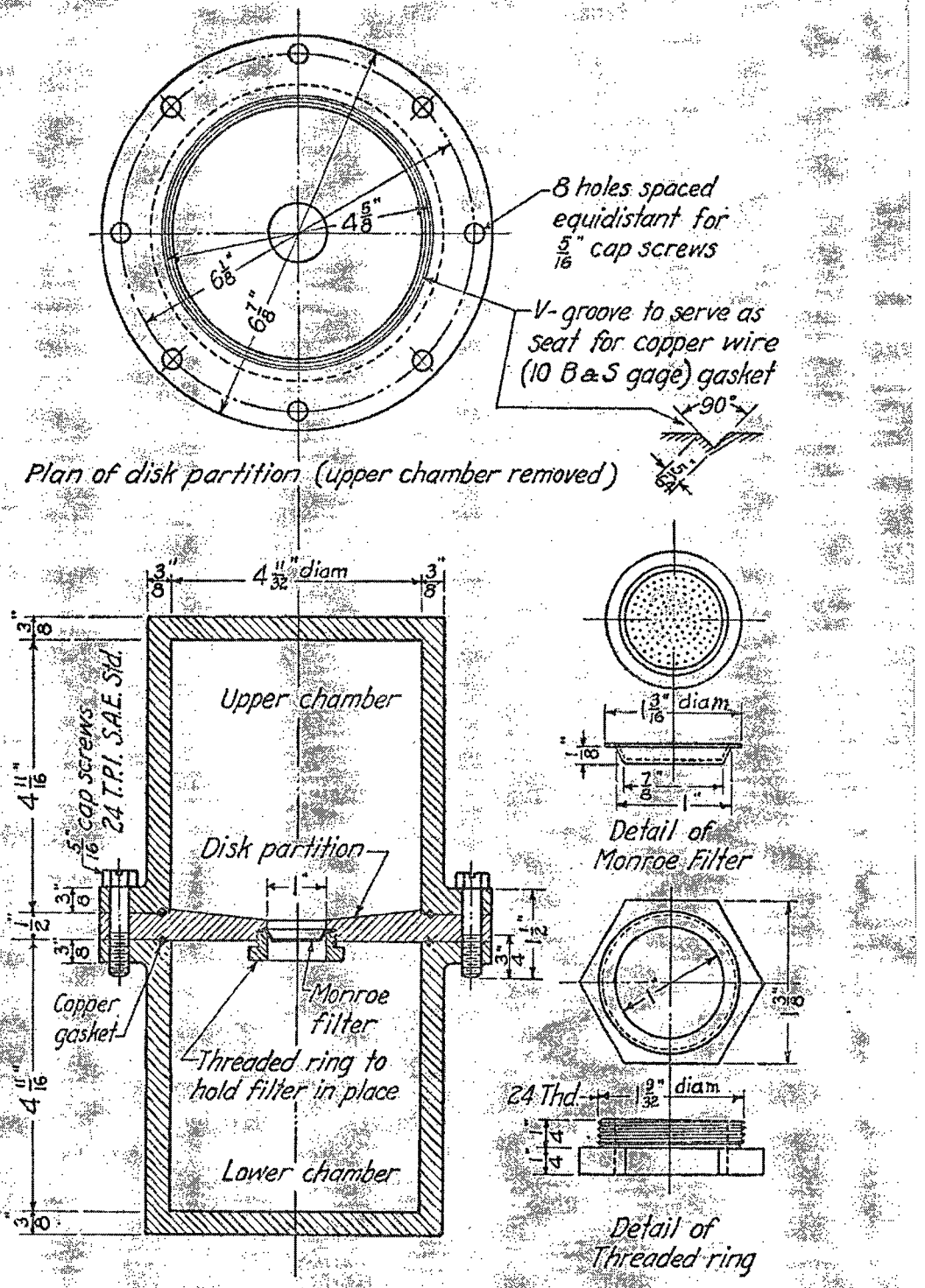

FIGURE 1.—*Bomb for hydrothermal synthesis (in position for filtering).*

was turned over and the lower chamber (fig. 1) placed in cold water. Condensation of steam in this chilled compartment forced the liquid through a Munroe platinum filter in the middle disk.

3. PRELIMINARY EXPERIMENTS

At a given temperature and pressure the composition of the product will depend not only on the composition of the starting material, but also on the relative solubilities of lime and silica in the liquid. The CaO/SiO_2 ratio of the product may be either raised or lowered, depending upon whether lime or silica has the greater concentration in the solution formed.

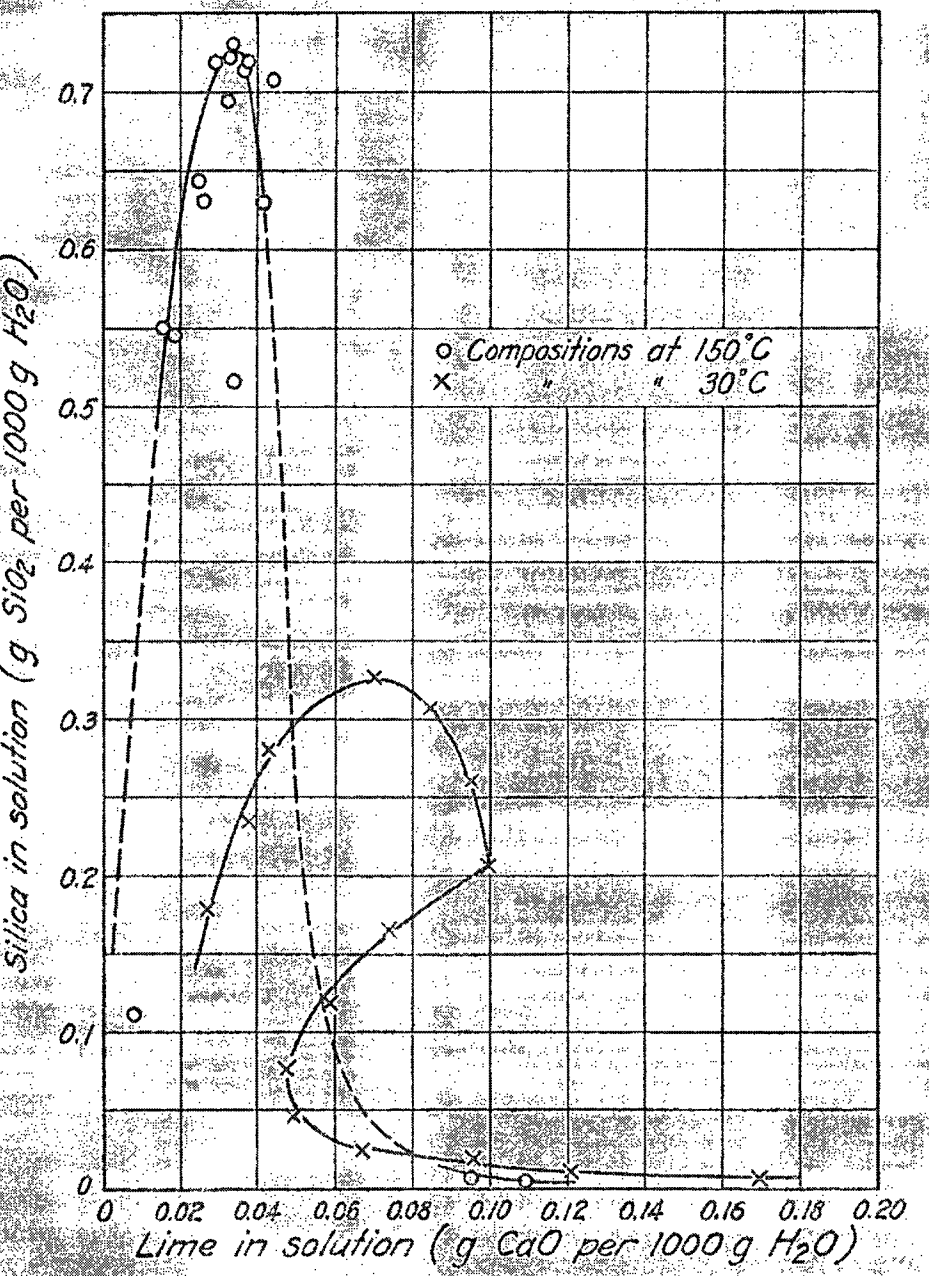

FIGURE 2.—*Solubilities of silica in lime solutions at 30° and 150° C.*

To obtain some information on this factor, a number of determinations were made of the solubility of amorphous silica in solutions of calcium hydroxide at 150° C. Silica gel in amounts between 1 and

10 g was treated with 700 ml of lime solution of various concentrations in the large bomb for 5 days with occasional shaking. The resulting solutions, which remained clear for a short time after cooling, were analyzed for lime and silica, and the results are shown in figure 2. The maximum silica concentration was 0.73 g/1,000 g of H_2O at 0.033 g of CaO/1,000 g of H_2O, and the silica content of the solutions decreased rapidly when the lime content either exceeded or fell below this value. The lower curve in figure 2 represents the solubility relations found at 30° C in a previous investigation [6]. In neither curve do the values represent the solubilities of any one of the crystalline forms of silica, but they were nevertheless fairly reproducible and to some extent indicative of the solubilities of the materials used in these experiments.

Several determinations were made also of the solubility of calcium hydroxide in the temperature range 100° to 200° C. The solubility at 100° C was found to be less than half the solubility at room temperature, or approximately 0.5 g of CaO/1,000 g of H_2O, and the solubilities at 150° and 200° C are approximately 0.25 and 0.1 g of CaO/1,000 g of H_2O, respectively.

In the case of experiments in the three small bombs, where 0.5-gram quantities of solid were treated with usually not more than 10 ml of water, the results indicate that the CaO/SiO_2 molar ratio of the product cannot be much different from that in the starting material. In some experiments in the large bomb, however, where a large excess of water was used, the molar ratio of the product may be considerably different from that of the starting material.

It is evident that the limited solubilities of lime and silica and their compounds would make a complete investigation of the liquid phase in this system very difficult.

4. HYDROTHERMAL TREATMENT OF CALCIUM SILICATES OF VARYING MOLAR RATIOS OF LIME TO SILICA

The effect of hydrothermal treatment on calcium silicates of CaO/SiO_2 molar ratios varying from 0.1 to 4.0 will be described in the following sections. For convenience, the various compositions are divided into groups of the same CaO/SiO_2 ratio or having a limited range of molar ratios. The lengths of time required for complete crystallization to occur varied with the different molar ratios and the periods listed are somewhat arbitrary. In general, however, the times of heating represent those necessary to form a well-crystallized sample as determined by preliminary experiments.

(a) MOLAR RATIO CaO/SiO_2 VARYING FROM 1:10 TO 1:2

The least basic of the known calcium hydrosilicates is the mineral okenite, $CaO.2SiO_2.2H_2O$. The results of treating calcium silicates having the molar ratio of okenite, as well as those of lower molar ratios are described in table 2.

TABLE 2.—*Results of experiments on compositions varying in molar ratio* CaO/SiO_2 *from 1:10 to 1:2*

Experiment number	Starting material	Temperature	Pressure	Time	Product
		°C	atm	Days	
1	0.1CaO:SiO_2:aq [1]	390	261	14	Cristobalite+xonotlite.
2	.2CaO:SiO_2:aq	450	420	12	Cristobalite+?
3	3CaO:SiO_2:aq	260	15	50	$4CaO.5SiO_2.5H_2O$+?
4	.5CaO:SiO_2 glass [2]	150	5	58	Cristobalite+glass.
5	do	225	25	21	Gyrolite+glass.
6	do	360	85	21	Do.
7	do	400	290	7	Do.
8	do	450	300	13	Pseudowollastonite+?

[1] "Aq" here and in following tables designates the indefinite water content of the amorphous calcium silicate precipitates.
[2] Contained 3 percent of B_2O_3.

The crystallization of cristobalite and psuedowollastonite at temperatures far removed from those at which they crystallize from anhydrous melts is of some interest. The cristobalite crystals were very small but good X-ray patterns were obtained. Other investigators have obtained cristobalite by hydrothermal treatment at corresponding temperatures, but usually from neutral or acidic solutions [9]. Xonotlite, $5CaO.5SiO_2.H_2O$, which crystallized with cristobalite in experiment 1, occurred in fairly large, well-formed crystals. Later experiments indicated that xonotlite crystallizes comparatively rapidly at 390° C, which may account for its formation here in preference to less basic hydrosilicates.

In experiment 3 the formation of the compound $4CaO.5SiO_2.5H_2O$, the synthesis of which will be discussed in a later section, cannot be accounted for. The formation of okenite or of gyrolite was more to be expected under these conditions.

The pseudowollastonite obtained in experiment 8 crystallized in aggregates of fibrous needles of parallel extinction and negative elongation. The X-ray pattern was identical with that of α-$CaO.SiO_2$.

The product in experiments 5, 6, and 7 gave the X-ray pattern of gyrolite. In the best crystallized of these preparations, No. 6, the product had the appearance of aggregates of parallel fibers. The ignition loss of this preparation, however, was only 4.8 percent as compared with a theoretical water content for $4CaO.6SiO_2.4H_2O$ of 10.97 percent, or for $4CaO.7SiO_2.5H_2O$ of 12.26 percent, which indicated that conversion was incomplete.

Attempts to obtain the mineral okenite were unsuccessful. A product which the authors suggested might be okenite was synthesized by Schlaepfer and Niggli [10] by treatment of mixtures of SiO_2, CaO, Al_2O_3, and KOH with water at 470° C. They reported similarities in appearance and mean index to the natural mineral. These criteria would seem to be insufficient in view of the fact that some of the other hydrated calcium silicates have almost the same index and crystal habit.

(b) MOLAR RATIO CaO/SiO_2 VARYING FROM 4:7 TO 2:3

The CaO/SiO_2 molar ratio 0.59 corresponds to the reported ratio of the minerals centrallasite and truscottite, and the ratio 0.66 corresponds to that of the mineral gyrolite. Results of treatment of such compositions are given in table 3.

TABLE 3.—*Results of experiments on compositions varying in molar ratio* CaO/SiO_2 *from 4:7 to 2:3*

Experiment number	Starting material [1]	Temperature	Pressure	Time	Product
		°C	atm	Days	
9	0.59CaO:SiO_2:aq	150	5	42	Gyrolite.
10	do	225	25	28	Do.
11	do	250	39	35	Gyrolite+xonotlite.
12	do	300	85	14	Gyrolite.
13	0.59CaO:SiO_2 glass	300	85	37	Do.
14	do	350	163	6	Do.
15	do	450	300	6	Pseudowollastonite+?.
16	0.66CaO:SiO_2:aq	250	39	40	Gyrolite.
17	0.66CaO:SiO_2 glass	300	85	35	Do.
18	do	500	330	14	Pseudowollastonite+?.

[1] The glasses contained no B_2O_3.

The gyrolite crystals occurred as bundles of parallel fibers with positive elongation, parallel extinction, uniaxial negative, and indices of refraction $\epsilon=1.536$, $\omega=1.548$. A photomicrograph of the preparation from experiment 16 is shown in figure 3. Figure 4 shows preparation 11, which in some portions contained large broom-shaped aggregates of xonotlite surrounded by gyrolite.

A chemical analysis of preparation 10, initial molar ratio 0.59, gave the composition: 34.18 percent of CaO, 55.96 percent of SiO_2, 9.86 percent of H_2O, corresponding to the ratios: $1.96CaO:3.00SiO_2:1.76H_2O$. An analysis of the best preparation, No. 16, initial molar ratio 0.66, gave the composition: 33.58 percent of CaO, 0.36 percent of R_2O_3,[4] 54.02 percent of SiO_2, 11.40 percent of H_2O; corresponding to the ratios: $2.00CaO:3.00SiO_2:2.11H_2O$. These analyses justify assigning to gyrolite the formula $2CaO.3SiO_2.2H_2O$. The fact that the CaO/SiO_2 molar ratio of 0.59 was unstable and increased to 0.65 in experiment 10, while a ratio of 0.66 remained unchanged in experiment 16, indicates that 0.66 is the stable ratio. In conjunction with the X-ray data, this evidence confirms the belief that centrallasite and truscottite are not distinct minerals but are rather impure forms of gyrolite.

The synthesis of gyrolite was claimed by E. Baur [11] from a mixture of SiO_2, Al_2O_3, KOH, and CaO treated with water at 450° C. The optical properties which he reported for his product were, however, not those of gyrolite. No other report on the synthesis of gyrolite was found in the literature.

(c) MOLAR RATIO CaO/SiO_2, 4:5

The results of these experiments are listed in table 4.

TABLE 4.—*Results of experiments on compositions varying in molar ratio* CaO/SiO_2, 4:5

Experiment number	Starting material	Temperature	Pressure	Time	Product
		°C	atm	Days	
19	0.80CaO:SiO_2:aq	150	5	42	$4CaO.5SiO_2.5H_2O$.
20	do	225	25	14	Do.
21	do	250	39	7	Do.
22	0.76CaO:SiO_2:aq	275	59	21	Do.
23	0.80CaO:SiO_2:aq	300	85	14	Xonotlite.
24	do	350	163	10	Do.
25	do	500	330	7	Wollastonite.

[4] The small percentages of R_2O_3 in the products of hydrothermal synthesis reported here and elsewhere in this paper are largely Fe_2O_3 as a contamination from the iron of the bomb.

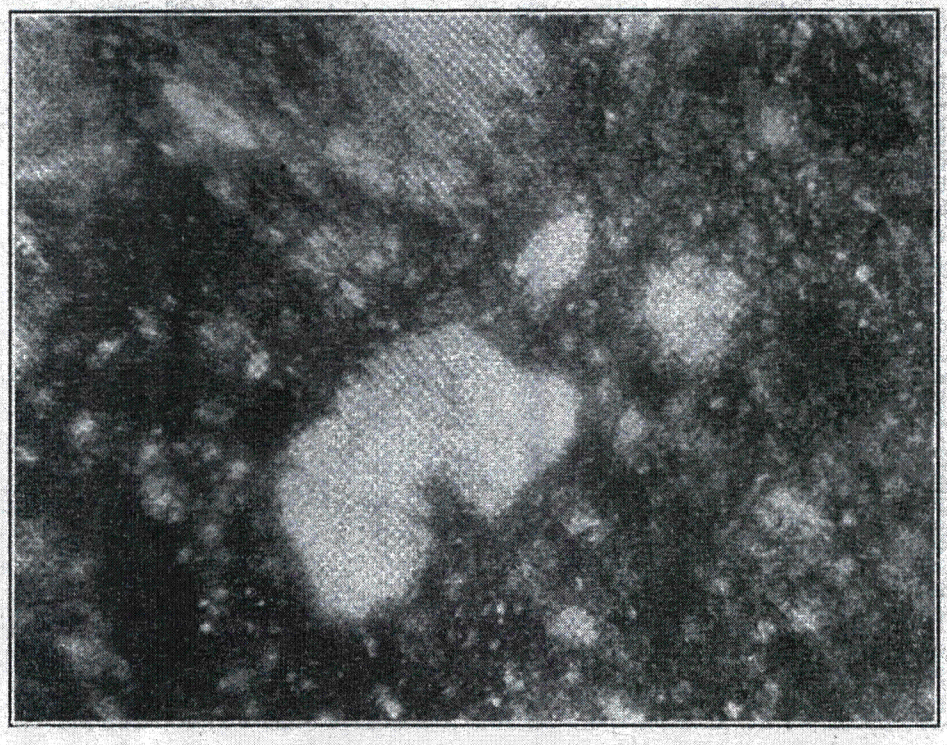

FIGURE 3.—*Synthetic gyrolite.*
Crossed nicols, magnification ×180

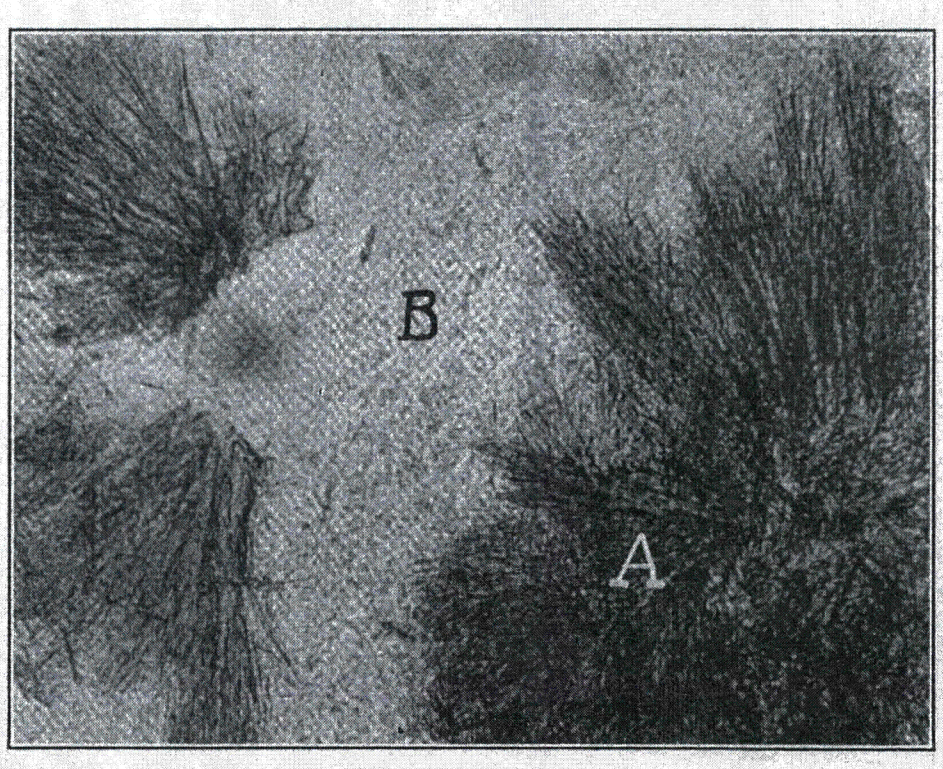

FIGURE 4.—*Synthetic (A) xonotlite + (B) gyrolite.*
Magnification ×180.

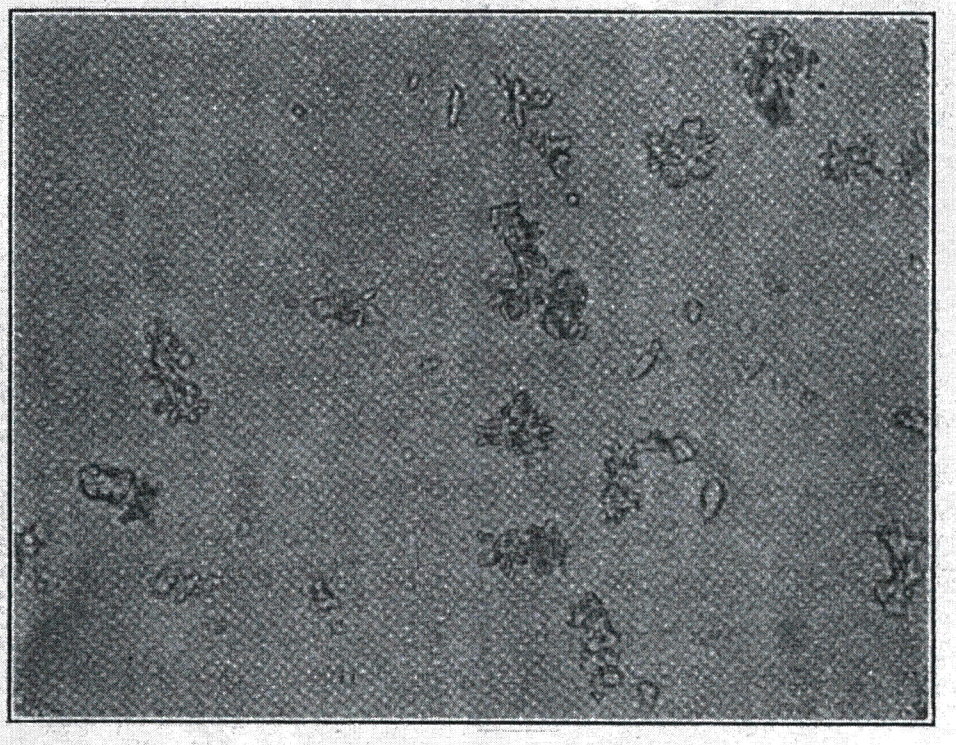

FIGURE 5.—*Synthetic* $CaO.SiO_2.H_2O$.
Magnification ×900.

FIGURE 6.—*Synthetic xonotlite.*
Magnification ×180.

The product of experiments 19, 20, and 21 consisted of very small needles of moderate birefringence and mean refractive index 1.54, positive elongation and parallel extinction. The X-ray pattern of this phase is distinctive. Analysis of preparations 19 and 21 gave the following results:

Components	Preparation 19	Preparation 21
	Percent	*Percent*
CaO	36.86	38.96
R_2O_3	0.37	
SiO_2	47.84	48.71
H_2O	14.44	11.84
Total	99.51	99.51

corresponding to the ratios $4.13CaO:5.00SiO_2:5.03H_2O$ in the case of preparation 19 and to $4.00CaO:5.00SiO_2:4.15H_2O$ for preparation 21. The ignition loss of preparation 20 was 13.97 percent, corresponding to $4CaO:5SiO_2:4.7H_2O$. The formula of this compound is therefore tentatively placed at $4CaO.5SiO_2.5H_2O$.

The mineral most similar to this preparation is tobermorite discovered by M. F. Heddle [12], who assigned to it the formula $3(4CaO.5SiO_2.H_2O).10H_2O$, or $4CaO.5SiO_2.4\frac{1}{3}H_2O$. P. Groth [13] suggested the formula $4CaO.5SiO_2.4H_2O$. Unfortunately, Heddle was unable to determine the crystalline form of the mineral and lists none of its optical properties, so no further comparison with the synthetic product is possible.

(d) MOLAR RATIO CaO/SiO_2, 1:1

The hydrated monocalcium silicate minerals are crestmoreite, $2CaO.2SiO_2.3H_2O$; and xonotlite, $5CaO.5SiO_2.H_2O$. Experiments on starting materials of this ratio are listed in table 5.

Experiments 26 and 40 involved pseudowollastonite, which underwent no transformation in 6 weeks at 150° C, but it was 50 percent transformed to wollastonite in 3 weeks at 500° C, 480 atmospheres.

TABLE 5.—*Results of experiments on* $1CaO:1SiO_2$ *compositions*

Experiment number	Starting material	Temperature	Pressure	Time	Product
		°C	atm	Days	
26	Pseudowollastonite	150	5	42	Unchanged.
27	$0.95CaO:SiO_2:aq$	150	5	42	Amorphous.
28	$1.04CaO:SiO_2:aq$	150	5	60	$CaO.SiO_2.H_2O$.
29	do	175	9	79	Xonotlite.
30	do	200	15	73	Do.
31	$1.0CaO:SiO_2$ glass [1]	250	39	10	Do.
32	$1.04CaO:SiO_2:aq$	320	109	7	Do.
33	do	370	207	4	Do.
34	do	380	225	4	Do.
35	do	390	225	4	Do.
36	Xonotlite	390	169	7	Do.
37	do	390	72	4	Do.
38	$1.04CaO:SiO_2:aq$	400	290	5	Wollastonite.
39	do	450	300	5	Do.
40	Pseudowollastonite	500	480	21	50 percent of wollastonite+50 percent of pseudowollastonite.

[1] Contained no B_2O_3.

Amorphous monocalcium silicate hydrate treated with water at 150° C for 6 weeks remained amorphous, but a sample treated for 60 days at the same temperature (experiment 28) crystallized to a single phase of the following composition: 41.97 percent of CaO, 43.97 percent of SiO_2, 14.47 percent of H_2O corresponding to the ratios: $1.02CaO:1.00SiO_2:1.10H_2O$, or a monohydrate of monocalcium silicate. The preparation was rather finely divided, but under the oil-immersion objective it appeared to be composed of thick needle- and lath-shaped crystals with parallel extinction, negative elongation, mean index 1.603. The X-ray pattern was distinctive and different from that of crestmoreite. A photomicrograph of these crystals is shown in figure 5.

Monocalcium silicate hydrate treated with water between 175 and 390° C for a sufficient time crystallized completely to a product having the optical properties and X-ray pattern of xonotlite, $5CaO.5SiO_2.H_2O$. A typical analysis is that of the preparation from experiment 33 which was: 46.15 percent of CaO, 50.10 percent of SiO_2, 3.35 percent of H_2O, corresponding to the ratios: $0.99CaO:1.00SiO_2:0.22H_2O$. A photomicrograph of these crystals is shown in figure 6. They are fibrous needles of parallel extinction, positive elongation, having indices of refraction: $\alpha=1.583\pm0.003$, $\gamma=1.594\pm0.003$.

Crystallization of xonotlite occurred most rapidly between 320° and 390° C, in which range it was complete in 4 to 7 days.

Experiments 37 and 38 fix the upper temperature limit at which xonotlite is stable at 395° ±10° C. Xonotlite remained the stable phase at 390° C, on reduction of the pressure from 225 to 72 atmospheres. Above this temperature complete crystallization to large well-formed laths of wollastonite occurred in heating periods of 5 days. A photomicrograph of these crystals is shown in figure 7.

Nieuwenburg and Blumendal [14] reported having obtained wollastonite by steaming a lime-silica mixture out of contact with the liquid for 2 days at 365° C. Their experiment was repeated by steaming monocalcium silicate hydrate out of contact with the liquid at 365° C for 3 days. The product was xonotlite.

Nagai [15] and Kohler [16] reported having synthesized xonotlite, but neither of these authors gives any confirmatory optical or X-ray data.

(c) MOLAR RATIO CaO/SiO_2, 3:2

The mineral afwillite, $3CaO.2SiO_2.3H_2O$, possesses the CaO/SiO_2 molar ratio used in experiments 41 to 49, inclusive, table 6.

TABLE 6.—*Results of experiments on* $3CaO:2SiO_2$ *compositions*

Experiment number	Starting material	Temperature	Pressure	Time	Product
		°C	*atm*	*Days*	
41	α-$3CaO.2SiO_2$	150	5	42	>50 percent unaltered.
42	$1.53CaO:SiO_2$:aq	150	5	70	$CaO.SiO_2.H_2O$+?
43	do	200	15	73	Do.
44	α-$3CaO.2SiO_2$ (prep. 41)	250	39	10	?
45	$1.44CaO:SiO_2$:aq	250	39	14	Xonotlite+?
46	$1.42CaO:SiO_2$:aq	300	85	14	Do.
47	$1.45CaO:SiO_2$:aq	350	163	14	Do.
48	$1.53CaO:SiO_2$:aq	400	270	5	Do.
49	α-$3CaO.2SiO_2$	500	380	14	β.$3CaO.2SiO_2$

FIGURE 7.—*Synthetic wollastonite.*
Magnification ×180.

FIGURE 8.—*β-tricalcium disilicate.*
Magnification ×900.

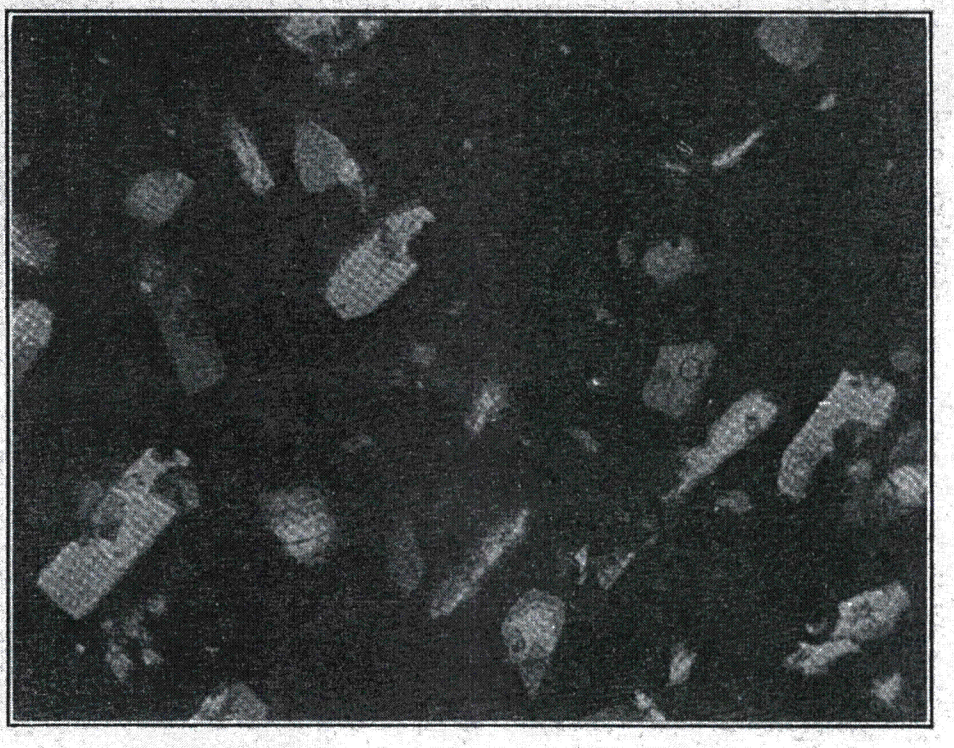

FIGURE 9.—*Synthetic* $10CaO.5SiO_2.6H_2O$.

Crossed nicols, magnification ×400.

In experiment 41 more than 50 percent of the anhydrous tricalcium disilicate, treated with water at 150° C for 6 weeks, remained unaltered. The alteration product consisted of irregular masses of low-birefringent material of refractive index 1.57, and was not identified. This material kept an additional 10 days at 250° C (experiment 44) was largely altered to low-birefringent aggregates of mean refractive index, 1.62+. The X-ray pattern was different from that of afwillite and could not be identified.

Treatment of anhydrous tricalcium disilicate with water at 500° C, 380 atmospheres, for 2 weeks (experiment 49) resulted in 90-percent conversion to a new phase. Inasmuch as the tricalcium disilicate contained a few percent of impurities (mostly dicalcium silicate) there were also present some alteration products of the impurities, including some dicalcium silicate hydrates, the hydrothermal formation of which will be described subsequently. The new phase consisted of small needle- and lath-shaped crystals of parallel extinction and positive elongation. The indices of refraction are: $\alpha=1.608 \pm 0.003$, $\gamma=1.615 \pm 0.003$. A photomicrograph of these crystals is shown in figure 8.

Determinations of ignition loss showed the new compound to be anhydrous. Its X-ray pattern proved to be different from that of ordinary tricalcium disilicate or any of the other anhydrous calcium silicates. Ignition for a few minutes over a Méker burner converted it back to the usual form of tricalcium disilicate.

The evidence indicated that the new phase was a low-temperature form of tricalcium disilicate. This was confirmed by experiments using the quenching method. A sample held overnight at 1,020° C gave an unchanged X-ray pattern, while a sample held at 1,027° C overnight gave the pattern of ordinary tricalcium disilicate. The inversion of the low-temperature form of tricalcium disilicate to the high-temperature form is therefore placed at 1,024°C ±5° C.

Attempts to prepare the mineral afwillite were unsuccessful. Amorphous hydrates having the CaO/SiO_2 molar ratio of this compound when heated at temperatures of 150° and 200° C in the presence of water crystallized largely to $CaO.SiO_2.H_2O$, and at temperatures ranging from 250° to 400° C crystallized largely to xonotlite. The secondary phases could not be distinguished petrographically or by the X-ray patterns. Raising the CaO/SiO_2 molar ratio has the effect of making both $CaO.SiO_2.H_2O$ and xonotlite stable at higher temperatures than was the case with the preparations of pure hydrated monocalcium silicate.

(f) MOLAR RATIO CaO/SiO_2, 5:3

The compositions treated in the experiments reported in table 7 corresponded in lime-silica ratio to the mineral foshagite, $5CaO.3SiO_2.3H_2O$.

TABLE 7.—*Results of experiments on* $5CaO:3SiO_2$ *compositions*

Experiment number	Starting material	Temperature	Pressure	Time	Product
		°C	*atm*	*Days*	
50	1.67CaO:SiO_2 glass [1]	200	15	73	?
51	do	300	85	53	Foshagite+glass.
52	do	350	163	17	Foshagite+glass.

[1] Contained 7 percent of B_2O_3.

The product of experiment 50 had the same X-ray pattern as that of the product obtained by treating anhydrous dicalcium silicate and dicalcium silicate glass with water at relatively low temperatures, and will be discussed in the next section.

The product of experiments 51 and 52 was a low-birefringent material without definite crystalline form and of mean index of refraction 1.595, which checks well with the mean index of foshagite. The X-ray patterns showed complete correspondence with the X-ray pattern of foshagite obtained from the United States National Museum. Conversion of the glass to the hydrate was not complete even in experiment 51, as the product gave an ignition loss of only 5.7 percent, compared with a theoretical loss for foshagite of 10.5 percent.

A sample of amorphous hydrate of CaO/SiO_2 molar ratio 1.68 steamed at 300° C out of contact with water gave a product having the X-ray pattern of $CaO.SiO_2.H_2O$. The manner of combination of the excess lime could not be determined.

(g) MOLAR RATIO CaO/SiO_2, 2:1

Results of experiments on compositions having a dicalcium silicate molar ratio, to which the mineral hillebrandite, $2CaO.SiO_2.H_2O$, corresponds, are listed in table 8.

TABLE 8.—*Results of experiments on* $2CaO:1SiO_2$ *compositions*

Experiment number	Starting material	Temperature	Pressure	Time	Product
		°C	*atm*		
53	β-$2CaO.SiO_2$	25	1	10 years	?
54	do	100	1	9 days	$10CaO.5SiO_2.6H_2O$+β-$2CaO.SiO_2$.
55	γ-$2CaO.SiO_2$	150	5	4 days	$10CaO.5SiO_2.6H_2O$+γ-$2CaO.SiO_2$.
56	β-$2CaO.SiO_2$	150	5	1 day	Scarce $10CaO.5SiO_2.6H_2O$ +β-$2CaO.SiO_2$.
57	do	150	5	7 days	Pure $10CaO.5SiO_2.6H_2O$.
58	$2CaO:SiO_2$ gel	150	5	10 days	95% of $10CaO.5SiO_2.6H_2O$.
59	$2CaO:SiO_2$ glass (12% of B_2O_3)	150	5	23 days	Same as preparation 53.
60	90% of γ-$2CaO.SiO_2$+ 10% of natural hillebrandite.	150	5	14 days	$10CaO.5SiO_2.6H_2O$+natural hillebrandite.
61	Preparation 53	175	9	41 days	Same product as preparation 53.
62	β-$2CaO.SiO_2$	200	15	3 days	$10CaO.5SiO_2.6H_2O$.
63	$2CaO:SiO_2$ gel	225	25	44 days	$2CaO.SiO_2.H_2O$.
64	$3CaO:2SiO_2$:aq+CaO	225	25	47 days	$CaO.SiO_2.H_2O$+?.
65	β-$2CaO.SiO_2$	250	39	15 days	$2CaO.SiO_2$ aq.
66	$10CaO.5SiO_2.6H_2O$	250	39	14 days	$10CaO.5SiO_2.6H_2O$.
67	90% of γ-$2CaO.SiO_2$+ 10% of natural hillebrandite.	250	39	14 days	Natural hillebrandite+$2CaO.SiO_2$aq.
68	$3CaO:2SiO_2$:aq+CaO	300	85	7 days	$CaO.SiO_2.H_2O$+?.
69	do	350	163	8 days	$CaO.SiO_2.H_2O$+$3CaO.SiO_2.2H_2O$.
70	$10CaO.5SiO_2.6H_2O$	450	400	7 days	$2CaO.SiO_2.2/3H_2O$.

Five g of β-dicalcium silicate treated with 500 ml of water for 10 years at room temperature (experiment 53) and shaken at intervals gave a product having a distinctive X-ray pattern and possessing a composition corresponding to the ratios $1.8CaO:1.0SiO_2:2.1H_2O$. It contained about 5 percent of calcite with the bulk of the material consisting of weakly birefringent masses without definite crystalline form. In order to effect further crystallization this material was

heated in the presence of water for 6 weeks at a temperature of 175° C (experiment 61). It was then completely crystallized to very fine needles of low birefringence and mean index of refraction 1.60. A chemical analysis gave the composition: 52.94 percent of CaO, 0.78 percent of R_2O_3, 36.50 percent of SiO_2, 9.69 percent of H_2O, which corresponds to the molar ratios: $1.55CaO:1.00SiO_2:0.88H_2O$. Allowing for the calcite which the sample contained, this analysis agrees fairly well with the formula $3CaO.2SiO_2.1.5H_2O$. The pattern is not like that of afwillite. The same X-ray pattern was given by dicalcium silicate glass (containing 12 percent of B_2O_3) treated with water at 150° C for 3 weeks (experiment 59) and also by $5CaO.3SiO_2$ glass (containing 7 percent of B_2O_3) at 200° C for 10 weeks (experiment 50, table 7).

Treating dicalcium silicate with water between 100° and 200° C usually produces an orthorhombic hydrate of dicalcium silicate. This compound is identical with crystals found by Thorvaldson and Shelton [17] in steam-cured portland cement and prepared in a pure state by Vigfusson, Bates, and Thorvaldson [18]. Reference to the preparation of the same compound from mixtures of lime, silica, and water and from tricalcium silicate and water has also been made by Flint and Wells [6]. The crystals are extremely thin (rarely more than 3 microns in thickness), lath-like plates often occurring as simple rectangular parallelopipeds but not infrequently with domatic faces bevelling the prismatic forms. The measured indices of refraction agree with those fixed by previous investigators: $\alpha=1.614\pm0.002$, $\beta=1.620\pm0.002$, $\gamma=1.633\pm0.002$. The crystals are biaxial positive. There is a perfect cleavage normal to the elongation. A photomicrograph is shown in figure 9.

Analysis of a typical preparation gave the composition: 56.64 percent of CaO, 0.46 percent of R_2O_3, 31.14 percent of SiO_2, and 11.34 percent of H_2O, corresponding to the ratios: $1.96CaO:1.00SiO_2:1.19H_2O$. Prolonged heating in an oven maintained at a temperature of 110° C reduced the water content to 10.90 percent, which corresponds to a H_2O/SiO_2 molar ratio of 1.17. Analysis of several other preparations also gave water contents corresponding closely to $1.2H_2O:1.0SiO_2$. The average of three analyses of this compound presented by Vigfusson, Bates, and Thorvaldson [18] likewise gave a H_2O/SiO_2 molar ratio of 1.24. It, therefore, appears probable that the water in excess of 1 mole is constitutional, and accordingly, the formula $10CaO.5SiO_2.6H_2O$ is suggested for the compound.

As shown in table 8, $10CaO.5SiO_2.6H_2O$ resulted from treatment with water of β- and γ-dicalcium silicates and $2CaO:1SiO_2$ mixtures of calcium oxide and silica gel. At 100° C (experiment 54), 9 days' boiling of 1 g of β-dicalcium silicate with 25 ml of water under a reflux gave about 30-percent conversion to $10CaO.5SiO_2.6H_2O$. Well-formed crystals of $10CaO.5SiO_2.6H_2O$ were also obtained by treatment of portland cement clinkers with water at 100° and 175° C. A photomicrograph of the product obtained at 175° C is given in figure 10.

Attempts to prepare hillebrandite by treating mixtures of natural hillebrandite and dicalcium silicate with water at 150° and 200° C (experiments 60 and 67) were unsuccessful. The results obtained by Kohler [16], who reported having prepared hillebrandite by heating a mixture of β-dicalcium silicate and water at temperatures ranging from 200° to 290° C, could not be duplicated. The synthesis of hille-

brandite from mixtures of CaO and amorphous SiO_2 in the presence of $CaCl_2$ heated with water at 470° C has been claimed by Schlaepfer and Niggli [10].

Treatment of $10CaO.5SiO_2.6H_2O$ at 250° C for 2 weeks (experiment 66) produced no change; treatment at 450° C, 400 atmospheres, for 1 week gave a product of unchanged crystal form but having the indices of refraction: $\alpha=1.642$, $\gamma=1.672$, which are about 0.03 higher than the corresponding indices of $10CaO.5SiO_2.6H_2O$. This material gave a distinctive X-ray pattern and its composition corresponded to the formula, $6CaO.3SiO_2.2H_2O$.

In experiment 65, β-dicalcium silicate heated in a bomb with water at 250° C crystallized to a granular product having a mean index of refraction of 1.64. The X-ray pattern was similar in spacing and intensity of lines to that of a finely crystalline monohydrate of dicalcium silicate obtained by Keevil and Thorvaldson [19]. Treatment of a $2CaO:1SiO_2$ mixture of CaO and silica gel at 225° C (experiment 63) gave complete crystallization to the other monohydrated dicalcium silicate described by Thorvaldson and coworkers [18, 19]. This occurs in very small needles of low birefringence and mean index 1.60. Analysis gave a composition corresponding to the ratios $2.0CaO:1.0SiO_2:1.1H_2O$.

In experiments 64, 68, and 69 amorphous hydrated calcium silicate of CaO/SiO_2 molar ratio 3:2 was mixed with sufficient CaO to give a ratio of 2:1 and in the presence of water heated at temperatures of 225°, 300°, and 350° C. The principal product in all three cases was $CaO.SiO_2.H_2O$. The secondary product was not identified except in experiment 69, where the optical properties and X-ray pattern showed it to be a hydrate of tricalcium silicate.

(h) MOLAR RATIO CaO/SiO_2, 3:1

The results of these experiments are shown in table 9.

In experiment 71, 1 g of tricalcium silicate treated with 500 ml of water for 9 years at room temperature was completely converted to a hydrated material of composition $1.3CaO:1.0SiO_2:1.7H_2O$. Petrographic examination showed less than 5 percent of calcite with the bulk of the material appearing as rounded grains of low birefringence having refractive indices ranging from 1.52 to 1.53. The X-ray pattern of this material was different from that of calcite or any of the other hydrous or anhydrous calcium silicates thus far investigated.

TABLE 9.—*Results of experiments on* $3CaO:SiO_2$ *compositions*

Experiment number	Starting material	Temperature	Pressure	Time	Product
		°C	atm		
71	$3CaO.SiO_2$	25	1	9 years	?
72	do	100	1	14 days	$10CaO.5SiO_2.6H_2O+Ca(OH)_2$.
73	do	150	5	5 days	Do.
74	do	200	15	35 days	$3CaO.SiO_2.2H_2O+10CaO.5SiO_2.6H_2O+Ca(OH)_2$.
75	do	250	39	12 days	$3CaO.SiO_2.2H_2O$.
76	β-$2CaO.SiO_2+CaO$	250	39	10 days	$2CaO.SiO_2$ hydrate$+Ca(OH)_2$.
77	$3CaO:2SiO_2:aq+3CaO$	275	59	16 days	$3CaO.SiO_2.2H_2O$.
78	$3CaO.SiO_2$	350	163	8 days	Do.
79	do	450	397	6 days	Do.

Tricalcium silicate treated with water at 100° C under a reflux condenser (experiment 72) and in the bomb at 150° C (experiment 73)

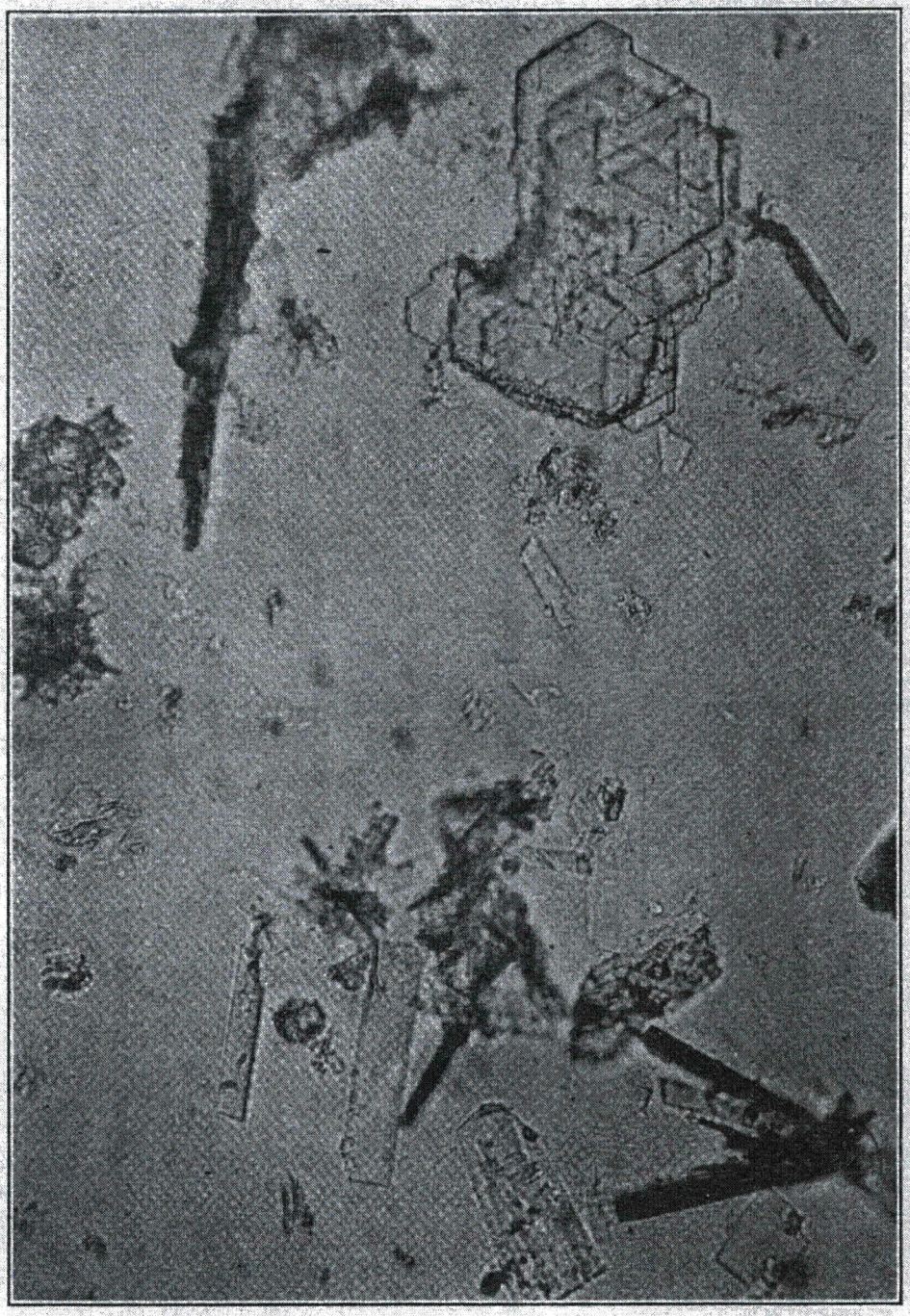

FIGURE 10.—*Lath-like orthorhombic plates of synthetic* $10CaO.5SiO_2.6H_2O$ *and hexagonal plates of* $Ca(OH)_2$ *obtained by treatment of portland cement clinker with water at 175° C.*

FIGURE 11.—*Synthetic* $3CaO.SiO_2.2H_2O$.
Magnification ×900.

was converted to $10CaO.5SiO_2.6H_2O$ and calcium hydroxide. At 250° C (experiment 75) direct hydration occurred without liberation of calcium hydroxide. The product consisted of broad fibrous crystals of positive elongation and parallel extinction. The indices of refraction were: $\alpha=1.590 \pm 0.003$, $\gamma=1.602 \pm 0.003$. Analysis of the preparation from experiment 75 gave the composition: 65.42 percent of CaO, 23.45 percent of SiO_2, 11.53 percent of H_2O, corresponding to the ratios: $2.98CaO:1.00SiO_2:1.63H_2O$. At 200° C (experiment 74) the product was primarily this compound with smaller amounts of $10CaO.5SiO_2.6H_2O$ and $Ca(OH)_2$ also present.

For experiment 77 the starting material was a mixture of amorphous hydrate of CaO/SiO_2 molar ratio 3:2 mixed with sufficient CaO to give a ratio of 3:1. After 16 days in the bomb at 275° C this preparation crystallized completely to large broom-shaped clusters of fibrous needles having the composition: 63.07 percent of CaO, 0.50 percent of R_2O_3, 22.38 percent of SiO_2, 13.56 percent of H_2O, corresponding to the ratios: $3.02CaO:1.00SiO_2:2.02H_2O$. A photomicrograph of this material is shown in figure 11. The X-ray pattern and optical properties were the same as those of the product from direct hydration of anhydrous tricalcium silicate. This preparation and that of experiment 75 gave negative tests for free lime by alcohol-glycerol extraction and by White's method.

This compound is identical with the product obtained by Keevil and Thorvaldson [19] by steaming tricalcium silicate between 110° and 375° C. By their procedure, however, only very finely crystalline material resulted.

Dehydration experiments proved the hydrated tricalcium silicate to be a very stable compound. A preparation heated in an oven for 16 hours at 215° C gave a loss in weight of only 0.2 percent. At 500° C for 16 hours the loss was 2.6 percent and at 700° C for 16 hours, 10.3 percent. Ignition for 5 minutes at 1,200° C gave complete conversion of the sample to β-dicalcium silicate and calcium oxide. Attempts to dehydrate the compound to tricalcium silicate were unsuccessful. Loss of water and liberation of free lime appear to take place concurrently.

In experiment 76 an attempt was made to prepare the hydrated tricalcium silicate from a $3CaO:1SiO_2$ mixture of β-$2CaO.SiO_2$ and CaO treated with water at 250° C. The product consisted of calcium hydroxide and the granular dicalcium silicate hydrate obtained by Keevil and Thorvaldson [19] and also identified in experiment 65, table 8 of this paper.

(i) MOLAR RATIO CaO/SiO_2, 4:1

Several experiments which were made to determine whether any hydrates richer in lime than $3CaO.SiO_2.2H_2O$ exist are recorded in table 10.

TABLE 10.—*Results of experiments on* $4CaO:1SiO_2$ *compositions*

Experiment number	Starting material	Temperature	Pressure	Time	Product
		°C	*atm*	*Days*	
79	β-$2CaO.SiO_2$+2CaO	250	39	27	$2CaO.SiO_2$ aq+$Ca(OH)_2$.
80	$3CaO.SiO_2$+CaO	250	39	12	$3CaO.SiO_2.2H_2O$.
81	$1.4CaO:SiO_2$ aq+2.6CaO	400	397	7	$3CaO.SiO_2.2H_2O$+$Ca(OH)_2$.
82	$1.3CaO:SiO_2$ aq+2.7CaO	450	400	6	$3CaO.SiO_2.2H_2O$+$Ca(OH)_2$.

The results indicate that dicalcium and tricalcium silicates form the same hydrates as they did in the absence of excess lime. The dicalcium silicate hydrate formed in experiment 79 occurred in small irregular plates having refractive indices ranging from 1.62 to 1.64. It was the same product as was obtained in experiment 76, table 9, and experiment 65, table 8 of this paper.

5. CEMENTITIOUS MATERIAL IN SAND-LIME BRICK

Some experiments similar to those of Grime and Bessey [2] were made in an attempt to isolate the hydrated calcium silicate in a commercial sand-lime brick of good quality. Half of the brick was crushed in a porcelain mortar with as little grinding as possible. Of this material the sample passing a No. 40 sieve and retained on a No. 70 sieve after brief shaking was used. It contained 4.4 percent of soluble silica determined according to the usual procedure. The material was screened on a No. 200 sieve for ½ hour and that passing was examined under the microscope. It appeared to consist almost wholly of calcite and was discarded. Screening was then continued another half hour. It was hoped by this method that the cementing material surrounding the sand grains might be rubbed off and concentrated. That this apparently occurred was shown by an increase in soluble silica to 16.2 percent in the material passing the No. 200 sieve. A number of pennies were then added to the material on the No. 200 sieve to assist the rubbing action, and the screening was continued for an hour. The material passing then showed a soluble silica content of 20.2 percent. However, in the X-ray patterns of both samples only the lines of calcite and quartz appeared.

It was thought that evidence of the presence of a crystalline hydrated calcium silicate might be obtained using a laboratory-prepared brick. For this purpose a mixture of 10 percent of hydrated lime and 90 percent of graded Ottawa sand (containing 0.13 percent of soluble silica) was molded into a bar in a hand press. The bar was then treated in contact with water at 175° C for 20 hours. After crushing the brick, the whole sample was found to contain 2.6 percent of soluble silica. This sample was rubbed with the fingers on a No. 20 sieve and the material passing in each case was rubbed successively on the No. 48, 100, and 200 sieves. The material passing the No. 200 sieve contained 16.8 percent of soluble silica. In the X-ray pattern the strongest lines were those of calcium hydroxide together with the lines of quartz.

Another bar was treated in the bomb at 175° C for 15 days. After a separation similar to that just described the material passing a No. 200 sieve was extracted for 75 hours with boiling ethylene glycol in an extractor of the type used in rubber analysis. The residue contained no free calcium hydroxide. Its X-ray pattern showed the lines of quartz with a few additional lines of moderate intensity which did not coincide with any of the lines of quartz, calcite, or calcium hydroxide. It was not possible, however, to assign these additional lines with certainty to any of the known hydrated calcium silicates.

IV. DISCUSSION

In the manufacture of sand-lime brick a wetted mixture of about 10 percent of hydrated lime and 90 percent of sand is pressed into forms, the resulting blocks removed, and steamed in an autoclave at 150° to 200° C (5 to 15 atm) for 8 to 12 hours. The nature of the cementing material formed by this treatment has never been established, but it is presumed to be a hydrated calcium silicate. X-ray and optical data [2] indicate that it may be amorphous. Some inferences regarding its potential crystalline composition may, however, be made from the results of this paper.

Lime usually constitutes only about 10 percent of the sand-lime brick mix, but its proportion to surface silica available for reaction will evidently be much higher owing to the relative coarseness of the sand particles. Thus, it is probable that the cementing material of the brick will be much richer in lime than the mix as a whole. Such a condition might permit the crystallization of compounds as highly basic as $10CaO.5SiO_2.6H_2O$. This compound appears to be by far the most easily formed of the hydrated calcium silicates at the temperatures employed in sand-lime brick manufacture. However, if the lime available for reaction with surface silica is insufficient to form this compound the potential crystallization of a less basic compound such as gyrolite might be favored.

Although the experiments with sand-lime brick failed to establish the identity of the cementing material in sand-lime brick, the greatly increased soluble silica content of the finer fractions of the crushed brick appears to indicate the formation of potentially crystalline compounds. That these combinations could not be identified by their X-ray patterns is not surprising in view of the fact that the various syntheses described in this paper all required much longer periods of time than those employed in sand-lime brick manufacture. The appearance of additional lines in the X-ray pattern of the sand-lime brick treated for a longer period is promising, and it is hoped that further work may reveal their source.

The crystalline materials obtained by reaction of water on β-dicalcium silicate and tricalcium silicate at room temperature are noteworthy with reference to end products in the setting of portland cement. There is a possibility that the product derived from dicalcium silicate, and which had a composition approximating $3CaO.2SiO_2.1.5H_2O$ on complete crystallization, may occur in set portland cement. This product could not be identified with any of the known calcium hydrosilicate minerals.

The poorly crystallized material which resulted from treatment of tricalcium silicate with water at room temperature had a CaO/SiO_2 molar ratio of only 1.3 owing to the extensive hydrolysis which had taken place in the presence of a large excess of water. Therefore, it probably would not form in the setting of portland cement when less water is used but might occur in hydrated puzzolanic cement where the proportion of silica to lime is higher. Unfortunately, the pattern of this material also could not be identified.

As has been pointed out by Thorvaldson and coworkers [17, 18, 19], the compounds designated in this paper as $10CaO.5SiO_2.6H_2O$ and $3CaO.SiO_2.2H_2O$ are probable products of the autoclave treatment of portland cements. Under such conditions it has also been

shown by Mather and Thorvaldson [20] that tricalcium aluminate will hydrate to $3CaO.Al_2O_3.6H_2O$ and tetracalcium aluminoferrite to $3CaO.Al_2O_3.6H_2O$ and $CaO.Fe_2O_3$ hydrate, which, in turn, will slowly decompose to $Ca(OH)_2$ and hematite. Thus it would appear possible to hydrate cement partially in the autoclave without the liberation of appreciable free lime. This is actually the case. A group of four high-tricalcium silicate cements all having ignition losses and free-lime contents of less than 1 percent was steamed in the autoclave at 200° C (15 atm) overnight. The ignition loss in each case was increased to 5 to 6 percent. The free-lime content of one cement remained the same, another showed a slight decrease, and the two remaining, an increase of a few tenths of a percent.

With regard to the 215° C autoclave test [1] for neat cement bars, the fact that calcium hydroxide can react with amorphous hydrated calcium silicate already formed, to give the hydrate of tricalcium silicate, is significant. This result, taken in conjunction with those of Mather and Thorvaldson [20], indicates that any expansion which results from autoclaving cannot be caused by crystallization of calcium hydroxide liberated from the cement compounds, but must be ascribed to other causes.

As was pointed out with reference to sand-lime brick, the crystallization of hydrated calcium silicates occurs slowly, requiring days or weeks to reach completion even at temperatures above 200° C. It is not to be expected, therefore, that well-developed crystals of any of the various hydrates described in this paper would be found in specimens steamed for the short period employed in the autoclave test. Only incipient crystallization would occur, but the products should be the same as those formed over longer periods.

V. SUMMARY

Table 11 gives a summary of optical properties of the natural and synthetic minerals identified in this investigation.

X-ray study of the hydrated calcium silicate minerals indicated that the following are distinct compounds:

Okenite	$CaO.2SiO_2.2H_2O$.
Gyrolite	$2CaO.3SiO_2.2H_2O$.
Crestmoreite	$2CaO.2SiO_2.3H_2O$.
Xonotlite	$5CaO.5SiO_2.H_2O$.
Afwillite	$3CaO.2SiO_2.3H_2O$.
Foshagite	$5CaO.3SiO_2.3H_2O$.
Hillebrandite	$2CaO.SiO_2.H_2O$.

Centrallasite, $4CaO.7SiO_2.5H_2O$, and truscottite, $4(Ca,Mg)O.7SiO_2.5H_2O$, seem to be impure forms of gyrolite. Riversideite, $2CaO.2SiO_2.H_2O$, is apparently not a distinct mineral and is probably the same compound as crestmoreite.

Preparations having X-ray patterns identical with those of gyrolite, xonotlite, and foshagite were synthesized by hydrothermal methods. Other compounds formed were cristobalite, wollastonite, pseudowollastonite, β-$3CaO.2SiO_2$, $4CaO.5SiO_2.5H_2O$, $CaO.SiO_2.H_2O$, $2CaO.SiO_2.H_2O$, $10CaO.5SiO_2.6H_2O$, and $3CaO.SiO_2.2H_2O$.

TABLE 11.—*Optical properties of natural and synthetic minerals identified in this study*

Composition	Optical properties					Crystal system and habit	Elongation	Mineral name	Obtained synthetically
	Sign	Optic angle	α or ω	β	γ or ϵ				
$CaO.2SiO_2.2H_2O$	–	Large	1.530		1.541	Orth. fibrous.	+	Okenite	No.
$2CaO.3SiO_2.2H_2O$	–	0	1.548		1.636	Trig. fibrous lamellae.	+	Gyrolite	Yes.
$4CaO.5SiO_2.5H_2O$				1.54		Acicular	+	Tobermorite(?)	Yes.
$5CaO.5SiO_2.H_2O$	+	Small	1.583	1.583	1.594	Orth. (?) fibrous.	+	Xonotlite	Yes.
$CaO.SiO_2.H_2O$				1.603		(?)	–		Yes.
$2CaO.2SiO_2.3H_2O$	–	Large	1.593	1.603	1.607	Fibrous	+	Crestmoreite	No.
$3CaO.2SiO_2.1.5H_2O$				1.60		do			Yes.
$3CaO.2SiO_2.3H_2O$	+	54°	1.617	1.620	1.634	Mon. prism.	–	Afwillite	No.
$5CaO.3SiO_2.3H_2O$	+	Small	1.594	1.594	1.598	Orth. fibrous.	+	Foshagite	Yes.
$2CaO.SiO_2.H_2O$	–	60° to 80°	1.605	1.61	1.612	do	+	Hillebrandite	No.
$2CaO.SiO_2.H_2O$				1.60		(?)	+		Yes.
$2CaO.SiO_2.H_2O$				1.64		(?)			Yes.
$10CaO.5SiO_2.6H_2O$	+	Medium	1.614	1.620	1.633	Orth.	+		No.
$6CaO.3SiO_2.2H_2O$			1.642		1.672	(?)			Yes.
$3CaO.SiO_2.2H_2O$			1.590		1.602	Fibrous	+		Yes.

Attempts to produce okenite synthetically were unsuccessful. Thus, a sample of calcium disilicate glass treated with water for 8 weeks at 150° C gave partial crystallization to cristobalite only.

Gyrolite was formed at 150° to 400° C from glasses and amorphous hydrates having CaO/SiO_2 molar ratios in the vicinity of 2:3.

Treating amorphous hydrate with CaO/SiO_2 molar ratio 0.80 at temperatures between 150° and 275° C gave a single phase of distinctive X-ray pattern, and a composition corresponding to $4CaO.5SiO_2.5H_2O$. This composition is similar to that reported for the rare mineral tobermorite. At 300° C the product was xonotlite.

Amorphous monocalcium silicate hydrate at 150° C crystallized to $CaO.SiO_2.H_2O$, which had a distinctive X-ray pattern. However, in the presence of higher molar ratios of lime to silica, $CaO.SiO_2.H_2O$ was formed at temperatures as high as 350° C.

Xonotlite, $5CaO.5SiO_2.H_2O$, crystallized from preparations of amorphous hydrated monocalcium silicate between 165° ±15° C and 395° ±5° C (70 to 225 atm). Above 395° C wollastonite crystallized.

Amorphous hydrate of molar ratio $3CaO/2SiO_2$ treated between 150° and 400° C did not yield afwillite, $3CaO.2SiO_2.3H_2O$, but instead crystallized partially to $CaO.SiO_2.H_2O$ at the lower temperatures and to xonotlite at the higher. These were probably metastable crystallizations resulting from the relatively high crystallization potential of the monocalcium silicate hydrates. Anhydrous tricalcium disilicate treated at 250° C was converted to an unidentified hydrate.

The usual form of anhydrous tricalcium disilicate treated at 500° C (380 atm) for 2 weeks was converted to a low-temperature or β form of the anhydrous compound. It inverts to the high-temperature form at 1,024° ±5° C.

Glass of composition $5CaO.3SiO_2$ treated at 300° and 350° C was converted to a product having an X-ray pattern identical with that of the mineral foshagite.

The compound $10CaO.5SiO_2.6H_2O$ was formed from β- and γ-dicalcium silicates, tricalcium silicate, and mixtures of lime and silica gel in the temperature range 100° to 200° C. Attempts to prepare a hydrate identical with natural hillebrandite were unsuccessful.

Tricalcium silicate treated with water between 200° and 450° C hydrated directly to $3CaO.SiO_2.2H_2O$. No hydrates of higher lime content than $3CaO.SiO_2.2H_2O$ appear to exist.

A number of unsuccessful attempts were made to isolate and identify the cementing material in sand-lime brick.

The authors gratefully acknowledge their indebtedness to Herbert Insley for his assistance in the X-ray and microscopic studies, to W. F. Foshag of the United States National Museum for supplying samples of most of the naturally occurring minerals, and to E. S. Newman for carrying out the experiments on sand-lime brick.

VI.—REFERENCES

[1] *Report of Committee C-1 on Cement.* Proc. Am. Soc. Testing Materials **37,** 290 (1937).

[2] G. Grime and G. E. Bessey, *The cementing material of sand-lime bricks. An X-ray and microscopic examination,* Ceram. Soc. Trans. **32** [1], 14 (1933).

[3] J. W. Mellor, A comprehensive treatise on inorganic and theoretical chemistry, **6,** 358 (Longmans, Green and Co., New York, N. Y., 1925).

[4] A. S. Eakle, *Minerals associated with the crystalline limestone at Crestmore, Riverside County, Calif.,* Univ. of Calif. Bul. Dept. Geology **10,** 327 (1917).

[5] V. A. Vigfusson, *The hydrated calcium silicates.* I. *The system* $CaO-SiO_2-H_2O$. II. *Hillebrandite and foshagite,* Am. J. Sci. **21,** 67 (1931).

[6] E. P. Flint and L. S. Wells, *Study of the system* $CaO-SiO_2-H_2O$ *at 30° C and of the reaction of water on the anhydrous calcium silicates,* BS J. Research **12,** 751 (1934) RP687.

[7] G. W. Morey and C. N. Fenner, *The ternary system* $H_2O-K_2SiO_3-SiO_2$. J. Am. Chem. Soc. **39,** 1173 (1917). G. W. Morey and Earl Ingerson, *A bomb for use in hydrothermal experimentation,* Am. Mineral. **22,** 1121 (1937).

[8] C. J. van Nieuwenburg and H. B. Blumendal, *The isotherms of water from 350° to 480° C and for pressures up to 600 kg/cm²,* Rec. trav. chim. **51,** 707 (1932).

[9] G. W. Morey and Earl Ingerson, *The pneumatolytic and hydrothermal alteration and synthesis of silicates,* Econ. Geology **32,** 629 (1937).

[10] M. Schlaepfer and P. Niggli, *Neue Beitrage zur hydrothermalen Silikatbildung,* Z. anorg. Chem. **87,** 52 (1914).

[11] E. Baur, *Ueber hydrothermale Silikate.* Z. anorg. Chem. **72,** 119 (1911).

[12] M. F. Heddle, *Preliminary notice on substances which may prove to be minerals,* Min. Mag. **4,** 119 (1880).

[13] P. Groth, *Tabellarische Uebersicht der Mineralien,* Munich and Berlin (1921).

[14] C. J. van Nieuwenburg and H. B. Blumendal, *The pneumatolytic synthesis of silicates,* I. Rec. trav. chim. **50,** 129 (1931).

[15] S. Nagai, *Hydrothermale Synthesen von Calciumsilikaten,* II, Z. anorg. Chem. **207,** 321 (1932).

[16] W. Kohler, *Ueber die Bildung kristallisierter Kalziumsilikathydrate,* Tonind. Ztg. **59,** 739; 754 (1935).

[17] T. Thorvaldson and G. R. Shelton, *Steam curing of portland cement mortars. A new crystalline substance.* Can. J. Research **1,** 148 (1929).

[18] V. A. Vigfusson, G. N. Bates, and T. Thorvaldson, *Hydrothermal synthesis of calcium hydrosilicates.* Can. J. Research **11,** 520 (1934).

[19] N. B. Keevil and T. Thorvaldson, *The hydration of dicalcium silicate and tricalcium silicate,* Can. J. Research **14,** 20 (1936).

[20] D. T. Mather and T. Thorvaldson, *The action of saturated steam on dicalcium ferrite and tetracalcium aluminoferrite,* Can. J. Research **15** [B] 331 (1937).

WASHINGTON, August 19, 1938.

WVMP SAR Reference 3-23

"The Hydration of Alite: A Time-Resolved Quantitative X-Ray Diffraction Approach Using the G-Factor Method Compared with Heat Release," Jansen, D., S. T. Berghold, F. Goetz-Neunhoeffer, and J. Neubauer, J. Appl. Cryst., 44, 895-901, 2011.

Journal of
Applied
Crystallography
ISSN 0021-8898

Received 21 March 2011
Accepted 30 June 2011

The hydration of alite: a time-resolved quantitative X-ray diffraction approach using the *G*-factor method compared with heat release

Daniel Jansen,* Sebastian T. Bergold, Friedlinde Goetz-Neunhoeffer and Jürgen Neubauer*

GeoZentrum Nordbayern, Chair for Mineralogy, University of Erlangen–Nuremberg, Schlossgarten 5a, Erlangen, Bavaria, 91054, Germany. Correspondence e-mail: danherjansen@googlemail.com, neubauer.gzn@me.com

The classical external-standard method derived from the work of O'Connor & Raven [*Powder Diffr.* (1988), **3**, 2–6] was used to examine the hydration of the major phase, alite, of ordinary Portland cements at different temperatures and different water/alite ratios. In order to estimate the accuracy of the method, heat-flow curves were calculated from the alite dissolution curves obtained from X-ray diffraction *in situ* experiments. The heat-flow curves calculated in this way were compared with heat-flow curves recorded using a calorimeter. It is shown that the calculated curves agree well with the curves obtained from heat-flow experiments.

1. Introduction

Even though ordinary Portland cements (OPCs) have been used and studied for decades, the hydration kinetics of their major phase, alite (doped tricalcium silicate, C_3S), are still not completely understood. Several theories have persisted alongside each other. The major concern of these theories has been to explain the reaction kinetics of alite hydration which are commonly determined from heat-flow calorimetric measurements (Fig. 1). An initial heat flow can be detected directly after mixing (I). This is followed by a period of slow reaction which is known as the induction period (II). This induction period is followed by the main hydration reaction (III), which is separated into the acceleration (III*a*) and the deceleration period (III*b*). The main hydration reaction is normally completed after the elapse of 24 h, but the hydration continues at low heat-flow levels for months. The hydration results in the formation of an amorphous calcium–silicate–hydrate (C–S–H) gel and crystalline portlandite. The Ca/Si ratio of C–S–H depends on the temperature (Escalante-Garcia & Sharp, 1999), on the water-to-cement ratio (Locher, 1967) and, in the case of an OPC, on the composition of the OPC used (Richardson, 1999). After 28 d, the Ca/Si ratio of a C–S–H gel formed in a hydrated OPC at 293 K with a water-to-cement ratio of 0.4 stands at 1.7, according to Allen *et al.* (2007). We thus arrive at equation (1) for the hydration of C_3S after this point in time:

$$C_3S + 3.9H \rightarrow C_{1.7}SH_{2.6} + 1.3CH, \quad \Delta H = -561\,J\,g^{-1}. \quad (1)$$

The enthalpy of reaction ΔH is the difference between the sum of the formation enthalpies of the products ($\Delta HF_{products}$) and the sum of the formation enthalpies of the reactants ($\Delta HF_{reactants}$).

The enthalpy for equation (1) was calculated using data acquired by means of the thermodynamic software *GEMS* (Kulik, 2010) using the *GEMS* version of the Nagra/PSI thermodynamic database (Hummel *et al.*, 2002; Thoenen & Kulik, 2003), the cemdata07 database (Lothenbach *et al.*, 2008) and the enthalpy of formation for $C_{1.7}SH_{2.6}$ derived following Fuji & Kondo (1983).

The most widely used theory for the hydration of alite predicts the formation of a metastable protective C–S–H layer on the C_3S grain surface directly after wetting. This protective layer suppresses further hydration of the C_3S and ends the initial period (Stein & Stevels, 1964; Gartner & Gaidis, 1989). At the end of the induction period, this protective layer is destabilized, giving rise either to a more permeable layer or to the dissolution of the layer, which allows the hydration reaction to start again. Livingston *et al.* (2010) assume, from the results of their nuclear resonance reaction analysis of C_3S

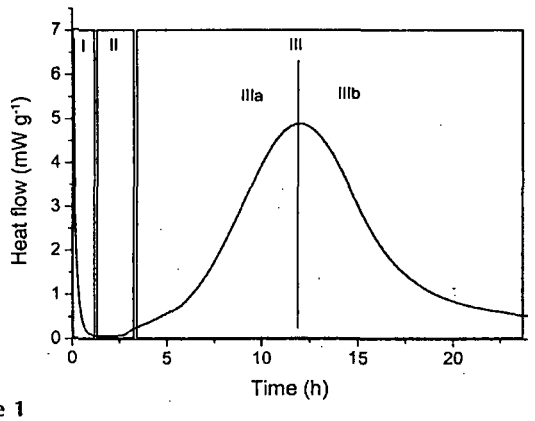

Figure 1
Heat-flow curve of alite; water/alite ratio = 0.5; T = 296 K.

doi:10.1107/S0021889811025933

hydration, that an existing protective layer breaks because of the osmotic pressure attained between the silicate-rich grain surface and the calcium-rich solution.

Another theory does not require this assumption of the emergence of a protective layer in order to explain the progress of alite hydration. For example, Garrault & Nonat (2001) and Peterson & Whitten (2009) assume that a single process is responsible for both the nucleation and the growth of C–S–H, which begins, according to Rodgers *et al.* (1988), directly after mixing. Thomas (2007) concludes, from mathematical calculation of a boundary nucleation and growth model, that the hydration continues at low levels during the period of slow reaction. This, he suggests, is because there are only a small number of C–S–H nucleons present, so that this period does not form a separate chemical process in itself. Assuming a constant rate for the C–S–H nucleation process (Thomas, 2007), the acceleration period would begin once a sufficient number of C–S–H nucleons have been precipitated. Juilland *et al.* (2010) suggest that there are different solution mechanisms working at different degrees of undersaturated solution, as described by Lasaga & Luttge (2001) for several minerals.

At a certain point, the hydration of alite becomes diffusion controlled, because the unreacted alite grains come to be covered by a continuous product layer. Some authors (*e.g.* Garrault & Nonat, 2001) claim that the diffusion regime has already begun with the onset of the deceleration period, while others consider it to begin only with the end of the deceleration period, when the hydration has reached very low levels, or at even later points in time (Thomas *et al.*, 2009).

X-ray diffraction (XRD) *in situ* analysis is a suitable method for examining the phase development of hydrating alite/water mixtures during the process of hydration. This is the case even though the C–S–H phase that is formed during this process is not detectable by X-ray diffraction in the first 24 h because of its low degree of crystallinity. Besides this, the water added to the alite cannot be quantified directly with X-rays.

Software for Rietveld (1969) refinement usually gives the total of the crystalline phases determined, normalized to 100 wt% (*ZMV* algorithm; Hill & Howard, 1987). In cases where amorphous phases are present (in the case of alite/water mixtures, there is likely to be at least C–S–H phase and water) the amounts of the crystalline phases calculated from Rietveld analysis will differ from the actual amounts. Moreover, any computing error of any phase of the mixture will have an influence on the calculated amounts of all phases in the mixture.

There exists the possibility of plotting peak areas or peak intensities in order to show phase developments in pastes in quantitative terms (Pöllmann *et al.*, 2009; Pelletier *et al.*, 2009) and without normalization to 100 wt%. Unfortunately it is not possible to calculate actual quantities, given in wt% of the alite/water mixture, by this method.

An internal-standard method can be applied in order to establish the phase composition of the crystalline phases as well as the amount of the amorphous content of an alite/water mixture (Scrivener *et al.*, 2004). If an internal standard is added to the cement, there exists the possibility of the standard material exerting an influence on the hydration of the cement.

Westphal *et al.* (2009) have examined the mathematical consequences of the internal-standard method and have concluded that there is such a thing as an optimal amount of internal standard that can be added to the sample. Assuming an amorphous content of 35 wt% on average in the first 22 h of hydration (depending on the C–S–H phase and water/alite ratio), the most advisable option, they propose, is to work with an amount of internal standard of at least 40 wt%. Where this is not done, the user will have to accept a considerable analysis error. Such a high amount of internal standard might possibly have an influence on the hydration inasmuch as it might bring about alterations in nucleation and growth kinetics or the water/alite ratio.

In order to avoid complications that might be caused by mixing an internal standard with the alite phase, we decided to make use of an external-standard method, which was first described by O'Connor & Raven (1988) but has not subsequently been used for the quantification of hydration reactions.

The scope set for this paper is to provide an answer to the question of whether or not XRD *in situ* analysis is a suitable method for characterizing the hydration process of the alite phase. It is also the intention of the authors to focus attention on the comparison between heat-flow curves as calculated from XRD data and heat-flow curves as measured from heat-flow experiments. The main focus is on the main hydration period of the cement, which sets in after several hours and is concluded within 24 h at room and higher temperatures.

However, a question that can be answered using XRD experiments is how the reaction from alite to portlandite and the C–S–H phase emerges. Assuming that there exist at least two processes here that release heat, namely the dissolution of the alite phase and the precipitation of portlandite and the C–S–H phase, it necessarily follows that dissolution and precipitation have to run synchronously in order to make it possible to calculate the heat flow using only the dissolution curve of the alite phase obtained from Rietveld analysis.

2. Materials and methods

Alite was synthesized using $CaCO_3$, Al_2O_3 and SiO_2 from Alfa Aesar and MgO from Merck. Al_2O_3 and MgO were added to stabilize a monoclinic (*M*3) alite structure (De La Torre *et al.*, 2002). The chemicals were homogenized in a vibration disc mill and placed in platinum crucibles. The thermal treatment was carried out three times at a temperature of 1673 K for 4 h in a chamber furnace. The synthesized alite was checked for phase purity using XRD. The specific surface of the synthesized alite was measured to be 0.29 $m^2 g^{-1}$, using the Blaine method.

For the *in situ* XRD analysis a custom-made sample holder with a heater/cooler unit was used (Hesse *et al.*, 2008). Cement and water were mixed by external stirring for 1 min. The paste was then put into the sample holder and covered by a 7.5 μm-

Table 1
Structure models used for Rietveld refinements.

Phase	ICSD code	Author
Alite	94742	De La Torre *et al.* (2002)
Silicon	51688	Többens *et al.* (2001)
Portlandite	34241	Greaves & Thomas (1986)

Table 2
Chemical composition of the samples (wt%).

CaO	71.8
Al_2O_3	0.6
SiO_2	25.9
MgO	1.8

thick Kapton polyimide film. The diffraction patterns were recorded using a D8 diffractometer (Bruker) equipped with a LynxEye position-sensitive detector. We made use of Cu $K\alpha$ radiation at 40 kV and 40 mA, and recorded from 7° 2θ to 40° 2θ with a step width of 0.0236 and 0.58 s counting time per step. Under these conditions, it is possible to record 88 ranges within the first 22 h of hydration. For the Rietveld refinements, the program *Topas* version 4.2 from Bruker AXS Inc. (Madison, Wisconsin, USA) (fundamental parameters approach) was used. There was no evidence for any difference in the results when working with a longer range from 7° 2θ to 70° 2θ.

The quantitative phase composition of the alite paste was determined using the *G*-factor method, which was first described by O'Connor & Raven (1988) and which has already been used successfully for the examination of cements and cement pastes (Jansen, Goetz-Neunhoeffer *et al.*, 2011; Jansen, Stabler *et al.*, 2011). In addition, the method was recommended by Schreyer *et al.* (2011) for the examination of organic mixtures. For this purpose, a well known standard (in our case silicon; Jansen, Stabler *et al.*, 2011) is used in order to calculate the *G* factor [equation (2)]:

$$G = s_{\mathrm{Si}} \frac{\rho_{\mathrm{Si}} V_{\mathrm{Si}}^2 \mu_{\mathrm{Si}}^*}{c_{\mathrm{Si}}}, \qquad (2)$$

where s_{Si} is the Rietveld scale factor of silicon from Rietveld analysis, ρ_{Si} the density of silicon, V_{Si} the unit-cell volume of silicon, c_{Si} the weight fraction of silicon (100 wt%) and μ_{Si}^* the mass attenuation coefficient of silicon.

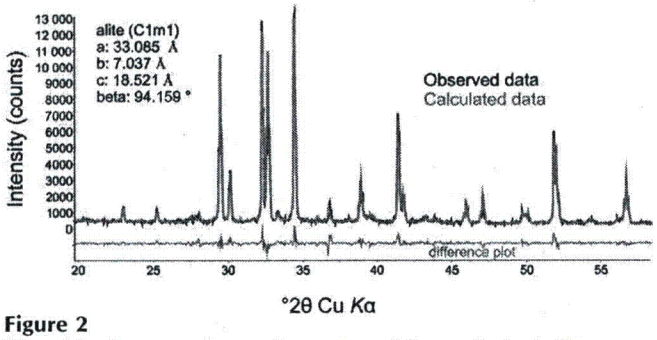

Figure 2
Rietveld refinement of a powder pattern of the synthesized alite.

Table 3
Mass attenuation coefficients (MAC) ($cm^2\ g^{-1}$) of the samples.

$MAC_{\mathrm{dry\ alite}}$	99
MAC_{H2O}	10.2
MAC(alite/water paste; water/alite ratio = 0.5)	69.4
MAC(alite/water paste; water/alite ratio = 1)	54.6

Table 4
Computed *G* factor and structural details regarding the silicon standard employed.

Scale factor from Rietveld refinement	0.007695
Cell volume	1.6×10^{-22} cm^3
Density	2.33 g cm^{-3}
Mass attenuation coefficient	63.7 cm^2 g^{-1}
G factor	2.92×10^{-44} cm^5 per wt%

The *G* factor was then used to determine the mass concentration of each crystalline phase *j* in the hydrating alite paste [equation (3)]:

$$c_j = s_j \frac{\rho_j V_j^2 \mu_{\mathrm{sample}}^*}{G}. \qquad (3)$$

This made it imperative that the sample be measured under the same conditions as the standard. Since the alite paste was covered during the measurement process with a Kapton film, which can cause absorption of X-rays and thereby intensity loss, it was necessary that the standard material be likewise covered with a Kapton film during its measurement process. The structure models and the respective ICSD codes are shown in Table 1. The chemical composition of the alite samples is shown in Table 2. The mass attenuation coefficients of the dry alite powder and the pastes are shown in Table 3. Mass attenuation coefficients for the various elements were drawn from *International Tables for Crystallography* (Prince, 2004). The mass attenuation coefficient of the alite powder was calculated from the chemical composition. More details about the standard used are shown in Table 4. The *G* factor was evaluated from six powder samples with individual preparations. The mean value of all measurements was used for the quantification of the water/alite pastes. The standard deviation of the mean value for the scale factor of the silicon powder was 0.8 wt%.

The *G*-factor method of O'Connor & Raven (1988) displays enormous advantages where it is applied to the quantification of alite hydration. Where this method is adopted, the crys-

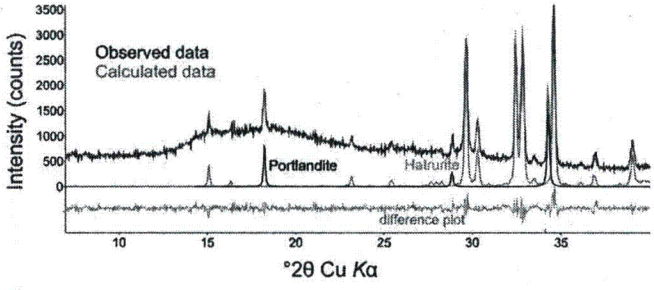

Figure 3
Rietveld refinement of a paste after 11 h hydration; water/alite ratio = 0.5; T = 310 K.

talline phases can be quantified directly from the scale factors. No error in the determination of any individual phase has any influence on the determined amounts of the other phases. In addition, the amorphous phases, namely water and the C–S–H phase, cannot be quantified using the standard Rietveld *ZMV* algorithm, which only considers the crystalline phases.

Heat-flow experiments were carried out using a commercial TAM Air calorimeter. Alite and water were equilibrated before the measurements in a calibrated heat chamber. Mixing of the alite with the water was carried out externally by means of a special mixer which allows reproducible stirring for 1 min. The samples were then put in the calorimeter. The first half-hour of the heat-flow experiments cannot be evaluated because of the disturbance of the signal caused by opening the calorimeter.

Heat-flow curves were calculated from the *in situ* XRD results (alite dissolution curves) using equation (4) (modified from Hesse *et al.*, 2011):

$$\mathrm{HF} = \frac{\partial \mathrm{wt\%\ alite}/\partial t}{100}\frac{\Delta H\mathrm{R}}{3.6}(-1), \qquad (4)$$

where ∂wt% alite/∂t is the derivation of the alite curve from XRD *in situ* experiments, and ΔHR is the enthalpy of reaction of equation (1).

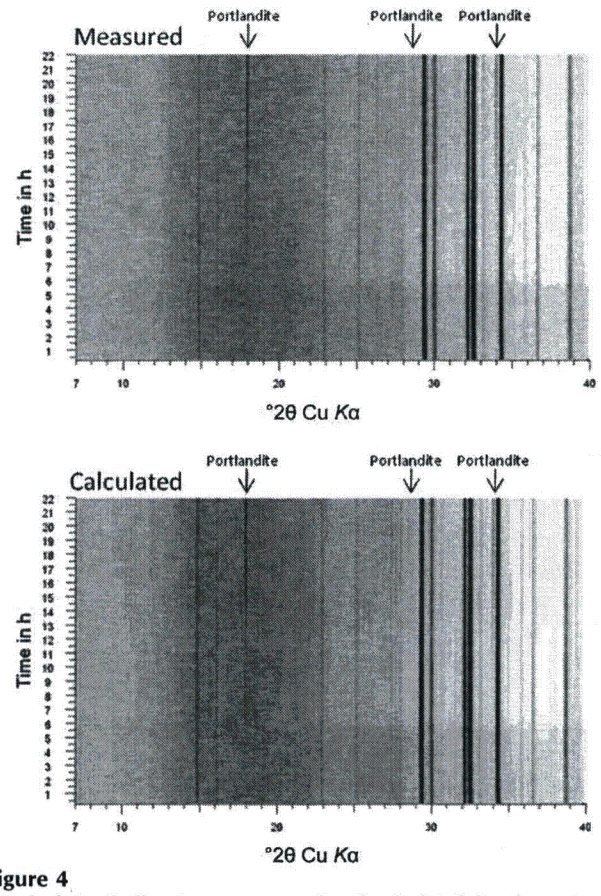

Figure 4
Level plots of all patterns measured and calculated for the system at 296 K and a water/alite ratio of 0.5. (Portlandite peaks are marked, the remaining peaks are alite peaks.)

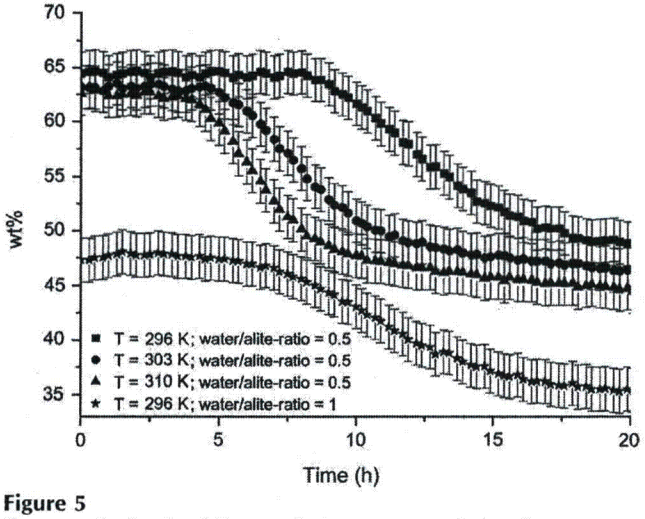

Figure 5
Content of alite in different alite/water pastes during the process of hydration.

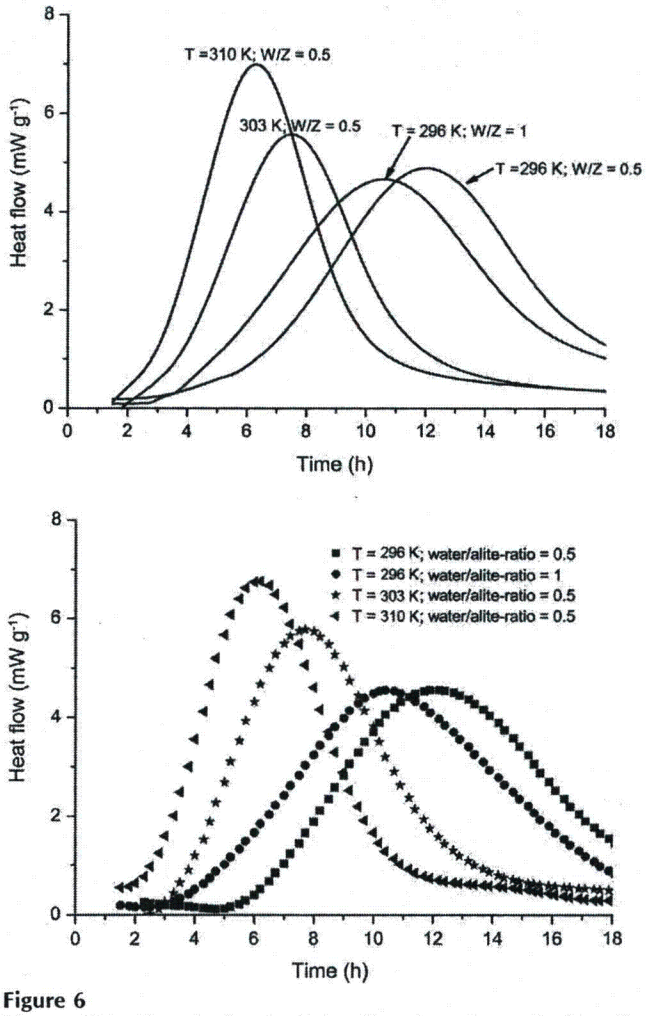

Figure 6
Measured heat flows (top) and calculated heat flows (bottom) of the alite/water pastes at different temperatures and water/alite ratios (from 1.5 h).

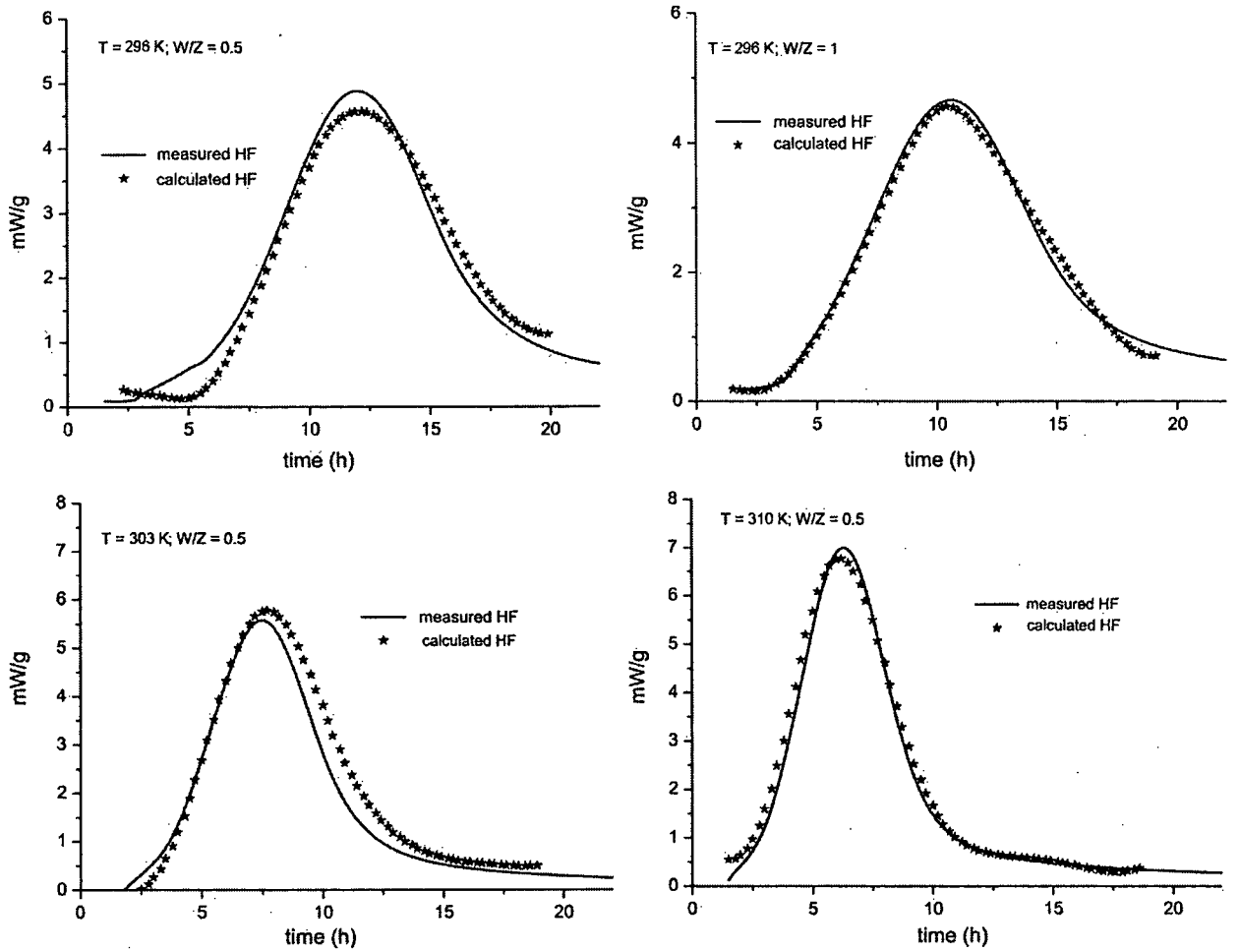

Figure 7
Comparison between measured and calculated heat flows of synthetic alite at different temperatures and water/alite ratios (from 1.5 h).

3. Results

The Rietveld refinement of the synthesized alite is shown in Fig. 2.[1] There was no sign of any phase except the alite phase. The calculation of the amount of alite using the G factor, which was derived from the standard material silicon, resulted in 96 (2) wt% of alite in our sample and 4 (2) wt% of amorphous or non-fitted phase. We assume that the structures used, as well as inaccurate dislocation parameters, might possibly be the reasons for the underquantification of the alite phase (Jansen, Stabler *et al.*, 2011). An amorphous, glassy phase is not verified.

The Rietveld refinement of the hydrating alite/water paste is shown in Fig. 3. There is close agreement between the intensity as observed and the intensity as calculated. The hump between 15° 2θ and 25° 2θ is created by the Kapton foil which covered the sample in order to avoid interaction with atmospheric CO_2 or water loss. The background of the Kapton foil and the water was considered using a special peaks phase model (Hesse *et al.*, 2009).

[1] Supplementary data for this paper are available from the IUCr electronic archives (Reference: CG5188). Services for accessing these data are described at the back of the journal.

Fig. 4 shows level plots of all patterns calculated and measured for the system at 296 K and a water/alite ratio of 0.5 as a function of time, representative of all measurements performed and refined. All Rietveld refinements were as good as the refinement shown in Fig. 4.

The results from the XRD *in situ* experiments are shown in Fig. 5. It can be seen that the reaction of the alite phase strongly depends on both the temperature and water/alite ratio. Since about 96 wt% of crystalline alite could be detected in the dry sample, we can expect an absolute alite content of around 64 wt% in the cement paste, when working with a water/alite ratio of 0.5. A water/alite ratio of 1 would result in an amount of 48 wt% of alite in the paste, assuming that no alite reacts immediately after mixing the alite with water. Fig. 5 shows that no dissolution of the alite phase directly after mixing could be proven by means of the G-factor method. This leads us to the conclusion that either no alite reacts immediately with water or only very low amounts of alite are dissolved immediately, the amounts being lower than the standard deviations of the results of our experiments (±2 wt%).

The heat-flow curves as measured and the heat-flow curves as calculated from XRD data using equation (4) are shown in

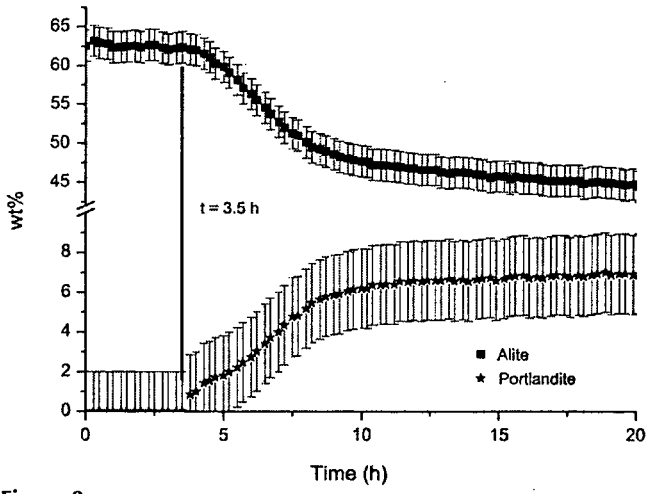

Figure 8
Quantitative phase development of alite and portlandite during the hydration of alite and water (water/alite = 0.5, T = 310 K).

Fig. 6. It can be seen that the calculated heat-flow curves accord to a great extent with the measured heat-flow curves. It is a fact that slow reactions are much harder to track by X-ray experiments than fast reactions. Therefore it is not surprising that the main period of the hydration is much easier to reproduce by means of X-ray diffraction than is the induction period.

The direct comparison of the curves is shown in Fig. 7. There is close agreement between the heat-flow curves as measured and the calculated heat-flow curves evaluated using the determined alite content measured by X-ray diffraction. It can be proven that the heat-flow curve obtained from the heat-flow experiments can be explained by the hydration reaction of the alite phase. This leads us to the conclusion that the quantification method chosen for the experiments can be recommended for the quantification of hydration reactions, such as the reaction of alite with water.

The fact that the complete hydration reaction [equation (1)] can be described by the alite dissolution curve can be interpreted in two ways. The first is that all heat is released during the dissolution of the alite phase. The precipitation of portlandite and the C–S–H phase does not contribute to the heat flow that can be detected from heat-flow experiments.

Another, more likely, explanation is that the dissolution of alite and the precipitation of portlandite and the C–S–H phase take place synchronously. This makes it conceivable that the heat-flow curve of alite with water is correctly described by the dissolution of alite.

A plot of the alite curve and the portlandite curve in the same diagram also shows that the dissolution of the alite phase and the precipitation of the portlandite phase emerge synchronously. Fig. 8 shows both curves at a water/alite ratio of 0.5 and at a temperature of 310 K, representative of all experiments performed. Under these conditions, the dissolution of alite and the precipitation of portlandite begin at a point in time some 3.5 h after mixing of the reactants.

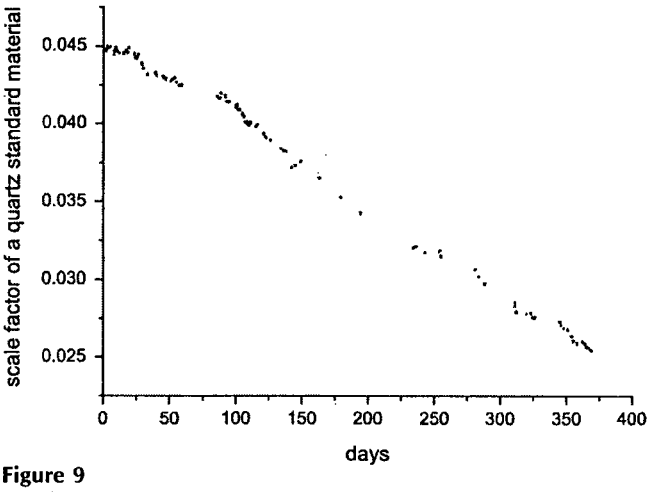

Figure 9
Development of the scale factor of a quartz standard material over time.

4. Conclusion

The method presented by O'Connor & Raven (1988) was a crucial step in developing a method for quantifying materials with amorphous portions. The implementation of this method for the characterization of hydration processes turned out to be very promising. It transpires that the calculation of a calibration factor G is of great practical use in the day-to-day work of a laboratory where hydration processes of materials containing crystalline phases are under examination.

It could be shown that the dissolution of alite, which was quantified by means of X-ray diffraction using the G-factor method, is suitable for characterizing the kinetics of the reaction of alite and water. The heat-flow curves obtained from heat-flow experiments could be simulated by using the quantitative XRD data for the calculation of heat-flow diagrams.

It is, however, imperative in every case that the user of the G-factor method always takes care to ensure that the right G factor is used. This is because the factor depends on the performance of the X-ray tube and the detector, and therefore strongly depends on time. As shown in Fig. 9, it is not advisable to calculate the G factor a long time before or after the point in time at which the experiment is actually performed.

The authors would like to thank Natalia Illenseer, Sebastian Klaus and Sebastian Scherb for their support during the experiments.

References

Allen, A. J., Thomas, J. J. & Jennings, H. M. (2007). *Nat. Mater.* **6**, 311–316.
De La Torre, A. G., Bruque, S., Campo, S. & Aranda, M. (2002). *Cem. Concr. Res.* **32**, 1347–1356.
Escalante-Garcia, J. I. & Sharp, J. H. (1999). *J. Am. Ceram. Soc.* **82**, 3237–3241.
Fuji, K. & Kondo, W. (1983). *J. Am. Ceram. Soc.* pp. C220–C221.
Garrault, S. & Nonat, A. (2001). *Langmuir*, **17**, 8131–8138.

Gartner, E. M. & Gaidis, J. M. (1989). *Materials Science of Concrete I*, pp. 95–125. Westerville: The American Ceramic Society.
Greaves, C. & Thomas, M. A. (1986). *Acta Cryst.* B**42**, 51–55.
Hesse, C., Degenkolb, M., Gäberlein, M., Goetz-Neunhoeffer, F., Neubauer, J. & Schwarz, V. (2008). *Cem. Int.* **6**, 68–78.
Hesse, C., Goetz-Neunhoeffer, F. & Neubauer, J. (2011). *Cem. Concr. Res.* **41**, 123–128.
Hesse, C., Goetz-Neunhoeffer, F., Neubauer, J., Braeu, M. & Gaeberlein, P. (2009). *Powder Diffr.* **24**, 112–115.
Hill, R. J. & Howard, C. J. (1987). *J. Appl. Cryst.* **20**, 467–474.
Hummel, W., Berner, U., Curti, E., Pearson, F. J. & Thoenen, T. (2002). *Nagra/PSI Chemical Thermodynamic Data Base 01/01*. Parkland: Universal Publishers/uPUBLISH.com.
Jansen, D., Goetz-Neunhoeffer, F., Stabler, C. & Neubauer, J. (2011). *Cem. Concr. Res.* **41**, 602–608.
Jansen, D., Stabler, C., Goetz-Neunhoeffer, F., Dittrich, S. & Neubauer, J. (2011). *Powder Diffr.* **26**, 31–38.
Juilland, P., Gallucci, E., Flatt, R. & Scrivener, K. (2010). *Cem. Concr. Res.* **40**, 831–844.
Kulik, D. (2010). *GEMS-PSI* 3.0 2010, PSI-Villingen, Switzerland, http://gems.web.psi.ch.
Lasaga, A. C. & Luttge, A. (2001). *Science*, **291**, 2400–2404.
Livingston, R. A., Schweitzer, J. S., Rolfs, C., Becker, H. W., Kubsky, S., Spillane, T., Zickefoose, J., Castellote, M., de Viedma, P. G. & Cheung, J. (2010). *Appl. Radiat. Isot.* **68**, 683–687.
Locher, F. W. (1967). *Zement-Kalk-Gips*, **20**, 402–407.
Lothenbach, B., Matschei, T., Möschner, G. & Glasser, F. P. (2008). *Cem. Concr. Res.* **38**, 1–18.
O'Connor, B. H. & Raven, M. D. (1988). *Powder Diffr.* **3**, 2–6.
Pelletier, L., Winnefeld, F. & Lothenbach, B. (2009). *Tagungsbericht 17. Internationale Baustofftagung, Weimar*, 1-0277-1-0282. Weimar: F. A. Finger-Institut für Baustoffkunde.
Peterson, V. K. & Whitten, A. E. (2009). *J. Phys. Chem. C*, **113**, 2347–2351.
Pöllmann, H., Fylak, M. & Wenda, R. (2009). *Tagungsbericht 17. Internationale Baustofftagung, Weimar*, 1-0161-1-0176. Weimar: F. A. Finger-Institut für Baustoffkunde.
Prince, E. (2004). Editor. *International Tables for Crystallography*, Vol. C. Dordrecht: Kluwer.
Richardson, I. G. (1999). *Cem. Concr. Res.* **29**, 1134–1147.
Rietveld, H. M. (1969). *J. Appl. Cryst.* **2**, 65–71.
Rodgers, S. A., Groves, G. W., Clayden, N. J. & Dobson, C. M. (1988). *J. Am. Ceram. Soc.* **71**, 91–96.
Schreyer, M., Guo, L., Tjahjono, M. & Garland, M. (2011). *J. Appl. Cryst.* **44**, 17–24.
Scrivener, K. L., Füllmann, T., Gallucci, E., Walenta, G. & Bermejo, E. (2004). *Cem. Concr. Res.* **34**, 1541–1547.
Stein, H. N. & Stevels, J. M. (1964). *J. Appl. Chem.* **14**, 338–346.
Thoenen, T. & Kulik, D. (2003). Nagra/PSI Chemical Thermodynamic Database 01/01 for the *GEM-Selektor* (V.2-PSI) Geochemical Modelling Code. Villingen, Switzerland.
Thomas, J. J. (2007). *J. Am. Ceram. Soc.* **90**, 3282–3288.
Thomas, J. J., Allen, A. J. & Jennings, H. M. (2009). *J. Phys. Chem. C*, **113**, 19836–19844.
Többens, D. M., Stuesser, N., Knorr, K., Mayer, H. M. & Lampert, G. (2001). *Mater. Sci. Forum*, pp. 378–381.
Westphal, T., Füllmann, T. & Pöllmann, H. (2009). *Powder Diffr.* **21**, 239–243.

WVMP SAR Reference 3-24

"A Study of Reaction between Calcium Oxide and Water," T. C. Miller, National Lime Association report, National Lime Association (Washington, DC), 1960.

AZBE AWARD NO. 1

A STUDY OF THE REACTION BETWEEN CALCIUM OXIDE AND WATER

BY

T. C. MILLER, TECHNICAL DIRECTOR
INDUSTRIAL SALES DIVISION
NATIONAL GYPSUM COMPANY
BUFFALO, NEW YORK

(1960 Winner of the Victor J. Azbe Lime Award for the Best Technical Paper on Lime)

Published by

NATIONAL LIME ASSOCIATION

WASHINGTON 5, D. C.

FOREWORD

In 1960 Victor J. Azbe, President of the Azbe Engineering Corp., Clayton, Missouri, generously established through an irrevocable trust an annual award of $1000 for the best technical paper on lime. Mr. Azbe, who has dedicated 40 years of his life as an international lime plant engineering consultant, hopes that this award will help stimulate greater interest in research on lime.

The National Lime Association -- administrator of this annual contest -- is pleased to publish the first award paper by T. C. Miller of the National Gypsum Company, which deals with the fundamental reaction between quicklime and water. If succeeding winning papers attain the high quality of Mr. Miller's, the lime industry will be the benefactor, and Mr. Azbe's generosity will be more than justified.

The Victor J. Azbe Lime Contest covers all aspects of lime manufacturing, including limestone processing, calcination, hydration, etc.; research on lime's physical and chemical properties; and methods of tests for evaluating lime's properties and quality. Further details of this contest can be obtained from the National Lime Association.

Robert S. Boynton, General Manager
National Lime Association
Washington 5, D.C.

A STUDY OF THE REACTION BETWEEN CALCIUM OXIDE AND WATER

By T. C. Miller
National Gypsum Co.

TABLE OF CONTENTS

I Introduction 5

II Methods of Evaluation of the Physical Properties of Calcium Hydroxide 6

A Settling Time and Rate 6
B Specific Surface 7

III Methods of Hydration 8

A Dry Hydration 8

1 Conventional Dry Hydrate 10
2 Special Dry Hydrate 11

B Wet Slaking 12

IV Heat Distribution Calculations 13

A Dry Hydration. 13
B Wet Slaking. 16

V Method of Wet Slaking. 19

A Procedure 19
B Method of Testing. 20

1 Specific Surface 20
2 Settling Time 20
3 Viscosity. 21

VI Results 22

A Slaking Temperature and Slaking Time 22
B Settling Time. 25
C Specific Surface 42
D Viscosity 47

VII Conclusions 50

I - INTRODUCTION

The reaction between calcium oxide (CaO) and water (H_2O) is an interesting and complex process. A great deal of confusion has existed in the use of calcium oxide by the chemical industry when it is required that the calcium oxide be converted to calcium hydroxide with water only, and ofttimes has resulted in unexpected results because of the unusual characteristics of such a calcium hydroxide. Commercial dry calcium hydroxide also has been criticized because of the varying degree of characteristics of a product from one producer. A study has been made of the reaction between calcium oxide and water for a wide range of variation in temperature to understand more fully the results to be expected when the reaction is carried out under specified conditions, from producing a dry product to that of producing suspensions with a large excess of water.

The physical analysis of products resulting from the dry hydration of calcium oxide under a variety of conditions indicates wide variations in settling time and specific surface or mean particle diameter. A similar study of aqueous suspensions of calcium hydroxide resulting from the wet slaking of calcium oxide in an excess of water under various conditions of temperature and concentration indicate that by this process of converting calcium oxide to calcium hydroxide a wide variation of settling times and specific surfaces is being obtained. Requests for the study of the process of a large number of chemical industries indicate the need for more technical knowledge of the hydration or slaking process and the resulting products. Results compiled from the study of industrial processes indicate the need for a search for a better understanding of conditions controlling the physical properties of calcium hydroxide and for better test methods which would more clearly define these physical properties.

It has been known for many years that the physical properties of settling rate and specific surface may vary over a relatively wide range with slight variations in a hydration process but these variations have never been studied in the effort to establish laws by which these variations take place. The data from industrial processes indicated that some law may exist by which these characteristics could be controlled and maintained. This paper deals with the results of such a study in slaking calcium oxide in an excess of water to produce aqueous suspensions of calcium hydroxide. It is not the intention at this time to include the results from a study of the dry hydration process.

It has been established during recent years that the specific surface of calcium hydroxide could be changed within certain limits by a change of either the concentration or the temperature of the water used for hydrating.

It is also known that there is correlation between specific surface and settling time of calcium hydroxide, but this correlation is not always in as close agreement as would be desired.

The cause for this disagreement has been studied with the result that physical limits have been established for standardizing the hydration of calcium hydroxide to produce the most desirable product available to increase the efficiency of a chemical process.

The single important fact to come from this study is the discovery of conditions that have given a clue to certain laws governing the control of particle diameter of calcium hydroxide resulting from the reaction of calcium oxide and water.

II METHODS OF EVALUATING THE PHYSICAL PROPERTIES OF CALCIUM HYDROXIDE

A Settling Time and Rate

The lack of understanding the physical properties of dry, as well as aqueous suspensions of calcium hydroxide has been primarily the result of the limited means of test methods. Since the introduction of commercial dry calcium hydroxide powder in 1904 the only test methods have been the settling time or rate determination and the sieve test. Although in use for an indeterminate number of years, the settling test did not become a standard test method until recently (A.S.T.M. C110-58). It is certainly a reliable and reproducible method of evaluation, but two major disadvantages make it difficult to become a popular test.

First, the time required to determine the settling time or rate on many types of calcium hydroxide, especially aqueous suspensions prepared by using an excess of water resulting in a slow settling product, make the test unsatisfactory as a control test. Second, when slight changes in the hydrating or slaking procedure are permitted, these changes influence a change in the viscosity of the suspension and consequently influence the settling time or rate. This gives the impression that changes in the quality of the calcium oxide are responsible for the differences in settling time or rate. Therefore, it appears that settling time tests of aqueous suspensions may require the determination of some other characteristic or characteristics to fully define the settling rate.

A sieve test is meaningless as far as defining a physical characteristic of calcium hydroxide is concerned. This test merely indicates the maximum size particle to which the calcium oxide has been slaked or the calcium hydroxide sieved or air separated. A sieve test gives no information on the size or distribution of particles finer than the finest sieve used.

A test method which would give more positive information in a short length of time has been desirable and is even in greater demand in present-day chemical processes where more definite physical characteristics are required. A study of various test methods has been undertaken over the years and very few have shown promise of becoming accepted methods for process control. Liquid elutration methods employing water, methanol, ethanol and various other organic suspending mediums have been ruled out for the same reason that has made the settling time test so unpopular as a process-control test - - its time-consuming aspects.

Gas absorption methods are the most precise even for research work, but the cost of equipment and the high skill required for operation will undoubtedly prevent the method of being accepted as a control test.

B Specific Surface

During the past 15 years the Blaine air permeability method for specific surface has been employed as a method for studying the characteristics of calcium hydroxide. The results have been very encouraging. The method has been used throughout the present work and it is concluded that it is the most economical and rapid method for process control. The inexpensive apparatus makes it possible to provide more than one imstrument for plant control where constant control must be maintained throughout more than one department. It is encouraging to cite that several of these testing instruments have been installed by industry for process-control testing. Approximately twenty to thirty minutes are required for testing a dry calcium hydroxide and approximately one and one-half hours for testing aqueous suspensions of calcium hydroxide.

The Blaine specific surface results are not influenced by viscosity or other physical properties. It is a test for the area exposed by one gram of calcium hydroxide which can be employed to calculate the theoretical mean particle diameter. The reader is referred to National Gypsum Company's Industrial Sales Department Technical Bulletin 2 BC for details of this method.

III METHODS OF HYDRATION

A Dry Hydration

The reaction between calcium oxide and water is not a simple one from any point of view. Calcium oxide is practically insoluble in water. Theoretically, 0.131 g dissolves in 100 ml water at 0° C and 0.07 g dissolves in 100 ml water at 100° C. Calcium oxide reacts with water to form calcium hydroxide. Calcium oxide is a member of a group of chemicals which liberates a considerable quantity of heat when reacting with water. This is known as an exothermic reaction. It is a remarkable property found in but a few materials which lime producers and consumers have failed to recognize to its fullest.

The reaction between calcium oxide and water takes place according to the equation

$$\underset{56.08}{CaO} + \underset{18.016}{H_2O} = \underset{74.096}{Ca(OH)_2} \qquad 27,500 \text{ Btu/lb-mol} \quad (1)$$

That is, 56.08 pounds of calcium oxide will react with 18.016 pounds of water to produce 74.096 pounds of calcium hydroxide. Each pound of calcium oxide will produce 1.3213 pounds of calcium hydroxide by combining with 0.3213 pound of water. The calcium hydroxide produced contains theoretically 75.7% calcium oxide and 24.3% water. Calcium hydroxide also is practically insoluble in water. The solubility at 0° C is 0.185 g per 100 ml of water and at 100° C is 0.077 g per 100 ml of water.

One significant property of this reaction is the liberation of 27,500 Btu of heat for each lb-mol (56.08 lbs) of calcium oxide. An idea of this amount of heat is illustrated by the fact that it is sufficient to raise the temperature of 194 pounds of water from 70° F to 212° F (boiling). Considering that only 18.016 pounds of water are theoretically required for each lb-mol of calcium oxide, a greater amount of heat is liberated than can be utilized with this amount of water simply to heat the product to 212° F and therefore the mass will become heated above 212° F unless a larger amount of water is used.

The extent of this exothermic reaction offers an opportunity to utilize the heat in three distinct methods of hydration according to the type of calcium hydroxide desired as determined by the utilization of this heat. These methods are outlined in Figure 1. The most familiar method of hydration used by commercial lime producers is the conventional one producing a dry powder at temperatures not exceeding 214° F. A second method produces

THE PRODUCTION OF CALCIUM HYDROXIDE FROM ROTARY KILN QUICKLIME

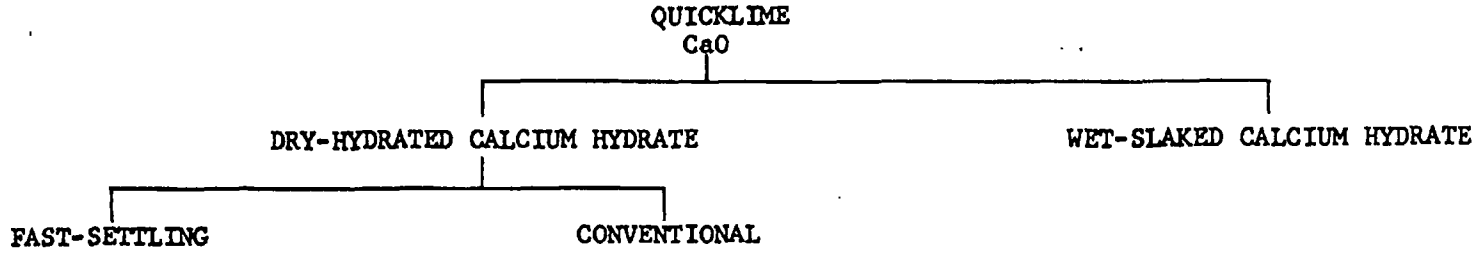

Specific Surface fairly low ranging from 13,000 cm^2/g to 17,000 cm^2/g.

Settling time -- 50 to 70 minutes.

Uses:

- Bleach manufacture
- Water Treatment
- Salt clarification
- Oil refining
- Any industry specifically requiring a fast-settling calcium hydroxide.

Specific Surface moderately high ranging from 25,000 cm^2/g to 36,000 cm^2/g.

Settling time -- 120 to 180 minutes.

Uses:

- Any chemical industry requiring a calcium hydroxide of moderate settling or where settling is no problem.

Specific Surface ranging from fairly low to high depending on slaking temperature and concentration. Range 15,000 cm^2/g to 58,000 cm^2/g with 2.5 to 25 parts water at $4^{\circ}C$ to $90^{\circ}C$.

Settling time -- 70 minutes to 1800 minutes or more. Many suspensions can be made which will not settle to one-half volume. This method of hydration has the greatest versatility.

FIG. 1

a dry product at temperatures above 212° F by taking advantage of the liberated heat to control the size of calcium hydroxide particles. The third method of hydration, known more commonly as slaking, employs an excess of water to produce an aqueous suspension of calcium hydroxide. The chemical industry employs this method of producing calcium hydroxide principally because more economical equipment can be used and a greater latitude of variation is permissible with less skill. But recent studies of this method of producing calcium hydroxide indicate that closer controls are necessary to maintain constant physical properties of the calcium hydroxide.

1. Conventional Dry Hydrate

Commercial dry calcium hydroxide is normally produced by reacting approximately one pound of calcium oxide with 0.75 to 1.0 pound of water in a continuously agitated machine or hydrator. The mixture of CaO and H_2O, in the very early stages of hydration, produces a wet or "soupy" mass just prior to the beginning of the heat reaction. This mass reaches the temperature of boiling water within a few minutes when the excess water begins to be evaporated. The temperature cannot exceed the boiling point of water (212° F) at atmospheric pressure as long as liquid water (not water vapor alone) is present. The process is regulated with sufficient water to be assured that liquid water is present until the hydration reaction is practically complete. Then the last trace of liquid water is evaporated to produce a finely divided dry powder practically free of excess moisture.

The degree of burning a limestone to produce a quicklime influences to a great extent the type of calcium hydroxide which can be produced. A soft-burned quicklime reacts very readily with water as indicated by the temperature rise test involving a small amount of lime in a comparatively large amount of water. On the other hand, an overburned lime reacts much slower with water to give a low temperature rise by this test. Rotary kiln or other similar quicklimes generally have a high temperature rise which indicates a soft burned product capable of producing a finely-divided calcium hydroxide. Shaft kiln quicklimes generally have a low temperature rise indicating their inability of producing as finely divided calcium hydroxide as rotary kiln quicklime. Both types of dry calcium hydroxide may have the same percentage passing a 325 mesh sieve, which might indicate equal quality as far as fineness is concerned, but this is not true. The real difference in the products is the size of the particles or distribution of sizes smaller than 325 mesh. Two evaluations may be used to denote this difference. One of these is the settling rate of a ten per cent suspension to one-half volume in a 100 ml graduated cylinder. Calcium hydroxide containing particles of large diameter will settle at a faster rate than a calcium hydroxide containing particles of small diameter.

Another method of evaluation is the determination of the specific surface or the mean particle diameter. This may be determined with the Blaine air permeability apparatus.

The difference between shaft kiln and rotary kiln quicklimes is illustrated by the results of Table I.

TABLE I

Settling Time, Specific Surface and Mean Particle Diameter of Calcium Hydroxides from Shaft Kiln and Rotary Kiln Quicklimes

Lime	Settling Time to 1/2 Volume Minutes	Specific Surface cm^2/g	Mean Diameter u
Shaft Kiln "A"	50	14,451	1.8
Shaft Kiln "B"	40	13,624	2.0
Rotary Kiln "A"	133	30,238	0.9
Rotary Kiln "B"	150	29,379	0.9

A great many chemical processes were established on calcium hydroxide produced from shaft kiln quicklime before the widespread production of rotary kiln quicklime. These industries may be able to use a hydrated lime produced from a rotary kiln quicklime, but most generally it means the investment in additional equipment or an alteration in the process to compensate for the differences in physical properties. A great many industries can use this finer product without disadvantage. Also, a great many industries can and do use a much finer calcium hydroxide than is obtainable commercially in a dry form from either shaft kiln or rotary kiln quicklimes. These industries must produce their calcium hydroxide from quicklime slaked in an excess of water.

2. Special Dry Hydrate

A study of the dry hydration of calcium oxide at temperatures greater than 212° F indicated that the diameter of the particles could be increased as denoted by a decrease in specific surface or an increase in mean particle diameter.

A decrease in specific surface or increase in mean particle diameter decreases the settling time of the dry product. This increase of particle diameter is proportional to the increase in temperature of hydration above 212° F. The increase in temperature of hydration is accomplished by regulating amount and rate of water addition to produce a high temperature that will maintain all the water as liquid and vapor, or vapor alone at atmospheric pressure until hydration is complete. This method of hydration can be used to reduce the settling time of dry calcium hydroxide to approximately one-third that of commercial dry rotary kiln calcium hydroxide produced by conventional methods and is comparable to calcium hydroxide produced from shaft kiln calcium hydroxide.

The reaction of calcium oxide in an excess of water, which we choose to call wet slaking, offers a great magnitude of variation of particle diameter control by a single method. Because the chemical industry uses this method exclusively in processing calcium oxide it offers great opportunity to standardize calcium hydroxide suspensions with constant physical properties.

B Wet Slaking

It is indeed interesting that the exothermic reaction of calcium oxide and water offers such control of particle diameter by slaking the calcium oxide in an excess of water. When a particle of soft burned calcium oxide is dropped in water, the lime immediately absorbs the water into the interstices left by the escaping carbon dioxide during the calcination process, and wets every part of the particle. Hydration begins immediately. When the lime is over-burned or when shaft kiln calcium oxide is used, the reaction rate is considerably slower. If the particle of calcium oxide is considered to be made up of many smaller particles, these very small particles will disintegrate during the hydration to produce even smaller particles of calcium hydroxide. The rate of reaction or the degree of hydration should then offer some means of controlling the size of the resulting calcium hydroxide particles. The process involving only sufficient water to produce a dry calcium hydroxide has been known as hydration, while the reaction utilizing an excess of water has been known as slaking. The two chemical reactions are identical as far as producing a calcium hydroxide is concerned, the only difference being that hydrating produces a dry product and slaking is spoken of as producing a suspension.

Realizing that the liberation of 27, 500 Btu of heat per lb-mol of calcium oxide could have considerable influence on the development of the particle diameter of calcium hydroxide, the reactions were carried out not only with water at various temperatures from 4° C (39° F) to 90° C (194° F), but also at concentrations from 2.5 pounds of water per pound of calcium oxide to 25 pounds of water per pound of calcium oxide. This range in temperature would give us all practical values between the freezing and boiling points of water. The range of concentration would likewise be from the most concentrated suspension to a diluted suspension which would be feasible in any chemical process.

IV HEAT DISTRIBUTION CALCULATIONS

The liberation of a large amount of heat from the reaction between calcium oxide and water makes it desirable to study the effect of this heat on the hydrating mass. It is desirable to determine the distribution of heat in dry hydrating as well as wet slaking to better understand the possibilities of particle size control. The amount of heat developed and its distribution or dissipation controls the particle size and the particle size distribution of a calcium hydroxide and these calculations may be helpful in better understanding its effect.

A Dry Hydration

1 Conventional Dry Hydrates

Nearly every lime producer operates a hydrating plant for the production of a dry commercial calcium hydroxide. These plants are normally operated by the conventional process of adding sufficient water to convert the calcium oxide to calcium hydroxide at temperatures not exceeding 214° F (elevation of the boiling point of water by about 2° F by the presence of the solid calcium hydroxide).

Theoretical calculations for the use of 0.75 pound water per pound of calcium oxide, without heat loss from radiation, are shown in Table II. These calculations show that theoretically 94.3% of the water is used for hydrating and dissipating the heat, leaving 5.7% in the finished product. This amount of water constitutes 3.14% of the finished product.

This calculation is not exactly true, because no corrections were made for radiation losses. Neither were allowances made for the amount of recovered water from escaping steam normally captured by one of the sprays in the system. The efficiency of the hydrating machine or the amount of heat losses will determine whether this amount of water is sufficient to completely convert the calcium oxide to calcium hydroxide. Practical operation of the process in a hydrator with low radiation losses produces a finished product with 0.5% or less free moisture.

2 Special Dry Hydration

It has been found that the development of higher temperatures in the production of a dry calcium hydroxide has a desirable effect on increasing the particle size. Calculations illustrating the temperatures possible by this process have been made.

Theoretical calculations for the operation of such a process above 212° F are shown in Table III. When 0.40 pound water per pound calcium oxide

(Con't - pg. 16)

TABLE II

Basis: Normal Hydration

56 lbs. CaO (1 lb-mol)
42 lbs. H_2O (0.75 lbs. H_2O per lb. CaO)

42 lbs. H_2O added to CaO at one time.
56 lbs. CaO will require the following amount of H_2O for theoretical hydration:

CaO	+	H_2O	=	$Ca(OH)_2$
56		18		74

Therefore 18 lbs. of water will be used for converting CaO to $Ca(OH)_2$
Excess H_2O will be 42 - 18 = 24 lbs.

Total heat evolved in combining 56 lbs. CaO + 18 lbs. H_2O = 27,500 Btu

Amount of heat required to raise the temperature of 24 lbs. H_2O from
70° F to 214° F = (24) (144) = 3452 Btu

Amount of heat required to raise the temperature of 74 lbs. $Ca(OH)_2$ from
70° F to 214° F = (74) (0.29) (144) = 3089 Btu

Therefore, the heat required to heat both $Ca(OH)_2$ and H_2O from
70° F to 212° F = 3452 + 3089 = 6541 Btu

Remaining Btu's available for heating 24 lbs. excess H_2O above 214° F is
27,500 Btu - 6451 Btu = 20,959 Btu

Quantity of water which can be evaporated at 212° F with this quantity of heat will be:

$$\frac{20,959}{970} = 21.6 \text{ lbs.}$$

Water as liquid at 212° F remaining in 74 lbs. $Ca(OH)_2$ will be
24.0 - 21.6 = 2.4 lbs. or

The composition of the finished product will be, therefore 74.0 lbs.
$Ca(OH)_2$ + 2.3 lbs. excess water or a total weight of 76.3 lbs.

Water	2.4 lbs.	3.14%
$Ca(OH)_2$	74.0 lbs.	96.86%
Total	76.5 lbs.	100.00%

TABLE III

Basis: Special Hydration for size control

56 lbs. (1 lb-mol)
22.4 lbs. (0.40 lbs. H_2O per lb. CaO)

22.4 lbs. H_2O added under controlled conditions
56 lbs. CaO will require the following amount of H_2O for theoretical hydration

CaO	+	H_2O	=	$Ca(OH)_2$
56		18		74

Therefore, 18 lbs. of H_2O will be used in converting CaO to $Ca(OH)_2$
Excess H_2O will be 22.4 - 18 = 4.4 lbs. H_2O per 56 lbs. CaO

Total heat evolved in combining 56 lbs. CaO + 18 lbs. H_2O = 27,500 Btu

Amount of heat required to raise the temperature of 4.4 lbs. H_2O from
70° F to 212° F = (4.4) (142) = 625 Btu

Amount of heat required to raise the temperature of 74 lbs. $Ca(OH)_2$ from
70° F to 212° F = (74) (0.29) (142) = 3057 Btu

Therefore, the heat required to heat both $Ca(OH)_2$ and H_2O from
70° F to 212° F = 625 Btu + 3057 Btu = 3682 Btu

Remaining Btu's available for heating 4.4 lbs. excess H_2O above 212° F is
27,500 Btu - 3682 Btu = 23,818 Btu

Quantity of water which can be evaporated at 212° F with this quantity of heat will be:

$$\frac{23,818}{970} = 24.6 \text{ lbs.}$$

Since there is less water than this in the mass, a different method calculation must be made. The amount of heat necessary to evaporate 4.4 lbs. of H_2O at 212° F is:

(4.4) (970) = 4268 Btu

Excess heat still available is 23,818 - 4268 = 19,550 Btu
Heat required for 74 lbs. $Ca(OH)_2$ from 212° F to 575° F will be
(74) (0.29) (363) = 7790 Btu

Heat available for heating water vapor only = 19,550 - 7790 = 11,760
Temperature attainable = (4.4) (0.48) (x - 212) = 15,516

$$\text{or } x = \frac{12,207}{2.11} = 578^\circ \text{ F}$$

is used and added at such a rate that evaporation is maintained throughout the process to provide vapor for hydration, it is shown that theoretically temperatures of 578° F can be maintained.

Greater quantities of water, to a maximum of 0.75 pound water per pound calcium oxide, will decrease the final temperatures to that for conventional hydration as shown in Table II. A decrease in final temperature results in a decrease in mean particle diameter or an increase in specific surface. An increase in specific surface is accompanied by an increase in settling time of the calcium hydroxide.

B WET SLAKING

The theoretical temperatures expected from the reaction of calcium oxide and water were calculated for water temperatures from 4°C (39° F) to 90° C (194° F) and for water-to-calcium oxide ratios from 2.5 pounds to 25 pounds. The calculations are based upon a constant weight to give 0.503 pound pure calcium oxide. Water ratios of 2.5, 7.5, 10.5, 13.5, 18.5 and 25 corresponding to excess weight of water of 1.16, 3.81, 5.39, 6.98, 9.36 and 13.06 pounds respectively were used.

Calcium oxide in the amount of 0.503 pound will produce 0.665 pound calcium hydroxide. The theoretical heat evolved by 0.503 pound calcium oxide during hydration is 246.9 Btu.

The amount of heat required to raise the temperature of water to any temperature up to and including 212°F (boiling), where

H = the heat in Btu
W = the weight of water
h = the heat capacity of water = 1
T_1 = the initial temperature of the water, and
T_2 = the final temperature of water

is calculated from the equation

$$H = (W)(h)(T_2 - T_1) \text{ or } (W)(T_2 - T_1) \qquad (2)$$

The amount of heat required to raise the temperature of calcium hydroxide where

H' = the heat in Btu
W' = the weight of calcium hydroxide
h' = the heat capacity of calcium hydroxide = 0.29
T'_1 = the initial temperature
T'_2 = the final temperature

is calculated from the equation

$$H' = (W')(h')(T'_2 - T'_1) \text{ or } (W')(0.29)(T'_2 - T'_1) \quad (3)$$

When a constant weight of 0.503 pound calcium oxide is used with a value for H of 246.9 Btu and a weight for calcium hydroxide of 0.665 pound the equations become

$$246.9 = (W)(T_2 - T_1) \quad (4)$$

and

$$H = (0.665)(0.29)(T'_2 - T'_1) = (0.193)(T'_2 - T'_1) \quad (5)$$

respectively.

The total heat derived from the hydration reaction is the distribution of the evolved heat from the calcium oxide between the water and the calcium hydroxide to the same temperature. It is the sum of the heat required to raise the temperature of the water and the heat required to raise the temperature of the calcium hydroxide to the same temperature.

The combined equation then becomes Equations (4) + (5) or

$$H = W(T_2 - T_1) + W'h'(T'_2 - T'_1) \quad (6)$$

or

$$H = (W)(T_2 - T_1) + 0.193(T'_2 - T'_1) \quad (7)$$

The final temperature of hydration can be calculated from this equation by solving for T_2 since H = 246.9 Btu. The equation then becomes

$$T_2 = \frac{H + (0.193 + W)\,T_1}{0.193 + W} \quad (8)$$

When it becomes desirable to calculate the temperature necessary to start a reaction with a given weight of calcium oxide to theoretically result in a final temperature of 212° F the equation becomes

$$T_1 = \frac{(0.193 + W)\,T_2 - 246.9}{0.193 + W} \quad (9)$$

The theoretical final temperatures expected from the same weight of pure calcium oxide (0.503 lb.) with various ratios of water at several temperatures as calculated by equation (7) are shown in Table IV.

TABLE IV

(following page)

TABLE IV

Theoretical Slaking Temperature (^{o}F) of calcium oxide with water at various temperatures and proportions.

Ratio H_2O/CaO	Excess H_2O lbs.	Temperatures of Slaking Water 4°C 39°F	10°C 50°F	20°C 68°F	40°C 104°F	60°C 140°F	90°C 194°F
2.5	1.16	221.4	232.5	250.3	286.3	322.5	376.4
7.5	3.81	100.7	111.8	129.7	165.7	201.7	255.7
10.5	5.39	83.2	94.2	112.2	148.2	184.2	238.2
13.5	6.98	73.4	84.4	102.4	138.4	174.4	228.3
18.0	9.36	64.8	75.9	93.9	129.8	165.7	210.7
25.0	13.06	57.6	68.6	86.6	122.6	158.6	212.6

Temperatures in excess of 212°F are shown above and to the right of a dotted line, indicating that insufficient water is present to absorb the liberated heat and therefore part of the water will be evaporated during the slaking cycle. Temperatures of calcium hydroxide suspensions less than boiling (212°F) can be expected from the reacting between calcium oxide and water for ratios greater than 7.5 and for all temperatures from 39°F (4°C) to 140°F (60°C).

The initial temperature of water for the reaction of all ratios of water to calcium oxide to give a final temperature of 212°F were calculated by equation (8). These initial temperatures are shown in Table V.

TABLE V

THEORETICAL INITIAL TEMPERATURE (T_1) (°F) OF SLAKING WATER TO GIVE A FINAL SLAKING TEMPERATURE (T_2) OF 212° F.

Ratio H_2O/CaO	Excess Water Lbs.	T_1 °F	T_1 °C	T_1 corrected for °F radiation loss	T_1 corrected for °C
2.5	1.16	29.6	-1.4	54.6	12.6
7.5	3.81	150.3	65.6	166.8	74.9
10.5	5.39	167.7	75.4	180.1	82.3
13.5	6.98	177.5	80.8	185.8	85.4
18.0	9.36	186.1	85.6	196.5	91.4
25.0	13.06	193.4	89.6	205.0	96.0

All of these calculations have been made to illustrate the wide temperature variations expected in using a variation of ratios and temperatures of water to effect the development of particle diameters of calcium hydroxide in aqueous suspension and to compare the theoretical values with the actual values. It should be emphasized that the degree of rotary kiln calcination of a limestone may affect the rate of slaking and therefore all calcium oxides may not reach these expected temperatures. Only soft-burned calcium oxide will check the values.

V METHOD OF WET SLAKING

A very reactive rotary kiln pebble calcium oxide was used for this study. The reactivity was measured by testing the temperature of 180 grams of the pebble calcium oxide in 900 ml of water at 24° C in an insulated stainless steel beaker. The temperature rise in 30 seconds was 33° C. The quality of the calcium oxide was determined by the sugar method for calcium oxide. If was found to contain 95% calcium oxide.

A Procedure

The procedure for preparing suspensions of calcium hydroxide employed 240 g of pebble calcium oxide for each sample. The amount of water for the preparation of the suspensions ranged from a ratio (R) of 2.5 to 25 times the weight of calcium oxide. A tabulation of the weight of calcium oxide and the volume of water are shown in Table VI.

TABLE VI

Weight of CaO and Volume of H_2O used for Preparing $Ca(OH)_2$ Suspensions

R	Rotary Kiln Pebble CaO	Total Water	Excess Water	
	g	ml	g	lbs.
2.5	240	600	527	1.16
7.5	240	1800	1727	3.81
10.5	240	2500	2447	5.39
13.5	240	3240	3167	6.98
18.0	240	4320	4247	9.36
25.0	240	6000	5927	13.06

The water for each slaking test was heated to the required temperature. The weighed amount of rotary kiln pebble calcium oxide was added to the water at one time. The mixture was mechanically stirred and the reaction temperature measured with a thermometer calibrated to 0.1°C. Agitation was continued until the temperature reached a maximum and began to recede.

The proper agitation of a mixture of calcium oxide and water during the hydration cycle is of the utmost importance. Agitation must be provided to prevent local overheating of the calcium oxide, especially in large quantities of water, and to assure that each particle of lime is supplied constantly with a fresh supply of necessary water to carry out the entire hydration reaction. The most satisfactory method of agitation was found to be supplied by a stirrer having two arms perpendicular to each other and of sufficient length to extend almost to the periphery of the reaction vessel. The agitator speed was controlled during the hydration cycle to provide maximum agitation without overflowing the vessel.

The suspensions of very high solids concentration were very difficult to agitate to a homogeneous mass. The evaporation of water was so rapid that it was difficult to prevent local drying before the temperature decreased below the boiling point. This condition may introduce errors of accurate temperature determination of the slaking reaction.

B Method of Testing

1. Specific Surface

A sample of each suspension was taken immediately after hydration was complete for a specific surface determination. Approximately 100 - 250 ml of the suspension were filtered on a 3-inch Buechner funnel under vacuum, washed with five portions of alcohol to remove the water and then washed with five portions of ether to remove most of the alcohol. The evacuated sample was then dried under infra-red heat until all of the ether and most of the alcohol had been evaporated. The sample was finally dried for approximately 30 minutes in an oven at 105 to 110°C.

A weight of 1.30 g of dried powder was used for determining the specific surface of each sample.

2. Settling Time

Each suspension was then stored in a 1/2 gallon sealed mason jar to allow cooling to room temperature. Then each well mixed suspension was analyzed by the sugar method to determine the concentration of calcium hydroxide in grams per liter. The suspension was then diluted with water or decanted of clear supernatant liquid to give 100 grams per liter of calcium hydroxide and rechecked by the sugar method. This concentration is equivalent to 10 grams of dry calcium hydroxide in 100 ml of suspension for the settling time test. Settling rate was then determined on 100 ml each of suspension by noting the time-rate required to settle to 50 ml (1/2 volume) for those samples which would settle to this point, or to determine the minimum volume each suspension of calcium hydroxide would assume when

no settling value could be obtained. The latter condition existed for those samples having a high specific surface, indicating a bulkiness for the extremely fine particles.

3. Viscosity

It is known that the viscosity of calcium hydroxide suspensions can be increased by dispersing the particles more completely in the liquid vehicle. It is also known that the increase in viscosity in a given suspension is accompanied by an increase in specific surface when there is no change in the water ratio of the suspension. The increase in specific surface increases the settling time of the particles in the suspension. The degree of dispersion of particles during wet slaking is proportional to the degree of calcination of the limestone and the temperature and ratio of the slaking water.

It is not the intention to go into details of the viscosity of calcium hydroxide suspensions in this report, but to briefly touch on the subject to show that some relation exists between the quality of the calcium oxide, the method of slaking and the characteristics of the resulting calcium hydroxide.

All types of calcium oxide will not produce aqueous suspensions of calcium hydroxide of equal viscosity at the same concentration by the same procedure of slaking. For example, one type of calcium oxide slaked in six parts water at 20° C (68° F) and stirred for five minutes produces a calcium hydroxide suspension with a viscosity of 46 centipoises while another type of calcium oxide slaked under exactly the same conditions of stirring and water temperature and ratio produced an aqueous suspension of calcium hydroxide with a viscosity of 273 centipoises. These same calcium oxides slaked in exactly the same manner but using water at a temperature of 60°C (140°F) produced suspensions of calcium hydroxide having viscosities of 716 centipoises and 395 centipoises respectively. Further agitation of these suspensions produced some surprising results. The suspensions produced with slaking water at 20°C and stirred for twenty-five minutes after slaking was complete yielded viscosities of 200 centipoises and 288 centipoises respectively. The suspensions produced with slaking water at 60°C and stirred for twenty-five minutes after slaking was complete had viscosities of 3875 centipoises and 390 centipoises respectively.

Far too little study has been made on the viscosity of calcium hydroxide suspensions from various types of calcium oxide to understand the mechanics of viscosity control. The viscosity of suspensions produced for this report was determined for various concentrations. The determinations were made with a standard Brookfield viscometer.

VI RESULTS

A Slaking Temperatures and Slaking Time

The slaking temperatures of samples for all concentrations and initial water temperatures are shown in Table VII.

TABLE VII

Maximum Slaking Temperatures of CaO with Various Amounts of Water at Various Temperatures

R	Initial Water Temperature											
	°C	4		10		20		40		60		90
	°F	39		50		68		104		140		194
		°C	°F	°C	°F	°C	°F	°C	°F	°C	°F	°C	°F
2.5		85	185	90	194	100	212	100	212	100	212	100	212
7.5		32.2	90	36.5	98.7	43.6	110.5	63	145.4	82	179.6	100	212
10.5		24.6	76.3	29	84.2	38	100.4	58	136.4	77	170.6	100	212
13.5		21.2	70.2	25.5	77.9	34.8	94.7	54	129.2	69	156.2	100	212
18.0		16.0	60.8	21.6	70.9	30.6	87.1	50	122.0	69	156.2	100	212
25.0		12.2	52	19.0	66.2	27.8	82.0	48	118.4	65	149.0	100	212

These values are also shown graphically in Figure 2.

Temperatures less than 100°C (212°F) are shown to the left and below a dotted line.

A comparison of these actual slaking temperatures with the theoretical expected temperatures indicated quite a variation. The percentage differences between these two values, based upon the theoretical, are shown in Table VII-A. No values are shown for tests with R at 2.5 or a temperature of 194°F.

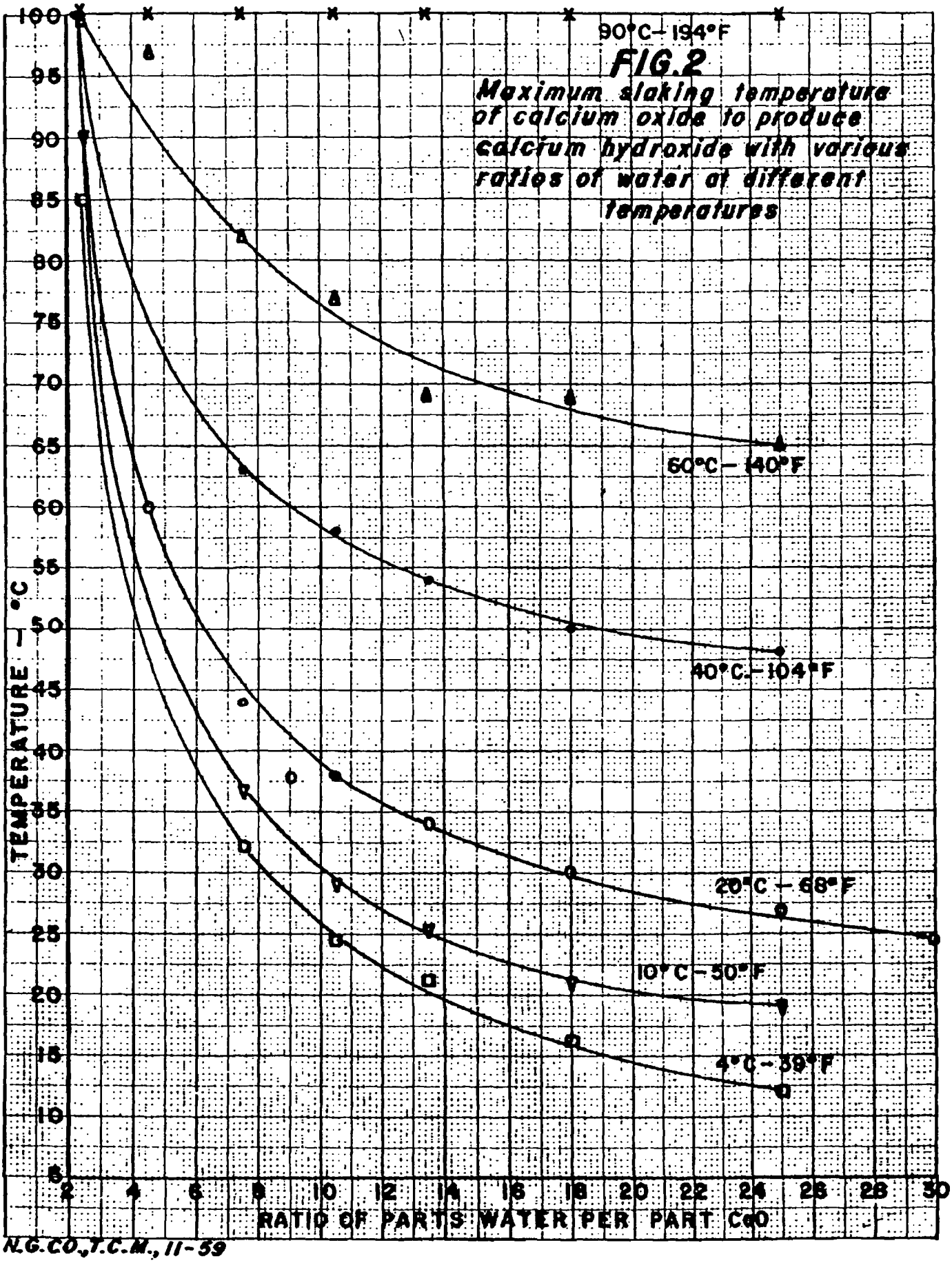

FIG. 2

Maximum slaking temperature of calcium oxide to produce calcium hydroxide with various ratios of water at different temperatures

N.G.CO.,T.C.M., 11-59

TABLE VII-A

Percentage Difference between Theoretical and Actual Slaking Temperature

	Initial Water Temperature °F				
R	39	50	68	104	140
7.5	10.6	11.7	14.8	12.3	11.0
10.5	8.3	10.6	10.5	7.97	7.4
13.5	5.5	7.7	7.5	6.6	4.7
18.0	6.2	6.6	7.2	6.0	5.7
25.0	9.7	3.5	5.3	3.4	6.0

No correction was made in the theoretical calculations for heat loss in the steel container or for the radiation loss. A correction for heat loss in the steel slaking vessel would have been constant to give a uniform lower percentage difference between the theoretical and actual results. Radiation losses would be expected to be greatest at the higher temperatures which would result in a greater temperature difference. This, however, is not exactly true. Greatest losses were found to be at the lower values of R. The initial temperature of the slaking water appears to have little influence in increasing these losses. For example, at initial temperature of 60°C (140°F) the final slaking temperature was approximately 150°F or greater with percentage difference between theoretical and actual less than many other tests at lower initial water temperature. There is a general trend for lower percentage differences between theoretical and actual slaking temperatures with an increase in the value of R.

All rotary kiln calcium oxides will not produce slaking temperatures corresponding exactly to these values. The activity or slaking rate of the calcium oxide (V-1, p. 19) and the viscosity of the calcium hydroxide suspension will affect the final slaking temperature. Regardless of the activity of the calcium oxide the slaking temperature will be proportionate to the values shown as changes in R and water temperature are made. These data indicate anticipated temperatures to be expected for changes in R and T_1.

The time for the reaction between calcium oxide and water to be completed is dependent upon both the solids concentration and the initial temperature of the water. An increase in the ratio of water at a given temperature increases the slaking time, but an increase in the initial water temperature at a given concentration decreases the slaking time.

The approximate slaking time for each sample prepared is shown in Table VIII. The values give the slaking time to the nearest minute for the temperature to reach a maximum.

TABLE VIII

Slaking Time (Minutes) of CaO with Various Amounts of Water at Various Temperatures

		Initial Water Temperature					
	°C	4	10	20	40	60	90
R	°F	39	50	68	104	140	194
2.5		4	3	6	1	2	1
7.5		8	16	7	3	2	1
10.5		18	20	7	4	2	1
13.5		13	23	8	4	2	1
18.0		14	20	7	4	2	1
25.0		18	12	8	4	2	1

These values are shown graphically in Figure 3.

B Settling Time

The settling rate of each suspension, adjusted to 100 gpl $Ca(OH)_2$, prepared at all concentrations and at temperatures of 4°, 10°, 20°, 40°, 60° and 90°C are shown in Tables IX, X, XI, XII, XIII and XIV respectively. The data is also shown graphically in Figures 4, 5, 6, 7, 8 and 9. A summary of the settling time to one-half volume (50 ml) for each sample is shown in Table XV and graphically in Figure 10. The volume occupied by the settled calcium hydroxide after 24 hours for each suspension is shown in Table XVI and shown graphically in Figure 11.

The settling time of a series of calcium hydroxide suspensions prepared with water of the same initial starting temperature increases as the ratio of water decreases for final temperatures less than 212°F. For example, using water at 4°C (39°F), the settling time is 80 minutes when the ratio is 25 pounds of water per pound of CaO and 480 minutes when the ratio of water has been decreased to 7.5 pounds water per pound CaO. Also, using water with an initial temperature of 60°C (140°F) the settling time is 835 minutes when the ratio is 25 pounds water per pound calcium oxide and 1800 minutes when the ratio is decreased to 7.5 pounds water per pound calcium oxide.

FIG. 3

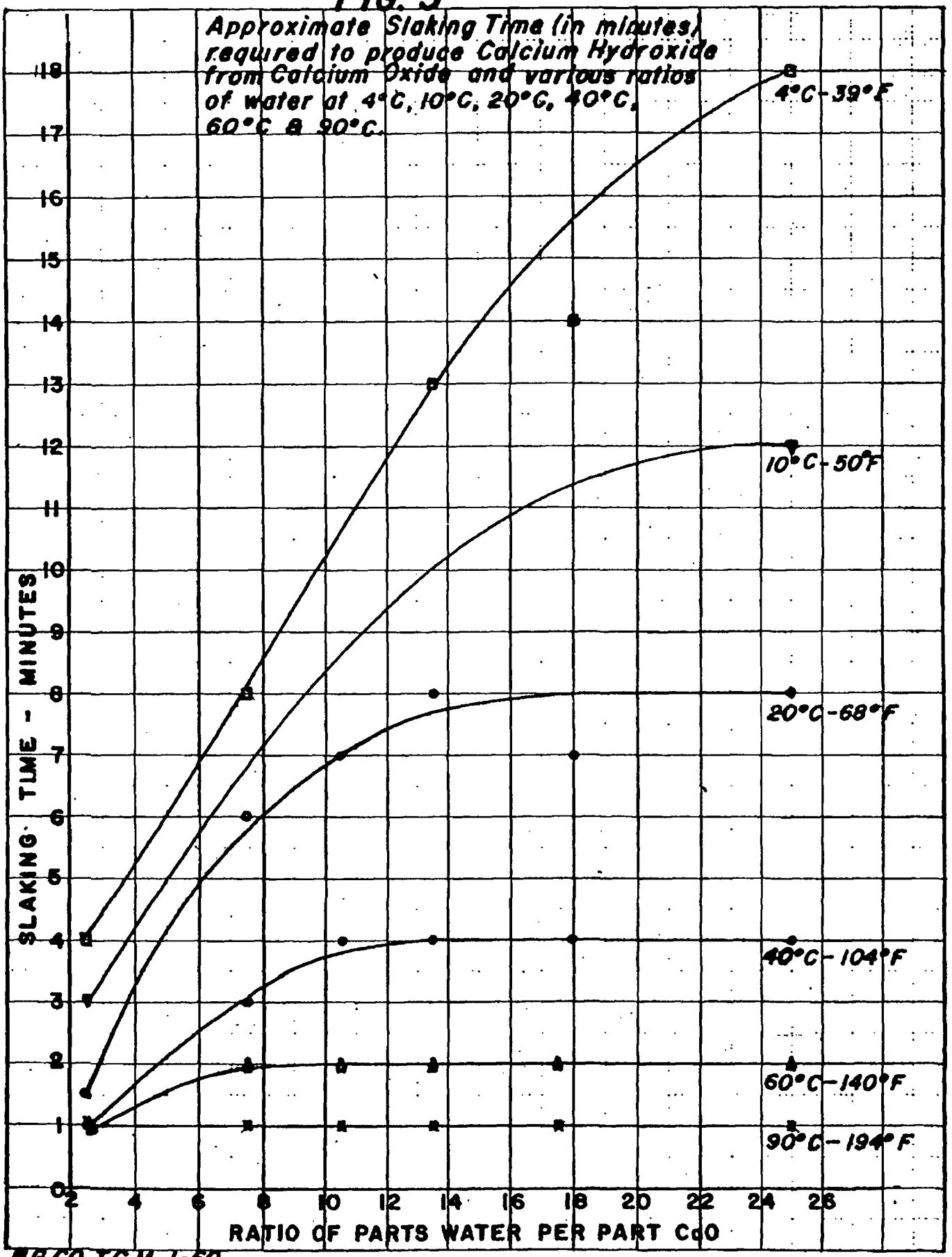

N.G.CO., T.C.M., 1-60

TABLE IX

SETTLING RATES OF HYDRATES

Temp. °C		4	4	4	4	4	4
°F		39	39	39	39	39	39
R		2.5	7.5	10.5	13.5	18	25
Min.	(hr.)						
0		0	0	0	0	0	0
5		1	1.5	1.5	1.5	3	1.5
10		2	2.5	4.0	5	5.5	7.5
15		2.5	4.5	7.0	9	8.5	14.5
20		3	6.5	10.5	13.0	11	22.5
25		3.5	9.5	15.0	18.5	14	32.0
30		4	11.5	18.0	22.5	16	37.0
35		5	13.5	21.5	26.5	18.5	40.0
40		6	16.5	25.5	32.5	21	42.0
45		7	18.5	30.5	37.0	23.5	43.0
50		9	21.0	34.0	39.0	26	44.5
55		11	24.5	36.0	41.0	28.5	45.5
60	(1)	13	28.5	37.0	42.0	31	46.5
70		15	31.5	39.0	44.0	37.5	48.5
80		-	33.5	40.5	45.0	-	50.0
90		18	35.0	42.0	46.5	46.5	51.0
100		-	36	43.0	47.5	-	52.0
110		20.0	37	43.5	48.5	49.0	53
120	(2)	20.5	38	44.5	49.0	50.0	54
135		21.5	39	45.5	50.0	51	55
150		22.5	40	46.5	51.0	52	56
165		23.5	41	47.5	52	53	57
180	(3)	24.0	41.75	48.25	52.75	54	58
195		25.0	42.5	49.0	53.5	55	58.5
210		-	43.25	49.75	54.0	-	59
225		27.0	43.75	50.00	54.75	57	59.75
240	(4)	-	44.25	50.5	55	-	60
270		28.0	45.5	52	56.5	57.5	61.5
300	(5)	29.0	46	52.75	57	58.5	62
330		30	47.0	53.5	58	59	62.5
360	(6)	31	48.0	54.25	58.75	59.5	63
390		31.5	48.5	55.0	59.25	59.75	63.5
420	(7)	32.25	49.25	55.5	59.75	60	64.0
480	(8)	33.5	50.0	56.0	60	60	64.0
540		-	50.5	56.5	60.5	-	64.5
1440	(24)	44	57	61	63.4	61	66

TABLE X

SETTLING RATES OF HYDRATES

Temp.° C		10	10	10	10	10	10
° F		50	50	50	50	50	50
R		2.5	7.5	10.5	13.5	18	25
Min.	(hr)						
0		0	0	0	0	0	0
5		0.5	1	1	0.5	1	1.5
10		1.5	3	3.5	2.5	3	8.5
15		2.5	4.5	5.5	5.0	6	15.0
20		4	7.0	8.5	8.0	10.5	21.5
25		6	10.0	12.0	12.0	15.5	30.0
30		8	12.0	14.0	14.5	20	37.0
35		9	14.0	17.0	17.5	25.5	41.5
40		10	16.0	19.5	20.5	32	43.5
45		11	19.0	23.0	24.0	37	45.0
50		12.5	22.0	26.0	27.0	39	46.0
55		13.5	25.0	30.0	32.0	40.5	47.5
60	(1)	14.25	29.5	34.5	36.5	41.5	48.5
70		15.5	33.0	38.0	40.0	43.75	50.0
80		16.5	35.0	40.0	42.0	45	51.0
90		17.5	36.5	41.5	44.0	46.5	52.5
100		-	37.5	43.0	45.0	-	53.0
110		19.5	38.5	43.5	46.0	48.5	54.0
120	(2)	20	39.5	44.5	47.0	49.5	55.0
135		21	40.5	45.5	48.0	50.75	56.0
150		22	41.5	46.5	49.0	51.75	56.75
165		23	42.5	47.5	50.0	52.75	57.5
180	(3)	23.75	43.25	48.5	51.0	53.5	58.25
195		24.5	44.0	49.0	51.75	54.25	59
210		25/	45.0	50.0	52.50	55	59.5
225		-	45.25	50.5	53.0	-	60.0
240	(4)	26.5	46.0	51.0	53.75	56	60.5
270		-	47.25	52.5	55	-	61.5
300	(5)	28.5	48.0	53.25	56	-	62
330		-	49.0	54.25	57	-	62.75
360	(6)	-	49.75	55.0	57.5	-	63.25
390		-	50.5	56.0	58.5	-	63.75
420	(7)	-	51/	56.5	59.0	-	64.0
480	(8)	-	51.75	57.0	59.5	-	64.25
540		-	52.5	57.75	60.0	-	64.5
1440	(24)	43	58	61.5	63	60	66

TABLE XI

SETTLING RATES OF HYDRATES

Temp. ° C		20	20	20	20	20	20
° F		68	68	68	68	68	68
R		2.5	7.5	10.5	13.5	18	25
Min.	(hr)						
0		0	0	0	0	0	0
5		0.5	1.0	1.0	2.0	2.0	2.0
10		1.0	2.5	2.5	4.5	4.5	6.0
15		1.5	4.5	4.0	7.0	8.0	10.5
20		2.0	7.0	6.0	10.0	12.0	15.0
25		2.75	9.0	8.0	13.0	15.5	19.5
30		3.25	11.0	10.0	15.5	19.0	24.0
35		3.75	13.5	12.25	18.75	23.0	28.5
40		4.25	15.5	14.5	21.75	26.75	34.0
45		4.75	17.5	16.0	24.0	30.0	39
50		5.0	20.0	18.5	27.5	34.5	42.5
55		5.5	23.0	21.25	31.0	39.5	44.5
60	(1)	6.0	25.75	24.5	35.0	42.5	45.75
70		6.75	31.5	31.0	42.0	44.75	47.5
80		7.5	37.5	34.5	43.0	46.5	49.0
90		8.0	39.5	36.5	45.5	47.75	50.0
100		8.75	41.0	38.0	46.75	49.0	51.5
110		9.0	42.0	39.0	47.5	50.0	52
120	(2)	10.0	43.0	40.0	48.5	50.5	53.0
135		10.5	44.5	41.0	49.75	51.75	54.0
150		11.25	45.5	42.0	50.75	52.5	55.0
165		12.00	46.5	43.0	51.75	53.25	56.0
180	(3)	12.75	47.5	44.0	52.5	54.0	57.0
195		13.5	48.0	45.0	53.5	55.0	57.5
210		13.75	48.5	45.0	54.0	55.5	58.0
225		14.5	49.5	46.0	54.5	56.0	58.5
240	(4)	15.0	49.75	46.5	55.0	56.5	59.0
270		16.0	51.0	47.5	56.0	57.75	60.0
300	(5)	17.0	52.0	48.75	57.0	58.75	61.0
330		18.0	53.0	49.75	58.5	59.75	62.0
360	(6)	18.75	54.0	50.5	59.0	60.0	62.5
390		19.5	54.75	51.0	59.5	61.0	63.0
420	(7)	20.5	55.5	52.0	60.25	61.5	63.25
480	(8)	22.0	56.5	53.0	61.0	62.50	64.0
540		23.0	57.5	54.0	62.0	63.0	64.5
600	(10)	24.5	58.5	55.0	62.5	63.5	65.0
660		26.0	59.0	55.75	63.0	64.0	65.0
960	(16)	31.75	60.75	58.5	64.0	65.0	65.75
1200	(20)	34.25	61.25	59.0	64.25	65.0	65.75
1440	(24)	37	61.5	59.0	64.25	65.0	66.0

TABLE XII

SETTLING RATES OF HYDRATES

Temp. ° C	40	40	40	40	40	40
° F	104	104	104	104	104	104
R	2.5	7.5	10.5	13.5	18	25
Min. (hr)						
0	0	0	0	0	0	0
5	5	1.0	1.0	1.0	2.0	2.0
10	1.0	2.5	1.5	1.5	2.0	3.0
15	2.0	2.5	3.0	3.0	4.0	5.5
20	2.5	4.0	4.0	5.0	6.0	7.75
25	3.0	4.75	5.25	6.5	7.75	10.0
30	4.0	6.0	7.0	8.25	9.75	12.0
35	4.75	7.0	8.0	10.0	11.5	14.5
40	6.0	8.5	9.75	12.0	13.5	17.0
45	7.0	10.0	11.0	13.5	15.5	19.0
50	8.5	11.0	12.25	15.5	17.5	21.25
55	10.0	12.5	14.0	17.5	20.0	23.0
60 (1)	12.0	14.0	15.5	20.0	22.0	27.0
70	15.0	17.0	18.5	24.0	27.0	33.0
80	16.0	20.0	22.0	28.5	32.0	39.5
90	17.25	23.5	26.0	34.0	38.0	42.0
100	18.5	28.0	30.5	37.75	40.25	43.50
110	19.0	31.5	34.5	39.0	41.5	44.5
120 (2)	20.0	33.0	36.5	40.0	42.5	45.5
135	21.0	35.0	38.0	41.75	44.0	47.0
150	21.75	36.0	39.75	43.0	45.0	48.0
165	22.75	37.0	41.0	44.0	46.0	49.0
180 (3)	23.5	38.0	42.0	45.0	47.0	50.0
195	24.0	39.0	42.5	45.5	47.75	50.5
210	24.5	39.5	43.0	46.0	48.0	51.0
225	25.0	40.0	44.0	47.0	49.0	51.5
240 (4)	25.75	40.75	44.5	47.5	49.5	52.5
270	27.0	42.0	45.5	48.5	50.5	53.5
300 (5)	28.0	43.0	46.75	49.75	52.0	54.5
330	29.0	44.0	48.0	50.5	53.0	55.5
360 (6)	29.5	44.5	48.5	51.5	53.75	56.25
390	30.0	45.5	49.5	52.0	54.5	57.0
420 (7)	31.0	46.0	50.0	53.0	55.0	57.5
480 (8)	32.25	47.25	51.5	54.25	56.5	58.75
540	33.5	48.5	52.5	55.25	57.5	59.5
600 (10)	34.5	49.5	53.5	56.0	58.5	60.5
660	35.5	50.5	55.0	57.0	59.0	60.75
960 (16)	40.0	54.0	58.0	59.5	61.0	62.25
1200 (20)	41.0	54.5	58.25	60.0	61.0	62.5
1320 (22)	42.0	54.75	58.5	60.0	61.0	62.5
1440 (24)	43.0	55.0	58.75	60.0	61.0	62.5

TABLE XIII

SETTLING RATES OF HYDRATES

Temp. °C	60	60	60	60	60	60
°F	140	140	140	140	140	140
R	2.5	7.5	10.5	13.5	18	25
Min. (hr)						
0	0	0	0	0	0	0
5	1	1	1	1	1	2
10	2	2	2	2	2	2.5
15	2.5	2.5	2.1	2.1	2.5	4.0
20	3.0	3.2	3.2	3.2	3.5	5.0
25	4.0	4.0	4.0	4.3	4.5	6.0
30	5.0	5.1	5.0	5.5	5.5	7.5
-	-	-	-	-	-	-
60 (1)	10.1	10.5	10.0	12.0	12.0	16.0
90	14	18.0	18.0	21.0	21.0	27.1
105	15	22.8	20.8	26.0	27.0	29.0
120 (2)	16	26.0	26.0	30	29.2	31
135	17	27.8	27.0	32	31.0	32.5
150	17.5	29.0	29.8	33	32.0	33.5
240 (4)	21	34	34.8	38	38	38.5
300 (5)	22.8	36	36.9	40	39.0	40.5
330	23.5	37	37.8	41	40.0	41.7
360 (6)	24.0	37.9	38.8	41.9	40.9	42.5
370	25.0	38.5	39.1	42.5	41.4	43.2
420 (7)	25.6	39.0	40.0	43.0	42.0	44.0
480 (8)	26.9	40.2	41.0	44.1	43.1	45.1
600 (10)	29.0	42.3	43.1	46.4	45.2	47.2
660 (11)	29.9	43.1	44.0	47.3	46.1	48.1
720 (12)	30.6	44.0	45.0	48.0	47.0	49.0
780 (13)	31.6	44.9	45.9	48.9	48.0	49.8
840 (14)	32.1	45.3	46.3	49.6	48.4	50.1
900 (15)	33.0	46.0	47.0	50.0	49.0	50.9
960 (16)	33.8	46.6	47.7	50.7	49.6	51.2
1230	36.3	48.3	49.2	51.9	51.1	52.9
1380 (23)	37.6	49.0	50.0	52.5	51.5	53.2
1440 (24)	38.0	49.2	50.0	52.5	51.7	53.5

TABLE XIV

SETTLING RATES OF HYDRATES

Temp. ° C	90	90	90	90	90
° F	194	194	194	194	194
R	4.5	7.5	10.5	13.5	18.0
Min (hr)					
0	0	0	0	0	0
5	1.0	1.0	1.0	0.5	0.5
10	1.0	1.0	1.0	0.5	1.0
15	1.8	2.0	2.0	1.0	1.4
20	2.6	2.6	3.0	2.0	2.1
25	3.4	4.0	3.8	2.4	3.1
30	4.5	5.0	4.9	3.5	4.0
35	5.0	5.8	5.6	4.2	4.8
40	6.0	7.0	6.8	5.0	5.2
45	7.1	8.0	7.5	6.0	6.0
50	8.0	9.0	8.0	6.6	7.2
55	9.0	10.0	9.0	7.2	7.9
60 (1)	10.0	10.9	10.0	8.2	9.2
70	11.1	12.8	12.8	10.0	11.8
80	13.0	15.1	13.8	11.9	14.9
100	17.5	20.8	17.8	15.8	22.0
110	20	24.1	20.0	18.1	24.0
120 (2)	23	27.2	22.9	21.1	25.1
150	29.6	30.4	31.0	29.9	28.1
165	31	31.6	32.1	31.2	29.1
180 (3)	32	32.8	33.8	32.8	30.0
210	33.8	34.1	35.0	34.3	32.0
240 (4)	34.1	35.8	36.8	36.0	33.2
300 (5)	37.4	37.7	38.8	38.1	35.3
330	38.1	38.5	39.8	39.1	36.6
360 (6)	39.1	39.1	40.5	40.0	37.1
390	40.0	40.0	41.1	40.9	38.0
420 (7)	40.6	40.6	41.9	41.7	38.9
480 (8)	42.0	41.9	43.1	43.0	39.9
540 (9)	43.0	43.0	44.2	44.0	41.1
660 (11)	44.8	44.8	46.2	46.0	43.0
780 (13)	46.2	46.1	48.0	47.8	44.5
900 (15)	47.8	47.4	49.4	49.0	45.9
1020 (17)	48.9	48.7	50.3	49.8	46.9
1080 (18)	49.2	49.0	50.9	50.0	47.1
1200 (20)	50.1	50.0	51.6	50.1	48.0
1260 (21)	50.6	50.1	51.9	50.4	48.2
1320 (22)	51.0	50.8	52.0	50.5	48.7
1380 (23)	51.2	51.0	52.1	50.8	48.9
1440 (24)	51.9	51.1	52.2	50.8	49.0

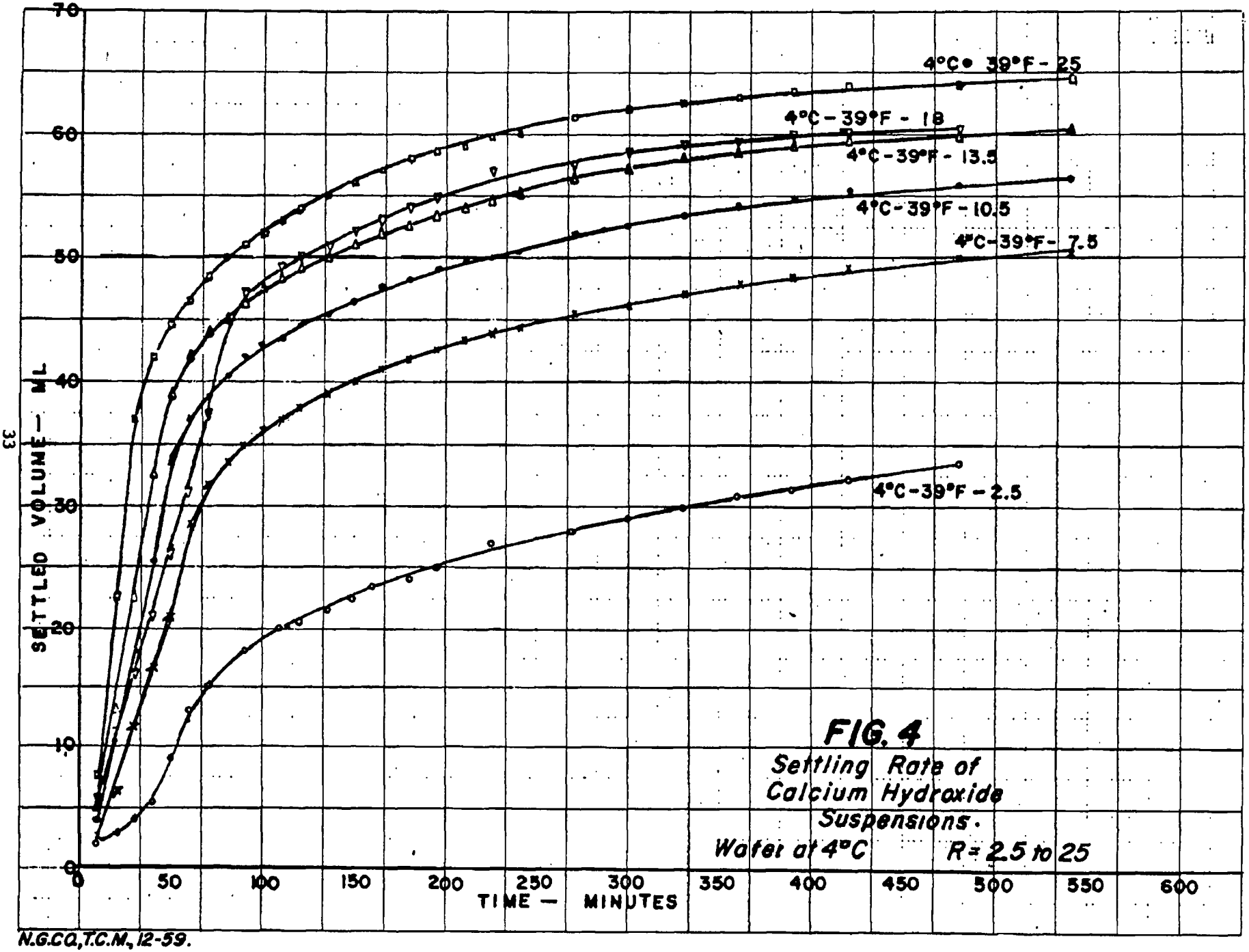

FIG. 4

Settling Rate of Calcium Hydroxide Suspensions.

Water at 4°C R = 2.5 to 25

N.G.C.A, T.C.M., 12-59.

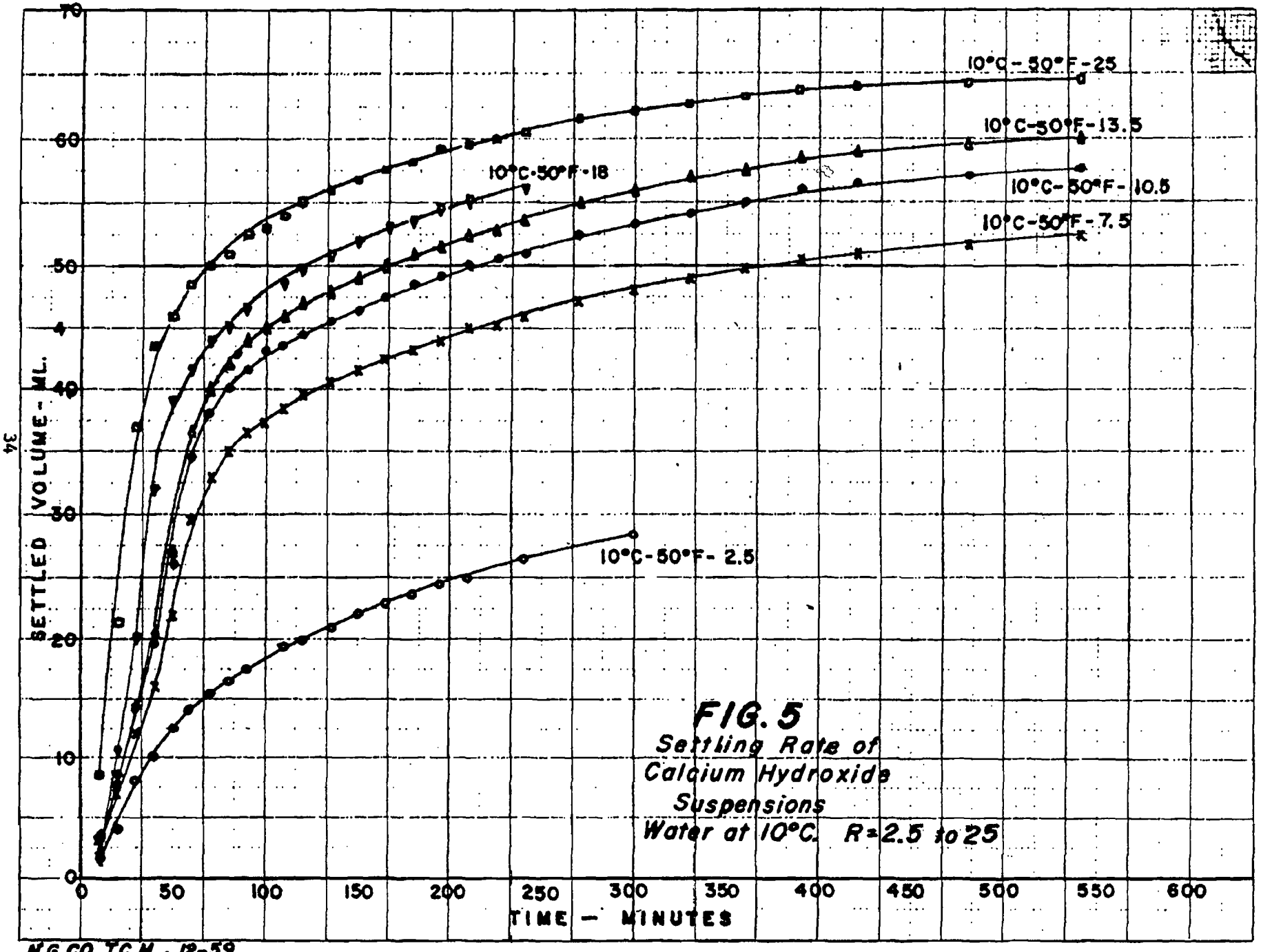

FIG. 5
Settling Rate of Calcium Hydroxide Suspensions Water at 10°C. R=2.5 to 25

N.G.CO., T.C.M., 12-59

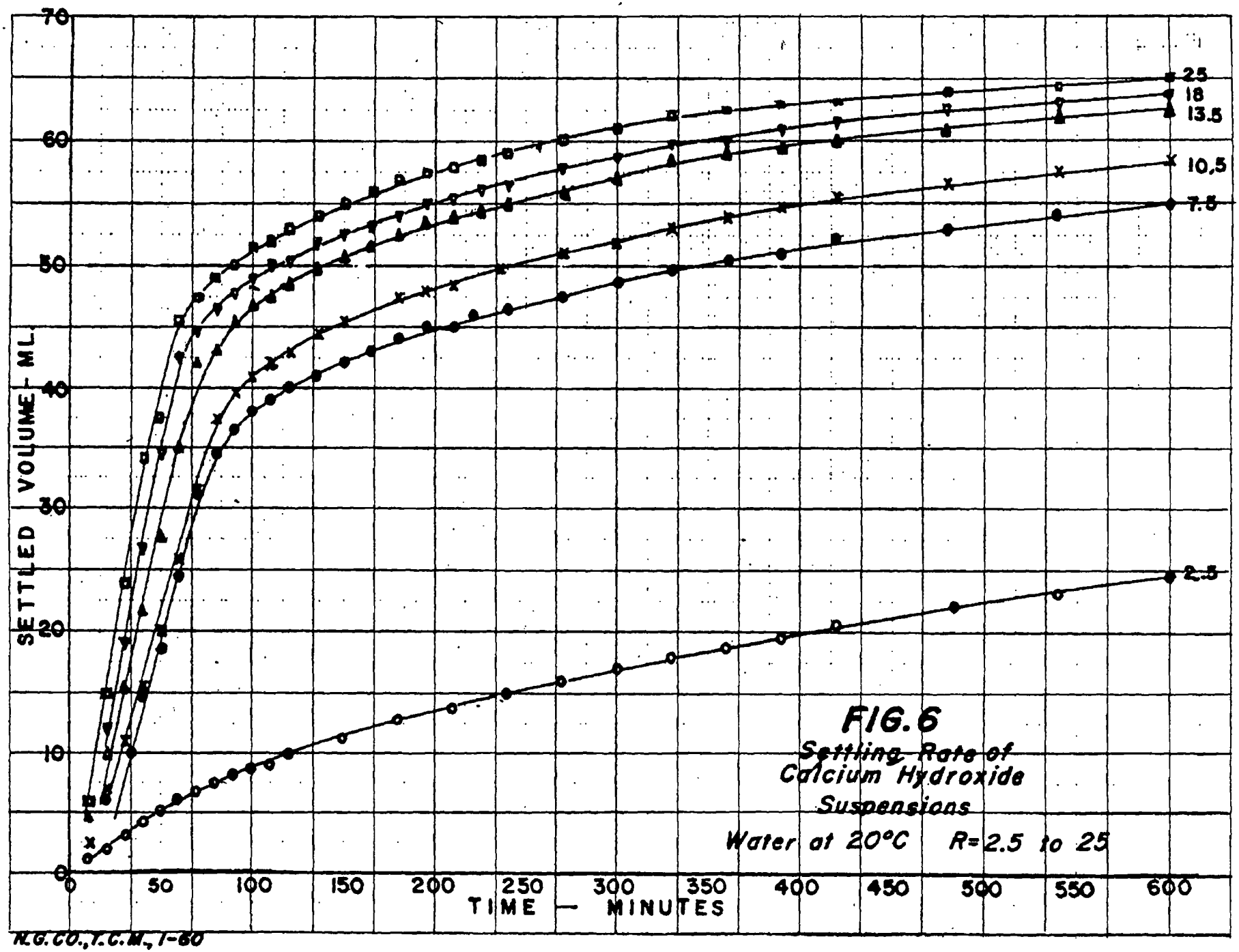

FIG. 6

Settling Rate of Calcium Hydroxide Suspensions

Water at 20°C R=2.5 to 25

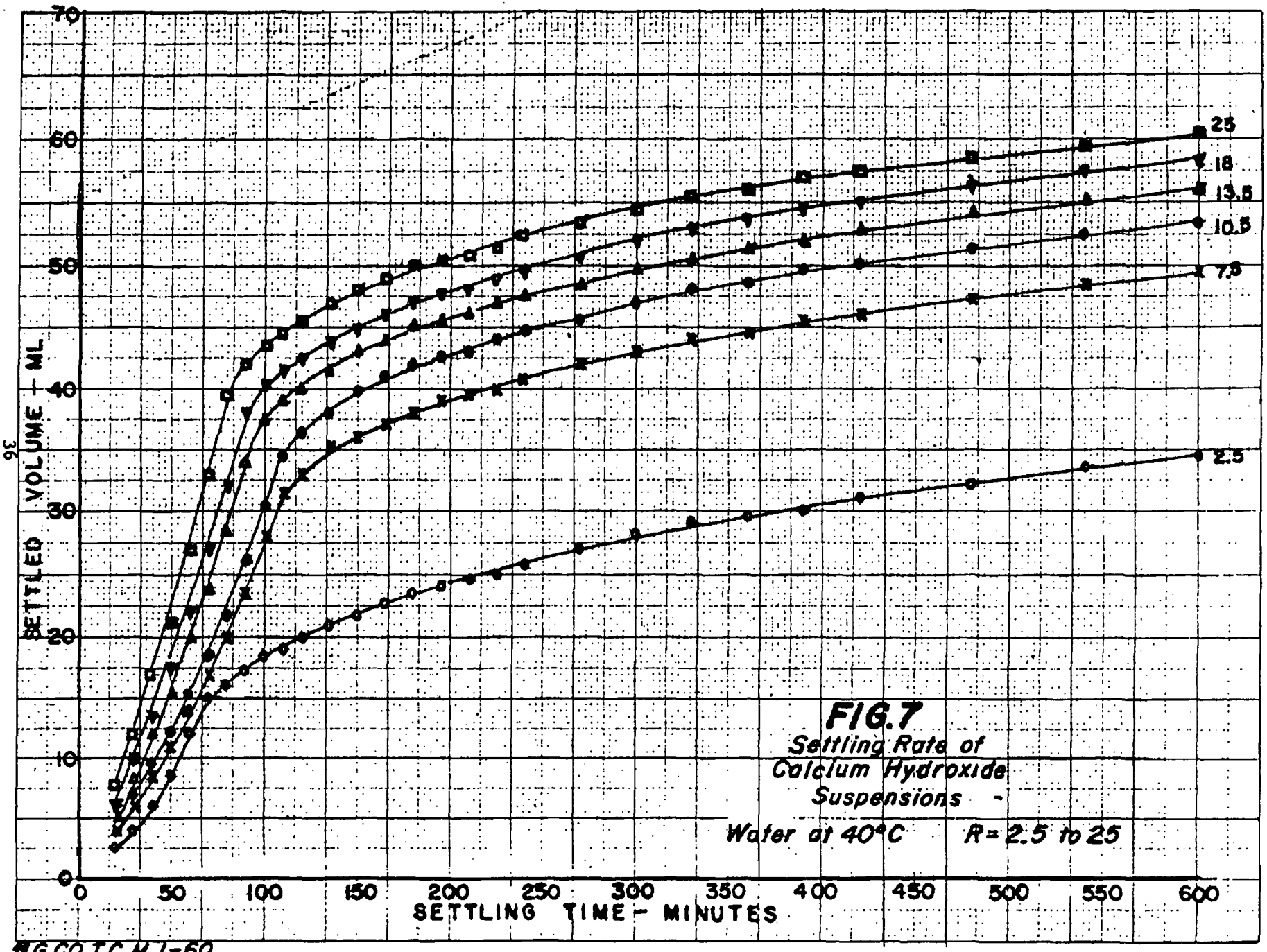

FIG. 7
Settling Rate of Calcium Hydroxide Suspensions - Water at 40°C R = 2.5 to 25

N.G.CO.,T.C.M.,1-60

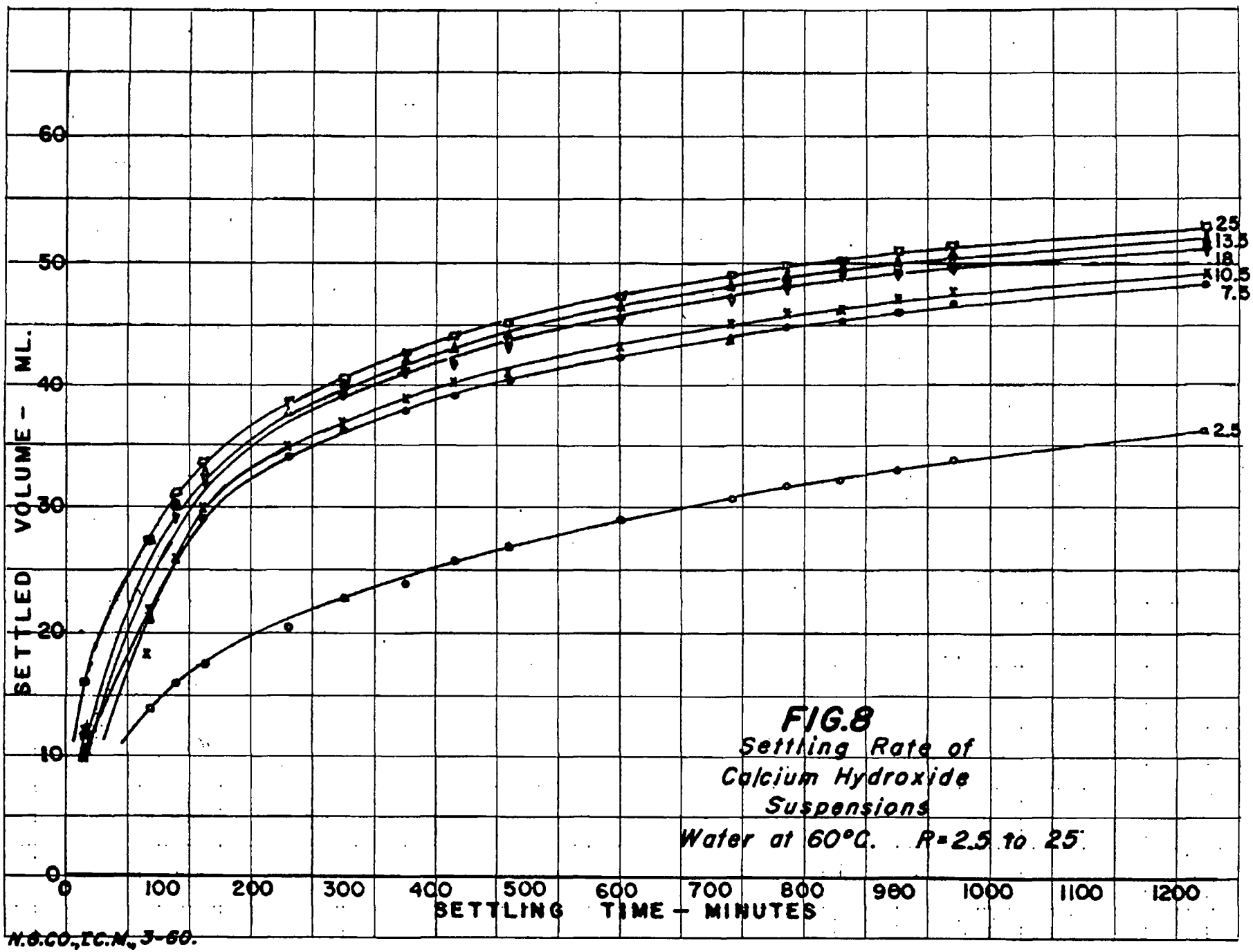

FIG.8
Settling Rate of Calcium Hydroxide Suspensions
Water at 60°C. R=2.5 to 25

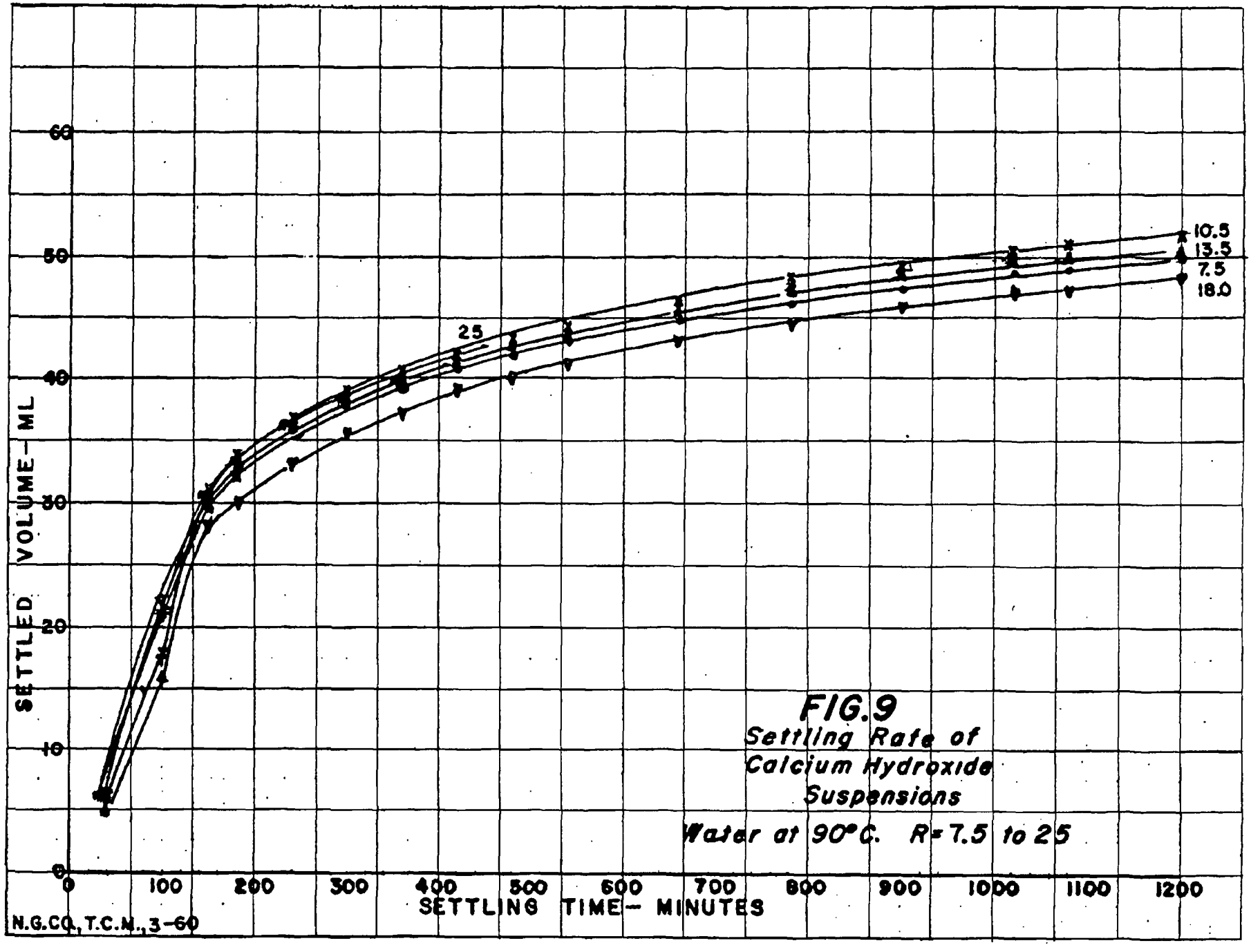

FIG. 9
Settling Rate of
Calcium Hydroxide
Suspensions
Water at 90°C. R = 7.5 to 25

TABLE XV

SETTLING TIME OF CALCIUM HYDROXIDE

PRODUCED WITH VARIOUS RATIOS OF WATER OF DIFFERENT TEMPERATURE

Temp. °C	4	10	20	40	60	90
°F	39	50	68	104	140	194
R(H_2O/CaO)						
2.5						
7.5	480	375	275	630	1800	1200
10.5	225	210	330	420	1380	980
13.5	135	165	140	310	900	1080
18.0	120	126	110	240	1180	1800
25.0	80	70	90	180	835	1100

TABLE XVI

VOLUME OCCUPIED BY CALCIUM HYDROXIDE

AFTER SETTLING 10% SUSPENSION FOR 24 HOURS

Temp. °C	4	10	20	40	60	90
°F	39	50	68	104	140	194
R(H_2O/CaO)						
2.5	56	57	63	57	62	--
4.5	--	--	--	--	--	--
7.5	43	42	38.5	45	50.8	48.9
10.5	39	38.5	41	51.25	50	47.8
13.5	36.6	37	35.75	40	47.5	49.2
18.0	39	40	35	39	48.3	51
25.0	34	34	34	37.5	46.5	50

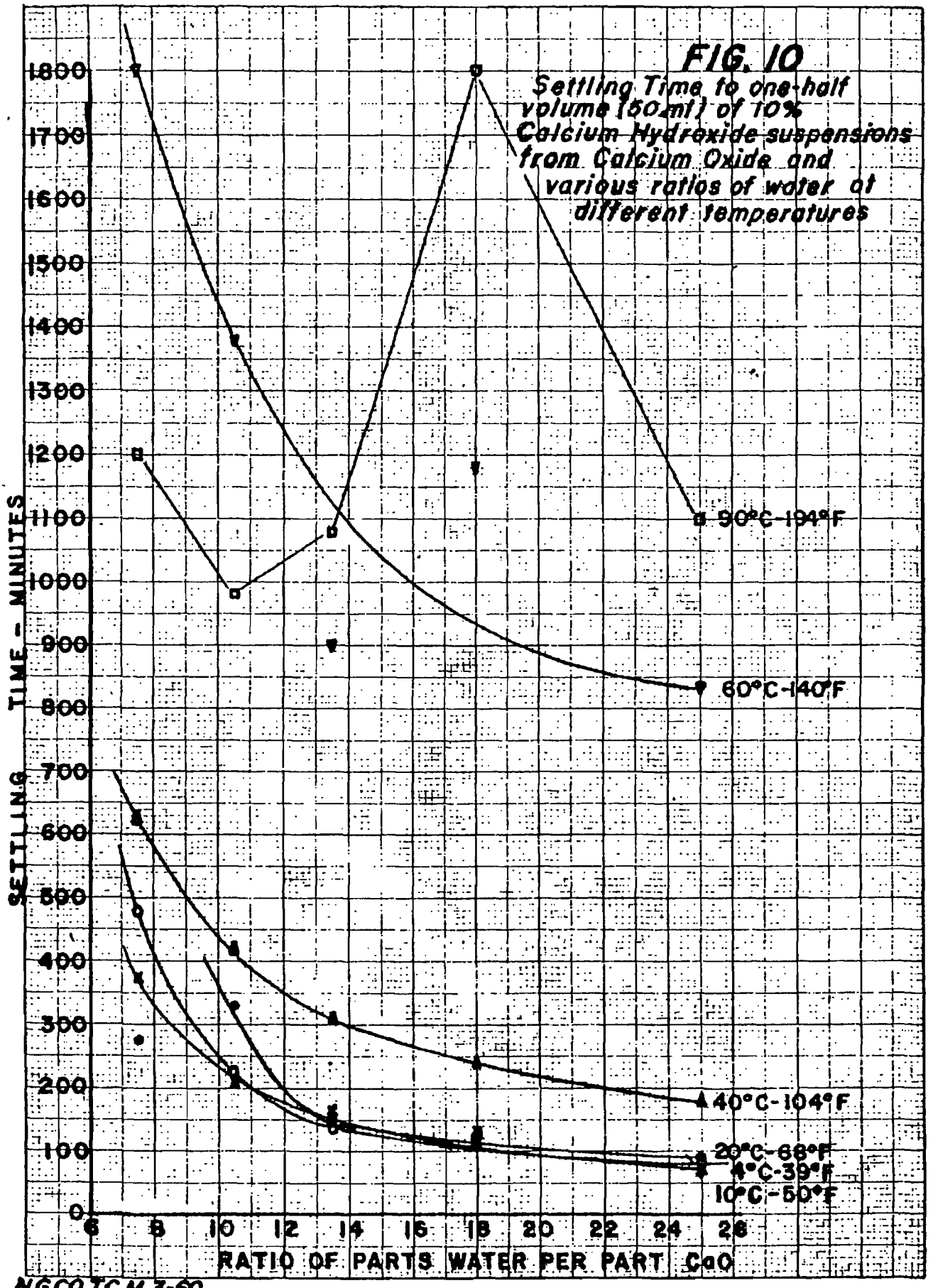
FIG. 10
Settling Time to one-half volume (50 ml) of 10% Calcium Hydroxide suspensions from Calcium Oxide and various ratios of water at different temperatures
SETTLING TIME - MINUTES
RATIO OF PARTS WATER PER PART CaO
90°C-194°F
60°C-140°F
40°C-104°F
20°C-68°F
4°C-39°F
10°C-50°F
0
100
200
300
400
500
600
700
800
900
1000
1100
1200
1300
1400
1500
1600
1700
1800
6
8
10
12
14
16
18
20
22
24
26

N.G.CO,T.C.M.3-60

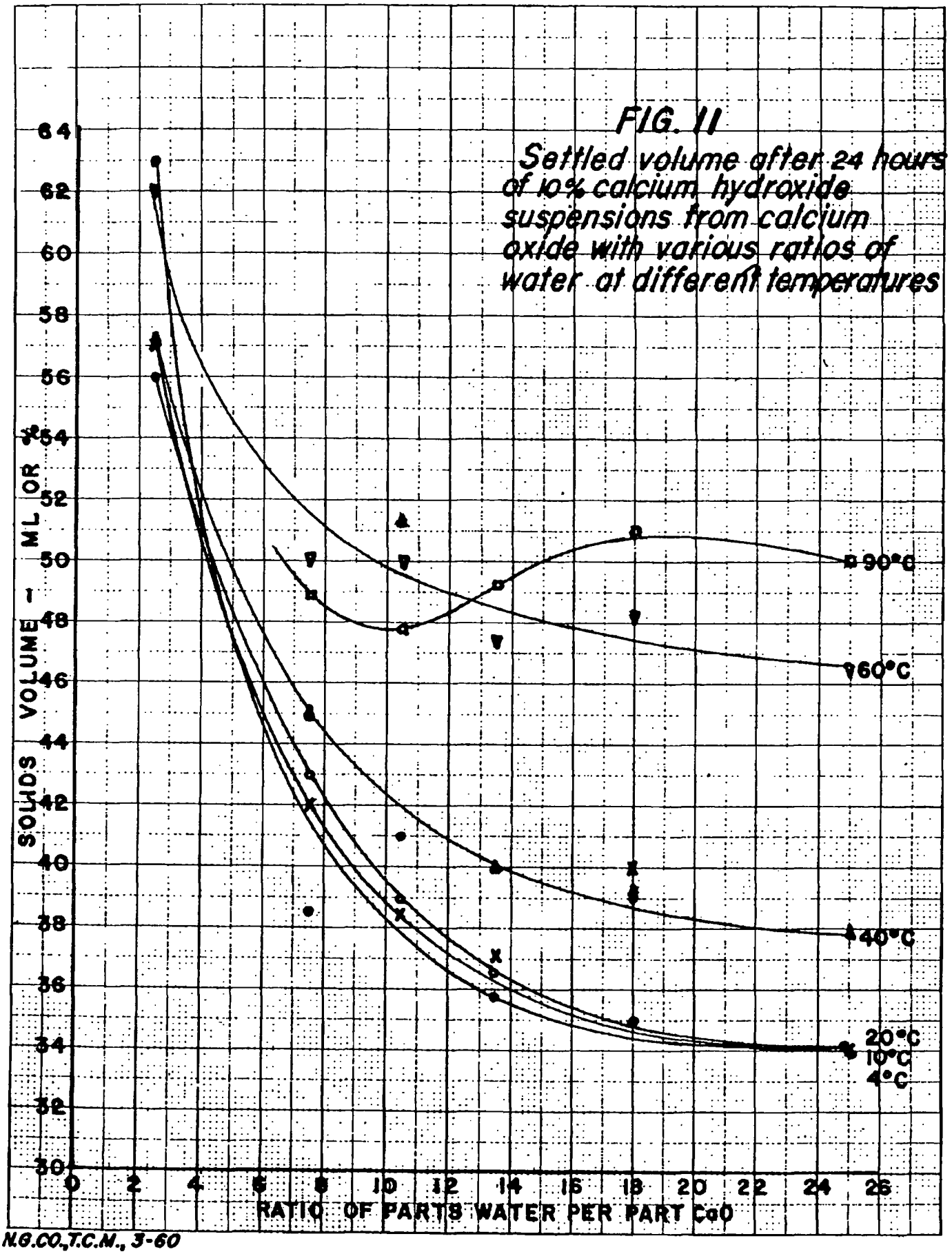
FIG. 11
Settled volume after 24 hours of 10% calcium hydroxide suspensions from calcium oxide with various ratios of water at different temperatures
SOLIDS VOLUME - ML OR %
64
62
60
58
56
54
52
50
48
46
44
42
40
38
36
34
32
30
0
2
4
6
8
10
12
14
16
18
20
22
24
26
RATIO OF PARTS WATER PER PART CaO
90°C
60°C
40°C
20°C
10°C
4°C
N.G.CO.,T.C.M., 3-60

None of the calcium hydroxides prepared with a ratio of 2.5 pounds water per pound calcium oxide settled to one-half volume even after one week (10,000 minutes). The settling time values for suspensions prepared with water between 4°C and 60°C fall between those values shown for 4°C and 60°C and are of the same increasing values with decrease in R.

The settling times for suspensions prepared with water at 90°C (194°F) are more constant for all values R than any of the suspensions prepared with water at lower temperatures. Some irregularity exists with changes in R, but this difference has not been fully explained. A decrease in settling time with an increase in the value of R does not occur at this temperature. The slaking temperatures for all values of R at this temperature theoretically exceeds 212°F (Table IV) and actually evaporated some of the slaking water during the reaction. This boiling temperature undoubtedly produced crystal growth of calcium hydroxide to increase both the settling time and the viscosity.

These data indicate that the settling time of calcium hydroxide can be controlled by choosing a combination of initial water temperature between 4°C and a temperature producing a final temperature less than 212°F, and ratio of water to calcium oxide to give the desired characteristic.

C Specific Surface

The time required to adjust the suspensions to the required 100 gpl calcium hydroxide and to determine the settling time was enormous, and would be unjustified as a control test in an industrial plant requiring several periodic checks per day. A shorter and more convenient method of testing involves the determination of specific surface. The specific surface of each sample is tabulated in Table XVII and shown graphically in Figure 12. The specific surface values range from a low of 15,314 cm^2/g produced with hydrating water at 4°C at R = 25 to a high of 58,300 cm^2/g produced with water at 90°C at R = 2.5. These specific surface values represent a mean particle diameter range from 1.74 microns (u) to 0.46 u respectively. The calculated mean particle diameters for the calcium hydroxide produced in all samples are shown in Table XVIII.

TABLE XVII

SPECIFIC SURFACE OF CALCIUM HYDROXIDE

PRODUCED WITH VARIOUS RATIOS OF WATER OF DIFFERENT TEMPERATURES

Temp. °C	4	10	20	40	60	90
°F	39	50	68	104	140	194
$R(H_2O/CaO)$						
2.5	50,736	54,293	52,790	56,606	57,355	58,300
4.5	--	--	48.307	--	52,260	55,255
7.5	35.246	34,534	--	47,035	49,183	53,070
10.5	29,133	29,840	--	45,203	48,920	51,126
13.5	23,166	24,419	36,520	41,080	45,967	52,658
18.0	17,833	18,968	31,556	37,620	48,307	53,925
25.0	15,314	18,597	29,405	40,910	48,244	53,295

TABLE XVIII

CALCULATED PARTICLE DIAMETER (MICRONS) OF CALCIUM HYDROXIDE

PRODUCED WITH VARIOUS RATIOS OF WATER OF DIFFERENT TEMPERATURES

Temp. °C	4	10	20	40	60	90
°F	39	50	68	104	140	194
$R(H_2O/CaO)$						
2.5	0.53	0.49	0.50	0.47	0.46	0.46
4.5	--	--	0.55	--	0.51	0.48
7.5	0.76	0.77	--	0.57	0.54	0.50
10.5	0.91	0.89	--	0.59	0.54	0.52
13.5	1.15	1.09	0.73	0.65	0.58	0.51
18.0	1.49	1.40	0.84	0.71	0.55	0.49
25.0	1.74	1.43	0.90	0.65	0.55	0.50

FIG. 12

Specific Surface of Calcium Hydroxide produced with various ratios of water of different temperatures

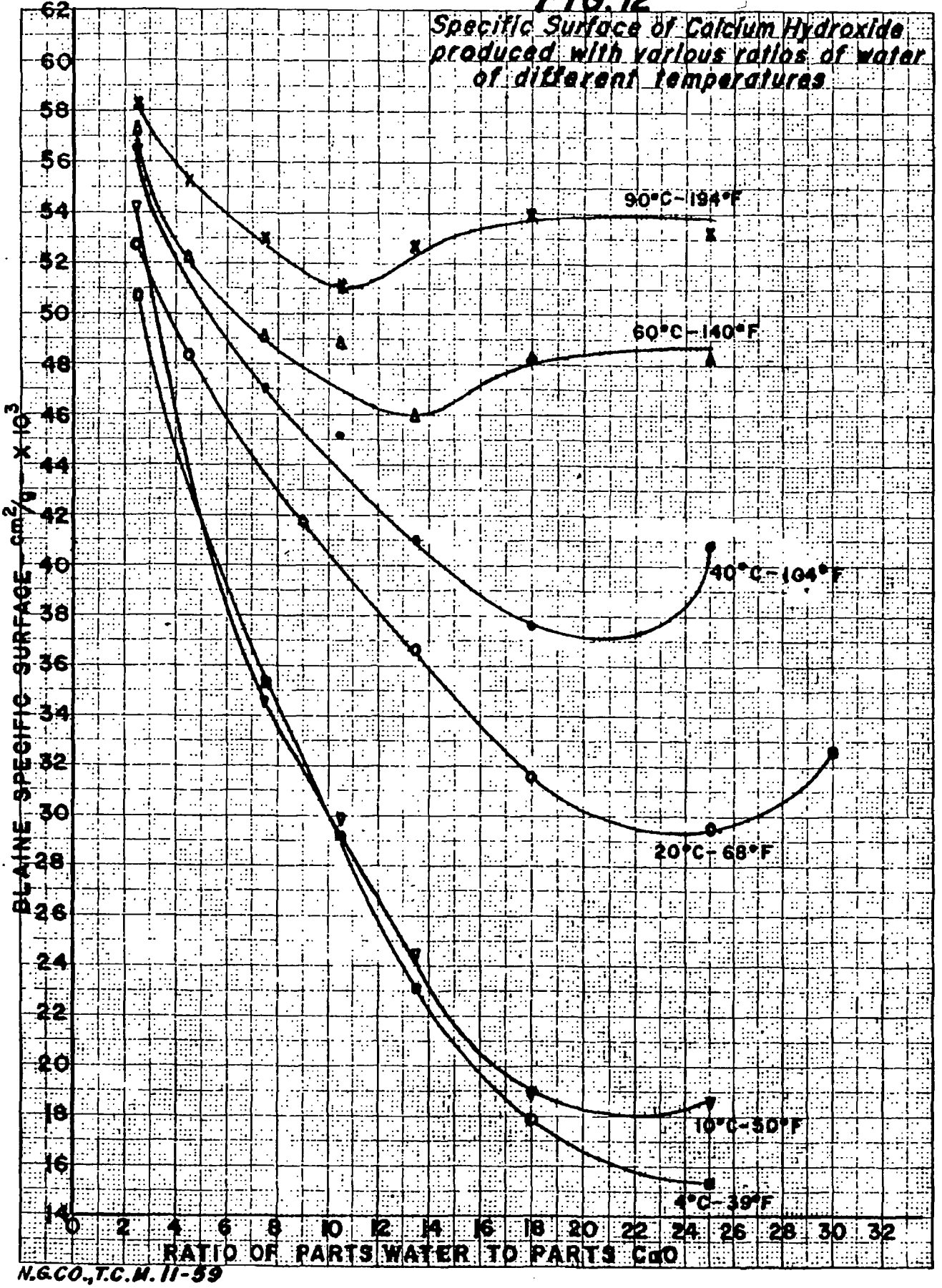

N.G.C.O., T.C.M. 11-59

An initial water temperature of 4°C (39°F) and a change in R from 2.5 to 25 pounds water to pounds calcium oxide produces calcium hydroxide with specific surfaces from 50,736 cm^2/g to 15,314 cm^2/g with corresponding mean particle diameters from 0.53 to 1.74 u. Settling times represented by particles of this size, according to Table IV, range from 480 minutes to 80 minutes respectively. A constant water temperature of 10°C (50°F) and R from 2.5 to 25 likewise produces calcium hydroxide of decreasing specific surfaces from 54,293 cm^2/g to 18,597 cm^2/g with corresponding mean particle diameter from 0.49 u to 1.43 u with increase in R. Particles of this range have settling times from 375 minutes to 70 minutes respectively. Water temperature of 20°C (68°F) follows a similar pattern with the usual change in R, but the change of a much smaller magnitude than either 4°C or 10°C.

The range of the calcium hydroxide at a water temperature of 20°C is from 52,790 cm^2/g to 32,610 cm^2/g specific surface with corresponding mean particle diameters of 0.50 u to 0.90 u, indicating that the higher temperature slaking water gives changes of less magnitude than at the two previous temperatures. Settling times of these samples more or less correlate this data by showing less variation of settling values from 235 minutes to 90 minutes. Water temperatures of 40°C (104°F) and 60°C (140°F) both show less mean particle size variation than the previous temperatures. At 40°C the change will be seen to be from 56,606 cm^2/g to 40,910 cm^2/g specific surface corresponding to mean particle diameters of 0.47 u to 0.65 u, while at 60°C the variation is from 57,355 cm^2/g to 48,244 cm^2/g specific surface with mean particle diameters of 0.46 u to 0.55 u. This narrow range of mean particle diameters would be expected to show longer settling time than previous series for all values of R.

Slaking water at 90°C (194°F) produces from 58,300 cm^2/g to 53,295 cm^2/g specific surfaces for all values of R with a mean particle diameter range of only 0.46 u to 0.50 u. Very long settling times would be expected from these suspensions. Table XIV and Figure 9 show active settling times from 980 minutes to 1200 minutes.

The specific surface decreases(mean particle diameter increases) for all initial water temperatures to 60°C as the ratio (R) of water increases from 2.5 to 25. Also, the specific surface increases (mean particle diameter decreases) for each value of R as the initial water temperature increases.

The highest specific surface calcium hydroxides were obtained from those tests producing final temperatures of or greater than 212°F. These temperatures were obtained with R at 2.5 for all initial slaking water temperatures investigated and for an initial slaking water temperature of 90°C at all values of R. The development of specific surface of a calcium hydroxide is therefore a function of the final slaking temperature. Final slaking temperatures less than 100°C (212°F) develop the specific surface of calcium hydroxide in proportion to the final temperature, which is another way of defining the ratio; R, of water. Higher ratios of water resulting in lower final temperatures produce the lower specific surfaces, and low ratios of water resulting in higher final temperatures produce higher specific surfaces. Investigating this condition further, the amount of water required for several ratios was heated to the calculated initial temperature (T_1) to result in a final temperature (T_2) approaching 100°C or 212°F (Table V), and used for slaking tests. The tabulation of data for the tests and the results of final temperature of the suspension and specific surface of the calcium hydroxide are shown in Table XIX.

TABLE XIX

Results from Volume and Temperature of H_2O (T_1) to Produce a Final Temperature (T_2) of approximately 212°F

R	Temperature °F		Specific Surface cm^2/g
	T_1	T_2	
2.5	57.2	210.9	55,100
7.5	167	211.1	52,300
13.5	190	211.6	51,600
25.0	205	212.7	53,200

The final temperature of each test approached the expected value of 212°F. The specific surface values are of the same magnitude. Therefore, these data offer further proof that to produce extremely high specific surface or small particle-diameter calcium hydroxide requires a high slaking temperature approaching 100°C (212°F). It is a matter of choice for the ratio of water to be used so long as the temperature calculated for this value of R will produce a final temperature approaching, but not exceeding, 212°F.

It is important that the calcium oxide have a high degree of activity to produce a high specific surface calcium hydroxide in a short slaking cycle. Otherwise, a low activity calcium oxide will increase radiation losses to reduce the slaking temperature below the necessary limit.

Very low values of R will produce high specific surface calcium hydroxide. However, at these concentrations, especially above an initial starting temperature 50°F (10°C) the final slaking temperature (T_2) will theoretically be above 212°F resulting in the evaporation of a large proportion of the water. Also, values of R at temperatures approaching 90°C (194°F) produce high specific surface calcium hydroxide. Final temperatures of these combinations will be theoretically above 212°F, so that a large amount of the slaking water will be evaporated.

Aqueous suspensions of calcium hydroxide exposed to heated bodies above 214°F have been shown to produce hexagonal crystals of fairly large size (Wire and Wire Products, October 1955). The specific surface of these suspensions increases as the crystallization increases because of the colloidal characteristics of aqueous suspensions of crystalline calcium hydroxide.

It has also been found optically that calcium hydroxide produced by the slaking of calcium oxide in water at values of R and T_1 to result in a final slaking temperature T_2 of 212°F or calculated theoretically to exceed 212°F also produces crystalline calcium hydroxide. The specific surface, settling time and viscosity of these suspensions are greatly increased because of this crystallization.

Suspensions produced at all values of R with T_1 at 194°F (90°C) contained large amounts of crystalline calcium hydroxide which account in part to the very high specific surfaces. Crystallization also increases the settling time as shown in Table XIV.

The initial slaking temperature (T_1) should be chosen to assure a final slaking temperature (T_2) of 212°F or less to prevent or reduce to a minimum the opportunity for crystal growth.

D VISCOSITY

The viscosity was determined on calcium hydroxide suspensions slaked with several ratios of water and temperatures then cooled to 70°F. Two of the suspensions were prepared at R of 7.5 and T_1 of 4°C (39°F) and 60°C (140°F). One suspension was prepared at R of 2.5 and T_1 of 14°C but was too viscous for a test. Three suspensions were prepared at R of 7.5, 13.5 and 25 and T_1 of 75° C (166.8°F), 88°C (190°F) and 96°C (205°F) respectively calculated to produce final temperatures (T_2) of 212°F. The values for T_2 and the viscosities, with the exception of the one prepared at R of 2.5, are shown in Table XX.

TABLE XX

Slaking Temperature and Viscosity (Centipoises) of Calcium Hydroxide Suspensions

Sample	R	°C Temperatures T_1	°C Temperatures T_2	Viscosity
1	7.5	4	33.8	38
2	7.5	60	88.3	163
3	2.5	14	99.4	--- *
4	7.5	75	99.5	241
5	13.5	88	99.8	28
6	25.0	96	100.4	10

* Suspensions prepared at this value of R are highly viscous and a viscosity test is meaningless.

The viscosity increased with an increase in temperature for a constant water ratio. When the water ratio was increased and the initial temperature of the water increased to produce a final temperature approaching 212°F the viscosity decreased at a very rapid rate.

The theoretical concentration of a suspension at R of 7.5 is approximately 162 gpl. The concentration at R of 13.5 and 25.0 are 91.4 gpl and 49.7 gpl respectively. The concentration at R of 2.5 is theoretically 456 gpl. Therefore it would be expected to find very low viscosities of suspension prepared with R of 13 and 25 as shown in samples 5 and 6. Samples 5 and 6 were allowed to settle and the calculated amount of supernatant water decanted to give a concentration equivalent to R of 7.5. Sample 3 required diluting with water to reduce the concentration from 456 to 162 gpl. The viscosities of these corrected suspensions are shown in Table XXI.

TABLE XXI

Viscosity (Centipoises) of Calcium Hydroxide Suspensions at approximately 177 gpl

Sample	R of Original Suspension	Viscosity of Suspension corrected to 162 gpl
3	2.5	131
4	7.5	241
5	13.5	360
6	25.0	291

The amount of water employed for slaking and its initial temperature has a decided effect on the viscosity of a calcium hydroxide during the slaking of calcium oxide. A ratio of water of 7.5 at a temperature of 75°C (167°F) produces a suspension of higher viscosity than a suspension prepared with a ratio of 13.5 even though the same final slaking temperature is reached. However, when both suspensions are made to the same concentration, the one prepared with the greater ratio of water has the higher viscosity. A suspension of calcium hydroxide prepared at a ratio of 25 and an initial temperature of 96°C does not produce the same viscosity when corrected to 162 gpl.

The viscosity of the calcium hydroxide suspensions at a concentration of 100 gpl were determined. It was anticipated the values would be relatively low at this low concentration, but it was thought that values for any differences, however slight, may help to explain some of the differences in the settling rates. The values for most of the samples produced are shown in Table XXII.

TABLE XXII

Viscosity (Centipoises) of Calcium Hydroxide Suspensions at Concentration of 100 gpl $(CaOH)_2$

		Initial Water Temperature					
	°C	4	10	20	40	60	90
R	°F	39	50	68	104	140	194
2.5		--	--	72	42	63	--
7.5		35	27	21	25	32	28
10.5		28	24	24	22	32	27
13.5		--	23	22	20	29	26
18.0		--	--	21	19	33	--
25.0		--	--	20	19	--	--

The viscosities of suspensions of this low concentration will be very low. The viscosities are higher at the lowest water ratio of 2.5. These samples are undoubtedly influenced by the presence of crystalline calcium hydroxide produced at this low water ratio. The viscosity decreases with an increase in the water ratio between 39°F and 104°F. The viscosity appears constant at ratios from 7.5 to 18 for initial water temperatures of 60°C (140°F) and 90°C (194°F).

The higher viscosities of suspensions prepared with water ratios of 2.5 indicate a change in physical properties which will decrease the settling time. Therefore, the settling time is not dependent upon mean particle diameter (or specific surface) of the suspended calcium hydroxide alone.

VII CONCLUSIONS

This preliminary study of the reaction between calcium oxide and water reveals the complexity of the reaction in producing results regarding settling time, specific surface and viscosity of calcium hydroxide suspension prepared with an excess of water.

Advantage can be taken of the thermodynamics of the reaction by altering the ratio and temperature of water per pound of calcium oxide to produce calcium hydroxide varying in particle diameter from fairly large to extremely small as determined by the Blaine air permeability method. Low ratios of water produce higher reaction temperatures and calcium hydroxide of high specific surfaces. Specific surfaces vary less with changes in water temperatures at low water ratios. Specific surfaces also vary less with water at high temperatures for all ratios. The specific surface of the calcium hydroxides vary over a very wide range at ratios of 7.5 to 25 and at temperatures from 4°C (39°F) to approximately 60°C (140°F).

Settling times of calcium hydroxide suspensions corrected to 100 gpl do not correlate changes in ratios and temperature of water as well as specific surface measurements. This may be caused by the influence of the viscosity of a suspension on the settling rate of the particles of calcium hydroxide. A considerable change in viscosity was found which has not been fully explained.

This study, although presenting encouraging data on specific surface control, indicates the need for more information on the factors influencing the difference in the rate of settling and a more thorough knowledge of particle size distribution with changes in the process.

Data on the control of specific surface or mean particle diameter by either a change in the ratio of water to calcium hydroxide or a change in the temperature of water at any given ratio of water to calcium hydroxide is presented which, to our knowledge, has not been previously available to the chemical industry. A better understanding of this principle offers the industry a new method of more consistent control at higher efficiency.

WVMP SAR Reference 3-25

Thermodynamics of the Liquid State: Generalized Predictions of Properties," K. M. Watson, Ind. Eng. Chem., 35(4), 398-406, 1943

Thermodynamics of the Liquid State

GENERALIZED PREDICTION OF PROPERTIES

K. M. Watson
UNIVERSITY OF WISCONSIN, MADISON, WIS.

On the basis of a modified application of the theorem of corresponding states, new methods are presented for the general prediction of the following thermodynamic properties of liquids: thermal expansion and compressibility, pressure correction to enthalpy, pressure correction to entropy, pressure correction to heat capacity at constant pressure, heat of vaporization, difference between heat capacity of a saturated liquid and its ideal gas, and difference between heat capacity of saturated liquid and heat capacity at constant pressure. The only data required are the boiling point, the critical temperature, critical pressure, and the liquid density at some one temperature.

Like all applications of the theorem of corresponding states, these relations are not rigorously correct. However, deviations from the available experimental data on a variety of compounds, both polar and nonpolar, are sufficiently small to warrant their use for many process problems where reliable data are not available, and for rationalizing fragmentary experimental data.

DURING the past ten years much attention has been directed (*2, 4, 7, 8, 10, 23–26*) toward the development of generalized relations which permit prediction of the thermodynamic properties of the gaseous state, even at extreme conditions of temperature and pressure, with accuracy sufficient for general engineering purposes. The similar properties of the liquid state have received little attention because of their lesser importance and because of the failure of the theorem of corresponding states to directly correlate liquid properties with accuracy. However, by a modified application of this theorem it is possible to correlate liquid properties with a degree of accuracy similar to the correlations of the gas phase.

THERMAL EXPANSION AND COMPRESSIBILITY

The equation of state for the gaseous phase is ordinarily written,

$$pv = zRT \tag{1}$$

where z, the compressibility factor, is a function of reduced temperature and pressure, approximately the same for all substances. If this relation were applied to the liquid state, an expression for liquid density might be written,

$$\rho = \frac{pM}{zRT} = \left(\frac{p_r}{zRT_r}\right)\frac{P_cM}{T_c} = \omega\frac{P_cM}{T_c} \tag{2}$$

where ω, which might be termed the "expansion" factor, would be a function only of reduced temperature and pressure.

Unfortunately it is found that factor ω of Equation 2 is not a generalized function of reduced conditions. Values of ω at the same reduced conditions may vary by more than 20 per cent for different compounds. Accordingly, Equation 2 is a rough approximation useful only where no direct liquid density data of any type are available.

Since at least one value of liquid density is available for almost any compound, a more useful relation results by applying Equation 2 to obtain an expression for the ratio of the density at any given condition to that at some reference state designated by subscript 1:

$$\frac{\rho}{\rho_1} = \frac{\omega}{\omega_1}$$

$$\text{or } \rho = \frac{\rho_1}{\omega_1}\omega \tag{3}$$

It has been found that if ω is evaluated as a function of reduced temperature and reduced pressure for one compound on which complete data are available, Equation 3 may be used with satisfactory accuracy for predicting the densities of any other compound for which one liquid density value is available to establish ρ_1/ω_1.

Table I. Values of Expansion Factor ω

T_r	Expansion Factor ω							
	$P_r = 0$	$P_r = 0.4$	$P_r = 0.8$	$P_r = 1.0$	$P_r = 1.5$	$P_r = 2$	$P_r = 3$	$P_r = 5$
0.5	(0.1328)	....	....	0.1332	....	0.1338	....	0.1350
0.6	0.1242	....	....	0.1250	....	0.1258	....	0.1275
0.7	0.1144	0.1150	....	0.1158	....	0.1170	0.1182	0.1202
0.8	0.1028	0.1042	0.1050	0.1056	0.1070	0.1077	0.1098	0.1125
0.9	....	0.0900	0.0915	0.0926	0.0949	0.0968	0.1002	0.1043
0.95	....	....	0.0810	0.0831	0.0872	0.0902	0.0943	0.1000
1.0	....	....	....	0.0440	0.0764	0.0818	0.0875	0.0954

Figure 1 and Table I give values of ω for isopentane, calculated from the measurements of Young (*11*) and extended to higher pressures by the data of Sage and Lacey (*16, 18*) on propane and *n*-pentane and Equation 3. Tables II and III compare liquid densities calculated from these curves and Equation 3 with experimental data from the indicated sources for compressed and saturated liquids of various polar and nonpolar types. The agreement is reasonably good with deviations, in general, less than 5 per cent, even for the case of water at 100° C. and above. The anomalous density changes of water at low temperature are not in agreement with the correlation, and selection of 4° C. as the reference conditions instead of 100° C. would increase the maximum deviations in the high-temperature range to approximately 10 per cent. In general, it is desirable to use the highest temperature at which data are available as the reference state, particularly when the high-temperature behavior of polar substances such as water are being calculated.

PRESSURE CORRECTION TO ENTHALPY

The effect of pressure on the enthalpy of any substance is expressed by the rigorous thermodynamic equation:

$$J\left(\frac{\partial H}{\partial p}\right)_T = V - T\left(\frac{\partial V}{\partial T}\right)_p \qquad (4)$$

Rearranging in terms of reduced conditions,

$$\frac{J}{P_c}\left(\frac{\partial H}{\partial p_r}\right)_T = V - T_r\left(\frac{\partial V}{\partial T_r}\right)_p \qquad (5)$$

Combining Equations 3 and 5,

$$\frac{J\rho_1}{P_c\omega_1}\left(\frac{\partial H}{\partial p_r}\right)_T = \frac{1}{\omega} - T_r\left(\frac{\partial \frac{1}{\omega}}{\partial T_r}\right)_p \qquad (6)$$

Through Equation 6 the group

$$\frac{J\rho_1}{P_c\omega_1}\left(\frac{\partial H}{\partial p_r}\right)_T$$

may be expressed as a general function of reduced temperature and pressure by the graphical differentiation of Figure 1, remembering that $\partial(1/\omega) = -(\partial\omega/\omega^2)$. The results of this operation are summarized in Figure 2 and Table IV for the range of conditions not close to the critical point.

The effect of pressure on enthalpy may be expressed in a more useful form by graphically integrating Equation 6 to obtain the differences between the enthalpy of a liquid under

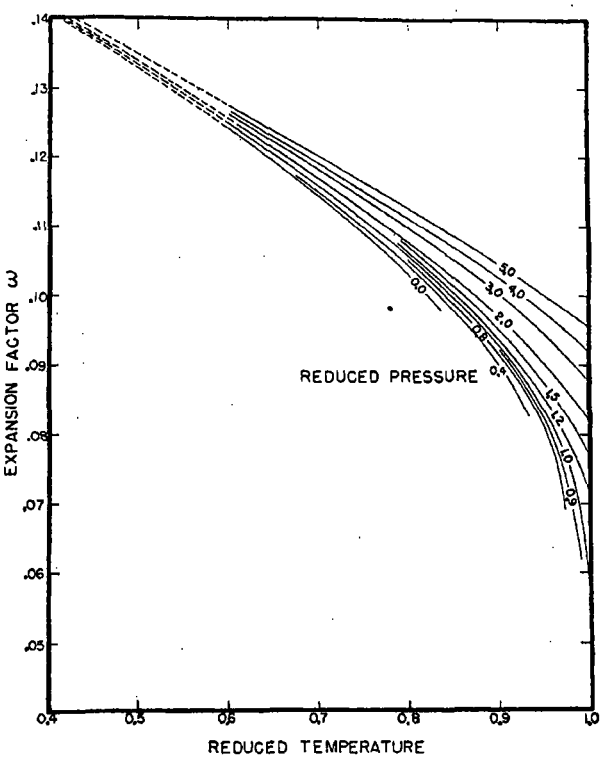

Figure 1. Thermal Expansion and Compressibility of Liquids

Table II. Densities of Compressed Liquids

Pressure, Lb./Sq. In.	Reduced Pressure	Density, Gram/Co. Calcd.	Exptl.	Calcd.	Exptl.	Calcd.	Exptl.
WATER (*12*): ρ_1/ω_1 = 7.586 AT 100° C., 1 ATM.		204.4° C., T_r = 0.738		348.9° C., T_r = 0.961		374.3° C., T_r = 1.0	
1000	0.312	0.842	0.864	....	....	....	....
3206	1.0	0.851	0.874	0.611	0.616	0.326	0.318
4000	1.248	0.854	0.878	0.633	0.639	0.551	0.543
5500	1.716	0.858	0.885	0.658	0.660	0.603	0.603
PROPANE (*17*): ρ_1/ω_1 = 4.807 AT 21.0° C., 200 LB./SQ. IN.		54.5° C., T_r = 0.878		71.1° C., T_r = 0.921		87.9° C., T_r = 0.966	
300	0.466	0.453	0.447	....	....	....	....
600	0.934	0.460	0.458	0.416	0.422	0.374	0.368
1500	2.35	0.485	0.482	0.460	0.458	0.431	0.430
3000	4.66	0.508	0.506	0.489	0.489	0.469	0.470
BUTANE (*19*): ρ_1/ω_1 = 5.037 AT 21.1° C., 250 LB./SQ. IN.		71.1° C., T_r = 0.809		104.4° C., T_r = 0.887		121.1° C., T_r = 0.926	
250	0.462	0.521	0.522	0.467	0.461	0.427	0.411
500	0.945	0.526	0.527	0.475	0.472	0.438	0.434
1500	2.84	0.546	0.545	0.508	0.501	0.487	0.475
3000	5.67	0.567	0.564	0.536	0.528	0.521	0.507

Table III. Densities of Saturated Liquids

Temperature, ° C.	Density, G./Co. Calcd.	Exptl.	Temperature, ° C.	Density, G./Co. Calcd.	Exptl.
AMMONIA (*81*): ρ_1/ω_1 = 5.463 AT −33.3° C., SATD. PRESSURE					
−73.3	0.729	0.730	37.8	0.586	0.584
−45.6	0.698	0.699	93.3	0.488	0.475
−17.8	0.664	0.664	121	0.388	0.380
+10	0.626	0.625	133 (T_c)	0.240	0.234
ETHYL ALCOHOL (*11*): ρ_1/ω_1 = 6.210 AT 20° C., SATD. PRESSURE					
0	0.809	0.806	60	0.746	0.755
40	0.768	0.772	80	0.721	0.735
			243.1 (T_c)	0.273	0.275

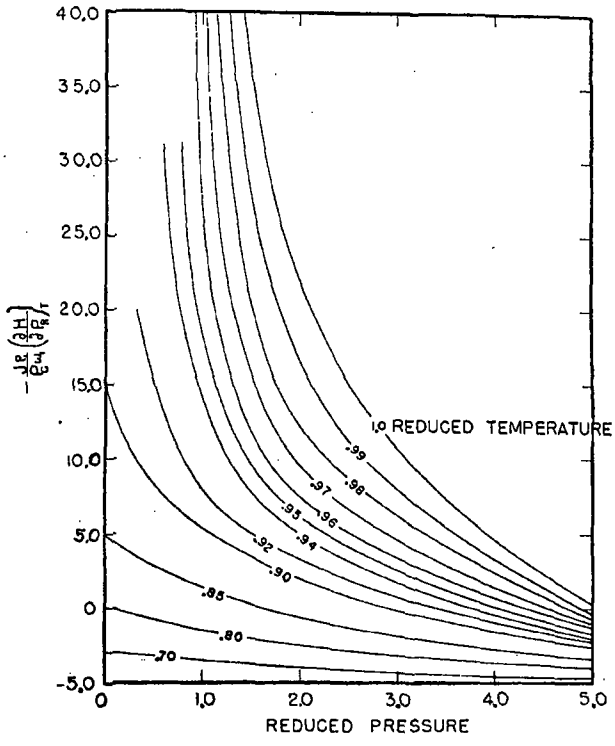

Figure 2. Differential Effect of Pressure on Enthalpy of Liquids

its critical pressure and the enthalpy at the same temperature and other pressures:

$$\frac{J\rho_1}{P_c\omega_1}(H_{cp} - H)_T = \int_{p_r}^{1.0} \frac{J\rho_1}{P_c\omega_1}\left(\frac{\partial H}{\partial p_r}\right)_T dp_r \qquad (7)$$

The results of this integration are summarized in Figure 3 and Table V.

Unfortunately few data are available with which to compare the enthalpy corrections calculated from Figure 3. Table VI compares the calculated values and those experimentally evaluated for water and propane. The agreement is reasonably good for both compounds. In view of the fact that the pressure correction is relatively small as compared to the enthalpy changes ordinarily encountered in industrial operations, it is believed that Figure 3 may be safely used for many engineering applications. The fact that a relation based on data for pentane is in even fair agreement with such dissimilar materials as water and propane is reassuring as to its generality.

PRESSURE CORRECTION TO ENTROPY

The effect of pressure on the entropy of any substance is expressed by the rigorous thermodynamic equation:

$$J\left(\frac{\partial S}{\partial p}\right)_T = -\left(\frac{\partial V}{\partial T}\right)_p \qquad (8)$$

Expressing in terms of reduced conditions and combining with Equation 3,

$$\frac{J\rho_1 T_c}{\omega_1 P_c}\left(\frac{\partial S}{\partial p_r}\right)_T = -\left(\frac{\partial \frac{1}{\omega}}{\partial T_r}\right)_p \qquad (9)$$

Equation 9 may be integrated to obtain a useful correction chart relating the difference between entropy under the critical pressure and entropy at any other pressure under the same temperature:

$$\frac{J\rho_1 T_c}{\omega_1 P_c}(S_{cp} - S)_T = \int_{p_r}^{1.0} -\left(\frac{\partial \frac{1}{\omega}}{\partial T_r}\right)_p dp_r \qquad (10)$$

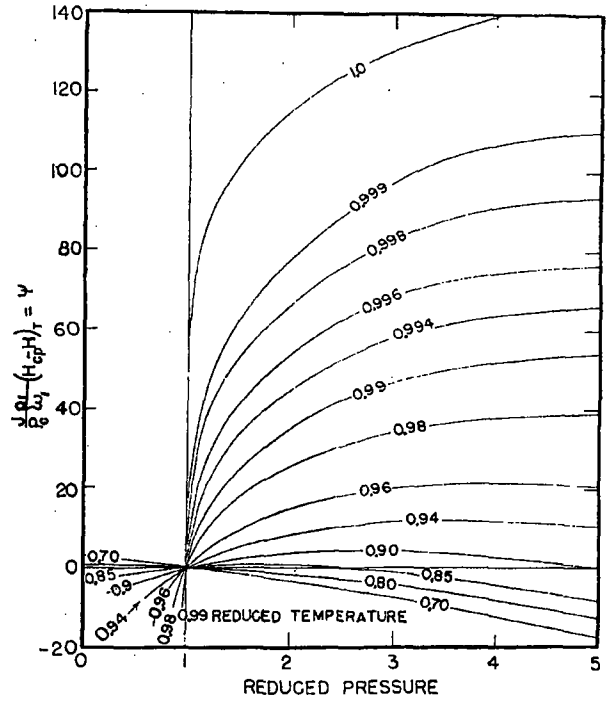

Figure 3. Pressure Correction to Enthalpy of Liquids

Table IV. Values of $-\frac{J\rho_1}{P_c\omega_1}\left(\frac{\partial H}{\partial P_r}\right)_T$

T_r	$P_r = 0$	$P_r = 0.4$	$P_r = 0.8$	$P_r = 1.0$	$P_r = 1.5$	$P_r = 2$	$P_r = 3$	$P_r = 5$
0.7	− 3.0	−3.2	− 3.4	− 3.5	− 3.8	− 4.0	− 4.4	−4.7
0.8	+ 0.1	−0.6	− 1.3	− 1.6	− 2.2	− 2.6	− 3.3	−4.1
0.85	+ 5.0	+3.1	+ 1.8	+ 1.3	+ 0.2	− 0.7	− 1.9	−3.4
0.90	+15.0	+9.1	+ 6.3	+ 5.3	+ 3.4	+ 1.9	− 0.2	−2.7
0.94	....	...	+19.0	+14.0	+ 7.7	+ 4.9	+ 1.7	−2.0
0.98	....	...	....	....	+20.3	+12.1	+ 6.2	−0.7
1.0	....	...	....	....	+36.0	+21.8	+10.7	+0.4

Table V. Values of $\frac{J\rho_1}{P_c\omega_1}(H_{cp} - H)_T = \psi$

T_r	$P_r = 0$	$P_r = 0.4$	$P_r = 0.8$	$P_r = 1.2$	$P_r = 1.5$	$P_r = 2$	$P_r = 3$	$P_r = 5$
0.7	+3.1	+2	+0.8	− 0.7	− 1.8	− 3.4	− 7.3	− 17.2
0.8	+0.8	+0.5	+0.1	− 0.2	− 0.7	− 1.4	− 4.0	− 12.3
0.85	−3.2	−1.8	−0.5	+ 0.4	+ 0.9	+ 1.0	− 0.9	− 8.0
0.9	...	−5.0	−1.7	+ 1.0	+ 2.2	+ 3.7	+ 4.4	+ 0.2
0.94	...	...	−3.5	+ 2.1	+ 5.2	+ 8.2	+ 11.8	+ 10.8
0.98	...	...	...	+10.0	+ 18	+ 25.8	+ 20.2	+ 39.3
0.99	...	...	...	+15.0	+ 24.9	+ 35.0	+ 47	+ 54.1
0.999	...	...	...	+46.5	+ 62.5	+ 77.8	+ 97.6	+110.3
1.0	...	...	...	+87.0	+101.5	+115.2	+130.5	.....

Values $[\partial(1/\omega)/\partial T_r]_p$ were obtained from Figure 1 in deriving Figure 2. The resulting integrated pressure correction to entropy is plotted against reduced temperature and pressure in Figure 4 and summarized in Table VII. Table VIII compares values calculated from Figure 4 with experimental values for water and propane. The agreement appears to be somewhat better than that of the enthalpy correction, indicating that generalization is sufficiently sound for useful application.

PRESSURE CORRECTION TO HEAT CAPACITY AT CONSTANT PRESSURE

A useful expression for the effect of pressure on heat capacity at constant pressure may be derived by designating the right-hand side of Equation 7 as ψ, a function of reduced temperature and pressure:

$$\frac{J\rho_1}{P_c\omega_1}(H_{cp} - H)_T = \psi \qquad (11)$$

Upon differentiation at constant pressure,

$$\frac{J\rho_1}{P_c\omega_1}\left[\left(\frac{\partial H_{cp}}{\partial T}\right)_p - \left(\frac{\partial H}{\partial T}\right)_p\right]_T = \frac{1}{T_c}\left(\frac{\partial \psi}{\partial T_r}\right)_p$$

$$\text{or} \quad \frac{J\rho_1 T_c}{\omega_1 P_c}(C_{cp} - C_p)_T = \left(\frac{\partial \psi}{\partial T_r}\right)_p \qquad (12)$$

The results of graphically differentiating Figure 3 in accordance with Equation 12 are summarized in Figure 5 and Table IX. A comparison of values calculated from Figure 5 with those derived from experimental data for water is shown in Table X. Additional data for testing this relation are scanty, but the agreement with the data on water is sufficiently good to indicate that the generalization did not lose greatly in accuracy through the series of manipulations employed in deriving Figure 5.

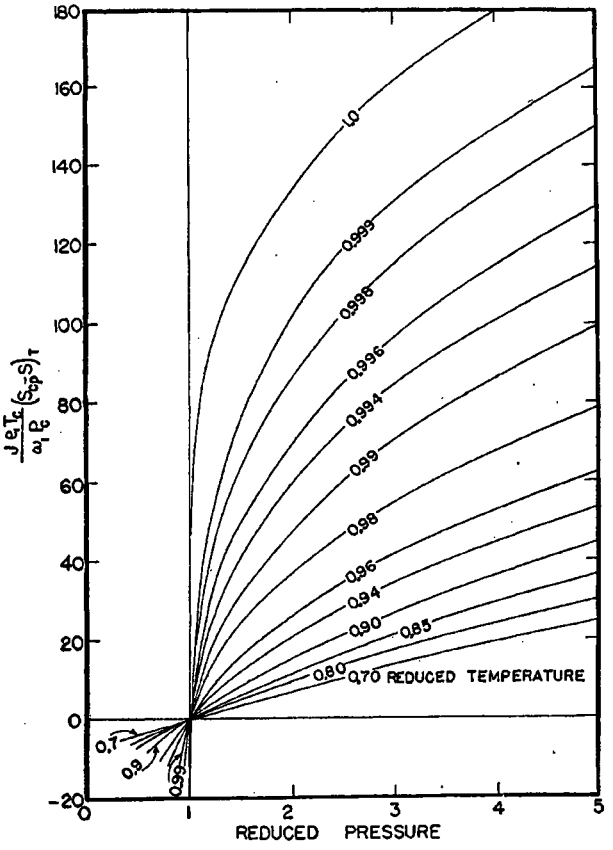

Figure 4. Pressure Correction to Entropy of Liquids

Table VI. Pressure Correction to Enthalpy

Pressure, Lb./Sq. In.	$(H_{cp} - H)_T$, cal./gram mole: 204.4° C. Calcd.	204.4° C. Exptl.	348.9° C. Calcd.	348.9° C. Exptl.	374.3° C. Calcd.	374.3° C. Exptl.
	WATER (18)					
1000	23	28	...	...	....	....
2500	8	10	−107	−115	....	....
4000	− 8	− 9	+ 75	+ 79	+1130	+1266
5500	−26	−32	+164	+172	+1370	1526
	PROPANE (17)					
	54.5° C.		71.1° C.		87.9° C.	
300	−29	−25	...	...	....	....
1500	+18	+12	+68	+63	+205	+200
3000	−28	−21	+58	+45	+260	+256

Table VII. Values of $\frac{J\rho_1 T_c}{\omega_1 P_c}(S_{cp} - S)_T$

T_r	$P_r = 0.4$	$P_r = 0.8$	$P_r = 1.2$	$P_r = 1.5$	$P_r = 2$	$P_r = 3$	$P_r = 5$
0.7	−4.6	−1.7	+ 1.1	+ 3.2	+ 6.9	+ 13.8	+ 25.0
0.9	...	−3.6	+ 3.8	+ 8.5	+ 15.5	+ 26.9	+ 44.9
0.94	...	−7.1	+ 5.6	+ 12.2	+ 20.8	+ 34.7	+ 53.8
0.98	...	...	+13.2	+ 24.6	+ 37.3	+ 55.1	+ 79.0
0.99	...	...	+18.3	+ 31.9	+ 47.7	+ 71.0	+ 99.9
0.996	...	...	+32.1	+ 50.0	+ 70.2	+ 96.9	+130.0
0.999	...	...	+50.7	+ 76.9	+102.0	+130.9	+165.6
1.0	...	...	+93.2	+113.0	+134.0	+161.5	.....

HEAT OF VAPORIZATION

An empirical graphical generalization was developed by the author (*22*) which satisfactorily represents the effect of temperature on the heat of vaporization of a variety of polar and nonpolar compounds. A curve, based on the available data for all materials, was presented from which the heat of vaporization at any reduced temperature can be calculated if one value at a known reduced temperature is available. The Kistiakowsky equation offers a satisfactory method of estimating heats of vaporization at the normal boiling points for nonpolar compounds but does not apply to polar materials.

A satisfactory generalized method for estimating the heat of vaporization of any substance at any temperature was developed by Meissner (*14*). This method shows good agreement with experimental results, particularly at high temperatures. It becomes somewhat unsound at low reduced temperatures, but even in this range the errors are not ordinarily serious. The method here presented is an alternate to Meiss-

Table VIII. Pressure Correction to Entropy

Pressure, Lb./Sq. In.	$(S_{cp} - S) \times 10^3$ cal./gram mole/° K.: 204.4° C. Calcd.	204.4° C. Exptl.	348.9° C. Calcd.	348.9° C. Exptl.	374.3° C. Calcd.	374.3° C. Exptl.
	WATER (18)					
1000	−115	−100	....	....	....	....
2500	− 37	− 32	− 249	−242	....	....
4000	+ 88	+ 33	+ 194	187	1900	2030
5500	+112	+ 96	+ 430	445	2400	2545
	PROPANE (17)					
	54.5° C.		71.1° C.		87.9° C.	
300	−235	−238	...	...	....	....
1500	+470	+442	+630	591	+915	+970
3000	+990	+984	+1215	1200	+1670	+1790

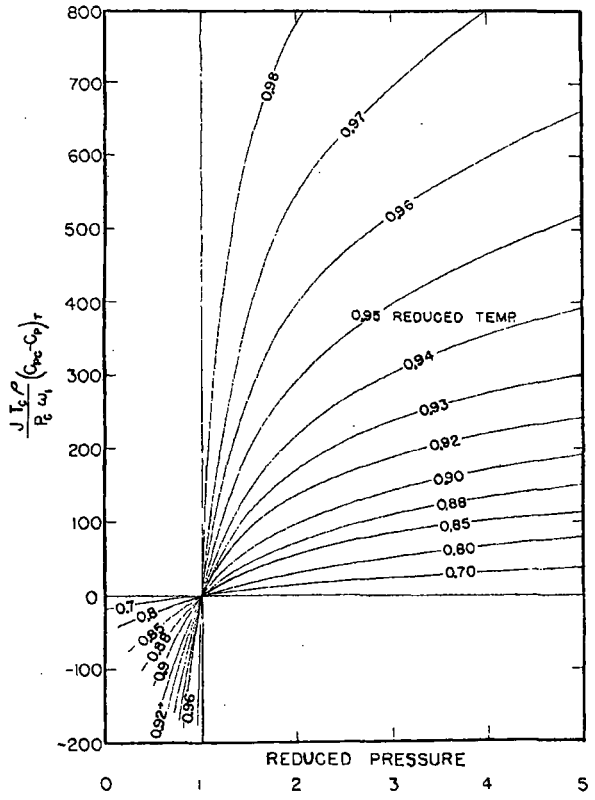

Figure 5. Pressure Correction to Heat Capacity at Constant Pressure of Liquids

ner's method, with the advantage of not involving any graphical relations and consequently being adaptable to mathematical manipulation for the derivation of other thermodynamic functions. It is perhaps somewhat more dependable than Meissner's method at low reduced temperatures.

It has been found that the general curve, referred to above (*22*) and expressing the relation between heat of vaporization and reduced temperature, is represented by the following empirical equation:

$$\lambda = \lambda_1 \left(\frac{1 - T_r}{1 - T_{r_1}}\right)^{0.38} \tag{13}$$

This equation is more convenient to use than the original curve and gives considerably more reproducible results, particularly at temperatures near the critical. It is in good agreement with the available data with the exception of water at low temperatures, below the normal boiling point. As previously mentioned, water is unusual in many of its characteristics in this region.

Heats of vaporization may be accurately calculated at any temperature from the rigorously correct Clapeyron equation:

$$\frac{dp_s}{dT} = \frac{\lambda}{T(v_g - v_l)} \tag{14}$$

The molal volume of the vapor, v_g, may be calculated from the generalized gas compressibility factors while the volume of the liquid, v_l, is obtained from Equation 3 and Figure 1. Where complete vapor pressure data are not available, excellent approximations can be obtained from only the boiling point and the critical temperature and pressure by use of a reference substance method of plot ting such as that introduced

Table IX. Values of $\frac{JT_c\rho_1}{P_c\omega_1}(C_{cp} - C_p)_T$

T_r	$P_r = 0.4$	$P_r = 0.8$	$P_r = 1.2$	$P_r = 1.5$	$P_r = 2$	$P_r = 3$	$P_r = 5$
0.7	− 9	− 3	+ 3	+ 7	+ 14	+ 23	+ 38
0.8	−28	− 9	+ 6	+ 16	+ 30	+ 52	+ 80
0.9	..	− 42	+ 30	+ 62	+ 98	+142	+192
0.94	..	− 75	+ 70	+143	+216	+303	+392
0.96	..	−190	+146	+272	+400	+518	+662
0.97	..	...	+208	+387	+550	+695	...
0.98	..	...	+385	+608	+778	...	...

by Cox (*5*) which permits ready determination of dp_s/dT from the corresponding values for the reference substance. However, this method is rather tedious, and the added labor is frequently not warranted by the improved accuracy obtained.

If the application of Equation 14 is restricted to the normal boiling point, a reasonably good approximation is obtained with the following modified form of the Clausius-Clapeyron equation in which the factor 0.95 represents the average deviation of the vapor from the ideal gas laws at these conditions, together with the effect of the liquid volume:

$$\left(\frac{dp_s}{dT}\right)_B = \frac{p_B\lambda_B}{0.95RT_B^2} \tag{15}$$

A simple relation between temperature and vapor pressure was developed by Calingaert and Davis (*3*) as a result of a study of the Cox method of vapor-pressure plotting:

$$\ln p_s = A - \frac{B}{T - 43} \tag{16}$$

where T is expressed in degrees Kelvin. This equation is not particularly reliable for many materials and is not recommended as a general method of predicting vapor pressures where considerable accuracy is required. However, it can be used satisfactorily for evaluating dp/dT for generalized thermodynamic relations where a high order of accuracy is not required or inherent in the other relations. Thus, differentiating Equation 16,

$$\frac{dp_s}{dT} = \frac{p_sB}{(T - 43)^2} \tag{17}$$

The constant B may be determined from any two vapor pressure values, such as the boiling point and critical point:

$$B = \frac{\ln \frac{p_c}{p_B}}{\frac{1}{T_B - 43} - \frac{1}{T_c - 43}} \tag{18}$$

Combining Equations 12 and 14,

$$\lambda_B = 0.95RB\left(\frac{T_B}{T_B - 43}\right)^2 \tag{19}$$

Table X. Pressure Correction to Heat Capacity of Water at Constant Volume (*12*)

Pressure, Lb./Sq. In.	$(C_{cp} - C_p)_T$ cal./gram mole/° K. 260° C., $T_r = 0.824$ Calcd.	Exptl.	315.6° C., $T_r = 0.910$ Calcd.	Exptl.	337.8° C., $T_r = 0.943$ Calcd.	Exptl.
1000	−0.88	−0.81	....	....	....	....
2000	−0.46	−0.38	−1.98	−1.93	....	....
2500	−0.27	−0.23	−1.15	−0.99	−2.48	−2.61
4000	+0.25	+0.27	+0.87	+0.90	+1.94	+2.02
6000	+0.74	+0.86	+2.18	+2.32	+4.40	+4.41

This equation gives results generally not differing from reliable experimental values by so much as 5 per cent when constant B is determined from the critical point and boiling point. Somewhat better results are obtained if B is evaluated from a vapor pressure value less distant from the normal boiling point than the critical temperature, and if the actual compressibility factor of the vapor is used instead of the average value of 0.95.

HEAT CAPACITY DIFFERENCE BETWEEN SATURATED LIQUID AND ITS IDEAL GAS

By combining the equations developed above with the generalized expression for the effect of pressure on the enthalpy of gases, it is possible to derive a generalized thermodynamic method for calculating the difference between the heat capacity of a saturated liquid and the same material as an ideal gas at the same temperature and zero pressure. Such a

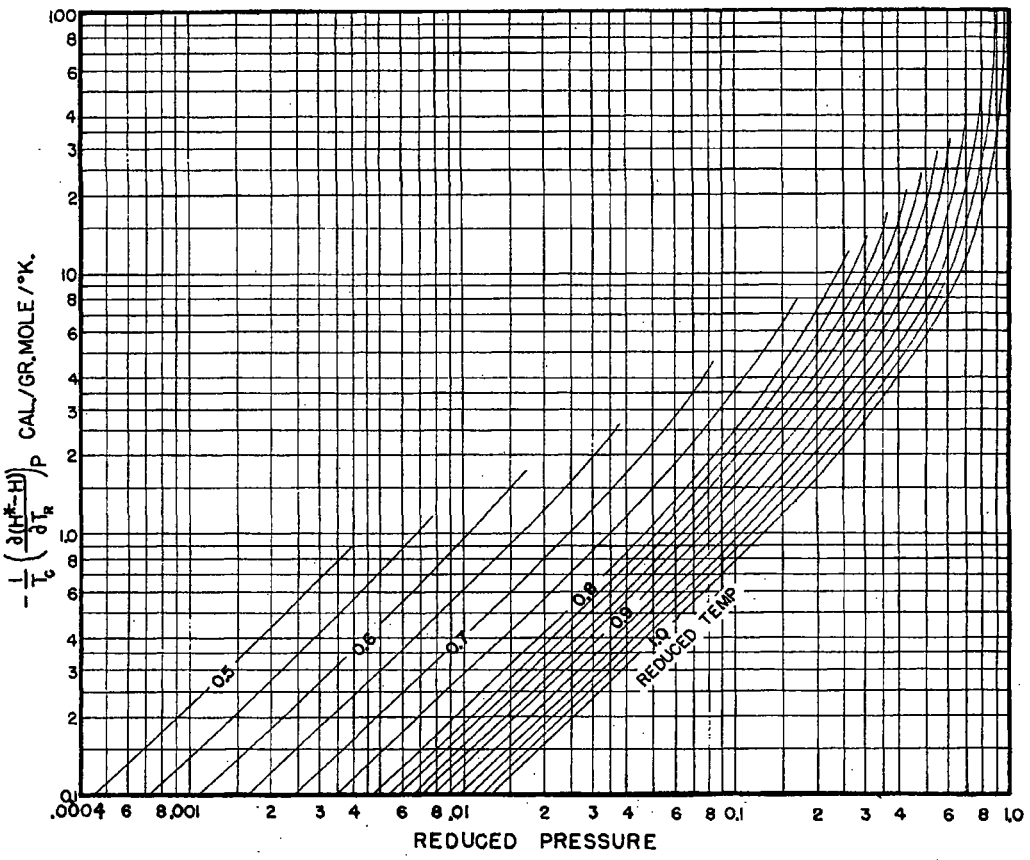

Figure 6. Differential Pressure Correction to Enthalpy of Gases

Combining Equations 13 and 19, an expression is obtained which permits calculation of the heat of vaporization of any substance at all conditions from a knowledge merely of the boiling point and critical temperature and pressure, since B is also found from T_c and P_c:

$$\lambda = 0.95RB\left(\frac{T_B}{T_B - 43}\right)^2\left(\frac{1 - T_r}{1 - T_{rB}}\right)^{0.38} \qquad (20)$$

Table XI compares values calculated from Equation 20 with experimental data for several compounds on which measurements were made at elevated temperatures. The deviations are of the same order as shown by Meissner's method; they are greater in some cases and less in others. Further comparisons indicated that the major source of error is Equation 19 rather than Equation 13, and the over-all accuracy is improved by using the actual compressibility factor at the boiling point instead of the average value of 0.95.

method is of considerable value because of the scarcity and general unreliability of heat capacity data. Recent development of generalized statistical methods (*1*, *6*) derived from spectroscopic observations permits reasonably satisfactory prediction of the heat capacities of the more simple molecules in the ideal gaseous state. These methods, combined with a thermodynamic relation between gaseous and liquid heat capacities and the relations for thermodynamic properties of liquids developed above, will permit complete prediction of heat capacities at all conditions, both liquid and gaseous. Conversely, for complex high-boiling liquids on which liquid heat capacity measurements have been made, such a thermodynamic relation may offer a more reliable method of estimating gaseous heat capacities than the statistical methods. The relation will also be useful in rationalizing experimental observations of gaseous and liquid heat capacities and making them consistent with each other.

There are several methods by which a saturated liquid at temperature T_1 may be converted into a saturated vapor at a

higher temperature T_2. One is to heat the liquid (maintaining saturation) to T_2 and vaporize it. Another is to vaporize the liquid at T_1, isothermally expand the vapor to zero pressure, heat the ideal vapor to T_2, and isothermally compress to saturation conditions. Since the initial and final states are the same in both cases, the enthalpy changes of the two operations must be equal:

$$\lambda_1 + (H_1^* - H_{s_{g_1}}) + C_{pg}^* (T_2 - T_1) - (H_2^* - H_{s_{g_2}}) = \lambda_2 + C_{sl}(T_2 - T_1) \quad (21)$$

Rearranging and applying to an infinitesimal temperature change, dT,

$$(C_{sl} - C_{pg}^*)\, dT = -d\lambda - d(H^* - H_{sg})$$

$$C_{sl} - C_{pg}^* = -\frac{d\lambda}{dT} - \frac{d(H^* - H_{sg})}{dT} \quad (22)$$

Since the term $d(H^* - H_{sg})$ involves both a temperature and a pressure change, it must be expressed in terms of partial differentials:

$$\frac{d(H^* - H_{sg})}{dT} = \left[\frac{\partial(H^* - H_{sg})}{\partial T}\right]_p + \left[\frac{\partial(H^* - H_{sg})}{\partial p}\right]_T \frac{dp_s}{dT} \quad (23)$$

All the terms on the right-hand side of Equation 24 may be obtained from generalizations, presumably applicable to all substances. Thus, differentiating Equation 20,

$$\frac{d\lambda}{dT_r} = \frac{-0.361RB}{(1 - T_{rB})^{0.38}} \left(\frac{T_B}{T_B - 43}\right)^2 \frac{1}{(1 - T_r)^{0.62}} \quad (25)$$

A generalized relation between $(H^* - H_s)$ and reduced temperature and pressure was introduced by Watson and Nelson (*23*) and improved by several others (*8*, *10*, *24*, *26*). Graphical differentiation of this relation with respect to reduced temperature at constant pressure permits evaluation of the second term of Equation 24. The first part of the third term similarly may be evaluated by differentiation with respect to reduced pressure at constant temperature. The last part of the third term is evaluated by Equation 17.

For differentiation, a pressure-enthalpy correction chart for the gaseous state was prepared, taking into account the improved data calculated by Edmister (*8*) and York and Weber (*26*) and extended to the low reduced temperature range by the Joule-Thomson data on water (*11*). This chart was graphically differentiated with respect to temperature and pressure, and the data obtained are summarized in Figures 6 and 7 and in Tables XII and XIII. Because of the uncertainty of the basic enthalpy correction chart at conditions in the saturated region, particularly at low temperatures, the curves of Figures 6 and 7 were adjusted by cross plotting to obtain consistent relations which, when incorporated in Equation 24, gave the best average agreement with the ex-

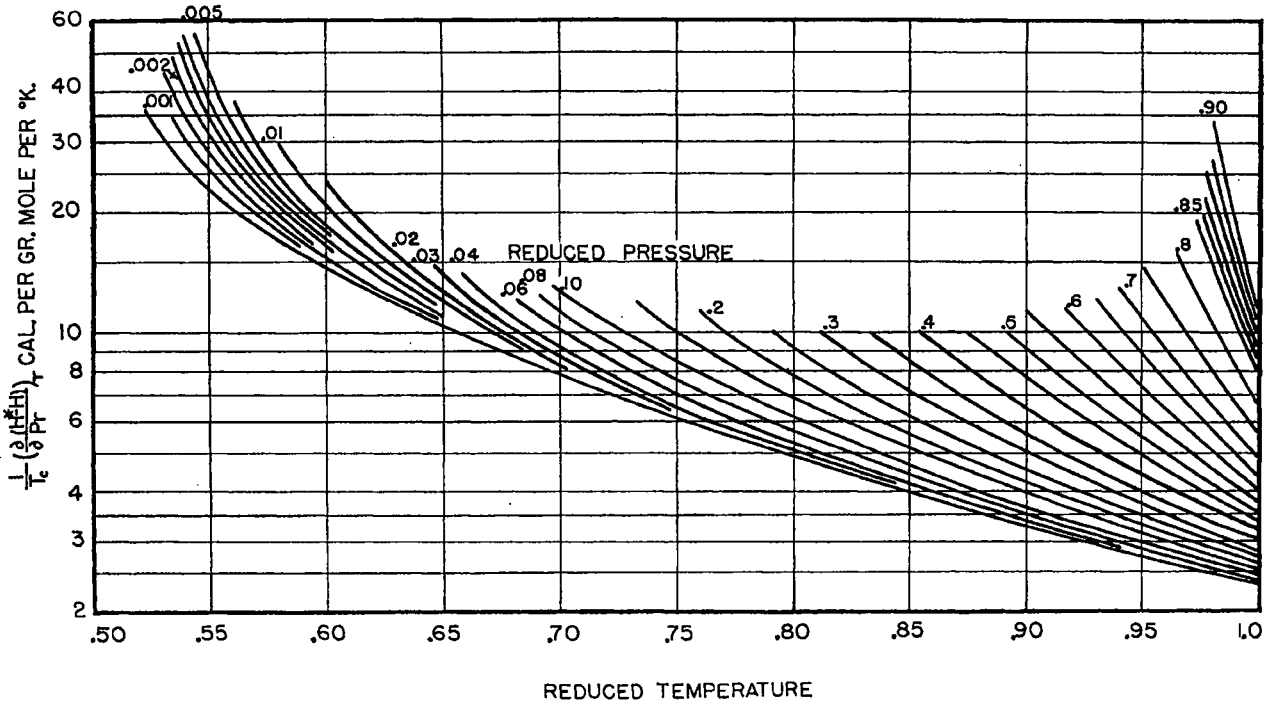

Figure 7. Differential Pressure Correction to Enthalpy of Gases

Substituting Equation 23 in 22 and writing in terms of reduced conditions,

$$C_{sl} - C_{pg}^* = -\left(\frac{d\lambda}{dT_r}\right)\frac{1}{T_c} - \left[\frac{\partial(H^* - H_s)}{\partial T_r}\right]_p \frac{1}{T_c} - \left[\frac{\partial(H^* - H_s)}{\partial p_r}\right]_T \frac{1}{P_c}\frac{dp_s}{dT} \quad (24)$$

Table XI. Heats of Vaporization

Temperature, ° C.	λ, cal./gram mole Calcd.	Exptl.	Temperature, ° C.	λ, cal./gram mole Calcd.	Exptl.
		WATER (*12*)			
83	9,680	9,890	277	6,380	6,720
115	9,250	9,530	307	5,460	5,740
147.5	8,800	9,110	322	5,020	5,240
180.5	8,300	8,660	335	4,500	4,670
210.5	7,740	8,140	348.5	3,850	3,980
245	7,100	7,470	364	2,960	3,040
			373.3	1,020	1,060
		AMMONIA (*21*)			
−49.9	5,870	5,770	91.8	3,310	(3,180)
− 9.5	5,340	5,260	100	3,045	(3,050)
+31.0	4,690	4,640	108.1	2,730	(2,700)
71.6	3,870	(3,780)	116.2	2,340	(2,250)
			124.8	1,800	(1,640)
		BENZENE (*11*)			
0	8,250	8,350	180	5,700	5,790
60	7,680	7,600	220	4,780	4,850
100	7,000	7,060	260	3,420	3,420
140	6,400	6,440	280	2,160	2,140
		ETHYL ALCOHOL (*11*)			
0	10,450	10,110	160	6,950	7,150
40	9,760	9,900	200	5,650	5,280
80	8,970	9,350	220	4,260	3,960
120	8,090	8,350	240	1,990	1,760
		BUTANE (*19*)			
24.9	5,140	5,050	110.9	3,380	3,170
67.9	4,400	4,310			
		PROPANE (*17*)			
20.8	3,680	3,460	88.1	1,785	1,490
54.8	2,960	2,780	98.1	916	610
73.8	2,410	2,210			
		SULFUR DIOXIDE (*11*)			
−10	5,930	6,090	40	5,180	4,950
+20	5,490	5,400	60	4,810	4,500

perimental values of $(C_{sl} - C_s^*)$ for water and ammonia. In all of this work Equations 16 and 18 were used for the calculation of vapor pressures, and it is recommended that this procedure be followed in using Figures 6 and 7.

Figure 7 is not in good agreement with $(\partial H/\partial P)_T$ data calculated by Kennedy, Sage, and Lacey (*13*) from their Joule-Thomson measurements on *n*-butane and *n*-pentane. Edmister (*8*) pointed out that the data of these investigators did not conform with his generalized relations. Similarly, Watson and Smith (*24*) found that a generalized plot of Joule-Thomson coefficients showed large differences from the experimental data. These discrepancies indicate that differentiation of the generalized enthalpy-pressure relation tends to magnify its inherent errors. It is probable that the absolute values of the functions plotted in Figures 6 and 7 may differ from experimental values for some substances by as much as 50 per cent. However, it is hoped that these errors will tend to compensate one another when the two charts are used together in conjunction with Equation 24 and Equations 16 and 18 for calculating pressures.

Heat capacity data in general are so unreliable that it is difficult to find good comparable values on both the liquid and gaseous state with which to test Equation 24. Table XIV compares values calculated from the equation with experimental data for water, ammonia, pentane, butane, and propane. The experimental values for the hydrocarbons were taken from the general correlation of Holcomb and Brown (*9*) at temperatures below 70° F. These are actually heat capacities at constant pressure, but at reduced temperatures below 0.8 the difference from the heat capacity of the saturated liquid becomes small. At higher temperatures the data of Sage and co-workers from the indicated sources were selected. These investigators made actual measurements of the heat capacities of the saturated liquid.

The agreement in Table XIV is reasonably good except in the case of butane at the higher temperatures. Although these few comparisons do not confirm the reliability of Equation 24, it is encouraging that agreement is obtained on both nonpolar and highly polar compounds of both low and high boiling points. Figures 6 and 7 are not recommended for reduced temperatures above 0.96 or below 0.55. At reduced temperatures below 0.55 the difference between the heat capacity of the liquid and the ideal gas appears to approach independence of temperature, and it is believed that this assumption is preferable to attempting to extend Figure 7.

In the recommended temperature range it seems probable that the calculated heat capacity differences should not be in error by more than 25 per cent. Although much better accuracy is to be desired, such errors are not too serious, particularly when one is working with materials of high molal heat capacities for which the difference in heat capacities is

Table XII. Values of $-\frac{1}{T_c}\left(\frac{\partial(H^* - H)}{\partial T_R}\right)_p$ in Small Calories per Gram Mole per ° K.

P_r	$T_r = 0.55$	$T_r = 0.6$	$T_r = 0.7$	$T_r = 0.8$	$T_r = 0.9$	$T_r = 0.95$	$T_r = 1.0$
0.001	0.140	...	...	...	....	....	....
0.002	0.275	0.181	...	...	....	....	....
0.003	0.415	0.270	0.121	...	....	....	....
0.006	0.88	0.55	0.242	0.126	....	....	....
0.01	...	0.95	0.40	0.210	0.128	....	....
0.02	...	...	0.80	0.42	0.254	0.195	0.158
0.03	...	...	1.23	0.63	0.38	0.29	0.186
0.06	...	...	2.82	1.33	0.77	0.59	0.47
0.1	...	...	...	2.46	1.34	1.0	0.79
0.2	...	...	...	7.0	3.12	2.20	1.63
0.4	...	...	...	...	9.5	5.7	4.0
0.5	...	...	...	...	18.5	8.6	5.7
0.7	...	...	...	...	.....	27	11.4
0.9	...	...	...	...	.....	....	33

Table XIII. Values of $\frac{1}{T_c}\left(\frac{\partial(H^* - H)}{\partial P_r}\right)_T$ in Small Calories per Gram Mole per ° K.

P_r	$T_r = 0.55$	$T_r = 0.6$	$T_r = 0.7$	$T_r = 0.8$	$T_r = 0.9$	$T_r = 0.95$	$T_r = 0.98$	$T_r = 1.0$
0.001	25.2	14.6	7.8	4.88	3.29	2.73	2.48	2.32
0.002	32.0	15.8	7.9	4.88	3.29	2.73	2.48	2.32
0.005	46	17.5	8.0	4.88	3.29	2.73	2.48	2.32
0.01	..	20.8	8.1	4.88	3.29	2.73	2.48	2.32
0.02	..	24.0	8.2	4.88	3.29	2.73	2.48	2.32
0.03	..	..	8.5	5.0	3.35	2.73	2.48	2.32
0.06	..	..	10.1	5.25	3.4	2.80	2.50	2.34
0.10	..	..	12.8	6.05	3.55	3.00	2.64	2.44
0.2	..	..	..	7.8	4.20	3.29	2.88	2.63
0.3	..	..	..	11.7	5.0	3.70	3.15	2.84
0.5	..	..	..	...	9.0	5.45	4.15	3.5
0.6	..	..	..	...	..	7.3	5.05	4.0
0.7	..	..	..	...	..	10.9	6.6	4.8
0.8	..	..	..	...	..	...	10.7	6.6
0.85	..	..	..	...	..	...	15.0	8.1
0.90	..	..	..	...	..	...	34.0	11.2

Table XIV. Difference between Heat Capacities of Saturated Liquid and Its Ideal Gas

		$(C_{sl} - C^*_{pg})$, cal./g. mole/° K.				$(C_{sl} - C^*_{pg})$, cal./g. mole/° K.	
T_r	T° C.	Calcd.	Exptl.	T_r	T° C.	Calcd.	Exptl.
			Water (*12*)				
0.55	83	11.0	10.0	0.85	277	14.4	13.6
0.60	115	11.5	10.1	0.90	307	17.0	16.4
0.65	147.5	11.5	10.3	0.92	322.5	18.6	18.0
0.70	180.5	11.8	10.7	0.94	335	20.7	20.7
0.75	210.5	11.9	11.2	0.96	348.5	28.0	25.1
0.80	243	12.3	11.6				
			Ammonia (*21*)				
0.55	−49.9	9.8	9.8	0.85	71.6	12.9	12.6
0.60	−29.8	9.9	1.0	0.90	91.8	15.1	14.7
0.65	− 9.5	9.8	10.2	0.92	100.0	17.1	16.2
0.70	+10.7	10.4	10.5	0.94	108.1	16.9	17.8
0.75	31.0	10.7	10.9	0.96	116.2	19.9	20.9
0.80	51.3	11.4	11.5				
			n-Pentane (*9*)				
0.55	−14.6	9.9	10.0	0.7	55.9	11.4	11.9
0.6	+ 8.9	10.1	10.4	0.8	103.9	11.6	13.6
			n-Butane (*9, 15, 20*)				
0.55	−39.1	8.7	7.6	0.8	67.9	10.3	14.4
0.6	−17.1	8.8	8.7	0.9	110.9	12.9	17.6
0.7	+24.9	9.4	10.9				
			Propane (*9, 15, 20*)				
0.55	−67.7	5.2	6.1	0.8	25.6	8.2	9.3
0.6	−49.1	5.8	6.4	0.9	63.0	13.5	13.4
0.7	−11.7	6.3	8.2				

small in comparison to the heat capacity of the vapor. At present no better general method for estimating these properties is available.

DIFFERENCE BETWEEN HEAT CAPACITY AT CONSTANT PRESSURE AND HEAT CAPACITY OF SATURATED LIQUID

The heat capacity of a saturated liquid C_{sl} expresses the change in enthalpy accompanying a simultaneous increase in both temperature and pressure:

$$C_{sl} = \left(\frac{\partial H}{\partial T}\right)_p + \left(\frac{\partial H}{\partial p}\right)_T \frac{dp_s}{dT} \qquad (26)$$

In terms of reduced conditions,

$$(C_{pl} - C_{sl})_{TP} = -\left(\frac{\partial H}{\partial p_r}\right)_T \frac{1}{P_c}\left(\frac{dp_s}{dT}\right) \qquad (27)$$

Values of $\frac{1}{P_c}\left(\frac{\partial H}{\partial p_r}\right)$ may be obtained from Figure 2, and dp_s/dT is calculated from Equation 17, permitting complete evaluation of Equation 27.

Table XV. Difference between Heat Capacity at Constant Pressure and Heat Capacity of Saturated Liquid (Water, *12*)

		$(C_p - C_s)$, cal./g. mole/° K.	
T° C.	T_r	Calcd.	Exptl.
204.4	0.738	−0.08	−0.09
287.8	0.867	+0.33	+0.54
315.6	0.910	+0.92	+1.11
326.7	0.927	+1.75	+2.16
337.8	0.943	+3.0	+3.64

Table XV compares results calculated from Equation 27 with the accepted values for water. The agreement is not particularly good, but the quantity sought is not large except at conditions near the critical. Furthermore, it is believed that maximum errors are probably encountered when Figure 2 is applied to water because of the unusually low reduced pressures corresponding to a given reduced temperature at saturation. As a result, saturation values for water fall on the extrapolated portion of Figure 2 at pressures below the range of the hydrocarbon data from which it was derived. Better accuracy should be obtained from Equation 27 when applied to other materials of lower critical pressures.

ACKNOWLEDGMENT

This investigation was carried out with the financial support of the Wisconsin Alumni Research Foundation, under the sponsorship of the University Research Committee. The helpful criticism and suggestions of O. A. Hougen are gratefully acknowledged.

NOMENCLATURE

A, B = constants in Calingaert-Davis vapor pressure equation
C = heat capacity
C^* = heat capacity of ideal gas
d = liquid density
H = enthalpy
H^* = enthalpy of ideal gas
J = mechanical equivalent of heat
M = molecular weight
p = pressure
P = pressure
R = gas law constant
S = entropy
T = absolute temperature
v = molal volume
V = volume of n moles
z = compressibility factor (gaseous)
λ = molal heat of vaporization
ρ = liquid density, mass per unit volume
ψ = $\frac{J\rho_l}{P_c\omega_l}(H_{ep} - H)_T$
ω = liquid expansion factor

Subscripts
B = normal boiling point
c = critical value
cp = critical pressure
g = gaseous state
l = liquid state
r = reduced value
s = saturated liquid or vapor

LITERATURE CITED

(1) Bennewitz and Rossner, *Z. physik. Chem.*, **39B**, 126 (1938).
(2) Brown, G. G., Souders, M., and Smith, R. L., Ind. Eng. Chem., 24, 513 (1932).
(3) Calingaert, G., and Davis, D. S., *Ibid.*, **17**, 1287 (1925).
(4) Cope, J. Q., Lewis, W. K., and Weber, H. C., *Ibid.*, **23**, 887 (1931).
(5) Cox, E. R., *Ibid.*, 15, 592 (1923).
(6) Dobratz, C. J., *Ibid.*, 33, 759 (1941).
(7) Dodge, B. F., *Ibid.*, 24, 1353 (1932).
(8) Edmister, W. C., *Ibid.*, 30, 352 (1938).
(9) Holcomb, D. E., and Brown, G. G., *Ibid.*, 34, 590 (1942).
(10) Hougen and Watson, "Industrial Chemical Calculations", 2nd ed., New York, John Wiley & Sons, 1936.
(11) International Critical Tables, New York, McGraw-Hill Book Co., 1926.
(12) Keenan and Keyes, "Thermodynamic Properties of Steam", New York, John Wiley & Sons, 1936.
(13) Kennedy, E. R., Sage, B. H., and Lacey, W. N., Ind. Eng. Chem., 28, 718 (1936).
(14) Meissner, H. P., *Ibid.*, 33, 1440 (1941).
(15) Sage, B. H., and Lacey, W. N., *Ibid.*, 27, 1484 (1935).
(16) *Ibid.*, 34, 730 (1942).
(17) Sage, B. H., Lacey, W. N., and Schaafsma, J. G., *Ibid.*, 26, 1218 (1934).
(18) *Ibid.*, 27, 48 (1935).
(19) Sage, B. H., Webster, D. C., and Lacey, W. N., *Ibid.*, 29, 1188 (1937).
(20) *Ibid.*, 29, 1309 (1937).
(21) U. S. Bur. of Standards, *Circ.* 142 (1923).
(22) Watson, K. M., Ind. Eng. Chem., 23, 360 (1931).
(23) Watson, K. M., and Nelson, E. F., *Ibid.*, 25, 880 (1933).
(24) Watson, K. M., and Smith, R. L., *Natl. Petroleum News*, July, 1936.
(25) York, R., Ind. Eng. Chem., 34, 535 (1942).
(26) York, R., and Weber, H. C., *Ibid.*, 32, 388 (1940).

WVMP SAR Reference 3-26

CRC Handbook of Chemistry and Physics, 75th. ed., CRC Press, Boca Raton, Florida, 1994.

Pages 6-10 to 6-11.

PROPERTIES OF WATER IN THE RANGE 0 — 100 °C

This table summarizes the best available values of the density, specific heat capacity at constant pressure (C_p), vapor pressure, viscosity, thermal conductivity, dielectric constant, and surface tension for liquid water in the range 0 — 100 °C. All values (except vapor pressure) refer to a pressure of 100 kPa (1 bar). The temperature scale is IPTS-68.

t / °C	Density / g/cm³	C_p / J/g K	Vap. pres. / kPa	Visc. / μPa s	Ther. cond. / mW/K m	Diel. const.	Surf. ten. / mN/m
0	0.99984	4.2176	0.6113	1793	561.0	87.90	75.64
10	0.99970	4.1921	1.2281	1307	580.0	83.96	74.23
20	0.99821	4.1818	2.3388	1002	598.4	80.20	72.75
30	0.99565	4.1784	4.2455	797.7	615.4	76.60	71.20
40	0.99222	4.1785	7.3814	653.2	630.5	73.17	69.60
50	0.98803	4.1806	12.344	547.0	643.5	69.88	67.94
60	0.98320	4.1843	19.932	466.5	654.3	66.73	66.24
70	0.97778	4.1895	31.176	404.0	663.1	63.73	64.47
80	0.97182	4.1963	47.373	354.4	670.0	60.86	62.67
90	0.96535	4.2050	70.117	314.5	675.3	58.12	60.82
100	0.95840	4.2159	101.325	281.8	679.1	55.51	58.91
Ref.	1—3	2	1, 3	3	3	4	5

REFERENCES

1. L. Harr, J. S. Gallagher, and G. S. Kell, *NBS/NRC Steam Tables*, Hemisphere Publishing Corp., 1984.
2. K. N. Marsh, Ed., *Recommended Reference Materials for the Realization of Physicochemical Properties*, Blackwell Scientific Publications, Oxford, 1987.
3. J. V. Sengers and J. T. R. Watson, Improved international formulations for the viscosity and thermal conductivity of water substance, *J. Phys. Chem. Ref. Data*, 15, 1291, 1986.
4. D. G. Archer and P. Wang, The dielectric constant of water and debye-huckel limiting law slopes, *J. Phys. Chem. Ref. Data*, 19, 371, 1990.
5. N. B. Vargaftik, et al., International tables of the surface tension of water, *J. Phys. Chem. Ref. Data*, 12, 817, 1983.

ENTHALPY OF VAPORIZATION OF WATER

The enthalpy (heat) of vaporization of water is tabulated as a function of temperature on the IPTS-68 scale.

REFERENCE

Marsh, K. N., Ed., *Recommended Reference Materials for the Realization of Physicochemical Properties*, Blackwell, Oxford, 1987.

t / °C	$\Delta_{vap}H$ / kJ/mol	t / °C	$\Delta_{vap}H$ / kJ/mol
0	45.054	200	34.962
25	43.990	220	33.468
40	43.350	240	31.809
60	42.482	260	29.930
80	41.585	280	27.795
100	40.657	300	25.300
120	39.684	320	22.297
140	38.643	340	18.502
160	37.518	360	12.966
180	36.304	374	2.066

FIXED POINT PROPERTIES OF H_2O AND D_2O

	Unit	H_2O	D_2O
Molar mass	g/mol	18.01528	20.02748
Melting point (101.325 kPa)	°C	0.00	3.82
Boiling point (101.325 kPa)	°C	100.00	101.42
Triple point temperature	°C	0.01	3.82
Triple point pressure	Pa	611.73	661
Triple point density (l)	g/cm^3	0.99978	1.1055
Triple point density (g)	mg/L	4.885	5.75
Critical temperature	°C	373.99	370.74
Critical pressure	MPa	22.064	21.671
Critical density	g/cm^3	0.322	0.356
Critical specific volume	cm^3/g	3.11	2.81
Maximum density (saturated liquid)	g/cm^3	0.99995	1.1053
Temperature of maximum density	°C	4.0	11.2

REFERENCES

L. Haar, J. S. Gallagher, and G. S. Kell, *NBS/NRC Steam Tables*, Hemisphere Publishing Corp., 1984.

J. M. H. Levelt Sengers, J. Straub, K. Watanabe, and P. G. Hill, Assessment of critical parameter values for H_2O and D_2O, *J. Phys. Chem. Ref. Data*, 14, 193, 1985.

J. Kestin, et. al., Thermophysical properties of fluid D_2O, *J. Phys. Chem. Ref. Data*, 13, 601, 1984.

J. Kestin, et. al., Thermophysical properties of fluid H_2O, *J. Phys. Chem. Ref. Data*, 13, 175, 1984.

P. G. Hill, R. D. C. MacMillan, and V. Lee, A fundamental equation of state for heavy water, *J. Phys. Chem. Ref. Data*, 11, 1, 1982.

THERMAL CONDUCTIVITY OF SATURATED H_2O AND D_2O

This table gives the thermal conductivity λ for water (H_2O or D_2O) in equilibrium with its vapor. Values for the liquid (λ_l) and vapor (λ_v) are listed, as well as the vapor pressure.

REFERENCES

1. J. V. Sengers and J. T. R. Watson, Improved international formulations for the viscosity and thermal conductivity of water substance, *J. Phys. Chem. Ref. Data*, 15, 1291, 1986.

2. N. Matsunaga and A. Nagashima, Transport properties of liquid and gaseous D_2O over a wide range of temperature and pressure, *J. Phys. Chem. Ref. Data*, 12, 933, 1983.

	H_2O			D_2O		
t/°C	*P*/kPa	λ_l/(mW/K m)	λ_v/(mW/K m)	*P*/kPa	λ_l/(mW/K m)	λ_v/(mW/K m)
0	0.6	561.0	16.49			
10	1.2	580.0	17.21	1.0	575	17.0
20	2.3	598.4	17.95	2.0	589	17.8
30	4.2	615.4	18.70	3.7	600	18.5
40	7.4	630.5	19.48	6.5	610	19.3
50	12.3	643.5	20.28	11.1	618	20.2
60	19.9	654.3	21.10	18.2	625	21.0
70	31.2	663.1	21.96	28.8	629	21.9
80	47.4	670.0	22.86	44.2	633	22.8
90	70.1	675.3	23.80	66.1	635	23.8
100	101.3	679.1	24.79	96.2	636	24.8
150	476	682.1	30.77	465	625	30.8
200	1555	663.4	39.10	1546	592	39.0
250	3978	621.4	51.18	3995	541	52.0
300	8593	547.7	71.78	8688	473	75.2
350	16530	447.6	134.59	16820	391	143.0

WVMP SAR Reference 3-27

COMSOL Multiphysics Version 4.3 Software Test Documentation, B-STP-A-00027, Revision 0, Kesterson, M.R., Savannah River National Laboratory, Aiken, South Carolina, December 3, 2012.

(Redacted version)

COMSOL Multiphysics

Versions 4.3

Software Test Documentation

B-STP-A-00027

Revision 0

December 3, 2012

Comsol Multiphysics

Software Revision Number: 4.3

Revision History Log

Revision #	Date	Description of Revision
0	10/29/12	Initial Issue

Approvals:

[redacted]

M.R. Kesterson, Author/Design Agency — Date
Applied Computational Engineering and Statistics

[redacted]

D.A. Tamburello, Independent Reviewer (IR-2) — Date
Applied Computational
Engineering and Statistics

[redacted]

W.A. Drown, Cognizant Quality Function — Date
Quality Engineering

[redacted]

S.J. Hensel, Design Authority — Date
Manager, Computational Engineering and Sciences

Table of Contents

Approvals: 3
1.0 SCOPE 5
2.0 SOFTWARE AND PRODUCT IDENTIFICATION 5
3.0 REFERENCE DOCUMENTS 5
4.0 RESOURCES 5
5.0 TESTING ACTIVITIES 6
5.1 Software Operating Environment 6
5.2 Existing Test Plans 6
5.3 Test Problems 6
5.4 Acceptance Criteria 7
5.5 Test Logs/Reports 7
5.6 Special Plant/System Configuration 7
5.7 Training Requirements 7
5.8 Schedule 7
5.9 Limiting Conditions 7
5.10 Initial Conditions 7
5.11 Error/Deficiencies Handling 8
5.12 Regression Testing 8
5.13 Recovery Plan 8
6.0 ACCEPTANCE 8
7.0 BASELINE ESTABLISHED 9
8.0 SUMMARY AND CONCLUSIONS 9
9.0 ATTACHMENTS 9

1.0 SCOPE

The software COMSOL Multiphysics is a general purpose engineering analysis program. The COMSOL software is divided into submodules that can be employed based on the type of problem being solved. For the purposes of this test plan, the Heat Transfer module is utilized to enable the modeling of heat transfer via conduction, convection, and radiation.

The Software Test Plan (STP) delineated in this document will cover the software testing, software acceptance, and software baseline of the COMSOL software.

2.0 SOFTWARE AND PRODUCT IDENTIFICATION

Project Name:	Not applicable
Software Product Name:	COMSOL Multiphysics
Operating Division:	Savannah River National Laboratory
Facility:	Applied Computational Engineering and Statistics
Location of Target System:	703-41A
Software Lead Engineer:	Matt Kesterson 703-41A, Room 255 (803) 725-5975

3.0 REFERENCE DOCUMENTS

3.1 B-SQP-A-00057, Rev. 0, "Software Quality Assurance Plan for COMSOL Multiphysics", January 2012.

3.2 IEEE Std. 829-1998, IEEE Standard for Software Test Documentation.

3.3 SRT-EMS-940084, "Heat Transfer Software Test Plan", February 1995, Attachement 9.1

4.0 RESOURCES

4.1 Test Lead Engineer

COMSOL – Matt Kesterson

4.2 Special Equipment

SRNL computer Lenovo Thinkstation 6493-AL7.

4.3 System Configuration
RedHat Enterprise Linux version 5.

5.0 TESTING ACTIVITIES

5.1 Software Operating Environment

COMSOL will operate under the RedHat Linux Operating Environment.

5.2 Existing Test Plans

None

5.3 Test Problems

For computer software, one acceptable method of testing is technical evaluation by tests which demonstrate its capability to produce valid results for the test cases. The test plan for validating the software requirements requires matching the requirements with the test problems, making sure that the test problem is well defined, building the model using the software, inputting required data such as, material properties, loading conditions, boundary conditions, setting the model for run, and finally comparing the results. One test problem can validate more than one requirement in a test run. Fifteen problems have been selected to test the code analysis options that are frequently used in analyses at SRS. These test problems are described in Attachment 9.1. These problems have been used in the past for the dedication of this type of software. For each problem, written and graphical descriptions are provided to define the problem. The option tested is identified and the expected solution is given along with the methodology used in arriving at the solution. The expected solution is obtained from an analytical solution, experimental results, or results from other industry standard software codes.

Attachment 9.1 consists of a set of problems for which solutions have been published, or for which solutions are derived using standard analytical methods, or solution comparison with other software codes, or recommended benchmark problems. The problems were selected with the intent of testing a wide range of: 1) element types, and 2) analysis procedures. 2-D, 3-D, and axisymmetric problems with radiation boundary conditions, Dirichlet (Temperature =constant), and Neumann (heat flux dT/dx = constant) boundary conditions have been solved. These test cases provide an excellent baseline for the analysis and development work which is performed in the SRNL at the SRS.

Note regarding units: When modeling heat transfer due to radiation, an absolute temperature system must be used. COMSOL does not currently have syntax for the Rankine system, the degrees F is used with input temperatures increased by 459.67, and output temperatures reduced by 459.67 (or else reported as Rankine temperatures).

5.4 Acceptance Criteria

The accuracy of solution should be within 0.5% for typical benchmark problems, and within 5% for non-standard problems in comparison with solutions from "industry accepted" codes or experiments.

5.5 Test Logs/Reports

The Test Engineer will create a test logbook for recording any errors or deficiencies encountered during testing, if necessary. The test cases and printed input/output files from the software shall also serve as test documentation. All result directories shall be preserved to verify the input parameters. Input/output files for the various test cases are listed in Attachment 9.4.

5.6 Special Plant/System Configuration

The computer system is a Lenovo Thinkstation 6493-AL7 with the RedHat Linux Enterprise Edition, version 5.

5.7 Training Requirements

The Test Engineer shall be trained in the use of the software. The Owner shall document the training and the background experience of the Test Engineer.

Testing Complete:

[redacted]

Owner, S.J. Hensel Date

[redacted]

Test Engineer, M.R. Kesterson Date

5.8 Schedule

Not Applicable.

5.9 Limiting Conditions

Not Applicable

5.10 Initial Conditions

Software shall be installed such that the program can run locally on the target machine. Material databases shall be installed along with the source file installation.

5.11 Error/Deficiencies Handling

If errors or deficiencies during testing are found, the Test Engineer shall take the following steps:

- immediately stop the testing
- contact the software Owner for error/deficiency resolution
- software Owner shall review the requirements, test method, or Test Engineer's steps to determine the source of error
- The software Owner may revise the requirement, revise the test method or revise the Test Engineer's steps to resolve the error/deficiency.

5.12 Regression Testing

If a requirement or test case is rewritten, all previously testing requirements shall be retested to ensure no adverse effects.

5.13 Recovery Plan

Not applicable.

6.0 ACCEPTANCE

Test results review and approval:

[redacted]

M.R. Kesterson, Design Agency Date

[redacted]

D.A. Tamburello, Date
Independent Reviewer (IR-2)

Owner Acceptance of Software:

[redacted]

S.J. Hensel, Owner Date

7.0 BASELINE ESTABLISHED

Test Lead Engineer:

[redacted]

M.R. Kesterson Date

Design Agency:

[redacted]

M.R. Kesterson Date

Design Authority:

[redacted]

S.J. Hensel Date

8.0 SUMMARY AND CONCLUSIONS

The COMSOL software is classified, tested, and maintained in accordance with the requirements set forth in QAP 20-1 of Manual 1Q. The test problems modeled and run on this software give results that meet the stated acceptance criteria. It is concluded that the COMSOL software will perform its intended safety function.

9.0 ATTACHMENTS

9.1 SRT-EMS-940084, Heat Transfer Software Test Plan, February 1995.
9.2 Test Results and Tester Comments.
9.3 Computer Files

ATTACHMENT 9.1
Heat Transfer Software Test Plan

Table of Contents

Problem 1: Infinitely Long Hollow Cylinder with Applied Heat Flux 3

Problem 2: Infinitely Long Cylinder with Internal Heat Generation and Convection 5

Problem 3: 1D Slab with Internal Heat Generation 7

Problem 4: Transient Conduction in a Semi-infinite Solid 9

Problem 5: Concentric Cylinders Modeled as 2-D Plates with Radiation 11

Problem 6: Freezing of a Square Solid - The Two Dimensional Stefan Problem 13

Problem 7: Insulated Slab with Radiation 15

Problem 8: Insulated Slab with Variable Temperature Boundary Condition 16

Problem 9: 2-D Slab with Convection 17

Problem 10: 1M X 1M Square Aluminum Plate 18

Problem 11: "Stiff" Thermal Problem with the Direct Solver 19

Problem 12: Infinitely Long Hollow Cylinder with Multiple Materials 20

Problem 13: 2-D Plate with Two Isothermal Boundaries 22

Problem 14: Radiation Exchange between Two Infinitely Long Cylinders and Space 25

Problem 15: 3-D Brick with Heat Flux, Convection, and Temperature Boundary Conditions 27

PROBLEM 1 :

Infinitely Long Hollow Cylinder with Applied Heat Flux

OPTION(S) TESTED:

Conduction with heat flux (Steady-state, British units)

DESCRIPTION:

A heat flux (q") is applied at the right wall (r_2) and temperature (T_o) is held constant at the left wall (r_1). Steady-state temperatures are calculated assuming an axisymmetric geometry.

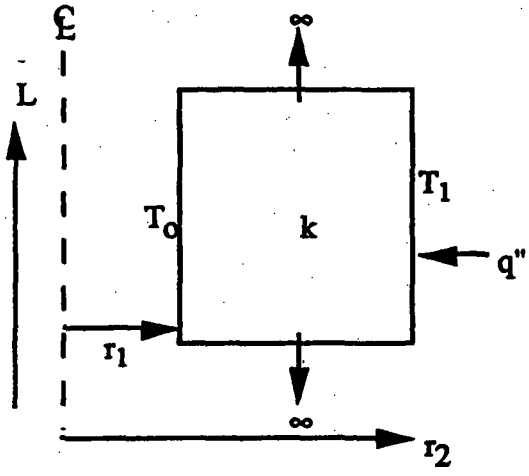

Parameters:

$q" = 20$ Btu/hr-ft^2	$r_2 = 3$ ft.
$T_o = 100°$ F	$k = 1$ Btu/hr-ft-°F
$r_1 = 2$ ft.	L = length (infinite)

EXPECTED SOLUTION:

The temperature at the right boundary (r_2) can be found from the expression:

$$q = \frac{2\pi Lk(T_1 - T_o)}{\ln(r_2/r_1)}$$

Rearranging,

$$T_1 = T_0 + \frac{\ln(r_2/r_1)q}{2\pi kL}$$

By definition the heat rate (q) in Btu/hr can be written as

$$q = 2\pi r_2 L q''.$$

Substituting into the previous equation yields

$$T_1 = T_0 + \frac{\ln(r_2/r_1)2\pi r_2 L q''}{2\pi k L}$$

Simplifying and substituting values gives

$$T_1 = T_0 + \frac{\ln(r_2/r_1) r_2 q''}{k}$$

$$T_1 = 100 + \frac{\ln(3/2)(3)(20)}{1}$$

$$T_1 = 100 + 24.328$$

$$T_1 = 124.328$$

The temperature at the right wall (r_2) is found analytically to be 124.328°F.

REFERENCE: Kreith, Frank, and Black, William Z. Basic Heat Transfer, Harper & Row, New York, 1980, pg 55.

PROBLEM 2 :

Infinitely Long Cylinder with Internal Heat Generation and Convection

OPTION(S) TESTED:

Internal heat generation and convection (Steady-state, British units)

DESCRIPTION:

Heat is generated internally (q''') throughout the solid and is conducted to the right wall at temperature T_s where it is transported by convection to the environment at temperature T_∞. The convective heat transfer coefficient is constant. Steady-state temperatures at the centerline (T(0))are calculated assuming an axisymmetric geometry.

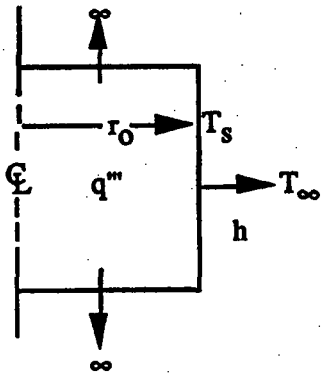

Parameters:

$q''' = 50$ Btu/hr-ft^3
$h = 1$ Btu/hr-ft-°F
$T_\infty = 100$ °F
$r_o = 1$ ft.
$k = 1$ Btu/hr-ft-°F

EXPECTED SOLUTION:

The temperature at the outside surface (r_o) can be found from Newton's law of cooling

$$q = hA(T_s - T_\infty)$$

where A is the surface area of the outside of the cylinder:

$$A = 2\pi r_o L.$$

The heat rate (q) in Btu/hr is found from the cylinder volume and volumetric heat generation (q'''):

$$q = q'''(\pi r_o^{\,2} L)$$

Rearranging Newton's law of cooling and substituting the volumetric heat source gives

$$T_s = T_\infty + \frac{q'''r_o}{2h}$$

$$T_s = 100 + \frac{50(1)}{2(1)}$$

$$T_s = 125$$

The centerline temperature (T(0)) can be found from:

$$T(r) = \frac{q'''r_o^2}{4k}\left(1 - \frac{r^2}{r_o^2}\right) + T_s$$

Substituting at $r = 0$

$$T(0) = \frac{50(1)}{4(1)} + 125$$

$$T(0) = 12.5 + 125$$

$$T(0) = 137.5$$

The temperature at the centerline(T(0)) is found analytically to be 137.5 °F.

REFERENCE:

Kreith, Frank, and Black, William Z. Basic Heat Transfer, Harper & Row, New York, 1980, pg 72.

PROBLEM 3 :

1D Slab with Internal Heat Generation

OPTION(S) TESTED:

Temperature dependent conductivity (Steady-state, British units)

DESCRIPTION:

Heat is generated internally (q‴) in a slab with thickness 2L. The heat is conducted through the solid slab to a fixed wall temperature of T_o. The conductivity is linearly dependent on temperature. Steady-state temperatures at the centerline (x=0) are calculated assuming a slab geometry.

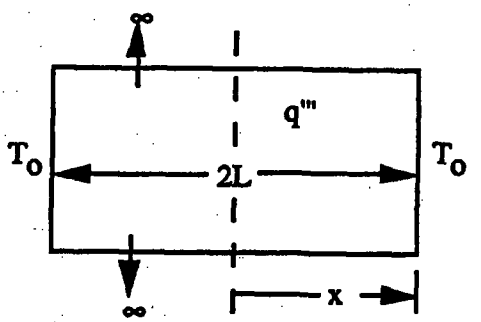

Parameters:

$T_o = 100°$ F
$q''' = 500$ Btu/hr-ft^3
$k_0 = 1$ Btu/hr-ft-°F
L = 1 ft
$k = k_0(1 + bT)$
$b = 0.1°$ F^{-1}

EXPECTED SOLUTION:

The thermal conductivity is expressed as $k = k_0(1 + bT)$.

The temperature at x=0 can be found from the expression:

$$\frac{(T(x) - T_0) + \frac{b}{2}(T^2(x) - T_0^2)}{q''' L^2/2k_0} = 1 - (x/L)^2$$

Substituting for $x = 0$ yields

$$\frac{(T(0) - T_0) + \frac{b}{2}(T^2(0) - T_0^2)}{q'''L^2/2k} = 1$$

$$T(0) - T_0 + \frac{b}{2}(T^2(0) - T_0^2) = \frac{q'''L^2}{2k}$$

$$T(0) - 100 + 0.05T^2(0) - 500 = 250$$

$$T(0) = \frac{-1 \pm \sqrt{1 + 4(0.05)(850)}}{0.1} = \frac{-1 \pm \sqrt{171}}{0.1} = 120.767, -140.770$$

Since −140.770 is a physically meaningless root for this problem, T(0) = 120.767.

The temperature at the centerline (x=0) is found analytically to be 120.767 °F.

REFERENCE: Arpaci, Vedat S. Conduction Heat Transfer, Addison-Wesley Publishing Company, Reading, MA., 1966, pg 131.

PROBLEM 4 :

Transient Conduction in a Semi-infinite Solid

OPTION(S) TESTED:

Transient solution (Transient, British units)

DESCRIPTION:

A heat flux (q") is conducted into a semi-infinite solid having an initial temperature (T_0) of 100°F. The temperature at the surface x=0 is calculated in 0.5 hr intervals from 0 to 2 hours.

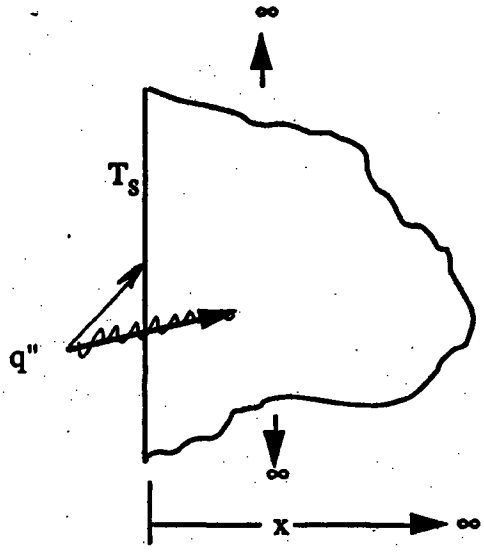

Parameters:

k = 1 Btu/ft-hr-°F **T_0 = 100°F**
c_p = 1 Btu/lbm-°F **q" = 10 Btu/hr-ft^2**
ρ = 1 lbm/ft^3

EXPECTED SOLUTION:

The transient temperature at the left boundary can be found from the expression:

$$T_s = T_0 + \frac{2q''\left(\frac{\alpha t}{\pi}\right)^{1/2}}{k}$$

Substituting values gives

$$T_s = T_0 + 20\sqrt{t/\pi}$$

Note: In the diagram, the heat flux is on the edge of the slab. The arrow pointing to the center was an error in the original document and marked out by hand on the original.

The temperatures at the surface in 0.5 hour intervals are found analytically:

time (minutes)	Temperature (°F) at x=0
0	100.000
0.5	107.979
1.0	111.284
1.5	113.820
2.0	115.958

REFERENCE:

Incropera, Frank P., and DeWitt, David.P. Fundamentals of Heat Transfer, John Wiley & Sons, New York, 1981. pg 205.

PROBLEM 5 :

Concentric Cylinders Modeled as 2-D Plates with Radiation

OPTION(S) TESTED:

Radiation (Transient, British units)

DESCRIPTION:

Radiative heat transfer occurs between concentric regions 2 and 4 (region 3 is void). All surface emmittances and absorptivites are 1. Region 2 radiates to region 4 and region 4 radiates to the ambient. Region 1 is a heat source of 3702.6 Btu/hr-ft.^{3}. The temperatures at locations T3, T8, and T4 are calculated for times of 0, 30, and 90 minutes.

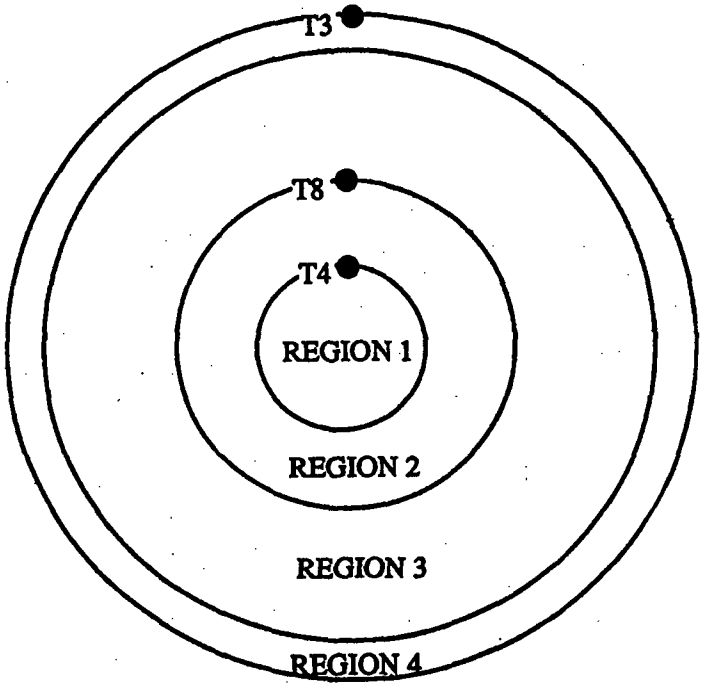

REGION	~~O.D.~~ RADIUS (inches)
1	~~6.9~~ ~~6.5~~
2	15.25
3	21.25
4	21.5

Material	Conductivity (Btu/hr-ft-°F)	Specific Heat (Btu/lb$_m$)	Density (lb$_m$/ft^3)
REGION 1	139.7	0.214	169
REGION 2	26	0.113	489
REGION 4	26	0.113	489

Table 1: Material Properties

Note: In the diagram, the radius of region 1 was incorrect in the original print of the test case and was corrected by hand before the original document submission

Time (minutes)	Ambient Temperature (°F)
0	130°F
0 - 30	1475°F
30 - 90	130°F

Table 2: Ambient Temperature

EXPECTED SOLUTION:

The temperatures at locations T3, T8, and T4 are shown below for times of 0, 30, and 90 minutes.

Time (minutes)	Temperatures (°F)		
	T3	T8	T4
0	278.6	399.2	417.5
30	1272.2	708.8	505.4
90	397.4	568.4	595.4

REFERENCE:

Glass, Robert E., Sample Problem Manual For Benchmarking of Cask Analysis Codes (SAND88-0190 TTC-0780 UC-71), Sandia National Laboratories, Albuquerue, NM 87185, February 1988.

PROBLEM 6 :

Freezing of a Square Solid - The Two Dimensional Stefan Problem

OPTION(S) TESTED:

Phase change (Transient, SI units)

DESCRIPTION:

This problem is the two-dimensional Stefan problem: a square block of material is initially liquid, just above the freezing temperature. The temperature of its outside perimeter is reduced suddenly by -45°, so that the block starts to freeze from the outside towards the core. The latent heat of freezing (70.26 J/kg) occurs between the solidus and liquidus temperatures of -0.25° C and -0.15° C, respectively. The initial temperature of the material is 0° C.

The block is a square with a side length of 8 meters. Symmetry allows the mesh to be generated on only one quarter of the model. A graphical ABAQUS solution is presented for the first 5 seconds of the transient at the points 'A' and 'B' which are shown in the figure below. The ABAQUS element used is type DC2D4 (four-node, bilinear quadrilateral).

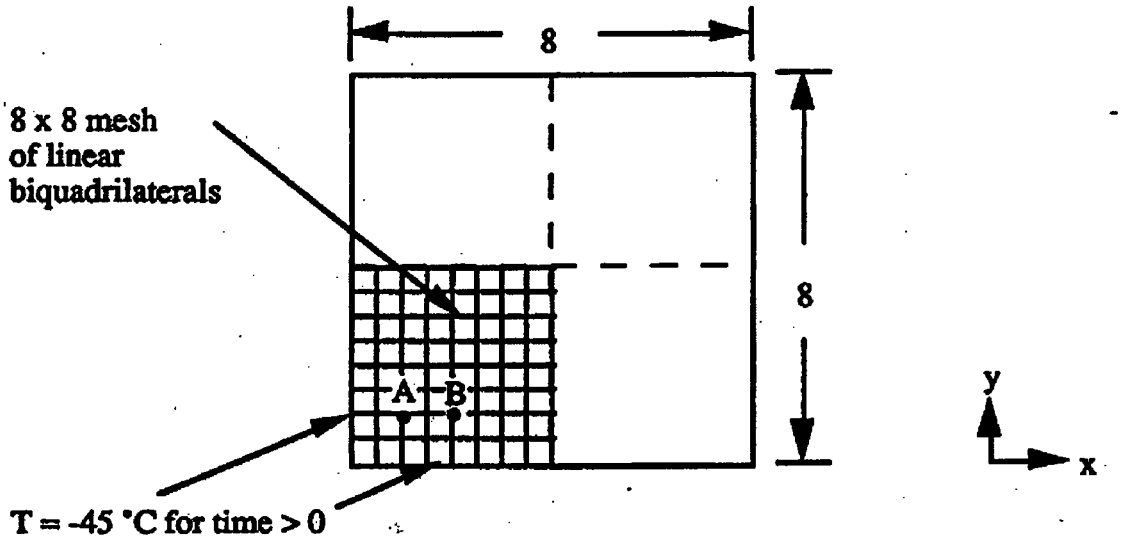

Parameters: $k = 1.08$ W/m-°C $\quad c_p = 1.0$ J/kg
$\rho = 1.0$ kg/m^3

EXPECTED SOLUTION:

Plots of the temperatures computed by COMSOL Multiphysics should be similar to those computed by ABAQUS.

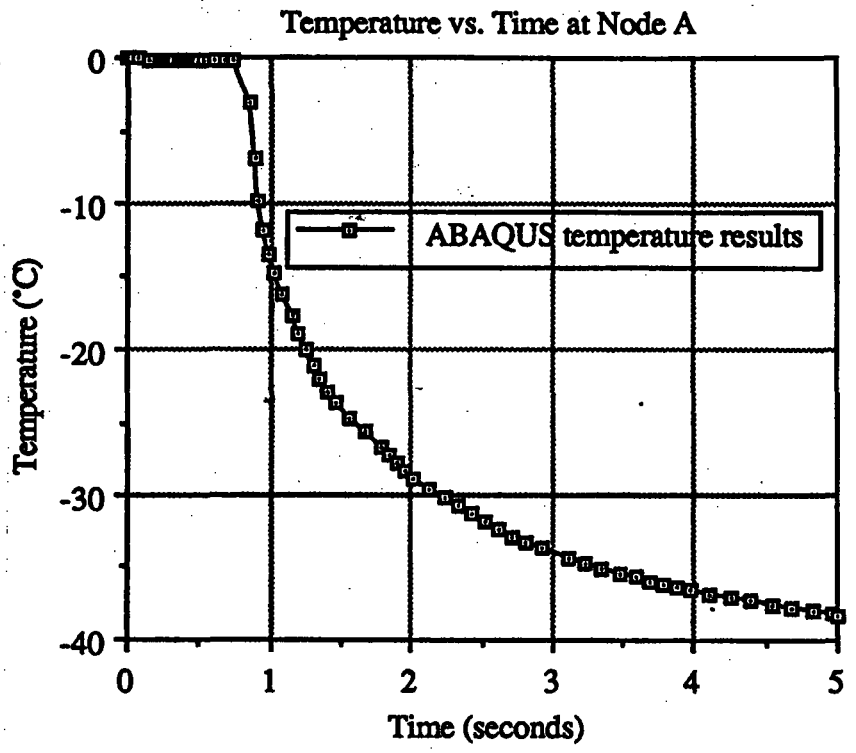
Temperature vs. Time at Node A
0
-10
-20
-30
-40
Temperature (°C)
ABAQUS temperature results
0
1
2
3
4
5
Time (seconds)

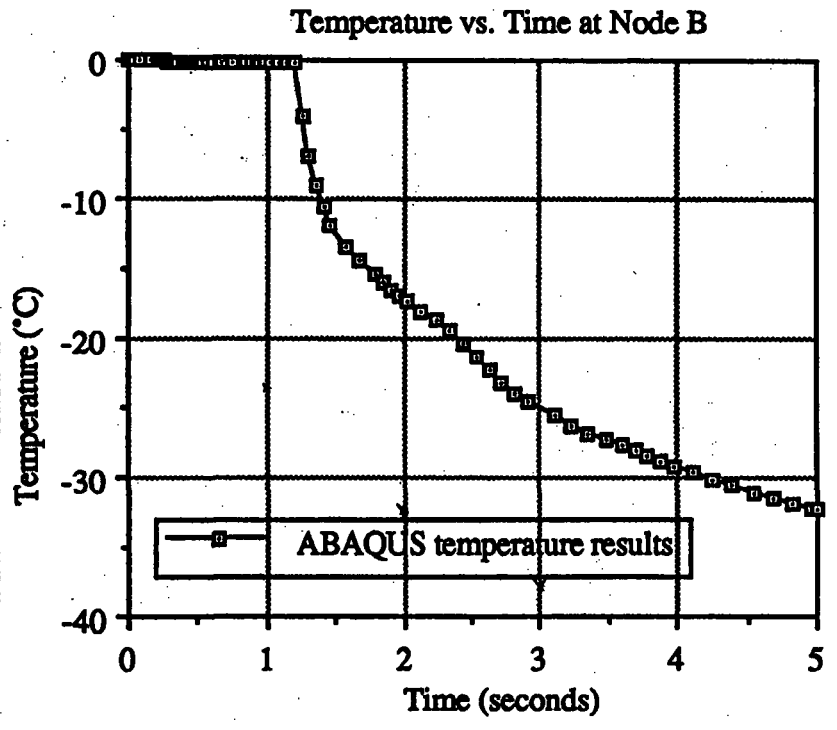
Temperature vs. Time at Node B
0
-10
-20
-30
-40
Temperature (°C)
ABAQUS temperature results
0
1
2
3
4
5
Time (seconds)

PROBLEM 7 :

Insulated Slab with Radiation

OPTION(S) TESTED:

Conduction and radiation (Steady-state, SI units)

DESCRIPTION:

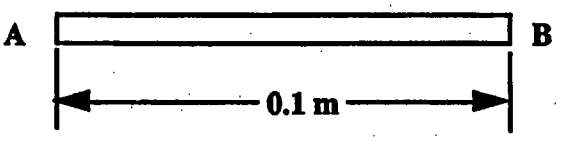

Parameters: $T_a = 1000$ K $\quad \varepsilon_b = 0.98$
$T_{ambient} = 300$ K $\quad k = 55.6$ W/m-° C

This problem is found in ABAQUS V5.2 Verification Manual, page 6.2.2. The ABAQUS element type tested is DC2D8 (8 noded quadrilateral elements). The model used a uniform mesh with 10 elements along the length.

Geometry consists of a rectangular region with zero heat flux along the top and bottom boundary, and fixed temperature (T_a) at the left end. Heat is conducted through the solid to the right end at temperature (T_b) which radiates to an environment at 300 K. The right end has an emissivity (ε_b). There is no internal heat generation.

This is a test recommended by the National Agency for Finite Element Methods and Standards (U.K.): Test T2 from NAFEMS publication TNSB, Rev. 3, "The Standard NAFEMS Benchmarks," October 1990. The temperature results are compared for point B.

EXPECTED SOLUTION:

The temperature at point B is computed by ABAQUS to be 653.80 °C.

PROBLEM 8 :

Insulated Slab with Variable Temperature Boundary Condition

OPTION(S) TESTED:

Transient analysis using a variable temperature boundary condition (Transient, SI units)

DESCRIPTION:

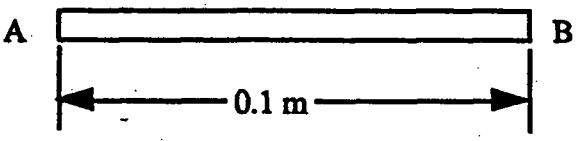

Parameters:

$T_a = 0°$ C
$T_b = 100\sin(\pi t/40)°$ C where t is in seconds
$\rho = 7200$ kg/m^3
$k = 35.0$ W/m-°C
$c_p = 440.5$ J/kg°C

This problem is found in ABAQUS V5.2 Verification Manual, pg 6.2.3. The ABAQUS element type tested is DC1D3 (1-D with 3 nodes per bar element).

Geometry consists of a rectangular region with zero heat flux along the top and bottom boundary, and fixed temperature (T_a) at the left end and with a varying temperature (T_b) at the right end. There is no internal heat generation.

This is a test recommended by the National Agency for Finite Element Methods and Standards (U.K.): Test T3 from NAFEMS publication TNSB, Rev. 3, "The Standard NAFEMS Benchmarks," October 1990. The temperature results are compared for .

EXPECTED SOLUTION:

The target solution is 36.60° C at x = 0.08 m and 32 secs .

PROBLEM 9 :

2-D Slab with Convection

OPTION(S) TESTED:

2-D with convection (Steady-state, SI units)

DESCRIPTION:

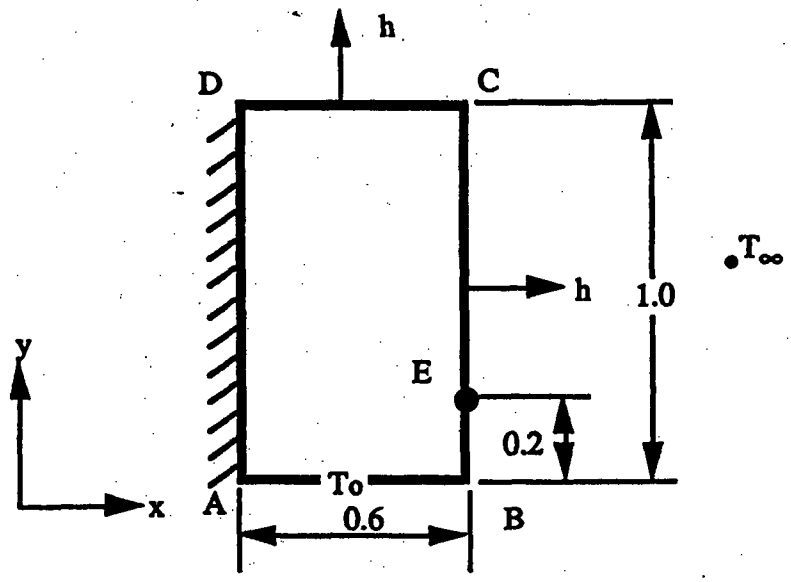

Parameters: $h = 750\ W/m^{2\circ}\ C$; $T_O = 100^\circ\ C$; $k = 52\ W/m^\circ\ C$, $T_\infty = 0^\circ\ C$

This problem is found in ABAQUS V5.2 Verification Manual, page 6.2.4. The ABAQUS element type tested is DC3D8 (3-D with 8 nodes per hexagonal element). The mesh is uniform and the width (Δx) and height (Δy) for each element is 0.1 m. There are four elements through the thickness (Δz) for the ABAQUS model.

Geometry consists of a rectangular region with zero heat flux along the left boundary, and convection to the ambient at T_∞ along right and top boundaries. The bottom is held at a constant temperature (T_O). There is no internal heat generation.

This is a test recommended by the National Agency for Finite Element Methods and Standards (U.K.): Test T4 from NAFEMS publication TNSB, Rev. 3, "The Standard NAFEMS Benchmarks," October 1990.

EXPECTED SOLUTION:

The temperature at point E as computed by ABAQUS is 18.26 °C.

PROBLEM 10 :

1M X 1M Square Aluminum Plate

OPTION(S) TESTED:

Nodal point heat source (Steady-state, SI units)

DESCRIPTION:

A square aluminum plate has a left boundary fixed at 100.0 K and a right boundary with a constant heat flux of 1000.0 W/m^2. At the bottom heat is lost to the environment at 300K through convection with a coefficient of 13.4 W/m^2-K. The top boundary is insulated. At the center of the plate (0.5, 0.5) is a nodal point heat source of 1000W. The plate is uniformly meshed (4x4) with sixteen 4-noded quadrilaterals. P3/THERMAL results are compared to ABAQUS results at the specified coordinates.

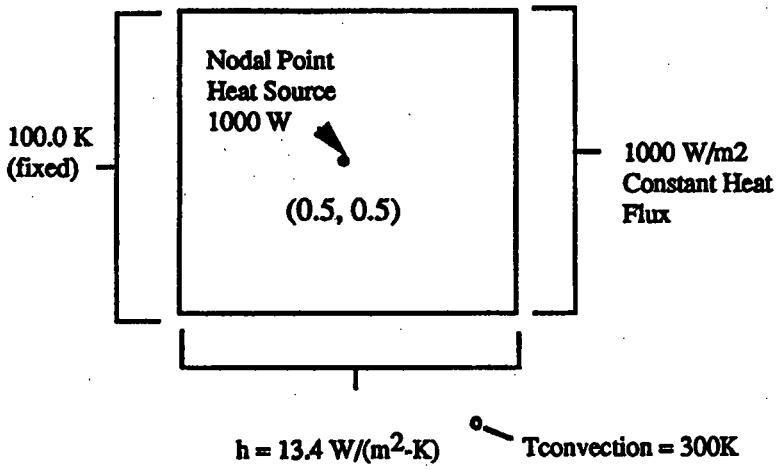

Parameters: $k_{aluminum}$ = 293.076 W/mK

EXPECTED SOLUTION:

The temperatures computed by ABAQUS at three coordinates are shown below:

Coordinates	Temperature (K)
(1, 1)	108.0906
(0.5, 0.5)	107.1976
(1, 0)	112.1438

PROBLEM 11 :

"Stiff" Thermal Problem with the Direct Solver

OPTION(S) TESTED:

Numerical convergence (Steady-state, SI units)

DESCRIPTION:

This problem has been designed to illustrate the thermally "stiff" problem. A material with a lower thermal conductivity and width of 0.5 m is sandwiched between two materials with a higher conductivity and width of 1 m. Temperature and heat flux boundary conditions are imposed on the surfaces as illustrated. QTRAN has Iterative (SOL = 0) and Direct (SOL=2) solution options. For "stiff" thermal problems iterative solvers tend to converge very slowly while direct solvers work very efficiently. This problem is solved using the direct solver. Temperature results are compared to ABAQUS V5.2 temperature results at the coordinates x = 1.0 and y = 9.0.

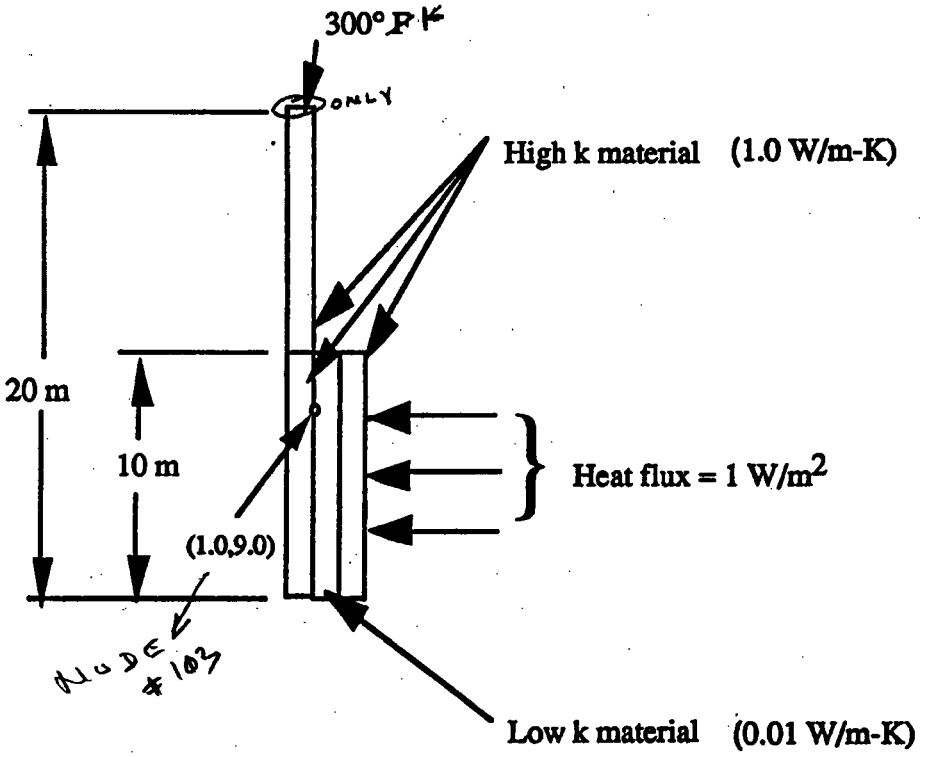

EXPECTED SOLUTION:

The temperature at coordinates (1.0,9.0) is computed by ABAQUS to be 409.690502 K.

PROBLEM 12 :

Infinitely Long Hollow Cylinder with Multiple Materials

OPTION(S) TESTED:

Conduction through multiple materials (Steady-state, British units)

DESCRIPTION:

An infinitely long hollow cylinder is composed of 9 concentric cylinders of various materials, some of which have temperature dependent thermal conductivities. There are constant temperature boundary conditions at the inner cylinder wall of 339° F and between the stainless steel/fiberglass interface of 190° F. The objective is find the temperature at the fiberfrax/stainless steel interface.

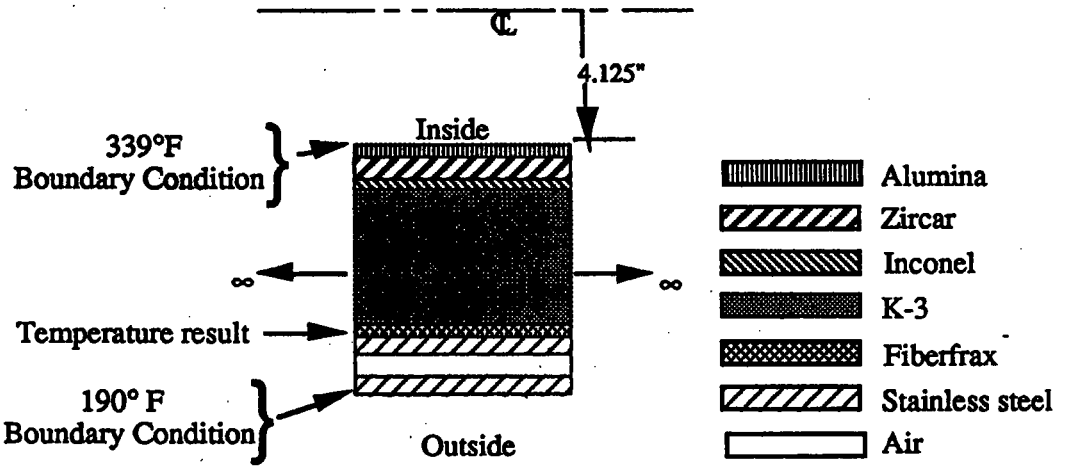

Parameters: $T_i = 339°$ F $\quad T_o = 190°$ F
$r_o = 14.275$ $\quad r_i = 4.125$
L = length (infinite)

Material	outer radius (r_o) (inches)	inner radius (r_i) (inches)	Conductivity (k) (Btu/hr-ft-°F)
Alumina	4.455	4.125	13.1 @ 339° F
Zircar	5.195	4.455	0.054 @ 305° F
Inconel	5.5	5.195	8.16 @ 271° F
K-3	11.25	5.5	2.5 @ 268° F
Fiberfrax	12.0	11.25	0.055 @ 251° F
Stainless steel	13.4	12.0	9.54 @ 237° F
Air	13.9	13.4	0.0184 @ 214° F
Stainless steel	14.275	13.9	9.23 @190° F

The rate of heat transfer by conduction across the materials (q) can be determined from

$$q = \frac{2\pi kL(T_i - T_o)}{\ln(r_o/r_i)} = \frac{(T_i - T_o)}{R_t}$$

The rate of heat transfer by conduction across the materials (q) can be determined from

$$q = \frac{2\pi kL(T_i - T_o)}{\ln(r_o/r_i)} = \frac{(T_i - T_o)}{R_t}$$

The total thermal resistance (R_t) is found by the summation of individual resistances:

$$R_t = \Sigma \frac{\ln(r_o/r_i)}{2\pi kL}$$

Substituting values between the 339° F boundary condition (T_i) and 190° F boundary condition (T_o) yields $R_t = 1.0064$. When $T_i = 339°$ F and $T_o = 190°$ F, q = 148.0451 Btu/hr.

The total thermal resistance (R_t) between the 190° F boundary condition and the stainless steel/fiberglass interface is calculated to be 0.3192. Substituting R_t = 0.3192, q = 148.0451, and $T_o = 190°$ F into the equation for heat transfer by conduction gives $T_i = 237.25°$ F.

EXPECTED SOLUTION:

The temperature at the stainless steel/fiberfrax interface is analytically found to be 237° F.

REFERENCE: Kreith, Frank, and Black, William Z. Basic Heat Transfer, Harper & Row, New York, 1980, pp 55, 56.

PROBLEM 13 :

2-D Plate with Two Isothermal Boundaries

OPTION(S) TESTED:

Spatially dependent temperature boundary condition (Steady-state, SI units)

DESCRIPTION:

A 2-D plate has a constant temperature of 0 K at the left and right boundaries. A spatially dependent temperature boundary condition is imposed at the top and bottom of the plate as shown below:

$$T(x, y) = x \qquad 0 \le x \le 1$$
$$T(x, y) = 2 - x \qquad 1 < x \le 2.$$

Temperatures are calculated analytically at three randomly selected nodal locations: (1.45, 1.1), (0.85, 1.5), and (0.15, 0.7).

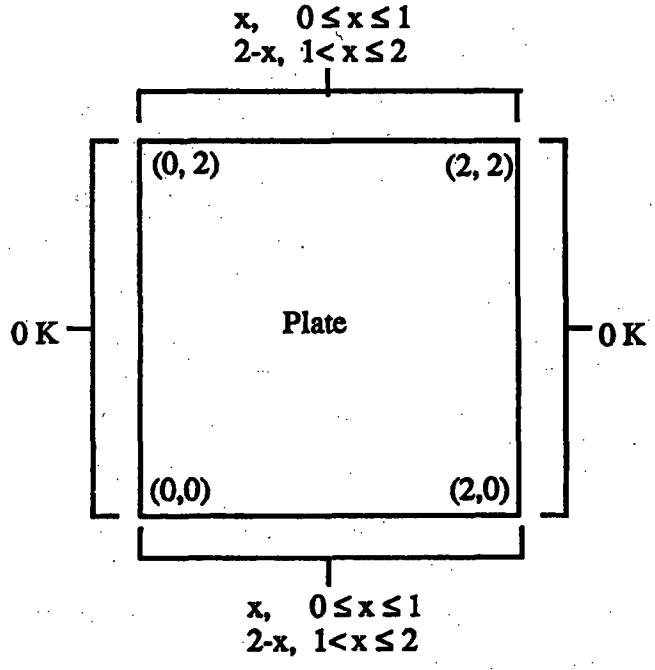

Parameters:

a = 2 m (plate length) **b = 2 m (plate width)**

EXPECTED SOLUTION:

The temperature at any (x,y) coordinate within the domain can be found from

$$T(x,y) = \frac{8}{\pi^2}\sum_{n=1}^{\infty}\frac{\sin(n\pi/2)}{n^2}\left\{\frac{\sinh\left(\frac{n\pi}{a}\right)y + \sinh\left[\frac{n\pi}{a}(b-y)\right]}{\sinh\left(\frac{n\pi}{a}\right)b}\right\}\sin\left(\frac{n\pi}{a}\right)x$$

The solution is found from the following FORTRAN program and output after substituting values for the plate length and width and summing the first 35 terms. Temperatures are calculated at the three arbitrarily selected points within the domain: (1.45, 1.1), (0.85, 1.5), and (0.15, 0.7).

PROGRAM

```
                program sum
c
      print*, 'Enter x : '
      read (*,*) x
      print*, 'Enter y : '
      read (*,*) y
c
      tsum = 0.0
      pi = 3.14159265
      do 10 n = 1, 35
       at = n*pi/2.0
       gin = (sinh(at*y) + sinh(at*(2-y)))/sinh(n*pi)
       sum = sin(at)/n**2 * gin * sin(at*x)
       tsum = tsum + sum
 10   continue
c
      write (*, *) 'sum = ', 8.0*tsum/pi**2
c
      stop
      end
```

OUTPUT

```
 f77 sum.f
% a.out
 Enter x :
1.45
 Enter y :
1.1
 sum =  0.2477080
% a.out
 Enter x :
0.85
 Enter y :
1.5
 sum =  0.4228634
% a.out
 Enter x :
0.15
 Enter y :
0.7
 sum =  8.1770860E-02
```

The temperatures calculated at the three points are shown below :

Node	Coordinates	Temperature (K)
472	(1.45, 1.1)	0.2477080
1479	(0.85, 1.5)	0.422863
1145	(0.15, 0.7)	0.081771

REFERENCE:

Powers, David L. Boundary Value Problems, Clarkson College of Technology, Academic Press, Inc., 1979. pp 182, 183.

PROBLEM 14 :

Radiation Exchange between Two Infinitely Long Cylinders and Space

OPTION(S) TESTED:

Radiation view factor calculations (Steady-state, SI units)

DESCRIPTION:

To test performance of P3/THERMAL's integrated viewfactor/radiation resistor generation program, a benchmark analysis was chosen that has an exact solution. This thermal radiation benchmark consists of two parallel cylinders, each 1-meter in radius, with the centerlines separated by 2.25 meters. A uniform heat flux of 1000 W/m^2 is applied on the outer surfaces. The cylinder material is assumed to be a near perfect conductor (thermal conductivity of 7920 W/m-K) to make the radial temperature gradient small so that the analytical solution can be easily shown. The surface emissivity is 1.0. The space temperature (T_∞) is taken as absolute zero. The relatively close proximity of the cylinders makes this benchmark a significant challenge to a radiation view factor code. This benchmark demonstrates P3/THERMAL's view factor program accuracy for a complicated view factor problem as well as the capability of the solver to model the radiation network.

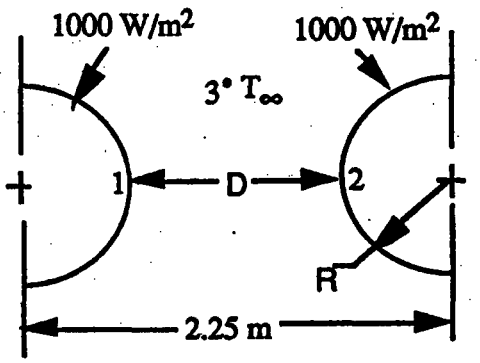

Parameters: D = 0.25 m R = 1 m
q" = 1000 W/m^2 $\sigma = 5.7(10)^{-8}$ W/m^2-K^4

EXPECTED SOLUTION:

The net heat flux between surface 1 and the environment is

$$q''_{1\text{-}3} = \sigma F_{1\text{-}3}(T_1^4 - T_3^4)$$

The viewfactors (F) for this arrangement can be expressed as

$$F_{1\text{-}2} + F_{1\text{-}3} = 1.0.$$

with

with

$$F_{1-2} = \frac{2}{\pi}\left[(X^2 - 1)^{1/2} + \frac{\pi}{2} - \cos^{-1}\left(\frac{1}{X}\right) - X \right]$$

$$\text{where } X = 1 + \frac{D}{2R}$$

Evaluating, $F_{1-2} = 0.30895$ and $F_{1-3} = 0.69105$.

Substituting these values into the expression for the net heat flux q''_{1-3} yields $T_1 = 399.700$ K.

The temperature of the cylinder surface is analytically found to be 399.700 K.

REFERENCES:

Siegel, Robert and Howell, John. Thermal Radiation Heat Transfer, 2nd. ed., Hemisphere Publishing Co., 1981. pg 205.

PROBLEM 15 :

3-D Brick with Heat Flux, Convection, and Temperature Boundary Conditions

OPTION(S) TESTED:

3-D conduction (Steady-state, SI units)

DESCRIPTION:

A brick has a width of 1.0 m (Δz), length of 2.0 m (Δx), and height of 1.0 m (Δy). A heat flux (q''_f) of 245 W/m^2 is applied at the plane z = 1. Convection (q''_c) with a convective heat transfer coefficient of 180 W/m^{2}K occurs to an environment at 250 K at the plane x = 2. The boundary at y = 0 is held at a constant temperature of 300 K. The remaining boundaries are insulated. The thermal conductivity of the brick is 40 W/mK.

The brick is uniformly meshed with 250 8-noded hexahedrons, each having an element edge length of 0.2 m. Temperatures computed by ABAQUS are shown at three arbitrarily selected nodal locations within the brick.

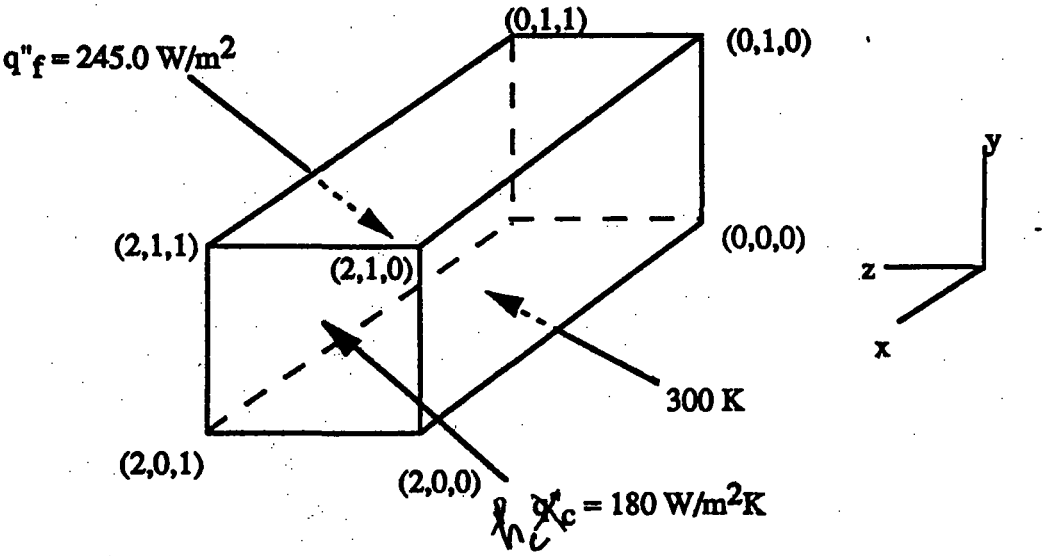

EXPECTED SOLUTION:

The temperatures at three nodes are found by ABAQUS as shown below:

Node	Coordinates (x,y,z)	Temperature (K)
305	(1.4, 0.6, 0.8)	287.566078
227	(1.2, 0.4, 0.6)	293.430702
82	(0.8, 0.2, 0.2)	298.230642

ATTACHMENT 9.2 – TEST RESULTS

The following results compare the COMSOL solutions to the theoretical or other solutions at the specified critical points. The test cases (Problem #s) identified in Attachment 9.1 were run on Redhat Linux Enterprise Edition version 5 and therefore satisfy the RSS #1 [B-SQP-A-00057, Attachment A]. Computer input and output files are listed in Attachment 9.4.

Test Problem 1: Infinitely Long Hollow Cylinder with Applied Heat Flux

Results: The temperature at the right boundary (r_2)

COMSOL 4.3 (°F)	Analytical (°F)	Error (%)
124.33	124.328	<0.01

The temperature contours are shown in Figure 1.

Tester's Comments: This problem satisfies the RSS # 3.2a, 3.2b, 3.2d, 3.3, 3.4b, 3.4e, and 3.6. Software calculated result meets the acceptance criteria.

Test Problem 2: Infinitely Long Hollow Cylinder with Internal Heat Generation and Convection

Results: The temperature at the centerline (r_o)

COMSOL 4.3 (°F)	Analytical (°F)	Error (%)
137.5	137.5	<0.01

The temperature contours are shown in Figure 2.

Tester's Comments: This problem satisfies the RSS # 3.2a, 3.2b, 3.2d, 3.3, 3.4a, 3.4b, 3.4g, and 3.6. Software calculated result meets the acceptance criteria.

Test Problem 3: 1-D Slab with Internal Heat Generation

Results: The temperature at centerline (x=0):

COMSOL 4.3 (°F)	Analytical (°F)	Error (%)
120.77	120.767	<0.01

The temperature contours are shown in Figure 3.

Tester's Comments: This problem satisfies the RSS # 3.2a, 3.2b, 3.2d, 3.3, 3.4b, 3.4e, 3.4g, and 3.6. Software calculated result meets the acceptance criteria.

Test Problem 4: Transient Conduction in a Semi-infinite solid

Results: The temperatures at x = 0, at 30 minute interval:

Time (Hours)	COMSOL 4.3 (°F)	Analytical (°F)	Error (%)
0	100.000	100.000	<0.01
0.5	107.978	107.977	<0.01
1.0	111.283	111.283	<0.01
1.5	113.812	113.821	<0.01
2.0	115.958	115.959	<0.01

The temperature contours are shown in Figure 4.

Tester's Comments: This problem satisfies the RSS # 3.2a, 3.2b, 3.2d, 3.2f, 3.2g, 3.3, 3.4b, 3.4e, and 3.6. Software calculated results meet the acceptance criteria.

Test Problem 5: Concentric Cylinders Modeled as 2-D Plates with Radiation

Results: The temperatures at T3, T4, and T8 are:

Time (min)	COMSOL 4.3 (°F)			**Reference (°F)**			4.3 Error (%)		
	T3	**T8**	**T4**	**T3**	**T8**	**T4**	**T3**	**T8**	**T4**
0	278.4	400.0	417.8	278.6	399.2	417.5	0.07%	0.20%	0.07%
30	1273.2	710.2	505.5	1272.2	708.8	505.4	0.08%	0.20%	0.02%
90	398.7	569.5	596.2	397.4	568.4	595.4	0.33%	0.19%	0.13%

The temperature contours are shown in Figure 5.

Tester's Comments: This problem satisfies the RSS # 3.2a, 3.2b, 3.2d, 3.2e, 3.2f, 3.3, 3.4b, 3.4f, 3.4g, and 3.6. Software calculated results meet the acceptance criteria.

Problem 6: Freezing of a Square Solid – The 2-D Stefan Problem

Results: The temperatures at Points A and B are given in Figure 6:

Tester's Comments: This problem satisfies the RSS # 3.2a, 3.2b, 3.2c, 3.2d, 3.f, 3.3, 3.4b, 3.4e, 3.5, and 3.6. Temperatures calculated by COMSOL are in good agreement with ABAQUS results. COMSOL does not have specific inputs for latent heat due to phase change, but COSOL does give the user great flexibility by allowing the user to input equations describing the systems phase change. Based on these observations, the results obtained using COMSOL are in good agreement with the ABAQUS results.

Problem 7: Insulated Slab with radiation

Results: The temperature at point B is:

COMSOL 4.3 (°C)	ABAQUS (°C)	Error (%)
653.85	653.80	<0.01

The temperature contours are shown in Figure 7.

Tester's Comments: This problem satisfies the RSS # 3.2a, 3.2b, 3.2d, 3.2e, 3.2f, 3.3, 3.4b, 3.4f, and 3.6. Software calculated result meets the acceptance criteria.

Problem 8: Insulated Slab with Variable Temperature Boundary Condition.

Results: The temperature at point B (x = 0.08 m and 32 secs) is:

COMSOL 4.3 (°C)	ABAQUS (°C)	Error (%)
36.60	36.60	<0.01

The temperature contours are shown in Figure 8.

Tester's Comments: This problem satisfies the RSS # 3.2a, 3.2b, 3.2d, 3.2f, 3.3, 3.4b, 3.4c, 3.4e, and 3.6. Software calculated result meets the acceptance criteria.

Problem 9: 2-D Slab with Convection

Results: The temperature at point E is:

COMSOL 4.3 (°C)	ABAQUS (°C)	Error (%)
18.25	18.26	<0.05

The temperature contours are shown in Figure 9.

Tester's Comments: This problem satisfies the RSS # 3.2a, 3.2b, 3.2d, 3.2f, 3.3, 3.4a, 3.4b, 3.4e, and 3.6. Software calculated result meets the acceptance criteria.

Problem 10: 1M X 1M Square Aluminum Plate

Results: The temperatures at three nodes are:

Node	Coordinates	COMSOL 4.3 (°K)	ABAQUS (K)	Error (%)
5	(1, 1)	108.1249	108.0906	0.032
3	(0.5, 0.5)	107.83248	107.1976	0.529
4	(1, 0)	112.14712	112.1438	<0.01

The temperature contours are shown in Figure 10.

Tester's Comments: This problem satisfies the RSS # 3.2a, 3.2b, 3.2d, 3.2f, 3.3, 3.4a, 3.4b, 3.4e, 3.4g, and 3.6. Software calculated results meet the acceptance criteria.

Problem 11: "Stiff" Thermal Problem with Direct Solver

Results: The temperature at coordinate (1.0, 9.0) is:

COMSOL 4.3 (°K)	ABAQUS (°K)	Error (%)
409.69505	409.690502	<0.01

The temperature contours are shown in Figure 11.

Tester's Comments: This problem satisfies the RSS # 3.2a, 3.2b, 3.2d, 3.2f, 3.3, 3.4b, 3.4e, and3.6. Software calculated result meets the acceptance criteria.

Problem 12: Infinitely Long Hollow Cylinder with Multiple Materials

Results: The temperature at the Fiberfrax/stainless steel interface is:

COMSOL 4.3 (°F)	Analytical (°F)	Error (%)
237.25	237.25	<0.01

The temperature contours are shown in Figure 12.

Tester's Comments: This problem satisfies the RSS # 3.2a, 3.2b, 3.2d, 3.2f, 3.3, 3.4b, 3.4e, and 3.6. Software calculated result meets the acceptance criteria.

Problem 13: 2-D Plate with Two Isotherm Boundaries

Results: The temperatures at the selected nodal points are:

Node	Coordinates	COMSOL 4.3 (°K)	Analytical (K)	Error (%)
932	(1.45, 1.1)	0.24815	0.2477080	0.18
1248	(0.85, 1.5)	0.42375	0.422863	0.21
578	(0.15, 0.7)	0.08189	0.081973	0.10

The temperature contours are shown in Figure 13.

Tester's Comments: This problem satisfies the RSS # 3.2a, 3.2b, 3.2d, 3.2f, 3.3, 3.4b, 3.4d, 3.4e, and 3.6. Software calculated results meet the acceptance criteria.

Problem 14: Radiation Exchange between Two Infinitely Long Cylinders and Space
Results: The temperature at the cylindrical surface is:

COMSOL 4.3 (°K)	Analytical (°K)	4.3 Error (%)
399.65	399.700	0.01

The temperature contours are shown in Figure 14.

Tester's Comments: This problem satisfies the RSS # 3.2a, 3.2b, 3.2d, 3.2e, 3.2f, 3.3, 3.4b, 3.4e, 3.4f, and 3.6. Software calculated result meets the acceptance criteria.

Problem 15: 3-D Brick with Heat Flux, Convection, and Temperature Boundary Conditions

Results: The temperature at the cylindrical surface is:

Node	Coordinates	COMSOL 4.3 (°K)	ABAQUS (°K)	4.3 Error (%)
623	(1.4, 0.6, 0.8)	287.34454	287.566078	0.08
1061	(1.2, 0.4, 0.6)	293.24771	293.430702	0.06
1939	(0.8, 0.2, 0.2)	298.17468	298.230642	0.02

The temperature contours are shown in Figure 15.

Tester's Comments: This problem satisfies the RSS # 3.2a, 3.2b, 3.2d, 3.2e, 3.2f, 3.3, 3.4a, 3.4b, 3.4e, and 3.6. Software calculated results meet the acceptance criteria.

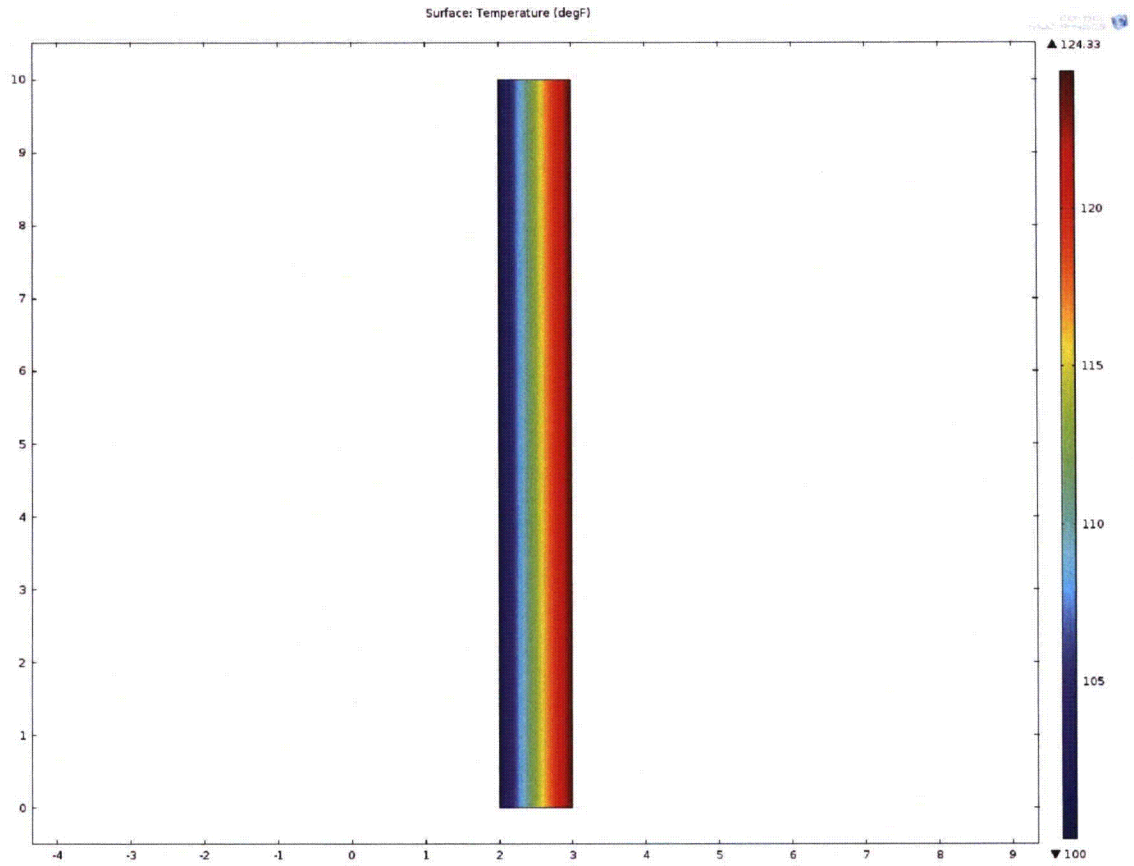

Figure 1 – Temperature Contours for Test Problem No. 1

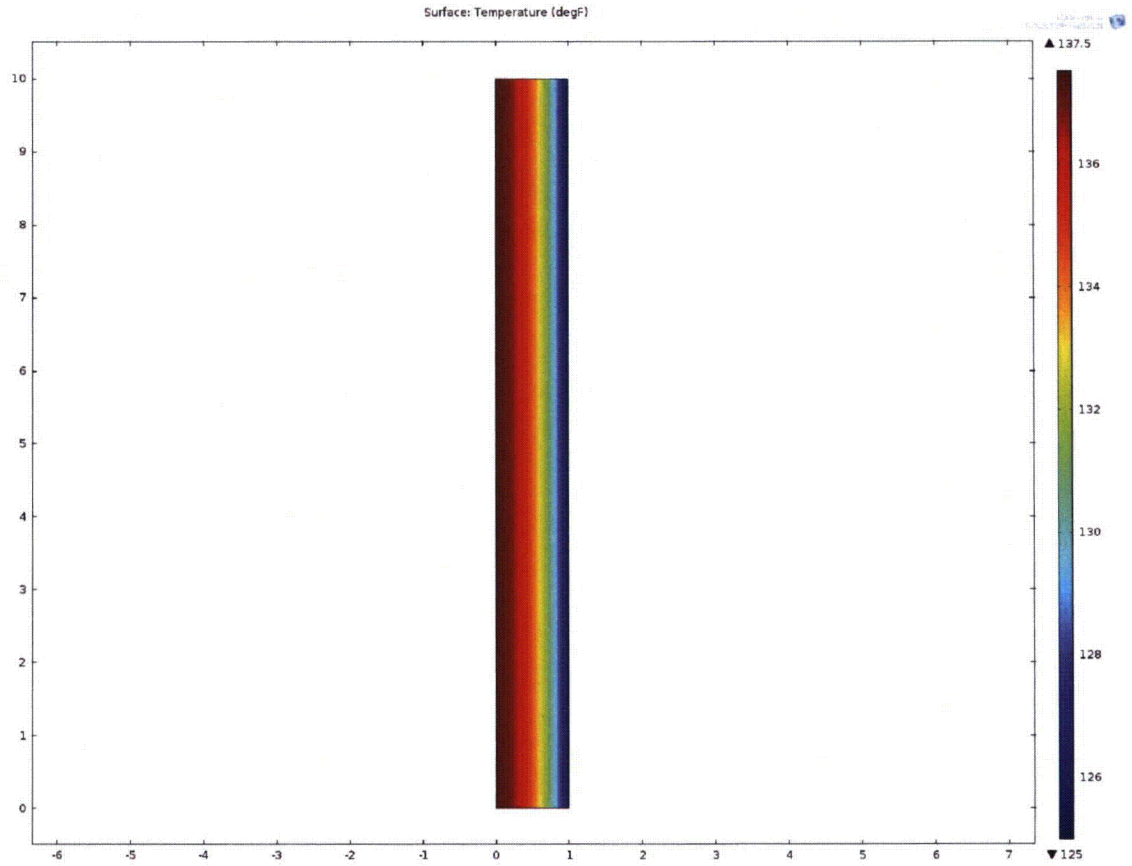

Figure 2 – Temperature Contours for Test Problem No. 2

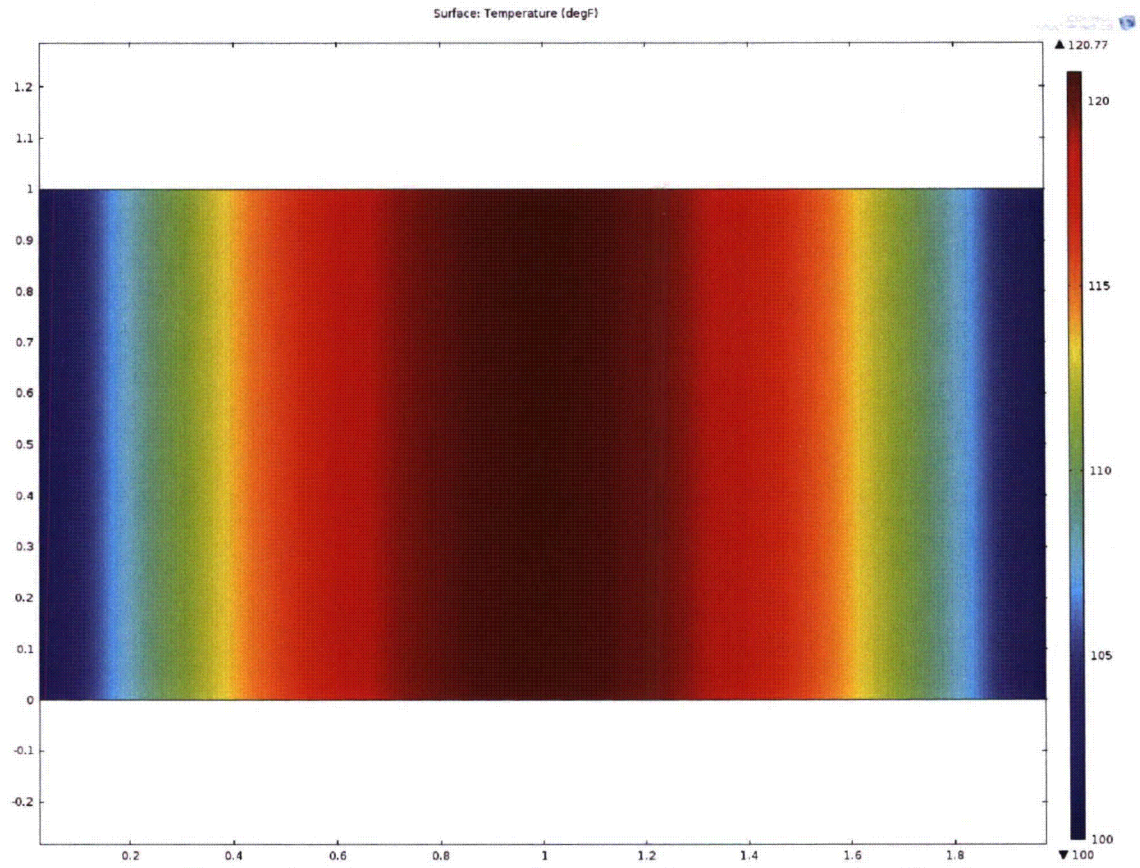

Figure 3 – Temperature Contours for Test Problem No. 3

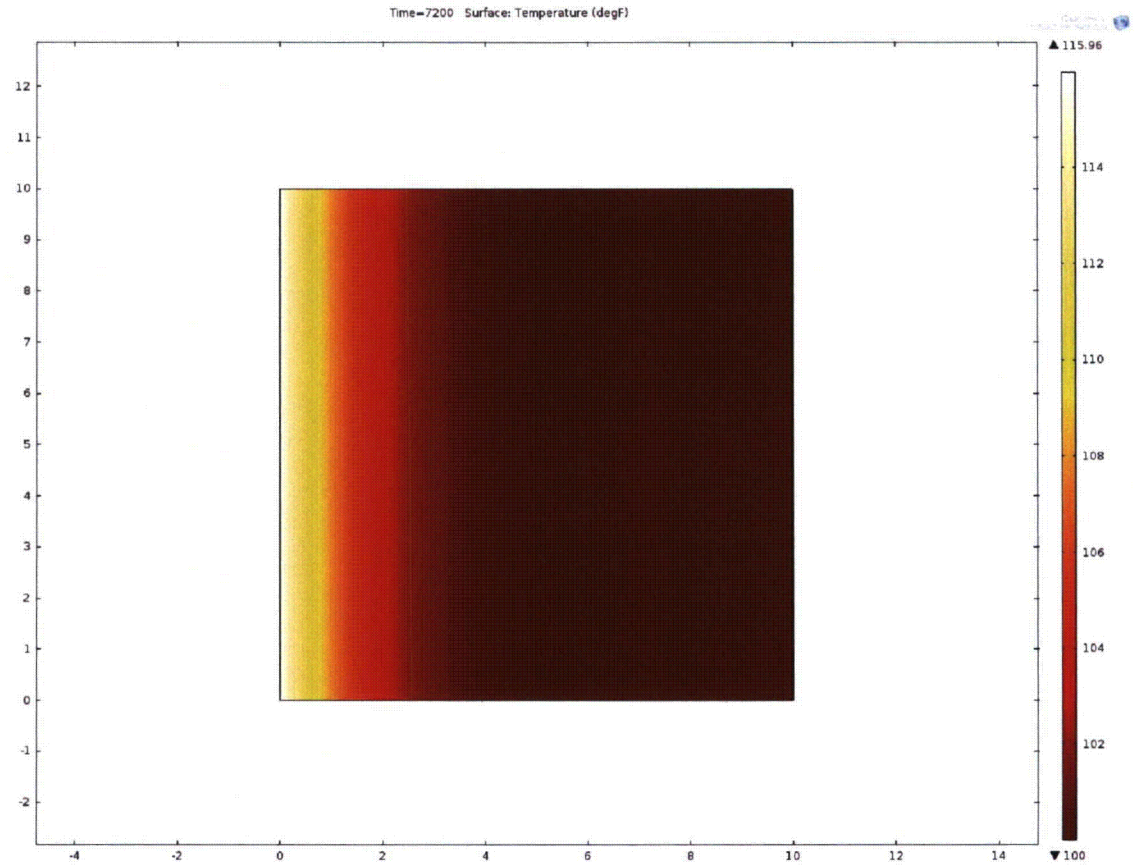

Figure 4 – Temperature Contours for Test Problem No. 4

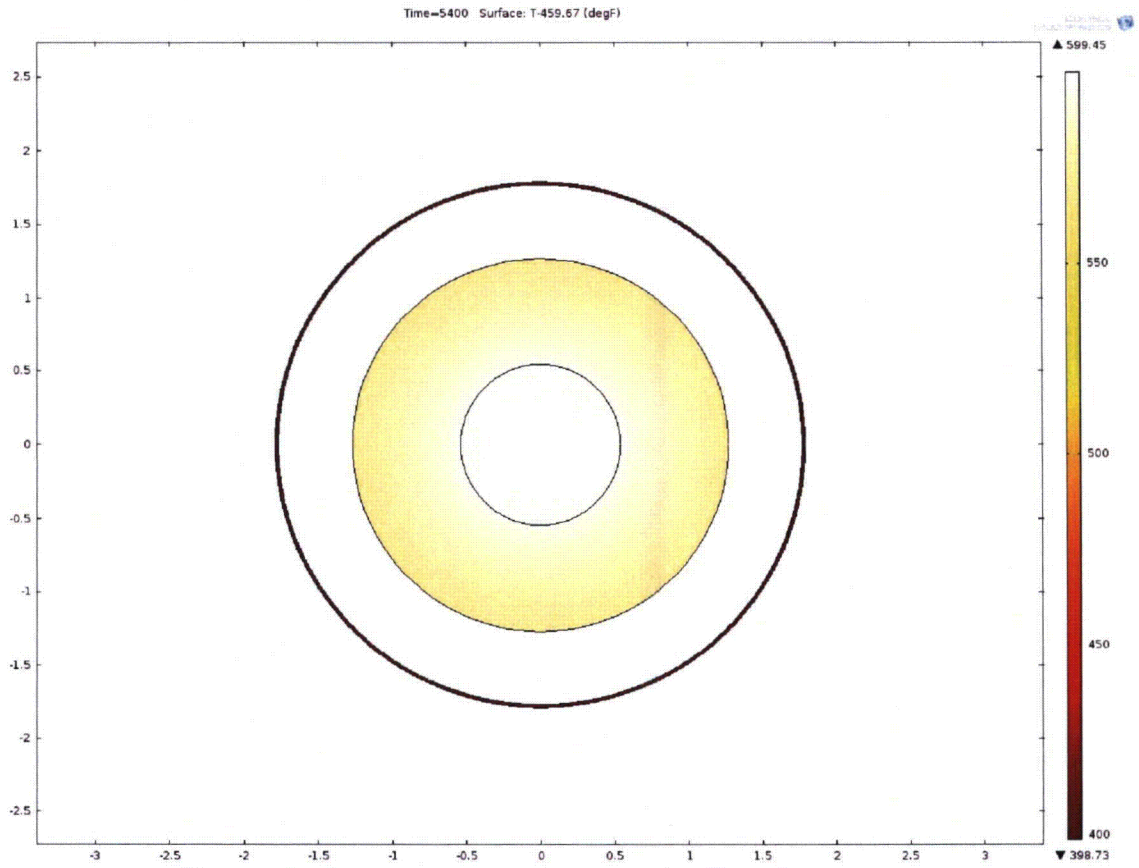

Figure 5 – Temperature Contours for Test Problem No. 5

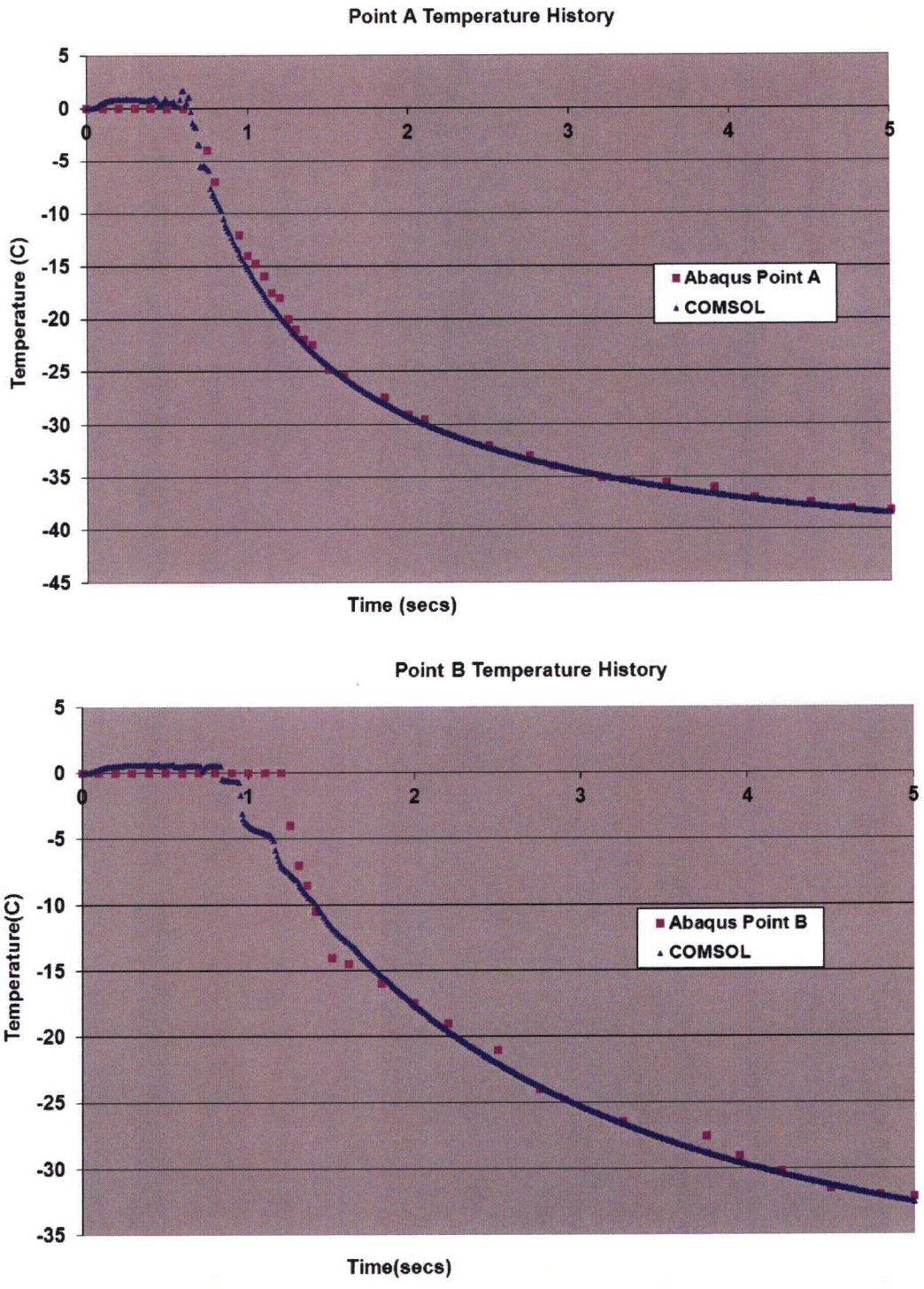

Figure 6 - Temperature Plots for Test Problem No. 6

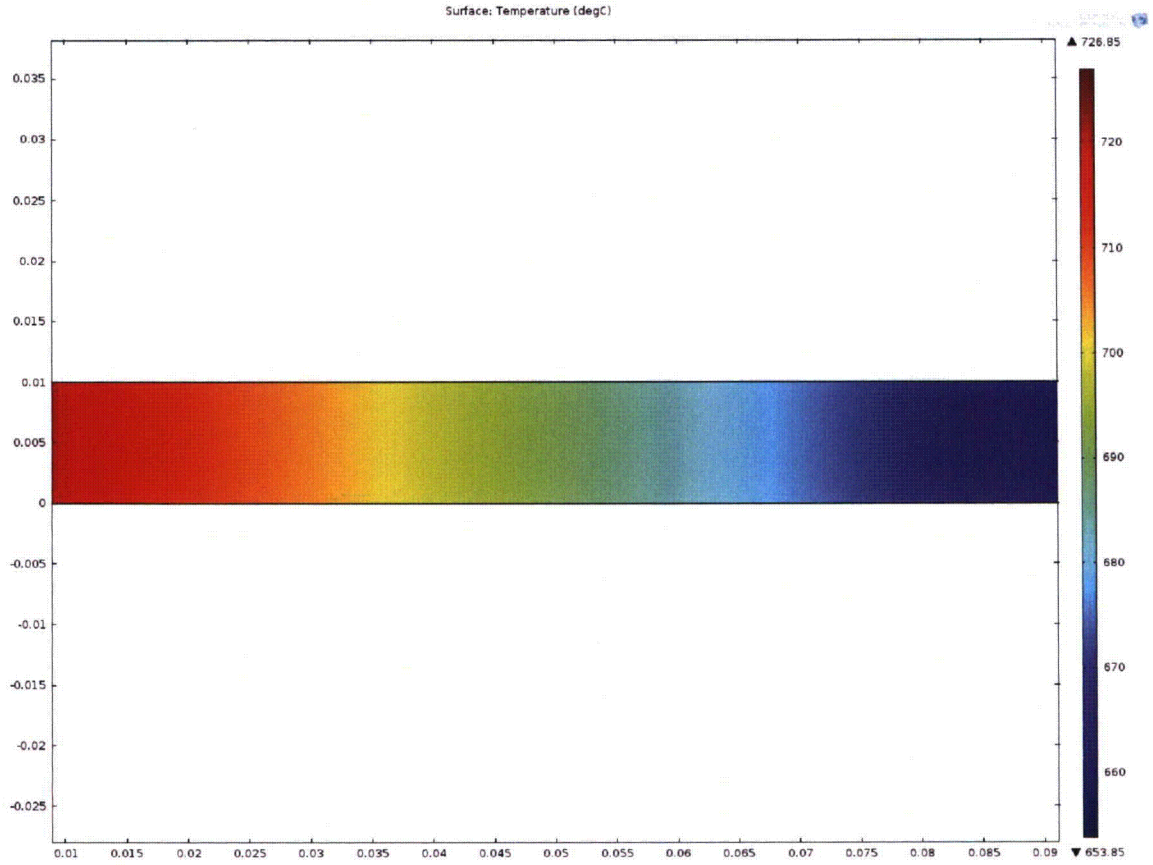

Figure 7– Temperature Contours for Test Problem No. 7

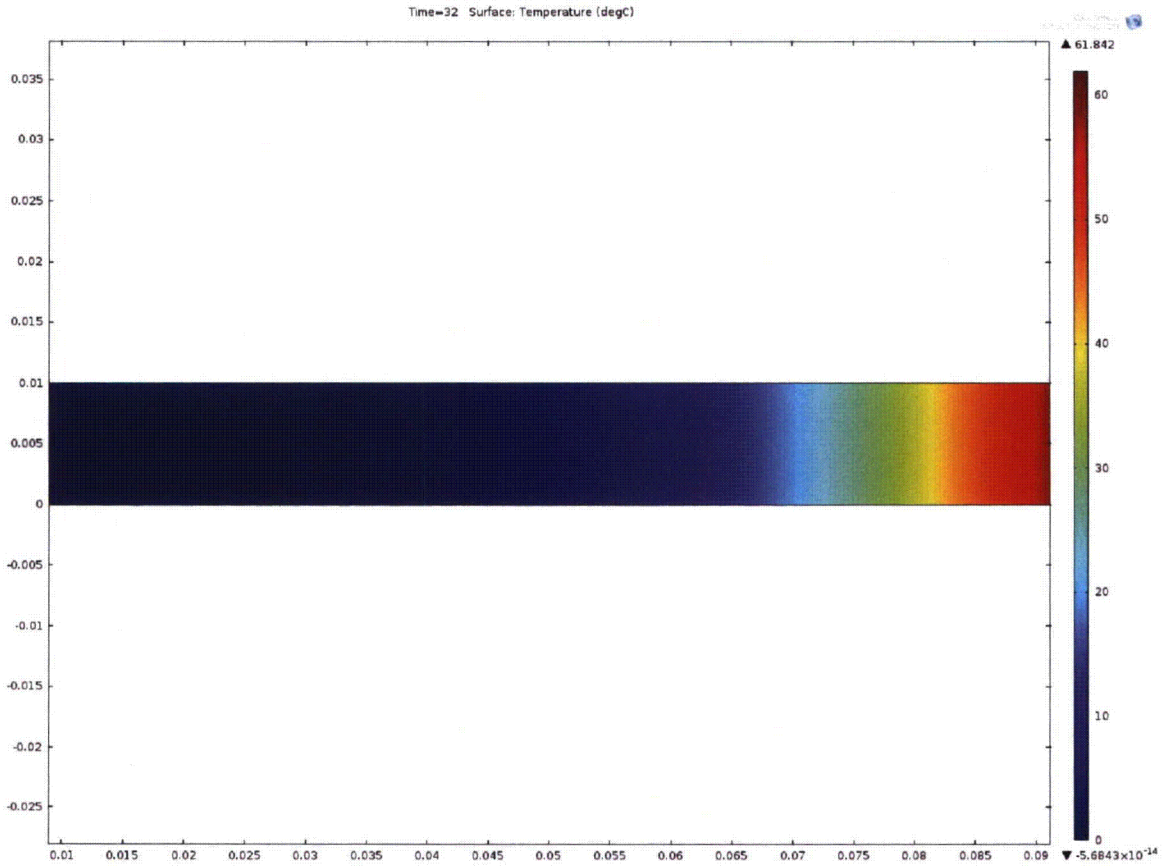

Figure 8– Temperature Contours for Test Problem No. 8

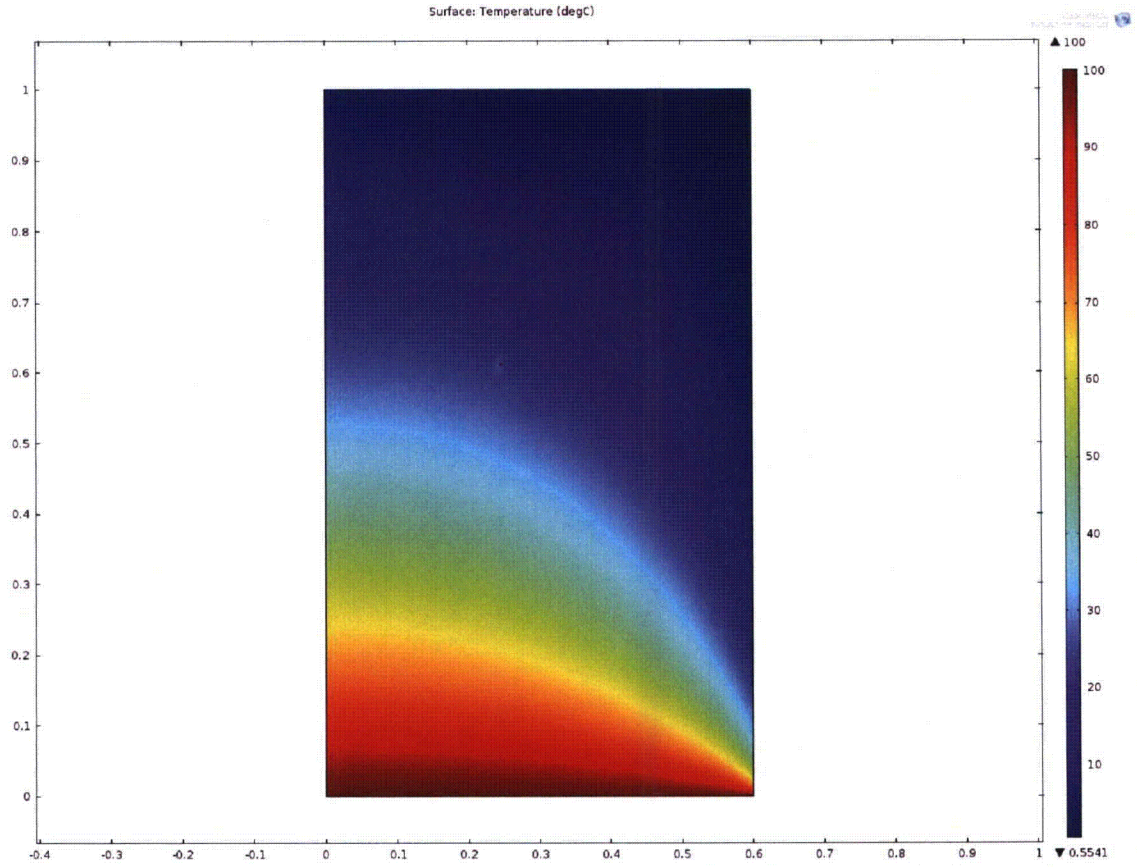

Figure 9– Temperature Contours for Test Problem No. 9

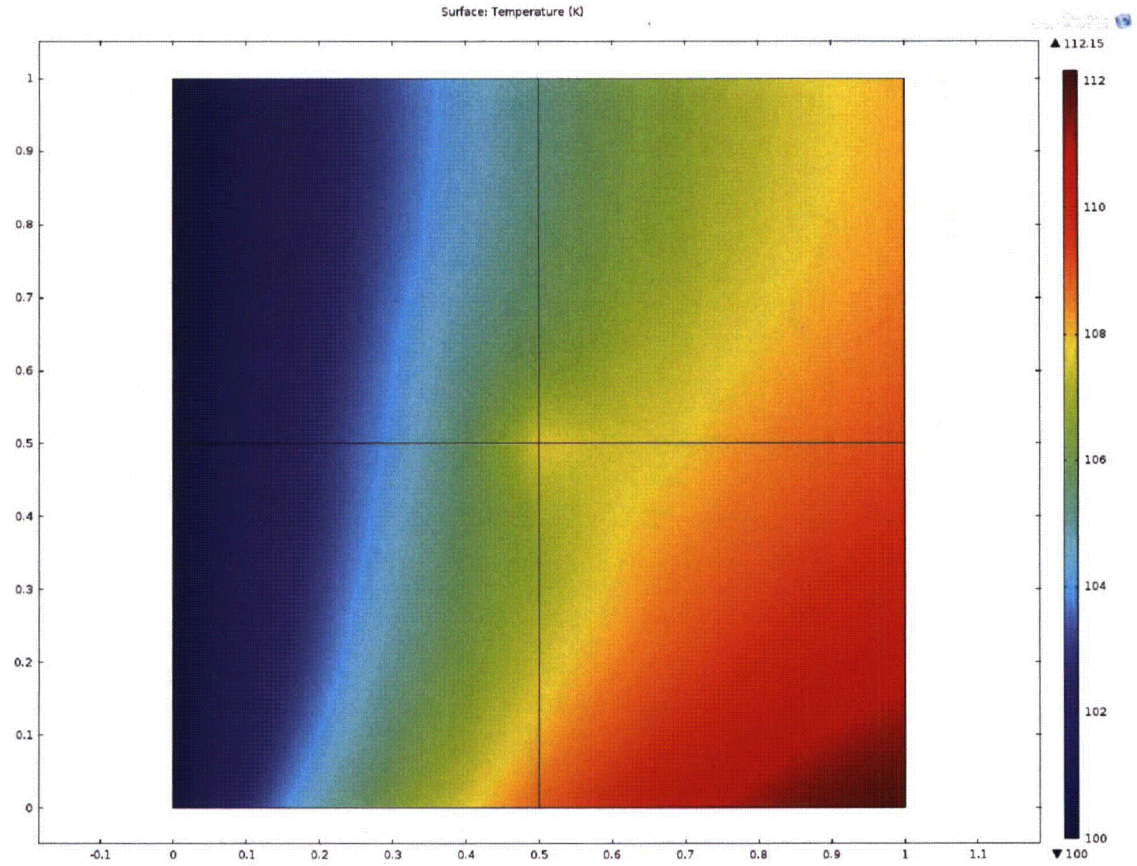

Figure 10– Temperature Contours for Test Problem No. 10

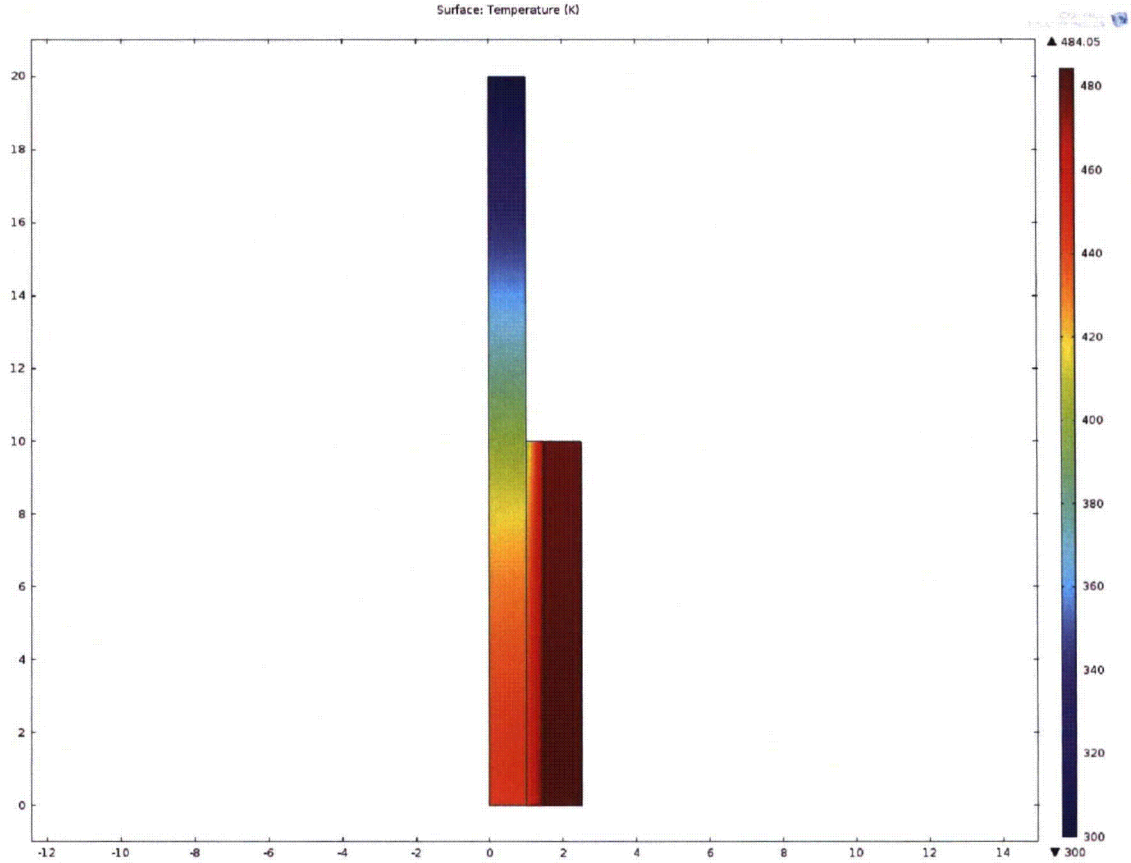

Figure 11– Temperature Contours for Test Problem No. 11

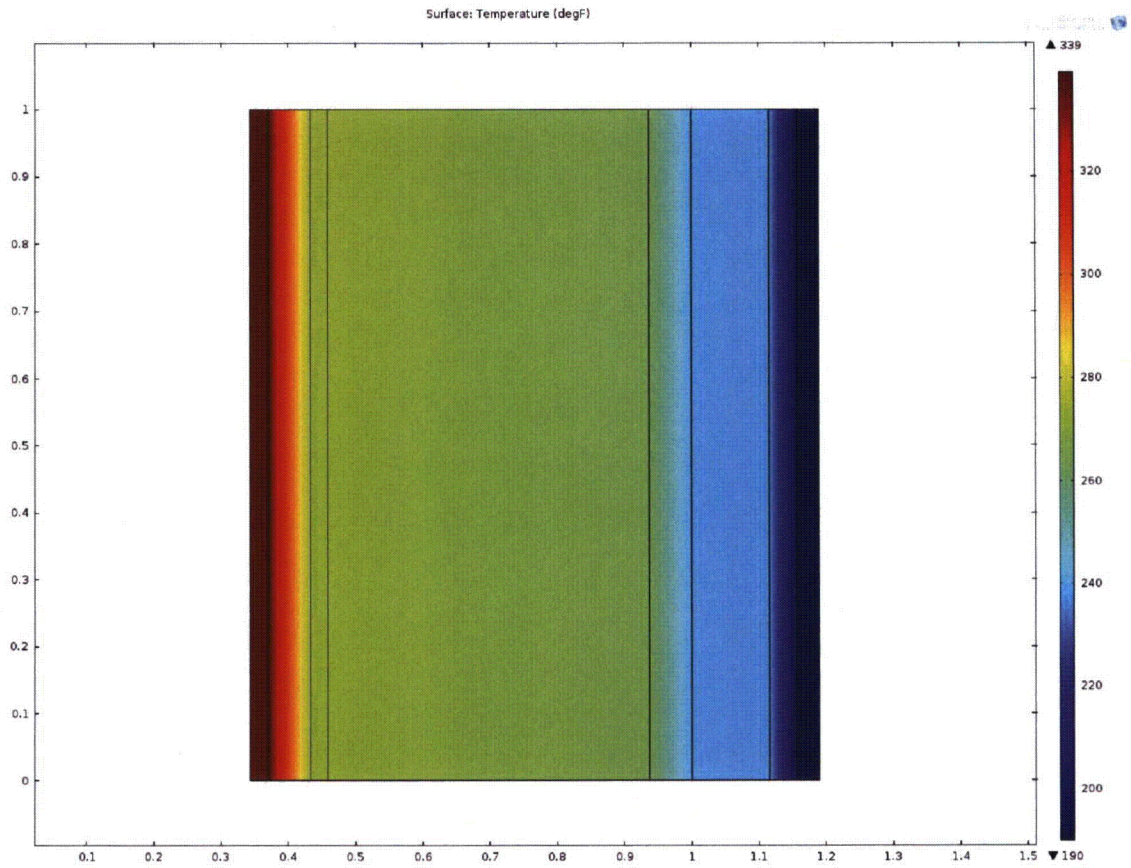

Figure 12– Temperature Contours for Test Problem No. 12

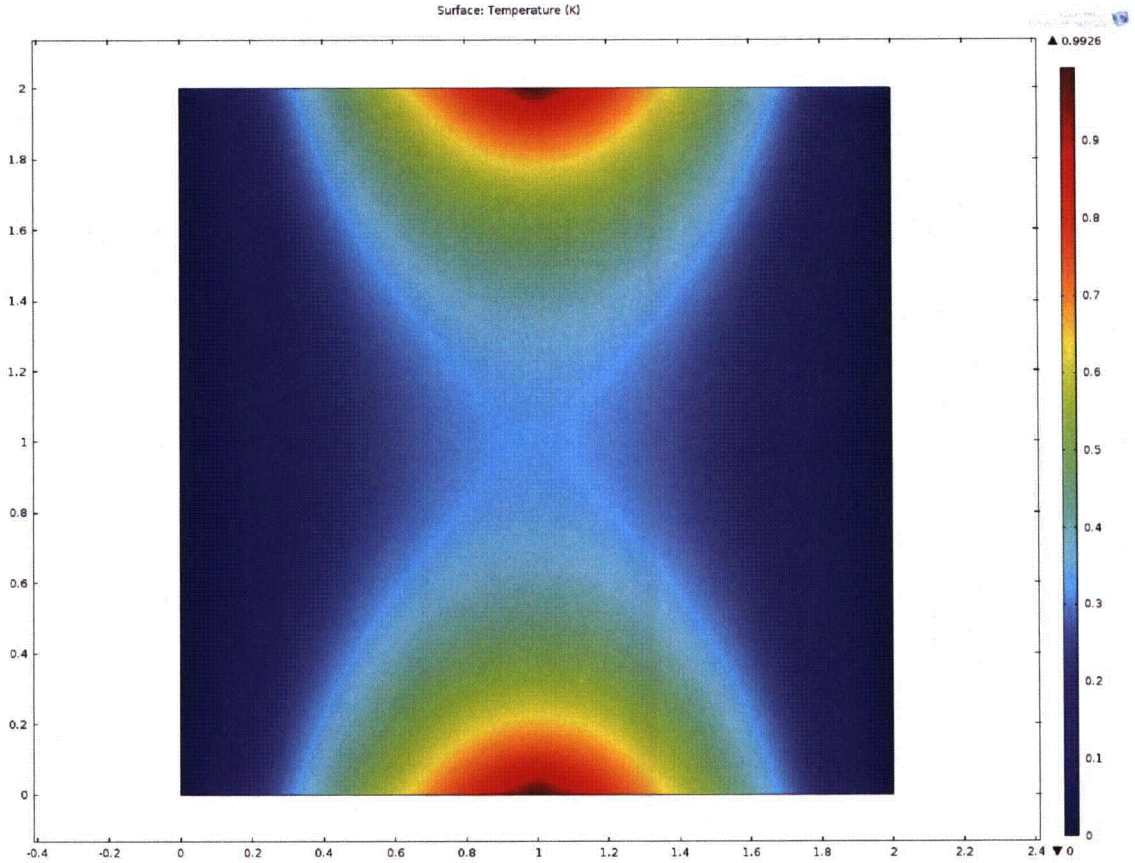

Figure 13– Temperature Contours for Test Problem No. 13

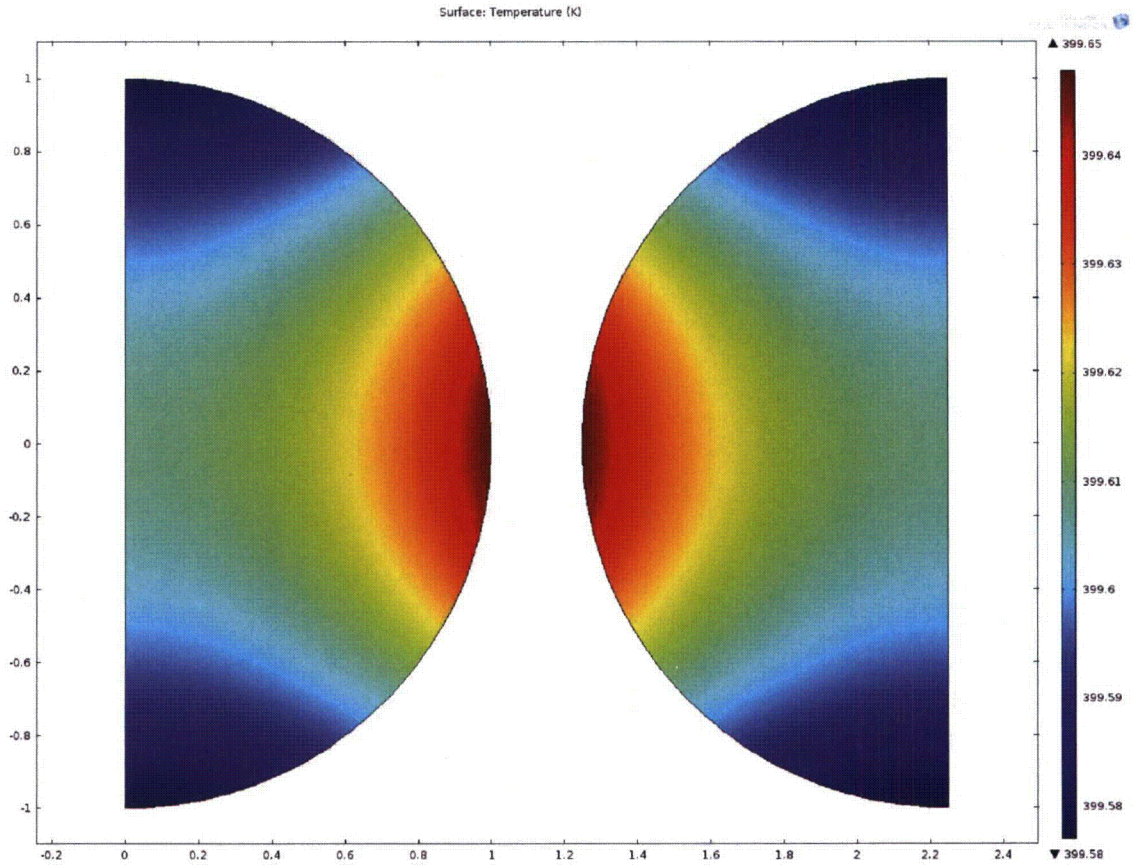

Figure 14– Temperature Contours for Test Problem No. 14

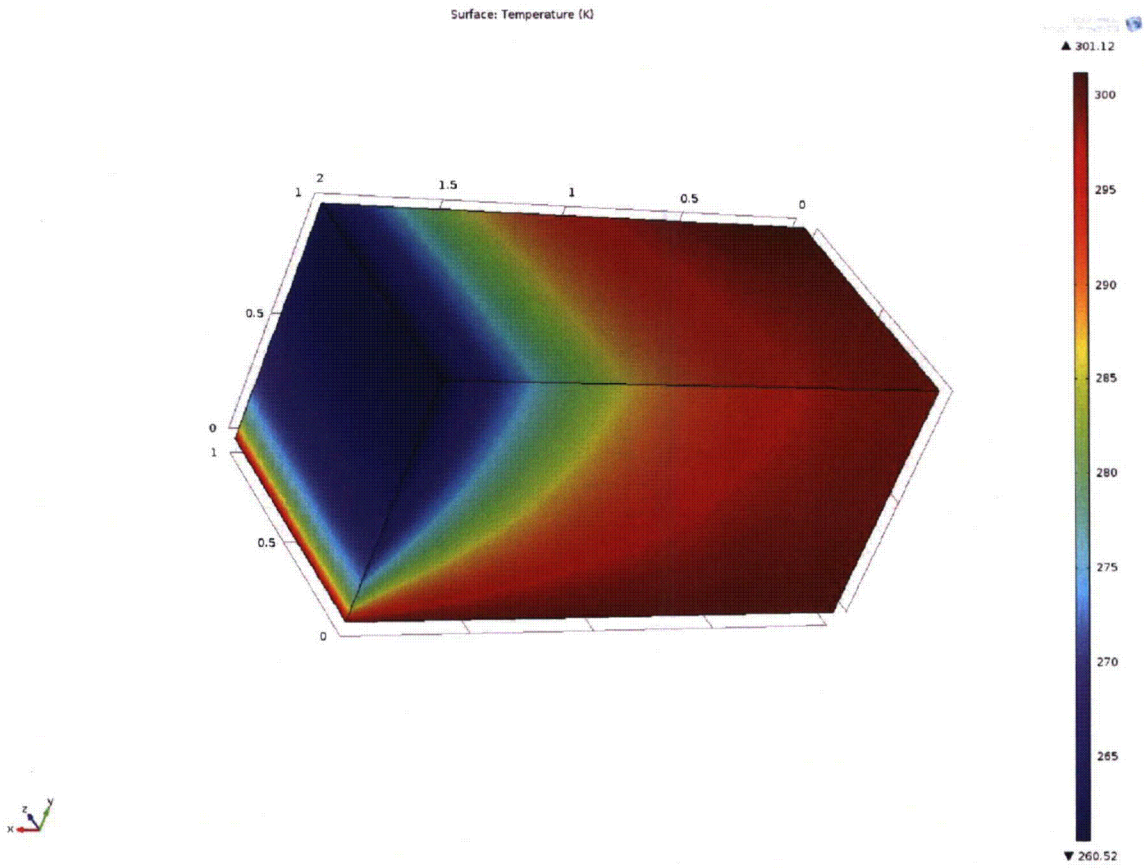

Figure 15– Temperature Contours for Test Problem No. 15

Attachment 9.3 - Computer Files

All folders are located in:

/hpc/archive/ems/qa/comsol/Comsol43

Test Case	Model File	Date/Time Stamp	SubFolder
1	Testcase1.mph	10/42012 11:49AM	TestCase1
2	Testcase2.mph	10/4/2012 11:52 AM	TestCase2
3	Testcase3.mph	10/4/2012 11:53 AM	TestCase3
4	Testcase4.mph	10/4/2012 12:01 PM	TestCase4
5	Testcase5.mph	10/4/2012 1:09 PM	TestCase5
6	Testcase6.mph	10/15/2012 6:52 AM	TestCase6
7	Testcase7.mph	10/15/2012 7:11 AM	TestCase7
8	Testcase8.mph	10/15/2012 7:15 AM	TestCase8
9	Testcase9.mph	10/15/2012 7:29 AM	TestCase9
10	Testcase10.mph	10/15/2012 8:09 AM	TestCase10
11	Testcase11.mph	10/15/2012 8:13 AM	TestCase11
12	Testcase12.mph	10/25/2012 2:49 PM	TestCase12
13	Testcase13.mph	10/25/2012 2:25 PM	TestCase13
14	Testcase14.mph	10/25/2012 2:36 PM	TestCase14
15	Testcase15.mph	10/25/2012 2:42 PM	TestCase15

WVMP SAR Reference 3-28

"NCT and HAC Thermal Analysis for the MC5PV," M-CLC-A-00448, Revision 1, Kesterson M.R., Savannah River National Laboratory, Aiken, South Carolina, July 25, 2013.

Redacted Version

OSR 45-24 (Rev 12-6-2012)

Proc. Ref. E7, 2.31

Calculation Cover Sheet

Sheet 1 of 23

Project/Task	Calculation Number	Project/Task Number
NA	M-CLC-A-00448	NA

Title	Functional Classification
NCT and HAC Thermal Analysis for the MC5PV	SC
	Discipline: Mechanical

Calculation Type	Type 1 Calculation Status
◉ Type 1 ○ Type 2	○ Preliminary ◉ Confirmed

Computer Program Number	Version/Release Number
COMSOL Multiphysics ☐ N/A	COMSOL 4.3a

Purpose and Objective

This calculation evaluates the thermal performance of the Bulk Tritium Shipping Package (BTSP) for the Normal Conditions of Transport (NCT) and Hypothetical Accident conditions (HAC) containin an Mound Configuration 5 Process Vessel package (MC5PV). Maximum temperatures of various components are calculated and compared against their design limits.

[redacted]

Summary of Conclusion

1. The NCT and HAC analyses show that the maximum component temperatures are below their design limits.

2. The analyses show that the BTSP Mound Configuration 5 Process Vessel package meets the thermal design requirements given in 10 CFR Part 71.

REVISIONS

Rev No.	Revision Description
0	Initial issue.
1	Updated tables 6, 7, and 8 to reflect current HAC temperature limits.

SIGN OFF

Rev No.	Originator (Print / Sign & Date)	Verification/Checking Method	Verification/Checker (Print / Sign & Date)	Manager (Print / Sign & Date)
1	M. R. Kesterson [redacted]	☐ Design Check (GS/PS only) ☒ Document Review ☐ Qualification Testing ☐ Alternate Calculation ☐ Operational Testing	S. Y. Lee [redacted]	M. K. Harris
		☐ Design Check (GS/PS only) ☐ Document Review ☐ Qualification Testing ☐ Alternate Calculation ☐ Operational Testing		

Additional Reviewer (Print Name)	Signature	Date
NA		

Design Authority (Print Name)	
Paul Blanton	[redacted]

Revisions

Revision	Description
0	Original Issue
1	Updated tables 6, 7, and 8 to reflect current HAC temperature limits.

Table of Contents

Section	Description	Page
1.0	INTRODUCTION	5
2.0	INPUTS AND ASSUMPTIONS	6
3.0	ANALYTICAL METHODS AND COMPUTATIONS	13
4.0	RESULTS	17
5.0	CONCLUSIONS	22
6.0	REFERENCES	23

Nomenclature and Units

h = Convection Heat Transfer Coefficient (Btu/hr-ft^2-°F)
k = Thermal Conductivity (Btu/hr-ft-°F)
ρ = Density (lb/ft^3)
C_p = Specific Heat (Btu/lb-°F)
L = Characteristic Length (ft)
T = Temperature (°F)

Acronyms and Abbreviations

CCSS	Configuration Control Support Structure
CCV	Contamination Control Vessel
CoC	Certificate of Compliance
CV	Containment Vessel
DOT	Department of Transportation
BTSP	Bulk Tritium Shipping Package
HAC	Hypothetical Accident Conditions
HAC/Solar	Hypothetical Accident Conditions (Steady State) with Insolation
HSV	Hydride Storage Vessel
HTV	Hydride Transport Vessel
MC5PV	Mound Configuration 5 Process Vessel
NCT	Normal Conditions of Transport
NCT/Solar	Normal Conditions of Transport with Insolation
NCT/Shade	Normal Conditions of Transport without Insolation
PV	Product Vessel
SARP	Safety Analysis Report for Packaging
SRNL	Savannah River National Laboratory
SS	Stainless Steel

1.0 INTRODUCTION

This document describes the thermal performance of the Bulk Tritium Shipping Package (BTSP) for the Normal Conditions of Transport (NCT) and the Hypothetical Accident Conditions (HAC) containing the Mound Configuration 5 Process Vessel (MC5PV) package. The BTSP has been previously evaluated for multiple product vessel (PV) configurations [1]. Figure 1 shows a schematic of the BTSP package with a generic PV content. This calculation evaluates the MC5PV within the BTSP. The MC5PV was previously authorized for shipment in the AL-M1 Nuclear Packaging (DOE CoC No. USA/9507/BLF)[2]. The general configuration of the MC5PV in a BTSP is shown in Figure 1 and a photo of the MC5PV are shown in Figure 2.

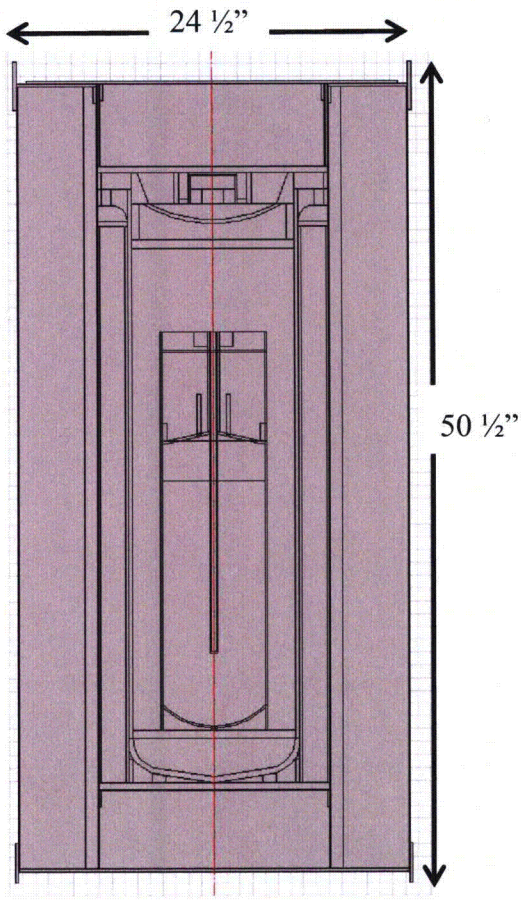

Figure 1 Schematic and dimensions of the BTSP package containing the CV.

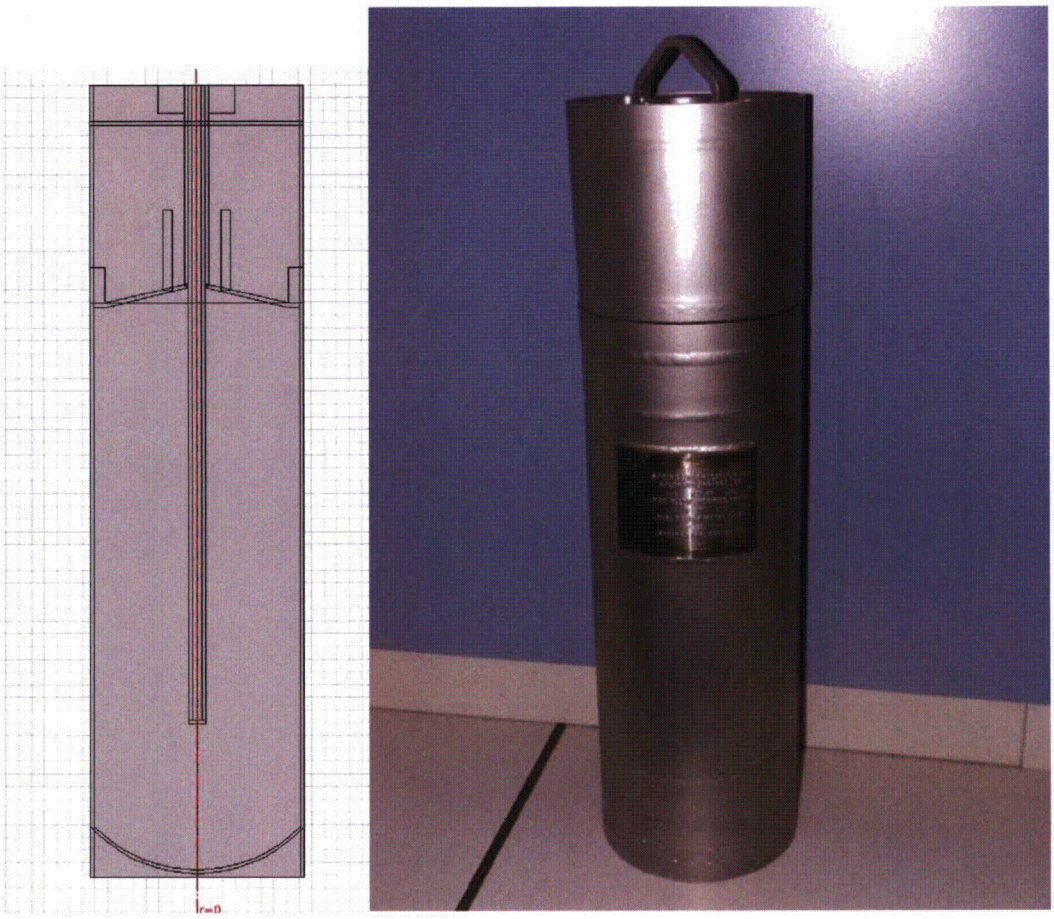

Figure 2 Sketch and Photo of the MC5PV Product Vessel

Technical specifications for the BTSP packaging components are provided on the BTSP engineering drawings[3]. Package design specifications relevant to the thermal analysis are summarized below.

2.0 INPUTS AND ASSUMPTIONS

2.1 Package Construction

Drum and Lid Assembly

The BTSP drum assembly consists of a 16 gauge Type 304L stainless steel (SS) drum shell with top and bottom bands welded to SS top and bottom plates and a 16 gage SS liner. A CV support shelf is welded to the bottom of the liner assembly. The drum top plate is fitted for a bolted-flange closure and is closed by a lid assembly. The closure lid incorporates a cylinder of Thermal Ceramics Vermiculite TR-19™ Block insulation. The drum assembly bottom is welded closed with a SS plate after the volume is fitted with a cylinder of the TR-19™ block insulation. The assembly construction details are defined on Drawings R-R4-G-00040, R-R3-G-00049 and R-R3-G-00051.[3]

Compressed Fiberfrax®, Last-A-Foam® and Vermiculite TR-19

Three layers of Fiberfrax® insulation blanket with density 7-10 lb/ft^3 are wrapped around outside of the drum liner. The drum fabrication process has liquid General Plastics Manufacturing Company Last-A-Foam® FR-3710[4] polyurethane foam being poured into the annular region between the insulation blanket and the drum wall. The Last-A-Foam® expands and becomes rigid as it cures, with a bulk density of 10 lb/ft^3. The expanding foam compresses the 1.5 inch layer of Fiberfrax® to approximately ¾ inch. Because the thickness of the Fiberfrax® is approximately halved, its density is assumed to double. This assumption is based on the compression of Fiberfrax® in the 9977 package that has similar construction [5]. Details are shown in Drawing R-R2-G-00051.[3] The Vermiculite TR-19 is block insulation with a bulk density of 23 lb/ft^3. The TR-19 blocks are located both above and below the CV and in contact with the drum lid and base.

Containment Vessel (CV)

The BTSP CV is a SS pressure vessel designed, analyzed and fabricated in accordance with Section III, Subsection NB of the ASME Code, with design conditions of 500 psig at 400°F. The CV is fabricated from Type 304L SS seamless pipe having a minimum 0.250 inch wall thickness terminated by a machined base welded at one end (R-R3-G-00013) with a flange welded to the other.

The CV body is closed by a 304/304L SS lid secured by bolts. The CV leaktight containment seal, per ANSI N14.5, is made by an inner Inconel Alloy 718 C-ring while an outer elastomeric O-ring provides the capability of post-load verification of the seal.[6] The CV Lid has a 1-inch valve assembly protected by a valve cap attached with cap screws. Valve assembly and the C-rings[6] that fit into these grooves complete the leaktight closure assembly. The construction details are given in Drawings R-R1-G-00024, R-R3-G-00013, R-R4-G-00037, and R-R4-G-00038.[3]

Honeycomb Cylinder

The honeycomb cylinder is fabricated using 5052 aluminum and is covered both inside and outside with a layer of resin impregnated fiberglass cloth to give it a smooth and abrasion resistance surface. The construction details are given in drawing R-R2-G-00054.[3] Figure 3 shows the end view of the honeycomb cylinder and the CV assembly with the insulating pad placed on the honeycomb cylinder.

Aluminum Foam Spacers

Two aluminum foam spacers, placed inside the top and bottom the CV, provide impact protection. The construction details are given in drawing R-R4-G-00039.[3]

Silicone Pad

A silicone rubber pad, reinforced with fiberglass, is placed at the bottom of the drum liner as a flexible wear surface for the CV. The details are given in the drawing R-R2-G-00070.[3]

Insulating Pad

An insulating pad placed on the CV closure lid (see Figure 3) provides added thermal protection

to the CV seals. The pad is made of KAO-Tex Superwool insulation made by Thermal Ceramics. The design details are given in the drawing R-R2-G-00069.[3] The pads thermal properties are assumed to be the same as the Fiberfrax® insulation blanket due to their similarity in materials and construction.

Fiberglass Coated Honeycomb Cylinder

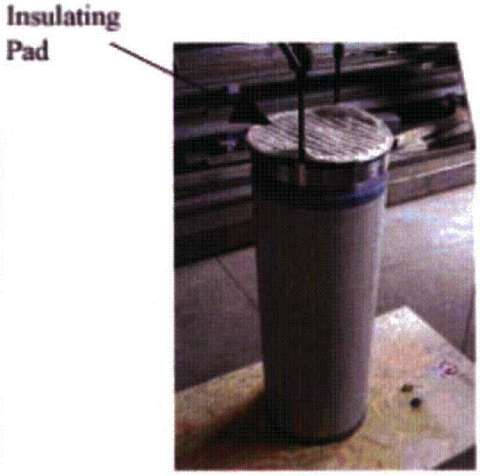

Honeycomb Cylinder and CV Assembly

Figure 3 Aluminum Honeycomb Cylinder and CV Assembly

2.2 Thermal Properties

Insulation Materials

The thermal conductivity *k* of the polyurethane foam is an important property for the NCT analyses. The foam vendor gives the thermal conductivity values at room temperature only. The values at higher temperatures were calculated previously[1] and are reported in **Table 1**. The density and specific heat values of the foam are modeled as constant values. The modified Sandia equation was validated for the 9977 package model [5].

The thermal conductivity of the compressed Fiberfrax® insulation blanket surrounding the liner is based on testing at SRNL.[8] Thermal properties of the compressed blanket are listed in **Table 1**. Vermiculite TR-19 Block insulation thermal properties are listed in Table 1.

Honeycomb Cylinder & Aluminum Foam Spacers

The honeycomb cylinder is procured based on a minimum strength and the foil thickness and cell size may vary to meet that requirement. The thermal properties of the aluminum honeycomb used in the analyses are based on testing and calculations. The radial plane *k* values are based on thermal conductivity tests[8] on aluminum 5052 honeycomb samples having appropriate cell size and foil thickness and a density of 12 lb/ft^3. The aluminum foam spacers are small compared to the honeycomb cylinder and are assumed to have the same thermal properties. The properties are modeled as constants and are listed in Table 2.

Other Materials

The properties of stainless steel and aluminum are listed in Table 2. Thermal properties of the silicone pad are approximated with grey silicone rubber [9]. The values are listed in Table 2.

Contents

The MC5PV contains a sorbent material with adsorbed tritiated water. The sorbent material can be a 4A, 5A, or 13X molecular sieve. The heat capacity of the various molecular sieves is constant and the density varies by 2% for the beaded material. The 5A molecular sieve density is an average of the other types of sieves. Therefore, for the purpose of this calculation, the thermal properties 5A molecular sieve used[10]. The heat generation of the contents is assumed to be the content maximum of 3.3 Watts [2]. A sensitivity analysis for the thermal properties of the contents is described in section 4.4.2.

In addition to the molecular sieve material, the contents can contain up to 2kg of water [2]. Water has a higher thermal conductivity than the molecular sieve materials and will therefore yield lower content temperatures for the steady state evaluations. The addition of water content will also add additional heat capacity to the content region, thereby also lowering the maximum temperatures attained in the transient case.

Gases

Tritium gas is assumed to fill the empty spaces inside the MC5PV. The space between the CV and the MC5PV is evacuated and filled with helium during the CV loading. The helium gas pressure is 1 to 5 psi [11] above the atmospheric pressure to ensure inert environment in the CV during transport. Air is assumed to fill any gaps between the CV and the silicon pad or honeycomb cylinder. Thermal properties of the tritium, helium and the air are given in Table 2.

Table 1 Thermal Properties of Insulating Materials

Material	Thermal Conductivity k, (Btu/hr-ft-°F)	Density ρ, (lb/ft^3)	Specific Heat Cp, (Btu/lb-°F)
Fiberfrax (compressed) Insulation Blanket (Values are based on tests at SRNL) [8] (Same for Insulating Pad)	2.14E-02 @ 70.0°F 2.25E-02 @ 122.0°F 2.43E-02 @ 185.0°F	20	0.27
Vermiculite TR-19 Block Insulation[12]	6.33E-02 @ 400.0°F 6.67E-02 @ 600.0°F 7.00E-02 @ 800.0°F 7.33E-02 @ 1000.0°F 7.75E-02 @ 1200.0°F 8.17E-02 @ 1400.0°F	23	0.20
Polyurethane Foam Insulation FR-3710 (During NCT and pre-fire)[7]	2.325E-02 @ 68.0°F 2.690E-02 @ 140.7°F 3.285E-02 @ 248.4°F 3.906E-02 @ 348.6°F	10	0.353

Table 2 Thermal Properties of Other Materials

Material	Thermal Conductivity k, (Btu/hr-ft-°F)	Density ρ, (lb/ft^3)	Specific Heat Cp, (Btu/lb-°F)
Honeycomb Cylinder (Radial plane) (Aluminum 5052)[8]	0.196	15.22 [a]	0.22
Honeycomb Cylinder (Axial plane) (Aluminum 5052)[8]	0.0982	15.22 [a]	0.22
Aluminum Foam Spacers (Radial) – Assumed same as honeycomb cylinder	0.196	16.9 [a]	0.22
Aluminum Foam Spacers (Axial) - Assumed same as honeycomb cylinder	0.0982	16.9 [a]	0.22
Aluminum (Type 6061 T-6)[13]	90.0	169.3	0.216
304L Stainless Steel[14]	7.74108 @ 32.0°F 9.43444 @ 212.0°F 12.5793 @ 932.0°F 14.9983 @ 1292.0°F	494.429	1.200E-01 @ 32.0°F 1.350E-01 @ 752.0°F
Tritium Gas (Hydrogen property values are used)[9]	0.105@80°F 0.119@170°F 0.132@260°F 0.145@350°F 0.169@530°F	5.11E-03@80°F 4.38E-03@170°F 3.83E-03@260°F 3.41E-03@350°F 2.79E-03@530°F	3.419@80°F 3.448@170°F 3.461@260°F 3.463@350°F 3.471@530°F
Helium[14]	8.177E-02 @ 32°F 8.685E-02 @ 77°F 9.096E-02 @ 120°F 9.846E-02 @ 212°F 1.226E-01@ 392°F 1.684E-01 @ 932°F 2.552E-01 @ 2192°F	0.01105	0.124
Air [14]	1.516E-02@80°F 1.735E-02@170°F 1.944E-02@260°F 2.142E-02@350°F 4.178E-02@1520°F	0.0735	0.240@80°F 0.237@212°F 0.265@1070°F 0.277@1520°F
Molecular Sieve 5A (Contents)[10]	0.48	44	0.19
Silicone Pad[9]	0.18	91.73	0.35
Aluminum shells[15]	0.185	28	0.22

Note: The numbers in brackets are the references at the end of the calculation.
[a] Based on bulk assembly

Surface Emissivities

Experience with the analyses for drum type packages (9975, 9977 and 9978) has shown that changes in the internal surface emissivities result in a relatively small change (< 5°F) in the predicted temperatures. The emissivity values for the various surfaces are listed in Table 3. These were used previously in certified drum type packages[1] and have shown acceptable agreement with test results. The emissivity values for honeycomb cylinder, silicone pad and insulating pad are obtained from the sources cited.

Table 3 Surface Emissivities

Surface		Emissivity
Component	**Material**	
CV	304L Stainless Steel	0.30
Drum Liner	304L Stainless Steel	0.30
Bottom of Lid	304L Stainless Steel	0.30
CCSS	Aluminum	0.20
Honeycomb Cylinder[1]	Aluminum/Fiberglass	0.75
Exterior of Drum (NCT & pre-fire)	304L Stainless Steel	0.21
Exterior of Drum (during HAC post-fire)	304L Stainless Steel	0.80
Silicone Pad (grey soft rubber)[2]	Silicone Rubber Pad	0.86
Insulating Pad (Kao-Tex with cover)[2]	Fiberglass Cloth Cover	0.77

[1] www.infracd-thermography.com/material-1.htm

[2] www.ib.cnea.gov.ar/~experim2/Cosas/omega/emisivity.htm

The surface emissivity values in Table 3 are for the gray and diffuse surfaces. The CV is a machined stainless steel component with clean surfaces. These surfaces are not polished. The drum surface is assumed as received (medium finish). For the NCT analyses, the drum surface thermal emissivity value (0.21) and solar absorptivity (0.498 or $\approx$ 0.50) are based on the detailed analysis for different types of drum surfaces.[22] The drum surface emissivity value during HAC post-fire phase is the minimum value (0.8) specified in the 10CFR 71.73. The corresponding solar absorptivity of the drum surface which is oxidized and is of dark gray color is assumed to be 0.9. A lower drum surface emissivity value results in higher component temperatures during post-fire cooling.

2.3 Geometry Modeling Assumptions

2.3.1 Drum and Lid Assembly

The dimensional details of the various components are given in drawings in Reference 3. The dimensions used in making the models are the nominal values and no attempt is made to incorporate tolerances in the dimensions. Nuts, bolts and welds are not included in the model because their impact on the temperature distribution is negligible. Since the gaps between components are small, it is assumed that the various components inside the drum remain concentric. A minor shifting of the components has only secondary effects on the package temperature field. The resulting thermal models are axisymmetric and are depicted in various figures only as half model.

2.3.2 Other Components

The gas valve assembly is located off-center in the CV Lid design but is modeled in the center. Valving and tubing connected on to the MC5PV are not amenable to accurately model in an axisymmetric model. Therefore, the MC5PV geometry is modified to include a ring at the top of the vessel representing the mass of the valving and tubing.

3.0 ANALYTICAL METHODS AND COMPUTATIONS

The mathematical equations describing the thermal models are solved by numerical methods. The general purpose conduction-radiation computer code COMSOL Multiphysics® was used to perform the computations.[16] This computer code meets site nuclear safety QA requirements.[17] Work was performed in accordance with the WSRC E7 manual.[18]

3.1 NCT Thermal Models

The NCT models for the NCT/Shade and NCT/Solar were developed using the COMSOL Multiphysics software. Boundary conditions, described in section 3.2, meet the intent of those specified for NCT in 10CFR71.71.[19] In the thermal analysis, the limiting components are the containment vessel, its C-ring seals, and the polyurethane foam insulation. Temperature limits for components of the BTSP for the NCT are tabulated, along with predicted maximum temperatures, for the MC5PV model in Tables 4 and 5. The BTSP model for NCT analyses includes interior metal surfaces, namely the drum shell and its liner, CV surfaces, and the metal surfaces between the drum lid, drum liner and the upper part of the CV lid.

Three modes of heat transfer - namely conduction, convection, and radiation - are considered in the analysis. Natural convection is evaluated on the outer drum surface but is ignored inside the CV cavity and in small gaps. This simplification is conservative since it yields higher local temperatures. Radiation is considered in all gas filled areas of the model. The pressures of gases in internal cavities are assumed to be one atmosphere.

The modeled MC5PV package contains maximum of 5.6 kg of molecular sieve material [2] with adsorbed tritiated water. The thermal properties of a loaded molecular sieve are not directly known. Therefore, a sensitivity analysis was performed, section 4.4.2, to determine the effect on the package temperature of a dry mixture and a mixture that is principally all water. For these

calculations the thermal properties of a 5A molecular sieve[10] were used. The maximum heat generation of the contents is assumed to be 3.3 Watts. Figure 4 shows the color representation of the materials with the MC5PV as the source model. The fill height of the molecular sieve was determined by the mass, density of the molecular sieve and the internal dimensions of the AL-M1 container. Having a lower mass or higher density molecular sieve will yield lower sieve volumes and if the decay heat remains constant, slightly higher (by 6°F) content temperatures will be seen. Section 4.4.2 discusses the effect of the molecular sieve density on the thermal analysis.

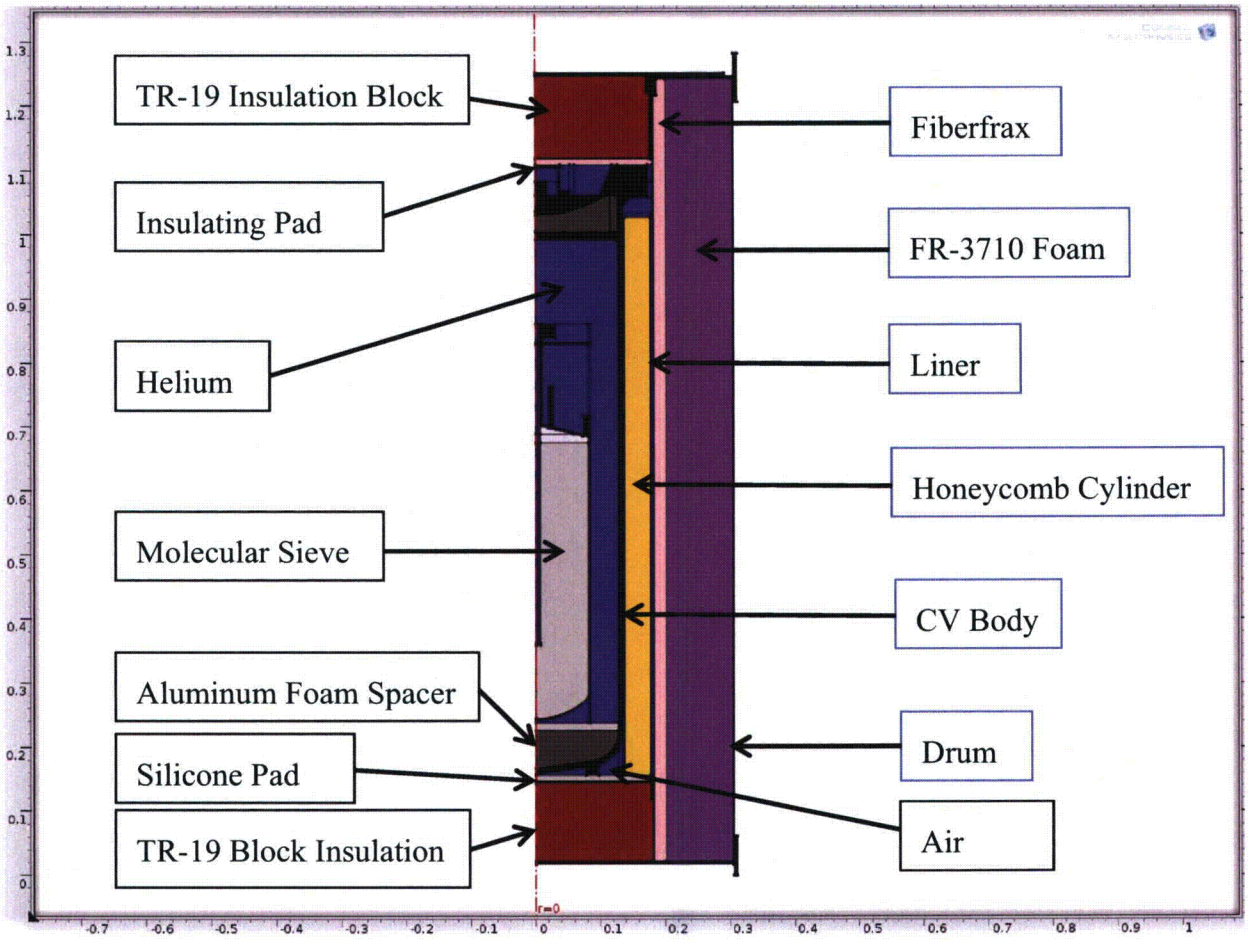

Figure 4 - Material Representation for BTSP with MC5PV.

3.2 Boundary Conditions

The boundary conditions used in the analytical models include the ambient temperature, solar heating, and convection and radiation heat exchange from the drum surfaces. Solar heating used in the NCT/Solar analyses is applied as heat flux to the drum's outer surface. 10CFR 71.71 prescribes a total insolation energy of 800 cal/cm^2 over a period of 12 hours on a horizontal surface and 400 cal/cm^2 over a period of 12 hours on the vertical surface, alternating 12 hours on and 12 hours off. The corresponding time averaged heat fluxes are 245.77 Btu/ft^2-hr on the top

of the package and 122.88 Btu/ft^2-hr on the side of the package. The applied solar fluxes using absorptivity of 0.50 are 122.88 Btu/ft^2-hr on the top of the package and 61.44 Btu/ft^2-hr on the side of the package. As listed in Table 3, the emissivity value for the outer surface of the drum is 0.21 for the pre-fire condition and 0.8 for the post-fire condition. Other specific parameters and related assumptions are summarized in the description of the NCT/Solar model below.

Description of the NCT/Solar Model

All NCT/Solar calculations were performed under the following conditions:

1. The drum is in an upright position and the contents are assumed to remain concentric during transport.
2. The drum bottom surface is adiabatic.
3. There is radiative heat transfer from the sides and top of the drum to the ambient.
4. There is natural convection heat transfer from the sides and top of the drum to the ambient.
5. The ambient temperature is 100°F.
6. Insolation is applied as solar heat flux. The applied solar fluxes are 122.88 Btu/ft^2-hr on the top of the package and 61.44 Btu/ft^2-hr on the side of the package. These heat fluxes are applied continuously rather than as a step function with a period of 12 hours.
7. The polyurethane foam thermal conductivity is the calculated value obtained from Reference [5]. The thermal conductivity values are validated by the environmental thermal test described in Reference [1].
8. The thermal properties for 50% compressed Fiberfrax® are used for the insulating blanket surrounding the drum liner.
9. The Content decay heat is 3.3 Watts.

The model for the NCT/Shade was the same as that for the NCT/Solar except that the insolation heat flux was omitted.

Description of the NCT/Shade Model

1. The drum is in an upright position.
2. The drum bottom surface is adiabatic.
3. There is radiation heat transfer from the sides and top of the drum to the ambient.
4. There is natural convection heat transfer from the drum sides and top to the ambient.
5. The ambient temperature is 100°F in shade
6. The polyurethane foam thermal conductivity is the calculated value obtained from Reference [5].Unburned foam properties are applied to the foam in the drum.
7. The Content decay heat is 3.3 Watts.

3.3 HAC Thermal Models

The HAC/solar analysis refers to the steady state analysis with a 100 °F ambient temperature and insolation during the post-fire phase where the drum surface optical properties reflect the dark gray surface appearance of the fire affected drum surface. For the HAC/solar analysis, the solar absorptivity is assumed 0.9 and the emissivity as 0.8. Lower emissivity gives higher steady state temperatures for this analysis. The analysis results are given in Section 4.0.

Description of the HAC/Solar Fire Model

1. The drum is in an upright position with contents.
2. The drum bottom surface is adiabatic.
3. There is radiation heat transfer from the sides and top of the drum to the ambient.
4. There is natural convection heat transfer from the drum sides and top to the ambient.
5. The ambient temperature is 1475°F.
6. Insolation is applied as solar heat flux assuming solar absorptivity of 0.9 for the drum surface during post-fire cooling. The applied solar fluxes are 221.18 Btu/ft^2-hr on the top of the package and 110.59 Btu/ft^2-hr on the side of the package. These heat fluxes are applied continuously rather than as a step function with a period of 12 hours.
7. Thermal properties for air are used in place of the polyurethane foam. This is due to charring of the foam during the fire phase.
8. The Content decay heat is 3.3 Watts.

Description of the HAC/Solar Model

1. The drum is in an upright position with contents.
2. The drum bottom surface is adiabatic.
3. There is radiation heat transfer from the sides and top of the drum to the ambient.
4. There is natural convection heat transfer from the drum sides and top to the ambient.
5. The ambient temperature is 100°F.
6. Insolation is applied as solar heat flux assuming solar absorptivity of 0.9 for the drum surface during post-fire cooling. The applied solar fluxes are 221.18 Btu/ft^2-hr on the top of the package and 110.59 Btu/ft^2-hr on the side of the package. These heat fluxes are applied continuously rather than as a step function with a period of 12 hours.
7. Pristine foam (10 lb/ft^3) thermal properties are applied to the char cavity in the drum. This is a highly conservative assumption for the transient post-fire model, due to the pristine foam having a higher density and heat capacity compared to air. The package will retain heat for a longer period of time and yield higher maximum temperature for the transient case.
8. The Content decay heat is 3.3 Watts.

4.0 RESULTS

4.1 NCT/Shade Model Results

The MC5PV NCT/Shade model examined a temperature profile for a 3.3 Watt heat source. The maximum predicted temperatures of the limiting components are listed in Table 4. Figure 5 is the package temperature contour.

Table 4 NCT/Shade Maximum Component Temperatures (°F)

Component	BSTP/MC5PV Model (°F)	Temperature Limit (°F)
CV Wall	112	400
CV C-ring	105	1200
Cap C-Ring	106	1200
Bellows Valve	106	400
Honeycomb Cylinder	111	350
MC5PV Contents	154	NA
Drum Surface	101	NA
Last-A-Foam® FR-3710	107	300
Gas in CV (Volume Average)	111	NA
Gas in MC5PV (Volume Average)	117	NA

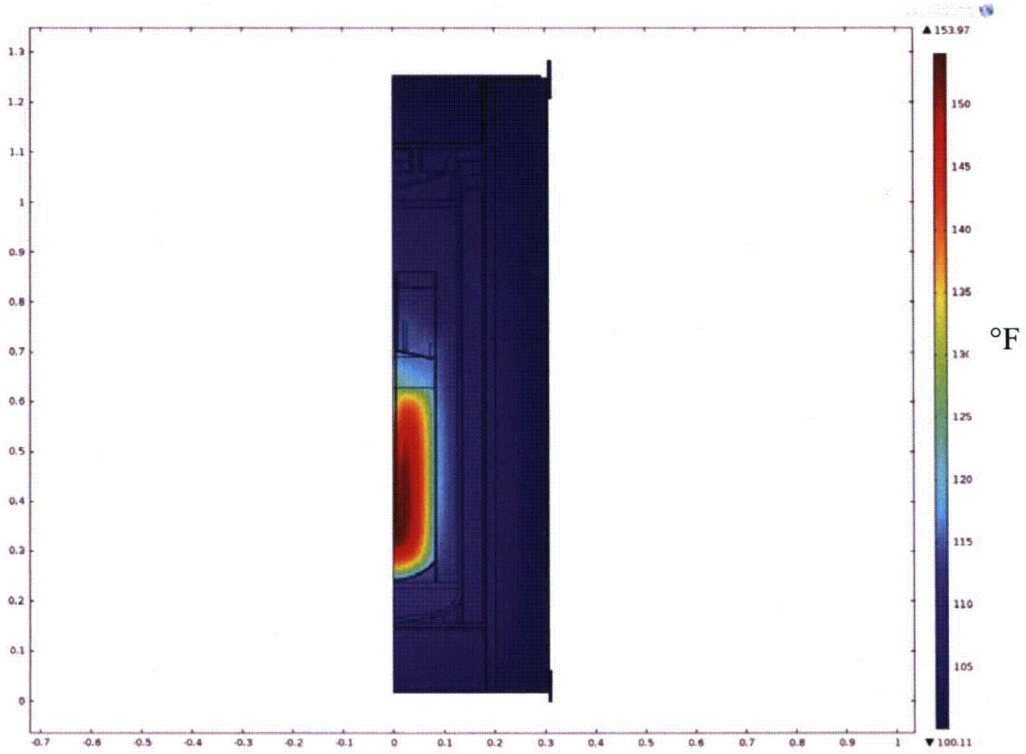

Figure 5 MC5PV Prefire Temperature Profiles for NCT/Shade

4.2 NCT/Solar Model Results

The MC5PV NCT/Solar model determined a temperature profile for a 3.3 Watt heat source. The maximum predicted temperatures of the limiting components are listed in Table 5. The package temperature contour is Figure 6.

Table 5– NCT/Solar Maximum Component Temperatures (°F)

Component	BTSP/MC5PV Model (°F)	Temperature Limit (°F)
CV Wall	158	400
CV C-ring	157	1200
Cap C-ring	158	1200
Bellows Valve	158	400
Honeycomb Cylinder	157	350
Contents	185	NA
Drum Surface	164	NA
Last-A-Foam® FR-3710	159	300
Gas in CV (Volume Average)	159	NA
Gas in MC5PV (Volume Average)	163	NA

4.2.1 Volume Average Gas Temperature

Volume average gas temperature is required for calculating the maximum normal operating pressure (MNOP) inside the CV. Average gas temperature was calculated by volume averaging of nodal temperatures in the CV cavity. The average gas temperature for the MC5PV NCT/Solar configuration is 163°F.

4.2.2 Volume Average Foam Temperature

The volume average foam temperature for the MC5PV configuration is 147°F. The volume average foam temperature data is required in assessing the structural performance of the BTSP during NCT.

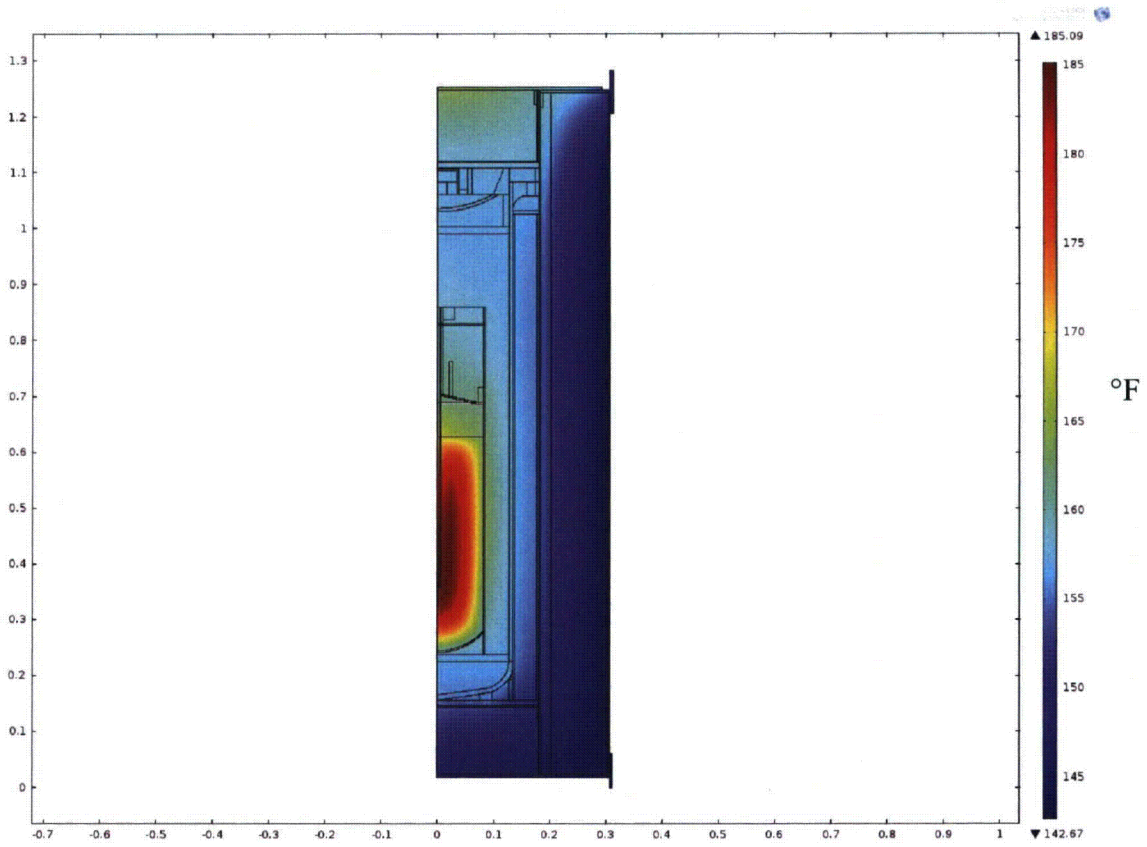

Figure 6 MC5PV Model Temperature Profiles for NCT/Solar

4.3 Results for the HAC/Solar Model

The HAC/Solar Fire model is used to calculate component temperatures during the fire event and refers to the thermal model with insolation effect during post-fire phase. Table 6 lists the maximum component temperatures of the MC5PV model during the fire phase while Table 7 lists the maximum component temperatures during the cooldown phase.

Table 6– HAC/Solar Maximum Component Temperatures During Fire

Component	BTSP/MC5PV Model (°F)	Temperature Limit (°F)
CV Wall	161	500
CV C-ring	161	1200
Cap C-ring	158	1200
Bellows Valve	158	400
Honeycomb Cylinder	180	NA
Contents	185	NA
Drum Surface	1474	NA
Last-A-Foam® FR-3710	1471	NA
Gas in CV (Volume Average)	159	NA
Gas in MC5PV (Volume Average)	163	NA

Table 7– HAC/Solar Maximum Component Post-Fire Temperatures

Component	BTSP/MC5PV Model (°F)	Temperature Limit (°F)
CV Wall	238	500
CV C-ring	236	1200
Cap C-ring	236	1200
Bellows Valve	236	400
Honeycomb Cylinder	273	NA
Contents	284	NA
Drum Surface	1474	NA
Last-A-Foam® FR-3710	1471	NA
Gas in CV (Volume Average)	236	NA
Gas in MC5PV (Volume Average)	218	NA

The post-fire temperatures are calculated using the HAC/Solar model. The only difference in this thermal model is the replacement of foam/char with air in the foam cavity. The steady state temperatures are given in Table 8.

Table 8 HAC/Solar Steady State Component Post Fire Temperatures

Component	BTSP/MC5PV Model (°F)	Temperature Limit (°F)
CV Wall	161	500
CV C-ring	160	1200
Cap C-ring	161	1200
Bellows Valve	161	400
Honeycomb Cylinder	160	NA
Contents	187	NA
Drum Surface	171	NA
Last-A-Foam® FR-3710 (replaced as Air post fire)	164	NA
Gas in CV (Volume Average)	161	NA
Gas in MC5PV (Volume Average)	166	NA

As shown in Table 7, the component temperatures are well below their design limits. Figure 7 is the temperature profiles for the MC5PVconfiguration during the HAC/Solar event.

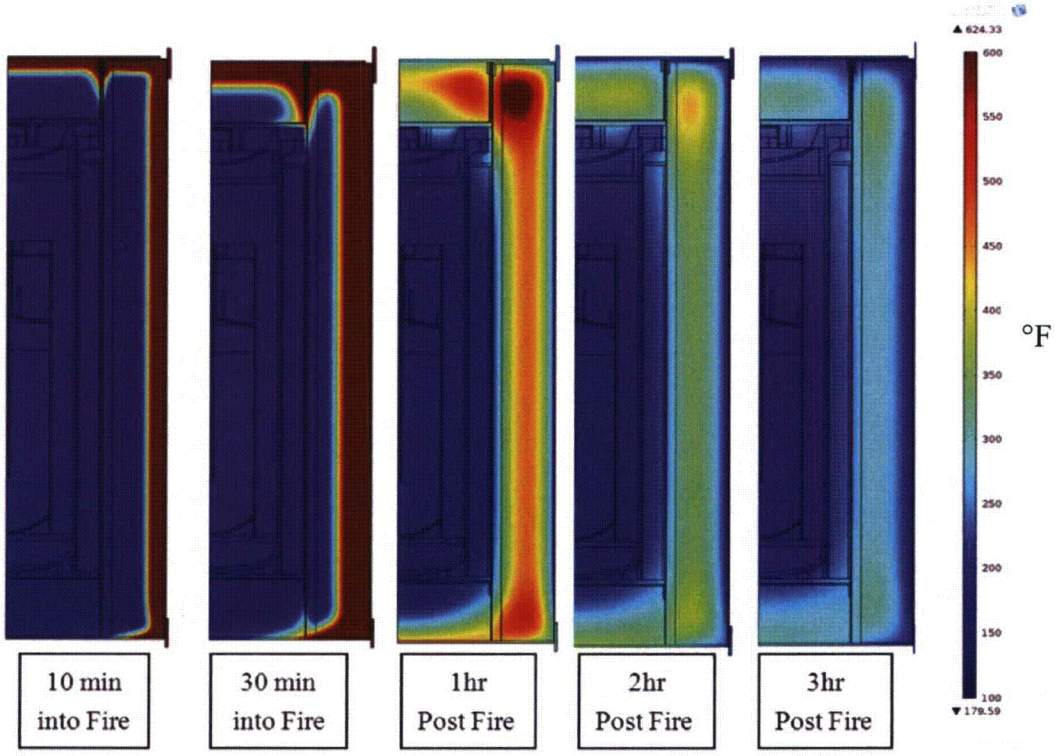

Figure 7 - HAC/Solar Temperature Profiles (peak temperatures are 30 minutes into fire). 1 hr post fire is at 1.5 hr simulation time.

Note: Temperature scale was set to a maximum of 600°F for comparison of plots. Any dark red color represents a value of 600°F or higher.

4.4 Uncertainty/Sensitivity Analyses

Uncertainties in thermal properties and other important parameters are minimized by making sure that their threshold values are used to yield conservative results. Uncertainties are addressed by performing simple sensitivity analyses. Sensitivity analyses were performed for finite element mesh size and thermal properties.

4.4.1 Mesh Size Sensitivity

A mesh sensitivity analysis was performed to ensure that the various thermal models had sufficient number of elements to give stable results. The number of elements was increased from 192,880 to 516,528 elements in the NCT/Solar. The maximum contents temperature with the increased number of elements was found to be less than 0.1% lower compared to the smaller number of elements. The model with the lower number of elements was used in the analyses.

4.4.2 Thermal Properties

FR-3710 foam free rise density of 10 lb/ft^3 and the corresponding thermal conductivity (k) values are used in the thermal analyses. However, the actual packed density of the FR-3710 foam in the prototype packages was found to be approximately 12.4 lb/ft^3 [21]. Since k of the foam increases with the density, the actual k would be higher.[4] For the NCT steady state analysis, higher k results in lower CV temperatures and therefore actual foam k does not impact the NCT analysis results. For the HAC analyses, higher density foam has lower thermal diffusivity than the lower density foam[4] and hence lower CV temperatures during HAC fire event.

The model was evaluated replacing the thermal properties of the 5A molecular sieve with water. Water having a higher thermal conductivity yielded steady state temperatures for the contents that were 20°F lower than when evaluated with the 5A molecular sieve material. For the transient case, water also has a higher heat capacity and therefore yields contents temperatures 80°F lower during the HAC fire.

The density of the molecular sieve material was varied to determine the effect on the steady state temperature of the package. A lower density was not simulated since a lower density will yield a larger molecular sieve volume. Using the same decay heat of 3.3 Watts over a larger volume will distribute the heat load and result in a lower maximum content temperature. A density that is 50% higher (66 lb/ft^3) yields a steady state maximum temperature 6°F higher for the contents.

5.0 CONCLUSIONS

1. The NCT and HAC analyses show that the maximum component temperatures are below their design limits.
2. The analyses show that the BTSP Mound Configuration 5 Process Vessel package meets the thermal design requirements given in 10 CFR Part 71.

6.0 REFERENCES

1. M-CLC-A-00340 Rev.1, BTSP Thermal Testing and Model Validation for Normal Conditions of Transport (NCT), Savannah River Nuclear Solutions, Aiken, SC (2010).
2. Safety Analysis Report for Packaging (SARP): Model AL-M1 Nuclear Packaging (DOE C of C No. USA/9507/BLF), MOUND, Miamisburg, OH, November 24, 1987.
3. Drawings:
   - R-R1-G-00022 – Packaging Assembly
   - R-R1-G-00023 – Drum Plug and Lid Assembly
   - R-R1-G-00024 – CV Assembly
   - R-R2-G-00048 – Drum Plug Sub Assembly
   - R-R2-G-00054 – Honeycomb Cylinder
   - R-R3-G-00013 – CV Weldment
   - R-R3-G-00049 – Drum Lid Weldment
   - R-R3-G-00051 – Drum and Liner Weldment
   - R-R4-G-00035 – CV Flange
   - R-R4-G-00036 – CV Base
   - R-R4-G-00037 – CV Lid
   - R-R4-G-00038 – CV Protection Cap
   - R-R4-G-00039 – CV Upper & Lower Spacers
   - R-R4-G-00040 – Drum and Liner Details
   - R-R2-G-00069 – Insulating Pad
   - R-R2-G-00070 – Silicone Pad
4. Design Guide for Use of Last-A-Foam FR-3700 for Crash and Fire Protection of Nuclear Material Shipping Containers (including data from cited references in this guide), General Plastics Manufacturing Company, Tacoma WA.
5. Safety Analysis Report for Packaging, Model 9977 B(M)f-96, S-SARP-G-00001, Rev. 2, Savannah River National Laboratory, 2007
6. • Parker O-ring Handbook, ORD-5700, Parker Hannifin Corp., Cleveland, OH (2007).
   • Seals for Extreme Environment, Parker-Hannifin Advanced Products Co., North Haven, CT.
7. E.G. Wenski, Properties of 30 lb/ft^3 Rigid Polyurethane Foams, SAND97-0120 (Appendix D), (March 1997).
8. W. L. Daugherty, Thermal Conductivity Data for Candidate Materials, SRNL-MST-2007-00127, (June 2008).
9. DC Products, www.dcproducts.com.au/RTV_Silicone_Solutions/Tech_Data_Sheets/RTV88-tds.pdf, May 2013
10. • Sigma Aldrich, www.sigmaaldrich.com/chemistry/chemical-synthesis/learning-center/technical-bulletins/al-1430/molecular-sieves.html, May 2013
    • Pnj Resources, LLC, www.pnjresources.com/Molecular%20Sieves.html, May 2013
11. Safety Analysis Report for Packaging, Bulk Tritium Shipping Package -1 (BTSP-1), S-SARP-G-00004, Rev. 4, Savannah River National Laboratory, (2012).
12. Morgan Thermal Ceramics http://www.morganthermalceramics.com/files/datasheets/4tr19tr19hstr201014-100.pdf, May 2013

13. ASME Boiler and Pressure Vessel Code, Section II, Part D, American Society of Mechanical Engineers, New York, NY (2004).
14. MSC.PATRAN THERMAL 2008 r1, Online Manual, MSC Software Company, Santa Ana, Ca (2008)
15. R. C. Dykhuizen and A. R. york, Packing Materials for Heat Producing Payloads, RAMTRANS, Vol. 3, No. 2/3, p. 135-139, Nuclear Technology Publishing (1992)
16. Comsol Multiphysics version 4.3a, COMSOL, Inc., Burlingame, Massachusetts (2012).
17. (1) G-SQP-A-00057 Rev. 0, Software Quality Assurance Plan for COMSOL Multiphysics (2012).
    (2) B-STP-A-00027 Rev. 0, COMSOL Multiphysics Version 4.3 Software Test Documentation, (2012).
18. Conduct of Engineering, Manual E-7, Engineering Calculations, Savannah River Nuclear Solutions, Savannah River Site, Aiken, SC.
19. Packaging and Transportation of Radioactive materials, Code of Federal Regulations, Title 10, Part 71, Washington, DC (2006).
20. Heat Transfer, by D. R. Pitts and L. E. Sissom, Schaum's Outline Series, McGraw-Hill Book Co. (1977).
21. M-CLC-A-00305 Rev.4, NCT and HAC Thermal Analysis for the BTSP, Savannah River Nuclear Solutions, Aiken, SC (2011).
22. M-TRT-A-00026, Solar Absorbance and Emittance of Stainless Steel at 400K, Savannah River Nuclear Solutions, Aiken, SC (2014)

WVMP SAR Reference 3-29

Fundamentals of Heat and Mass Transfer, 5th ed.,
Incropera, F.P., and D. P. DeWitt, John Wiley & Sons, Inc.,
Hoboken, New Jersey (2002).

Chapter 9, pages 605, 610.

where the Rayleigh number,

$$Ra_L = Gr_L Pr = \frac{g\beta(T_s - T_\infty)L^3}{\nu\alpha} \tag{9.25}$$

is based on the characteristic length L of the geometry. Typically, $n = \frac{1}{4}$ and $\frac{1}{3}$ for laminar and turbulent flows, respectively. For turbulent flow it then follows that $\bar{h}_L$ is independent of L. Note that all properties are evaluated at the film temperature, $T_f \equiv (T_s + T_\infty)/2$.

9.6.1 The Vertical Plate

Expressions of the form given by Equation 9.24 have been developed for the vertical plate [5–7]. For laminar flow ($10^4 \lesssim Ra_L \lesssim 10^9$), $C = 0.59$ and $n = 1/4$, and for turbulent flow ($10^9 \lesssim Ra_L \lesssim 10^{13}$), $C = 0.10$ and $n = 1/3$. A correlation that may be applied over the *entire* range of Ra_L has been recommended by Churchill and Chu [8] and is of the form

$$\overline{Nu}_L = \left\{0.825 + \frac{0.387\,Ra_L^{1/6}}{[1 + (0.492/Pr)^{9/16}]^{8/27}}\right\}^2 \tag{9.26}$$

Although Equation 9.26 is suitable for most engineering calculations, slightly better accuracy may be obtained for laminar flow by using [8]

$$\overline{Nu}_L = 0.68 + \frac{0.670\,Ra_L^{1/4}}{[1 + (0.492/Pr)^{9/16}]^{4/9}} \qquad Ra_L \lesssim 10^9 \tag{9.27}$$

When the Rayleigh number is moderately large, the second term on the right-hand side of Equations 9.26 and 9.27 dominates, and the correlations are the same form as Equation 9.24, except that the constant, C, is replaced by a function of Pr. Equation 9.27 is then in excellent quantitative agreement with the analytical solution given by Equations 9.21 and 9.20. In contrast, when the Rayleigh number is small, the first term on the right-hand side of Equations 9.26 and 9.27 dominates, and the equations yield the same behavior since $0.825^2 \approx 0.68$. The presence of leading constants in Equations 9.26 and 9.27 accounts for the fact that, for small Rayleigh number, the boundary layer assumptions become invalid and conduction parallel to the plate is important.

It is important to recognize that the foregoing results have been obtained for an isothermal plate (constant T_s). If the surface condition is, instead, one of uniform heat flux (constant q_s''), the temperature difference $(T_s - T_\infty)$ will vary with x, increasing from the leading edge. An approximate procedure for determining this variation may be based on results [8, 9] showing that $\overline{Nu}_L$ correlations obtained for the isothermal plate may still be used to an excellent approximation, if $\overline{Nu}_L$ and Ra_L are defined in terms of the temperature difference at the midpoint of the plate, $\Delta T_{L/2} = T_s(L/2) - T_\infty$. Hence, with $\bar{h} \equiv q_s''/\Delta T_{L/2}$, a correlation such as Equation 9.27 could be used to determine $\Delta T_{L/2}$ (for example, using a trial-and-error technique), and hence the midpoint surface temperature $T_s(L/2)$. If it is assumed that $Nu_x \propto Ra_x^{1/4}$ over the entire plate, it follows that

$$\frac{q_s'' x}{k\Delta T} \propto \Delta T^{1/4} x^{3/4}$$

or

$$\Delta T \propto x^{1/5}$$

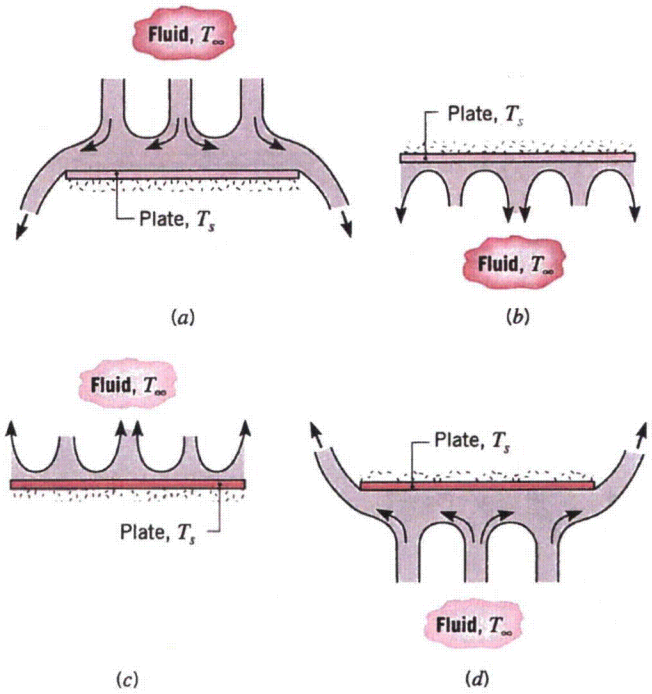

FIGURE 9.7 Buoyancy-driven flows on horizontal cold ($T_s < T_\infty$) and hot ($T_s > T_\infty$) plates: (*a*) Top surface of cold plate. (*b*) Bottom surface of cold plate. (*c*) Top surface of hot plate. (*d*) Bottom surface of hot plate.

where A_s and P are the plate surface area (one side) and perimeter, respectively. Using this characteristic length, the recommended correlations for the average Nusselt number are

Upper Surface of Hot Plate or Lower Surface of Cold Plate [19]:

$$\overline{Nu}_L = 0.54\, Ra_L^{1/4} \quad (10^4 \lesssim Ra_L \lesssim 10^7, Pr \gtrsim 0.7) \tag{9.30}$$

$$\overline{Nu}_L = 0.15\, Ra_L^{1/3} \quad (10^7 \lesssim Ra_L \lesssim 10^{11}, \text{all } Pr) \tag{9.31}$$

Lower Surface of Hot Plate or Upper Surface of Cold Plate [20]:

$$\overline{Nu}_L = 0.52\, Ra_L^{1/5} \quad (10^4 \lesssim Ra_L \lesssim 10^9, Pr \gtrsim 0.7) \tag{9.32}$$

Additional correlations can be found in [21].

EXAMPLE 9.3

Airflow through a long rectangular heating duct that is 0.75 m wide and 0.3 m high maintains the outer duct surface at 45°C. If the duct is uninsulated and exposed to air at 15°C in the crawlspace beneath a home, what is the heat loss from the duct per meter of length?

SOLUTION

Known: Surface temperature of a long rectangular duct.

Find: Heat loss from duct per meter of length.

WVMP SAR Reference 3-30

"Correlating Equations for Laminar and Turbulent Free Convection from a Vertical Plate," Churchill, S.W. and H. H. S. Chu, Int. J. Heat Mass Transport, 18(11), 1323-1329, 1975.

Int. J. Heat Mass Transfer. Vol. 18, pp. 1323–1329. Pergamon Press 1975. Printed in Great Britain

CORRELATING EQUATIONS FOR LAMINAR AND TURBULENT FREE CONVECTION FROM A VERTICAL PLATE

STUART W. CHURCHILL and HUMBERT H. S. CHU
Department of Chemical and Biochemical Engineering, University of Pennsylvania, Philadelphia, PA 19174, U.S.A.

(*Received* 2 *August* 1974 *and in revised form* 10 *February* 1975)

Abstract—A simple expression is developed for the space-mean *Nu* (or *Sh*) for all *Ra* and *Pr* (or *Sc*) in terms of the model of Churchill and Usagi. The development utilizes experimental values for *Ra* approaching zero and infinity, and the theoretical solutions obtained from laminar boundary-layer theory. The expression is applicable to uniform heating as well as to uniform wall temperature and for mass transfer and simultaneous heat and mass transfer. The correlation provides a basis for estimating transfer rates for non-Newtonian fluids and for inclined plates. Even simpler expressions are developed for restricted ranges of conditions. The general and restricted expressions are compared with representative experimental data. The structure of the correlating equation shows why the common power-law-type equations cannot be successful over an extended range of *Ra* and *Pr*.

NOMENCLATURE

a, arbitrary exponent;
A, dimensionless coefficient;
b, arbitrary exponent;
c, dimensionless coefficient;
$\mathscr{D}$, diffusivity [m^2/s];
$f\{Pr\}$, dimensionless function of Pr in equation (2);
$F\{m\}$, dimensionless function of power-law coefficient in equation (16);
g, acceleration due to gravity [m/s^2];
h, local heat-transfer coefficient [$J/m^2.s.°K$];
$\bar{h}$, mean heat-transfer coefficient over 0–z [$J/m^2.s.°K$];
k, thermal conductivity [$J/m.s.°K$];
k', local mass-transfer coefficient [s^{-1}];
$\bar{k}'$, mean mass-transfer coefficient over 0–z [s^{-1}];
K, coefficient defined by equation (15) [$kg/m\text{-}s^{2-m}$];
m, exponent defined by equation (15);
n, exponent in equation (1);
Nu, hz/k, local Nusselt number at z;
$\overline{Nu}$, $\bar{h}z/k$, mean Nusselt number over 0–z;
Pr, ν/α, Prandtl number;
q, heat flux density [$J/m^2\text{-}s$];
Ra, $g\beta(T_s-T_b)z^3/\nu\alpha$, Rayleigh number;
Ra', $g\gamma(\omega_s-\omega_b)z^3/\nu\mathscr{D}$, Rayleigh number for mass transfer;
Ra^*, $g\beta qz^4/k\nu\alpha$, modified Rayleigh number based on heat flux density;
Sc, $\nu/\mathscr{D}$, Schmidt number;
Sh, $k'z/\mathscr{D}$, local Sherwood number;
$\overline{Sh}$, $\bar{k}'z/\mathscr{D}$, mean Sherwood number over 0–z;
T, temperature [°K];
x, independent variable [m];
y, dependent variable [m];
z, distance up plate [m].

Greek symbols

α, thermal diffusivity [m^2/s];
β, thermal coefficient of expansion [$°K^{-1}$];
γ, dimensionless coefficient for expansion due to change in composition;
ω, mass fraction;
ν, kinematic viscosity [m^2/s];
$\varphi\{Pr\}$, dimensionless function of Pr in equation (8);
θ, angle of inclination of the plate from the vertical;
τ, shear stress [$kg/m\text{-}s^2$].

Subscripts

b, bulk;
s, surface;
0, limiting behavior for small z;
∞, limiting behavior for large z.

INTRODUCTION

A VARIETY of theoretical expressions, graphical correlations and empirical equations have been developed to represent the coefficients for heat and mass transfer by free convection from vertical plates. However, the discrepancies between the expressions proposed for correlation and the various sets of experimental data have still not been completely resolved or explained. The experimental anomalies are apparently due in part to physical property variations and undefined differences in the environment. The theoretical results are mostly limited to the intermediate range of Rayleigh number for which the postulates of laminar boundary-layer theory are applicable; a completely satisfactory theory has not been developed for either the diffusive regime (low Rayleigh numbers) or the turbulent regime (high Rayleigh numbers). The primary shortcoming of the empirical correlations is their failure to take into

proper account the *varying* dependence on the Rayleigh and Prandtl (or Schmidt) numbers.

This paper presents simple but very general correlations for the space-mean value of the transfer rate for free convection. The correlations are developed wholly in terms of the model of Churchill and Usagi [1]:

$$y^n\{z\} = y_0^n\{z\} + y_\infty^n\{z\} \tag{1}$$

and thus require appropriate expressions for the limiting behavior for both large and small values of the independent variable z.

Ede [2] provides a thorough review of the literature for heat transfer through 1964. In the interest of brevity, correlations, theoretical solutions and experimental data since that date will not be reviewed or analyzed except insofar as they are directly relevant to the derivations herein. The correlation is first developed in terms of heat transfer from an isothermal plate. Uniform heating, mass transfer, simultaneous heat and mass transfer, non-Newtonian fluids and inclined plates are subsequently considered.

LAMINAR REGIME

Boundary-layer theory has been utilized to derive relationships of the form:

$$Nu = Ra^{1/4} f\{Pr\} \tag{2}$$

where $f\{Pr\}$ represents a tabulation of values such as those summarized by Ede [2] for a number of values of Pr. Churchill and Usagi [1] derived an empirical expression in the form of equation (1) to provide a continuous approximation for these tabulated values of $f\{Pr\}$. This expression can be rewritten as follows in terms of $\overline{Nu}$:

$$\overline{Nu} = 0{\cdot}670 Ra^{1/4}/[1 + (0{\cdot}492/Pr)^{9/16}]^{4/9}. \tag{3}$$

Equation (3) represents the various computed values within 1 per cent from $Pr = 0$ to $Pr = \infty$ and is in general agreement for $10^5 < Ra < 10^9$ with the widely scattered experimental values compiled by Ede [2].

Equation (2) and hence equation (3) would be expected to become invalid for $Ra > 10^9$ owing to the onset of turbulence and as $Ra \to 0$ owing to thickening of the boundary layer relative to the distance from the starting edge of the plate. A generally accepted solution has not been derived for this latter regime. For pure conduction ($Ra = 0$) from an infinite strip $\overline{Nu} = 0$, but for a plate of finite dimensions $\overline{Nu}$ has a finite value. The experimental data of Saunders [5] indicate a limiting value of approximately 0·68, probably due to edge effects.

Utilizing 0·68 for $y_0\{z\}$ and the right side of equation (3) for $y_\infty\{z\}$ in equation (1) yields the following test expression for the entire laminar regime:

$$\overline{Nu}^n = 0{\cdot}68^n + \left(\frac{0{\cdot}670 Ra^{1/4}}{[1 + (0{\cdot}492/Pr)^{9/16}]^{4/9}}\right)^n. \tag{4}$$

A test plot of representative experimental data [2–13] in the form proposed by Churchill and Usagi [1] indicates that $n = 1$ is a reasonable choice, yielding

$$\overline{Nu} = 0{\cdot}68 + \frac{0{\cdot}670 Ra^{1/4}}{[1 + (0{\cdot}492/Pr)^{9/16}]^{4/9}}. \tag{5}$$

Equation (5) is seen in Fig. 1 to provide a good representation for all $Ra < 10^9$ while equation (3) is seen to be increasingly in error for $Ra < 10^5$.

LAMINAR PLUS TURBULENT REGIME

An asymptotic solution is not available for $Ra \to \infty$, but Churchill [14] has asserted on the basis of dimensional analysis that

$$Nu \to ARa^{1/3}\varphi\{Pr\} \tag{6}$$

where A is an empirical constant and $\varphi\{Pr\}$ is a function which approaches unity for $Pr \to \infty$ and is proportional to $Pr^{1/3}$ for $Pr \to 0$. Equations (5) and (6) could be combined in the form of equation (1) to obtain a test expression for all Ra and Pr. However the limiting value of 0·68 proves to combine with equation (6) to produce a simpler and equally successful correlation. The resulting test expression is

$$\overline{Nu}^n = 0{\cdot}68^n + [ARa^{1/3}\varphi\{Pr\}]^n. \tag{7}$$

Equation (7) provides a dependence of Nu on Ra for any positive n which increases continuously from the zeroth power to the 1/3-power as Ra increases. If equation (7) is to provide the same interrelationship between Ra and Pr in the laminar boundary-layer regime as equation (5) it is necessary that:

$$\varphi\{Pr\} = \left([1 + (0{\cdot}492/Pr)^{9/16}]^{-4/9}\right)^{4/3} = [1 + (0{\cdot}492/Pr)^{9/16}]^{-16/27} \tag{8}$$

The expression resulting from insertion of equation (8) in (7) also conforms to the asserted dependence for $Pr \to 0$ and ∞ as $Ra \to \infty$.

Bosworth [15] proposed an equation of the form of equation (7) with $\varphi\{Pr\} = 1{\cdot}0$ and $n = 1/2$ for $\overline{Nu}$ for free convection from horizontal cylinders in air. Trial plots indicate that $n = 1/2$ is a reasonable choice for the vertical plate as well. The straight line with a slope of 1/6 drawn in Fig. 2 through the same representative data as in Fig. 1 yields a value of $A = 0{\cdot}150$ and hence the final correlation:

$$\overline{Nu}^{1/2} = 0{\cdot}825 + \frac{0{\cdot}387 Ra^{1/6}}{[1 + (0{\cdot}492/Pr)^{9/16}]^{8/27}}. \tag{9}$$

This value of A is in reasonable accord with the value of $A\varphi\{Pr\} = 0{\cdot}10$, hence $A = 0{\cdot}12$, derived by Bayley [16] for air and also with the value of 0·13 proposed by Kutateladze [17] for a correlation in the form of equation (6) for turbulent free convection from vertical plates, cylinders and spheres to a number of fluids.

Equations (3) and (5) are plotted also in Fig. 2 for comparison and to indicate their limits of applicability. The undoubted superiority of equation (9) for $Ra > 19^9$ is somewhat obscured by the lack of data for truly high Ra, the scatter of the available data and the very condensed scale of the ordinate.

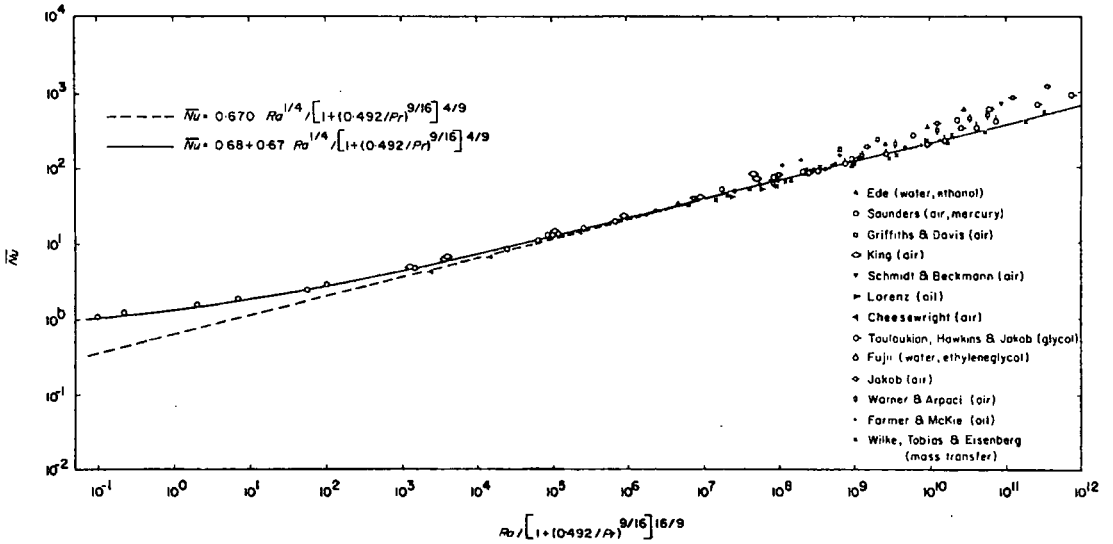

FIG. 1. Correlating equations for the laminar regime of isothermal, vertical plates.

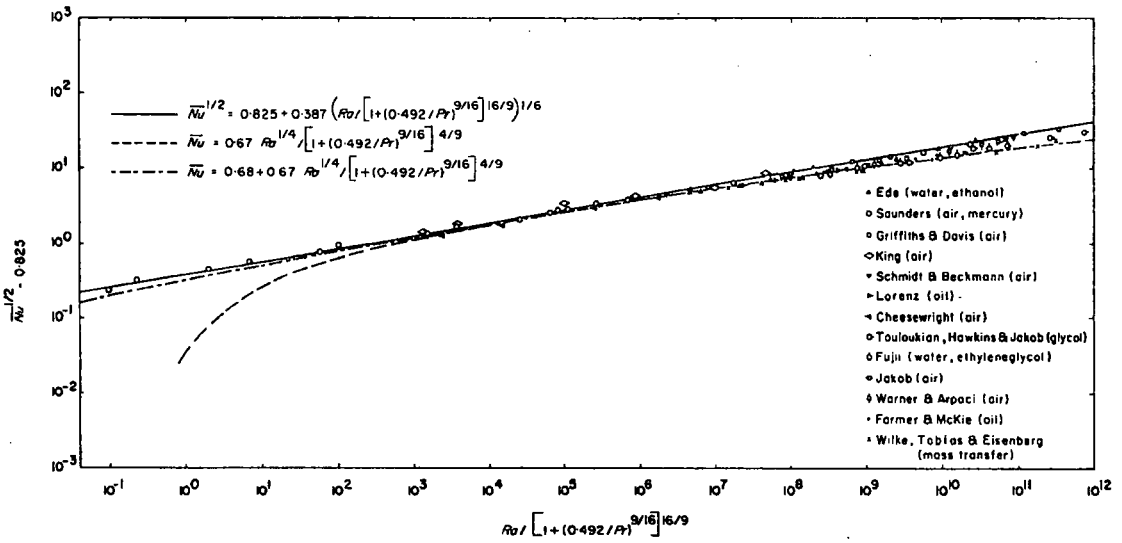

FIG. 2. Comparison of correlating equations with experimental data for isothermal, vertical plates.

INTERPRETATION

Computed values of $f\{Pr\}$ and $\varphi\{Pr\}$ for representative fluids are given in Table 1. The significant deviations for air and water from the limiting dependence for $Pr \to \infty$ indicate why the customary empirical equations of the form of equation (2) with $f\{Pr\} = 1{\cdot}0$ and equation (6) with $\varphi\{Pr\} = 1{\cdot}0$ have not proven satisfactory for a variety of fluids with a wide range of Pr. Table 1 also indicates that somewhat lesser but still significant discrepancies are to be expected with the simplified correlations for liquid metals based on the limiting form for $Pr \to 0$. A further variation in the dependence on Pr and Ra arises from the additive constant in equations (5) and (9). Thus empirical correlations of the form:

$$Nu = CRa^{a}Pr^{b} \tag{10}$$

cannot be expected to be successful over an extended range of Ra or Pr. Instead, the deviations from the correlations in the literature must be due in part to the choice of this form rather than wholly to experimental error. Such correlations appear to have outlived their usefulness.

Equation (9) provides a smooth transition from the laminar to the turbulent regime whereas the actual transition is known to be essentially discrete. The representation provided by equation (9) for this region is thus an oversimplification of reality and is numerically successful only because the effect of the transition is dampened by the integration which leads from the local to the mean Nusselt number. A correlation for the local Nusselt number extending through the transition from laminar to turbulent motion would need to be more complicated in structure than equation (9).

Table 1. Correction factor for various fluids from asymptotic behavior

Pr	Fluid	$f\{Pr\}$	$\varphi\{Pr\}$	$(0.492/Pr)^{1/4}f\{Pr\}$	$(0.492/Pr)^{1/3}\varphi\{Pr\}$
∞		1.000	1.000		
100	oil	0.978	0.971	0.259	0.165
7.0	water	0.914	0.887	0.471	0.366
0.70	air	0.766	0.701	0.702	0.623
0.024	mercury, 50°F	0.436	0.331	0.928	0.905
0.004	sodium, 1200°F	0.292	0.194	0.912	0.962
0				1.000	1.000

For large temperature differences such that the physical properties vary significantly, Ede [2] recommends that the physical properties be evaluated at the mean of the surface and the bulk temperature. Wylie [18] provides more detailed theoretical guidance for the laminar boundary-layer regime.

UNIFORM HEAT FLUX

The definition of the mean Nusselt number for uniform heating is somewhat arbitrary. However, Sparrow and Gregg [19] have shown that for a laminar boundary layer the use of the temperature difference at the midpoint of the plate yields values in better agreement with those for uniform wall temperature than the use of either the integrated mean temperature difference or the integrated mean heat-transfer coefficient. With this definition the following expression can be derived from the empirical representation of Churchill and Ozoe [20] for the local heat-transfer coefficient for uniform heating in a laminar boundary layer.

$$\overline{Nu} = 0.670Ra^{1/4}/[1+(0.437/Pr)^{9/16}]^{4/9}. \quad (11)$$

It may be noted that for $Pr \to \infty$ the coefficient of the Rayleigh number is indeed the same as that of equation (3) and that these expressions differ only by $((0.492/0.437)^{1/4}-1)100 = 3$ per cent even for $Pr \to 0$. [Equation (11) can be converted to one for the integrated mean temperature difference by multiplying the coefficient 0.670 by $(6/5)^{5/4}/2^{1/4}$ giving 0.708 and to the one for the integrated mean heat-transfer coefficient by multiplying by $(5/4)^{5/4}/2^{1/4}$ giving 0.745.]

Neither experimental data nor theoretical results appear to provide a limiting value of $\overline{Nu}$ for $Ra \to 0$. Hence the same value as for uniform wall temperature will arbitrarily be used. The exponent in equation (1) has generally been found to be the same for similar processes as illustrated by comparison of equations (3) and (11). Hence in the absence of experimental data the following expression is proposed for the entire laminar regime with uniform heating:

$$Nu = 0.68 + \frac{0.670Ra^{1/4}}{[1+(0.437/Pr)^{9/16}]^{4/9}}. \quad (12)$$

An equation of the form of equation (6) would be expected to hold for uniform heating as well as uniform wall temperature. Combining equation (6) with $\overline{Nu}_0 = 0.68$, forcing the same relationship between Ra and Pr as in equation (11) and assuming that 1/2 is again a satisfactory choice for n results in:

$$\overline{Nu}^{1/2} = 0.825 + \frac{A^{1/2}Ra^{1/6}}{[1+(0.437/Pr)^{9/16}]^{8/27}}. \quad (13)$$

A plot of a random selection from the limited sets of experimental data for uniform heating [21–24], in Fig. 3 in the form suggested by equation (13) again yields a value of $A = 0.15$, producing the following correlation for uniform heating for all Ra and Pr:

$$\overline{Nu}^{1/2} = 0.825 + \frac{0.387Ra^{1/6}}{[1+(0.437/Pr)^{9/16}]^{8/27}}. \quad (14)$$

Churchill [14] has asserted that Nu for fully developed turbulent motion ($Ra \to \infty$) should be the same for uniform heating as for wall temperature if a value independent of z, corresponding to a proportionality of Nu to $Ra^{1/3}$ is attained. This assertion is tested by plotting equation (9) for $Pr = 0.70$ in Fig. 3. Good agreement with the data may be noted as would be expected since equations (9) and (14) differ only slightly in one coefficient.

Free convection with uniform heating is often correlated in terms of Ra^* in order to avoid explicit inclusion of the surface temperature. Equations (11), (12) and (14) can be rewritten in terms of Ra^* simply by replacing $\overline{T_s}-\overline{T_b}$ with $q/\bar{h}$, hence Ra with $Ra^*/\overline{Nu}$. However, this re-expression disguises the important result that the dependence of $\overline{Nu}$ on Ra is essentially the same as for uniform wall temperature.

INCLINED SURFACES

Vliet [25] has reviewed prior results for inclined surfaces and presented additional results for uniform heating. He concludes that for the laminar regime the solutions and correlations for a vertical plate may be used for a plate inclined up to at least 60° from the vertical if the component of gravity parallel to the surface is used in the Rayleigh number. However, the Rayleigh number for transition from laminar to turbulent motion is decreased drastically as the angle of inclination from the vertical is increased and his local results for the turbulent regime were better correlated in terms of g than in terms of $g \sin \varphi$.

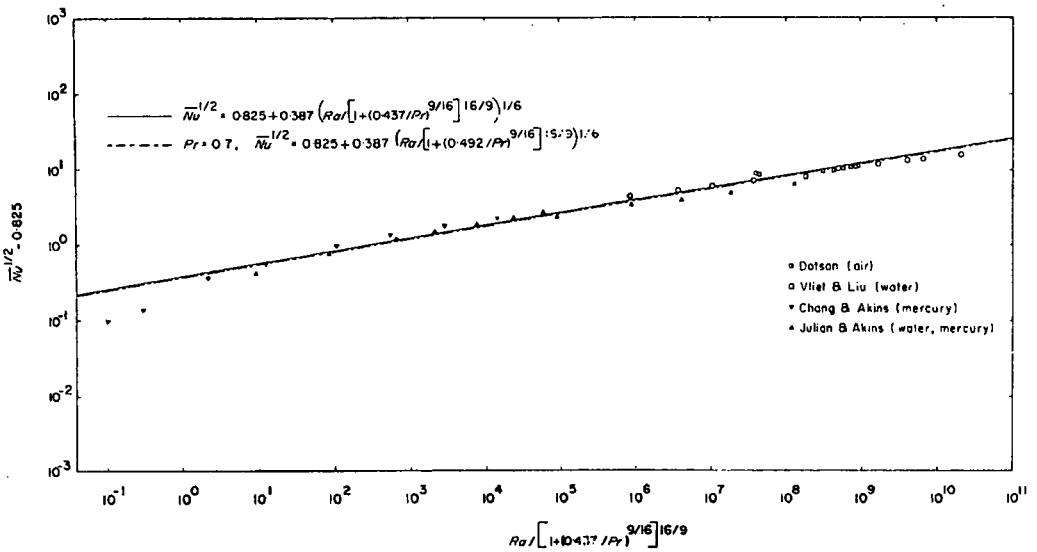

FIG. 3. Comparison of correlating equations with experimental data for uniformly heated, vertical plates.

MASS TRANSFER

Equations (5) and (9) with $\overline{Sh}$ substituted for $\overline{Nu}$, Sc for Pr, and Ra' for Ra are expected to hold for mass transfer as long as the net rate of mass transfer is not so high as to affect the velocity field significantly. Representative mass-transfer data [26] are included in Fig. 2 and reasonable agreement with equations (5) and (9) is apparent.

SIMULTANEOUS HEAT AND MASS TRANSFER

On the basis of the results of Saville and Churchill [27] and Lightfoot [28] for mass transfer due to a temperature gradient only $(\alpha(\omega_s-\omega_b)/\beta(T_s-T_b)\to 0$ and $Pr/Sc\to 0)$ $\overline{Sh}$ can be substituted for $\overline{Nu}$ and $Ra(Sc/Pr)^{4/3}$ for Ra in equation (9).

Also, on the basis of the results of Saville and Churchill [27] for simultaneous heat and mass transfer, $\overline{Nu}$ and Sh can be calculated from equation (9) for the special case of $Sc = Pr$ merely by substituting $Ra+Ra'$ for Ra. For $Sc \neq Pr$, the asymptotic solutions are not explicit and simple substitution in equation (9) is not possible [29].

NON-NEWTONIAN FLUIDS

For a power-law fluid such that:

$$\tau = -K\left|\frac{du}{dy}\right|^{m-1}\frac{du}{dy}. \qquad (15)$$

Acrivos [30] has derived for $Pr\to\infty$ the following generalized form of equation (2):

$$Nu = F\{m\}\left(\frac{\rho g\beta(T_s-T_b)z^{2m+1}}{K\alpha^m\rho}\right)^{1/(3m+1)} \qquad (16)$$

where $F\{m\}$ is a weak function of m and $F\{1{\cdot}0\} = 0{\cdot}670$. Equation (16) has been confirmed as a good representation for a number of fluids with $0{\cdot}6 \leqslant m \leqslant 1{\cdot}0$ by Agarwal *et al.* [30] for uniform wall temperature, and the analogue of equation (16) for uniform heating with $0{\cdot}4 < m < 1{\cdot}0$ by Chen and Wollersheim [32]. It follows that equation (5) with $f\{Pr\} = 1$ and equation (9) with $\varphi\{Pr\} = 1$ should be applicable for such fluids if $(\rho\beta(T_s-T_b)z^{2m+1}/K\alpha^m)^{4/3m+1}$ is susbsituted for Ra.

Fujii *et al.* [33] have obtained numerical solutions for a Sutterby fluid at finite Pr, and experimental results for aqueous solutions of polyethylene oxide. Their results indicate that Acrivos' solution may be a reasonable approximation for real fluids if the coefficients K and m are evaluated at the shear stress at the midheight of the heated plate.

CONCLUSIONS

1. Equation (9) based on the model of Churchill and Usagi provides a good representation for the mean heat transfer for free convection from an isothermal vertical plate over a complete range of Ra and Pr from 0 to ∞ even though it fails to indicate a discrete transition from laminar to turbulent flow.

2. Equation (14) provides an equivalent representation for heat transfer by free convection from a uniformly heated vertical plate. However, equation (9) is also an adequate representation for this boundary condition.

3. Equation (9) is applicable to mass transfer with $\overline{Sh}$, Ra' and Sc substituted for $\overline{Nu}$, Ra and Pr and can be applied for simultaneous heat and mass transfer for the special case of $Pr = Sc$ if $Ra+Ra'$ is substituted for Ra. Other such extensions are also possible.

4. More accurate representations for the laminar regime are provided by equations (5) and (12) and these simpler expressions should be used rather than equations (9) and (14) for $Ra < 10^9$. The expressions for the laminar regime are also applicable to mass transfer and simultaneous heat and mass transfer with the indicated substitutions.

5. Equations (5) and (12) are proposed as tentative representations for laminar convection from plates inclined up to at least 60° from the vertical if $g\sin\varphi$ is substituted for g. Based on the results of Vliet [25], equations (9) and (14) may be applicable for the turbulent regime without this modification. Fortunately

these equations are quite insensitive to the point of transition from laminar to turbulent motion.

6. Equations (9) with $Pr \to \infty$ is applicable to non-Newtonian fluids whose behavior can be represented by a power-law if $(\rho g \beta (T_s - T_b) z^{2m+1}/K\alpha^m)^{4/3m+1}$ is used for Ra.

7. The principal uncertainty in the correlations proposed herein arises from the uncertainty in the limiting solutions and experimental data for $Ra \to 0$ and ∞.

8. General correlations of the simple power-law type such as equation (10) are seen to be fundamentally unsound for any extended range of the variables and their use is no longer justified.

REFERENCES

1. S. W. Churchill and R. Usagi, A general expression for the correlation of rates of transfer and other phenomena, *A.I.Ch.E. Jl* **18**, 1121–1128 (1972).
2. A. J. Ede, Advances in free convection, in *Advances in Heat Transfer*, edited by J. P. Hartnett and T. F. Irvine, Jr., Vol. 4, pp. 1–64. Academic Press, New York (1967).
3. O. A. Saunders, Effect of pressure upon natural convection in air, *Proc. R. Soc.* **A157**, 278–291 (1936).
4. E. Griffiths and A. H. Davis, The transmission of heat by radiation and convection, DSIR Special Report No. 9, His Majesty's Stationary Office, London (1922).
5. W. J. King, The basic laws and data of heat transmission free convection, *Mech. Engng* **54**, 347–353 (1932).
6. E. Schmidt and W. Beckmann, Das Temperatur- und Geschwindigkeitsfeld vor einer Wärme abgebenden senkrechten Platte bei natürlichen Konvektion, *Tech. Mech. Thermo-dynam, Berlin* **1**, 341, 391 (1930).
7. N. H. Lorenz, Die Wärmeübertragung von einer ebenen senkrechten Platte an Öl bei natürlichen Konvektion, *Z. Tech. Phys.* **15**, 362–366 (1934).
8. R. Cheesewright, Turbulent natural convection from a vertical plane surface, *J. Heat Transfer* **90C**, 1–8 (1968).
9. Y. S. Touloukian, G. A. Hawkins and M. Jakob, Heat transfer by free convection from heated vertical surfaces to fluids, *Trans. Am. Soc. Mech. Engrs* **70**, 13–23 (1948).
10. T. Fujii, Experimental studies of free convection heat transfer, *Bull. J.S.M.E.* **2**(8), 555–558 (1959).
11. M. Jakob, Data as reported in Ede [2] above.
12. C. Y. Warner and V. S. Arpaci, An experimental investigation of turbulent natural convection at low pressure along a vertical heated flat plate, *Int. J. Heat Mass Transfer* **11**, 397–406 (1968).
13. W. P. Farmer and W. T. McKie, Natural convection from a vertical isothermal surface in oil, ASME Paper 64-WA/HT-12 (1964).
14. S. W. Churchill, An analysis of heat and component transfer by turbulent free convection from a vertical plate, *Proc. Chemeca '70*, Session 6A, pp. 1–16. Butterworths of Australia, Sydney (1970).
15. R. L. C. Bosworth, *Heat Transfer Phenomena*, p. 101. Wiley, New York (1952).
16. F. J. Bayley, An analysis of turbulent free convection heat transfer, *Proc. Instn Mech. Engrs* **169**(20), 361–370 (1955).
17. S. S. Kutateladze, *Fundamentals of Heat Transfer*, p. 294. Edward Arnold, London (1963).
18. R. G. Wylie, The transfer coefficients of a laminar boundary layer with variable fluid properties, *Chem. Engng* **6**, 1–14 (1973).
19. E. M. Sparrow and J. L. Gregg, Laminar free convection from a vertical plate with uniform surface heat flux, *Trans. Am. Soc. Mech. Engrs* **78**, 435–440 (1956).
20. S. W. Churchill and H. Ozoe, A correlation for laminar free convection from a vertical plate, *J. Heat Transfer* **95C**, 540–541 (1973).
21. J. P. Dotson, Heat transfer from a vertical plate by free convection, M.S. Thesis, Purdue University, Lafayette, Indiana (1954).
22. G. C. Vliet and C. K. Liu, An experimental study of turbulent natural convection boundary layers, *J. Heat Transfer* **91C**, 517–531 (1969).
23. B. H. Chang and R. G. Akins, An experimental investigation of natural convection in mercury at low Prandtl numbers, *Int. J. Heat Mass Transfer* **15**, 513–515 (1972).
24. D. V. Julian and R. G. Akins, Experimental investigation of natural convection heat transfer to mercury, *I/EC Fundamentals* **8**, 641–646 (1969).
25. G. C. Vliet, Natural convection local heat transfer on constant-heat-flux inclined surfaces, *J. Heat Transfer* **91C**, 511–516 (1969).
26. C. R. Wilke, C. W. Tobias and M. Eisenberg, Free convection mass transfer at vertical plates, *Chem. Engng Prog.* **49**, 663–674 (1953).
27. D. A. Saville and S. W. Churchill, Simultaneous heat and mass transfer in free convection boundary layers, *A.I.Ch.E. Jl* **16**, 268–273 (1970).
28. E. N. Lightfoot, Free-convection heat transfer: The limiting case of $Gr_{AB}/Gr \to 0$ and $Pr/Sc \to 0$, *Chem. Engng Sci.* **23**, 931 (1968).
29. J. W. Taunton, B. N. Lightfoot and W. E. Stewart, Simultaneous heat and mass transfer in laminar boundary layers, *Int. J. Heat Mass Transfer* **25**, 1927–1937 (1970).
30. A. Acrivos, A theoretical analysis of laminar natural convection heat transfer to non-Newtonian fluids, *A.I.Ch.E. Jl* **6**, 584–590 (1960).
31. B. K. D. Agarwal, K. S. Lieu and M. Adelman, Experimental verification of Acrivos' equation for laminar natural heat convection to non-Newtonian fluids, Personal communication.
32. T. Y. W. Chen and D. E. Wollersheim, Free convection at a vertical plate with uniform flux condition in non-Newtonian power law fluids, *J. Heat Transfer* **95C**, 123–124 (1973).
33. T. Fujii, O. Mujatake, M. Fujii, H. Tanaka and K. Murakami, Natural convective heat transfer from a vertical isothermal surface to a non-Newtonian Sutterby fluid, *Int. J. Heat Mass Transfer* **16**, 2177–2187 (1973).

LOIS DE CORRELATION EN CONVECTION NATURELLE LAMINAIRE ET TURBULENTE SUR UNE PLAQUE VERTICALE

Résumé—Une expression simple pour le nombre de Nusselt (ou de Sherwood) moyen est obtenue à l'aide du modèle de Churchill et Usagi pour tout nombre de Rayleigh et de Prandtl (ou de Schmidt). Au cours des développements il est fait usage de valeurs expérimentales du nombre de Rayleigh tendant vers zéro ou vers l'infini et de solutions théoriques obtenues en théorie de la couche limite laminaire. L'expression est applicable au transfert thermique à flux constant aussi bien qu'à température constante ainsi qu'au transfert de masse et au transfert simultané de chaleur et de masse. La loi de corrélation fournit une base de calcul des taux de transfert pour des fluides non newtoniens et pour des plaques inclinées. Des expressions tout aussi simples sont développées pour des domaines limités correspondant à des conditions particulières. Les expressions d'application générale et d'application restreinte sont comparées aux

données expérimentales représentatives. La structure de l'équation de corrélation fait apparaitre la raison pour laquelle les lois habituelles de type puissance ne peuvent s'appliquer sur un domaine étendu de nombres de Rayleigh et de Prandtl.

KORRELATIONEN FÜR LAMINARE UND TURBULENTE FREIE KONVEKTION AN EINER SENKRECHTEN PLATTE

Zusammenfassung—Nach einem Modell von Churchill und Usagi wurde eine einfache Beziehung für mittlere *Nu*-Zahlen (oder *Sh*) für alle *Ra* und *Pr* (oder *Sc*) entwickelt. Es sind dazu experimentelle Werte für *Ra* die gegen Null und unendlich gehen herangezogen und theoretische Lösungen, wie sie aus der Grenzschichttheorie erhalten werden. Die Beziehung ist anwendbar für gleichförmige Heizung, einheitliche Wandtemperatur, für Stoffübergang und gleichzeitigen Wärme- und Stoffübergang. Die Korrelation vermittelt eine Grundlage zur Bestimmung des Übergangs bei nichtnewtonischen Flüssigkeiten und für geneigte Platten. Für bestimmte Anwendungsbereiche werden einfachere Beziehungen angegeben. Die allgemeine Gleichung und die spezielle Beziehung werden vergliechen mit repräsentativen experimentellen Daten. Die Struktur der Korrelationsbeziehung gibt Aufschluß über das Versagen der allgemeinen Exponential-Gleichungen für einen ausgedehnten Bereich von *Ra* und *Pr*.

КОРРЕЛЯЦИОННЫЕ УРАВНЕНИЯ ДЛЯ ОПИСАНИЯ ЛАМИНАРНОЙ И ТУРБУЛЕНТНОЙ СВОБОДНОЙ КОНВЕКЦИИ ОКОЛО ВЕРТИКАЛЬНОЙ ПЛАСТИНЫ

Аннотация — С помощью модели Черчилля и Узаги получено простое выражение для осредненного по пространству значения числа *Nu* (или *Sh*) при любых значениях чисел *Ra* и *Pr* (или *Sc*). При выводе использовались экспериментальные данные для числа *Ra*, стремящегося к нулю и бесконечности, и аналитические решения, полученные на основе теории ламинарного пограничного слоя. Выражение применимо к случаям постоянного теплового потока, постоянной температуры стенки, а также для описания процессов массообмена и одновренемного тепло- и массообмена. Корреляция дает возможность рассчитать скорости переноса в неньютоноских жидкостях и в случае наклонных пластин. Аналогичные, но более простые выражения получены для ограниченных диапазонов условий. Общее и частные выражения сравниваются на достоверных экспериментальных данных. Структура корреляционного уравнения позволяет объяснить тот факт, почему обычные уравнения типа степенных зависимостей не могут успешно применяться при больших диапазонах значений *Ra* и *Pr*.

WVMP SAR Reference 3-31

"Natural Convection Adjacent to Horizontal Surface of Various Platforms," Lloyd, J.R. and W. R. Moran, J. Heat Transf., 96(4), 1974.

Pages 443 through 447

J. R. Lloyd
Assoc. Professor.
University of Notre Dame,
Notre Dame, Ind.
Assoc. Mem. ASME

W. R. Moran[1]
Graduate Assistant,
University of Notre Dame,
Notre Dame, Ind.

Natural Convection Adjacent to Horizontal Surface of Various Planforms

Natural convection adjacent to horizontal surfaces of circular, square, rectangular, and right triangular planforms has been studied experimentally. Electrochemical techniques were employed involving a fluid with a Schmidt number of about 2200. The results encompass a wide range of Rayleigh numbers thus providing information on both the laminar and the turbulent regimes. The data for all planforms are reduced to a single correlation in the laminar and turbulent regimes using the characteristic length, as recommended by Goldstein, Sparrow, and Jones, $L^* = A/p$, where A is the surface area and p is the surface perimeter. The laminar data for all planforms are correlated by the expression

$$\mathrm{Sh} = 0.54\,\mathrm{Ra}^{1/4} \quad (2.2 \times 10^4 \leq \mathrm{Ra} \leq 8 \times 10^6)$$

and the data for the turbulent regime are correlated by the expression

$$\mathrm{Sh} = 0.15\,\mathrm{Ra}^{1/3} \quad (8 \times 10^6 \leq 1.6 \times 10^8)$$

Transition is found to occur at about $\mathrm{Ra} = 8 \times 10^6$. The present work thus significantly extends the Rayleigh number range of validity for the use of L^* through the $\frac{1}{4}$ power laminar regime into the turbulent $\frac{1}{3}$ power regime. It also demonstrates the validity of the use of L^* to correlate natural convection transfer coefficients for highly unsymmetrical planforms, which heretofore had not been demonstrated. Comparisons to analytical solutions and other experimental heat and mass transfer data are presented.

Introduction

This paper presents an experimental investigation of natural convection adjacent to horizontal surfaces of various planforms. The results encompass a wide range of Rayleigh numbers, including the laminar and turbulent flow regimes, for circular, square, rectangular, and right triangular planforms. An electrochemical technique was employed to obtain the natural convection mass transfer measurements. This technique has been used by many investigators in recent years to study mass transfer, as evidenced by the recently published review by Mizushina [1].[2] The electrolyte employed in the present investigation was an aqueous solution of cupric sulphate and sulphuric acid, wherein the Cu^{++} ions were the transferred ions and the sulphuric acid served as the supporting electrolyte. The boundary condition for these experiments was uniform concentration at the test surface, which is the counterpart of uniform surface temperature in the corresponding heat transfer problem. The Schmidt numbers were on the order of 2200 so that these results apply to the analogous high Prandtl number heat transfer problem. One of the advantages of using the present mass transfer technique over heat transfer experiments for high Prandtl number fluids is the fact that the property variations for the mass transfer experiments are essentially zero, whereas the corresponding heat transfer experiments exhibit large variation in properties. The present results apply to either the heated upward facing heat transfer surface or the cooled downward facing heat transfer surface.

A review of the literature reveals both analytical and experimental investigations of horizontal surfaces of various planforms. Analyses of the natural convection [2, 3, 4, 5] generally employ a boundary layer model applied to the two-dimensional problem of long thin rectangles. Suriano and Yang [6] solved the problem numerically for small and moderate Grashof numbers. It should be noted that the analyses give a $\frac{1}{3}$-power dependence of the dimensionless transfer coefficients on the Rayleigh number for the laminar regime.

Experimentally, both heat and mass transfer investigations have been presented for horizontal surfaces e.g., [7–16]. The correlation between Nusselt number and Rayleigh number for the heat transfer problem which is the most widely accepted is that of Fishenden and Saunders [7]. Their experiments involved square planforms situated in air. The temperature differences involved were as high as 1000°F indicating extreme property variations and radiation corrections. Bosworth [8] provides very little information on his experiments, and Mikheyev [9] apparently used rectangular planforms, although this is not certain. Fujii and Imura [10] and Hassan and Mohamed [11] considered the horizontal upward facing surface as part of larger studies of heat transfer to inclined surfaces.

[1] Present address: Pratt and Whitney Aircraft, East Hartford, Conn.
[2] Numbers in brackets designate References at end of paper.

Contributed by the Heat Transfer Division and presented at the Winter Annual Meeting, New York, N. Y., November 17–22, 1974, of THE AMERICAN SOCIETY OF MECHANICAL ENGINEERS. Manuscript received by the Heat Transfer Division April 8, 1974. Paper No. 74-WA/HT-66.

Mass transfer natural convection experiments are provided by Fenech and Tobias [12], Wragg [13], Wragg and Loomba [14], Tobias and Boelfard [15], and Goldstein, Sparrow, and Jones [16]. References [12-15] used the same electrochemical technique employed herein. Fenech and Tobias [12] used electrodes embedded in the floor of the test cell. The electrodes had various widths and the length of each electrode stretched from one wall of the test cell to the other. Due to experimental difficulties only their wider test strips were used in their correlation and thus their results were only for the turbulent regime. Wragg [13] and Wragg and Loomba [14] used circular disks, but again embedded them flush in a surrounding collar. Tobias and Boelfard [15] studied both circular and rectangular horizontal electrodes surrounded by side walls. The side walls were both vertical and coplanar in nature. The object of this study was to determine the effect of the side walls and to determine the effect of electrode size on the mass transfer.

The work by Goldstein, Sparrow, and Jones [16] deserve special attention. They performed their experiments using naphthalene vapor sublimation. They investigated unshrouded circles, squares, and equilateral triangles, and proposed a characteristic length so that the results from these planforms could be correlated by a common expression. Heretofore this had not been possible. Unfortunately, their results did not span the full Rayleigh number range of the laminar flow regime, and did not contain any irregular or nonsymmetrical planforms.

The present results, to the best of the authors' knowledge, provide the only electrochemical mass transfer data for any free-standing, unshrouded planform. The results of the investigation are also the first for any mode of transfer involving the nonsymmetrical right triangle planforms. The Rayleigh numbers based on Goldstein, Sparrow, and Jones characteristic length range from 2.6×10^4 to 1.55×10^9, thus providing laminar, transition, and turbulent mass transfer information. By analogy, the results also apply to the corresponding isothermal horizontal surface heat transfer problem.

Data Analysis

In the present electrochemical mass transfer experiments, the total mass transfer rate of copper ions to the test surface was a result of three basic transfer mechanisms [21]: migration, convection, and diffusion

$$\dot{N} = \dot{N}_m + \dot{N}_c + \dot{N}_d \tag{1}$$

The three fluxes can be defined by the following relations which are all evaluated at the test surface

$$\dot{N}_m = Uc\frac{\partial \phi}{\partial y} \tag{2}$$

$$\dot{N}_c = vc \tag{3}$$

$$\dot{N}_d = -D\frac{\partial c}{\partial y} \tag{4}$$

The relative importance of each mechanism is revealed by examining their magnitudes under limiting current conditions. As explained in reference [1], under certain operating conditions, termed limiting current conditions, the concentration of the transferred species is essentially zero at the test surface.

Considering first the migration term, it is seen that $\dot{N}_m$ contains the transferred species conentration. Since this concentration is essentially zero at the surface, the entire term is, while in the presence of the supporting electrolyte where $\partial\phi/\partial y$ is small, negligibly small.

Next, consider the convection and diffusion terms together. Modeling the electrolyte solution as a binary mixture of copper ions as one component and the rest as the other component, reference [30] shows that $v = D/(1 - c/\rho)\,\partial(c/\rho)/\partial y$. Realizing that the concentration of the transferred species is approximately zero, the following is obtained

$$\dot{N}_c + \dot{N}_d = -\left(\frac{c/\rho}{1 - c/\rho} + 1\right) D\frac{\partial c}{\partial y} \cong -D\frac{\partial c}{\partial y} \tag{5}$$

Thus

$$\dot{N} \cong \dot{N}_d = -D\frac{\partial c}{\partial y} \tag{6}$$

The total rate of ion transfer is given in reference [21] as

$$\dot{N} = \frac{i}{n\mathrm{F}} \tag{7}$$

It is thus clear that the surface mass transfer is diffusive in nature which establishes the analogy between the present mass transfer experiments and the corresponding heat transfer problem.

It is possible now to define the mass transfer coefficient k in the same manner as is done in the analogous heat transfer problem

$$k = \frac{i}{n\mathrm{F}(c_\infty - c)} \cong \frac{i}{n\mathrm{F}c_\infty} \tag{8}$$

The dimensionless mass transfer number (analogous to the Nusselt number for the corresponding heat transfer problem) is given by the Sherwood number

$$\mathrm{Sh} = \frac{kL^*}{D} \tag{9}$$

Here D is the diffusion coefficient of the transferred species and L^* is the characteristic length. The characteristic length defined by Goldstein, Sparrow, and Jones [16] is

$$L^* = \frac{A}{P} \tag{10}$$

where A is the transfer area of the test surface and P is the perimeter. The Rayleigh number is

$$\mathrm{Ra} = \left[\frac{\zeta g(\zeta_\infty - \zeta_w)L^{*3}}{\mu^2}\right]\mathrm{Sc} \tag{11}$$

where Sc is the Schmidt number (analogous to the Prandtl num-

Nomenclature

- A = surface area of transfer surface
- c = transferred species concentration
- D = diffusion coefficient of transferred species
- F = Faraday number
- g = gravitational acceleration
- i = current density
- k = mass transfer coefficient
- L^* = characteristic length $L^* = A/p$
- n = valence of transferred species
- $\dot{N}$ = rate of mass transfer
- p = perimeter of transfer surface
- Pr = Prandtl number
- Ra = Rayleigh number
- Sc = Schmidt number
- Sh = Sherwood number
- t = transference number
- U = ion mobility
- v = convection velocity normal to test surface
- y = distance normal to test surface
- μ = viscosity
- ζ = density
- ϕ = electric field potential

Subscripts

- c = due to convection
- d = due to diffusion
- m = due to migration
- w = surface conditions
- ∞ = bulk conditions

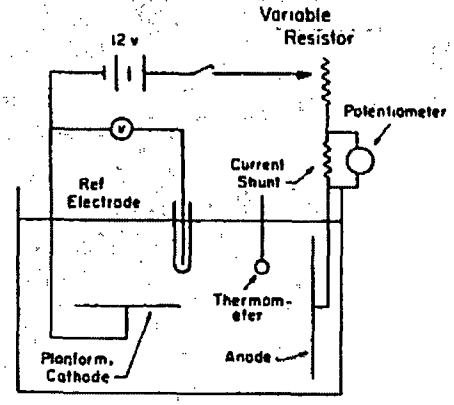

Fig. 1 Schematic of experimental apparatus

Table 1 Characteristic dimensions of various planforms

PLANFORM	CHARACTERISTIC DIMENSIONS, cm
CIRCLE (Diameter)	0.318
	0.635
	1.27
	5.08
	10.16
SQUARES (Length x Width)	0.635 x 0.635
	1.27 x 1.27
	12.7 x 12.7
RECTANGLES (Length x Width)	0.635 x 1.27
	2.54 x 1.27
	3.81 x 1.27
	6.35 x 1.27
	12.7 x 1.27
	12.7 x 2.54
	12.7 x 5.18
RIGHT TRIANGLES (Base x Height x Hypotenuse)	1.91 x 2.54 x 3.18
	1.27 x 1.91 x 3.29
	7.62 x 10.17 x 12.7
	15.35 x 20.3 x 25.4

ber) $\mu/\zeta D$; μ, ζ, and D are viscosity, density, and diffusion coefficient, respectively, at the average concentrations; and ζ_∞ and ζ_w are the fluid densities in the bulk and at the test surface, respectively. The properties were evaluated using the data of references [22–28], as described in reference [17]. As noted previously, property variations were practically nonexistent being 3 percent maximum. This is where this electrochemical technique has its major advantage over high Prandtl number heat transfer experiments.

Experimental Apparatus and Measurement Technique

A schematic of the experimental apparatus is presented in Fig. 1. A 30 gal polyethelene tank 61 cm × 45.6 cm × 45.6 cm (length × width × depth) served as the test chamber. The tank contained the electrolyte which was made up using reagent grade chemicals. The electrolyte solution was approximately 0.035 M $CuSO_4$ as the transferred species and 1.5 M H_2SO_4 as the supporting electrolyte.

The test surface was the cathode in the circuit. Table 1 provides a listing of the planforms tested and their characteristic dimensions. Each cathode was constructed of 0.635 cm thick copper. To the back side of each of the surfaces was attached a lead wire which connected to the main electrical circuit. The back and sides of the test pieces were carefully insulated with epoxy and Glyptal (an insulating paint). The test surface was held in position by a plexiglass holder. The lead wire was connected to a 12^v automotive storage battery to provide the electric power. The potential of the cathode was measured relative to a reference electrode which consisted of a bare copper wire inserted into a glass tube. The glass tube had a small hole in the bottom to provide electrical contact between the reference electrode and the electrolyte solution. The potential was controlled with a series of precision variable resistors. The current flowing in the circuit, which is directly proportional to the mass transfer rate, was obtained by measuring the potential drop across a calibrated precision resistor, called a current shunt, with a Leeds and Northrup 8686 potentiometer. The anode was a large thin copper sheet 50 cm × 50 cm (length by width). It was purposely larger than the cathode so that the reaction would be totally controlled by conditions at the cathode.

To obtain a datum point the following procedure was followed. Prior to each test run the anode and cathode were carefully resurfaced and cleaned, essentially as described in reference [17], and then placed in the tank. The cathode was carefully leveled to provide a horizontal surface located about 15 cm off the bottom of the tank, and time was allowed for the system to come to complete equilibrium. Limiting currents, where the concentration of the transferred species is zero at the test surface [21], were determined in each run by noting the characteristic plateau in the current-potential curves in the voltage range between 0.40^v and 0.50^v as will be discussed further in a later section. The copper ion and sulphuric acid concentrations of the bulk solution were determined for each run by standard spectrometric and titration methods [18, 19]. Vertical bulk concentration gradients at the time of data acquisition were determined for each run to insure that all data would not be influenced by stratification. Finally, it should be noted that the length of each run was critical since it was necessary to operate long enough to insure steady operating conditions, but not so long as to generate any recirculation effects on the transfer at the surface. All data were taken so as to insure steady operating conditions without recirculation effects.

Results and Discussion

Before discussing the results of the experiments, a short discussion of the characteristic length is presented. The characteristic length employed in this investigation is that proposed by Goldstein, Sparrow, and Jones [16]. It was their "expectation" that this particular characteristic length would enable all horizontal planforms to exhibit a common correlation. Unfortunately, they investigated a more limited number of planforms and smaller Rayleigh numbers than in the present investigation. The present investigation should serve to prove or disprove their expectations.

As discussed earlier, limiting current-voltage curves as shown in Fig. 2 were generated in each run. Plotted in the figure on rectangular coordinates is the current density at the cathode versus the cathode voltage. As indicated in the figure, the plateau, signifying limiting current conditions, was reached in several steps. At each step, the system was allowed to reach steady conditions. All data were taken at cathode voltages of 0.40^v to 0.50^v to insure that limiting conditions had been reached. Current shunt signals for the laminar flow regime were very steady and could be read directly. In the turbulent regime the shunt signals fluctuated making it necessary to time average the data over a period of approximately two minutes, which was determined in the present investigation to be sufficient to obtain accurate time averages without encountering stratification effects. This time averaging was accomplished by recording the data digitally on the tape unit of a Hewlett Packard 2019A Data Acquisition System and then statistically averaging them on a computer.

Fig. 3 presents the data for the laminar flow regime. The Sher-

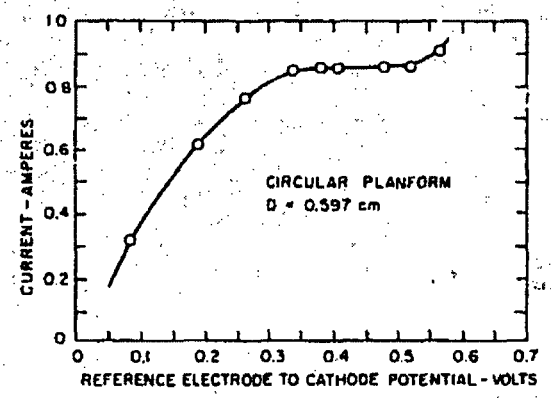

Fig. 2 Limiting current plateau

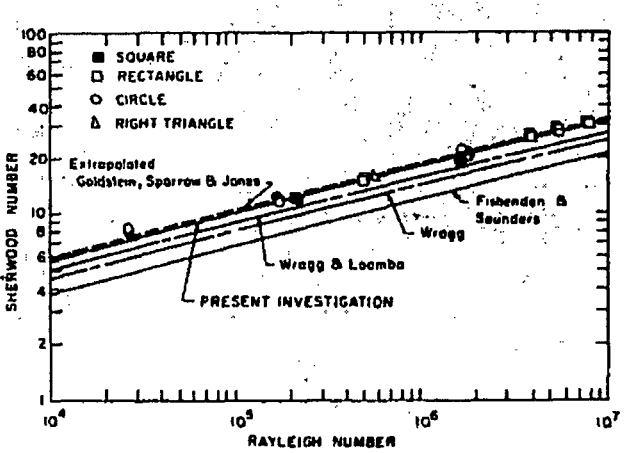

Fig. 3 Laminar mass transfer results

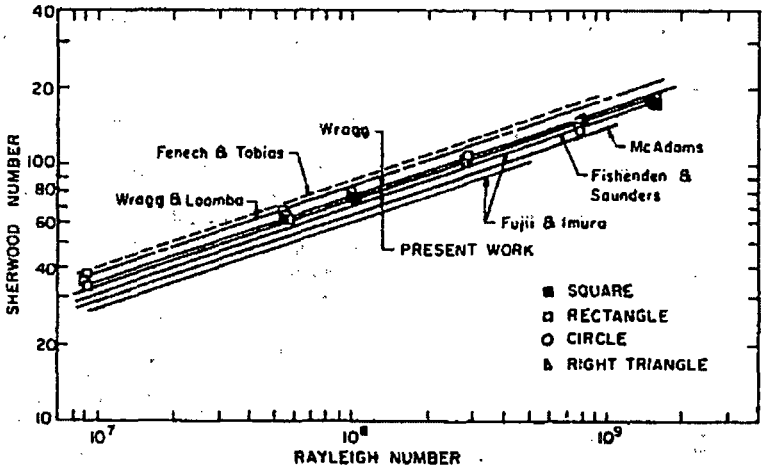

Fig. 4 Turbulent mass transfer results

wood number is plotted as a function of the Rayleigh number on logarithmic coordinates. The shape of the symbols reflect the planforms of the various surfaces as indicated in the upper left corner of the figure. It is immediately obvious that within the scatter of the data, approximately ± 5 percent, the data from all planforms are correlated through the use of L^*, including the nonsymmetric right triangle planform. This confirms the expectations of Goldstein, Sparrow, and Jones. A least squares fit through the data yields the relation

$$\mathrm{Sh} = 0.50\,\mathrm{Ra}^{0.255}$$

Forcing a slope of ¼, as has been reported in the literature for the heat transfer experiments, one finds the relation

$$\mathrm{Sh} = 0.54\,\mathrm{Ra}^{1/4}$$

for the data in the Rayleigh number range from 2.6×10^4 to 8×10^6.

Since L^* appears to correlate all the horizontal planforms, other published experimental results can be appropriately modified and compared to the present work. The data of Wragg and Loomba [14] and Wragg [13] can be compared directly to the present work since the same electrochemical technique was employed. Wragg and Loomba, it should be noted, is a revision of Wragg. They concerned themselves with circular surfaces which had a flush fitting collar surrounding their free-standing test surface. The revised data of Wragg and Loomba fall 10 percent below the present results. This difference could be a result, at least in part, from the presence of the surrounding collar.

The prediction of Goldstein, Sparrow, and Jones also involved mass transfer but at a much lower Schmidt number, approximately 2.5. Although their data only extended up to a Rayleigh number of 7×10^3, it is interesting that extension of their prediction into the Rayleigh number range covered in the present investigation falls very close to the present result. This would indicate that the Rayleigh number may be sufficient to account for Schmidt or Prandtl number variations.

Fig. 4 presents data for the turbulent flow regime. The Sherwood number is plotted as a function of the Rayleigh number on logarithmic coordinates. As in Fig. 3 the symbols reflect the planforms of the various surfaces. There does not appear to be any difference in the data for the various planforms. A least squares fit through the data for Rayleigh numbers greater than 8×10^6 provide the following correlation

$$\mathrm{Sh} = 0.169\,\mathrm{Ra}^{0.327}$$

If a ⅓ slope is enforced the best fit expression becomes

$$\mathrm{Sh} = 0.15\,\mathrm{Ra}^{1/3}$$

With the exception of two data points, the data scatter ±7 percent about this correlation.

The results of other investigators are also presented. The heat transfer correlations of Fishinden and Saunders [7] and McAdams [29] are seen to fall 4 to 12 percent lower than the present investigation. The data of Fujii and Imura [10] using water as the working fluid are perhaps the most interesting heat transfer data for comparison to the present work. They present two Nusselt num-

ber expressions, for the turbulent regime. Both have the form $Nu = C\ Ra^{1/3}$, but the value for C is 0.13 for Ra less than 5×10^8 and 0.16 for Ra greater than 2×10^8. The difference, they state, is due to edge effects on the surface. These experimental results using water as the surrounding medium have, within experimental scatter, essentially the same correlation as the present work when their edge effects are minimal. This would indicate again that the use of the Rayleigh number may be sufficient to account for Prandtl or Schmidt number effects.

The data of Fenech and Tobias [12], Wragg [13], and Wragg and Loomba [14] employed the same electrochemical techniques but with the previously discussed differences in the experimental setup. The data of Fenech and Tobias fall about 12 percent higher than the present data. This difference is in all probability due to the differences in the experimental setup as have been discussed earlier. The data of Wragg and Loomba are about 8 percent higher than the present work. It is important to note, however, that the correlation of Wragg and Loomba is a revised version of Wragg, due to the use of different physical properties, and that the correlation of Wragg, which uses almost the same values for properties as the present work, falls within the scatter of the present data. In this regime, the effect of the surrounding collar appears to be negligible, based on comparisons of Wragg's data to the present investigation.

Finally, the work of Tobias and Boeffard [15] deserves special mention. They considered the effect of both vertical and coplanar surrounding walls on the mass transfer to horizontal surfaces using the same experimental techniques. They found that the surrounding walls had no effect on the mass transfer correlation if the surfaces were large enough. For smaller electrodes their correlation underpredicts and it must be multiplied by a factor d_n, a number which is larger than one. When one considers their data in the light of the present investigation it appears that their size effect is related to the transition noted in the present work from the turbulent range to the laminar range. Indeed, if one takes Schmidt and Grashof numbers characteristic of the present data and use their expression to predict the Sherwood number for the turbulent regime, it is found that their prediction falls within the scatter of the present turbulent data. If one considers the small electrodes found in the laminar regime of the present work and applies the d_n correction discussed in their work, their Sherwood number prediction falls approximately within the scatter of the present work. Thus, it appears to be possible that their size effects, even with the surrounding walls, may be related to the difference between the laminar and turbulent flow regimes discussed in the present work.

Concluding Remarks

The present data are the first electrochemical mass transfer investigations of truly free-standing unshrouded horizontal surfaces. They also present the only data available for any mode of transfer involving right triangular planforms. The characteristic length as proposed by Goldstein, Sparrow, and Jones appears to bring all the data into a common correlation, even the nonsymmetrical surfaces such as the right triangles, for all Rayleigh numbers investigated. Special note should be made that the experimentally determined laminar correlation involves the ¼ power of the Rayleigh number whereas the laminar boundary layer analyses indicate a ⅕ power dependence. This is probably the result of using a boundary layer approach in the analyses.

It is highly encouraging to see data from circular, square, rectangular, and right triangular planforms exhibit a common correlation through the use of the characteristic length proposed by Goldstein, Sparrow, and Jones. There are indications that the use of the Rayleigh number in the mass or heat transfer relations is sufficient to account for Schmidt or Prandtl number variations. These observations, based on the experimental data, will enable calculation of transfer rates involving any shaped upward facing horizontal surface provided the transfer surface area and perimeter are known.

Acknowledgment

The authors gratefully acknowledge the support for this work provided by the National Science Foundation under Grant Number GK 32658.

References

1 Mizushina, T., "The Electrochemical Method in Transport Phenomena," *Advances in Heat Transfer*, Vol. 7, J. P. Hartnett and T. F. Irvine eds., Academic Press, New York, 1971.

2 Levy, S., "Integral Methods in Natural Convection Flow," *Journal of Applied Mechanics*, Vol. 77, No. 5, May 1955, pp. 515-525.

3 Stewartson, K., "On the Free Convection From a Horizontal Plate," *Z. Angew. Math. Phys.*, Vol. 9 a, 1958, p. 276.

4 Gill, W. N., Zeh, D. W., and del Casal, E., "Free Convection on a Horizontal Plate," *Z. Angew. Math. Phys.*, Vol. 15, 1965, p. 539.

5 Roten, Z., and Classen, L., "Natural Convection Above Unconfined Horizontal Surfaces," *Journal of Fluid Mechanics*, Vol. 39, Part 1, Oct. 23, 1969, pp. 173-192.

6 Suriano, F. J., and Yang, K. T., "Laminar Free Convection About Vertical and Horizontal Plates at Small and Moderate Grashof Numbers," *International Journal of Heat and Mass Transfer*, Vol. 11, No. 3, Mar. 1968, pp. 473-490.

7 Pishenden, M., and Saunders, O. A., *An Introduction to Heat Transfer*, Oxford University Press, London, 1950.

8 Bosworth, R. L. C., *Heat Transfer Phenomena*, Wiley, New York, 1952.

9 Mikheyev, M., *Fundamentals of Heat Transfer*, Peace Publishers, Moscow, 1968.

10 Fujii, T., and Imura, H., "Natural Convection Heat Transfer From a Plate With Arbitrary Inclination," *International Journal of Heat and Mass Transfer*, Vol. 15, No. 4, Apr. 1972, pp. 755-767.

11 Hassan, K., and Mohamed, S. A., "Natural Convection From Isothermal Flat Surfaces," *International Journal of Heat and Mass Transfer*, Vol. 13, No. 12, Dec. 1970, pp. 1866-1873.

12 Fenech, E. S., and Tobias, C. W., "Mass Transfer by Free Convection at Horizontal Electrodes," *Electrochem. Acta*, Vol. 2, No. 3, Mar. 1960, pp. 311-321.

13 Wragg, A. A., "Free Convection Mass Transfer at Horizontal Electrodes," *Electrochem. Acta*, Vol. 13, No. 12, Dec. 1968, pp. 2159-2165.

14 Wragg, A. A., and Loomba, R. P., "Free Convection Flow Patterns at Horizontal Surfaces With Ionic Mass Transfer," *International Journal of Heat and Mass Transfer*, Vol. 13, No. 2, Feb. 1970, pp. 439-442.

15 Tobias, C. W., and Boeffard, A. L., "Ionic Mass Transport by Free Convection at Horizontal Electrodes," 17th General Meeting of CITCE, Sept. 5-9, 1966, Tokyo, Japan, pp. 23-24.

16 Goldstein, R. J., Sparrow, E. M., and Jones, D. C., "Natural Convection Mass Transfer Adjacent to Horizontal Plates," *International Journal of Heat and Mass Transfer*, Vol. 16, No. 5, May 1973, pp. 1025-1034.

17 Lloyd, J. R., Sparrow, E. M., and Eckert, E. R. G., "Local Natural Convection Mass Transfer Measurements," *J. Electrochem. Soc.*, Vol. 119, No. 6, June, 1972, pp. 702-707.

18 Sandell, E. B., *Colorimetric Determination of Traces of Metal*, Interscience Publishers, New York, 1950.

19 Kolthoff, I. M., and Sandell, E. B., *Textbook of Quantitative Inorganic Analysis*, Macmillan, New York, 1965.

20 Lloyd, J. R., Sparrow, E. M., and Eckert, E. R. G., "Laminar Transition and Turbulent Natural Convection Adjacent to Inclined and Vertical Surfaces," *International Journal of Heat and Mass Transfer*, Vol. 15, No. 3, Mar. 1972, pp. 457-473.

21 Wilke, C. R., Eisenberg, M., and Tobias, C. W., "Correlation of Limiting Currents Under Free Convection Conditions," *J. Electrochem. Soc.*, Vol. 100, No. 11, Nov. 1953, pp. 513-523.

22 Eisenberg, M., Tobias, C. W., and Wilke, C. R., "Selected Physical Properties of Ternary Electrolytes Employed in Ionic Mass Transfer Studies," *J. Electrochem. Soc.*, Vol. 103, No. 7, July 1956, pp. 413-416.

23 Vinal, G. W., and Craig, D. N., *J. Res. Nat. Bur. Std.*, Vol. 10, 1933, p. 781.

24 Cole, A. F. W., and Gordon, A. R., "The Diffusion of Copper Sulphate in Aqueous Solutions of Sulphuric Acid," *J. Phys. Chem.*, Vol. 40, No. 9, Sept. 1935, pp. 773-775.

25 James, W. A., Hollingshead, E. A., and Gordon, A. R., "The Differential Diffusion Constants of Hydrochloric and Sulphuric Acids," *J. Chem. Phys.*, Vol. 7, No. 2, Feb. 1939, pp. 89-92.

26 Hollingshead, E. A., and Gordon, A. R., "The Variation of the Differential Diffusion Constant of Sulphuric Acid With Temperature," *J. Chem. Phys.*, Vol. 8, No. 5, May, 1940, pp. 423-425.

27 Landolt-Bornstein, "Physikalish-Chemische Tabellen," *5 Auflage*, Vol. 1, 1936, pp. 248-397.

28 Dorsey, E. N., *Properties of Ordinary Water Substance in All Its Phases; Water Vapor, Water, and All the Ices*, Hafner Publishing Co., 1968.

29 McAdams, W. H., *Heat Transmission*, McGraw-Hill, New York, 1954.

30 Eckert, E. R. G., and Drake, Jr., R. M., *Heat and Mass Transfer*, McGraw-Hill, New York, 1959.

WVMP SAR Reference 3-32

Perry's Chemical Engineers' Handbook, 6th ed., McGraw-Hill, New York (1984).

Page 10-13

fluid friction, it has greater utility than other expressions for the heat-transfer coefficient.

The classical (and perhaps more familiar) form of dimensionless expressions relates, primarily, the Nusselt number hD/k, the Prandtl number $c\mu/k$, and the Reynolds number DG/μ. The L/D and viscosity-ratio modifications (for Reynolds number <10,000) also apply.

The **dimensional equations** are usually expansions of the dimensionless expressions in which the terms are in more convenient units and in which all numerical factors are grouped together into a single numerical constant. In some instances, the combined physical properties are represented as a linear function of temperature, and the dimensional equation resolves into an equation containing only one or two variables.

NATURAL CONVECTION

Natural convection occurs when a solid surface is in contact with a fluid of different temperature from the surface. Density differences provide the body force required to move the fluid. Theoretical analyses of natural convection require the simultaneous solution of the coupled equations of motion and energy. Details of theoretical studies are available in several general references (Brown and Marco, *Introduction to Heat Transfer*, 3d ed., McGraw-Hill, New York, 1958; and Jakob, *Heat Transfer*, Wiley, New York, vol. 1, 1949; vol. 2, 1957) but have generally been applied successfully to the simple case of a vertical plate. Solution of the motion and energy equations gives temperature and velocity fields from which heat-transfer coefficients may be derived. The general type of equation obtained is the so-called Nusselt equation:

$$\frac{hL}{k} = a\left(\frac{L^3\rho^2 g\beta\,\Delta t}{\mu^2}\,\frac{c\mu}{k}\right)^m \qquad (10\text{-}32a)$$

$$N_{Nu} = a(N_{Gr}N_{Pr})^m \qquad (10\text{-}32b)$$

Nusselt Equation for Various Geometries Natural-convection coefficients for various bodies may be predicted from Eq. (10-32). The various numerical values of a and m have been determined experimentally and are given in Table 10-1. Fluid properties are evaluated at $t_f = (t_s + t')/2$. For **vertical plates and cylinders** and $1 < N_{Pr} < 40$, Kato, Nishiwaki, and Hirata [*Int. J. Heat Mass Transfer*, 11, 1117 (1968)] recommend the relations

$$N_{Nu} = 0.138N_{Gr}^{0.36}(N_{Pr}^{0.175} - 0.55) \qquad (10\text{-}33a)$$

for $N_{Gr} > 10^9$, and

$$N_{Nu} = 0.683N_{Gr}^{0.25}N_{Pr}^{0.25}[N_{Pr}/(0.861 + N_{Pr})]^{0.25} \qquad (10\text{-}33b)$$

for $N_{Gr} < 10^9$.

Simplified Dimensional Equations Equation (10-32) is a dimensionless equation, and any consistent set of units may be used. Simplified dimensional equations have been derived for air, water, and organic liquids by rearranging Eq. (10-32) into the following form by collecting the fluid properties into a single factor:

$$h = b(\Delta t)^m L^{3m-1} \qquad (10\text{-}34)$$

Values of b in SI and U.S. customary units are given in Table 10-1 for air, water, and organic liquids.

Simultaneous Loss by Radiation The heat transferred by radiation is often of significant magnitude in the loss of heat from surfaces to the surroundings because of the diathermanous nature of atmospheric gases (air). It is convenient to represent radiant-heat transfer, for this case, as a **radiation film coefficient** which is added to the film coefficient for convection, giving the combined coefficient for convection and radiation ($h_c + h_r$). In Fig. 10-7 values of the film coefficient for radiation h_r are plotted against the two surface temperatures for emissivity = 1.0.

Table 10-2 shows values of ($h_c + h_r$) from single horizontal oxidized pipe surfaces.

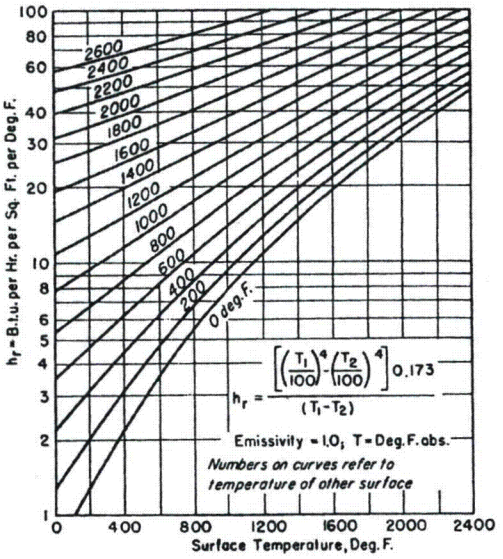

FIG. 10-7 Radiation coefficients of heat transfer h_r. To convert British thermal units per hour–square foot–degrees Fahrenheit to joules per square meter–second–kelvins, multiply by 5.6783; °C = (°F − 32)/1.8.

TABLE 10-1 Values of a, m, and b for Eqs. (10-32) and (10-34)

Configuration	$Y = N_{Gr}N_{Pr}$	a	m	b, air at 21°C	b, air at 70°F	b, water at 21°C	b, water at 70°F	b, organic liquid at 21°C	b, organic liquid at 70°F
Vertical surfaces	$<10^4$	1.36	1/5						
L = vertical dimension <3 ft	$10^4 < Y < 10^9$	0.59	1/4	1.37	0.28	127	26	59	12
	$>10^9$	0.13	1/3	1.24	0.18				
Horizontal cylinder	$<10^{-5}$	0.49	0						
L = diameter <8 in	$10^{-5} < Y < 10^{-3}$	0.71	1/25						
	$10^{-3} < Y < 1$	1.09	1/10						
	$1 < Y < 10^4$	1.09	1/5						
	$10^4 < Y < 10^9$	0.53	1/4	1.32	0.27				
	$>10^9$	0.13	1/3	1.24	0.18				
Horizontal flat surface	$10^5 < Y < 2 \times 10^7$(FU)	0.54	1/4	1.86	0.38				
	$2 \times 10^7 < Y < 3 \times 10^{10}$(FU)	0.14	1/3						
	$3 \times 10^5 < Y < 3 \times 10^{10}$(FD)	0.27	1/4	0.88	0.18				

NOTE: FU = facing upward; FD = facing downward. b in SI units is given in °C column; b in U.S. customary units, in °F column.

Proc. Ref. E7, 2.31

Calculation Cover Sheet

Sheet 1 of 38

Project/Task	Calculation Number	Project/Task Number
N/A	M-CLC-A-00498	N/A

Title
Thermal Analysis for West Valley Melter Package

Functional Classification
General Services

Discipline
Mechanical

Calculation Type
◉ Type 1 ○ Type 2

Type 1 Calculation Status
○ Preliminary ◉ Confirmed

Computer Program Number
COMSOL Multiphysics ☐ N/A

Version/Release Number
4.3a

Purpose and Objective
SRNL has been asked to provide a safety evaluation to the U. S. Nuclear Regulatory Commission (NRC) for the shipment of the West Valley Melter Package (WVMP). This report provides a thermal analysis for the shipment as part of this safety evaluation. Thermal analyses are provided for Normal Conditions of Transport (NCT) and Hyothetical Accident Conditions (HAC).

[redacted]

Summary of Conclusion
The maximum temperature for NCT with exposure to 100 °F ambient air and no insolation is 105.36 °F, well below the limit established by 10 CFR 71.51. The maximum temperature for NCT with exposure to 100 °F and insolation of 800 cal/cm² on the top surface and 200 cal/cm² on the sides is 209.42 °F. The maximum pressure for these conditions is 12.0 psig. The minimum temperatures for NCT with exposure to -20 °F air and -40 °F air do not drop below the ambient temperature. The maximum temperature for HAC with 30 min exposure to a 1475 °F fire, followed by exposure to 100 °F air with insolation of 800 cal/cm² on the top surface and 200 cal/cm² on the sides, is 1221.09 °F, at the corners of the WVMP. The temperature of the container walls except the very corners is below 800 °F. The maximum pressure for HAC is 73.0 psig.

REVISIONS

Rev No.	Revision Description
0	Original issue

SIGN OFF

Rev No.	Originator (Print / Sign & Date)	Verification/Checking Method	Verification/Checker (Print / Sign & Date)	Manager (Print / Sign & Date)
0	Matthew R. Kesterson James E. Laurinat	☐ Design Check (GS/PS only) ☒ Document Review	Neal M. Askew	Maximilian B. Gorensek
	[redacted]			
		☐ Design Check (GS/PS only) ☐ Document Review ☐ Qualification Testing ☐ Alternate Calculation ☐ Operational Testing		

[redacted]

Table of Contents

Section Page

1.0 Introduction 3
2.0 Inputs and Assumptions 4
3.0 Analysis Method 11
3.1 Thermal Analysis 13
3.2 Approach to Transient Modeling 18
3.3 Calculation of Maximum Pressures 18
4.0 Calculation Method 19
5.0 Open Items 19
6.0 Uncertainty Analysis 20
7.0 Results of NCT and HAC Thermal Analyses 20
8.0 Conclusion 28
9.0 References 29
Appendix A: Summary of Radionuclide Content and Radiolytic Heating for GMP 31
Appendix B: Parameter and Variable Lists for COMSOL® Multiphysics Model 37

1.0 Introduction

SRNL has been asked to provide a safety evaluation to the U. S. Nuclear Regulatory Commission (NRC) for the shipment of the West Valley Melter Package (WVMP). This report provides a thermal analysis for the shipment as part of this safety evaluation. DOE plans to ship the WVMP to the Waste Control Specialists (WCS) facility in Texas for disposal. The West Valley Melter operated from 1996 to 2002 to vitrify radioactive wastes from the West Valley Demonstration Project located south of Buffalo, New York.

Thermal analyses are provided for Normal Conditions of Transport (NCT) and Hypothetical Accident Conditions (HAC). The conditions for NCT and HAC are stipulated in 10 CFR Part 71. NCT covers conditions for outdoor storage of the waste package, including heat transfer to ambient air and sun exposure (insolation). The HAC assume exposure to a 1475 °F fire. The thermal analysis does not account for the presence of the Impact Limiter (IL) added to the exterior of the WVMP. For the thermal analysis, the omission of the IL is conservatively bounding in that it does not include the insulation that it provides. The WVMP without the IL component is referred to as the Grouted Melter Package (GMP) component.

The analysis of temperatures for NCT follows the guidelines of 10 CFR 71.71 [1]. The required temperatures are:

1. The maximum temperatures for exposure to 100 °F air at steady state.
2. The maximum temperatures for exposure to 100 °F still air with insolation of 800 cal/cm^2 on the top surface and 200 cal/cm^2 on the side surfaces for a period of 12 hours. The package bottom is assumed to be an insulated (adiabatic) surface.
3. The minimum (surface) temperature for exposure to a cold environment of -20 °F, with no insolation.
4. The minimum (surface) temperature for exposure to a maximum cold environment of -40 °F, with no insolation.

The WVMP accessible surface temperature in still air at 100 °F, with no insolation, must not exceed the exclusive use shipment limit of 185 °F, as specified in 10 CFR 71.43(g) [2]. In addition, there must be no loss of the radioactive contents, no significant increase in external surface radiation level, and no significant decrease in package effectiveness, as stated in 10 CFR 71.43(f) [2]and 71.51(a)(1) [3]. To address this requirement, the maximum pressure that can develop inside the WVMP during NCT is calculated for use in a structural analysis.

The analysis of temperatures for HAC follows the guidelines of 10 CFR 71.73 [4]. These guidelines specify that the package is exposed to an engulfing 1475 °F (800 °C) fire for a duration of 30 minutes, followed by a cool down to ambient conditions. The fire emissivity is specified as 0.9 and the surface emissivity for the surface of the package is set at 0.8. The guidelines also specify the use of a convective heat transfer coefficient appropriate for the fire.

The HAC analysis must demonstrate that the activity release during the HAC will not exceed the limits established by 10 CFR 71.51(a)(2) [3]. To demonstrate that no release of activity will

occur, the maximum pressure that can develop inside the WVMP during the HAC is calculated for use in a structural analysis.

2.0 Inputs and Assumptions

1. The WVMP consists of a container that encloses a 12-ft, 4.75-in. long by 11-ft, 4-in. wide by 11-ft, 4-in. high volume [5]. The melter is grouted in place inside this container by Low Density Cellular Concrete (LDCC). The LDCC fills the container to within 10 in. of the inside top surface [6]. The top and bottom container thickness is 4 in.; the sides of the container are 6 in. thick [5]. The container also includes steel rails, gaskets, and sacrificial shock absorbers at each of the eight corners [5]; these components are not modeled in the heat transfer analysis. Exclusion of these components yields conservatively bounding values for the calculated temperatures, since they provide added insulation for the interior of the WVMP when it is heated by either insolation or by the fire.

2. The mass of the melter is 107,500 lbm (48,761 kg) [6]. The LDCC mass is 70,738 lbm (32,086 kg) [6]. The mass of the melter glass is 467.2 kg (1030 lbm) [7].

3. Evaluation of thermal conductivities, densities, and heat capacities is required for the thermal analysis. The LDCC contains waters of hydration that may dehydrate to form water vapor when the GMP is exposed to the sun under NCT or, more particularly, to fire under HAC. The dehydration reaction is endothermic, so the dehydration process will act as a heat sink in the thermal analysis. The water vapor from dehydration will pressurize the GMP. Therefore, the fractional dehydration as a function of temperature and the heats of hydration and vaporization are needed inputs. Finally, the radionuclide contents of the melter glass and the decay heats for each of the isotopes in the glass are needed to compute the rate of radiolytic heating of the glass.

4. The volumes occupied by each type of material can be calculated by dividing the estimated mass of material by its density. The volume of the refractory material is estimated indirectly from the equation

$$V_{ref} = V_i - V_{air,l} - \frac{m_{LDCC}}{\rho_{LDCC}} - \frac{m_{glass}}{\rho_{glass}} \qquad (2\text{-}1)$$

where

V_{ref} = refractory volume, m^3

V_i = total interior volume of the WVMP, m^3

$V_{air,1}$ = volume air pocket above LDCC inside the WVMP, m^3

m_{LDCC} = mass of LDCC, kg

ρ_{LDCC} = LDCC density, kg/m^3

m_{glass} = mass of glass in melter, kg

ρ_{glass} = glass density, kg/m^3

The melter structure is comprised of Inconel®, Type 304 stainless steel, and Type 304L stainless steel [5]. As an approximation, the properties of the melter steel are set equal to the properties of Type 304L stainless steel. The refractory material is a combination of Monofrax™ K-3 and Zirmul™ [7]. Accordingly, the volume of the structural metal inside the melter is given by

$$V_{ss} = \frac{m_m - \rho_{Mono} V_{Mono} - \rho_{Zirm} V_{Zirm}}{\rho_{ss}} \quad (2\text{-}2)$$

where

V_{ss} = volume of metal inside melter, m^3

m_m = total melter mass, kg

ρ_{Mono} = density of Monofrax™, kg/m^3

V_{mono} = volume of Monofrax™ refractory inside melter, m^3

ρ_{Zirm} = density of Zirmul™, kg/m^3

V_{Zirm} = volume of Zirmul™ refractory inside melter, m^3

ρ_{ss} = density of Type 304L stainless steel, kg/m^3

Any portion of the melter volume that is not metal or refractory is assumed to be an air pocket. The melter air pocket volume is calculated by subtracting the metal and refractory volumes from the total refractory volume given by equation (2-1):

$$V_{air,2} = V_{ref} - V_{ss} - V_{Mono} - V_{Zirm} \quad (2\text{-}3)$$

where

$V_{air,2}$ = volume of air pocket inside melter, m^3

5. The density of the glass is 2600 kg/m^3 [7].

® Inconel is a registered trademark of Special Metals Corporation of New Hartford, New York.

™ Monofrax is a trademark of RHI Monofrax Ltd. of Falconer, New York.

™ Zirmul is a trademark of North American Refractories Co. of Pittsburgh, Pennsylvania. Zirmul is a contraction of the minerals names zirconia and mullite.

6. The average LDCC density is assumed to be equal to the density of the concrete batch with the lowest measured compressive strength, which was 71.2 lbm/ft^3 (1140 kg/m^3) [6].

7. The total refractory volume is 92.7 ft^3, of which 61.88 ft^3 is Monofrax™ K-3 and 30.82 ft^3 is Zirmul™ [7]. The thermal analysis uses the crystalline densities of these materials, 3900 kg/m^3 for Monofrax™ K-3 and 3140 kg/m^3 for Zirmul™, and the corresponding thermal conductivities at 100 °C, 4.19 W/m/K for Monofrax™ K-3 and 0.20 W/m/K for Zirmul™ [8]. The heat capacities are calculated from the compositions of Monofrax™ K-3 and Zirmul™ [8] and the estimated heat capacities of the crystalline phases of the oxide constituents [9,10]. The compositions and density calculations are summarized in Table 1; the resulting heat capacities are 774 J/kg/K for Monofrax™ K-3 and 709 J/kg/K for Zirmul™. The Monofrax™ and Zirmul™ heat capacities are computed using the weighted averages of only those consituents listed in Table 1, despite the fact that their weigtht fractions do not sum to one.

Table 1. Compositions and Heat Capacities for Monofrax™ K-3 and Zirmul™

Oxide	Mol. Wt. (g/mole)	Heat Capacity (J/mol/K)	Monofrax™ K-3 (wt %)	Monofrax™ K-3 (J/g/K)	Zirmul™ (wt %)	Zirmul™ (J/g/K)
Al_2O_3	101.96	79	44	0.341	70	0.542
CaO	56.08	42	0.18	0.001	0	0
Cr_2O_3	151.99	118.7	19	0.148	0	0
Fe_2O_3	159.69	103.9	5.85	0.038	0	0
Na_2O	62	69.1	0.2	0.002	0	0
MnO_2	86.94	54.1	0.06	0.000	0	0
MgO	40.3	37.2	3.71	0.034	0	0
SiO_2	60.08	44.4	0.6	0.004	10.2	0.075
TiO_2	79.88	55	0.16	0.001	0	0
ZrO_2	123.22	56.2	0	0	19.5	0.089
Total				0.774		0.709

8. As stated previously, the melter metal is assigned the properties of Type 304L stainless steel. The container walls are fabricated from Type SA516 carbon steel [5]. The density of Type 516 carbon steel is 483.8 lbm/ft^3 (7749.7 kg/m^3), and the density of Type 304L stainless steel is 499.4 lbm/ft^3 (7999.6 kg/m^3) [11]. The heat capacities and thermal conductivities are correlated as functions of temperature as shown in Figures 1 and 2 [11].

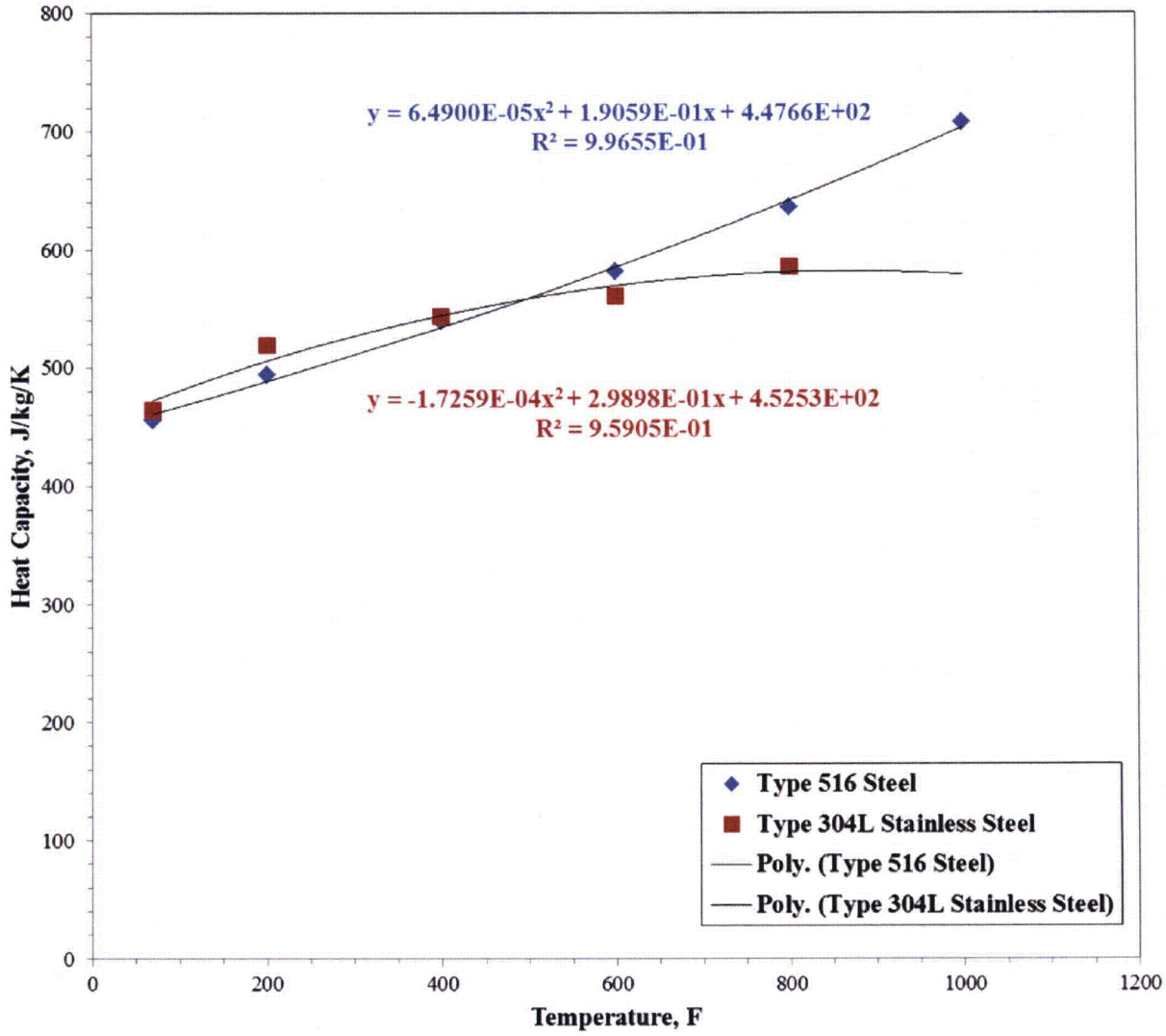

Figure 1. Correlation of Heat Capacities for Types 516 and 304L Steels [11].

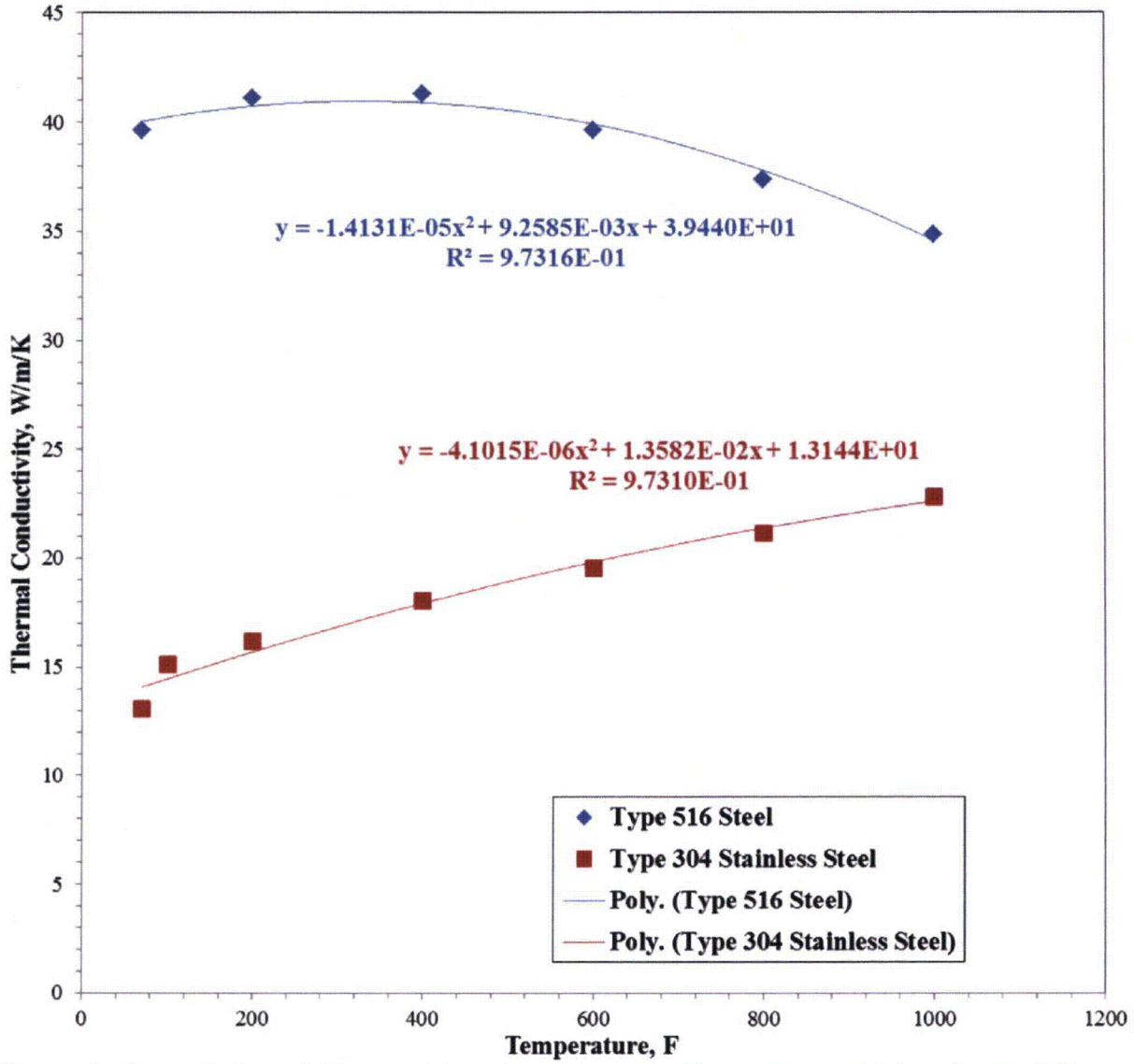

Figure 2. Correlation of Thermal Conducitivities for Types 516 and 304L Steels [11].

9. From equations (2-1), (2-2), and (2-3), and the densities listed, the volumes occupied by the different components of the GMP can be calculated. The volumes are listed in Table 2. The melter volumes are modeled as cubes inside the container. This modeling arrangement minimizes the heat transfer area, maximizes the amount of insulation, and therefore conservatively maximizes the temperatures inside the melter structure.

Table 2. West Valley Melter Shipping Package Content Volumes

Component	Volume (m^3)
Melter (total)	13.64
Glass	0.18
Steel	4.84
Refractory	2.62
Melter Air Pocket	5.99
LDCC	28.13
Air Pocket	3.32
Total Interior Volume	45.09

10. The glass heat capacity is fit to typical values for borosilicate glass [12], using the empirical correlation

$$c_{p,gl} = \min\left(\frac{0.19242 + 0.001081T_{gl}}{1 + 0.00251T_{gl}}, 0.2\right) \quad (2\text{-}4)$$

where

$c_{p,gl}$ = thermal conductivity of the melter glass, cal/g/K

T_{gl} = glass temperature, °C

11. The heat capacity of the LDCC is set equal to a typical value for a cement mix with a water content close to that estimated for LDCC. LDCC contains on average 510 lbm/yd^3 cement, with added water amounting to 20% of the cement by weight, and enough sand to increase the density to the specified value. The result for the given density of 71.2 lbm/ft^3 is 18.89 lbm/ft^3 cement, 48.53 lbm/ft^3 sand (SiO_2), and 3.78 lbm/ft^3 water [13, 14]. The water content is 5.3 wt %. The closest value for which a cement heat capacity is reported is a mix with 3 wt % water, for which the heat capacity was measured to be 765 J/kg/K [15].

12. The thermal conductivity for the glass is set at its minimum value for borosilicate glass of 0.42 W/m/K [12]. The LDCC thermal conductivity is set at its minimum value for its density, which is approximately 0.26 W/m/K [16].

13. The heat generation rate in the glass is calculated from a RADCALC® analysis of the activity in the glass [7, 17, 18, 19] and tabulations of the energy emissions for each radionuclide from the International Committee on Radiological Protection (ICRP) tables [20]. The full list of radionuclides from the RADCALC® output is included in the tabulation. The radiolytic heat generation calculations are summarized in Appendix A.

14. The Arrhenius correlation of the fractional dehydration is based on data for crystalline calcium silicates, which are by far the major constituents of typical cement. It is assumed

® RADCALC is a registered tradename of LifeLine Software, Inc., of Austin, Texas.

that the LDCC is fully cured so that there is no free water in the cement pores and so that, consequently, all dehydration involves the breaking of crystalline bonds, followed by evaporation of liquid water. For tricalcium silicate hydrate ($3CaO:SiO_2:2H_2O$), the fractional dehydration is correlated as an Arrhenius function of the form [21]

$$\alpha = A_r \exp\left(-\frac{E_a}{R_g T}\right) \tag{2-6}$$

where

α = cumulative fraction of calcium silicate oxides that have undergone dehydration

A_r = pre-exponential Arrhenius constant for cement dehydration, dimensionless

E_a = activation energy for cement dehydration, J/mole

R_g = gas constant, J/mole/K

The Arrhenius equation was fit to the dehydration data as shown by Figure 3.

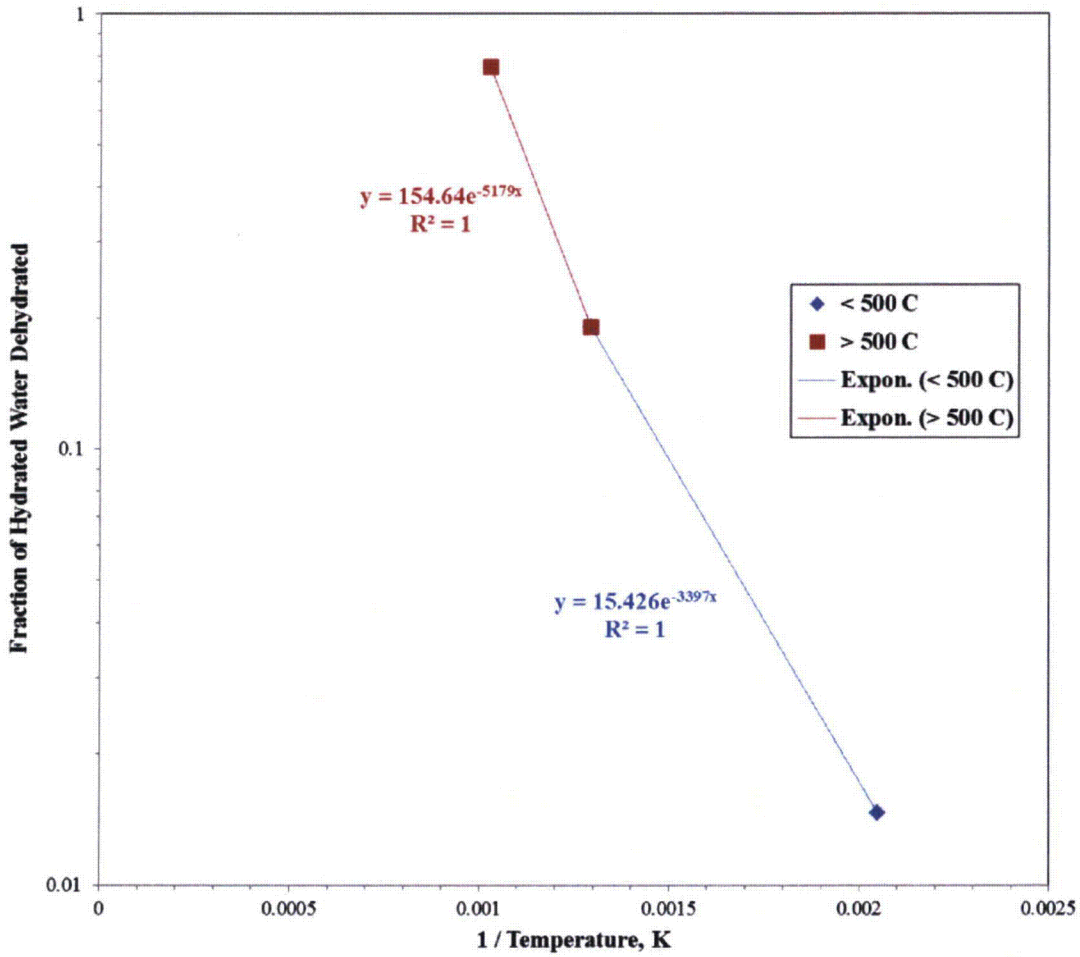

Figure 3. Correlation of Measurements for Dehydration of $3CaO:SiO_2:2H_2O$

As indicated by the figure, the Arrhenius constants, for temperatures below 500 °C, are

$$A_r = 15.426, \frac{E_a}{R_g} = 3397 \text{ K} \quad (2\text{-}7)$$

15. The heat of hydration for tricalcium silicate is 65.59 kJ/mole H_2O [22], and the heat of hydration for calcium oxide is 63.92 kJ/mole H_2O [23]. The tricalcium silicate heat of hydration is used in the thermal analysis, since it is more representative of the LDCC composition.

16. The heat of vaporization for water is added to the heat of reaction for dehydration. The heat of vaporization is correlated as a function of temperature by [24]

$$\lambda = \lambda_b \left(\frac{1 - T_r}{1 - T_{r,b}} \right)^{0.38} \quad (2\text{-}8)$$

where

λ = heat of vaporization, J/mole

λ_b = heat of vaporization at the normal boiling point (373.15 K), J/mole

T_r = relative temperature

$T_{r,b}$ = relative temperature at the normal boiling point

The relative temperature is normalized with respect to the critical temperature for water, which is 373.99 °C or 647.14 K [25]. The heat of vaporization of water at the normal boiling point is 40657 J/mole [25].

3.0 Analysis Method

The thermal analysis is performed using Version 4.3a of the finite element modeling code COMSOL® Multiphysics. COMSOL® Multiphysics is approved for use in heat transfer modeling at the Savannah River National Laboratory and has been used to calculate NCT and HAC temperatures for other waste transfer packages [26, 27]. The COMSOL® model uses the actual outer dimensions for the container and approximates the contents of the WVMP as a nested series of cubes, with the innermost cube comprised of the radioactive glass in the melter heel, the spout, and any glass dispersed into the refractory of the melter. In the model, this inner core is surrounded by a layer comprised of the melter refractory and structural steel, a layer of the LDCC used to grout the melter in the package, and the steel container walls. There also is a 10-in. thick air space between the top surface of the LDCC and the top container wall. This air pocket is present because the WVMP was not completely filled with LDCC.

® COMSOL is a registered tradename of COMSOL, Inc., of Burlingame, Massachusetts.

To simplify the heat transfer analysis, it is assumed that the glass, steel, refractory, and LDCC layers form concentric, symmetrical cubes within the container walls and upper air pocket. The symmetry provides a conservative, lower bound to the actual overall rate of heat transfer in that it averages out any variations in the thicknesses of the insulation provided by the LDCC and the refractory. Any asymmetrical variations would increase the local, and the average, rate of heat transfer. A lower bound to the heat transfer rate is desired because it maximizes the surface temperature for insolation and fire exposure and maximizes increases in the glass temperature due to radiolytic heating for the case of no insolation. (The maximum glass temperature is used to estimate the bounding surface temperature without insolation, to account for asymmetries in the thickness of the LDCC around the melter.)

The COMSOL® model utilizes bilateral symmetry along the length and width of the WVMP to reduce the volume analyzed to a one-quarter corner of the WVMP that extends from the top surface to the bottom surface. Figure 4 depicts the simplified COMSOL model, with the various materials shown. Figure 5 shows the discretization mesh for the finite element calculations. The total number of calculation nodes is 125,148. Trial calculations were performed to ensure that the discretization was sufficiently fine to calculate the WVMP temperature profile with a high degree of precision.

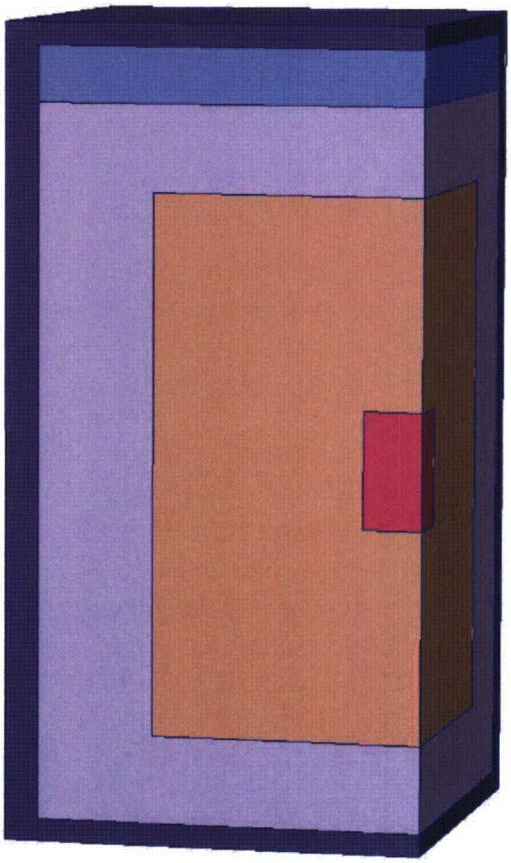

Key:

Dark Blue	**Container**
Medium Blue	**Air Space**
Light Violet	**LDCC**
Tan	**Melter Structural Steel and Refractory**
Pink	**Glass**

Figure 4. Schematic of COMSOL® Multiphysics Model of WVMP

® COMSOL is a registered tradename of COMSOL, Inc., of Burlingame, Massachusetts.

Figure 5. Meshing for COMSOL® Multiphysics Model of WVMP

3.1 Thermal Analysis

The COMSOL heat transfer equation for the glass takes the form

$$\rho c_p \frac{\partial T}{\partial t} - \nabla \bullet k \nabla T = \frac{Q}{V_{glass}} \tag{3-1}$$

where

ρ = density of the material, kg/m^3
c_p = heat capacity of the material, J/kg/K
∇ = dispersion operator, 1/m
t = time, s
k = thermal conductivity of material, W/m/K
T = temperature, K
Q = internal heat generation rate for radiolytic heating of the glass, W
V_{glass} = glass volume, m^3

The radiolytic heat generation rate is expressed as the sum of the products of the specific activity of the isotopes that are present in the glass and the decay energy for each isotope:

$$Q = \sum_j a_j e_j \tag{3-2}$$

where

a_j = activity of the j^{th} isotope, Ci

e_j = decay energy of the j^{th} isotope, W/Ci

The total radiolytic heat generation rate is the sum of the individual heat generation rates for the glass in the melter heel, the glass in the melter spout, and the glass embedded in the melter refractory. In the model it is assumed that radiolytic heating occurs at a uniform rate throughout the glass. In itself, this is not necessarily a conservative assumption. However, because the melter glass has a relative high thermal conductivity compared to the LDCC, when it is modeled as a monolith, the melter glass should be at a relatively uniform temperature regardless of the distribution of the radiolytic heating. The assumption that the glass is concentrated in one central volume should yield a conservatively high estimate for the maximum temperature in the glass.

The heat transfer equation for the melter steel and refractory and the LDCC is

$$\rho c_p \frac{\partial T}{\partial t} - \nabla \bullet k \nabla T = 0 \tag{3-3}$$

The equivalent thermal conductivity of the melter steel and refractory is computed by taking the volume average of the individual thermal conductivities of the steel and refractory:

$$k_{eq} = \frac{V_{ref} k_{ref} + V_{ss} k_{ss}}{V_{ref} + V_{ss} + V_{air,2}} \tag{3-4}$$

where

k_{eq} = equivalent thermal conductivity for mixture of melter refractory and steel, W/m/K

k_{ss} = thermal conductivity of melter steel, W/m/K

V_{fb} = volume of refractory, m^3

This linear averaging method is consistent with an arrangement where structural steel beams radiate outward from the melter glass to the inner edge of the LDCC and provide a continuous path for heat transfer through the steel. The averaging accounts for the fraction of the total cross-sectional heat transfer area occupied by the refractory. Linear averaging provides a more realistic model for heat transfer in the melter than reciprocal averaging, which would follow from an assumption that the refractory and structural steel were randomly mixed. Melter glass temperatures calculated using a reciprocal averaging method for the combined thermal conductivity of the refractory and steel would yield calculated glass temperatures that would be

unrealistically high. The same linear volume averaging is used to compute the equivalent density and heat capacity for the melter steel and refractory.

Heat losses and heat transfer associated with dehydration of cement hydrates in the LDCC are included in the COMSOL model by incorporating the heat of dehydration into the effective heat capacity for the LDCC. The contribution of the combined heats of dehydration and evaporation equals the product of the heats of dehydration and evaporation, the mass fraction of hydrate in the LDCC, and the derivative of the fractional dehydration with respect to temperature.

Differentiation of the Arrhenius expression for the fraction dehydration (equation (2-6)) and substitution in the expression for the effective LDCC heat capacity yields the following equation.

$$c_p = c_{p,s} + \frac{(\Delta H_r + \lambda) m_{H_2O} A_r E_a}{m_{LDCC} M_{H_2O} R_g T^2} \exp\left(-\frac{E_a}{R_g T}\right) \tag{3-5}$$

where

$c_{p,s}$ = ordinary heat capacity for cement solids exclusive of reaction or phase change, J/kg/K

ΔH_r = heat of reaction for breaking hydrate bond, J/mole H_2O

M_{H_2O} = molecular mass of water, 0.018 kg/mole

m_{H_2O} = mass of water in LDCC hydrate, kg

m_{LDCC} = total mass of LDCC, kg

During NCT, the heat transfer equation for the steel frame is

$$\rho c_p \frac{\partial T}{\partial t} - \nabla \bullet k \nabla T = q''_i A_i - h_i A_i (T_{s,i} - T_a) \tag{3-6}$$

where

q''_i = surface heat flux due to insolation over the i^{th} surface (applies only to surface nodes), W/m^2

A_i = surface area for the i^{th} surface, m^2

h_i = surface heat transfer coefficient for the i^{th} surface (applies only to surface nodes), $W/m^2/K$

$T_{s,i}$ = temperature of the i^{th} surface, K

T_a = ambient temperature (or fire temperature for the HAC), K

For the fire exposure portion of the HAC transient, the heat transfer equation for the frame is

$$\rho c_p \frac{\partial T}{\partial t} - \nabla \bullet k \nabla T = \varepsilon_i \sigma A_i \left(T_{fire}^4 - T_{s,i}^4\right) + h_i A_i (T_{fire} - T_{s,i}) \tag{3-7}$$

where

ε_i = emissivity for i^{th} surface, dimensionless
σ = Stefan-Boltzmann constant, $W/m^2/K^4$
T_{fire} = fire temperature, K

During the cool down portion of the HAC transient, the heat transfer equation for the frame becomes

$$\rho c_p \frac{\partial T}{\partial t} - \nabla \bullet k\nabla T = q''_i A_i - \varepsilon_i \sigma A_i \left(T_{s,i}^4 - T_a^4\right) - h_i A_i \left(T_{s,i} - T_a\right) \quad (3\text{-}8)$$

As stipulated by 10 CFR 71.71 [1], it is assumed that the air surrounding the WVMP during NCT is still. It is assumed that still air also surrounds the WVMP during the HAC transient. Consequently, the heat transfer coefficients are based on natural convection from exterior surfaces. Different correlations are applied for natural convection to the top surface of the WVMP, to the vertical side surfaces, and to the bottom surface. All three correlations are for turbulent natural convection; due to the large size of the WVMP, the natural convection flow is in the turbulent range for any significant temperature differences. The COMSOL® correlation for the side walls is given by Churchill and Chu [28, 29]

$$h_v = \left(\frac{k_{air}}{L_v}\right)\left(0.825 + \frac{0.387Ra^{1/6}}{\left(1+\left(\frac{0.492}{Pr}\right)^{9/16}\right)^{8/27}}\right)^2 \quad (3\text{-}9)$$

where

h_v = heat transfer coefficient for natural convection to the sides of the WVMP, $W/m^2/K$
k_{air} = thermal conductivity of air, W/m/K
L_v = GMP height, m
Ra = Rayleigh number
Pr = Prandtl number

For natural convection from the top of the WVMP, COMSOL® uses a natural convection correlation recommended by Lloyd and Moran [28, 30]:

$$h_u = \left(\frac{k_{air}}{L_u}\right)0.15Ra^{1/3} \quad (3\text{-}10)$$

where

h_u = heat transfer coefficient for natural convection to the top of the WVMP, $W/m^2/K$

L_u = GMP width at the top of the GMP, m

Finally, for convection from the bottom surface of the GMP, COMSOL® utilizes the following generalized correlation [31]

$$h_d = \left(\frac{k_{air}}{L_d}\right) 0.27 Ra^{1/4} \tag{3-11}$$

where

h_d = heat transfer coefficient for natural convection to the bottom of the WVMP, $W/m^2/K$

L_d = GMP width at the bottom of the GMP, m

The heat transfer coefficient given by equation (3-11) is used only for the HAC analysis.

The Rayleigh number in the preceding correlations is defined by

$$Ra = \frac{\rho_{air} \Delta\rho_{air} c_{p,air} g L^3}{\mu_{air} k_{air}} \tag{3-12}$$

where

ρ_{air} = air density, kg/m^3

$\Delta\rho_{air}$ = difference between the density of air at ambient temperature and the average density at the WVMP surface, kg/m^3

$c_{p,air}$ = air heat capacity, J/kg/K

g = gravitational acceleration, m/s^2

L = GMP height or equivalent width, m

μ_{air} = air viscosity, kg/m/s

The Prandtl number is given by

$$Pr = \frac{c_{p,air} \mu_{air}}{k_{air}} \tag{3-13}$$

All gas properties except the density difference are evaluated at a temperature midway between the ambient temperature and the average temperature at the WVMP surface.

3.2 Approach to Transient Modeling

Bounding temperatures for NCT with insolation are evaluated using a transient calculation in which 12-hour periods of insolation at the specified rates are followed by 12 hours of no insolation. This approach is consistent with the intent of 10 CFR 71.71 [1], which implies that the limiting condition is continual outdoor exposure of the WVMP, with insolation during daylight hours and no insolation at night. The heat losses to the ambient air are assumed to continue day and night. The ambient air temperature is conservatively set equal to 100 °F for nighttime exposure as well as daytime exposure. The COMSOL® calculations were extended to 30 days to assure an approach to a limiting diurnal temperature cycle. The limiting NCT conditions are evaluated at the end of the 12-hour period of insolation on the 30th day.

The HAC is modeled using a transient calculation in which the WVMP is fully engulfed by the 1475 °F fire. The initial temperature distribution is set equal to the limiting NCT temperature distribution. The fire is applied for 30 minutes, after which time it is assumed that the WVMP loses heat to 100 °F ambient air and receives insolation at the same rate as during NCT. The transient calculation is continued 720 minutes into the cool-down period to ensure that maximum local temperatures are reached and that the maximum amount of dehydration has occurred. (It is assumed that the dehydration reaction is reversible in the sense that the cement will rehydrate as it cools.)

The orientation of the WVMP during HAC is not specified by 10CRF71.73 [4]. To maximize the temperature of the air pocket inside the WVMP and hence the pressurization due to heating, it was assumed that the WVMP is upside down, so that natural convection heat losses from the wall adjacent to the air pocket were minimized during the cool-down period, when the interior temperatures reached their maximum values. (The natural convection heat transfer coefficient for heated surfaces facing down is less than the corresponding heat transfer coefficients for heated surfaces facing up or for vertical surfaces.)

3.3 Calculation of Maximum Pressures

The maximum pressure is calculated by assuming that all of the hydrated water content that is released as vapor due to heating of the LDCC accumulates in the upper air pocket. It is assumed that any pressure that might develop internally in the concrete pores is contained within the LDCC layer. The gas volume inside the LDCC pores is conservatively neglected in the pressure calculation. The air pocket pressure computation is based on the ideal gas law and is performed separately from the COMSOL® heat transfer calculations. The equation for the maximum pressure is

$$P = P_0\left(1+\frac{n_{H_2O}}{n_{air}}\right)\frac{T}{T_0} \qquad (3\text{-}14)$$

where

P = maximum pressure for NCT or HAC, atm or psia

P_0 = initial pressure, assumed to be equal to atmospheric pressure, atm or psia

n_{H_2O} = number of moles of water vapor generated by dehydration of the LDCC

n_{air} = number of moles of air initially in the air gap

T = average temperature in the air gap, K

T_0 = initial temperature in the air gap, assumed to be equal to 20 °C or 293.15 K

The number of moles of air at the start of the NCT transient is calculated using the ideal gas law relation

$$n_{air} = \frac{P_0 V_{air}}{R_g T_0} \tag{3-15}$$

where

V_{air} = volume of the air gap, m^3

R_g = gas law constant, 8.2057E-5 m^3 atm/mol/K

The number of moles of water evaporated is computed by taking the difference between the number of moles of hydrated water initially in the LDCC and the minimum number of moles that remain hydrated at any time during the HAC fire or cool-down period:

$$n_{H_2O} = \left(\rho_{H_2O,LDCC,0} - \overline{\rho}_{H_2O,LDCC}\right) V_{LDCC} \tag{3-16}$$

where

$\rho_{H_2O,LDCC,0}$ = initial concentration of hydrated water in the LDCC, kg/m^3

$\overline{\rho}_{H_2O,LDCC}$ = minimum average bulk concentration of hydrated water in the LDCC, kg/m^3

V_{LDCC} = total LDCC volume, m^3

4.0 Calculation Method

Thermal modeling was performed using Version 4.3a of COMSOL® Multiphysics on a Linux Red Hat operating system. The pressurization calculations and the evaluation of input items for the thermal analysis were performed using Microsoft Excel 2010 for Windows 7.

5.0 Open Items

There are no open items associated with this calculation note.

6.0 Uncertainty Analysis

A formal uncertainty analysis is not included. The thermal analysis uses conservative bounding assumptions, so a formal analysis of the uncertainties is not required as would be the case for a best estimate calculation.

7.0 Results of NCT and HAC Thermal Analyses

Table 3 summarizes the results of the NCT thermal analysis. The maximum temperature for exposure to 100 °F air is 105.36 °F, for the melter glass. Although the COMSOL® model predicts a surface temperature very close to the ambient air temperature, the glass temperature must be assigned as the bounding maximum surface temperature, because of the close approach of one arm of the melter to the door on one side of the WVMP. The maximum glass temperature of 105.36 °F does not closely approach the limiting surface temperature of 185 °F. The minimum temperatures for exposure to -20 °F and -40 °F ambient air are -19.89 °F and -39.89 °F, respectively. The maximum temperature with insolation is 209.42 °F, for the container. The maximum WVMP pressure of 12.0 psig is calculated from an assumption that the active pressurization of the container is from the air pocket at the top of the WVMP. The calculated pressure is based on heating of this air from an assumed initial temperature of 68 °F to an average temperature of 184.30 °F. The pressurization also accounts for the vaporization of 62 moles of hydrated water to add to the 126 moles of air initially present in the air pocket.

Table 4 reports the results of the HAC thermal analysis. The maximum temperature of 1221.09 °F is located at the corners of the WVMP. The average temperature of the LDCC increases to 204.00 °F, and the average temperature of the air pocket rises to 599.39 °F. The temperatures of the melter and the melter glass are virtually unaffected by the 30-minute fire. The maximum pressure for HAC of 73.0 psig is calculated based on the maximum average air pocket temperature and a maximum amount of evaporation of 249 moles of water. The maximum pressure conditions occur after the end of the fire exposure, during the cool-down period. The exact time at which the pressure peaks is not listed because the maximum pressure is based on a combination of the maximum air pocket temperature and the maximum amount of hydrated water that evaporates, these maximums are reached at different times.

Figure 6 shows the variation of the average LDCC and air pocket temperatures during the HAC fire transient. The average LDCC temperature reaches its maximum value of 204.00 °F 592 min after the start of the fire (and 562 min after the end of the fire exposure), and the average air pocket temperature peaks at 599.39 °F 88 min after the start of the fire. Figure 7 depicts the variation of the average bulk hydrated water content of the LDCC during the fire transient. The minimum hydrated water content, with the evaporation of a maximum 249 moles of water, occurs 256 min after the start of the fire.

Figures 8, 9, and 10 illustrate the development of the NCT temperature profile at the end of the 12-h heating cycle, after one day, 10 days, and 30 days. It may be seen that the transient temperature distribution approaches a limiting profile reasonably closely after one cycle and quite closely after 10 days. The maximum temperature is 209.32 °F and the minimum temperature is 133.1 °F. Temperatures in the melter and the LDCC are close to the minimum

temperature due to the relatively low thermal conductivity of the LDCC. The temperature increases toward the maximum only in the air pocket and the top wall of the WVMP.

Figure 11 shows the HAC temperature profile at the end of the 30-min. fire exposure, when the WVMP wall temperature is at its maximum. It may be noted that the 1221.1 °F maximum temperature is confined to the eight corners of the WVMP. The average container plate temperatures remain below 800 °F. The average temperature of the hottest plate, adjacent to the air pocket, is 782.20 °F on the outer surface oand 626.94 °F on the inside surface. The average plate temperature is approximately equal to the average of these two temperatures, which is 711.12 °F. Except for that portion of the LDCC closest to the container and the air pocket at the end of the WVMP, the temperatures inside the WVMP do not vary significantly from their initial values for NCT with insolation.

Table 3. Limiting Conditions for NCT

No Insolation, 100 °F Ambient Air

Component	Maximum Temperature (°F)	Maximum Pressure (psig)
Overall	105.36	----
Glass	105.36	
Melter	101.51	
LDCC	100.96	
Air Pocket	100.32	
Container	100.22	

No Insolation, -20 °F Ambient Air

Component	Minimum Temperature (°F)	Limiting Pressure (psig)
Overall	-19.89	----
Glass	-18.74	
Melter	-19.21	
LDCC	-19.88	
Air Pocket	-19.89	
Container	-19.89	

No Insolation, -40 °F Ambient Air

Component	Minimum Temperature (°F)	Limiting Pressure (psig)
Overall	-39.89	----
Glass	-38.73	
Melter	-39.20	
LDCC	-39.88	
Air Pocket	-39.89	
Container	-39.89	

Table 3. Limiting Conditions for NCT (continued)

With Insolation, 100 °F Ambient Air

Component	Max. Temperature (°F)	Maximum Pressure (psig)
Overall	209.42	12.0
Glass	146.30	
Melter	144.56	
LDCC	183.49	
Air Pocket	208.90	
Container	209.42	

Table 4. Limiting Conditions for HAC

With Insolation, 100 °F Ambient Air, 1475 °F Fire Exposure for 30 min.

Component	Max. Temp. (°F)	Avg. Temp. (°F)	Max. Pressure (psig)	Time for Max. Temp. (min)
Overall	1221.09		73.0	30
Glass	146.30[c]			750 +[d]
Melter	145.21			750 +[d]
LDCC	692.98	204.00		68
Air Pocket	727.92	599.39		68
Container	1221.09			30

[c] The maximum glass temperature for HAC is the same as for NCT.

[d] The glass and melter temperatures had not peaked 750 min after the start of the fire (720 min after the end of the fire exposure), but are judged to have been within 1 °F of their peak values.

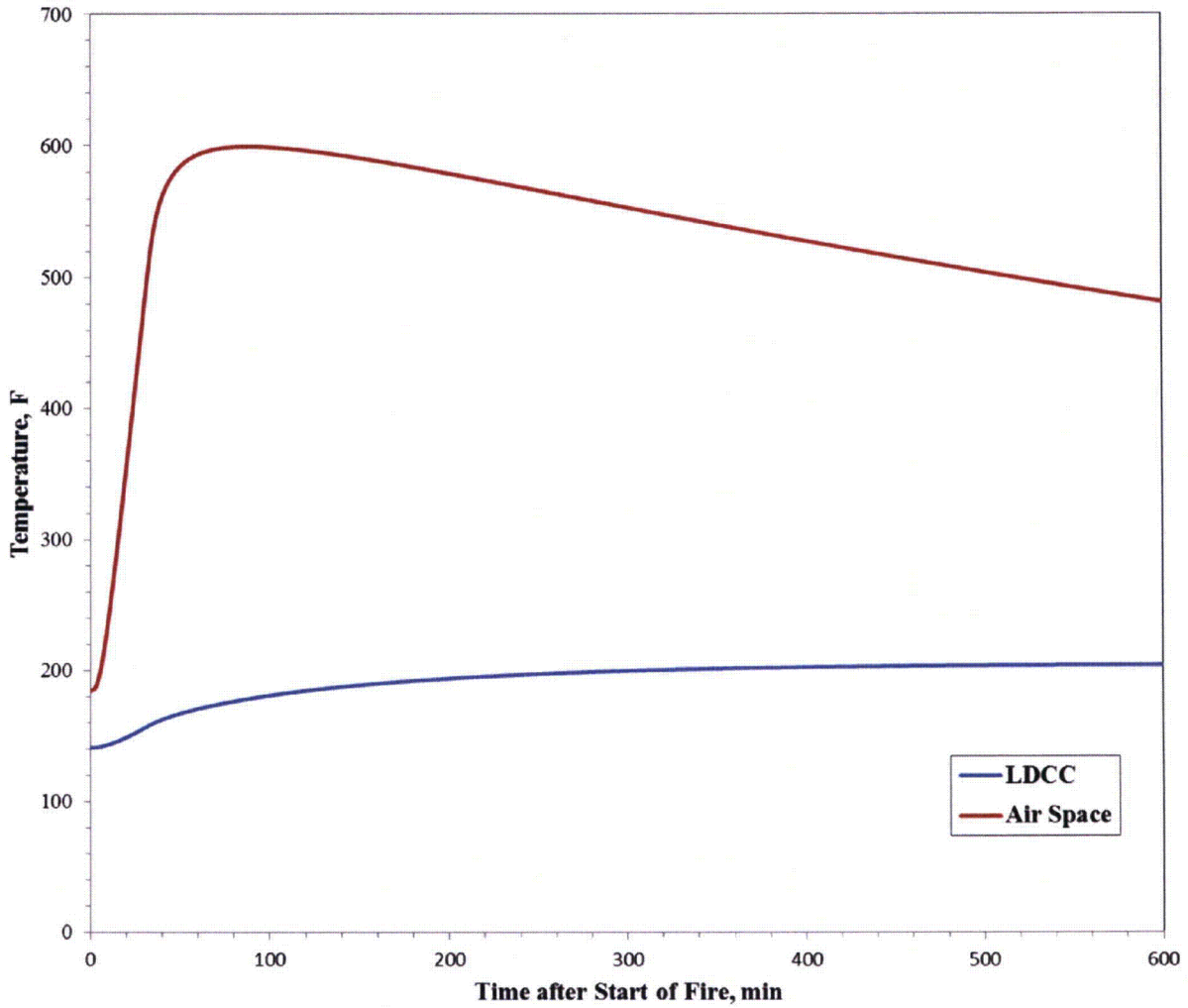

Figure 6. Variation of Average LDCC and GMP Air Pocket Temperatures during the HAC Fire Scenario

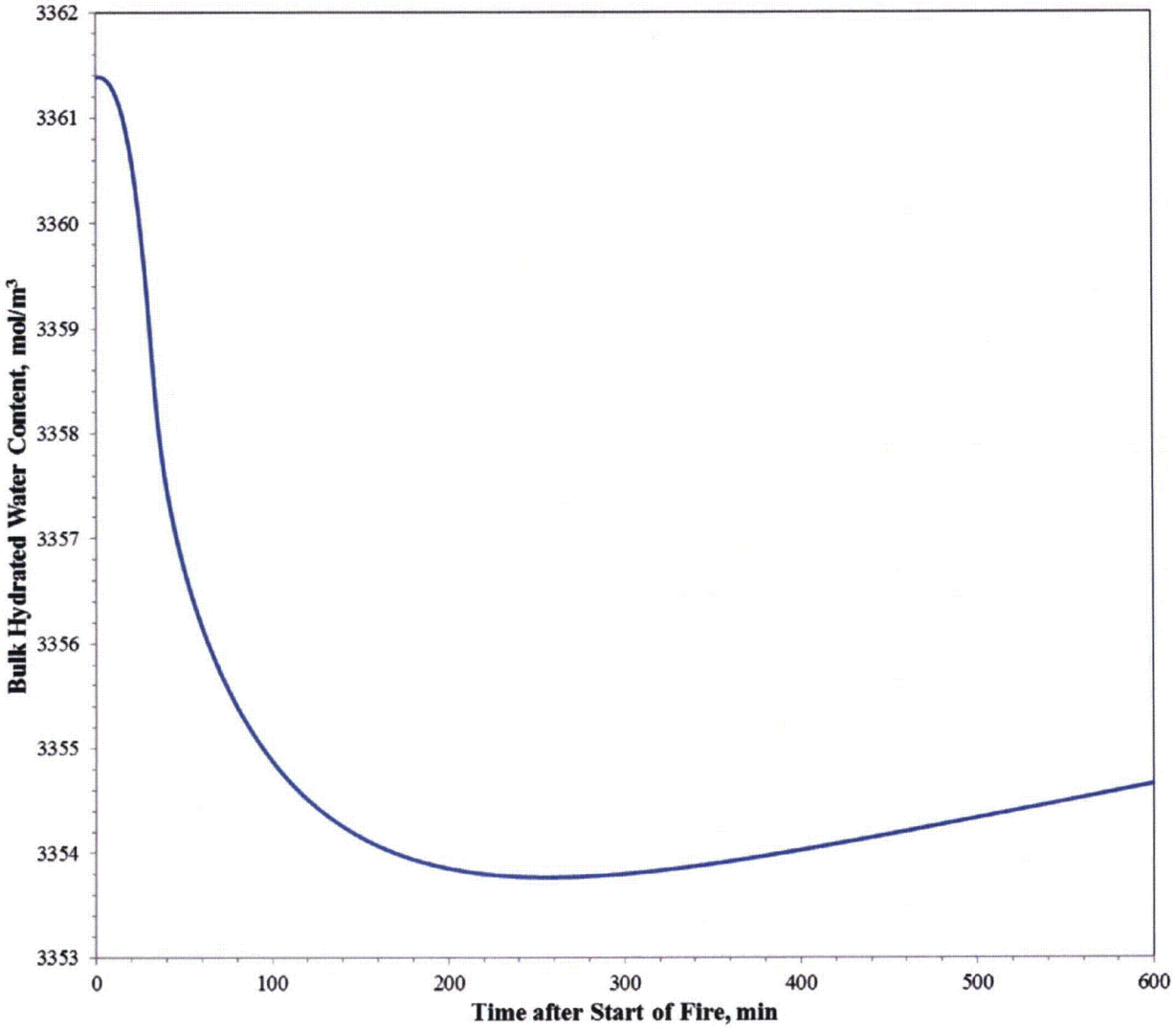

Figure 7. Variation of Average Bulk Hydrated Water Content in LDCC during HAC Fire Scenario

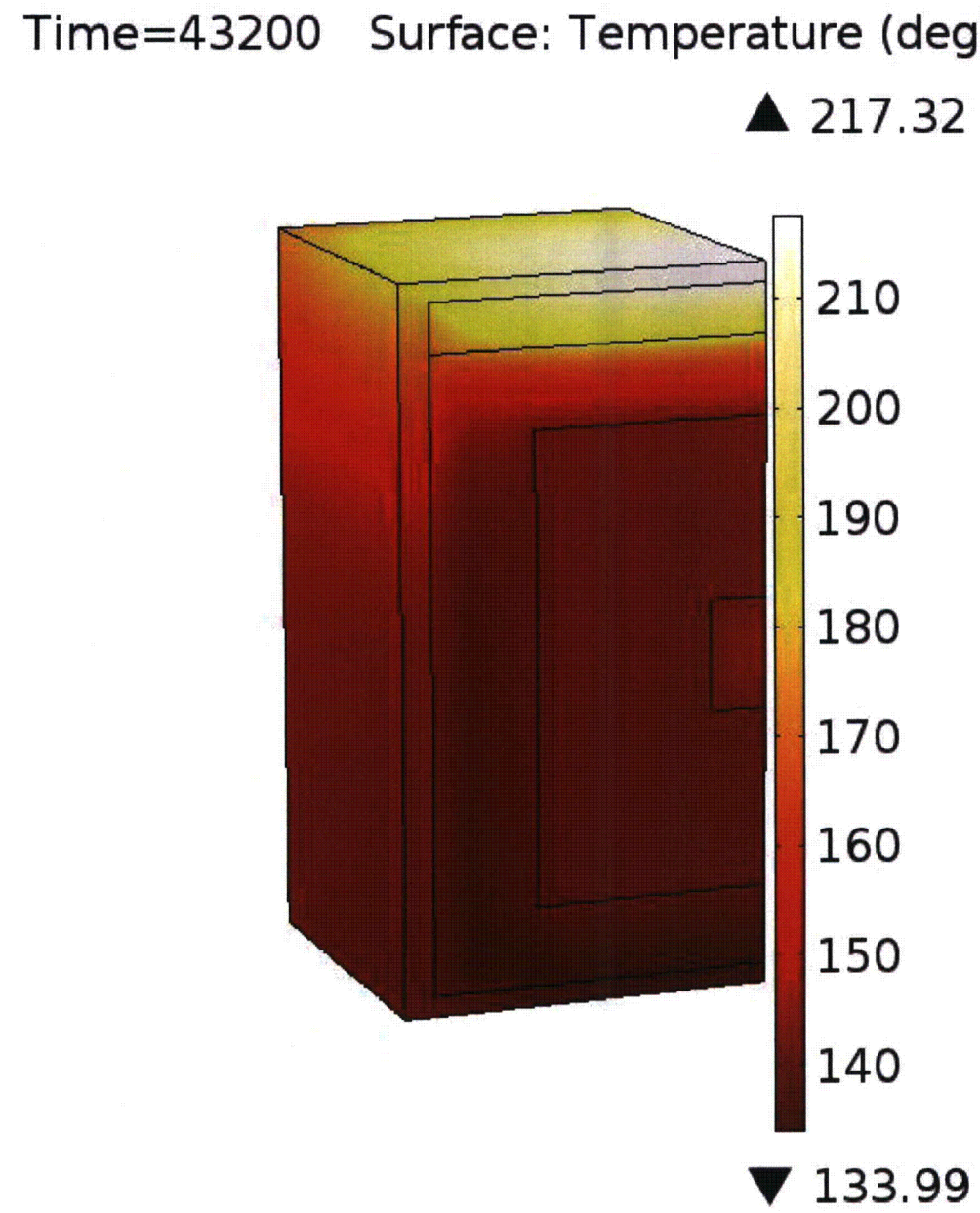

Figure 8. Temperature Profile for NCT with Insolation after One Day

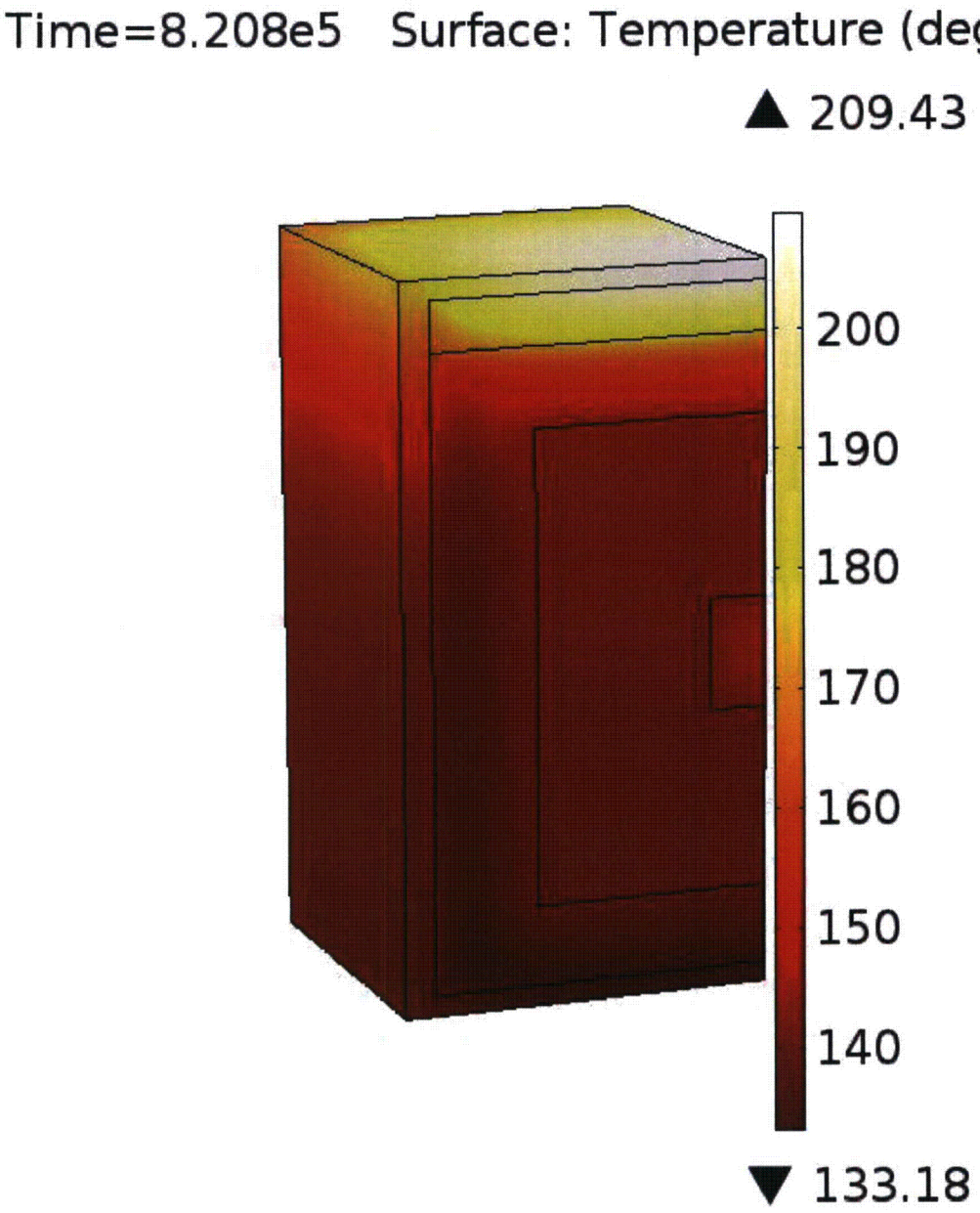

Figure 9. Temperature Profile for NCT with Insolation after 10 Days

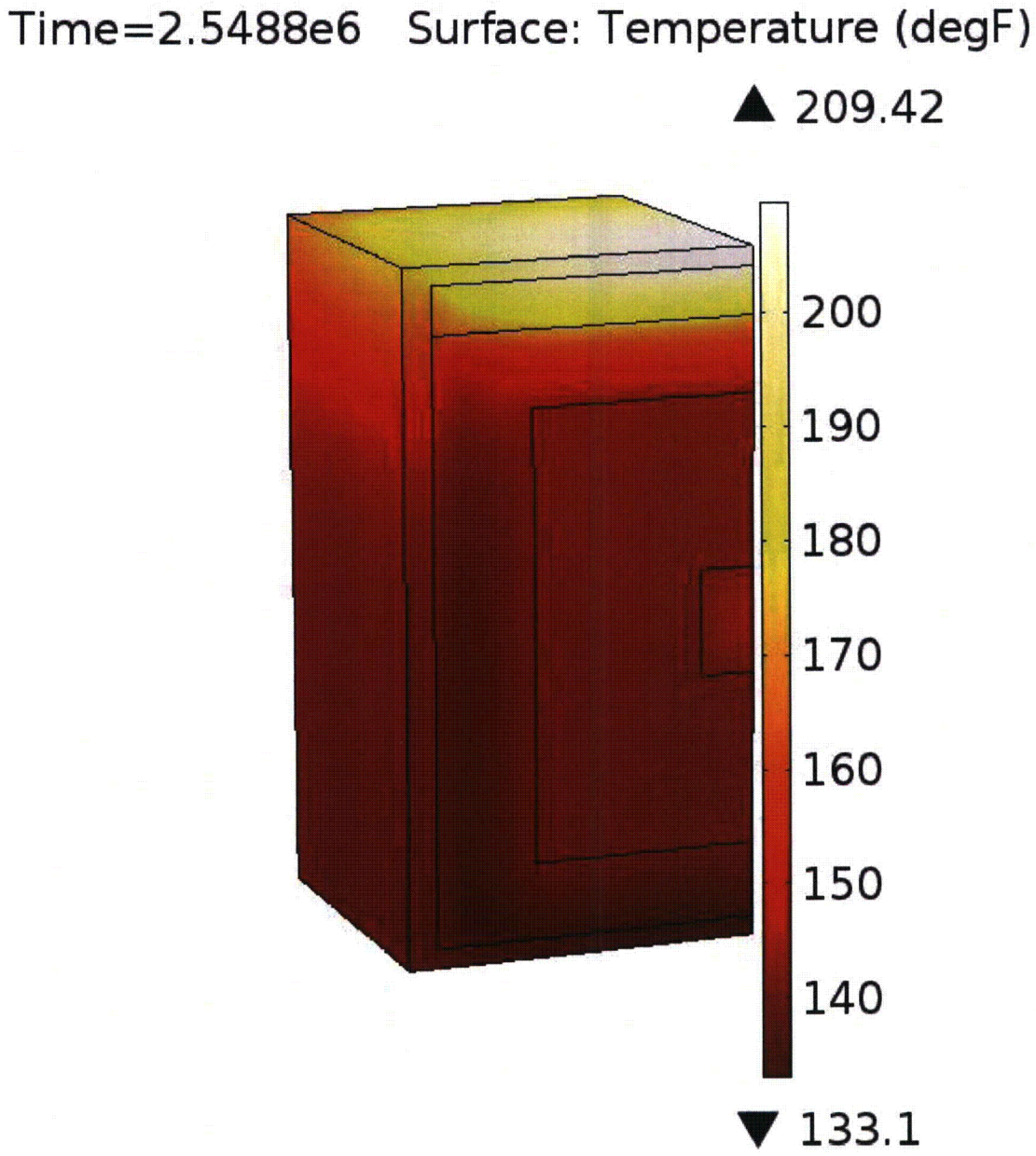

Figure 10. Temperature Profile for NCT with Insolation after 30 Days

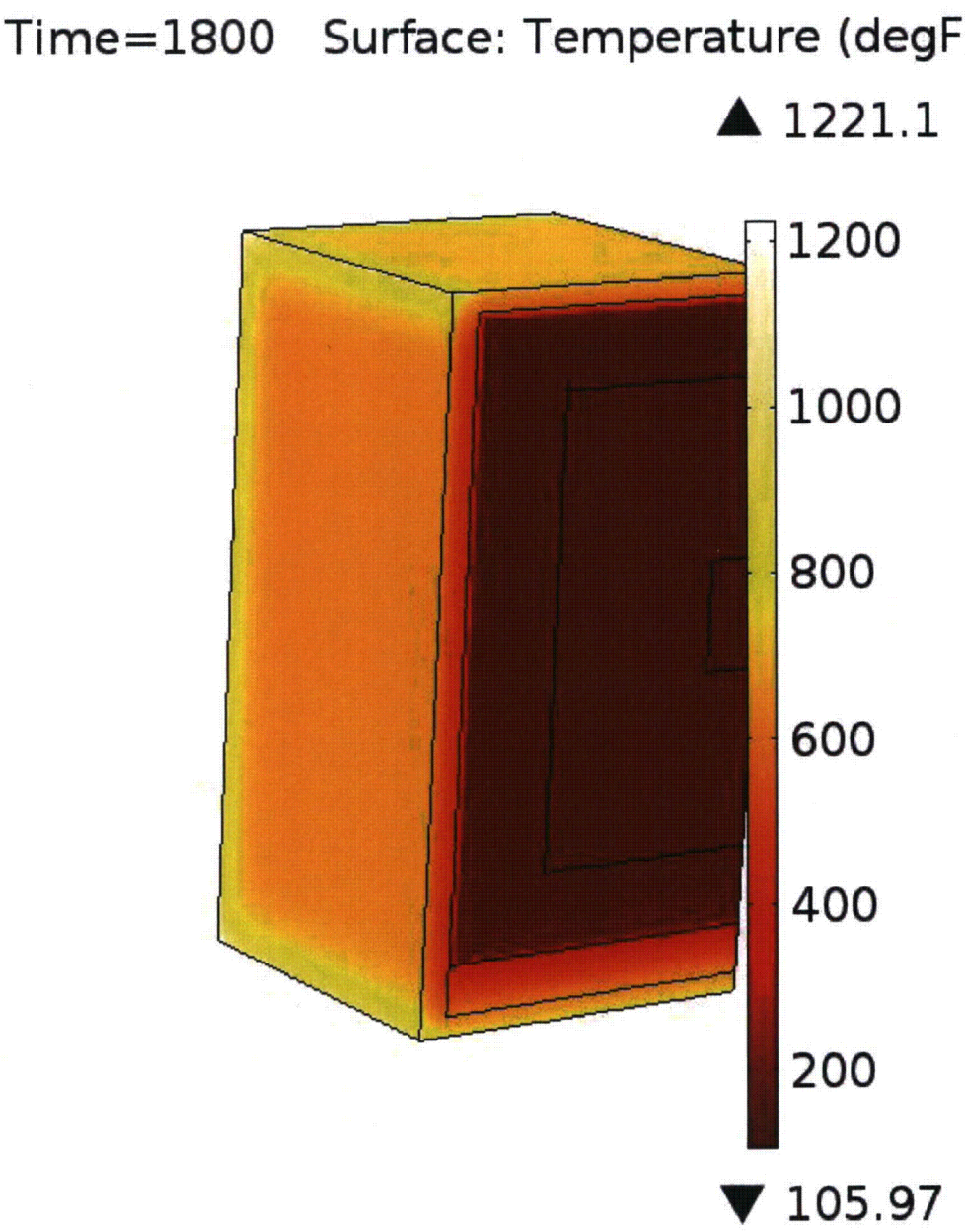

Figure 11. Surface Temperature Profile for HAC after 30 Minutes Fire Exposure

8.0 Conclusions

The maximum temperature for NCT with exposure to 100 °F ambient air and no insolation is 105.36 °F, well below the limit established by 10 CFR 71.51. The maximum temperature for NCT with exposure to 100 °F and insolation of 800 cal/cm^2 on the top surface and 200 cal/cm^2 on the sides is 209.42 °F. The maximum pressure for these conditions is 12.0 psig. The minimum temperatures for NCT with exposure to -20 °F air and -40 °F air do not drop below the ambient temperature.

The maximum temperature for HAC with 30 min exposure to a 1475 °F fire, followed by exposure to 100 °F air with insolation of 800 cal/cm^2 on the top surface and 200 cal/cm^2 on the

sides, is 1221.09 °F, at the corners of the WVMP. The temperature of the container walls except at the very corners is below 800 °F. The maximum pressure for HAC is 73.0 psig.

9.0 References

1. Code of Federal Regulations, Title 10, Part 71.71, "Packaging and Transportation of Radioactive Material: Normal conditions of transport," July 2013.
2. Code of Federal Regulations, Title 10, Part 71.43, "General Standards for All Packages," July 2014.
3. Code of Federal Regulations, Title 10, Part 71.51, "Additional Regulations for Type B Packages," July 2014.
4. Code of Federal Regulations, Title 10, Part 71.73, "Packaging and Transportation of Radioactive Material: Hypothetical accident conditions," July 2013.
5. WMG, Inc., Drawing 4005-DW-001, "West Valley Melter Container," June 26, 2013 (Proprietary).
6. C. A. McKeel, "Structural Evaluation of WVMP to Specific Requirements of 10 CFR 71.71," M-CLC-A-00497, Rev. 0, September 2014.
7. C. Brandjes and T. Pieczynski, "West Valley Demonstration Project Waste Characterization of Vitrification Melter," Ameriphysics Report, September 2014.
8. S. M. Barnes and D. E. Larsen, "Materials and Design Experience in a Slurry-Fed Electric Glass Melter," Pacific Northwest Laboratory Report PNL-3959, UC-70, August 1981.
9. CRC Handbook of Chemistry and Physics, 75th ed., CRC Press, Boca Raton, Florida (1994), Chapter 5.
10. J. Leitner, P. Chuchvalec, D. Sedmidubský, A. Strejc, and P. Abrman, "Estimation of Heat Capacities of Solid Mixed Oxides," Thermochim. Acta, 395, 27-46, 2003.
11. H. E. Adkins, Jr., J. M. Cuta, B. J. Koeppel, A. D. Guzman, and C. S. Bajwa, "Spent Fuel Transportation Package Response to the Baltimore Tunnel Fire Scenario," U. S. Nuclear Regulatory Commission Report NUREG/CR-686, Rev. 2, Pacific Northwest National Laboratory Report PNNL-15313, February 2009.
12. R. G. Baxter, "Defense Waste Processing Facility Wasteform and Canister Description," DP-1606, Rev. 2, December 1988.
13. J. F. Lamond and J. H. Pielert, Significant of Tests and Properties of Concrete and Concrete-making Materials, ASTM Report STP 169D, ASTM International, West Conshohocken, Pennsylvania (2006), p. 564.
14. ACI Manual of Concrete Inspection, 10th ed., American Concrete Institute Committee 311 Report SP-2(07), American Concrete Institute (2008), p. 126.
15. D. R. Flynn, "Response of High Performance to Fire Conditions: Review of Thermal Property Data and Measurement Techniques," NIST Report GCR 99-767, March 1999.
16. R. W. Steiger and M. K. Hurd, "Lightweight Insulating Concrete for Floors and Roof Decks," Concr. Constr., 23(7), 411-422, 1978.
17. C. Brandjes, "Refractory with Ave. Geomean 6-77 Act.rad," June 26, 2014.
18. C. Brandjes, "Melter Heal (sp) with Shard Data_062714.rad," June 27, 2014.
19. C. Brandjes, "Melter Spout_062614.rad," June 26, 2014.
20. "Nuclear Decay Data for Dosimetric Calculations," Ann. ICRP, 38(3), 1-96, 2008, ICRP Paper P107.

21 E. P. Flint, H. F. McMurdie, and L. S. Wells, "Formation of Hydrated Calcium Silicates at Elevated Temperatures and Pressures," J. Res. Nat. Bur. Stand., 21, 617-638, 1938.
22. D. Jansen, S. T. Berghold, F. Goetz-Neunhoeffer, and J. Neubauer, "The Hydration of Alite: A Time-Resolved Quantitative X-Ray Diffraction Approach Using the G-Factor Method Compared with Heat Release," J. Appl. Cryst., 44, 895-901, 2011.
23. T. C. Miller, "A Study of Reaction between Calcium Oxide and Water," National Lime Association report, National Lime Association (Washington, DC), 1960.
24. K. M. Watson, "Thermodynamics of the Liquid State: Generalized Predictions of Properties," Ind. Eng. Chem., 35(4), 398-406, 1943.
25. CRC Handbook of Chemistry and Physics, 75th. ed., CRC Press, Boca Raton, Florida (1994), pp. 6-10 to 6-11.
26. M. R. Kesterson, "COMSOL Multiphysics Version 4.3 Software Test Documentation," Savannah River National Laboratory Document B-STP-A-00027, Rev. 0, December 3, 2012.
27. M. R. Kesterson, "NCT and HAC Thermal Analysis for the MC5PV," Savannah River National Laboratory Document M-CLC-A-00448, Rev. 0, July 25, 2013.
28. F. P. Incropera and D. P. DeWitt, Fundamentals of Heat and Mass Transfer, 5th ed., John Wiley & Sons, Inc., Hoboken, New Jersey (2002), Chapter 9.
29. S. W. Churchill and H. H. S. Chu, "Correlating Equations for Laminar and Turbulent Free Convection from a Vertical Plate," Int. J. Heat Mass Tran., 18(11), 1323-1329, 1975.
30. J. R. Lloyd and W. R. Moran, "Natural Convection Adjacent to Horizontal Surface of Various Platforms," J. Heat Transf., 96(4), 443-447, 1974.
31. Perry's Chemical Engineers' Handbook, 6th ed., McGraw-Hill, New York (1984), p. 10-13.

Appendix A: Summary of Radionuclide Content and Radiolytic Heating for GMP

Table A-1. Radionuclide Content and Radiolytic Heating for Glass in Melter

Isotope	Ci	Mev/d	W/Ci	W
C-14	3.47E-03	0.0495	2.93E-04	1.02E-06
K-40	1.50E-02	0.6785	4.02E-03	6.03E-05
Mn-54	1.44E-06	0.8402	4.98E-03	7.16E-09
Co-60	3.16E-03	2.6007	1.54E-02	4.87E-05
Ni-63	1.52E-01	0.0174	1.03E-04	1.57E-05
Sr-90	3.12E+01	0.1957	1.16E-03	3.62E-02
Y-90	3.12E+01	0.9331	5.53E-03	1.73E-01
Zr-95	1.30E-20	0.8506	5.04E-03	6.55E-23
Nb-95	2.86E-20	0.8091	4.80E-03	1.37E-22
Nb-95m	1.49E-22	0.2497	1.48E-03	2.20E-25
Tc-99	2.01E-03	0.1013	6.01E-04	1.21E-06
Cs-137	5.42E+02	0.1884	1.12E-03	6.05E-01
Ba-137m	5.12E+02	0.6617	3.92E-03	2.01E+00
Eu-154	8.12E-02	1.5223	9.02E-03	7.33E-04
Hg-206	9.79E-16	0.5426	3.22E-03	3.15E-18
Tl-206	6.88E-14	0.5399	3.20E-03	2.20E-16
Tl-207	2.56E-09	0.4975	2.95E-03	7.55E-12
Tl-208	2.72E-03	3.9716	2.35E-02	6.40E-05
Tl-209	8.09E-08	2.8302	1.68E-02	1.36E-09
Tl-210	6.54E-11	4.0331	2.39E-02	1.56E-12
Pb-209	3.75E-06	0.1974	1.17E-03	4.38E-09
Pb-210	5.16E-08	0.0457	2.71E-04	1.40E-11
Pb-211	2.57E-09	0.5187	3.07E-03	7.89E-12
Pb-212	7.56E-03	0.3217	1.91E-03	1.44E-05
Pb-214	3.11E-07	0.5481	3.25E-03	1.01E-09
Bi-209	8.10E-25	----	----	----
Bi-210	5.14E-08	0.3889	2.31E-03	1.18E-10
Bi-211	2.57E-09	6.733	3.99E-02	1.02E-10
Bi-212	7.56E-03	2.8247	1.67E-02	1.27E-04
Bi-213	3.75E-06	0.6963	4.13E-03	1.55E-08
Bi-214	3.11E-07	2.1436	1.27E-02	3.96E-09
Bi-215	2.10E-15	0.9228	5.47E-03	1.15E-17
Po-210	4.71E-08	5.4075	3.21E-02	1.51E-09
Po-211	7.01E-12	7.5944	4.50E-02	3.15E-13
Po-212	4.84E-03	8.9541	5.31E-02	2.57E-04
Po-213	3.67E-06	8.537	5.06E-02	1.86E-07
Po-214	3.11E-07	7.8335	4.64E-02	1.45E-08
Po-215	2.57E-09	7.5263	4.46E-02	1.14E-10
Po-216	7.56E-03	6.9064	4.09E-02	3.10E-04
Po-218	3.11E-07	6.1135	3.62E-02	1.13E-08
At-215	1.03E-14	8.178	4.85E-02	4.97E-16
At-217	3.75E-06	7.2011	4.27E-02	1.60E-07
At-218	5.92E-11	6.8053	4.03E-02	2.39E-12
At-219	2.17E-15	6.1343	3.64E-02	7.87E-17
Rn-217	4.50E-10	7.8856	4.67E-02	2.10E-11
Rn-218	5.92E-14	7.2626	4.31E-02	2.55E-15
Rn-219	2.57E-09	6.9456	4.12E-02	1.06E-10
Rn-220	7.56E-03	6.4047	3.80E-02	2.87E-04
Rn-222	3.11E-07	5.5903	3.31E-02	1.03E-08

Table A-1. Radionuclide Content and Radiolytic Heating for Glass in Melter (continued)

Isotope	Ci	Mev/d	W/Ci	W
Fr-221	3.75E-06	6.4582	3.83E-02	1.43E-07
Fr-223	3.61E-11	0.4415	2.62E-03	9.44E-14
Ra-223	2.57E-09	5.9895	3.55E-02	9.11E-11
Ra-224	7.56E-03	5.7893	3.43E-02	2.60E-04
Ra-225	3.76E-06	0.1194	7.08E-04	2.66E-09
Ra-226	3.12E-07	4.8716	2.89E-02	9.00E-09
Ra-228	5.14E-05	0.0163	9.66E-05	4.97E-09
Ac-225	3.75E-06	5.9338	3.52E-02	1.32E-07
Ac-227	2.61E-09	0.0853	5.06E-04	1.32E-12
Ac-228	5.14E-05	1.3166	7.80E-03	4.01E-07
Th-227	2.55E-09	6.1955	3.67E-02	9.36E-11
Th-228	7.56E-03	5.5202	3.27E-02	2.47E-04
Th-229	3.78E-06	5.1772	3.07E-02	1.16E-07
Th-230	6.05E-05	4.7702	2.83E-02	1.71E-06
Th-231	6.15E-05	0.1891	1.12E-03	6.89E-08
Th-232	6.74E-05	4.0829	2.42E-02	1.63E-06
Th-234	3.74E-04	0.0728	4.32E-04	1.61E-07
Pa-231	1.55E-08	5.158	3.06E-02	4.75E-10
Pa-233	1.05E-03	0.438	2.60E-03	2.73E-06
Pa-234	5.61E-07	1.8755	1.11E-02	6.24E-09
Pa-234m	3.74E-04	0.8334	4.94E-03	1.85E-06
U-232	7.31E-03	5.4135	3.21E-02	2.35E-04
U-233	3.35E-03	4.9085	2.91E-02	9.75E-05
U-234	1.60E-03	4.8587	2.88E-02	4.62E-05
U-235	6.15E-05	4.6891	2.78E-02	1.71E-06
U-235m	2.61E-02	0	0.00E+00	0.00E+00
U-236	1.84E-04	4.5723	2.71E-02	4.99E-06
U-237	7.37E-06	0.3433	2.04E-03	1.50E-08
U-238	3.74E-04	4.2691	2.53E-02	9.46E-06
Np-237	1.05E-03	4.9529	2.94E-02	3.09E-05
Np-239	5.97E-03	0.4469	2.65E-03	1.58E-05
Pu-238	1.04E-01	5.593	3.32E-02	3.44E-03
Pu-239	2.61E-02	5.2442	3.11E-02	8.11E-04
Pu-240	2.01E-02	5.2559	3.12E-02	6.25E-04
Pu-241	2.99E-01	0.0054	3.20E-05	9.57E-06
Am-241	4.95E-01	5.6379	3.34E-02	1.66E-02
Am-243	5.97E-03	5.4402	3.22E-02	1.93E-04
Cm-242	3.08E-10	6.2156	3.68E-02	1.14E-11
Cm-243	2.16E-03	6.1624	3.65E-02	7.90E-05
Cm-244	4.70E-02	5.9014	3.50E-02	1.64E-03
Totals:	**1.12E+03**			**2.85E+00**

Table A-2. Radionuclide Content and Radiolytic Heating for Glass in Spout

Isotope	Ci	Mev/d	W/Ci	W
C-14	2.22E-03	0.0495	2.93E-04	6.51E-07
K-40	8.60E-03	0.6785	4.02E-03	3.46E-05
Mn-54	5.00E-07	0.8402	4.98E-03	2.49E-09
Co-60	5.47E-03	2.6007	1.54E-02	8.43E-05
Ni-63	9.80E-02	0.0174	1.03E-04	1.01E-05
Sr-90	6.33E+01	0.1957	1.16E-03	7.35E-02
Y-90	6.33E+01	0.9331	5.53E-03	3.50E-01
Zr-95	3.17E-22	0.8506	5.04E-03	1.60E-24
Nb-95	6.99E-22	0.8091	4.80E-03	3.35E-24
Nb-95m	3.63E-24	0.2497	1.48E-03	5.37E-27
Tc-99	1.57E-02	0.1013	6.01E-04	9.43E-06
Cs-137	8.57E+02	0.1884	1.12E-03	9.57E-01
Ba-137m	8.09E+02	0.6617	3.92E-03	3.17E+00
Eu-154	1.04E-01	1.5223	9.02E-03	9.41E-04
Hg-206	7.14E-16	0.5426	3.22E-03	2.30E-18
Tl-206	5.01E-14	0.5399	3.20E-03	1.60E-16
Tl-207	1.86E-09	0.4975	2.95E-03	5.49E-12
Tl-208	1.73E-03	3.9716	2.35E-02	4.08E-05
Tl-209	5.58E-08	2.8302	1.68E-02	9.36E-10
Tl-210	4.50E-11	4.0331	2.39E-02	1.07E-12
Pb-209	2.58E-06	0.1974	1.17E-03	3.02E-09
Pb-210	3.76E-08	0.0457	2.71E-04	1.02E-11
Pb-211	1.87E-09	0.5187	3.07E-03	5.74E-12
Pb-212	4.82E-03	0.3217	1.91E-03	9.20E-06
Pb-214	2.14E-07	0.5481	3.25E-03	6.95E-10
Bi-209	5.97E-25	----	----	----
Bi-210	3.75E-08	0.3889	2.31E-03	8.63E-11
Bi-211	1.87E-09	6.733	3.99E-02	7.46E-11
Bi-212	4.82E-03	2.8247	1.67E-02	8.08E-05
Bi-213	2.58E-06	0.6963	4.13E-03	1.07E-08
Bi-214	2.14E-07	2.1436	1.27E-02	2.72E-09
Bi-215	1.53E-15	0.9228	5.47E-03	8.35E-18
Po-210	3.45E-08	5.4075	3.21E-02	1.11E-09
Po-211	5.10E-12	7.5944	4.50E-02	2.30E-13
Po-212	3.09E-03	8.9541	5.31E-02	1.64E-04
Po-213	2.53E-06	8.537	5.06E-02	1.28E-07
Po-214	2.14E-07	7.8335	4.64E-02	9.94E-09
Po-215	1.87E-09	7.5263	4.46E-02	8.33E-11
Po-216	4.82E-03	6.9064	4.09E-02	1.97E-04
Po-218	2.14E-07	6.1135	3.62E-02	7.76E-09
At-215	7.47E-15	8.178	4.85E-02	3.62E-16
At-217	2.58E-06	7.2011	4.27E-02	1.10E-07
At-218	4.07E-11	6.8053	4.03E-02	1.64E-12
At-219	1.57E-15	6.1343	3.64E-02	5.72E-17
Rn-217	3.10E-10	7.8856	4.67E-02	1.45E-11
Rn-218	4.07E-14	7.2626	4.31E-02	1.75E-15
Rn-219	1.87E-09	6.9456	4.12E-02	7.69E-11
Rn-220	4.82E-03	6.4047	3.80E-02	1.83E-04
Rn-222	2.14E-07	5.5903	3.31E-02	7.10E-09
Fr-221	2.58E-06	6.4582	3.83E-02	9.89E-08
Fr-223	2.62E-11	0.4415	2.62E-03	6.87E-14
Ra-223	1.87E-09	5.9895	3.55E-02	6.63E-11
Ra-224	4.82E-03	5.7893	3.43E-02	1.66E-04

Table A-2. Radionuclide Content and Radiolytic Heating for Glass in Spout (continued)

Isotope	Ci	Mev/d	W/Ci	W
Ra-225	2.59E-06	0.1194	7.08E-04	1.83E-09
Ra-226	2.14E-07	4.8716	2.89E-02	6.19E-09
Ra-228	3.41E-05	0.0163	9.66E-05	3.29E-09
Ac-225	2.58E-06	5.9338	3.52E-02	9.09E-08
Ac-227	1.90E-09	0.0853	5.06E-04	9.61E-13
Ac-228	3.41E-05	1.3166	7.80E-03	2.66E-07
Th-227	1.85E-09	6.1955	3.67E-02	6.81E-11
Th-228	4.82E-03	5.5202	3.27E-02	1.58E-04
Th-229	2.60E-06	5.1772	3.07E-02	7.99E-08
Th-230	3.89E-05	4.7702	2.83E-02	1.10E-06
Th-231	3.95E-05	0.1891	1.12E-03	4.43E-08
Th-232	4.34E-05	4.0829	2.42E-02	1.05E-06
Th-234	2.41E-04	0.0728	4.32E-04	1.04E-07
Pa-231	1.07E-08	5.158	3.06E-02	3.26E-10
Pa-233	7.09E-04	0.438	2.60E-03	1.84E-06
Pa-234	3.62E-07	1.8755	1.11E-02	4.02E-09
Pa-234m	2.41E-04	0.8334	4.94E-03	1.19E-06
U-232	4.66E-03	5.4135	3.21E-02	1.50E-04
U-233	2.16E-03	4.9085	2.91E-02	6.29E-05
U-234	1.03E-03	4.8587	2.88E-02	2.98E-05
U-235	3.95E-05	4.6891	2.78E-02	1.10E-06
U-235m	3.01E-02	0	0.00E+00	0.00E+00
U-236	1.19E-04	4.5723	2.71E-02	3.23E-06
U-237	4.56E-06	0.3433	2.04E-03	9.27E-09
U-238	2.41E-04	4.2691	2.53E-02	6.10E-06
Np-237	7.09E-04	4.9529	2.94E-02	2.08E-05
Np-239	4.55E-03	0.4469	2.65E-03	1.20E-05
Pu-238	1.14E-01	5.593	3.32E-02	3.78E-03
Pu-239	3.01E-02	5.2442	3.11E-02	9.35E-04
Pu-240	2.29E-02	5.2559	3.12E-02	7.15E-04
Pu-241	1.85E-01	0.0054	3.20E-05	5.92E-06
Am-241	3.80E-01	5.6379	3.34E-02	1.27E-02
Am-243	4.55E-03	5.4402	3.22E-02	1.47E-04
Cm-242	1.05E-11	6.2156	3.68E-02	3.86E-13
Cm-243	1.85E-03	6.1624	3.65E-02	6.77E-05
Cm-244	4.07E-02	5.9014	3.50E-02	1.42E-03
Totals:	**1.79E+03**			**4.57E+00**

Table A-3. Radionuclide Content and Radiolytic Heating for Glass in Refractory

Isotope	Ci	Mev/d	W/Ci	W
Co-60	1.33E-02	2.6007	1.54E-02	2.05E-04
Sr-90	1.07E+02	0.1957	1.16E-03	1.24E-01
Y-90	1.07E+02	0.9331	5.53E-03	5.91E-01
Tc-99	5.22E-02	0.1013	6.01E-04	3.13E-05
Cs-137	2.13E+02	0.1884	1.12E-03	2.38E-01
Ba-137m	2.01E+02	0.6617	3.92E-03	7.89E-01
Eu-154	5.53E-01	1.5223	9.02E-03	4.99E-03
Hg-206	2.54E-16	0.5426	3.22E-03	8.16E-19
Tl-206	1.78E-14	0.5399	3.20E-03	5.70E-17
Tl-207	2.96E-09	0.4975	2.95E-03	8.73E-12
Tl-208	1.81E-04	3.9716	2.35E-02	4.25E-06
Tl-209	1.43E-08	2.8302	1.68E-02	2.41E-10
Tl-210	1.67E-11	4.0331	2.39E-02	4.00E-13
Pb-209	6.64E-07	0.1974	1.17E-03	7.77E-10
Pb-210	1.34E-08	0.0457	2.71E-04	3.62E-12
Pb-211	2.97E-09	0.5187	3.07E-03	9.13E-12
Pb-212	5.03E-04	0.3217	1.91E-03	9.58E-07
Pb-214	7.96E-08	0.5481	3.25E-03	2.59E-10
Bi-209	1.46E-25	----	----	----
Bi-210	1.33E-08	0.3889	2.31E-03	3.07E-11
Bi-211	2.97E-09	6.733	3.99E-02	1.18E-10
Bi-212	5.03E-04	2.8247	1.67E-02	8.42E-06
Bi-213	6.64E-07	0.6963	4.13E-03	2.74E-09
Bi-214	7.96E-08	2.1436	1.27E-02	1.01E-09
Bi-215	2.43E-15	0.9228	5.47E-03	1.33E-17
Po-210	1.22E-08	5.4075	3.21E-02	3.92E-10
Po-211	8.10E-12	7.5944	4.50E-02	3.65E-13
Po-212	3.22E-04	8.9541	5.31E-02	1.71E-05
Po-213	6.50E-07	8.537	5.06E-02	3.29E-08
Po-214	7.96E-08	7.8335	4.64E-02	3.70E-09
Po-215	2.97E-09	7.5263	4.46E-02	1.32E-10
Po-216	5.03E-04	6.9064	4.09E-02	2.06E-05
Po-218	7.96E-08	6.1135	3.62E-02	2.89E-09
At-215	1.19E-14	8.178	4.85E-02	5.75E-16
At-217	6.64E-07	7.2011	4.27E-02	2.83E-08
At-218	1.51E-11	6.8053	4.03E-02	6.10E-13
At-219	2.50E-15	6.1343	3.64E-02	9.10E-17
Rn-217	7.97E-11	7.8856	4.67E-02	3.73E-12
Rn-218	1.51E-14	7.2626	4.31E-02	6.51E-16
Rn-219	2.97E-09	6.9456	4.12E-02	1.22E-10
Rn-220	5.03E-04	6.4047	3.80E-02	1.91E-05
Rn-222	7.96E-08	5.5903	3.31E-02	2.64E-09
Fr-221	6.64E-07	6.4582	3.83E-02	2.54E-08
Fr-223	4.17E-11	0.4415	2.62E-03	1.09E-13
Ra-223	2.97E-09	5.9895	3.55E-02	1.05E-10
Ra-224	5.03E-04	5.7893	3.43E-02	1.72E-05
Ra-225	6.66E-07	0.1194	7.08E-04	4.72E-10
Ra-226	7.97E-08	4.8716	2.89E-02	2.30E-09
Ra-228	3.21E-05	0.0163	9.66E-05	3.10E-09
Ac-225	6.64E-07	5.9338	3.52E-02	2.34E-08
Ac-227	3.02E-09	0.0853	5.06E-04	1.53E-12
Ac-228	3.21E-05	1.3166	7.80E-03	2.51E-07
Th-227	2.95E-09	6.1955	3.67E-02	1.08E-10

Table A-3. Radionuclide Content and Radiolytic Heating for Glass in Refractory (continued)

Isotope	Ci	Mev/d	W/Ci	W
Th-228	5.02E-04	5.5202	3.27E-02	1.64E-05
Th-229	6.70E-07	5.1772	3.07E-02	2.05E-08
Th-230	1.52E-05	4.7702	2.83E-02	4.31E-07
Th-231	6.92E-05	0.1891	1.12E-03	7.76E-08
Th-232	4.18E-05	4.0829	2.42E-02	1.01E-06
Th-234	1.16E-04	0.0728	4.32E-04	5.01E-08
Pa-231	1.78E-08	5.158	3.06E-02	5.43E-10
Pa-233	8.49E-04	0.438	2.60E-03	2.21E-06
Pa-234	1.74E-07	1.8755	1.11E-02	1.93E-09
Pa-234m	1.16E-04	0.8334	4.94E-03	5.73E-07
U-232	4.41E-04	5.4135	3.21E-02	1.41E-05
U-233	5.85E-04	4.9085	2.91E-02	1.70E-05
U-234	2.84E-04	4.8587	2.88E-02	8.18E-06
U-235	6.92E-05	4.6891	2.78E-02	1.92E-06
U-235m	3.72E-02	0	0.00E+00	0.00E+00
U-236	2.08E-04	4.5723	2.71E-02	5.64E-06
U-237	5.08E-06	0.3433	2.04E-03	1.03E-08
U-238	1.16E-04	4.2691	2.53E-02	2.94E-06
Np-237	8.49E-04	4.9529	2.94E-02	2.49E-05
Np-239	6.72E-03	0.4469	2.65E-03	1.78E-05
Pu-238	1.41E-01	5.593	3.32E-02	4.67E-03
Pu-239	3.72E-02	5.2442	3.11E-02	1.16E-03
Pu-240	2.85E-02	5.2559	3.12E-02	8.87E-04
Pu-241	2.06E-01	0.0054	3.20E-05	6.61E-06
Am-241	8.45E-01	5.6379	3.34E-02	2.82E-02
Am-243	6.72E-03	5.4402	3.22E-02	2.17E-04
Cm-242	4.49E-11	6.2156	3.68E-02	1.65E-12
Cm-243	3.04E-03	6.1624	3.65E-02	1.11E-04
Cm-244	6.77E-02	5.9014	3.50E-02	2.37E-03
Totals:	**6.30E+02**			**1.79E+00**

Table A-4. Total Radiolytic Heating Rate

Glass in Melter	2.85 W
Glass in Spout	4.57 W
Glass in Refractory	1.79 W
Total	**9.21 W**

Appendix B: Parameter and Variable Lists for COMSOL® Multiphysics Model

Parameter List for COMSOL® Multiphysics Model

Parameter	Value or Formula
SidePlateTh	6[in]
TopPlateTh	4[in]
BottomPlateTh	4[in]
GlassSide	1.851377[ft]
FireBrick	7.838387[ft]
SteelCase	7.838387[ft]
Tamb	100[degF]
k_304L	20[W/m/K]
rho_304L	7850[kg/m^3]
cp_304L	475[J/(kg*K)]
FireT	1475[degF]
Rig	8.314[J/mol/K]
CaO_init	1 / 3 * CementRho / CaO_MW
CaSiO_init	2 / 3 * CementRho / CaSiO_MW
CaO_MW	56[g/mol]
CaSiO_MW	84[g/mol]
LDCC_Bulk	71.2[lb/ft^3]
CementRho	18.89[lb/ft^3]
Sand_rho	48.53[lb/ft^3]
BoundWater	3.78[lb/ft^3]
Total	BoundWater + Sand_rho + CementRho
BH2O_init	BoundWater / H2O_MW
H2O_MW	18[g/mol]
delH1	63.92[kJ/mol]
delH2	65.59[kJ/mol]
DelH_vap_Norm	40657[J/mol]
Tc	647.14[K]
AirGap	10[in]
Ea_Rg	3397[K]
Ar	15.426
ConcreteCP	765[J/kg/K]
glass_rho	2.6[g/cm^3]
glass_cp	810.9179[J/kg/K]

Variable List for COMSOL Multiphysics Model

Variable	Formula
FireT	(1475[degF] - Tamb) * (t[1/s] <= 1800) + Tamb
alpha	Ar * exp(-Ea_Rg / mod1.T)
delH_Vap	gamma_func(mod1.T)
Tr	mod1.T / Tc
Trb	100[degC] / Tc
Concrete_effCp	ConcreteCP + (delH2 + delH_Vap) * BoundWater / Total / H2O_MW * Ea_Rg /T^2 * exp(-Ea_Rg / T)
CCaO	CaO_init * (1 - alpha)
CCaSiO	CaSiO_init * (1 - alpha)
CBH2O	BH2O_init - ((CaO_init - CCaO) + (CaSiO_init - CCaSiO))
CycleTime	flc2hs(sin(pi*t[1/s] / 43200), 0.01)
SS_516_k	(-1.4131e-5 * (T[1/degF])^2 + 0.0092585 * (T[1/degF]) + 39.440)[W/m/K]
SS_516_Cp	(6.49e-5 * (T[1/degF])^2 + 0.19059 * (T[1/degF]) + 447.66)[J/kg/K]
SS_516_rho	7749.7[kg/m^3]

Note: flc2hs is a continuous variable Heaviside step function in which the step change is applied using a continuous ramp. The first argument of this function is the independent variable value at the midpoint of the ramp, and the second argument is the width of the ramp from the midpoint to either end.
Note: mod1.T is the nodal temperature.
Note: The unit 1/degF in the formulas for SS_516_k and SS_516_Cp are input as a reciprocal unit to cancel the temperature units.
Note: Some parameters and variables are entered directly into the COMSOL user interface and thus do not appear in the preceding lists.